Analysis of nanostructures based on diffraction of X-ray radiation

Zur Erlangung des akademischen Grades eines

DOKTORS DER NATURWISSENSCHAFTEN

von der Fakultät für Physik des
Karlsruher Instituts für Technologie (KIT)

genehmigte

DISSERTATION

von

Dipl.-Phys. Martin Köhl
aus Burghausen (Oberbayern)

Tag der mündlichen Prüfung: 5. Dezember 2014

Referent:	Prof. Dr. Tilo Baumbach
Korreferent:	Prof. RNDr. Václav Holý, CSc.

Contents

Introduction

The structure of matter — as found in nature or artificially engineered — is of fundamental importance for its physical and chemical properties. For the investigation of the structure of matter on length scales down to the order of the size of a single atom or typical interatomic distances in solids and liquids, electromagnetic radiation with photon energies in the order of some keV ("X-ray radiation") proofed highly valuable. The wavelength of such radiation is in the order of Angstroms and, therefore, is able to reveal correlations down to this length scale. In this manuscript, we focus on the extraction of information about crystalline structures from their X-ray scattering.

Arrangements which are invariant upon (discrete) translational shifts give rise to the concept of the reciprocal lattice ("Bragg peaks"). Its elements define the admissible momentum transfers of an incident X-ray photon after interacting with the structure. We point out that the structure is necessarily infinitely extended in the directions which correspond to the discrete translational symmetry. Each (ideal, infinitely extended) crystal exhibits such discrete translational symmetries. As soon as a crystalline structure is truncated to finite dimensions, but much larger in dimension than the period of the translational shifts, the momentum transfer is still limited to values close to the elements of the reciprocal lattice ("size broadening"). The smaller the dimensions of the truncated crystalline structure are, the larger is the size broadening.

In addition to such size broadening of the signal in reciprocal space, the atoms in the crystal may be displaced inhomogeneously with respect to their ideal positions which results in an inhomogeneous strain distribution in the crystalline structure. If the displacement field fulfills certain conditions, the scattering signal of such structures is still aggregated in the vicinity of the Bragg peaks but additional broadening takes place ("strain broadening").

Such inhomogeneous strain distributions may, for example, result from non-zero temperature gradients in case of a single material or from cooling as well as heating of (at least) two cohesive materials with different thermal expansion coefficients. Moreover, the strain distribution is also of high relevance at the interface of two different materials.

If the atomic ordering of one material is crystalline and a second material is connected to its surface such that the atomic ordering at the surface is preserved along the interface without the formation of defects, the interface is referred to as epitaxial. Since the second material typically has different native lattice constants, a non-zero inhomogeneous strain distribution is induced in both materials in the vicinity of their interface.

Specifically, the aim of this manuscript is the exploration of the capabilities and limitations to extract valuable information on crystalline nanostructures from their scattered X-ray intensity distribution in the vicinity of a Bragg peak given the following two scenarios:

- In the first part of this manuscript, we consider the scattering of a large number of (nano)objects where the interior of *each* object consists of a sequence of two alternating, epitaxially linked atomic arrangements ("polytypes", see Sec. 1.4) with slightly different lattice constants. The thickness of each polytypic segment of this sequence is obtained from a stochastic process and, thus, is non-deterministic.

The understanding of the scattering of such systems is the main goal of the first part of the manuscript, because it is of high importance for the proper interpretation of X-ray investigations of free-standing, polytypic nanowires (see Sec. 1.4) and such X-ray measurements have been performed recently time-resolved and *in-situ* in the portable molecular beam epitaxy (PMBE) growth chamber at ANKA (currently equipped for growing GaInAs structures). We derive and discuss its capabilities for X-ray investigation in Sec. 2.

During these time-resolved *in-situ* X-ray measurements, a fixed planar cut in reciprocal space through the $(111)_{\mathrm{z}\curvearrowright\mathrm{c}}$ Bragg reflection of zinc blende GaAs has been recorded time-resolved during the growth ("*in-situ*") of GaAs nanowires on Si-111 substrates (see Sec. 4.1). If the interplanar spacings of the $[111]_{\mathrm{z}\curvearrowright\mathrm{c}}$ planes in the zinc blende polytype and the $[00.2]_{\mathrm{w}\curvearrowright\mathrm{h2}}$ planes in the wurtzite polytype were equal, the scattering angles of these two reflections would coincide. By virtue of the small difference of the interplanar spacings of the polytypes, their scattering angles differ slightly. Thus, the intensity distribution in the vicinity of the $(111)_{\mathrm{z}\curvearrowright\mathrm{c}}$ reflection of GaAs contains information on the polytypism in the nanowires. For illustration, we consider the limiting cases of polytypic nanowires with either very large or very small segments of the alternating polytypes:

As long as the mean thicknesses of the segments of both polytypes are large, the signals from individual polytype segments do not overlap in reciprocal space (due to their different lattice constants and the small size broadening). In consequence, two well-separated peaks are observed close to the $(111)_{\mathrm{z}\curvearrowright\mathrm{c}}$ Bragg reflection of GaAs. Nonetheless, the signals from all segments of the *same* polytype are centered around the same position in reciprocal space and, therefore, strongly overlap. If the mean thicknesses of the segments of the polytypes decrease, the scattering of the individual segments of the *different* polytypes additionally starts to overlap. Since the lattice constants of the polytypes differ only slightly, this overlapping must be considered for yet very thick segments.

The smaller the thicknesses of the segments are, the stronger is the overlap of the scattering signals of the different polytypes near the $(111)_{\mathrm{z}\curvearrowright\mathrm{c}}$ reflection. In the limit of segments with a thickness of one layer of the crystalline arrangement of the respective polytype only – the shortest possible segments – we obtain a perfect, defect-free super-lattice. Instead of two peaks as observed for very pure wires (large polytype segments), the scattering signal contains only a single peak – centered at the mean lattice constants of the two polytypes.

The full intensity distribution near a Bragg peak is determined by a complicated interplay of (i) the coherence properties of the impinging beam, (ii) the spatial distribution of the different nanoobjects and (iii) the statistical properties of segments of the both polytypes. We assume that the properties of the impinging beam were such that (a) a large number of nanowires has been illuminated simultaneously, (b) the scattered photons from (at least) one nanowire interfere fully coherent, and (c) the number of illuminated coherence volumes is much larger than the number of wires per coherence volume.

In Sec. 4.3, we simulate the X-ray signal in the vicinity of a Bragg peak for such beam conditions. Specifically, we investigate the behavior of the X-ray signal for a variety of statistical distributions for the thicknesses of the polytypic segments and, thereby reveal which features of the statistical distributions induce which features of the scattered X-ray intensity distributions. In particular, we focus on the experimentally measured vicinity of the $(111)_{\mathrm{z}\curvearrowright\mathrm{c}}$ Bragg reflection of GaAs. Nonetheless, we also present simulations of the $(333)_{\mathrm{z}\curvearrowright\mathrm{c}}$ reflections (see Sec. 4.3.2.5) and discuss the possibilities to access other reflections than $(111)_{\mathrm{z}\curvearrowright\mathrm{c}}$ in future experiments (see Sec. 2.2), e.g. the polytype and twin selective series of reflections $(220)_{\mathrm{z}\curvearrowright\mathrm{c}}$, $(10.3)_{\mathrm{w}\curvearrowright\mathrm{h2}}$, and $(311)_{\mathrm{z}\curvearrowright\mathrm{c}}$ on the asymmetric truncation rod.

The interpretation of the currently available experimental data of the $(111)_{\mathrm{z}\curvearrowright\mathrm{c}}$ Bragg reflection is further complicated by the fact that parasitic growth ("crystallites") must be considered in addition to the growth of nanowires. For proper evaluation and interpretation of the experimental data, we thus also discuss (i) additional measurements of the full three dimensional vicinity of the corresponding Bragg reflection in reciprocal space, which have been performed *in-situ* directly after the growth (see Sec. 3.1), and (ii) spatially resolved post-growth *ex-situ* measurements with a highly focussed beam (see Sec. 3.2).

From the latter, we do not only obtain valuable information for the separation of the contributions from the nanowires and the crystallites to the $(111)_{\mathrm{z}\curvearrowright\mathrm{c}}$ Bragg reflection, but are also able to extract an estimate for the ratio $d_{\mathrm{WZ}}/d_{\mathrm{ZB}}$ of the thickness d_{ZB} of a GaAs layer in $[111]_{\mathrm{z}\curvearrowright\mathrm{c}}$ direction in zinc blende versus the thickness d_{WZ} of a GaAs layer in $[00.2]_{\mathrm{w}\curvearrowright\mathrm{h2}}$ direction in wurtzite.

Finally, the (time-resolved) experimental data is interpreted in Sec. 4.4 in the framework of a Markov model with time-dependent transition probabilities. Thereby, we obtain the temporal evolution of the phase purities of both polytypes during growth (see Sec. 4.4.1) and rough estimates for the differences of the nucleation barriers for continuing growth of the current polytype and for continuing growth with the other polytype and their temporal evolution (see Sec. 4.4.2).

Considering the perspectives of time-resolved *in-situ* X-ray-investigations of growth (including early growth stages like nucleation of initial droplets as well as the last growth phase of solidification of the droplet in case of nanowire growth, non-constant temporal evolution of the external growth conditions [substrate temperature and material fluxes in case of MBE growth] or the cool-down after growth) and annealing (in vacuum, air, or specific artificial atmospheres) of nanostructures in general, we are convinced that the results presented in this work are also useful for planning, performing, evaluating and interpreting many future experiments.

- In the second part of the manuscript we investigate the extraction of the displacement field and strain distribution inside a nanoobject (“reconstructions”) from its (fully) coherently scattered intensity distribution in the vicinity of a Bragg peak. In addition to the intensity distribution in the vicinity of a Bragg peak, we always assume that the geometrical shape of the nanostructure under investigation is known.

Commonly, linear elasticity theory serves as a model for determination of the displacement field and strain distribution in the interior of a nanostructure by finite element modeling — given its geometry, its chemical composition, the constants of elasticity and appropriate boundary conditions. However, in some cases, the chemical composition profile or adequate constants of elasticity are not known (or linear elasticity theory is not applicable for other reasons). Nonetheless, it is desirable to extract the displacement field and strain distribution inside such nanostructures.

For this, we give an introduction to the relevant physical, mathematical and algorithmic details in Sec. 6. After introduction of a test system for benchmarking our reconstructions (see Sec. 7.1) and an illustration of the shortcomings (Sec. 7.2) of the currently most widely used reconstruction algorithm – the HIO+ER-algorithm – we improve this algorithm in order to increase its range of applicability towards higher strain.

First, we demonstrate the benefits of appropriate randomization of the HIO-part of this algorithm (see Sec. 7.3). This modification is solely a mathematical modification: no additional *a priori* knowledge in comparison to the traditional HIO+ER-algorithm is required.

In contrast, Sec. 7.4 is dedicated to a detailed analysis of mathematical constraints during the reconstruction procedure which proofed valuable for the extraction of the displacement field from some particular experimental data sets. A closer investigation of these particular constraints is highly interesting because (i) they are applicable for a large variety of nanostructures and (ii) the parameters required as input are estimated easily from *a priori* knowledge on the nanostructure. Nonetheless, a thorough investigation of these constraints — in order to evaluate and benchmark their benefits for a reconstruction — had not yet been performed.

The outcome of the considerations in Secs. 7.2 and 7.3 is the $\mathrm{HIO}^{\mathrm{A}}_{\mathrm{O_R}}+\mathrm{ER}^{\mathrm{A}}$-algorithm – an extension of the traditional HIO+ER-algorithm with significantly better reconstruction capabilities.

The extraction of the displacement field and strain distribution from the output of the reconstruction process may be hindered by vortex defects. Their detection and elimination is discussed in Sec. 7.5.

The results in chapter 7 are based on simulated "ideal data" within the model for coherent diffractive imaging as derived in Sec. 6.1. The investigations in chapter 8 look at the impact of typical experimental artifacts and limitations. Specifically, we demonstrate that an artificially introduced small damping in low intensity domains in reciprocal space as regularization during the reconstruction process is beneficial for the quality of its output (see Sec. 8.1). The influence of Poisson photon noise in the detected intensity distribution and adequate counter-measures are presented in Sec. 8.2. In the last section of this chapter – Sec. 8.3 – we consider the effect of inconsistencies along the crystal truncation rod between experimental and modelled data. Adequate modifications of $\mathrm{HIO}^{\mathrm{A}}_{\mathrm{O_R}}+\mathrm{ER}^{\mathrm{A}}$-algorithm, which significantly improve its capabilities for providing successful reconstructions in presence of such inconsistencies, are presented and investigated.

Both parts of the manuscript are ended by a separate conclusion.

Parts of this work have already been published in:

- M. Köhl, A. A. Minkevich, T. Baumbach, *Improved success rate and stability for phase retrieval by including randomized overrelaxation in the hybrid input output algorithm*, Optics Express **20**, 17093-17106, 2012
- M. Köhl, P. Schroth, A. A. Minkevich, T. Baumbach, *Retrieving the displacement of strained nanoobjects: the impact of bounds for the scattering magnitude in direct space*, Optics Express **21**, 27734-27749, 2013
- M. Köhl, P. Schroth, A. A. Minkevich, J.-W. Hornung, E. Dimakis, C. Somaschini, L. Geelhaar, T. Aschenbrenner, S. Lazarev, D. Grigoriev, U. Pietsch and T. Baumbach, *Polytypism in GaAs nanowires: Determination of the interplanar spacing of wurtzite GaAs by X-ray diffraction*, Journal of Synchrotron Radiation **22**, 67-75, 2015

Figures taken from these manuscripts are labelled by (©2012 The Optical Society (OSA), from [1]), (©2013 The Optical Society (OSA), from [2]) or (©2014 International Union of Crystallography (IUCr), from [3]) and are reproduced here in accordance with the copyright transfer agreement of the Optical Society of America (OSA) [4, 5] or the International Union of Crystallography (IUCr) [6] respectively.

Part I.

Time-resolved in-situ investigation of the growth of nanowires

1. Introduction to the growth of nanowires

We start this manuscript with an overview over the growth process of nanowires. We summarize important and useful experimental results about the growth as well as those relevant for modelling and understanding the growth process. First, we provide a broad overview of the relevant aspects of nanowire growth. Then, we illustrate the complexity of III–V nanowire growth even for nanowires with only a single crystalline phase: On the one hand, we show the influence of limited amount of type V atoms in the droplet which acts as a reservoir for the growth of the crystalline nanowire (Sec. 1.2). On the other hand, we discuss the the implications from a model by Dubrovskii (Sec. 1.3) which focusses on the coupled dynamics of radial and axial growth. Finally, we introduce and discuss polytypism – the occurrence of multiple phases even in a single nanowire – in III-V nanowires in Sec. 1.4.

1.1. Overview over the dynamics of nanowire growth

Current state-of-the-art research already demonstrated a variety nanowire structures that are interesting for fundamental research (e.g. on qubits [7], single photon sources [8], Majorana fermions [9]) as well as for applications [10–12]. Such applications include transistors [13, 14], lasing [15, 16], solar cells [17], thermoelectric materials [18] and sensors [19, 20]. Even the physics of single spins in seminconductor nanowires has already been studied extensively (see e.g. Ref. [21]).

Depending on the application, the requirements span from single phase pure wires over superlattice structures to complicated heterostructures [22–26]. Such heterostructures include core-shell heterostructures as well as axial heterostructures and may require controlled embedding of specific objects like quantum dots. One advantage of free-standing, thin, vertical nanowires is their ability to relax lateral strain on short distances, which typically results in a strongly reduced dislocation density as compared to conventional two-dimensional layer growth in lattice-mismatched heteroepitaxy [27–29]. Consequently, a profound understanding of nanowire growth, which facilitates comprehensive control of the growing structures, is required. Many aspects of this growth have already been studied which we now shortly review.

In Fig. 1.1, we depict the growth process of gallium arsenic (GaAs) nanowires in a molec-

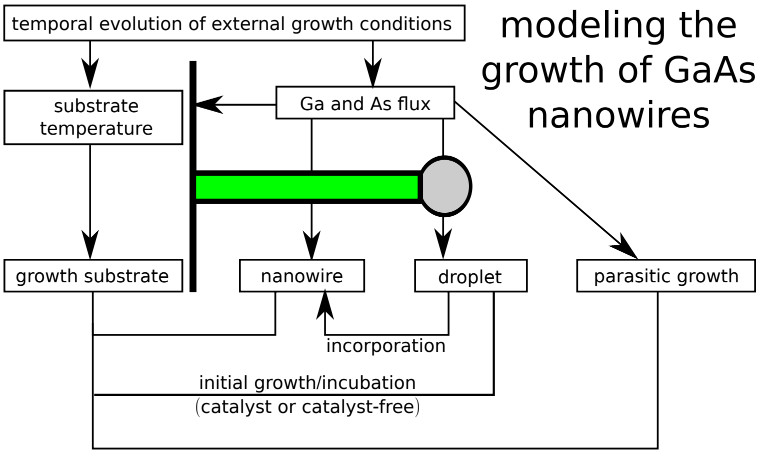

Figure 1.1.: Overview over nanowire growth from a bird's-eye view.

ular beam epitaxy (MBE) [30, 31] growth chamber from a bird's eye view:[1]

The temporal evolution of the external growth conditions is controlled by a suitable growth chamber. Most importantly, by this growth chamber, the temperature of the substrate for growth and the impinging fluxes of growth material are controlled. Often, the flux of Ga is provided before the arsenic flux is turned on. In this case, liquid Ga-droplets on the surface of the substrate accumulate. Then, the arsenic flux is turned on and arsenic accumulates in the liquid Gallium droplets [33–37]. Given appropriate conditions, crystalline GaAs forms layer by layer below the liquid droplet which results in vertical nanowire growth. The incorporated material of such additional layers is consumed from the liquid Ga droplet. However, the consumption of the Ga droplet is anticipated by the impinging fluxes of Ga and As which interact with the substrate, the nanowire side facets and the droplet directly. Although growth without a liquid droplet has been observed for various conditions and material systems (see for example [38–44]), we mainly focus on growth with such a liquid droplet (VLS growth mechanism introduced by Wagner and Ellis in 1964 for silicon whiskers [45–49] which has been applied to many other material systems than silicon since that time).

The above described case is referred to as self-catalyzed (or self-induced) growth. Early results about self-catalyzed nanowires are, for example, presented in Ref. [50] and is becoming now more and more popular (see e.g. Refs. [41–43, 49, 51–58]).

In contrast, the initial droplets may be formed by some catalyst – instead of Gallium. Often, gold is employed as such a catalyst (see e.g. Refs. [46, 59–63]). The catalyst substitutes the "self" in self-catalyzed growth, e.g. Au-catalyzed growth. However, gold modifies the resulting optical and electronic properties [26, 58, 64, 65], typically in a non-desired way.

In addition to the growth of nanowires, we also have parasitic growth (any growth beside the growth of the desired nanowires) for many conditions.

This rough overview barely illustrates the complexity of the dynamics and physics involved in nanowire growth. Consequently, we present a more detailed and more abstract overview in Fig. 1.2:

For a profound understanding of nanowire growth, (at least) the four "subsystems" growth substrate, liquid droplet, the (crystalline) nanowire and parasitic growth as well as their

---

[1] Although it is possible to grow GaAs nanowires also with other growth techniques such as MOVPE (see e.g. [32]), we restrict our discussion to MBE growth.

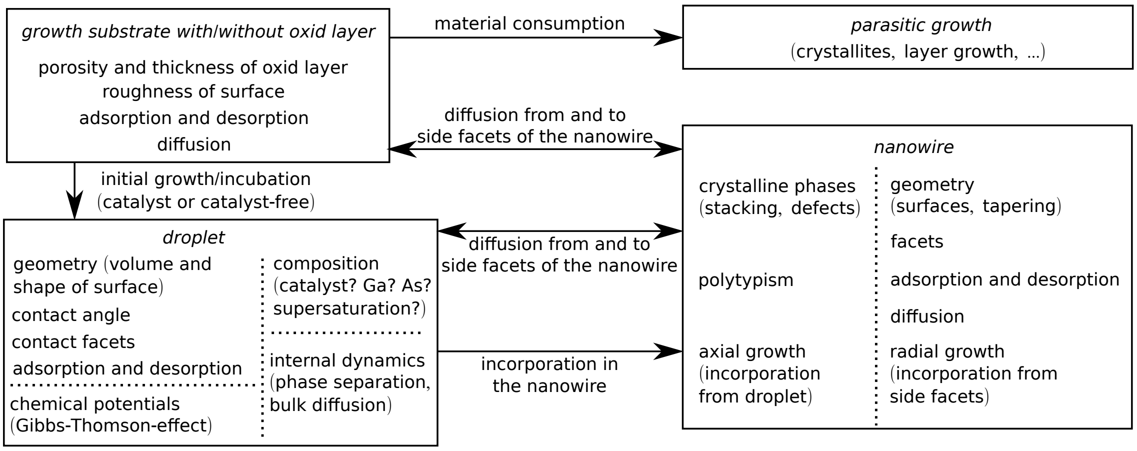

Figure 1.2.: Overview over the most important aspects of nanowire growth on a more detailed and more abstract level than in Fig. 1.1.

interaction must be modelled and analyzed: Each of these subsystems has already rich and complicated dynamics for its own which we now discuss [25, 66]:

- *growth substrate*: First of all, the substrates can be either cleaned from oxide coverage or intentionally oxidized for a specific amount of time [67, 68]. The limit of long oxidation time at room temperature is referred to as native oxide. If such an oxide layer is present, its thickness and porosity is crucial for nanowire growth. In any case – with or without an oxide layer – the roughness of the surface highly influences the diffusion and nucleation dynamics of the Ga and As on top of this surface. Moreover, the adsorption and desorption of these species from the surround gas phase must be modelled and taken properly into account.
- *droplet*: In the initial growth stage, the liquid droplets form on the substrate. These initial droplets as well as their evolution must be modelled. With and without catalyst atoms complicated dynamical features have been found: In addition to the adsorption and desorption from the gas phase, the geometrical aspects [69, 70] (most importantly the involved crystallographic facets [71]) and the composition [59, 69] (most importantly the supersaturation [59]) of the droplet must be modelled. The geometrical aspects mainly influence the geometry of the growing nanowires (radius, tapering) whereas the composition strongly influences the axial growth rates as well as the crystallographic properties of the nanowires. For determination of the chemical potentials of the species in the droplet, the composition as well as the geometry are relevant, since the Gibbs-Thomson effect relates both quantities [72, 73]. In contrast to the (solid) nanowire and (solid) substrate subsystem, where only surface diffusion seems relevant, the liquid droplet additionally allows for bulk diffusion. We would like to mention that even metastable crystalline phases have been found in the droplet [74]. As already mentioned before, for some conditions, nanowire growth without a liquid droplet has been observed. However, these systems are beyond the scope of this introductory overview.
- *nanowire*: For the nanowires, we also have to distinguish its bulk and its surface dynamics: Whereas for the surface, the most relevant aspects are the involved facets (and their energies), adsorption from and desorption to the gas phase, surface diffusion and, finally, incorporation of GaAs for radial growth of the nanowires, the crystalline bulk consists of stacked crystalline layers – possibly with all kinds of defects. In particular, these defects include substitutional and interstitial foreign atoms, which have strong influence on the final electronic and optical properties,

  and errors in the stacking sequence with respect to the expected stacking sequence from the bulk material. For some growth conditions, nucleation in two competing "ideal" stacking sequences has been observed. This phenomenon is referred to as polytypism and will be discussed in detail in Sec. 1.4 and will be of major importance for the first part of this manuscript. Finally, the bulk of the nanowire grows by axial growth.

- *parasitic growth*: All growth that does not result in nanowires is attributed to the parasitic growth. Possible parasitic growth includes growth of continuous two-dimensional layers or growth of small crystallites [67]. However, two-dimensional layer growth can typically be avoided (which would change the surface diffusion of the substrate). For most samples, only the material consumption of the parasitic growth is relevant for modelling the growth of the nanowires.

An example of a recent, extensive parameter study of nanowire growth, which investigates the influence of the thickness of the silicon oxide layer, the growth time, the substrate temperature and the Ga and As fluxes can be found in Ref. [68], whereas the book [66] written by Dubrovskii – which also includes many recent results – gives an extensive overview over the theoretical aspects of nanowire growth.

We point out that on this abstract layer, the gas phase in the growth chamber is not considered a dynamical system, but only an infinite reservoir of (directional) impinging flux and its "interaction" with the four above subsystem is only modelled by adsorption and desorption. Moreover, the growth of different nanowires starts to interact above a certain density and size due to shadowing of the impinging flux and reduction of the effective material collection area on the substrate due to competing nanowires. This multi-wire interaction has not been depicted in Fig. 1.2.

In addition to the dynamics in each of the subsystems, these subsystems are highly coupled and this couplings are *essential* for the growth of the nanowires.

During the initial growth stage, the growth substrate directly interacts with the initial droplets. At any later growth stage, no direct interaction between the substrate the droplets of the nanowires takes place. Instead, the nanowire separates these two subsystems. Consequently, diffusion along side-facets of the nanowires links the composition and volume of the droplet with the properties of the substrate [75, 76]. However, we again point out, that material on the side facets can also be incorporated directly in the nanowire which results in radial growth – instead of refilling the droplet reservoir on the tip of the nanowire.

Moreover, the interaction between the solid topmost layers of the nanowire and the liquid droplet reservoir must be modelled. This interaction is rather complicated: Recent studies with environmental transmission electron microscopy (ETEM) indicate that the nucleation does not take place directly at the triple phase line of the system [49, 77, 78] and this assumption would be an oversimplification. Instead, crystallographic surfaces and geometric factors must likely be considered.

This complicated interplay of all the above-mentioned factors poses a major challenge which needs to be resolved in order to gain maximum control during nanowire growth. In order to gain such understanding, sophisticated experiments with various techniques such as environmental TEM or *in-situ* X-ray diffraction have been performed.

It is a main goal of part I of this thesis to investigate the perspectives and limitations of *in-situ* X-ray diffraction with the current PMBE growth chamber (see Sec. 2) at the synchrotron source ANKA for studying polytypism (see Sec. 1.4) in GaAs nanowires. In Sec. 2.1, a short motivation for this approach by comparison with other experimental approaches is given.

1.2. Fluctuations of the height of nanowires (anti-bunching)

Before we focus on the wurtzite zincblende polytypism in GaAs nanowires in Sec. 1.4, we present in this section a detailed illustration of the complexity of nanowire growth even if only a single phase is contained in a nanowire. As an example, we discuss anti-bunching during growth as, e.g., observed by Glas et al. in Ref. [79]. In this work, Glas et al. investigated the fluctuations of the number of nucleation events after a particular growth time. Experimental observation – based on periodic modulation of the growth conditions [79, 80] – revealed constant fluctuations of the number of grown layers with respect to growth time. They explained the behavior of their sample by a non-linear self-regulatory process based on the memory of the droplet at the nanowire tip. In this section, we also study this self-regulatory mechanism.

First, we give a detailed presentation of the model which is studied afterwards numerically. We assume a nanowire which grows by successive single layer nucleation. The material which is incorporated in a newly grown layer is taken from a material reservoir ("droplet") located at the tip of the nanowire. The rate of nucleation of an additional layer is proportional to the Boltzmann factor $\mathrm{e}^{-\beta E}$ where $\beta = 1/(k_\mathrm{B} T_\mathrm{S})$ and E is the energy barrier for creation of a nucleus to form the next crystalline layer. k_B is the Boltzmann constant and T_S is the temperature of the substrate ("growth temperature"). However, the energy is not constant over time due to an accumulation of type V atoms (As in the case of GaAs nanowires) in the droplet after the depletion resulting from a nucleation event. Thus, E is a function of this concentration. The Boltzmann factor only describes the mean rate, which in turn determines the mean nucleation time μ_N. The statistical distribution resulting in this mean rate is not determined. To the best of the author's knowledge, this distribution is currently not known. A good review on the dynamics of systems with intrinsic fluctuations can be found in Ref. [81].

In the framework of this thesis, we illustrate the self-regulatory mechanism for

$$\mathbf{p}\left(t, \mu_\mathrm{N}\right) \propto \Theta(t) \frac{1}{\mu_\mathrm{N}} \, \mathrm{e}^{-t/\mu_\mathrm{N}} \ , \tag{1.1}$$

for nucleation of the next, additional layer on top of nanowire after time t. Here, $\Theta(t)$ is the Heaviside step function and μ_N is the mean nucleation time. It is a function of the number of type V atoms N_V in the droplet and, therefore, also a function of time. The normalization of every probability distribution to one fixes the proportionality constant in Eq. (1.1). For constant μ_N, this proportionality factor is equal to one.

μ_N has to fulfill certain limits: Below a minimum number of type V atoms $N_\mathrm{V}^{(\mathrm{Min})}$, no additional layer can nucleate. Thus, $\mu_\mathrm{N}(N_\mathrm{V} \leq N_\mathrm{V}^{(\mathrm{Min})}) = \infty$. On the other hand, for large N_V the mean nucleation approaches its minimum value $\mu_\mathrm{N}(N_\mathrm{V} \to \infty) = \mu_\mathrm{Min}$. These limits hold for the parametrization

$$\mu_\mathrm{N}(N_\mathrm{V}) = \mu_\mathrm{Min} + \frac{1}{f(N_\mathrm{V})} \ , \tag{1.2a}$$

$$f(N_\mathrm{V} \leq N_\mathrm{V}^{(\mathrm{Min})}) = 0^+ \quad , \quad f(N_\mathrm{V} \to \infty) = \infty \quad , \quad f(N_\mathrm{V}) > 0 \ . \tag{1.2b}$$

For the purpose of illustration of the non-linear self-regulatory mechanism, we employ

$$f(N_\mathrm{V}) = \alpha_1 \left(\frac{N_\mathrm{V}}{N_\mathrm{V}^{(\mathrm{Min})}} - 1 \right)^{\alpha_3} \cdot \Theta\left(\frac{N_\mathrm{V}}{N_\mathrm{V}^{(\mathrm{Min})}} - 1 \right) \ . \tag{1.3}$$

as a model. It is based on the relative abundance $\frac{N_\mathrm{V} - N_\mathrm{V}^{(\mathrm{Min})}}{N_\mathrm{V}^{(\mathrm{Min})}}$ (to some power α_3), incorporates the lower bound $N_\mathrm{V}^{(\mathrm{Min})}$ for nucleation by the Heaviside function and continuously goes to zero at $N_\mathrm{V} = N_\mathrm{V}^{(\mathrm{Min})}$ for $\alpha_3 > 0$. The parameter α_1^{-1} gives the linear slope in Eq. (1.2a). The parameter α_3 is dimensionless and the parameter α_1 has dimension s^{-1} which, however, we suppress in the subsequent discussion for simplicity.

Finally, we model N_V as a function of time. We consider an affine linearly increasing number of type V atoms with respect to time t which is measured starting from the previous nucleation event. The offset $N_\mathrm{V}^{(\mathrm{Offset})}(t_0, n(t_0))$ of this linear model is determined by the filling at time t_0 which refers to nucleation of the previous layer. $n(t_0)$ is the number of layers grown at time t_0. Consequently, we have in total

$$N_\mathrm{V}(t) = r \cdot t + N_\mathrm{V}^{(\mathrm{Offset})}(t_0, n(t_0)) \tag{1.4a}$$

$$= r \cdot t + r \cdot t_0 - n(t_0) \cdot N_\mathrm{V}^{(\mathrm{CPL})} + N_\mathrm{V}^{(\mathrm{Initial})} \ . \tag{1.4b}$$

Here, r is the refill rate of type V atoms, $N_\mathrm{V}^{(\mathrm{CPL})}$ is the cost of type V atoms per nucleated layer and, finally, $N_\mathrm{V}^{(\mathrm{Initial})}$ the amount of type V atoms in the droplet at the beginning of growth. We point out that Eq. (1.1) to (1.4b) should be generalized in more sophisticated models for the nanowire growth, but the simple model is sufficient for illustration.

In total, Eq. (1.1) yields

$$\mathbf{p}\,(t) = \frac{1}{\mathcal{N}} \, \frac{f(N_\mathrm{V}(t)) \cdot \Theta(t)}{1 + \mu_\mathrm{Min} \cdot f(N_\mathrm{V}(t))} \, \mathrm{e}^{\frac{-\,f(N_\mathrm{V}(t)) \cdot t}{1 + \mu_\mathrm{Min} \cdot f(N_\mathrm{V}(t))}} \ , \tag{1.5a}$$

$$\mathcal{N} = \int_0^\infty \frac{f(N_\mathrm{V}(t)) \cdot \Theta(t)}{1 + \mu_\mathrm{Min} \cdot f(N_\mathrm{V}(t))} \, \mathrm{e}^{\frac{-\,f(N_\mathrm{V}(t)) \cdot t}{1 + \mu_\mathrm{Min} \cdot f(N_\mathrm{V}(t))}} \ \mathrm{d}t \ , \tag{1.5b}$$

where $f(N_\mathrm{V})$ is defined in Eq. (1.3) and $N_\mathrm{V}(t)$ in Eq. (1.4b). The dependence of $\mathbf{p}(t)$ on μ_N, α_1, α_3, r, $N_\mathrm{V}^{(\mathrm{CPL})}$, $N_\mathrm{V}^{(\mathrm{Min})}$, and $N_\mathrm{V}^{(\mathrm{Initial})}$ has been suppressed.

It is necessary to carefully distinguish between the mean nucleation time μ_N in Eq. (1.1) and the mean nucleation time

$$\mu_r = \int_0^\infty t \cdot \mathbf{p}\,(t, \mu_\mathrm{N}(t)) \ \mathrm{d}t \tag{1.6}$$

of the full time dependent model in Eq. (1.5b).

The generation of random events according to a predefined probability density distribution is described in appendix A. The example defined by Eq. (9.6) in that section of the appendix is taken from the model described here.

If at time $t = 0$, the droplet concentration of the type V atoms is below the minimum $N_\mathrm{V}^{(\mathrm{Min})}$ which is required for nucleation of a new layer, the probability $\mathbf{p}$ in Eq. (1.5b) is equal to zero until the number of atoms in the droplet exceeds $N_\mathrm{V}^{(\mathrm{Min})}$ due to the refill rate r. From that point on, nucleation of a new layer is possible. If at time $t = 0$, N_V is greater than $N_\mathrm{V}^{(\mathrm{Min})}$, the Heaviside function $\Theta(t)$ eliminates nucleation at negative times $t < 0$. However, the probability for immediate re-nucleation at $t = 0$ is greater than zero in this case.

The self-regulatory mechanism works in the following way: By balancing incoming material and material incorporated in the nanowire, we expect a mean growth time

$$t_\mathrm{MGT} = \frac{N_\mathrm{V}^{(\mathrm{CPL})}}{r} \tag{1.7}$$

and respective mean growth rate t_MGT^{-1}. If several layers grow faster than expected by the mean layer growth time t_MGT as a result of statistical fluctuations, the amount of type

V atoms in the droplet is depleted. As a result, the expected time for the nucleation of the next layer is increased, thus decreasing the fluctuations of the number of layers grown in a particular time interval. In contrast, if several layers grow slower than expected by the mean layer growth time t_{MGT}, the amount of type V atoms increases and it is more likely for the next layer to grow faster than t_{MGT}. Consequently, the fluctuations around the expectation value for the number of grown layers are also reduced for that case. Whereas the maximum number of grown layers after a particular time is bound from above with this self-regulatory mechanism[2], this bound does not hold without the self-regulatory mechanism.

For the numerical simulations, we point out that only the ratio $\frac{N_{\mathrm{V}}}{N_{\mathrm{V}}^{(\mathrm{Min})}}$ determines $f(N_{\mathrm{V}})$ (see Eq. (1.3)). Thus, the solution of the model is invariant upon simultaneous rescaling of N_{V} and $N_{\mathrm{V}}^{(\mathrm{Min})}$. Therefore, we interpret the parameters r, $N_{\mathrm{V}}^{(\mathrm{CPL})}$ and $N_{\mathrm{V}}^{(\mathrm{Initial})}$ of the model (1.4b) as multiples of $N_{\mathrm{V}}^{(\mathrm{Min})}$. By rescaling and assuming a particular value for $N_{\mathrm{V}}^{(\mathrm{Min})}$, we can interpret the model in terms of “number of atoms of type V”. The initial filling $N_{\mathrm{V}}^{(\mathrm{Initial})}$ is irrelevant for the long time limit. Unless stated otherwise, we set $N_{\mathrm{V}}^{(\mathrm{Initial})} = 0$. The parameters μ_{Min}, α_1, and α_3 determine the fluctuations of the number of grown layers and the equilibrium value of N_{V} in the droplet.

First, we consider the deterministic limit of our model before we proceed to the full statistic model for the nucleation time of the new layer. In this deterministic limit, no random event according to the distribution (1.5b) is drawn. Instead, the mean nucleation time μ_r of the full time-dependent model in Eq. (1.5b) is taken as time difference to the subsequent nucleation event.

In Fig. 1.3, the time required for growing a particular number of layers as well as the nucleation time are depicted as a function of the number of grown layers for various values of the parameter μ_{Min}. The parameters are $r = 0.1\mathrm{s}^{-1}$ and $N_{\mathrm{V}}^{(\mathrm{CPL})} = 0.05$ (both understood as multiples of $N_{\mathrm{V}}^{(\mathrm{Min})}$), whereas α_1 and α_3 are set equal to one. Thus, the mean growth time t_{MGT} per layer as defined in Eq. (1.7) is 0.5s.

For values $\mu_{\mathrm{Min}} \lesssim 0.5\mathrm{s}$, the mean nucleation time t_{MGT} decreases quickly to the static limit $t_{\mathrm{MGT}} = 0.5\mathrm{s}$ after some initial accumulation of type V material in the droplet (see Figs. 1.3). After this initial phase, the amount of type V material in the droplet converges to a static limit (see Fig. 1.3(c)).

If the linear increase of the number of grown layers at layer growth times is extrapolated to zero layers, i.e., neglecting the transient behavior during the early growth phase, the intersection of this linear approximation with the time axis provides one approach to define the incubation time of the growth process.

However, once μ_{Min} exceeds the critical value[3] $\mu_{\mathrm{Min}} = t_{\mathrm{MGT}} = 0.5\mathrm{s}$, the type V material accumulates more and more in the droplet (see Fig. 1.3(c)). For such huge values of μ_{Min}, the type V material can no longer be incorporated sufficiently fast in newly grown layers. The mean nucleation time remains above the expected static limit t_{MGT} (see Fig. 1.3). As a consequence, the time that is required to grow a given number of layer increases (see Fig. 1.3). Physically, limiting the mean of the distribution in Eq. (1.5b) might, for example, model a dynamic process in the droplet which needs to take place after every nucleation event prior to the formation of a new nucleus. One example for such a process

---

[2] The bound is obtained if all material exceeding $N_{\mathrm{V}}^{(\mathrm{Min})}$ which has been accumulated by the refilling r plus the initial material $N_{\mathrm{V}}^{(\mathrm{Initial})}$ has been incorporated in the nanowire.

[3] The true critical value for μ_{Min} is slightly below the static limit t_{MGT} since the mean value of the distribution defined in Eq. (1.5b) is always larger than μ_{Min}. However, for practical purposes, it is typically sufficient to approximate the critical value by the static limit t_{MGT}.

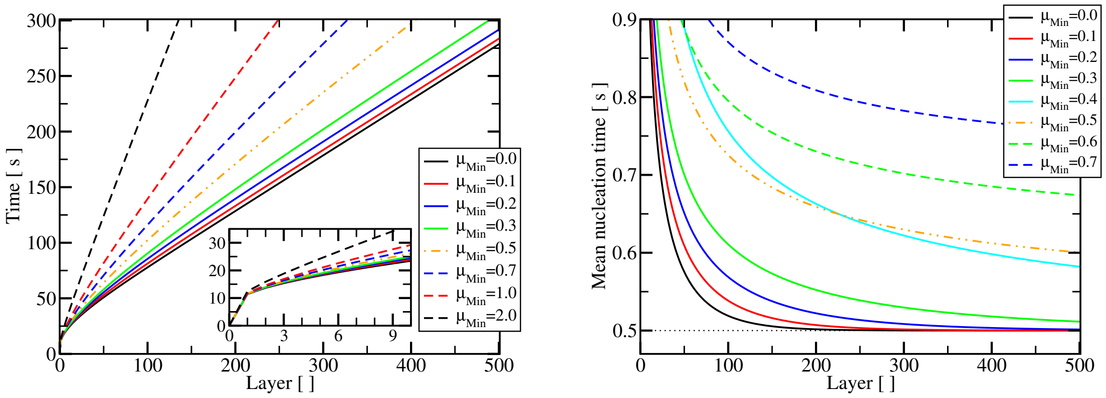

(a) Time requirements for growing a particular number of layers

(b) Mean nucleation time after a particular number of layers

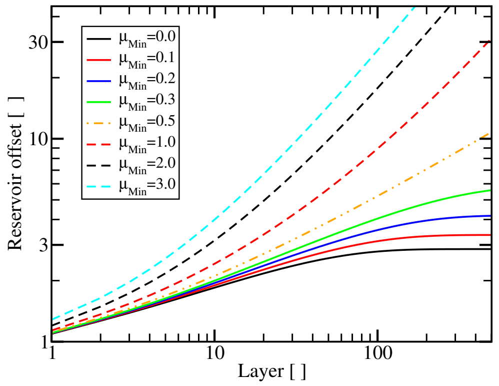

(c) Reservoir filling after a particular number of layers in units of multiples of $N_{\mathrm{V}}^{(\mathrm{Min})}$

Figure 1.3.: Deterministic limit of the model for reservoir based growth: Instead of random nucleation times, the mean of the distribution (1.5b) is used as nucleation time of the next layer. Figures illustrate the transient initial behaviour as well as the resulting equilibrium state.

would be a diffusion process in the droplet which transports new type V material towards the nucleated layer on top of which the new nucleus has to form.

Now, we include statistical fluctuations in the growth time of a new layer as described by the time-dependent model in Eq. (1.5b). Some results are depicted in Fig. 1.4: Unless stated otherwise, the parameter μ_{Min} is zero. In Figs. 1.4(a) and 1.4(b), we again depict the growth time for a particular number of layers and the filling of the reservoir for various parameter α_i. The deterministic limit – as described in the previous paragraphs – is depicted as dashed-dotted line. The statistical model is depicted as solid line. First, we observe, that the time required to grow a given number of layers essentially follows the deterministic limit. Only small fluctuations on top are present. Variation of α_1 only affects the growth of the early layers. After this, the (mean) slope in Fig. 1.4(a) is identical and equivalent to the mean nucleation time given by Eq. (1.7) as long as $\mu_{\mathrm{Min}} \lesssim 0.5$s. This result supports the widely used linear approximation of the nanowire height versus growth time. Again, we are able to define the incubation time in the same manner as before in the deterministic limit.

For increasing value of the parameter α_1, the static limit is reached faster. On the contrary, the mean filling of the reservoir decreases with increasing α_1 (see Fig. 1.4(b)). Note that

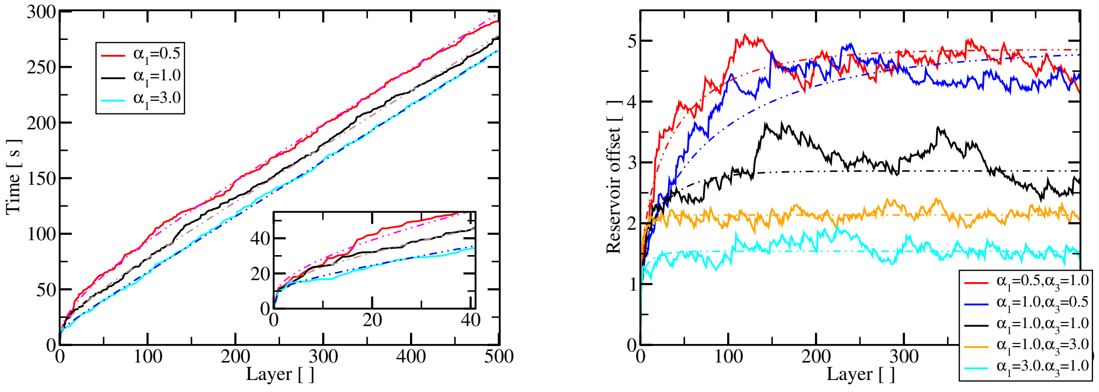

(a) Time requirements for growing a particular number of layers. The deterministic limit is plotted as dashed-dotted line.

(b) Filling of reservoir with type V atoms (unit: multiples of $N_{\mathrm{V}}^{(\mathrm{Min})}$). The deterministic limit is plotted as dashed-dotted line.

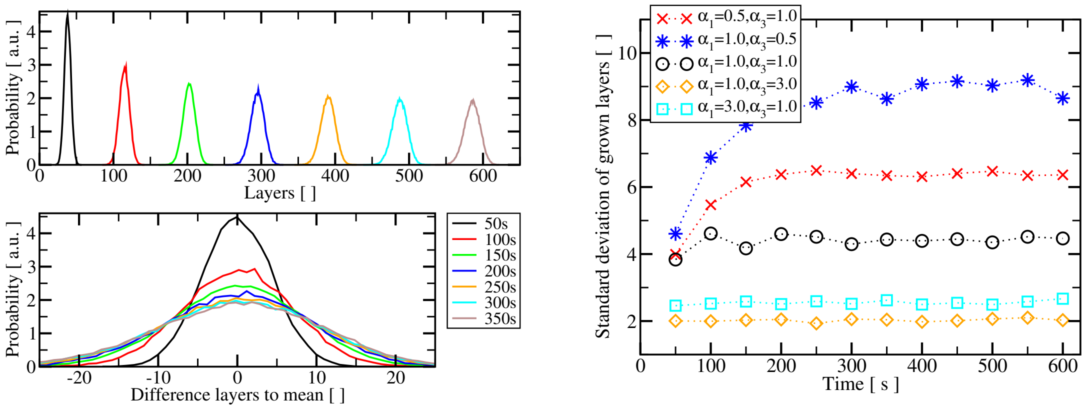

(c) Layer growth distribution after various growth times for parameters $\mu_{\mathrm{Min}} = 0.3\mathrm{s}$ and $\alpha_i = 1.0$

(d) Standard deviation of layer distribution after various growth times for different parameters α_i

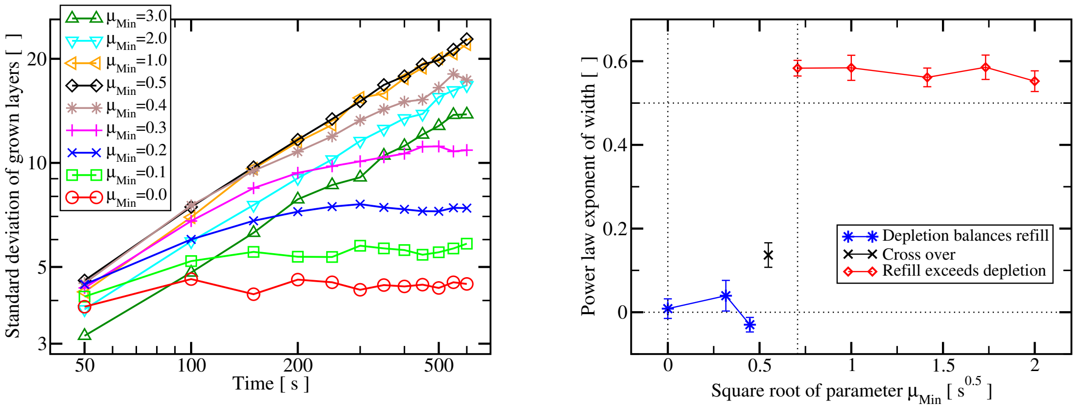

(e) Standard deviation of layer distribution after various growth times for different parameter μ_{Min}

(f) Power law exponents from fits to the curves in Fig. 1.4(e) for $t > 250\mathrm{s}$

Figure 1.4.: Statistical model for layer by layer growth from a reservoir of single phase nanowire. The nucleation time of a newly grown layer is drawn randomly from the distribution (1.5b).

depending on the parameters, the mean filling of the reservoir offset may be only slightly above $N_{\mathrm{V}}^{(\mathrm{Min})}$ – the minimum amount of type V atoms which is required for nucleation of a new layer.

The parameter α_3 influences the reservoir offset in the same way: Increasing α_3 reduces the mean reservoir offset after some initial growth stage. Like the parameter α_1, the parameter α_3 also influences the duration of the initial growth stage – until the static mean conditions are reached.

In Fig. 1.4(c), we depict the distributions of the number of grown layers after various growth times. At first, this distribution is very narrow. Then, its width increases with increasing growth time during the initial growth stage. After this, however, the shape of the distribution remains constant, only its center increases linearly. For better illustration of the evolution of the shape of the layer distribution, the center of all distributions has been shifted to zero in the lower part of Subfig. 1.4(c). Note, that for *independent* random nucleation times for every newly nucleated layer, i.e., without modelling the self-regulatory mechanism, the width of the nanowire height distribution grows strictly monotonously.

This observation is quantified in Fig. 1.4(d) for the set of parameters α_i which is also depicted in Fig. 1.4(b). Clearly, the width of the layer distribution converges to a static value after the initial growth stage. The width of the layer distribution decreases with increasing α_i, $i = \{1, 3\}$. We want to point out that even if the mean filling of the droplet with type V material is equal (e.g., $(\alpha_1, \alpha_3) = (0.5, 1.0)$ and $(\alpha_1, \alpha_3) = (1.0, 0.5)$ in Fig. 1.4(b)), the width of the resulting nanowire height distribution can vary. This clearly demonstrates the importance of this self-regulatory process for growing nanowires with narrow height distribution.

The remaining Figs. 1.4(e) and 1.4(f) are devoted to the behavior of the model for increasing μ_{Min}. As soon as the parameter μ_{Min} exceeds the mean nucleation time t_{MGT}, no static limit for the mean reservoir filling (as depicted in Fig. 1.3(c) for the deterministic limit of the model) exists and the stabilization of the width of the layer distribution breaks down. Instead, its width increases as a power law with an exponent close to 0.5 (see Fig. 1.4(f)). This clearly demonstrates the complicated dynamics and huge variation of possible dynamics during the growth of a nanowire – even if only a single phase is present in the grown wires and most aspects of nanowire growth as given in Fig. 1.2 are strongly simplified.

However, in case of polytypic nanowires (see Sec. 1.4), competing nuclei for the competing atomic arrangements need to be taking into account, possibly on different nucleation facets. As a consequence, the nucleation energy barriers for continuing growth of the current phase may depend on the current phase, and, moreover, the static limits for both phases as well. However, transitions from one polytype to the other polytype might prevent reaching the static limits at all. Therefore, the dynamics during growth of polytypic nanowires is far more complicated than the single phase model which we discussed in the previous section. On the contrary, such dynamics may open additional possibilities for controlling nanowire growth. As a consequence, we study the wurtzite zinc blende polytypism in III-V nanowires with X-ray radiation in the first part of this manuscript. In particular, we will also investigate the possibilities to conclude on information about the nucleation barriers and, thereby, help to understand the dynamic of nanowire growth (see Sec. 4).

1.3. Scaling laws in nanowire growth

The first example was dedicated to the effects of the "memory" of the droplet reservoir of the type V atoms on the axial growth of nanowires. Radial growth was neglected throughout this section. Our second example for illustrating the complexity of nanowire growth even without polytypism is a scaling law which relates axial and radial growth of nanowires in some cases.

More specifically, Dubrovskii et al. derived in [82] the temporal evolution of the height

$L(t)$ of self-induced GaN nanowires synthesized by MBE and their radius $R(t)$ as

$$L(t) = L(t_0) \cdot \left(1 + \frac{\alpha+1}{\alpha} \cdot \frac{a \cdot V}{L(t_0) \cdot R(t_0)} (t - t_0)\right)^{\alpha/(\alpha+1)} \tag{1.8a}$$

$$R(t) = R(t_0) \cdot \left(1 + \frac{\alpha+1}{\alpha} \cdot \frac{a \cdot V}{L(t_0) \cdot R(t_0)} (t - t_0)\right)^{1/(\alpha+1)} \tag{1.8b}$$

Here, t is the growth time. As a conclusion, the nanowire length and radius fulfill the scaling law $L(t)/L(t_0) = (R(t)/R(t_0))^\alpha$ and its parameter α can be easily extracted from a log-log plot of $L(R)$.

We now shortly discuss some implications of the Eq. (4)

$$\frac{1}{V}\left(\frac{\partial \mathrm{L}}{\partial t}\right) = \frac{a}{R(t)} \quad ; \quad \frac{1}{V}\left(\frac{\partial \mathrm{R}}{\partial t}\right) = \frac{b}{L(t)} \tag{1.9}$$

in Ref. [82] which are not explicitly discussed therein. For details on the derivation of this coupled system of partial differential equations and the physical interpretation of the parameters a, b and V, we refer the reader to Ref. [82]. However, we point out, that only the products aV and bV influence the results for $R(t)$ and $L(t)$, and, thus, the model has only two independent parameters. Moreover, all changes in the experimental conditions such that these two products remain equal will produce nanowires with the same geometric features $L(t)$ and $R(t)$. The parameter α is given by the ratio $a/b = (aV)/(bV)$. The most interesting aspect of the model is the coupling of the axial growth rate to the current radius, and of the radial growth rate to the current length of the nanowire.

First of all, we point out that the time-derivative of the product $L(t)R(t)$

$$\left(\frac{\partial(\mathrm{LR})}{\partial t}\right) = \left(\frac{\partial \mathrm{L}}{\partial t}\right) R + L \left(\frac{\partial \mathrm{R}}{\partial t}\right) = (a+b)V \ , \tag{1.10}$$

is constant with respect to time. Stated differently, the curvature (i.e., second derivative) of the product $L(t)R(t)$ is zero and the parameter combination $\gamma \equiv (a+b)V$ can be extracted easily from a linear fit to $L(t)R(t)$.

Consequently, from the parameters $\alpha = a/b = (aV)/(bV)$ and $\gamma = aV + bV$ which are both easily accessible from post-growth *ex-situ* studies, it is possible to extract the products aV and bV as

$$aV = \frac{\gamma\alpha}{1+\alpha} \quad ; \quad bV = \frac{\gamma}{1+\alpha} \ . \tag{1.11}$$

We also point out that the scaling law $L \propto R^\alpha$ can be nicely derived directly from the differential equations Eq. (1.9) by application of the chain rule without explicitly solving for $L(t)$ and $R(t)$, since

$$\left(\frac{\partial \mathrm{L}}{\partial t}\right) = \left(\frac{\partial \mathrm{L}}{\partial R}\right)\left(\frac{\partial \mathrm{R}}{\partial t}\right) = \left(\frac{\partial \mathrm{L}}{\partial R}\right)\left(\frac{bV}{L(R)}\right) \tag{1.12a}$$

$$\Rightarrow \quad \frac{aV}{R} = \left(\frac{\partial \mathrm{L}}{\partial R}\right)\left(\frac{bV}{L(R)}\right) \tag{1.12b}$$

$$\Rightarrow \quad \frac{R}{L(R)}\left(\frac{\partial \mathrm{L}}{\partial R}\right) = \frac{a}{b} = \alpha \tag{1.12c}$$

Consequently, the expression $\frac{R}{L(R)}\left(\frac{\partial \mathrm{L}}{\partial R}\right)$ remains constant. This equation is easily solved by separation:

$$\frac{1}{L(R)}\left(\frac{\partial \mathrm{L}}{\partial R}\right) = \frac{\alpha}{R} \quad \overset{\text{Integration}}{\Rightarrow} \quad \ln\left(\frac{L(R)}{L(R_0)}\right) = \alpha \cdot \ln\left(\frac{R}{R_0}\right) \tag{1.13a}$$

$$\Rightarrow \quad L(R) = L(R_0)\left(\frac{R}{R_0}\right)^\alpha \tag{1.13b}$$

If we interpret R as a function of time, this scaling relation implies in particular that

$$L(t) = L(t_0) \left(\frac{R(t)}{R(t_0)} \right)^{\alpha} \; . \tag{1.14}$$

Consequently, knowledge of α and either $L(t)$ or $R(t)$ determines the other quantity.

From a fundamental point of view, it is also interesting to consider the following scenario: Suppose, the power law (1.13b) has been observed empirically (no pronounced tapering of the nanowires is assumed). What would be the implications on the *differential equations* for $L(t)$ and $R(t)$ which describe the temporal evolution of axial and radial growth?

If this scaling law holds true, the derivative $\left(\frac{\partial \mathrm{L}}{\partial R}\right)$ is equal to

$$\left(\frac{\partial \mathrm{L}}{\partial R} \right) = \frac{\alpha \cdot L}{R} \overset{!}{=} \frac{\left(\frac{\partial \mathrm{L}}{\partial t}\right)}{\left(\frac{\partial \mathrm{R}}{\partial t}\right)} \tag{1.15}$$

where the chain rule has been used in the last step. Consequently, we have

$$\frac{1}{L} \left(\frac{\partial \mathrm{L}}{\partial t} \right) = \frac{\alpha}{R} \left(\frac{\partial \mathrm{R}}{\partial t} \right) \; . \tag{1.16}$$

Consequently, if $\left(\frac{\partial \mathrm{L}}{\partial t}\right) = f(L, R)$ describes the temporal evolution of the nanowire height, the growth dynamics of radial growth is

$$\left(\frac{\partial \mathrm{R}}{\partial t} \right) = \frac{1}{\alpha} \left(\frac{R}{L} \right) \cdot f(L, R) \; . \tag{1.17}$$

Here, $f(L, R)$ is arbitrary two-dimensional function of L and R. Eq. (1.9) follows for $f(L, R) = aV/R$.

However, if constant axial growth with time is observed, we have $f(L, R) = \tilde{A}$. Consequently, the power law (1.13b) is *only* observed for

$$\left(\frac{\partial \mathrm{R}}{\partial t} \right) = \frac{1}{\alpha} \left(\frac{R}{L} \right) \cdot \tilde{A} \; . \tag{1.18}$$

This nicely illustrates the implications which can be deduced from empirically observing the scaling law (1.13b) and a constant axial growth rate of non-tapered nanowires on differential equations governing nanowire growth.

From solving this equation by separation or by Eq. (1.14) (together with $L(t) = L(t_0) + \tilde{A} \cdot (t - t_0)$), we have

$$R(t) = R(t_0) \cdot \left(1 + \frac{\tilde{A} \cdot (t - t_0)}{L(t_0)} \right)^{1/\alpha} \; . \tag{1.19}$$

We now come back to the original model of Dubrovskii as defined in Eq. (1.9) and decouple this system of differential equations (1.9) for $L(t)$. From

$$\left(\frac{\partial \left(1 / \left(\frac{\partial \mathrm{L}}{\partial \mathrm{t}} \right) \right)}{\partial t} \right) = \frac{1}{a \cdot V} \left(\frac{\partial \mathrm{R}}{\partial t} \right) = \frac{1}{\alpha} \frac{1}{L(t)} \tag{1.20}$$

we obtain the equation

$$\alpha \cdot L(t) \cdot \left(\frac{\partial^2 \mathrm{L}}{\partial^2 t} \right) + \left(\frac{\partial \mathrm{L}}{\partial t} \right)^2 = 0 \; . \tag{1.21}$$

This non-linear differential equation for $L(t)$ contains *only* α as a parameter. Consequently, the parameter α solely determines the *dynamics* of growth. The absolute value of the product aV only influences this dynamics by the initial condition

$$\left(\frac{\partial \mathrm{L}(\mathrm{t}_0)}{\partial t}\right) = \frac{aV}{R(t_0)} \ . \tag{1.22}$$

If we modify Eq. (1.9) such that radial growth is constant with time, but without requiring the scaling relation (1.13b), i.e.,

$$\frac{1}{V}\left(\frac{\partial \mathrm{L}}{\partial t}\right) = \frac{a}{R(t)} \quad ; \quad \frac{1}{V}\left(\frac{\partial \mathrm{R}}{\partial t}\right) = \frac{\tilde{b}}{V} \ , \tag{1.23}$$

we have a linear increase in radius with $R(t) = \tilde{b} \cdot (t - t_0) + R(t_0)$ and, consequently,

$$\left(\frac{\partial \mathrm{L}}{\partial t}\right) = \frac{aV}{\tilde{b} \cdot (t - t_0) + R(t_0)} = \frac{aV}{\tilde{b}} \cdot \frac{1}{(t - t_0) + R(t_0)/\tilde{b}} \tag{1.24a}$$

$$\Rightarrow \quad L(t) \overset{t \geq t_0}{=} L(t_0) + \left(\frac{aV}{\tilde{b}}\right) \cdot \ln\left(1 + \frac{\tilde{b} \cdot (t - t_0)}{R(t_0)}\right) \ . \tag{1.24b}$$

For comparison, *if* we modify Eq. (1.9) such that either no radial growth takes place ($b = 0$) or that the impinging flux on the droplet dominates the growth dynamics, we would end up with

$$\frac{1}{V}\left(\frac{\partial \mathrm{L}}{\partial t}\right) = \frac{\tilde{A}}{V} \quad ; \quad \frac{1}{V}\left(\frac{\partial \mathrm{R}}{\partial t}\right) = \frac{b}{L(t)} \ . \tag{1.25}$$

This immediately implies linear behavior of the nanowire height versus growth time (in contrast to Eq. (1.8)) and logarithmic growth of the radius, i.e.,

$$L(t) = \tilde{A} \cdot (t - t_0) + L(t_0) \ , \tag{1.26a}$$

$$R(t) \overset{t \geq t_0}{=} R(t_0) + \left(\frac{bV}{\tilde{A}}\right) \cdot \ln\left(1 + \frac{\tilde{A} \cdot (t - t_0)}{L(t_0)}\right) \ . \tag{1.26b}$$

In this scenario, we therefore end up with a logarithmic increase of length $R(t)$ only – instead of a linear or power-law behavior.

Although this model is formulated for GaN nanowires, we choose this model because it nicely illustrates typical characteristics of growth models and its implications can be derived fast and easily. Attempts to formulate growth models specifically for GaAs nanowires can for example be found in Refs. [49, 66, 83–86]. Also, additional information on modelling the growth of nanowires can be found in Refs. [63, 66, 87–91].

1.4. The wurtzite zinc blende polytypism in GaAs nanowires

We now introduce polytypism in GaAs nanowires in more detail which describes an important aspect of the crystalline structure of the grown nanowires.

We would like to mention, that this polytypism is not only observed in GaAs nanowires, but also for other nanowires [61, 92] such as InAs [60, 93–95] or InP [96] nanowires. Although our discussion mainly aims at GaAs structures, some aspects or references refer to nanowires composed of other III/V materials.

Polytypism in III–V nanowires refers to the observation that for some growth conditions, two different periodic atomic arrangements ("stackings"), namely the zinc blende and the

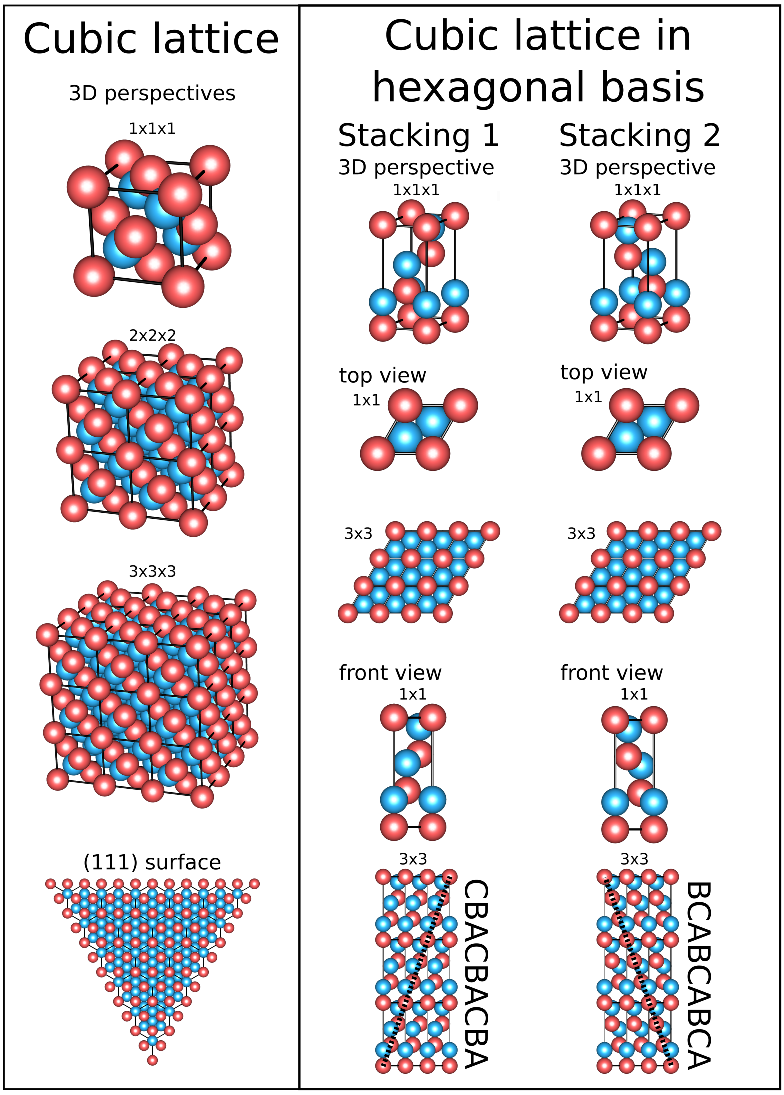

Figure 1.5.: Illustration of the crystal structure of zinc blende GaAs (hexagonality 0). In the left column the structure is described in a basis of a simple cubic lattice. The lowest image is a view from the top on a $[111]_{\mathrm{z}\frown\mathrm{c}}$ surface. A description of cubic zinc blende GaAs in a hexagonal basis can be constructed if the *c*-axis is perpendicular to this $(111)_{\mathrm{z}\frown\mathrm{c}}$ plane. The right column in the figure illustrates this hexagonal description. Two twins which are linked to each other by a rotation of 60° around the *c*-axis are depicted. The respective stackings of atomic bilayers are ABC and ACB. Ga atoms are depicted as blue, As atoms as red spheres.

wurtzite stacking, are observed in the grown nanowires in $[111]_{\mathrm{z}\frown\mathrm{c}}$ direction, typically even within the same wire (see e.g. Ref. [25] for a short review). Understanding and controlling this polytypism is particularly important for advancing applications of nanowires, since it typically deteriorates electronic and optical properties of III/V nanowires [86, 97–100].

These two atomic arrangements are visualized in Figs. 1.5 (zinc blende) and 1.6 (wurtzite). In addition, Fig. 1.6 also contains an illustration of the $4H$-polytype which is structure that consists of 50% of zinc blende and 50% of wurtzite.

For better comparison of these atomic arrangements, it is useful to transform basis of the zinc blende structure such that the cubic $[111]_{\mathrm{z}\frown\mathrm{c}}$ direction corresponds to the $[00.2]_{\mathrm{w}\frown\mathrm{h2}}$

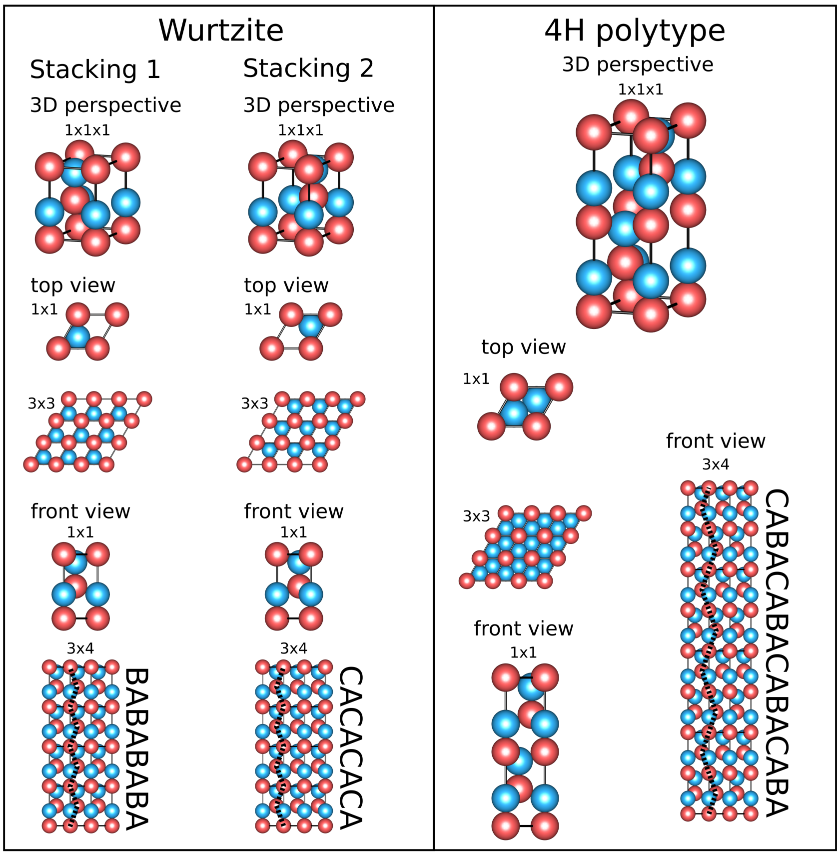

Figure 1.6.: Illustration of the crystal structure of GaAs for a hexagonality of 100% (wurtzite) and of 50% (4H polytype). In the left column the structure for a stacking sequence of AB and AC is depicted. The right column illustrates the 4H polytype: Its unit cell twice as high as the unit cell of wurtzite and is defined by the stacking *ABAC* (and equivalent). Ga atoms are depicted as blue, As atoms as red spheres.

direction in this transformed basis [101]. The planes perpendicular to the original, cubic $[111]_{\mathrm{z}\curvearrowright\mathrm{c}}$ direction contain either only Gallium (Ga) atoms or only Arsenic (As) atoms. In addition, these planes containing only one kind of atoms are alternating with the planes of the other atoms. Consequently, the primitive unit cell projected in $[111]_{\mathrm{z}\curvearrowright\mathrm{c}}$ direction consists of a set of one Ga plane next to one As plane. For simplicity, we refer to this set of two planes as a layer which consists of two sublayers. The crystal is then formed by periodic repetition of these layers in cubic $[111]_{\mathrm{z}\curvearrowright\mathrm{c}}$ direction but a shift perpendicular to this direction. For the wurtzite structure, two such layers with different in-plane positions are repeated in the stacking sequence. For the zinc blende structure, three such layers with different in-plane shifts are repeated.

For clarity, we distinguish coordinates with respect to the three involved crystallographic basis as

crystallographic basis vector	notation (example)
cubic basis of conventional zinc blende unit cell	$[111]_{\mathrm{z}\curvearrowright\mathrm{c}}$
hexagonal basis for zinc blende structure (c-axis $\parallel$ to $[111]_{\mathrm{z}\curvearrowright\mathrm{c}}$)	$[00.3]_{\mathrm{z}\curvearrowright\mathrm{h1}}$
hexagonal basis of wurtzite structure	$[00.2]_{\mathrm{w}\curvearrowright\mathrm{h2}}$

where the second letter in the index refers to the basis system and the first index to the crystalline structure which is described with this basis. The choice of basis vectors in this

cubic basis for zinc blende	$\begin{pmatrix} \boldsymbol{a_1} & \boldsymbol{a_2} & \boldsymbol{a_3} \end{pmatrix} = a_c \cdot \begin{pmatrix} 1 & 0 & 0 \\ 0 & 1 & 0 \\ 0 & 0 & 1 \end{pmatrix}$
hexagonal basis for zinc blende	$\begin{pmatrix} \boldsymbol{a_1} & \boldsymbol{a_2} & \boldsymbol{a_3} \end{pmatrix} = a_{h1} \cdot \begin{pmatrix} \frac{1}{2} & \frac{1}{2} & 0 \\ \frac{-\sqrt{3}}{2} & \frac{\sqrt{3}}{2} & 0 \\ 0 & 0 & \sqrt{6} \end{pmatrix}$
hexagonal basis for wurtzite	$\begin{pmatrix} \boldsymbol{a_1} & \boldsymbol{a_2} & \boldsymbol{a_3} \end{pmatrix} = a_{h1} \cdot \begin{pmatrix} \frac{1}{2} & \frac{1}{2} & 0 \\ \frac{-\sqrt{3}}{2} & \frac{\sqrt{3}}{2} & 0 \\ 0 & 0 & \sqrt{\frac{8}{3}}(1 + \frac{d_{\mathrm{WZ}}}{d_{\mathrm{ZB}}}) \end{pmatrix}$

Table 1.1.: Choice of crystallographic basis vectors for investigating polytypism in GaAs nanowires. $\frac{d_{\mathrm{WZ}}}{d_{\mathrm{ZB}}}$ is the ratio of the inter-layer spacing between wurtzite and zinc blende (see Sec. 3.2). a_c is the cubic lattice constant of GaAs which is equal to 5.6533Å [102]. Equivalent in-plane lattice parameters have been assumed.

structure	Ga atoms	As atoms
zinc blende in cubic basis c	$(\frac{1}{4} \quad \frac{1}{4} \quad \frac{1}{4})$	$(0 \quad 0 \quad 0)$
	$(\frac{3}{4} \quad \frac{3}{4} \quad \frac{1}{4})$	$(\frac{1}{2} \quad \frac{1}{2} \quad 0)$
	$(\frac{3}{4} \quad \frac{1}{4} \quad \frac{3}{4})$	$(\frac{1}{2} \quad 0 \quad \frac{1}{2})$
	$(\frac{1}{4} \quad \frac{3}{4} \quad \frac{3}{4})$	$(0 \quad \frac{1}{2} \quad \frac{1}{2})$
zinc blende in hexagonal basis h1	$(0 \quad 0 \quad \frac{1}{4})$	$(0 \quad 0 \quad 0)$
	$(\frac{2}{3} \quad \frac{1}{3} \quad \frac{7}{12})$	$(\frac{2}{3} \quad \frac{1}{3} \quad \frac{1}{3})$
	$(\frac{1}{3} \quad \frac{2}{3} \quad \frac{11}{12})$	$(\frac{1}{3} \quad \frac{2}{3} \quad \frac{2}{3})$
wurtzite in hexagonal basis h2	$(0 \quad 0 \quad \frac{3}{8})$	$(0 \quad 0 \quad 0)$
	$(\frac{2}{3} \quad \frac{1}{3} \quad \frac{7}{8})$	$(\frac{2}{3} \quad \frac{1}{3} \quad \frac{1}{2})$

Table 1.2.: Coordinates α_i of the Ga and As atoms $\boldsymbol{R} = \sum_{i=1}^{3} \alpha_i \boldsymbol{a_i}$ in each unit cell in various basis coordinate systems [101].

manuscript is given in Tab. 1.1. We point out, that $\frac{c_{h1}}{\sqrt{3}} = a_c = \sqrt{2}\, a_{h1}$. The coordinates α_i of the Ga and As atoms $\boldsymbol{R} = \sum_{i=1}^{3} \alpha_i \boldsymbol{a_i}$ in each unit cell in various basis coordinate systems are summarized in Tab. 1.2.

Finally, the distances in direct space of two planes $d_{hkl} = 2\pi / |\boldsymbol{G}_{hkl}|$ are given as [101, 103, 104]

$$d_{[hkl]_{\mathrm{z}\curvearrowright\mathrm{c}}} = a_c / \sqrt{h^2 + k^2 + l^2} \tag{1.27a}$$

$$d_{[hkl]_{\mathrm{w}\curvearrowright\mathrm{h2}}} = a_{h2} / \sqrt{\frac{4}{3}\left(h^2 + k^2 + hk\right) + \left(\frac{a_{h2}}{c_{h2}}\right)^2 l^2} \tag{1.27b}$$

where a_c is cubic lattice constant of the conventional unit cell and a_{h2} and c_{h2} are the magnitudes of the basis vectors in $[10.0]_{\mathrm{w}\curvearrowright\mathrm{h2}}$ and $[00.1]_{\mathrm{w}\curvearrowright\mathrm{h2}}$ direction respectively.

The Bravais-Miller indices [103, 104] of these basis representations are transformed by the matrices (see Ref. [101] and references therein)

$$\begin{pmatrix} h \\ k \\ l \end{pmatrix}_{\mathrm{z}\curvearrowright\mathrm{c}} = \mathcal{M}_{h1\leftarrow c} \begin{pmatrix} h \\ k \\ l \end{pmatrix}_{\mathrm{z}\curvearrowright\mathrm{h1}} \quad \text{with } \mathcal{M}_{h1\leftarrow c} = \begin{pmatrix} 2/3 & -2/3 & 1/3 \\ 2/3 & 4/3 & 1/3 \\ -4/3 & -2/3 & 1/3 \end{pmatrix} \tag{1.28a}$$

and

$$\begin{pmatrix} h \\ k \\ l \end{pmatrix}_{\mathrm{z}\curvearrowright\mathrm{h1}} = \mathcal{M}_{h1\leftarrow h2} \begin{pmatrix} h \\ k \\ l \end{pmatrix}_{\mathrm{w}\curvearrowright\mathrm{h2}} \quad \text{with } \mathcal{M}_{h1\leftarrow h2} = \begin{pmatrix} 1 & 0 & 0 \\ 0 & 1 & 0 \\ 0 & 0 & 3/2 \end{pmatrix} . \tag{1.28b}$$

Consequently, we have, for example, the equivalence of $(111)_{\mathrm{z}\curvearrowright\mathrm{c}} = (00.3)_{\mathrm{z}\curvearrowright\mathrm{h1}} = (00.2)_{\mathrm{w}\curvearrowright\mathrm{h2}}$.

We point out, that for zinc blende as well as for wurtzite, non-equivalent stacking sequences are obtained by rotations of 60° around the $(00.3)_{\mathrm{z}\curvearrowright\mathrm{h1}}$ direction ("twin structure"). A rotation by 120° maps the structure on itself. The reflections of such twin and symmetry related structures can be found in Sec. B in the appendix.

We would also like to mention that the wurtzite stacking is obtained if consecutive stacking faults after each layer of zinc blende are incorporated (and direct repetitions of the same layer are excluded), i.e., after AB a layer of type C would be expected. However, a stacking fault produces ABA. For zinc blende, now C is again expected. Another stacking fault would produce a layer of type B, and, thus, the wurtzite sacking sequence $ABAB$.

If only a single stacking fault occurs in a zinc blende sequence – as an example, consider the sequence $ABCABCACBACB$ – a single wurtzite layer is observed and the nanowire continues in the stacking of the equivalent twinned structure with respect to the previous structure (i.e., ACB instead of ABC). For low probability of (repeated) stacking faults, super-lattice structures with zinc-blende and twinned zinc blende can be constructed [22, 24, 25, 44, 56, 96].

Up to now, we illustrated the geometrical properties of the two polytypes in GaAs nanowires. These geometrical properties of the crystalline structures will be linked to X-ray scattering in Sec. 3.2.

Here, we now summarize the current understanding of the origin of this polytypism which has been studied extensively by various approaches (e.g. Refs. [55, 59, 105–107]) – theoretically and experimentally.

For example, Akiyama et al. estimated in Ref. [89] that wurtzite structure is stabilized for small diameters (depending on the nanowire's composition up to 22nm) as a results of different number of dangling surface bonds of wurtzite and zinc blende phase. For some intermediate range of diameter (depending in the ionicity of the involved semiconductors in the range of $12 - 32$nm), zinc blende and wurtzite phase can coexist in a single wire. From this perspective, the emergence of wurtzite structures in GaAs nanowires is a result of the increased ratio of surface to bulk – which is relevant for many nanostructures.

Similar observations have been reported by Magri et al. in Ref. [108]. These authors found a critical diameter of 6.3nm in first principle simulations: below this critical diameter the gain in surface energy for formation in wurtzite exceeds the costs in bulk volume for wurtzite formation and stable wurtzite nanowires are possible. However, such low critical radii are too low if compared with experimental data.

For comparison, the fraction of wurtzite in Au-assisted InAs nanowires as a function of their diameter has been studied experimentally by Johansson et al. in Ref. [109] where typical critical radii in the order of 35nm to 60nm have been observed – depending on the growth temperature.

In Ref. [105], Glas et al. attribute the growth of wurtzite segments in GaAs nanowires based on the energetics of the involved surface energies to nuclei forming close to the triple-phase-line, i.e., close to the surface of the nanowires (see also S5 in supporting information of Ref. [60]). For nuclei away from the triple-phase-line – deep inside the droplet – the layers which originate from such nuclei are likely to produce a zinc blende structures.

The precise behavior strongly depends on the involved facets [71, 107] which in return are coupled to shape and composition of the droplet [55, 57, 69, 105]. In particular, it is also of high importance if the droplet on the nanowire tip covers only the $[111]_{\mathrm{z}\curvearrowright\mathrm{c}}$ facet (regime 1 in Ref. [69]) or also wets the side facets (regime 2 in Ref. [69]). In the first case, zinc blende structures are favored whereas in the latter case, wurtzite arrangements are preferred.

In addition to wurtzite and zinc blende, other polytypes [110, 111] can also be considered: For example, Dubrovskii and Sibirev predict in Ref. [111] that the $4H$ polytype (see Fig. 1.6) has the lowest formation energy within their model. Such higher polytypes become particularly important if deviations from simple Markov models (see Sec. 4.3 and Refs. [24, 25, 110]) such as the axial next nearest neighbor interaction (ANNNI) model (see Ref. [110] and references therein) are investigated.

For examination of the intrinsic statistical properties of the nucleation process, the energy barriers E for creation of a nucleus for the next grown layer are of high relevance (e.g., in Boltzmann factors $\mathrm{e}^{-\beta E}$, where $\beta = 1/(k_\mathrm{B} T_\mathrm{S})$) [24, 59, 105]. More specifically, (at least) four nucleation barriers $E_{\mathrm{P}|\mathrm{P}}$ and $E_{\bar{\mathrm{P}}|\mathrm{P}}$ should be distinguished, where $\mathrm{P} \in \{\mathrm{ZB}, \mathrm{WZ}\}$ and $\bar{\mathrm{P}}$ is the complementary phase of P. Here, $E_{\mathrm{P}|\mathrm{P}}$ and $E_{\bar{\mathrm{P}}|\mathrm{P}}$ correspond to continuing growth of the current phase $\mathrm{P} \in \{\mathrm{ZB}, \mathrm{WZ}\}$ or for beginning a segment of the complementary phase $\bar{\mathrm{P}}$ on top of the current phase P respectively.

On the one hand, their absolute values are of particular interest for the growth rate (number of layers grown per unit of time) of the nanowire [79, 88].

On the other hand, the nucleation barrier *differences* $\delta E_{\bar{\mathrm{P}}|\mathrm{P}} = E_{\bar{\mathrm{P}}|\mathrm{P}} - E_{\mathrm{P}|\mathrm{P}}$ determine the polytypic behavior [24, 59, 96, 105]. If the nucleation barrier differences $\delta E_{\bar{\mathrm{P}}|\mathrm{P}}$ significantly exceed the thermal energy scale $k_\mathrm{B} T_\mathrm{S}$, transitions from one polytype to the other polytype are very unlikely – with the result of wires with low stacking fault density in growth direction.

On the contrary, the frequent observation of polytypism in III-V nanowires implies, that $\delta E_{\bar{\mathrm{P}}|\mathrm{P}} \gtrsim \mathrm{k}_\mathrm{B} T_\mathrm{Growth}$ for typical growth conditions.

The nucleation barrier differences $\delta E_{\bar{\mathrm{P}}|\mathrm{P}}$ will be estimated by means of *in-situ* X-ray diffraction for self-catalyzed GaAs nanowires on Si(111) in Sec. 4.4.2 – without explicit assumptions on the geometry of the nucleus, the exact mechanisms of nucleation and the catalyst dynamics (see in particular Refs. [25, 45, 49, 59, 60, 69, 70, 74, 77, 88, 96, 105, 106]).

In conclusion, considerable theoretical and experimental efforts aim at understanding and controlling polytypism in order to facilitate phase engineering in nanowires.

We now turn to experimental aspects which are relevant for the investigation of polytypism: we first motivate studying the growth of nanowires *in-situ* and in a time-resolved manner with X-ray diffraction based methods (see e.g. Ref. [54]) and then discuss the possibilities (and limitations) of the portable MBE growth chamber of the synchrotron source ANKA for such X-ray measurements.

2. The portable molecular beam epitaxy (PMBE) growth chamber at ANKA

Up to now, the fundamentals of the growth of nanowires have been discussed. We now motivate time-resolved *in-situ* X-ray diffraction as a valuable approach in order to provide additional insights in the growth dynamics of nanowires — despite great results and advances obtained with other techniques (see Sec. 2.1). We then discuss in Sec. 2.2 the feasible X-ray measurements with the current PMBE growth chamber for GaAs nanostructures located at the German synchrotron source ANKA.

2.1. Motivation for time-resolved X-ray growth studies

To motivate time-resolved *in-situ* X-ray diffraction studies, we first provide a rough overview over the various experimental techniques which are currently employed for understanding the physics of nanowire growth.

One very powerful experimental technique for accessing the dynamics of nanowire growth is environmental transmission electron microscopy (eTEM). By eTEM, a lot of insights in the dynamics of the nucleation of a new layer and the composition and geometry of the droplet on the tip of a growing nanowire have been revealed [70, 74, 77, 95]. However, transmission electron microscopy (TEM) – including eTEM – directly images the direct space structures of a rather limited field of view. If the crystalline arrangement (zinc blende or wurtzite) is the aim of the investigation, atomic resolution is required and, thus, only a limited number of objects or even only a fraction of a single objected can be investigated.

Scanning electron microscopy (SEM) does not provide sufficient resolution for investigation of the crystalline arrangement on an atomic level. However, it is extremely valuable for studying geometrical aspects of nanowire growth – from the geometry of the droplet to the crystallographic surfaces on the side facets as well as correlating the growth rates and diameters of nanostructures with the growth conditions.

In addition, reflection high energy electron diffraction (RHEED) is well established for time-resolved *in-situ* monitoring of the growth of nanostructures. Since the wavelength of the impinging electrons is of similar order of magnitude as the interplanar spacings of the growing nanostructures, RHEED is capable of revealing information on the types of growing nanostructures (wires, dots, layers) and the growing phases. However, typically, data quality of RHEED is rather poor and, therefore, a quantitative analysis rather difficult. Moreover, it is limited to studying few atomic layers below the surface of the grown material. Thus, buried structures cannot be studied.

Another powerful technique for studying grown nanostructures is photoluminesence. However, photoluminesce typically requires to measure the nanostructures at low temperatures in order to avoid thermal broadening and obtain sharp spectra. Thus, such photoluminesce measurements are incompatible with the substrate temperatures of the nanostructures during growth (typically several hundred Kelvin). In consequence, such measurements are not well suited for time-resolved *in-situ* investigations.

We will not discuss techniques based on electronic transport or probe based microscopy (e.g., atomic force microscopy, scanning tunneling microscopy, ...), although these approaches are also capable of providing very valueable insights in the behavior of nanostructures [97, 112–116]. Most importantly, most of these techniques can also be applied *in-situ* or *in-operando* (e.g., Refs. [116, 117]). However, such techniques typically study only a limited number of objects (as TEM) and, thus, are of limited statistical significance.

Finally, the interaction of photons with matter at wavelengths similar to the interatomic spacings is highly suitable for investigation of the structural properties (see Ref. [54] for an example of *in-situ* X-ray measurements). By this approach, it is possible to resolve correlations in the growing nanostructures. For crystalline structures, experiments exploiting diffraction by particular planes can be performed. Some reflections only contain scattered photons from one polytype in the III-V nanowires whereas scattered photons from both polytypes contribute to other reflections. In contrast to RHEED, very fine details of the diffracted signal can be observed with X-ray investigations due to the long propagation distances from the sample to the detector and the high quality of the impinging beam at current synchrotron facilities. Therefore, the investigation of polytypism in nanowires based on X-ray diffraction is highly interesting.

Since the lattice constant in polytypic III-V nanowires typically depends on the local phase in nanowires [92, 118, 119], the reflections which contain scattered photons from both phases are particularly promising for time-resolved *in-situ* investigations. The difference in lattice constants results in slightly different positions of the signal of the pure phases involved in the polytypic nanowires. On the one hand, the distance of the centers might allow splitting of the contributions from the polytypic phases. On the other hand, the signals are still close enough that capturing the information of both phases with modern two-dimensional detectors such as the PILATUS 100K-S [120] should be possible with little or no movement of the detector and the sample during the time-resolved growth studies.[1]

Depending on the properties of the beam, X-ray diffraction experiments with high statistical significance [54, 101, 119, 121, 122] as well as single wire experiments [101, 123] are feasible. In both cases, the changes in the scattered intensity distribution over time in time-resolved *in-situ* growth studies reveal the evolution of the properties of the nanowires with increasing growth time. Details will be discussed in Sec. 4.3.

In the first part of this manuscript we focus on X-ray measurements of a huge ensemble of nanowires. For example, we are able to measure the scattering of 10^6 nanowires, if we assume a spot size of 1mm^2 of the X-ray beam and a density of only a single wire per $1\mu\text{m}^2$. This high statistical significance will facilitate the detection of a gradient in the phase purity L_{P} in growth direction of the nanowires in a range that is currently not accessible by other methods and despite huge fluctuations of the length of individual phase segments.

---

[1] Based on the results of Sec. 2.2, it is straight forward to measure even a series of polytype specific reflections during growth in the current PMBE chamber with no movement of a current 2D detector (e.g. PILATUS 100K-S [120]) and very little movement of the sample only (see outlook of part I).

Suppose randomly distributed independent size of each *individual* faultless phase segment in the nanowires. Moreover, assume the standard deviation of the size distribution to be similar to its mean value μ. These assumptions resembles the behavior of some models discussed in Sec. 4.3. In this case, the error σ of the mean value scales as $\mu/\sqrt{N}$ where N is the number of segments in the estimation of the mean value. Therefore, estimation of the mean value μ with a relative error of 10% requires evaluation of $N = 100$ segments. If the wire has 6500 layers (approximately two microns in height), a single wire is only sufficient if the mean segment size is below 65 layers. For larger mean segment size, multiple wires need to be evaluated.

Further assume that the mean segment size changes with increasing height: For estimation of the mean gradient, it is necessary to estimate the mean segment size at the beginning of the wire and at the end of the wire with a precision higher than the mean value. For that purpose, we define ranges with width w for estimation of the mean layer size at the beginning (μ_B) and the end (μ_E) of growth, for example the ranges 0–1000 and 5500–6500 for $w = 1000$ and wires with a height of 6500 layers. Moreover, we assume a gradient $\delta\sigma = |\mu_B - \mu_E|$ between the two ranges. In order to resolve this gradient, the mean values μ_B and μ_E need to be estimated with a precision much better than this gradient $\delta\sigma$. Therefore, the error σ of the mean value must fulfill

$$\mu_{B/E}/\sqrt{N} = \sigma \overset{!}{\ll} \delta\sigma \ , \tag{2.1}$$

which implies for the number of individual segments N that need to be evaluated

$$N \gg \left(\mu_{B/E}/\delta\sigma\right)^2 \ . \tag{2.2}$$

However, if consider our ranges of width w, this number of individual faultless segments N is approximately equal to $(w/\mu_{B/E}) \cdot \mathrm{N_W}$ where $\mathrm{N_W}$ is the number of measured wires. Therefore,

$$\mathrm{N_W} w \gg \mu_{B/E} \cdot \left(\mu_{B/E}/\delta\sigma\right)^2 \ , \tag{2.3}$$

i.e., the expectation value divided by the square of the relative deviation $\delta\sigma/\mu_{B/E}$. For our example $w = 1000$, $\mu_{B/E} \approx 50$ layer and a relative deviation of $\delta\sigma/\mu_{B/E} \approx 0.1$, we have $\mathrm{N_W} \gg 5$. However, a study of $\mathrm{N_W} \approx 50 - 500$ with TEM for each set of “interesting” growth conditions is non-feasible. If we restrict to $\mathrm{N_W} = 1$ and solve for the relative deviation, we are only capable of detecting a relative deviation of $\delta\sigma/\mu_{B/E} \gg 22\%$.

In conclusion, the detection of the mean segment size and small gradients thereof are not feasible with TEM studies for large mean values μ. On the contrary, X-ray diffraction based studies are very promising for overcoming these limitations: time-resolved *in-situ* measurements of an ensemble of nanowires can detect large mean segment sizes and the gradient thereof as will be discussed in the next sections. In fact, the larger the mean segment lengths of the polytypes are, the more powerful are diffraction techniques which operate in reciprocal space (in contrast to direct space as TEM).

Since diffraction detects the grown *crystalline* structures, this approach is complementary to modeling or studying the droplet directly. Instead, the consequences of the complicated dynamics of the droplet and the nucleus on the growing crystalline material of the nanostructure are observed. This complicated interplay of the crystalline wire and the droplet determines the energetic nucleation barriers $E_{\mathrm{P|P}}$ and $E_{\mathrm{\bar{P}|P}}$ for continuing the growth of phase $\mathrm{P} \in \{\mathrm{ZB}, \mathrm{WZ}\}$ or for beginning a segment of the complementary phase $\bar{\mathrm{P}}$ on top of the current phase P (see Sec. 1.4).

In Sec. 4.4.2, we will infer these nucleation barrier differences $\delta E_{\mathrm{\bar{P}|P}}$ and the temporal evolution thereof based on a model for the length distribution of faultless segments of each polytype (“phase purity”).

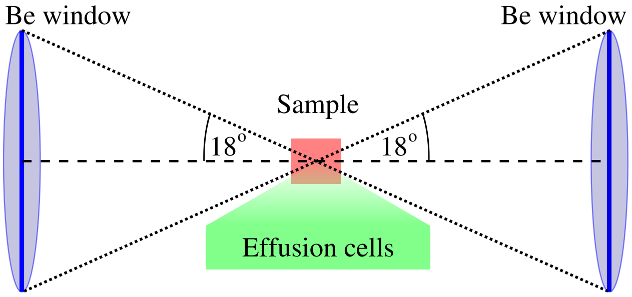

Figure 2.1.: Scheme of the *in-situ* MBE growth chamber: The Beryllium windows limit the angle with respect to the axis defined by the center of both Beryllium windows to 18° (if a proper safety margin is included). For more information, see Refs. [67, 124, 126, 127].

However, obtaining such data *during growth* (instead of post-growth *ex-situ* measurements) requires special growth equipment: On the one hand, it must have windows which are transparent for the incident and scattered X-ray beam. On the other hand, it must allow for proper orientation of the sample and the detector with respect to the incident beam.

One such special growth chamber — suitable for time-resolved *in-situ* X-ray diffraction during molecular beam epitaxy (MBE) growth of GaAs structures — has been developed at the synchrotron source ANKA [124, 125] (see Fig. 4.1(a) on page 50). For a description of the chamber, in particular its *growth* capabilities, we refer the reader to Refs. [67, 124, 126, 127]. For example, the chamber has been used to successfully investigate buried quantum dots (QDs) using grazing incidence X-ray diffraction (GID) [125].

The calibration of the growth chamber for growth of self-catalzed GaAs nanowires on $[111]_{z\frown c}$ oriented silicon substrates has been performed by Philipp Schroth and Jean-Wolfgang Hornung with strong support of the Paul-Drude-Institut für Festkörperphysik in Berlin.[2]

2.2. Possibilities and limitations of the PMBE chamber

We now provide a detailed discussion on the possibilities and limitations of this growth chamber [67, 124, 126, 127] with respect to X-ray diffraction based *in-situ* investigations of GaAs structures on $[111]_{z\frown c}$ oriented silicon substrates.

This growth chamber has been specifically designed for monitoring the growth of nanostructures *in-situ* with X-rays. For this purpose two Beryllium (Be) windows are positioned directly opposite to each other. The axis which is defined by the centers of the Be windows is tangential to the surface of the substrate for growth. As a result, the solid angle of X-ray radiation entering or leaving the chamber through the Be windows is limited to a maximum of approximately $\Theta_{\text{In}}^{(\text{Max})} = \Theta_{\text{Out}}^{(\text{Max})} \approx 18^\circ$ (if a safety margin of 2.4° is included with respect to the specification which states 20.4° [128]) with respect to the afore-mentioned axis (see Fig. 2.1). In addition to the limitations imposed by the Be windows, the growth chamber needs to be positioned and rotated during measurements by a suitable set-up. Although fixed constructions for particular Bragg reflections are in principle possible, the highest flexibility in positioning is provided by a suitable heavy load diffractometer. However, the limitations of such a heavy load diffractometer could impose additional restrictions on the set of possible X-ray measurements, in particular the set of available Bragg reflections.[3]

---

[2] For more information on this calibration of the chamber, we refer the reader to the PhD thesis of Philipp Schroth [67] and the diploma thesis of Jean-Wolfgang Hornung [126].

[3] Additional limitations may originate in collisions with detector arms of the diffractometer and the chamber. However, such limitations are not discussed in this manuscript.

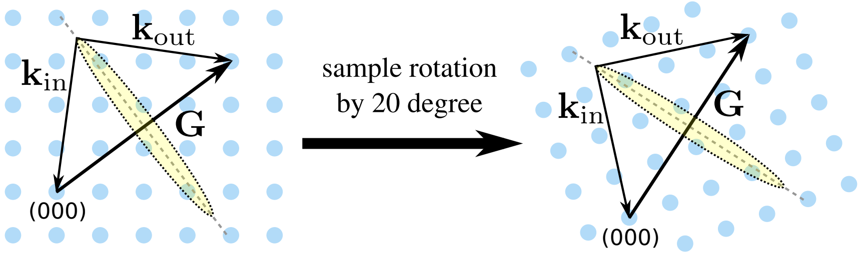

Figure 2.2.: Illustration of energy and momentum conservation for scattering by crystalline structures: For a momentum transfer $\boldsymbol{G}$ of the reciprocal lattice, a one dimensional, circular manifold of solutions with $\|\boldsymbol{k}_{\text{Out}}\|_2 = \|\boldsymbol{k}_{\text{In}}\|_2$ exists.

First, we discuss the relation between the geometry in direct space and a particular Bragg reflection in reciprocal space. Then, we give a list of measurable reflections of cubic and wurtzite GaAs at an energy of 15keV in the current growth chamber.[4] Our presentation includes three cases: First, the full solid angle in Fig. 2.1 can be used, i.e., no limitations are imposed by the diffractometer. Second, we assume limitations of the heavy load diffractometer similar to the conditions at the NANO beamline at ANKA. Finally, we consider the case of an increased angle $\Theta_{\text{In}}^{(\text{Max})} = \Theta_{\text{Out}}^{(\text{Max})} \approx 28°$ and without restrictions originating from the diffractometer. The last case corresponds to a (hypothetical) chamber after an upgrade planned for the future.

Physically, energy conservation and momentum conservation constrain the interaction of the X-ray photons and matter. For elastic scattering, the magnitude of the incoming and outgoing wave vector $\boldsymbol{k}_{\text{In}}$ and $\boldsymbol{k}_{\text{Out}}$ are equal. This magnitude is determined by the energy E of the incoming radiation as

$$\|\boldsymbol{k}_{\text{Out}}\|_2 = \|\boldsymbol{k}_{\text{In}}\|_2 = \frac{2\pi}{\lambda} = \frac{E}{\hbar c} , \tag{2.4}$$

where $\hbar$ is the Planck constant divided by 2π and c is the vacuum speed of light. For an ideal, infinite crystal the momentum transfer $\boldsymbol{k}_{\text{Out}} - \boldsymbol{k}_{\text{In}}$ is limited to the set of reciprocal lattice vectors $\boldsymbol{G}$ which are defined by the crystal structure. The result of those constraints is a circular set of solutions for each vector $\boldsymbol{G}$ (see Fig. 2.2). The center of this circular set of solutions is $\boldsymbol{G}/2$ and the radius of the circle is

$$r_0 = \sqrt{\|\boldsymbol{k}_{\text{In}}\|_2^2 - \|\boldsymbol{G}/2\|_2^2} \tag{2.5}$$

which is only real if

$$\|\boldsymbol{k}_{\text{In}}\|_2 \geq \|\boldsymbol{G}/2\|_2 \quad \Leftrightarrow \quad E \geq \hbar c \,\|\boldsymbol{G}/2\|_2 \ . \tag{2.6}$$

Thus, $\hbar c \,\|\boldsymbol{G}/2\|_2$ is the minimum energy required for measuring the Bragg reflection $\boldsymbol{G}$.

The set of possible vectors $\boldsymbol{k}_{\text{In}}$ and $\boldsymbol{k}_{\text{Out}}$ is characterized by the parametrization

$$\boldsymbol{k}_{\text{In}}(\eta) = r_0\big(\cos(\eta)\,\hat{\mathbf{e}}_1 + \sin(\eta)\,\hat{\mathbf{e}}_2\big) - \frac{\boldsymbol{G}}{2} , \tag{2.7a}$$

$$\boldsymbol{k}_{\text{Out}}(\eta) = r_0\big(\cos(\eta)\,\hat{\mathbf{e}}_1 + \sin(\eta)\,\hat{\mathbf{e}}_2\big) + \frac{\boldsymbol{G}}{2} , \tag{2.7b}$$

where $\hat{\mathbf{e}}_1$ and $\hat{\mathbf{e}}_2$ are two orthonormal vectors perpendicular to $\boldsymbol{G}$ and $\eta \in [0, 2\pi[$.

---

[4] We will not include reflections in this list for which the incoming and exit beam pass through the same Be window since those reflections are associated with high Bragg indices and, thus, typically weak in intensity and, therefore, of minor importance.

Suitable vectors $\hat{\mathbf{e}}_1$ and $\hat{\mathbf{e}}_2$ can be obtained either numerically by Gram-Schmidt process [129, 130] or analytically. For example, one such analytical parametrization, which will be used later, is given by

$$\hat{\mathbf{e}}_1 = \frac{1}{G_r} \begin{pmatrix} G_y \\ -G_x \\ 0 \end{pmatrix} \quad , \quad G_r = \sqrt{G_x^2 + G_y^2} \ , \tag{2.8a}$$

$$\hat{\mathbf{e}}_2 = \frac{1}{G \cdot G_r} \boldsymbol{G} \otimes \hat{\mathbf{e}}_1 = \frac{1}{G \cdot G_r} \begin{pmatrix} G_x G_z \\ G_z G_y \\ -G_r^2 \end{pmatrix} \quad , \quad G = \|\boldsymbol{G}\|_2 = \sqrt{G_r^2 + G_z^2} \ . \tag{2.8b}$$

The motivation for this particular parametrization is given by the fact that the third component of $\hat{\mathbf{e}}_1$ is equal to zero which simplifies a variety of calculations (see later).

Since valid vectors

$$\boldsymbol{G} = \sum_{i=1}^{3} n_i \boldsymbol{b}_i \tag{2.9}$$

are linked to the lattice in direct space – constituted by $\mathbf{a}_i$ – via

$$\begin{pmatrix} \boldsymbol{b}_1 & \boldsymbol{b}_2 & \boldsymbol{b}_3 \end{pmatrix}^T = 2\pi \begin{pmatrix} \mathbf{a}_1 & \mathbf{a}_2 & \mathbf{a}_3 \end{pmatrix}^{-1} , \tag{2.10}$$

a particular orientation of this direct space lattice and a fixed reflection $(n_1\, n_2\, n_3)_{\mathrm{z} \curvearrowright \mathrm{c}}$ is associated with the compact one-dimensional manifold (2.7) of solutions $(\boldsymbol{k}_{\mathrm{In}}, \boldsymbol{k}_{\mathrm{Out}})$. Any such $\boldsymbol{k}_{\mathrm{In}}$ can be chosen for investigation of this reflection $(n_1\, n_2\, n_3)_{\mathrm{z} \curvearrowright \mathrm{c}}$ and will result in an outgoing beam characterized by the respective $\boldsymbol{k}_{\mathrm{Out}}$ (i.e., same η).

By rotating the sample, its crystallographic axis $\mathbf{a}_i$ are rotated. As a result, the reciprocal basis vectors $\boldsymbol{b}_i$ and thereby the reciprocal lattice are rotated, too. $\hat{\mathbf{e}}_1$ and $\hat{\mathbf{e}}_2$ remain perpendicular to $\boldsymbol{G}$, if they are transformed in the same way as the reciprocal basis vector. Therefore, $\boldsymbol{k}_{\mathrm{In}}$ and $\boldsymbol{k}_{\mathrm{Out}}$ transform identically to the reciprocal basis vectors. The magnitudes of neither $\boldsymbol{G}$ nor $\boldsymbol{k}_{\mathrm{In}}$ or $\boldsymbol{k}_{\mathrm{Out}}$ are modified by such isometric transformations. Moreover, their relative angles are invariant upon isometric transforms. One such angle is the Bragg angle of a particular reflection $(n_1\, n_2\, n_3)_{\mathrm{z} \curvearrowright \mathrm{c}}$: it is defined as

$$\cos\left(2\Theta_{\mathrm{Bragg}}^{n_1 n_2 n_3}\right) = \frac{\boldsymbol{k}_{\mathrm{In}} \cdot \boldsymbol{k}_{\mathrm{Out}}}{\|\boldsymbol{k}_{\mathrm{In}}\|_2 \, \|\boldsymbol{k}_{\mathrm{Out}}\|_2} \ , \tag{2.11}$$

and does not depend on the orientation of the sample.

However, depending on the set-up, the orientation of the crystallographic axis $\mathbf{a}_i$ of the sample is limited: For example, substrates mounted inside the PMBE chamber can only be rotated around its surface normal (without moving the chamber as a whole). This restriction of the orientation of the sample must be included in the consideration if a particular reflection can be measured with the PMBE growth chamber.

Additionally, rotations of the chamber itself are typically limited — due to various reasons: one important aspect is that the heavy load diffractometer at the NANO beamline at ANKA is capable of inclining the growth chamber only by $\Psi_{\mathrm{In}}^{(\mathrm{Max})} \approx 5°$. Therefore, the beam cannot enter the growth chamber in the full solid angle of the Be windows, but only through a limited fraction of the surface of the respective Be window. On the contrary, we assume that the detector can be moved freely to all positions resulting from the full solid angle of the exit Be window. Thus, the constraints on $\boldsymbol{k}_{\mathrm{In}}$ and $\boldsymbol{k}_{\mathrm{Out}}$ are no longer identical.

From those considerations, it is reasonable to introduce the following set of orthonormal right-handed coordinate systems:

1. *chamber system*: This coordinate system is defined such that the first basis vector connects the centers of both Be windows (positive direction in direction of outgoing Be window) and the third basis vector points in direction of the surface normal of the substrate.
2. *sample surface system*: The third basis vector points in direction of the surface normal of the substrate. However, the other two directions are not constrained (beside being orthonormal right-handed). Therefore, it is only unique up to an arbitrary rotation around the surface normal.
3. *crystallographic basis* $\mathbf{a}_i$: This basis is defined by the conventional unit cell.

Note, that the chamber system and the sample surface system coincide up to a rotation around the surface normal of the substrate.[5] Typically, the crystalline surface of Si substrates is either $[111]_{\mathrm{z}\curvearrowright\mathrm{c}}$ or $[001]_{\mathrm{z}\curvearrowright\mathrm{c}}$. Here, we restrict to $[111]_{\mathrm{z}\curvearrowright\mathrm{c}}$ oriented substrates.

For calculation of the feasibility to study a particular (hexagonal or cubic) reflection $(n_1\, n_2\, n_3)_{\mathrm{z}\curvearrowright\mathrm{c}}$, we perform the following approach:

1. Crystalline basis:
    - Calculate $\boldsymbol{G}$ and r_0.
    - Calculate the set of solutions $(\boldsymbol{k}_{\mathrm{In}}(\eta), \boldsymbol{k}_{\mathrm{Out}}(\eta))$ for a step width $\eta \lesssim 1°$.
2. Transform to sample surface basis:[6] [7]
    - Verify for each solution $(\boldsymbol{k}_{\mathrm{In}}(\eta), \boldsymbol{k}_{\mathrm{Out}}(\eta))$ that it corresponds to Bragg geometry (i.e., incoming and outgoing beam leave the sample). Drop otherwise. Determine the incidence angle α_{In} and exit angle α_{Out} with respect to the sample surface (not surface normal).
    - Additional constraints such as specific ranges for the incidence angle (e.g. $0.1° \leq \alpha_{\mathrm{In}} \leq 1.0°$ for grazing incidence) can also be used for filtering at this point.
    - For each solution $(\boldsymbol{k}_{\mathrm{In}}(\eta), \boldsymbol{k}_{\mathrm{Out}}(\eta))$, determine the out-of-plane scattering angle ϕ_{oop} by projecting out the third coordinate of both vectors and calculation of the angle between the resulting two vectors. For coplanar scattering, this angle is zero.

---

[5] As long as the first vector of the chamber coordinate system is parallel to the surface of the sample, the prescription can be simplified and the chamber system and sample surface system can be merged. However, we intend to describe the prescription in a more general manner.

[6] It is valid to choose any of the non-uniquely defined orthonormal right-handed basis but it must be kept during the procedure.

[7] For the transformation of a vector $\boldsymbol{v}$ from an orthonormal basis $\boldsymbol{a}_i$ to any other (not necessarily orthonormal) basis $\boldsymbol{b}_k$, we have

$$\boldsymbol{v} = \sum_{i=1}^{d} \boldsymbol{a}_i \alpha_i = \sum_{i=1}^{d} \sum_{j=1}^{d} \boldsymbol{a}_j \delta_{ji} \alpha_i = \sum_{i=1}^{d} \sum_{j=1}^{d} \sum_{k=1}^{d} \boldsymbol{a}_j \left(M\right)_{jk} \left(M^{-1}\right)_{ki} \alpha_i \equiv \sum_{k=1}^{d} \boldsymbol{b}_k \beta_k \ , \tag{2.12}$$

where we defined

$$\boldsymbol{b}_k = \sum_{j=1}^{d} \boldsymbol{a}_j \left(M\right)_{jk} \quad , \quad \beta_k = \sum_{i=1}^{d} \left(M^{-1}\right)_{ki} \alpha_i \ . \tag{2.13}$$

The entries of the matrix M underlying the coordinate transformation can be extracted directly from Eq. (2.13) by projection on $\boldsymbol{a}_i$ which yields

$$\left(M\right)_{ik} = \boldsymbol{a}_i \cdot \boldsymbol{b}_k \ . \tag{2.14}$$

We emphasize that the transformation of the components α_i has to be performed with the inverse of the matrix M.

3. For each solution $(\boldsymbol{k}_{\text{In}}(\eta), \boldsymbol{k}_{\text{Out}}(\eta))$ which has not been dropped, all possible orientations of the sample need to be considered. For that purpose, each solution $(\boldsymbol{k}_{\text{In}}(\eta), \boldsymbol{k}_{\text{Out}}(\eta))$ must be transformed to each sample orientation. In the PMBE chamber, only the rotation around the surface normal (1 degree of freedom) has to be considered and the set of possible orientations can be sampled uniformly without significant computational effort.[8]

4. Transform each orientation of each solution $(\boldsymbol{k}_{\text{In}}(\eta), \boldsymbol{k}_{\text{Out}}(\eta))$ to chamber coordinates which are most suited for evaluation of the restrictions implied by the chamber. For that purpose, $\boldsymbol{k}_{\text{In}}$ and $\boldsymbol{k}_{\text{Out}}$ are parametrized as

$$\begin{aligned} \boldsymbol{k}_{\text{In}}(1) &= k \cdot \cos(\Theta_{\text{In}}) & \boldsymbol{k}_{\text{Out}}(1) &= k \cdot \cos(\Theta_{\text{Out}}) \\ \boldsymbol{k}_{\text{In}}(2) &= -k \cdot \sin(\Psi_{\text{In}}) & \boldsymbol{k}_{\text{Out}}(2) &= k \cdot \sin(\Psi_{\text{Out}}) \\ \boldsymbol{k}_{\text{In}}(3) &= -k \cdot \sin(\Omega_{\text{In}}) & \boldsymbol{k}_{\text{Out}}(3) &= k \cdot \sin(\Omega_{\text{Out}}) \end{aligned}$$

   and where $k = \|\boldsymbol{k}_{\text{In}}\|_2 = \|\boldsymbol{k}_{\text{Out}}\|_2$. These angles $(\Theta_{\text{In}}, \Psi_{\text{In}}, \Omega_{\text{In}})$ and $(\Theta_{\text{Out}}, \Psi_{\text{Out}}, \Omega_{\text{Out}})$ relate the directions of the incoming and outgoing beam to deviations from the coordinate axis of the chamber coordinate system. Thus, a large set of constraints is easily evaluated.[9] For example:

   - For a given distance of the Be windows to the sample and their diameters, the mathematical constraints are $\Theta_{\text{In}} \leq \Theta_{\text{In}}^{(\text{Max})}$ and $\Theta_{\text{Out}} \leq \Theta_{\text{Out}}^{(\text{Max})}$. For the current chamber we have $\Theta_{\text{In}}^{(\text{Max})} = \Theta_{\text{Out}}^{(\text{Max})} = 18°$ as already stated.
   - The inclination of the chamber can be constrained by $\Psi_{\text{In}} \leq \Psi_{\text{In}}^{(\text{Max})}$.

With this procedure, we can detect if a given reflection can be studied with the chamber (including possibly desired additional constraints as restrictions of the incidence angle) and extract information about the specific geometry which has to be set in the experiment.

Some results of this procedure are summarized in Fig. 2.3 and Tabs. 2.1 (zinc blende) and 2.2 (wurtzite) for an X-ray energy of 15keV.

In Fig. 2.3, the ordinate is the scattering component parallel to the surface normal of the sample. The axis of abscissae is the magnitude of the scattering vector component which is perpendicular to this normal. For this choice of coordinates, the information about the rotation of the sample around its normal is projected out, but the data can be visualized nicely as a two-dimensional plot.

All cases mentioned in the beginning of this section are depicted in this figure: For Be windows which limit $\Theta_{\text{In}}^{(\text{Max})}$ and $\Theta_{\text{Out}}^{(\text{Max})}$ to 28°, an enormous number of reflections can be measured. If $\Theta_{\text{In}}^{(\text{Max})}$ and $\Theta_{\text{Out}}^{(\text{Max})}$ is limited to 18°, it is still possible to find all kind of reflections: phase selective and quasi-forbidden reflections are available as well as reflection to which all structures (zinc blende, zinc blende twin, wurtzite) contribute. If the inclination of the chamber is limited, the maximum scattering vector component perpendicular to the sample surface is reduced. However, even for those strong experimental constraints, a large set of reflections with different properties can be studied at the chosen X-ray energy of 15keV. A detailed list can be found in Tab. 2.1 for zinc blende and Tab. 2.2 for wurtzite. If the inclination of the chamber is not restricted, the respective tables can be found in appendix C. We point out that GID reflections are not contained in those tables: since we neglect refraction in our considerations, either the incident or exit angle are slightly

---

[8] For a set-up with a high number of degrees of freedom, Monte-Carlo based sampling or more advanced sampling strategies may be needed.

[9] Note that due to the limitations in orienting the sample in the current PMBE growth chamber, it holds $\alpha_{\text{In}} = \Omega_{\text{In}}$ and $\alpha_{\text{Out}} = \Omega_{\text{Out}}$.

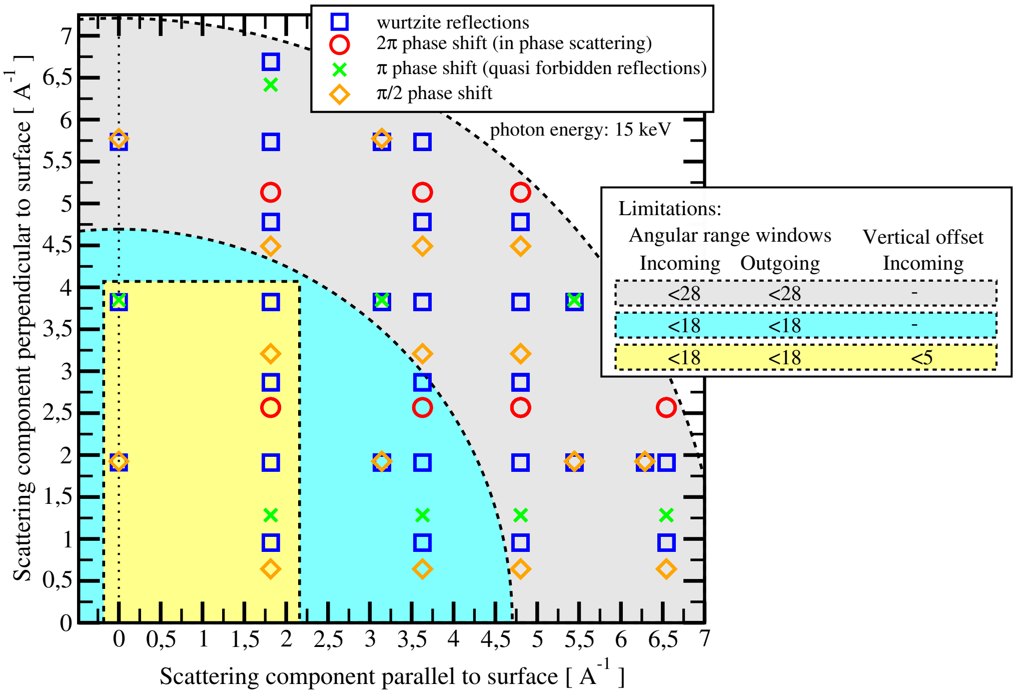

Figure 2.3.: Available Bragg reflections with the *in-situ* MBE growth chamber for a X-ray energy of 15keV: The limitation in angular space to $\Theta_{\mathrm{In}}^{(\mathrm{Max})} = \Theta_{\mathrm{Out}}^{(\mathrm{Max})} = 28°$ corresponds to a hypothetical upgraded chamber with larger Beryllium windows. The constraint of angular space to $\Theta_{\mathrm{In}}^{(\mathrm{Max})} = \Theta_{\mathrm{Out}}^{(\mathrm{Max})} = 18°$ corresponds to the currently available growth chamber (after subtraction of a proper safety margin). If the current chamber is mounted at the current heavy load diffractometer at NANO beamline at ANKA, restrictions in the diffractometer motors imply to limit the vertical offset to approximately $\Psi_{\mathrm{In}}^{(\mathrm{Max})} \approx 5°$. For more information, see main text, Tabs. 2.2 and 2.1), Sec. C in the appendix and the relevant discussions in Refs. [67, 124, 126, 127].

smaller than zero as a consequence of numerical rounding errors. As a consequence, these reflections are discarded when validating Bragg geometry.

In addition, the square of the magnitude of the structure factors $|\mathcal{S}|^2$ for the reflections given in these tables is listed (see, for example, Ref. [101]). For a cubic lattice, the structure factor of the reflection $(hkl)_{\mathrm{z}\frown\mathrm{c}}$ is

$$\mathcal{S}_{(hkl)_{\mathrm{z}\frown\mathrm{c}}} = 4 \cdot \begin{cases} f_{\mathrm{As}} + f_{\mathrm{Ga}} & \text{if } h,\ k,\ l \text{ even and } h+k+l = 4n \text{ with } n \in \mathbb{Z} \\ f_{\mathrm{As}} - f_{\mathrm{Ga}} & \text{if } h,\ k,\ l \text{ even and } h+k+l \neq 4n \text{ with } n \in \mathbb{Z} \\ f_{\mathrm{As}} \pm \mathrm{i} f_{\mathrm{Ga}} & \text{if } h,\ k,\ l \text{ odd} \\ 0 & \text{else} \end{cases} \tag{2.16}$$

whereas for the wurtzite reflection $(hk.l)_{\mathrm{w}\frown\mathrm{h2}}$, the structure factor is

$$\mathcal{S}_{(hkl)_{\mathrm{w}\frown\mathrm{h2}}} = f_{\mathrm{As}} \cdot \left(1 + \mathrm{e}^{-2\pi i\left(\frac{h+2k}{3}+\frac{l}{2}\right)}\right) + f_{\mathrm{Ga}} \cdot \left(\mathrm{e}^{-2\pi i\left(\frac{3l}{8}\right)} + \mathrm{e}^{-2\pi i\left(\frac{h+2k}{3}+\frac{7l}{8}\right)}\right) \ . \tag{2.17}$$

For reflections of the type $(00.l)_{\mathrm{w}\frown\mathrm{h2}}$, this expression simplifies to

$$\mathcal{S}_{(00.l)_{\mathrm{w}\frown\mathrm{h2}}} = 2 \cdot \left(f_{\mathrm{As}} + f_{\mathrm{Ga}}\,\mathrm{e}^{-\pi i \frac{3}{4} l}\right) \tag{2.18}$$

for even l. For odd l, $\mathcal{S}_{(00.l)_{\mathrm{w}\frown\mathrm{h2}}}$ is equal to zero. For the estimations for $|\mathcal{S}|^2$, the atomic for factors f_{As} and f_{Ga} have been approximated by their atomic number.

Table 2.1.: List of Bragg reflections of *cubic* GaAs which can be studied with the current PMBE growth chamber at an X-ray energy of 15keV and $[111]_{\mathrm{z}\curvearrowright\mathrm{c}}$ oriented surface. Constraints are $\Theta_{\mathrm{In}}^{(\mathrm{Max})} = 18°$, $\Theta_{\mathrm{Out}}^{(\mathrm{Max})} = 18°$ and $\Psi_{\mathrm{In}}^{(\mathrm{Max})} = 5°$.

reflection (cubic)	$\lvert\mathcal{S}\rvert^2$ [electrons]	(q_z,q_r) [1/Å]	$\lVert\boldsymbol{G}\rVert_2$ [1/Å]	$\Theta_{\mathrm{Bragg}}^{\mathrm{reflec.}}$ [°]	reflection (wurtzite)
[-1 1 1]	2050	(0.6417,1.8149)	1.9250	7.27	[-1 1 0.67]
[0 0 2]	4	(1.2834,1.8149)	2.2228	8.41	[-1 0 1.3]
[0 2 0]	4	(1.2834,1.8149)	2.2228	8.41	[0 1 1.3]
[0 2 2]	4096	(2.5667,1.8149)	3.1436	11.93	[-1 1 2.7]
[1 -1 1]	2050	(0.6417,1.8149)	1.9250	7.27	[0 -1 0.67]
[1 1 -1]	2050	(0.6417,1.8149)	1.9250	7.27	[1 0 0.67]
[1 1 1]	2050	(1.9250,0.0000)	1.9250	7.27	[0 0 2]
[1 1 3]	2050	(3.2084,1.8149)	3.6862	14.03	[-1 0 3.3]
[1 3 1]	2050	(3.2084,1.8149)	3.6862	14.03	[0 1 3.3]
[2 0 0]	4	(1.2834,1.8149)	2.2228	8.41	[1 -1 1.3]
[2 0 2]	4096	(2.5667,1.8149)	3.1436	11.93	[0 -1 2.7]
[2 2 0]	4096	(2.5667,1.8149)	3.1436	11.93	[1 0 2.7]
[2 2 2]	4	(3.8501,0.0000)	3.8501	14.67	[0 0 4]
[3 1 1]	2050	(3.2084,1.8149)	3.6862	14.03	[1 -1 3.3]

Table 2.2.: List of Bragg reflections of *wurtzite* GaAs which can be studied with the current PMBE growth chamber at an X-ray energy of 15keV and $[00.1]_{\mathrm{w}\curvearrowright\mathrm{h2}}$ oriented surface. Constraints are $\Theta_{\mathrm{In}}^{(\mathrm{Max})} = 18°$, $\Theta_{\mathrm{Out}}^{(\mathrm{Max})} = 18°$ and $\Psi_{\mathrm{In}}^{(\mathrm{Max})} = 5°$.

reflection (wurtzite)	$\lvert\mathcal{S}\rvert^2$ [electrons]	(q_z,q_r) [1/Å]	$\lVert\boldsymbol{G}\rVert_2$ [1/Å]	$\Theta_{\mathrm{Bragg}}^{\mathrm{reflec.}}$ [°]	reflection (cubic)
[-1 0 1]	452	(0.9558,1.8149)	2.0512	7.75	[-0.17 -0.17 1.8]
[-1 0 2]	513	(1.9117,1.8149)	2.6360	9.98	[0.33 0.33 2.3]
[-1 0 3]	2623	(2.8675,1.8149)	3.3936	12.90	[0.83 0.83 2.8]
[-1 0 4]	1	(3.8233,1.8149)	4.2322	16.16	[1.3 1.3 3.3]
[-1 1 1]	452	(0.9558,1.8149)	2.0512	7.75	[-0.83 1.2 1.2]
[-1 1 2]	513	(1.9117,1.8149)	2.6360	9.98	[-0.33 1.7 1.7]
[-1 1 3]	2623	(2.8675,1.8149)	3.3936	12.90	[0.17 2.2 2.2]
[-1 1 4]	1	(3.8233,1.8149)	4.2322	16.16	[0.67 2.7 2.7]
[0 -1 1]	452	(0.9558,1.8149)	2.0512	7.75	[1.2 -0.83 1.2]
[0 -1 2]	512	(1.9117,1.8149)	2.6360	9.98	[1.7 -0.33 1.7]
[0 -1 3]	2623	(2.8675,1.8149)	3.3936	12.90	[2.2 0.17 2.2]
[0 -1 4]	1	(3.8233,1.8149)	4.2322	16.16	[2.7 0.67 2.7]
[0 0 2]	2050	(1.9117,0.0000)	1.9117	7.22	[1 1 1]
[0 0 4]	4	(3.8233,0.0000)	3.8233	14.57	[2 2 2]
[0 1 1]	452	(0.9558,1.8149)	2.0512	7.75	[-0.17 1.8 -0.17]
[0 1 2]	512	(1.9117,1.8149)	2.6360	9.98	[0.33 2.3 0.33]
[0 1 3]	2623	(2.8675,1.8149)	3.3936	12.90	[0.83 2.8 0.83]
[0 1 4]	1	(3.8233,1.8149)	4.2322	16.16	[1.3 3.3 1.3]
[1 -1 1]	452	(0.9558,1.8149)	2.0512	7.75	[1.8 -0.17 -0.17]
[1 -1 2]	513	(1.9117,1.8149)	2.6360	9.98	[2.3 0.33 0.33]
[1 -1 3]	2623	(2.8675,1.8149)	3.3936	12.90	[2.8 0.83 0.83]
[1 -1 4]	1	(3.8233,1.8149)	4.2322	16.16	[3.3 1.3 1.3]
[1 0 1]	452	(0.9558,1.8149)	2.0512	7.75	[1.2 1.2 -0.83]
[1 0 2]	513	(1.9117,1.8149)	2.6360	9.98	[1.7 1.7 -0.33]
[1 0 3]	2623	(2.8675,1.8149)	3.3936	12.90	[2.2 2.2 0.17]
[1 0 4]	1	(3.8233,1.8149)	4.2322	16.16	[2.7 2.7 0.67]

We now shortly discuss how a scan in reciprocal space can be realized. We focus on scans at 15keV with $q_r = 1.815\text{Å}^{-1}$. For wurtzite, the set of reflections $(10.l)_{\mathrm{w}\curvearrowright\mathrm{h2}}$, $l = 1, 2, 3$, belongs to this class. For these reflections, the vertical scattering component increases with increasing l. Each of these four reflections is accessible with the current set-up (see Tab. 2.2). Although we use this set of reflections for illustration of our discussion, most of our considerations are independent of the particular reflection.

At this point, we come back to Eq. (2.7) and (2.8) and exploit it in orthonormal surface coordinates such that the surface normal is given by the $\hat{\mathbf{n}} = (001)$ direction. For this choice of a basis, the incidence angle and exit angle with respect to the sample surface is given by

$$\sin(\alpha_{\mathrm{In}}) = \cos\left(\frac{\pi}{2} - \alpha_{\mathrm{In}}\right) = \frac{\boldsymbol{k}_{\mathrm{In}} \cdot (-\hat{\mathbf{n}})}{k} \tag{2.19a}$$

$$\sin(\alpha_{\mathrm{Out}}) = \cos\left(\frac{\pi}{2} - \alpha_{\mathrm{Out}}\right) = \frac{\boldsymbol{k}_{\mathrm{Out}} \cdot \hat{\mathbf{n}}}{k} \tag{2.19b}$$

By virtue of the choice of $\hat{\mathbf{e}}_1$, the contribution of the term with $\cos(\eta)$ drops out in the projection on the surface normal and we obtain

$$\sin(\alpha_{\mathrm{In}}) = \nu_1 + \nu_2 \cdot \sin(\eta) \ , \tag{2.20a}$$

$$\sin(\alpha_{\mathrm{Out}}) = \nu_1 - \nu_2 \cdot \sin(\eta) \ , \tag{2.20b}$$

where we defined

$$\nu_1 = \frac{G_z}{2k} > 0 \quad , \quad \nu_2 = \frac{r_0}{k}\frac{G_r}{G} > 0 \ . \tag{2.20c}$$

First, we evaluate which values can be realized for α_{In} in Bragg geometry. In Bragg geometry, α_{In} and α_{Out} need to be bigger than zero, which is equivalent to the constraint that the sin of these angles is larger than zero. From

$$0 \le \nu_1 + \nu_2 \cdot \sin(\eta) \overset{\nu_2 \neq 0}{\Leftrightarrow} \sin(\eta) \ge \frac{-\nu_1}{\nu_2} < 0 \ , \tag{2.21a}$$

$$0 \le \nu_1 - \nu_2 \cdot \sin(\eta) \overset{\nu_2 \neq 0}{\Leftrightarrow} \sin(\eta) \le \frac{\nu_1}{\nu_2} > 0 \ , \tag{2.21b}$$

we see, that only values for η from the two intervals[10] $[-\eta_{\mathrm{Max}}, \eta_{\mathrm{Max}}]$ and $[\pi - \eta_{\mathrm{Max}}, \pi + \eta_{\mathrm{Max}}]$ provide Bragg geometry, where η_{Max} is given by

$$\eta_{\mathrm{Max}} = \begin{cases} \arcsin\left(\frac{\nu_1}{\nu_2}\right) & \text{if } \nu_1/\nu_2 \le 1 \\ \pi/2 & \text{else} \end{cases} \ . \tag{2.22}$$

Therefore, *irrespective* of the limitations imposed by the chamber or diffractometer, we have the limitations

$$0 \le \sin(\alpha_{\mathrm{In}}) \le 2\nu_1 \quad \text{if } \nu_1/\nu_2 \le 1 \ , \tag{2.23a}$$

$$\nu_1 - \nu_2 \le \sin(\alpha_{\mathrm{In}}) \le \nu_1 + \nu_2 \quad \text{otherwise} \ . \tag{2.23b}$$

In Tab. 2.3, the limitations for the incidence angle of the current experimental setup are summarized for several hexagonal and cubic Bragg reflections. The first column in this table ignores the restrictions imposed by the experiment setup. The angles in the second column correspond to the opening angle of 18° of the current *in-situ* MBE growth chamber. For the third column, the limitations in the vertical offset of the diffractometer to 5° are

---

[10] The transformation $\eta \to \eta + 180°$ transforms $\boldsymbol{k}_{\mathrm{In}} \to \boldsymbol{k}_{\mathrm{Out}}$ and $\boldsymbol{k}_{\mathrm{Out}} \to \boldsymbol{k}_{\mathrm{In}}$.

	incidence angle		
reflection	Bragg geometry	+ chamber limits	+ diffractometer limits
$(11\underline{1})_{\mathrm{z}\frown\mathrm{c}}$	0°-4.8°	0°-4.8°	0°-4.8°
$(10.1)_{\mathrm{w}\frown\mathrm{h2}}$	0°-7.2°	0°-7.2°	0°-7.2°
$(200)_{\mathrm{z}\frown\mathrm{c}}$	0°-9.7°	0°-9.7°	0°-9.7°
$(10.2)_{\mathrm{w}\frown\mathrm{h2}}$	0°-14.6°	0°-14.6°	0°-14.6°
$(220)_{\mathrm{z}\frown\mathrm{c}}$	0°-19.7°	1.7°-18°	3.8°-18°
$(10.3)_{\mathrm{w}\frown\mathrm{h2}}$	0°-22.2°	3.9°-18°	6.1°-18°
$(311)_{\mathrm{z}\frown\mathrm{c}}$	0°-25.0°	6.5°-18°	8.7°-18°

Table 2.3.: Limitations on the incidence angle for some particular Bragg reflections.

included in the calculations. The same restrictions apply to the equivalent reflections according to the Tabs. B.1 and B.2 in the appendix.

These considerations provide the following important *conclusions*:

Despite the limitations imposed by the growth chamber and the diffractometer, we are capable of scanning the full set of reflections $(10.1)_{\mathrm{w}\frown\mathrm{h2}}$, $(200)_{\mathrm{z}\frown\mathrm{c}}$, $(10.2)_{\mathrm{w}\frown\mathrm{h2}}$, $(22.0)_{\mathrm{z}\frown\mathrm{c}}$, $(10.3)_{\mathrm{w}\frown\mathrm{h2}}$ (and symmetry equivalents thereof) as well as the trajectories in between these reflections with a (fixed) incident angle of, e.g., 6.6°. If we choose a (fixed) incident angle of approximately 9.2°, we can instead measure the full set of reflections $(200)_{\mathrm{z}\frown\mathrm{c}}$, $(10.2)_{\mathrm{w}\frown\mathrm{h2}}$, $(220)_{\mathrm{z}\frown\mathrm{c}}$, $(10.3)_{\mathrm{w}\frown\mathrm{h2}}$, $(311)_{\mathrm{z}\frown\mathrm{c}}$ (and symmetry equivalents thereof). During such a scan with fixed incidence angle, it is only required to rotate the sample around its normal and simultaneously position the detector accordingly. No inclination of the sample itself with respect the chamber is required.

Finally, the series $(220)_{\mathrm{z}\frown\mathrm{c}}$, $(10.3)_{\mathrm{w}\frown\mathrm{h2}}$, and $(311)_{\mathrm{z}\frown\mathrm{c}}$ of asymmetric, polytype and twin specific reflections can even be measured at an energy of 15keV without inclination of the chamber itself, modification of the incidence angle ($\alpha_{\mathrm{In}} = 15.5°$), or repositioning of a current 2D detector placed at a distance of approximately 50cm from the sample.

Our derivations also provide all essential information for actually performing a scan along any suitable trajectory $(q_x(\tau), q_y(\tau), q_z(\tau))$ parametrized by τ with a fixed angle of incidence: For a given incidence angle α_{In} and parameter τ, we obtain a solution for η. Substituting this value for η in Eqs. (2.7) and (2.8), we obtain the full vectors $\boldsymbol{k}_{\mathrm{In}}$ and $\boldsymbol{k}_{\mathrm{Out}}$ in surface coordinates for the respective $\boldsymbol{q}(\tau)$ point. A simple coordinate transformation from surface coordinates to the lab coordinate system for the source and detector provides the information about the positioning of the source (in case of a lab diffractometer), the chamber (in case of a heavy load diffractometer at a synchrotron beamline) and the detector.

At this point we end the discussion on the capabilities and limitations of the PMBE growth chamber for time-resolved *in-situ* X-ray measurements.

3. Post-growth investigations of GaAs nanowires grown in the PMBE

In this chapter, we present the results of some post-growth measurements of three GaAs nanowire samples that have been grown in the PMBE growth chamber by Philipp Schroth (see Sec. 2 and Ref. [67]). We begin this chapter with a discussion of the three-dimensional intensity distribution in reciprocal space (close to the $(111)_{\mathrm{z}\curvearrowright\mathrm{c}}$ Bragg reflection of silicon and GaAs) in Sec. 3.1. This information has been measured after growth – without exposing the sample to air ("post-growth *in-situ* measurement"). In Sec. 3.2, we investigate two GaAs nanowire samples with a nano-focus setup. By virtue of the nano-sized beam, we obtain valuable information for the proper interpretation of the time-resolved *in-situ* measurements which we will discuss in Sec. 4. In addition, we extract the ratio $d_{\mathrm{WZ}}/d_{\mathrm{ZB}}$ of the thickness d_{ZB} of a GaAs layer in $[111]_{\mathrm{z}\curvearrowright\mathrm{c}}$ direction in zinc blende versus the thickness d_{WZ} of a GaAs layer in $[00.2]_{\mathrm{w}\curvearrowright\mathrm{h2}}$ direction in wurtzite. The latter results have already been published in Ref. [3].

Experimental investigations can be classified in two categories: *ex-situ* and *in-situ* investigations. The term *in-situ* refers to investigations of objects in their natural surrounding, possibly even in operation ("*in-operando*"). Since we aim to study the growth of nanowires, their natural surrounding during growth is a growth chamber – such as the PMBE growth chamber which has been presented in Sec. 2.

If the physical question under consideration can be answered by an *in-situ* investigation before and after growth only, the X-ray flux is typically no major concern for such investigations and the combination of the growth chamber with a lab setup could be also feasible. However, if *time-resolved in-situ* X-ray investigations are required, hard X-ray synchrotron sources become of relevance. We will discuss such *time-resolved in-situ* X-ray investigations in Sec. 4.[1]

Nevertheless, extended post-growth *in-situ and ex-situ* measurements are highly valuable:

On the one hand, for post-growth *in-situ* measurements, the final state can be measured with higher signal-to-noise ratio since time-resolution need not be considered. Moreover, supplemental scans of other reflections (which may require additional time-consuming alignment) can be recorded for the same reason.

On the other hand, post-growth *ex-situ* measurements typically provide higher experimental flexibility (and, typically, also accuracy) than feasible *in-situ*. The possibilities

---

[1] We point out that time-resolution is not only required for studying the growth process itself, but also for investigation of the cool-down after growth as well as for annealing studies.

and limitations of the PMBE growth chamber at ANKA concerning the geometry of the measurements have already been discussed in Sec. 2.2. In addition to those geometrical constraints, it is highly challenging to combine such a growth chamber with nano-positioning and a nano-focus for highly localized X-ray investigations.

Equally important is the characterization after growth by complementary techniques (such as SEM and TEM). Although the UHV laboratory at ANKA facilitates some post-growth characterizations without exposure to air, the most important characterization of grown GaAs nanowires is provided by SEM, which is not available in this laboratory. Consequently, the post-growth SEM investigations have been performed *ex-situ*.

Characteristic SEM images of the samples which are relevant for this part of the manuscript are depicted in the appendix in Sec. D. Extensive discussions of the information which has been extracted from the large amount of SEM images of a large number of samples grown in the PMBE growth chamber are given in Refs. [3, 67, 126, 131]. Moreover, detailed information on the calibration of the Ga and As fluxes and the growth protocol of these samples can be found in these references. The latter is shortly summarized now:

As substrates, p-doped Si(111) covered by a thin native oxide layer has been used. All three samples were grown at a substrate temperature $T_{\mathrm{S}} = 590°$. Sample 1 has been grown at a V-III ratio of approximately 3.2, whereas sample 2 and sample 2e have been grown at a V-III ratio of approximately 4.9. Whereas sample 1 and sample 2 have been grown for $t_{\mathrm{G}} = 60\mathrm{min}$ after opening the Ga shutter, sample 2e has been grown for only $t_{\mathrm{G}} = 30\mathrm{min}$. After the time t_{G}, the Ga and As shutters were closed, the substrate heating was stopped, and its temperature was ramped down to $T_{\mathrm{Final}} = 100°\mathrm{C}$ in 8min.

3.1. *In-situ* measurement of the $(111)_{\mathrm{z}\curvearrowright\mathrm{c}}$ reflection of GaAs

We now start with the discussion of the three-dimensional intensity distribution in reciprocal space close to the $(111)_{\mathrm{z}\curvearrowright\mathrm{c}}$ Bragg reflection of silicon and GaAs measured *in-situ after growth*. The results for sample S1 and sample S2 are depicted in Fig. 3.1.

In addition to the signal from the silicon substrate – its Bragg peak, its diffuse scattering and its crystal truncation rod – we observe a cloud of intensity close to the position of GaAs which is absent before growth. This cloud close to the position of GaAs is rather smooth and wide-spread in q_x and q_y direction which is advantageous for *time-resolved in-situ* measurements:

We can record any steep cut through this intensity cloud close to the center and, thereby, acquire a good approximation to the intensity distribution in the q_y-q_z plane in reciprocal space. Here, q_z is defined to be the momentum transfer perpendicular to the $(111)_{\mathrm{z}\curvearrowright\mathrm{c}}$ planes of the nanowires grown along $[111]_{\mathrm{z}\curvearrowright\mathrm{c}}$ direction.

We will in Sec. 4 exploit the q_z information obtained from such steep cuts through the $(111)_{\mathrm{z}\curvearrowright\mathrm{c}}$ Bragg reflection of GaAs recorded time-resolved during the growth of the samples S1 and S2 in order to investigate the evolution of the wurtzite zinc blende polytypism (see Sec. 1.4) of the growing nanowires.

However, the post-growth *ex-situ* SEM images of the final state of both samples S1 and S2 (see Sec. D in the appendix) show “crystallites” – nanostructures with aspect ratios $\Delta h/\Delta r$ in the order of one (“parasitic growth”) in addition to nanowires with aspect $\Delta h/\Delta r \gg 1$. Here, h is the height and r is the radius of the nanoobject. The presence of the crystallites on the samples complicates the interpretation of the cloud of intensity close to the GaAs position because the contributions from a large number of crystallites (“parasitic growth”) and a large number of (likely polytypic) nanowires superimpose.

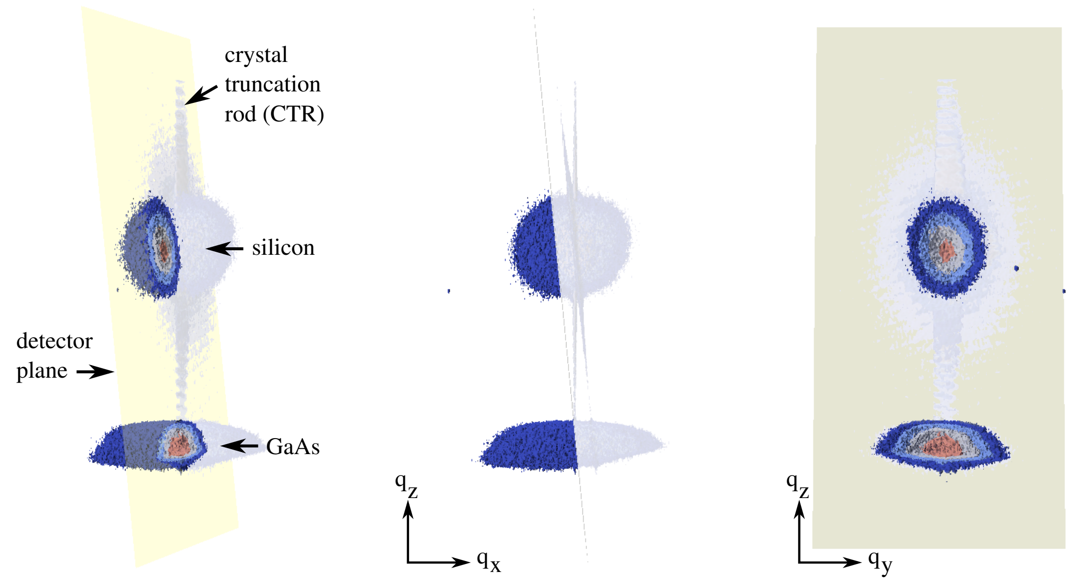

(a) sample 1: perspective view (b) sample 1: q_x-q_z view (c) sample 1: q_y-q_z view

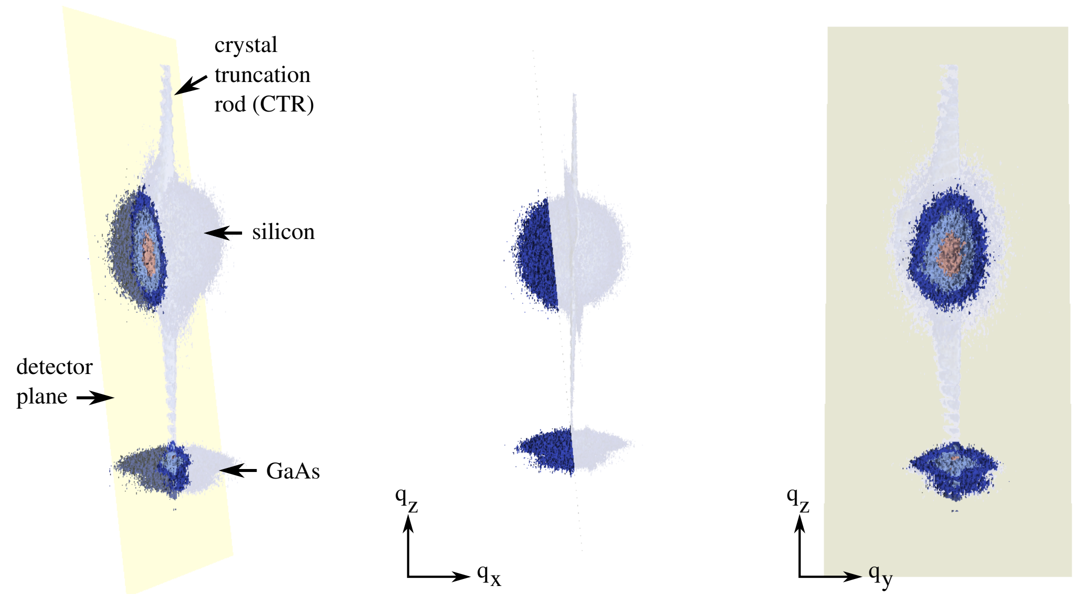

(d) sample 2: perspective view (e) sample 2: q_x-q_z view (f) sample 2: q_y-q_z view

Figure 3.1.: Intensity distribution in reciprocal space close to the $(111)_{\mathrm{z}\curvearrowright\mathrm{c}}$ Bragg reflection of silicon and GaAs of samples S1 and S2 measured *in-situ* after growth. The information in reciprocal space which is obtained during the time-resolved *in-situ* measurements that are discussed in Sec. 4 by the fixed arrangement of the detector, incident beam and sample is highlighted. A photograph of the experimental setup (i.e., the PMBE growth chamber mounted at the NANO beamline at ANKA) can be found on page 50.

Consequently, it is instructive to first study the signal of a single or few nanoobjects only before we return to the cumulative signal from a large number of two kinds of objects (crystallite/wire) each possibly with two kinds of internal structure (wurtzite/zinc blende). Therefore, we will first discuss post-growth *ex-situ* measurements with a highly focused X-ray beam in Sec. 3.2 before we proceed with the ensemble-averaged time-resolved *in-situ* measurements in the PMBE growth chamber in Sec. 4.

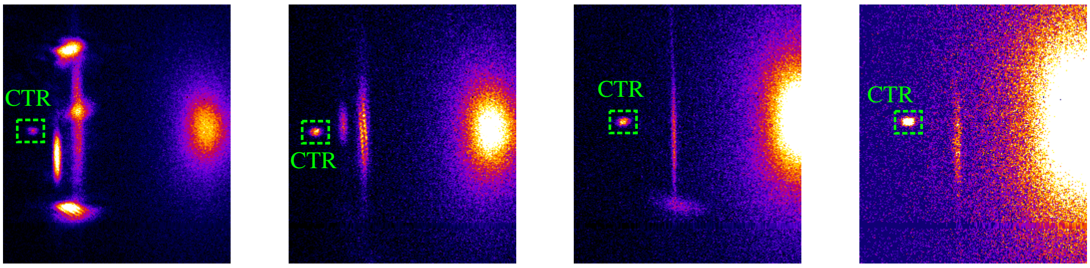

(a) Signal of a nanowire and a crystallite (sample S1)

(b) Nanowire signal with two pronounced subpeaks (sample S1)

(c) Signal of a nanowire mainly consisting of zinc blende next to a weak signal of a crystallite (sample S2e)

(d) Nanowire signal with two subpeaks in the q_z profile (sample S2e). The second subpeak is barely visible in the raw frame.

Figure 3.2.: Typical detector frames scanned with the nanofocus setup at ID13@ESRF. Counts of the detector have been converted to colored images by the lookup table "Fire" in imageJ [133]. The CTR is marked by a dashed green box.

3.2. *Ex-situ* measurements with nano focus at ID13@ESRF

In this section, we discuss post-growth *ex-situ* measurements which have been performed at ID13 at the ESRF in Grenoble [3, 132]. This beamline provides a nanofocus setup (Gaussian beam profile with a FWHM of 250nm at an energy of 14.9keV) which is essential for the results presented in this section. We again measured two-dimensional cuts in reciprocal space through the $(111)_{\mathrm{z}\frown\mathrm{c}}$ Bragg reflection of GaAs nanowire samples with a 2D detector as discussed in Secs. 3.1 and 4. However, instead of the temporal evolution during growth averaged over a large number of nanowires, we measured a huge number of such cuts in reciprocal space at different *positions* of the X-ray beam on two samples after growth and thereby obtain spatially resolved information on the scale of a single or a few wires. This way, we (i) gain important information about the composition of the spatially averaged, time-resolved *in-situ* data which will be analyzed in Sec. 4 and (ii) are able to derive an estimate on the ratio of the lattice constants in $[111]_{\mathrm{z}\frown\mathrm{c}}$ direction in the GaAs zinc blende polytype and the $[00.2]_{\mathrm{w}\frown\mathrm{h2}}$ direction of the GaAs wurtzite polytype.

The sample S1 studied at ID13@ESRF is a sample grown during the time-resolved *in-situ* X-ray growth studies discussed in Sec. 4. The other sample (sample S2e) has been grown with the same growth conditions as sample S2 in Sec. 4, but the growth time was only 30 min (compared to 60 min for sample S2). For a more detailed description of the samples, we refer the reader to the thesis of Philipp Schroth [67] and Ref. [3].

3.2.1. Contributions from nanowires and parasitic growth

In Fig. 3.2, some typical detector frames captured by the nanofocus grid scan of our samples are depicted. All frames show intense diffuse scattering from the silicon substrate. In addition, most detector frames of sample S1 reveal contributions from both, wires and crystallites (see Fig. 3.2(a)). Wire contributions are attributed to the signals with high aspect ratio and are typically rather extended in q_y direction (i.e., perpendicular to q_z). Clearly, the signal of crystallites has different characteristics: Most importantly, it shows a different aspect ratio. For this sample, we classified 194 frames mainly originating from wire scattering, 27 frames mainly originating from crystallites only and 453 frames which show simultaneous contributions from wires and crystallites by manual inspection. We do not require that a single detector frame resembles only the scattering of a single object. We only require that a single detector frame only shows scattering information of one class of objects. Fig. 3.2(b) shows a detector frame attributed to the class “wire scattering” with two pronounced and well distinguished subpeaks. Those two subpeaks are attributed to rather pure domains of zinc blende and wurtzite in the GaAs nanowires. We cannot distinguish if both subpeaks originate from a single wire or from two (or more) wires which may be illuminated simultaneously despite the nanofocus. However, this is of minor importance for our considerations.

In Figs. 3.2(c) and 3.2(d), the detectors frames illustrate scattering attributed to nanowires of sample S2e. The first example shows one peak only in q_z direction, whereas for the second example, two subpeaks along q_z are found in the q_z profile after integrated perpendicular to q_z and subtraction of the background of the diffuse silicon (see profile 24 later). However, in the two dimensional raw detector signal, the second subpeak is not or only barely visible. We point out that the signals are typically much stronger for the sample S1 since (i) its wire density is higher, (ii) the mean wire diameter is thicker and (iii) the mean wire height is larger [3, 67].

We now investigate the cumulative signal of the nanowires and the crystallites separately and compare it to the total cumulative signal “all” (obtained from all three classes of classification “wires-only”, “crystallites-only” and “both”). We focus on the q_z direction. Therefore, we integrate the frames in q_y direction, i.e., perpendicular to the line connecting the CTR and the center of the silicon peak. We then fit a Pearson VII function [134] to the silicon peak to obtain the center of the diffuse silicon signal in q_z direction. We shift the q_z profiles from each frame in such way that the silicon center is pixel zero.[2] The GaAs signal is thereby shifted to negative pixel values. We stick to detector pixels since a q_z calibration with the required high accuracy is very challenging and is neither required for the extraction of the ratio $d_{\mathrm{WZ}}/d_{\mathrm{ZB}}$ nor for the understanding of the contributions in the ensemble-averaged signal. For simplicity, we still refer to the respective axis as q_z axis.

We then summed all (shifted) profiles of each class “wires”, ”crystallites” and ”all” for both samples. This way, we obtain cumulative one dimensional q_z profiles which are depicted in Fig. 3.3(a) for sample S1 and in Fig. 3.3(b) for sample S2e. In both figures, the signal before and after background correction is depicted.

If we take a closer look on the q_z profiles in Fig. 3.3(a), we observe that

- neither the wires nor the crystallites show a pronounced fine structure,
- both signals are almost symmetric with respect to the maximum (the wire signal shows a weak asymmetric tail towards negative pixel distances),
- the full width half maximum of the peak from the crystallites (≈ 17.7 pixel) is larger than the full width half maximum of the peak of the nanowires (≈ 8.7 pixel), and,
- the maximum of both peaks is shifted by approximately 2.7 pixel (center of wires at -128.7, center of crystallites at -131.4).

For sample S2e, we determine the center of the crystallite signal at -132.7 pixel. Again, the signal of the crystallites is essentially a symmetric peak without fine structure. The full width half maximum of the respective peak is 26.7 pixel. The wire signal, however, is non-symmetric and, thus, is not compatible with a Gaussian shape. The additional weight in the wire frames stems from regions in the nanowire with larger interplanar lattice spacing — as in wurtzite segments [101, 119]. As a consequence of the disorder in the arrangement of both phases, scattered intensity is not only present at the pure phase positions, but also in between the two peaks. We will come back to this when we extract the interplanar lattice spacing from our data and when discussing the *in-situ* data for sample S1 and S2e.

---

[2] Since the center is – in general – a non-integer value, linear interpolation of the shifted data is performed.

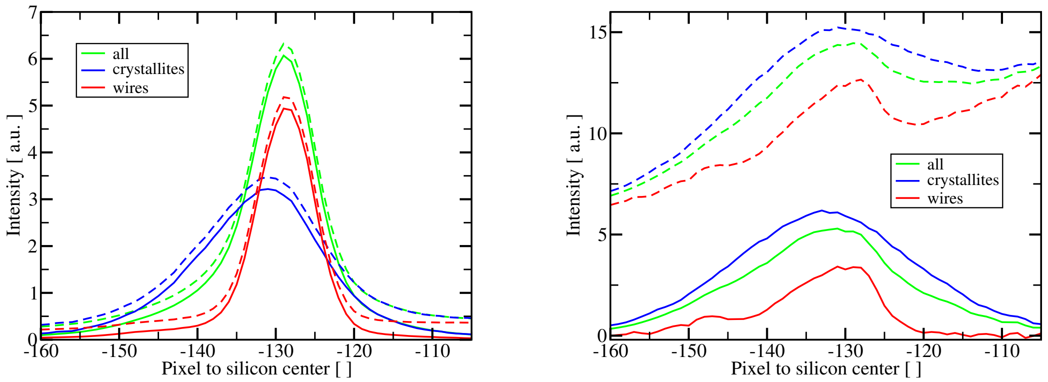

(a) Cumulative q_z intensity profiles of sample S1 (before [dashed line] and after [continuous line] correction of background).

(b) Cumulative q_z intensity profiles of the sample S2e (before [dashed line] and after [continuous line] correction of background). Note, that the integrated intensity of the crystallites is stronger than of the nanowire signal. Moreover, we point out the asymmetric profile of the nanowire signal.

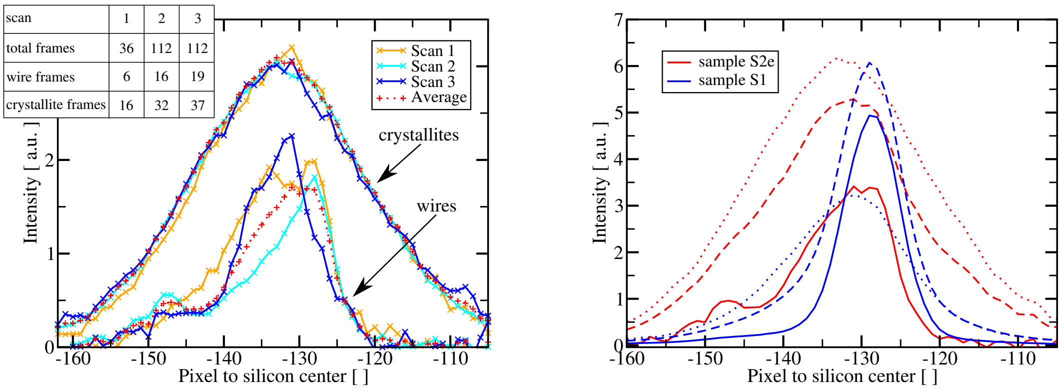

scan	1	2	3
total frames	36	112	112
wire frames	6	16	19
crystallite frames	16	32	37

(c) q_z intensity profile of wires and crystallites of three different scans of the sample S2e: Scans are marked by color line style. Whereas the signal of the crystallites is almost equal for all three scans, fluctuations from scan to scan are observed in the wire signal.

(d) Comparison of the signal of sample S1 (blue) and S2e (red). A dotted line corresponds to the signal of the crystallites of the respective sample, a continuous line to the wire signal and, finally, a dashed line to the overall signal of all observed frames.

Figure 3.3.: q_z intensity profiles of the samples S1 and S2e. The first two figures are normalized to the decay of the diffuse silicon peak. The third figure is normalized such that all three scans and the total average have the same crystallite weight. The comparison of both samples has been normalized such that the maximum of the strongest signal of both samples is approximately equal (overall signal for sample S1, crystallite signal for sample S2e). [Figs. (c) and (d): (©2014 International Union of Crystallography (IUCr), adopted from [3])]

The cumulative signal of sample S2e is constituted by three scans on the sample. The third subfigure (Fig. 3.3(c)) shows the cumulative q_z profile for the wires and the crystallites for each of these three scans separately. For better comparison, the intensity of each scan has been rescaled such, that the weight of the crystallites is equal. Clearly, the shape and the center of the crystallite signal is very similar in all three scans. However, the signal of the wires shows rather strong fluctuations: Whereas “scan 1” shows a rather broad signal with plateau , “scan 2” and “scan 3” show a pronounced peak. However, the maximum of this peak is shifted by two pixel. “scan 2” shows a second peak close to -148, which is absent in “scan 3”. In the latter, only a plateau can be observed near this position. “scan 1” does

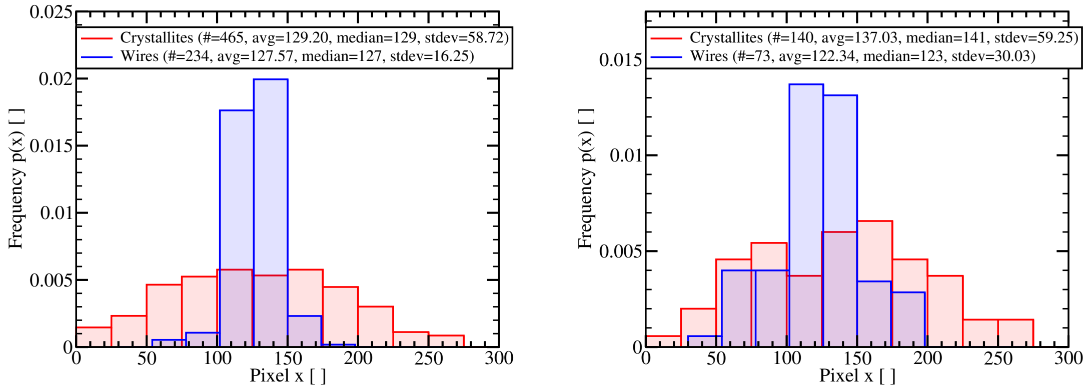

(a) sample S1

(b) sample S2e

Figure 3.4.: Distribution of centers of the wire and crystallite signals in q_y direction. For each histogram, the total number of objects "#", the mean value, the median and the standard deviation is given.

not even show this plateau, but decays continuously from pixel -135 to pixel -155 without plateau or second peak. These rather strong fluctuations demonstrate the importance of measuring the properties of nanowires with similar properties as samples S1 and S2e on a statistical level – beyond the investigations of single or few objects.

In Fig. 3.3(d), we compare the wire, crystallites and total overall signal of both samples. Since the detector was placed at the same position for both samples within experimental precision, the q_z distance associated with a single pixel is comparable: If we assume an error of 1% – resulting from small deviations in the experimental calibration for each sample and small deviations in the position of the detector – we can compare both samples within a precision of 1.3 pixel. Within this precision, the center of the crystallites is equal for both samples. Moreover, for both samples, the maximum of the wire signal is close to a pixel distance of 130 with respect to the center of the diffuse scattering of the silicon substrate. However, the asymmetric tail in the pixel range $[-155, -135]$ is only present for sample S2e. Again, we see the different relative total weight of the crystallites and the wires: Whereas the signal of the crystallites is stronger for sample S2e, the signal of the wires is stronger for sample S1. If we attribute the pixel distance to silicon close to -130 to the zinc blende phase, we see that sample S1 has a very high fraction of the zinc blende phase. The fraction of zinc blende in sample S2e is lower than the one in sample S1, but still above 50% since the peak at the zinc blende contains more intensity weight than the peak at the wurtzite position which should be located close to a pixel distance of -150 to silicon according to the results presented in Refs. [101, 119].

Before we turn to the extraction of the ratio of the lattice constants in $[111]_{z\frown c}$ direction in the GaAs zinc blende polytype and the $[00.2]_{w\frown h2}$ direction of the GaAs wurtzite polytype, we consider the behaviour of our signals in q_y direction.

For this, we estimated the center of mass of our wire signals as well as for the crystallites. The distributions of these centers are depicted in Fig. 3.4 for both samples. In both cases, the distribution of the crystallites has a width in the order of 60 pixel. On the contrary, the distribution for the wires is smaller by a factor of four for sample S1 and a factor of two for sample S2e.

We point out that the width of the wire distribution in Fig. 3.4(a) is systematically underestimated as compared to the intrinsic true physical width of the distribution. This systematic underestimation stems from the simultaneous illumination of multiple wires which becomes relevant for sample S1 due to its high density of wires. It can be understood if we assume that the signal on a single detector frame results from two wires with different q_y center. If the splitting of the centers is not larger than the width of the signal in q_y direction, a separation of the two contributions is not possible if we also take into account that almost all photons from the nanowires are located at very similar q_z positions. Since the width of the nanowire signal in q_y direction is very large, their signals tend to overlap in that manner once multiple wires are illuminated. As a consequence, the signal from the two wires is mistaken as a single wire with a center q_y typically shifted towards the center of the distribution. Thus, the width of the distribution of the center of the wires along q_y is systematically estimated too low. For the crystallites, such overlapping is far less likely due the typically lower width in q_y direction (see e.g. the three clearly separable crystallites in Fig. 3.2(a)). For sample S2e, the wire density is lower and their mean height is smaller. Therefore, the probability for simultaneous illumination of two wires also decreases. As a result, the standard deviation estimated from the measured data is much closer to the true physical value.

We will come back to this discussion of the q_y direction when we discuss the processing of the experimental *in-situ* data during growth in Sec. 4.1.

3.2.2. Ratio of the inter-layer spacings in zinc blende and wurtzite GaAs

We now turn to the extraction of the ratio $d_{\mathrm{WZ}}/d_{\mathrm{ZB}}$ of the lattice constants in $[111]_{\mathrm{z}\curvearrowright\mathrm{c}}$ direction in the GaAs zinc blende polytype and the $[00.2]_{\mathrm{w}\curvearrowright\mathrm{h2}}$ direction of the GaAs wurtzite polytype. We will also compare this ratio $d_{\mathrm{WZ}}/d_{\mathrm{ZB}}$ in our nanowires with the few results for this ratio in the in GaAs which we found in literature [101, 118, 119, 121, 135–138]. An overview over the existing results is given in Tab. 3.1.

If we consider the discrepancies of the ratio $d_{\mathrm{WZ}}/d_{\mathrm{ZB}}$ in the available results for nanowires grown on Si-111 and GaAs-111 substrates and for nanowires and bulk GaAs, the importance of re-estimation of the ratio — in particular for samples similar (or identical) to the *in-situ* samples discussed in Sec. 4 — is obvious.

It will turn out that our result close resembles the results given in Refs. [101, 119, 138], but discrepancies to the value for bulk GaAs [135, 136] and results for nanowires grown on GaAs-111B substrates [121, 137] are found.[3]

For that purpose, we select a subset of our detector frames which contain typical wire signals and show a two-peak splitting after subtraction of the background. In order to be able to evaluate frames which contain contributions of wires and crystallites, we define a specific q_y range as region of interest (ROI). From 36 candidates for determining the splitting of the two subpeaks as well as the positions of pure cubic and hexagonal GaAs, we selected in a second step the best five q_z profiles. This second selection was based on the requirements of sufficient signal to noise ratio, almost Gaussian shape of both subpeaks, and, finally, as few counts as possible in the intermediate domain. The last requirement is very important since such counts indicate that the illuminated structures are most likely not as pure as required: the mean lattice constant of the illuminated structures might differ from the pure structures which may result in a drift of one or both subpeaks towards each other. Therefore, such candidates systematically underestimate the splitting of pure wurtzite and zinc blende.

The resulting five detector frames, ROIs and q_z profiles are depicted in Fig. 3.5. For all 36 candidates, the respective q_z profiles — integrated along q_y inside the ROI and after subtraction of the diffuse silicon background which, again, has been modelled as a

---

[3] We point out, that – since we cannot obtain an estimate for the change of the in-plane lattice parameter from our data – we cannot compare the c/a-ratios which are provided e.g. in Refs. [121, 137].

Reference	$\frac{d_{\mathrm{WZ}}-d_{\mathrm{ZB}}}{d_{\mathrm{ZB}}}$ [%]	Δ [nm]	l [μm]	S	C	T [°C]	M
[135]	$0.554^{+0.015}_{-0.015}$	bulk	bulk	—	—	—	SXRD
[118]	-1.3	—	—	—	—	—	DFT
[136]	0.55	—	—	—	—	—	DFT
[137]	0.52	10-35	0.25-0.45	$\mathrm{GaAs}^{\mathrm{BL}}_{111\mathrm{B}}$	Au	570	TEM
[121]	$1.49^{+0.06}_{-0.06}$	75	0.5	$\mathrm{GaAs}^{\mathrm{R}}_{111\mathrm{B}}$	Au	510	LXRD
[138]	0.62	50	2.1	$\mathrm{Si}^{\mathrm{R}}_{111}$	Au	500	LXRD
[101, 119]	$0.70^{+0.05}_{-0.05}$	90-285	0.02-1.2	$\mathrm{Si}^{\mathrm{NO}}_{111}$	Ga	580	SXRD
—	$0.66^{+0.02}_{-0.02-0.06}$	18-25	1.2-2.2	$\mathrm{Si}^{\mathrm{NO}}_{111}$	Ga	590	SXRD

Table 3.1.: Summary of the published values $d_{\mathrm{WZ}}/d_{\mathrm{ZB}}$ in GaAs. All nanowire samples have been grown by MBE. No dopants have been added to the nanowires (apart from possibly catalyst atoms). Δ refers to the diameter of the nanowires, l to their length. S refers to the substrate (NO=native oxide layer; BL=buffer layer; R=oxide layer removed), C to the catalyst, T to the substrate temperature during growth, and M to the measurement technique (LXRD=XRD with laboratory source; SXRD=XRD at synchrotron source). The last line anticipates the result of this manuscript. Errors are given for $(d_{\mathrm{WZ}} - d_{\mathrm{ZB}})/d_{\mathrm{ZB}}$ whenever available. The first value in the superscript and subscript text for the ratio $d_{\mathrm{WZ}}/d_{\mathrm{ZB}}$ refers to bounds for the statistic uncertainties, the second to bounds for the systematic uncertainties. (©2014 International Union of Crystallography (IUCr), from [3])

Pearson VII — have been fitted by two Gauss distributions. We point out, that data points in between the two subpeaks need to be ignored if photons have been counted in this region. Otherwise, the centers of the two Gaussians are systematically shifted towards each other. As a consequence, the difference of the center of the two subpeaks is systematically estimated too low. For those candidates for which the fitting of both subpeaks was successful, the retrieved splittings are depicted in Fig. 3.6. The five splittings based on the profiles after the second selection ("best profiles") are highlighted in red. Clearly, we see from Fig. 3.6 that most "non-optimal" candidates indicate systematically a smaller splitting than the value retrieved from the five best profiles.

Since the number of estimations for the mean splitting is low and the error bounds vary by a factor as big as six, the error of each single value should be included in the calculation of the mean splitting of both phases and a weighted average is evaluated.[4] The result for the mean splitting of the two subpeaks – based on the five best profiles – is[5]

---

[4] The weighted average has been calculated by

$$\mu = \sum_i w_i x_i \quad , \quad w_i = \frac{e_i^{-1}}{\sum_j e_j^{-1}} \quad , \quad \sigma = \sqrt{\frac{1}{N} \sum_i w_i (x_i - \mu)^2} \; , \tag{3.1}$$

where σ estimates the error of the mean value. Note, that σ refers to the expected error of the mean value μ and not to an intrinsic width of a distribution. The weights w_i have been chosen as the reciprocal of the error e_i obtained from the confidence bounds of the centers from the fit to two Gaussians of each single profile.

[5] The numerical values for the splitting of both subpeaks, the error thereof and the weight for the calculation of a weighted average for the best five profiles are:

profile	single frame splitting [pixel]	error [pixel]	weight [ ]
4	19.924	0.228	0.365
13	20.897	0.468	0.178
18	21.743	0.848	0.098
19	20.891	0.281	0.296
24	23.632	1.337	0.062

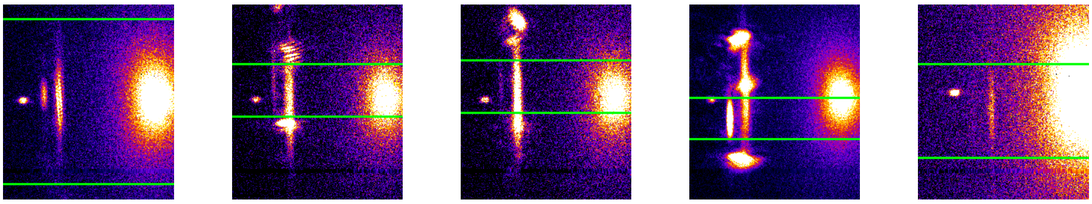

(a) detector frame for profile 4 with ROI (sample S1, see Fig. 3.2(b))

(b) detector frame for profile 13 with ROI (sample S1)

(c) detector frame for profile 18 with ROI (sample S1)

(d) detector frame for profile 19 with ROI (sample S1, see Fig. 3.2(a))

(e) detector frame for profile 24 with ROI (sample S2e, see Fig. 3.2(d))

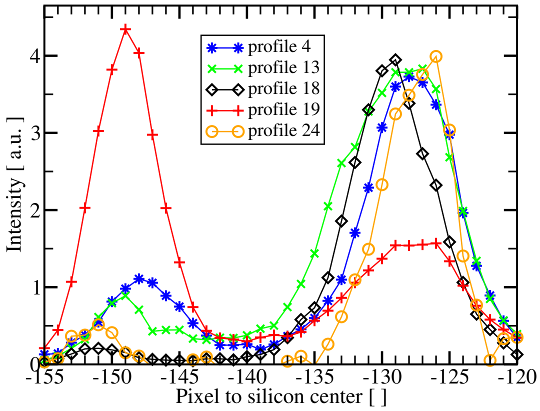

(f) q_z intensity profiles obtained from q_y-integration of the region of interest (green lines) in Figs. (a) to (e) after subtraction of the background of the silicon signal.

Figure 3.5.: Details on the five best candidates for determining the ratio of the interplanar distances in wurtzite and zinc blende structures in $[111]_{z\frown c}$ direction. (©2014 International Union of Crystallography (IUCr), from [3])

	mean splitting [pixel]	error of mean splitting [pixel]
reciprocal weight	20.793	0.502
equal weight	21.417	0.624

where the case of equally weighted data points has been included for comparison (only). If we include all 20 profiles (out of our 36 candidates) for which a difference has been extracted successfully, we obtain the strict lower bound (due to systematic under-estimation of some data points)

	mean splitting [pixel]	error of mean splitting [pixel]
reciprocal weight	18.880	0.493
equal weight	18.507	0.532

for the splitting of wurtzite and zinc blende. This lower bound is only 9.2% smaller than the weighted mean of the best profiles. However, we are convinced that the selection of the five best profiles more accurately represents the true physical value due to the reduced systematic errors. Thus, we will not discuss this lower bound in more detail. Nevertheless, this low bound will be important later for comparison of our results with values presented in current literature.

Since this difference is measured in pixel, we need to compare it to a second scale in pixel. We choose to compare the splitting to the distance of the cubic GaAs subpeak

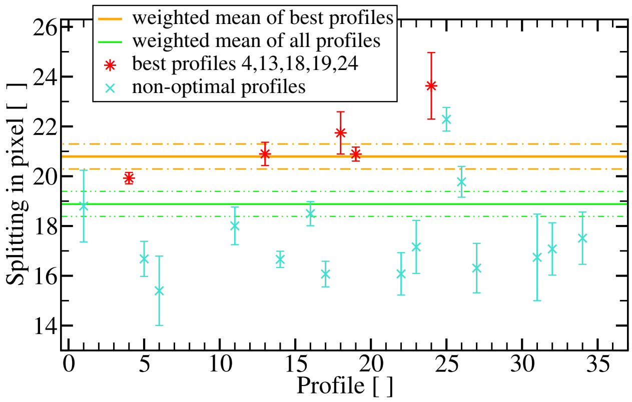

Figure 3.6.: Splittings of the two subpeaks in reciprocal space resulting from the different interplanar distance of cubic and wurtzite GaAs structures. The five best profiles (see Fig. 3.5) are highlighted by red stars. Most other candidates underestimate the splitting of the position of pure cubic and wurtzite GaAs (see discussion in main text). For some candidates, no splitting could be extracted in a robust and stable manner and, thus, those candidates have been discarded. The (weighted) mean value for the splitting (and the error thereof) are included as vertical lines (orange=best five profiles, green=all 20 profiles for which a difference could be extracted from a single frame). [(©2014 International Union of Crystallography (IUCr), adopted from [3])]

(i.e., the subpeak closer to the silicon signal) to the center of the diffuse silicon peak. By construction, the center of the silicon peak is located at zero. Therefore, the difference of the silicon peak to the GaAs peak is given by the (negative) center of the cubic GaAs subpeak. However, the uncertainty in the estimation of the Si center and the cubic GaAs center adds up. Again, we perform a weighted average[6] and obtain 128.253 ± 0.279 pixel for the distance of cubic GaAs and silicon.

Therefore, the splitting of hexagonal GaAs to cubic GaAs is

$$s = \frac{q_{\mathrm{ZB}} - q_{\mathrm{WZ}}}{q_{\mathrm{Si}} - q_{\mathrm{ZB}}} = \frac{20.793 \pm 0.502}{128.253 \pm 0.279} = 16.2\% \pm 0.4\% \tag{3.2}$$

of the splitting of cubic GaAs to silicon. If we convert this to reciprocal Angstroms – based on the lattice constants at room temperature – we obtain[7]

$$\delta q_z = (16.2\% \pm 0.4\%) \cdot 0.07883\text{Å}^{-1} = (0.1277 \pm 0.0032)\,\mathrm{nm}^{-1} \tag{3.3a}$$

Since the position of q_z is proportional to the inverse interplanar spacing, we have for the ratio of the interplanar spacing of wurtzite and zinc blende

$$\frac{d_{\mathrm{WZ}}}{d_{\mathrm{ZB}}} = \frac{q_{\mathrm{ZB}}}{q_{\mathrm{WZ}}} = \frac{1}{1 - \frac{q_{\mathrm{ZB}} - q_{\mathrm{WZ}}}{q_{\mathrm{ZB}}}} = \left[1 - \frac{s \cdot (q_{\mathrm{Si}} - q_{\mathrm{ZB}})}{q_{\mathrm{ZB}}}\right]^{-1} = \left[1 - s \cdot \frac{d_{\mathrm{ZB}} - d_{\mathrm{Si}}}{d_{\mathrm{Si}}}\right]^{-1} \tag{3.4a}$$

$$= \left[1 - s \cdot \frac{a_{\mathrm{ZB}} - a_{\mathrm{Si}}}{a_{\mathrm{Si}}}\right]^{-1} \approx 1 + s \cdot \frac{a_{\mathrm{ZB}} - a_{\mathrm{Si}}}{a_{\mathrm{Si}}} = 1 + 0.66\% \pm 0.02\%\ , \tag{3.4b}$$

---

[6] From the best five profiles, we obtain for the center of the cubic GaAs subpeak:

profile	distance GaAs-cub to Si [pixel]	error [pixel]	weight [ ]
4	127.728	0.0941	0.3511
13	128.416	0.2168	0.1522
18	129.183	0.1210	0.2728
19	128.033	0.2886	0.1144
24	127.619	0.3003	0.1099

[7] For GaAs, we used $q_z = 1.925055\,\text{Å}^{-1}$ and for Si, we used $q_z = 2.003886\,\text{Å}^{-1}$.

where we have set $\frac{a_{\mathrm{ZB}}-a_{\mathrm{Si}}}{a_{\mathrm{Si}}} = 4.092\%$. Therefore, the interplanar distance in the wurtzite phase structure is approximately 0.66% larger than the one in cubic GaAs. The relative statistical error of the deviation is approximately 3%, the absolute statistical error is 0.02%.

The systematic lower bound corresponds to $s = 14.7\% \pm 0.4\%$ or $\frac{d_{\mathrm{WZ}}}{d_{\mathrm{ZB}}} = 1 + 0.60\% \pm 0.02\%$.

We emphasize that the results for s are specific for the nanowires only, since we were able to split their signal from the signal from the crystallites by virtue of the highly focussed X-ray beam. Only for the ratios $\frac{d_{\mathrm{WZ}}}{d_{\mathrm{ZB}}}$ – evaluated by Eq. (3.4b) – we assume that the lattice constant of zinc blende GaAs in the bulk and in the nanowires coincides.

We now compare this ratio with the existing literature (see Tab. 3.1).

Within the error margins, our value is fully compatible with the value obtained in Refs. [101, 119] where a relative increase of inter planar spacing in $[111]_{\mathrm{z}\curvearrowright\mathrm{c}}$ direction of wurtzite phase of $0.70\% \pm 0.05\%$ has been observed. We point out that the wires which have been investigated in Refs. [101, 119] have diameters in the range from 90nm ± 8nm to 285nm ± 65nm whereas our wires are *much* smaller in diameter which reaches values as small as 18nm and 25nm for our wires [3, 67]. Moreover, our result closely resembles the result of Breuer [138]. Therefore, the inter planar spacing of wurtzite and zinc blende phase in $[111]_{\mathrm{z}\curvearrowright\mathrm{c}}$ direction is independent of the nanowire radius at least in the range from 15nm to approximately 300nm.

We point out that our result for the ratio $d_{\mathrm{WZ}}/d_{\mathrm{ZB}}$ in nanowires as well as the results given in Refs. [101, 119, 138] is larger than for *bulk* GaAs (see Ref. [135] for an experimentally obtained value and Ref. [136] for a recent[8] *ab-initio* DFT+LDA prediction in Tab. 3.1).

In Ref. [137], Tchernycheva et al. observed an interplanar spacing of $d^{(\mathrm{WZ})} = 3.281\text{Å}$ from the inter-spot distance of TEM diffraction patterns of gold-catalyzed GaAs nanowires. If we compare this to $d^{(\mathrm{ZB})} = a^{(\mathrm{ZB})}/\sqrt{3} = 3.26391\text{Å}$, it corresponds to an increase of the interplanar spacing of 0.52%. This value is smaller by approximately 25% than our value and, most importantly, smaller than our lower bound $0.60\% \pm 0.02\%$ for the increase of the interplanar spacing. However, the authors of Ref. [137] did not provide an error estimate for the results on the interplanar spacing, and, thus, we cannot draw conclusions if either their value is compatible with our estimate within their errors, if our reference $d^{(\mathrm{ZB})} = 3.26391\text{Å}$ is not valid for their sample, or, finally, if their interplanar spacing is physically different from the value which we observed. Nonetheless, it is interesting that their result for the ratio $d_{\mathrm{WZ}}/d_{\mathrm{ZB}}$ in nanowires is very similar to the current results for bulk GaAs.

On the contrary, Mariager et al. extracted an interplanar spacing of $d^{(\mathrm{WZ})} = 3.3125\text{Å} \pm 0.002\text{Å}$ for gold catalyzed GaAs nanowires in Ref. [121]. They could not observe any difference of the in-plane lattice parameter of cubic and hexagonal GaAs structures. Hence, the reference is $d^{(\mathrm{ZB})} = 3.26391\text{Å}$ which corresponds to an increase of the interplanar spacing of $1.49\% \pm 0.06\%$. This value is twice as large as our value or the value in [101, 119]. However, we cannot understand this discrepancy without further research on GaAs nanowires grown GaAs-111 substrates.

We believe that our result together with the result from Refs. [101, 119] provides an accurate estimate for the increase of the interplanar scaling $d_{\mathrm{WZ}}/d_{\mathrm{ZB}}$ in self-catalyzed GaAs nanowires grown on Si-111, but additional research for GaAs nanowires grown on GaAs-111 substrates is needed in future to elucidate the discrepancies to the results for Si-111.

---

[8] Considering the advances in computational power in the last two decades, we discard the result obtained by Yeh et al. [118] in our discussion and restrict to the recent result by Panse et al. [136].

4. Time-resolved *in-situ* X-ray studies of GaAs nanowires during growth

In this section, we present results of a *in-situ* X-ray investigation of self-catalyzed GaAs nanowires on a $[111]_{\mathrm{z\curvearrowright c}}$ oriented Si substrate with native oxide layer.

For this study, the portable MBE growth chamber (see Sec. 2) was installed at the NANO beamline at the synchrotron radiation source ANKA [67, 139, 140]. A two dimensional detector – a PILATUS 100K-S [120] — was placed at a fixed position in space (distance to sample $\approx$ 1m). From the set of possible reflections discussed in Sec. 2.2, the $(111)_{\mathrm{z\curvearrowright c}}$ Bragg reflection of GaAs has been chosen for the *in-situ* investigation: For that reflection, scattered photons of both phases are collected with slightly different diffraction angles as a result of the dependence of the lattice constant on the polytype. Moreover, as the lowest indexed symmetric reflection, its integrated scattered intensity is highest, which is advantageous for time-resolved measurements. Thus, it is a reasonable starting point for time-resolved *in-situ* investigations of GaAs nanowires.

A highly monochromatic ($\Delta E/E \approx 10^{-4}$) and parallel beam at an energy of 14keV has been used for the measurements underlying this section. The Bragg angles of Si and GaAs for this energy are $\Theta_{\mathrm{Bragg}}^{(111)_{\mathrm{z\curvearrowright c}}} = 8.119°$ and $\Theta_{\mathrm{Bragg}}^{(111)_{\mathrm{z\curvearrowright c}}} = 7.797°$ [141]. The incident angle α_{i} of the impinging X-ray beam was chosen slightly smaller than the $\Theta_{\mathrm{Bragg}}^{(111)_{\mathrm{z\curvearrowright c}}}$ of Si, near but not equal to the Bragg angle of GaAs. From the three dimensional post-growth measurement of the vicinity of the $(111)_{\mathrm{z\curvearrowright c}}$ Bragg reflection (see Fig. 3.1), we see that a single detector frame essentially corresponds to the (q_y, q_z) plane close to the GaAs signal. Nonetheless, diffuse scattering of the Si substrate is still seen in this cut through reciprocal space.

The experimental setup at the NANO beamline at ANKA is depicted in Fig. 4.1(a). The essential ingredients for time-resolved *in-situ* X-ray investigations are labelled (for growth: effusion cells and vacuum growth chamber with heating stage for the substrate; for X-ray measurements: Be windows, detector and heavy load diffractometer). The time-resolved *in-situ* growth experiments at the NANO beamline have been performed by Philipp Schroth et al. [67, 131]. Here, we discuss the evaluation of thereby obtained data: First, we describe the processing of the experimentally measured detector frames in Sec. 4.1 (joint work with Philipp Schroth [67]). Then, we present in Sec. 4.3 the results of extensive numerical simulations which have been performed in order to explore and understand the possibilities and limitations of X-ray measurements of the $(111)_{\mathrm{z\curvearrowright c}}$ reflection of polytypic GaAs nanowires. Finally, we provide in Sec. 4.4 an interpretation of the data based on the Markov model which is discussed in detail in Sec. 4.3.

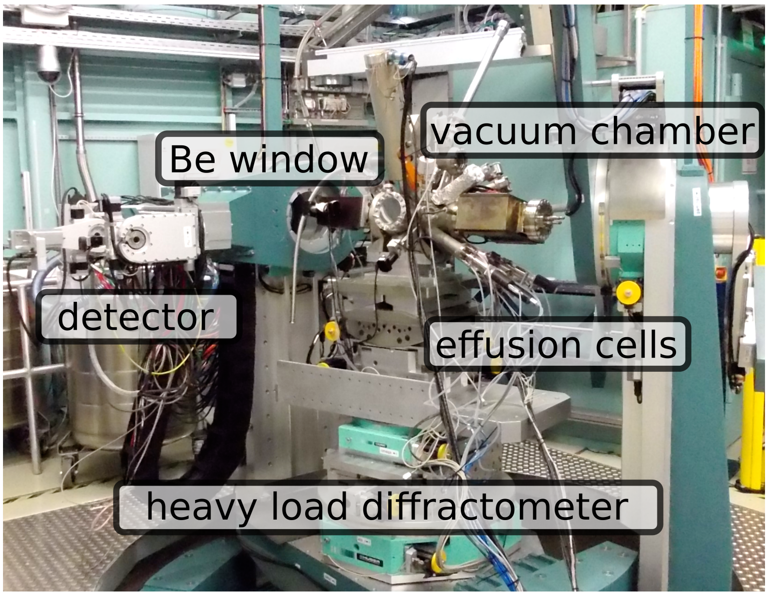

(a) Experimental setup at NANO@ANKA

Figure 4.1.: Illustration of the experimental setup for obtaining *in-situ* X-ray diffraction measurements during the growth of GaAs nanowires in the PMBE growth chamber at the NANO beamline of the synchrotron souce ANKA.

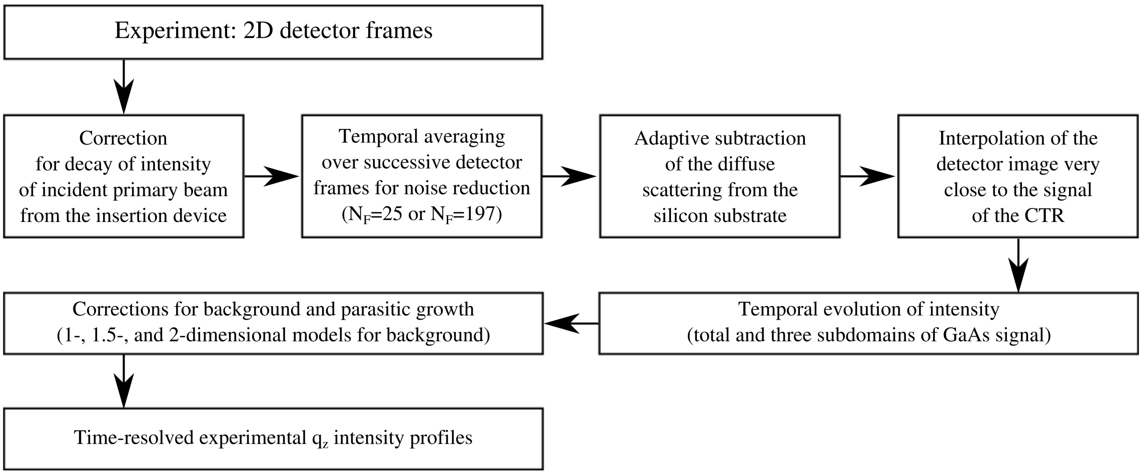

Figure 4.2.: Illustration of the processing pipeline of the experimentally measured time-resolved *in-situ* data. Details are provided in the main text.

4.1. Preprocessing of data measured at NANO@ANKA

In this section, we describe the data processing of time-resolved *in-situ* X-ray diffraction data for two samples. We point out, that sample 1 is the same sample which was also studied *ex-situ* with a nano-focus setup at ID13@ESRF after growth in Sec. 3.2.

Figure 4.2 illustrates the processing pipeline which has been applied to this experimentally measured data. First, the decay of the incoming flux from the insertion device has been corrected for each detector frame. Then, the signal-to-noise ratio of each time point was increased at the cost of lower temporal resolution by averaging over successive frames. Depending on the derived quantities, either $\mathrm{N_F} = 197$ (low temporal resolution, $\delta t \approx 4$min) or $\mathrm{N_F} = 25$ (low temporal resolution, $\delta t \approx 30$s) have been averaged after opening the Ga shutter of the effusion cells.

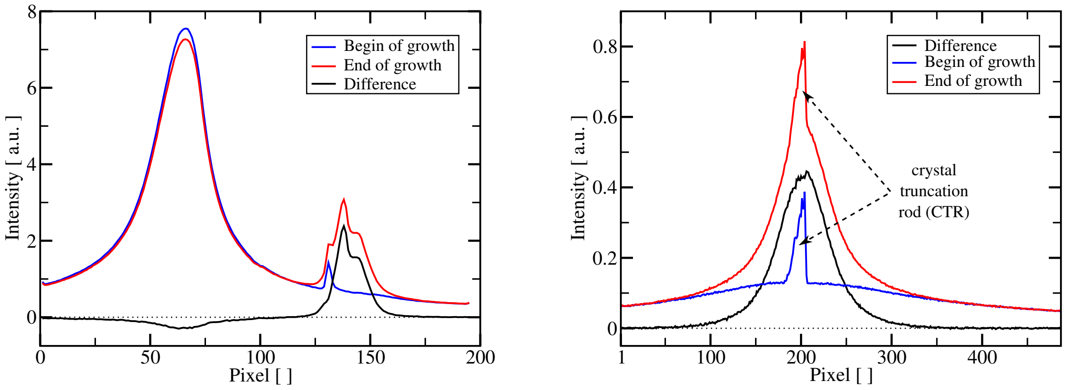

(a) Sample 2: q_z profile (full q_y integration)

(b) Sample 2: q_y profile (integration from channel $q_z = 116$ to $q_z = 195$)

Figure 4.3.: One dimensional line profiles of the (averaged) detector signal at the beginning and end the growth. Additionally, the difference thereof has been plotted.

Before we discuss the further processing of two dimensional detector frames, we shortly compare the q_z profile (integration of full q_y range) and the q_y profile for integration from channel $q_z = 116$ to $q_z = 195$ for sample 2 before and after growth without any additional preprocessing (see Fig. 4.3):

We observe that the intensity of the silicon peak slightly drops during the growth (see "Difference" in Fig. 4.3(a)). Therefore, proper background correction requires an adaptation of the strength of the silicon background. Moreover, we observe a peak close to pixel 145 with highly non-trivial shape – as in case of the sample S2e in Sec. 3.2. We point out, that in this section q_z decreases with increasing pixel, whereas in Sec. 3.2 q_z is increasing with increasing pixel.

The q_y profile in Fig. 4.3(b) reveals a non-gaussian shape of the signal from the crystal truncation rod (CTR). Nonetheless, the difference of the q_y profiles of the beginning of the growth and the end of the growth looks smooth: no fine structure is observed.

We now return to the processing of the two-dimensional detector images.

For subtraction of the diffuse background from the silicon substrate, the first $\mathrm{N_F} = 100$ (or $\mathrm{N_F} = 25$ for high time resolution) frames have been averaged. This initial signal is depicted in Fig. 4.4. This meta-frame is subtracted from all averaged meta-frames obtained during growth in such a way that the intensity in the range from q_z channel equal to 33 up to q_z channel 91 is equal. The center of silicon peak is approximated by pixel 66 for both samples.

The resulting meta-frames show a pronounced signal at the position of the $(111)_{\mathrm{z}\frown\mathrm{c}}$ Bragg reflection of GaAs as can be seen in Fig. 4.5. In both cases, a very small change in the shape of the silicon signal is observed as well as a very small drift of the signal from the crystal truncation rod. The artifacts from the latter have been minimized by interpolation of those few pixel by a multidimensional Taylor series from the close-by vicinity.

After these processing steps, we obtain (after q_y integration) the time-resolved q_z profiles depicted in Fig. 4.6:

For both samples, we observe an increasing overall intensity with increasing growth time. However, the peak shapes as well as their temporal evolution are clearly different for the two samples (see normalized intensity in the upper figures in Fig. 4.6).

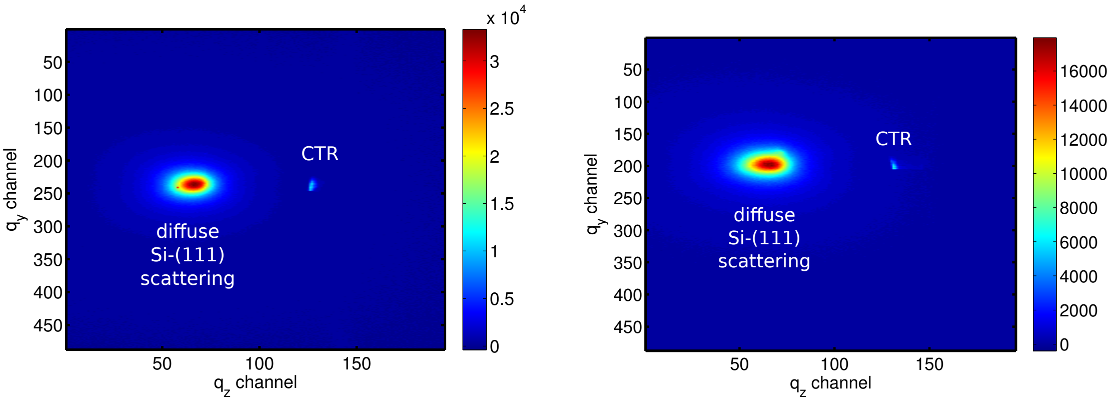

(a) Sample 1 (b) Sample 2

Figure 4.4.: Signal on the PILATUS detector at the beginning of growth. The exposure time for a single frame was $t_{\mathrm{Exp}} = 1\mathrm{s}$, read-out took 0.22s. The depicted image is the average of $\mathrm{N_F} = 100$ frames. The strongest signal is the diffuse cloud of the Si $(111)_{z\frown c}$ Bragg peak. Moreover, the intersection of the Ewald sphere with the crystal truncation rod (CTR) can be seen.

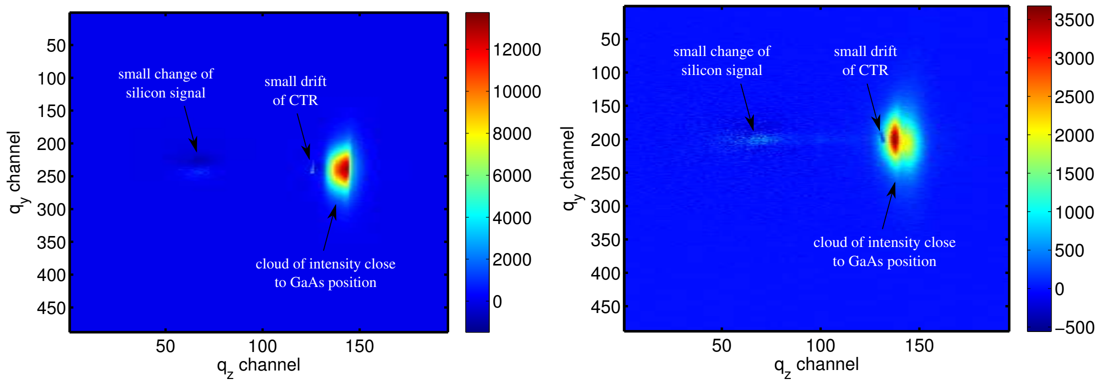

(a) Sample 1 (b) Sample 2

Figure 4.5.: Signal on the PILATUS detector at the end of growth after (adaptive) correction of the substrate signal (see Fig. 4.4). The exposure time for a single frame was $t_{\mathrm{Exp}} = 1\mathrm{s}$, read-out took 0.22s as before. The depicted image is the average of $\mathrm{N_F} = 197$ frames.

For sample 1, the change of the shape of the profile with increasing growth time is rather limited: Whereas a small increase of the scattered intensity is seen close to pixel 138, some intensity disappears for pixels greater than 146. As a consequence, the kink at early times $t_{\mathrm{G}} = 23\mathrm{min}$ at pixel 146 becomes less pronounced. The kink at pixel 132 remains almost identical in shape with increasing growth time.

In contrast, sample 2 exhibits rather pronounced temporal dynamics: In all depicted profiles, we observe a plateau in the range from pixel 141 to 145 in addition to a peak centered close to pixel 138. With increasing growth time, the peak height grows faster than the plateau. As a consequence, the ratio plateau height vs. peak height decreases with increasing growth time from approximately 0.93 at $t_{\mathrm{G}} = 26\mathrm{min}$ to approximately 0.61 at $t_{\mathrm{G}} = 58\mathrm{min}$. Moreover, we observe asymmetric tails, in particular at early growth times $t_{\mathrm{G}} = 26\mathrm{min}$.

From the post-growth *ex-situ* investigations which have been presented in Sec. 3.2 we know that the signal which we observe is composed of the two contributions, namely the

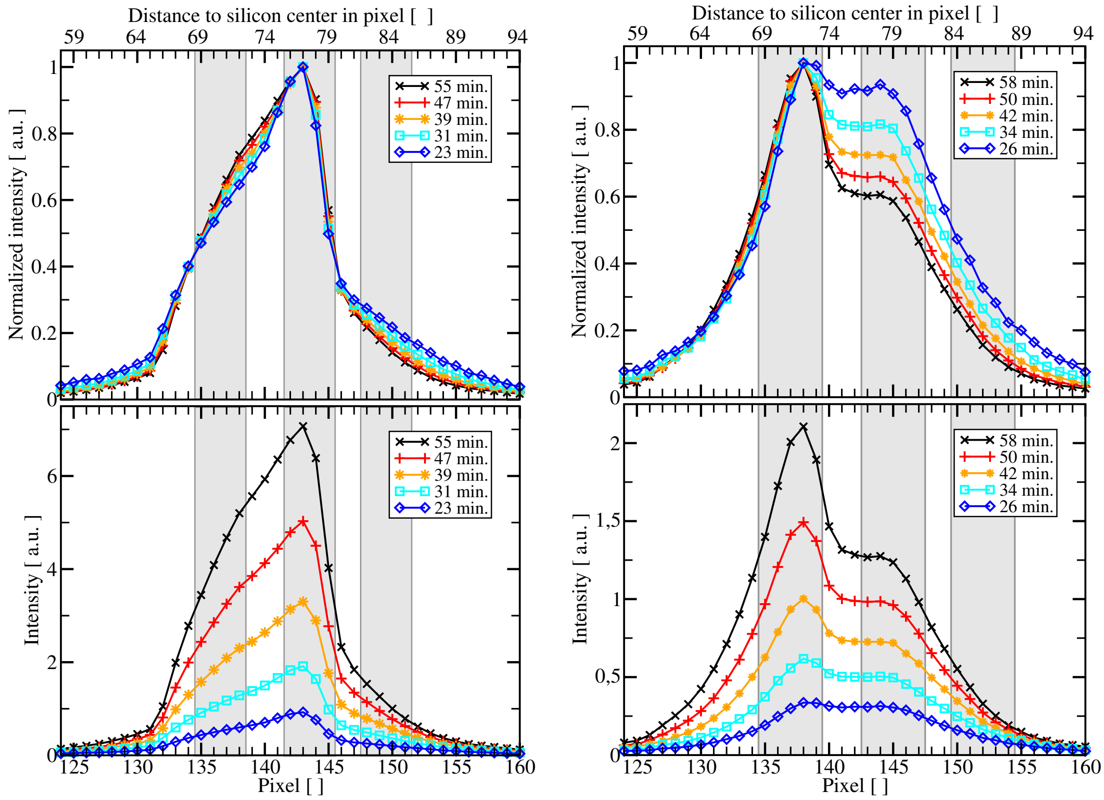

(a) Sample 1

(b) Sample 2

Figure 4.6.: Resulting time-resolved intensity profiles $\mathcal{I}(q_z, t)$. The lower figures illustrate the increase in overall intensity with increasing growth time. The upper figures are dedicated to the change of their shape: Each profile has been normalized such that its maximum is equal to one. In addition, the ranges defining the "sub-peaks" which are investigated in Fig. 4.7 are marked by gray boxes.

growing nanowires and the parasitic growth ("crystallites"). In particular, the signal from the parasitic growth was broader in q_z as well as in q_y direction. Therefore, we expect to observe mainly parasitic growth in the tails of the signal, for example in the pixel range 148-151 in case of sample 1 and 150-154 for sample 2. In addition, the central range has been divided in two subpeaks to study the temporal evolution of the signal.

The temporal evolution of these three subpeaks — as well as the entire GaAs signal — are investigated in Fig. 4.7. In case of sample 1, the subpeaks 1 and 2 behave almost identical. This is not true for sample 2. Here, subpeak 1 and 2 behave rather different. For both samples, subpeak 1 increases faster than the overall GaAs signal. However, subpeak 2 increases similar to subpeak 1 in case of sample 1 whereas for sample 2 it first increases similar to the overall GaAs signal ($t \lesssim t_\mathrm{G} = 35\mathrm{min}$), i.e., the ratio to the overall GaAs signal is almost constant. Then, its ratio *slightly* decreases, but not as fast as in case of subpeak 3. The ratio of subpeak 3 vs. the overall GaAs signal decreases in case of sample 1 and sample 2.

Before we interpret these results, we also consider the q_y information of our time-resolved *in-situ* data in the q_z ranges of subpeak 1-3. For that purpose, we fit a single Pearson VII function [134] in the form

$$\mathcal{P}(x; A, m, b, s) = \frac{2 \cdot A \cdot \sqrt{2^{1/m} - 1}}{\beta(m - 0.5, 0.5) \cdot \left(1 + 4 \cdot \left(\frac{x-b}{s}\right)^2 \cdot \left(2^{1/m} - 1\right)\right)^m} \tag{4.1}$$

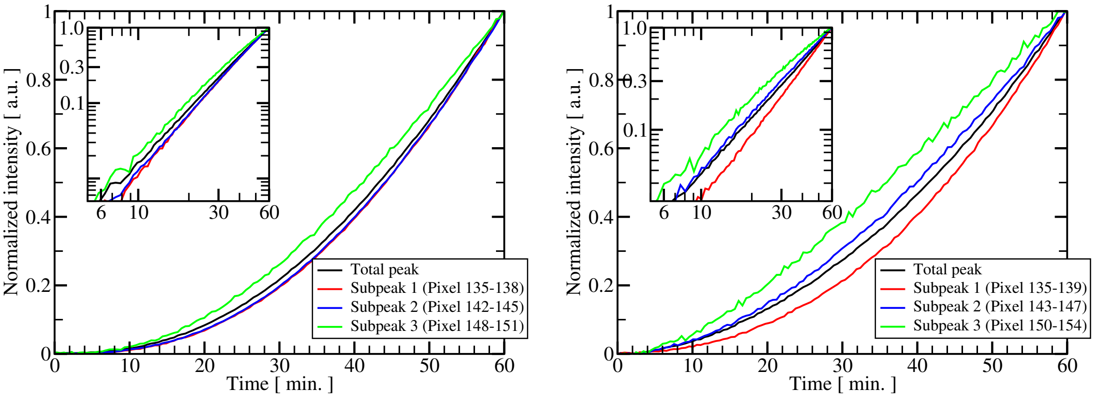

(a) Sample 1 (b) Sample 2

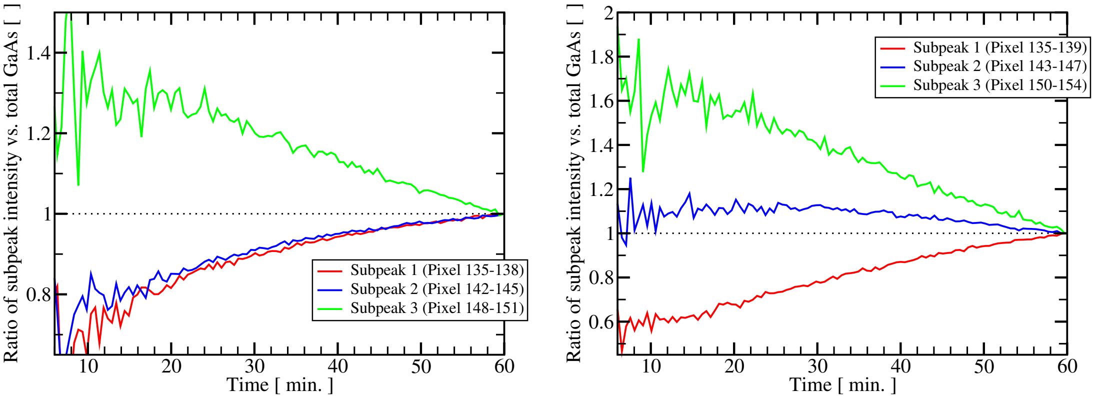

(c) Sample 1 (d) Sample 2

Figure 4.7.: Integrated intensity of the GaAs signal and the three sub-domains highlighted in Fig. 4.6. The depicted data points have a temporal resolution of approximately 30s. In Figs. (a) and (b), the value after $t_{\mathrm{G}} = 60\mathrm{min}$ ("final state") has been normalized to 1. In addition, the inset depicts the data on a log-log scale. In Figs. (c) and (d), the ratio of the (normalized) subpeaks vs. the (normalized) total GaAs signal is shown.

to the q_y profile which is obtained if each subpeak domain is integrated along q_z. Here, β is the beta-function. This function empirically describes the profiles very well. The temporal evolution of the width s for both samples and each subpeak is depicted in Fig. 4.8. For both samples, subpeak 3 is much broader than the other two subpeaks. Moreover, the width of the other subpeaks decreases with increasing growth time.

If we combine this information on the width s of the time-resolved *in-situ* data in q_y direction with the temporal evolution of the intensity (see Fig. 4.7(d)), we formulate the following hypothesis:

The signal is composed of two partially overlapping contributions, namely a rather broad one with a width of approximately $s = 80$ pixel in q_y and rather extended in q_x direction and a second contribution which is smaller in width in q_y ($s \leq 55$ pixel). The signal of subpeak 1 mainly stems from the second contribution, especially at later growth times, whereas the signal of subpeak 3 originates mainly from the broad signal. The behavior of subpeak 2 is a result of interplay of both signals and strongly depends on the relative strength of both contributions. The overall GaAs signal is the sum of those contributions and, thus, we deduce from Fig. 4.7(d) that the broad signal grows slower than the second

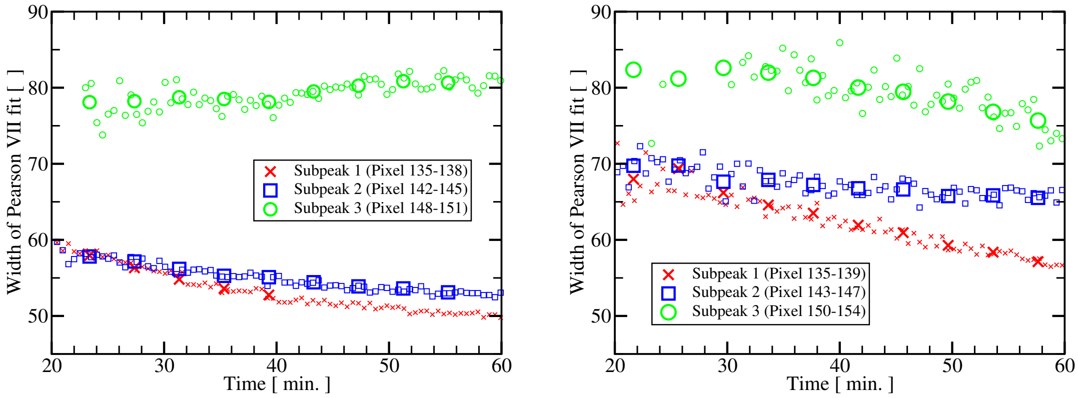

(a) Sample 1

(b) Sample 2

Figure 4.8.: Width of a Pearson VII fit to the q_y profile of the three sub-domains highlighted in Fig. 4.6 (integrated along q_z). The large symbols are obtained from the low time resolution, the small symbols from the high time resolution. Values are only depicted if the coefficient of determination R^2 of a fit exceeds 0.9.

contribution with increasing growth time. Therefore, the width of the fits for subpeak 3 is closest to the true value of the broad signal at early growth times, whereas this statement is true for subpeak 1 at latest growth times. In particular, the width of subpeak 1 (and 3) does no longer change in case of sample 1 for growth times $t_{\mathrm{G}} \geq 50$min.

In case of sample 1, the signal of subpeak 2 behaves very similar as subpeak 1 with time. Thus, the relative contribution of the broad signal in the range of subpeak 1 and 2 is rather weak, especially at larger growth times. Since the width of subpeak 3 remains constant – despite the decrease of its relative contribution – we can conclude that the second contribution does not produce a significant contribution in the domain of subpeak 3. Thus, it is rather narrow in q_z if compared to the broad signal.

In case of sample 1, we observe a similar width at early growth times – as in case of sample 2. However, for later growth times, the width of subpeak 3 decreases. If we assume a constant width of the broad signal with increasing growth time, this implies that the second contribution, which is narrower in q_y, contributes at later growth times and shifts the width of subpeak 3 to smaller values. On the contrary, the broad signal strongly influences the width of subpeak 1 and 2, if we also assume a constant width of the second contribution. Since the width of subpeak 1 does not yet stabilize after $t_{\mathrm{G}} = 60$min in case of sample 2 – in constrast to sample 1 – it is very likely that the relative contribution of the broad signal is higher in case of sample 2 than for sample 1. In addition, the second contribtuion is broader in q_z than in case of sample 1 as a consequence of the gradient of width of subpeak 3.

We attribute the broad signal to the parasitic growth ("crystallites") and the second contribution to the nanowires. This identification is fully consistent with the post-growth *ex-situ* measurements presented in Sec. 3.2 where the characteristics of these contributions have been studied with the nanofocus setup at ID13@ESRF. However, the two contributions must now be separated to study the temporal evolution of the nanowire signal.

In principle, the following strategies might be feasible for extraction of the nanowire signal:

First, the integration along q_y direction could be restricted to a small q_y region around the center with a width approximately equal to the width of the the wire signal. This way, the systematic error would be reduced, since a reduced fraction of the broad background is collected as compared to the nanowire signal. However, systematic errors persist in this approach irrespective of noise level of the data. A second approach could thus be to use the tails in the *one*-dimensional profiles for estimating the contribution from the broad signal, and, then, subtracting it from the measured data. However, evaluation of the central amplitude by such an extrapolation implies rather large statistical errors and, thus, should be avoided as far as possible. As a third approach, the background could be obtained directly from the tails in the *two*-dimensional intensity distribution. This way, many more data points are available and evaluation of the amplitude is much more stable than for the one-dimensional profiles.

However, the shape of the broad crystallite background profile must be known *a priori* in the second and third approach, in particular the properties of its tails. As a first approximation, this background in the third approach could be modelled by a Gaussian

$$\mathcal{G}(q_y, q_z) = A \cdot \mathrm{e}^{-0.5\left(\frac{q_z - q_{z\mathrm{C}}}{\sigma_Z}\right)^2} \cdot \mathrm{e}^{-0.5\left(\frac{q_y - q_{y\mathrm{C}}}{\sigma_y}\right)^2} \,. \tag{4.2}$$

We will refer to this approach as “two-dimensional background correction”.

In addition, we aim to split the profiles of the nanowires also by the following procedure:

For each q_z pixel, we fit the corresponding q_y profile for each time step by the sum of two Pearson VII functions. This way, we are able to adopt the tails – in contrast to fits based Gaussians – and allow for non-Gaussian variation in q_z direction. Nevertheless, Gaussian behavior is included as the limit $m \to \infty$. Since this approach is in between a a single one-dimensional background fit to the tails of the overall signal and a single two-dimensional fit to the tails of the two-dimensional meta-frames of the detector, we refer to it as “1.5 dimensional approach”.

Such an evaluation is rather difficult for the available data quality. Without prior constraints for some parameters, the fitting procedure is highly unstable. However, we can estimate some parameters of the two Pearson VII functions from the discussions on subpeak 1-3 and the diameter of the nanowires which has been obtained from post-growth SEM. For the width as well as for the m-coefficient of the broad background, we average these values over the last 15 time steps of subpeak 3 of sample 1. For this sample, no traces of significant overlapping of subpeak 2 and subpeak 3 have been observed in Figs. 4.7 and 4.8. The result is $m_2 = 2.79$ and $s_2 = 80.61$ pixel. These values are then used as estimate for both samples and all time steps. The width of the second peak is bound from above by $s_1 \approx 50$ in case of sample 1 and by $s_1 \approx 55$ in case of sample 2 due to the results depicted in Fig. 4.8. In addition, it is bound from below by $s_1 \approx 25 - 30$ pixel if the diameter of the nanowires in direct space and the approximate resolution element of the X-ray beam in q_y direction is considered. Finally, we constrain the centers of the two Pearson VII functions to the range $[230, 250]$ for sample 1 and $[190, 215]$ for sample 2. Thus, all parameters beside m_1 and the two weights of the sum are fixed. As a consequence, the 1.5 dimensional approach becomes feasible.

We now turn to the results of the separation of the contributions from the nanowires and from the crystallites.

In Fig. 4.9, the results after a background correction of a two dimensional Gaussian as defined in Eq. (4.2) are collected: As a result of the subtracting of the smooth broad Gaussian background all essential features of the profiles remain unchanged, but get more pronounced. For example, the ratio of the height of the plateau near pixel 145 to the maximum of the peak decreases to approximately 0.45 (see Fig. 4.9(b)) after 58min of growth — as compared to 0.6 for the unprocessed data depicted in Fig. 4.6. The background for sample S1 is less broad in q_y direction than for sample S2. For both samples, this

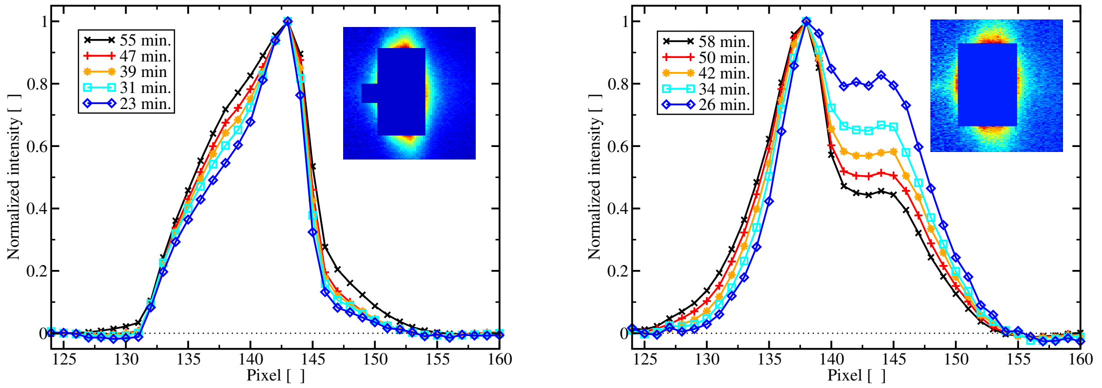

(a) Intensity profiles along q_z direction from the nanowires for sample 1

(b) Intensity profiles along q_z direction from the nanowires for sample 2

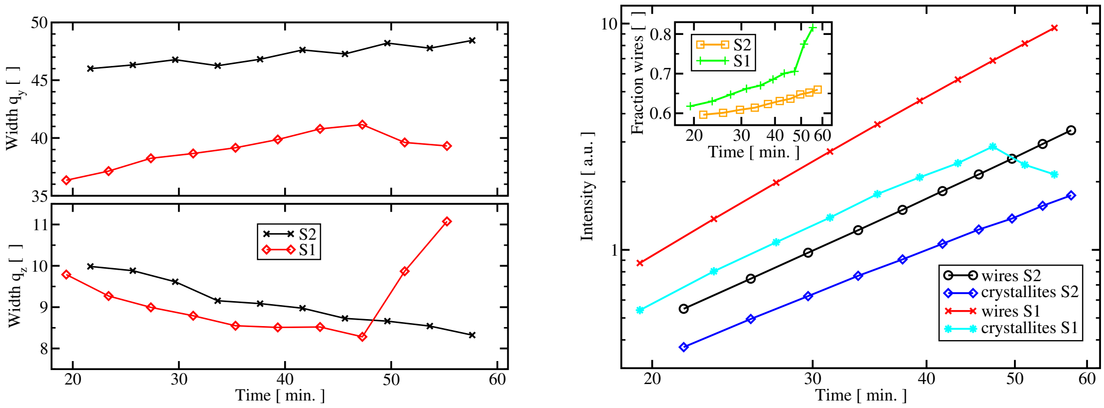

(c) Widths of the Gaussian background in q_z and q_y direction

(d) Total intensity from the nanowires and the crystallites as a result of a q_y and q_z integration of either the nanowire signal or the background signal. In addition, the ratio of the total intensity from the nanowires divided by the total intensity from the crystallites is depicted as inset.

Figure 4.9.: Temporal evolution of the intensity profiles along q_z direction resulting from the nanowires as well as temporal evolution of the Gaussian background correction. The mask in Figs. (a) and (b) covers the q_y range from pixel 100 to 300 and from 116 to 195 in q_z direction.

width increases slightly with time on average. On the contrary, the width in q_z direction decreases slightly with time. However, the last two data points for sample 1 do not resemble this trend. With the current data, it is not possible to uniquely identify if those two points are the result of an erroneous model for the background, problems with fitting of the background within the two-dimensional Gaussian model or of physical origin. Thus, they are discarded in subsequent discussions.[1] As expected from the discussion of Figs. 4.7 and 4.8(b), we observe a trend towards a larger contribution of the nanowires compared to the parasitic growth with increasing growth time. Moreover, we point out that the tails of the nanowire signal are modified by the subtraction of the Gaussian background.

Before we discuss these results further, we also collect the results for the 1.5 dimensional approach in Fig. 4.10. Within this approach, the best data quality has been achieved if the extracted two dimensional data with high temporal resolution has been processed and,

---

[1] Since the influence of these deviations on the last two temporal profile shapes of the nanowires is rather limited, the respective profiles need not be discarded in the subsequent discussions.

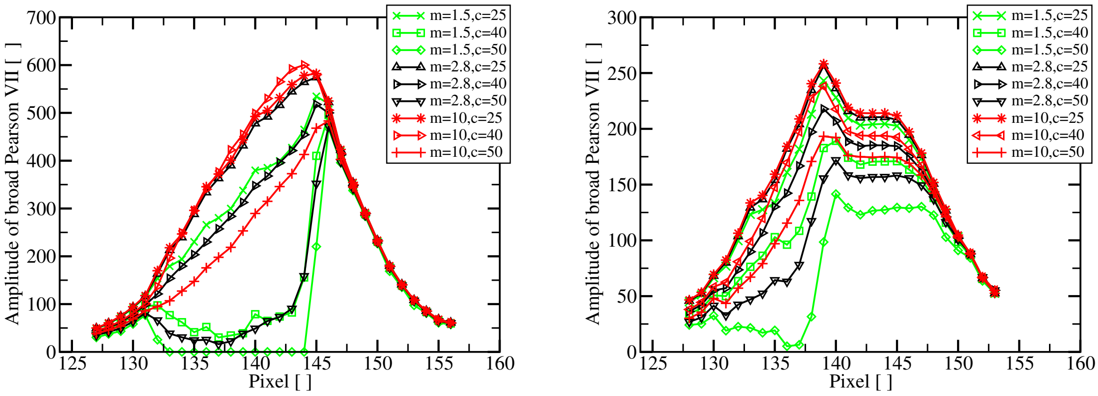

(a) Amplitudes of the broad Pearson VII contribution at the final time step in case of sample 1

(b) Amplitudes of the broad Pearson VII contribution at the final time step in case of sample 2

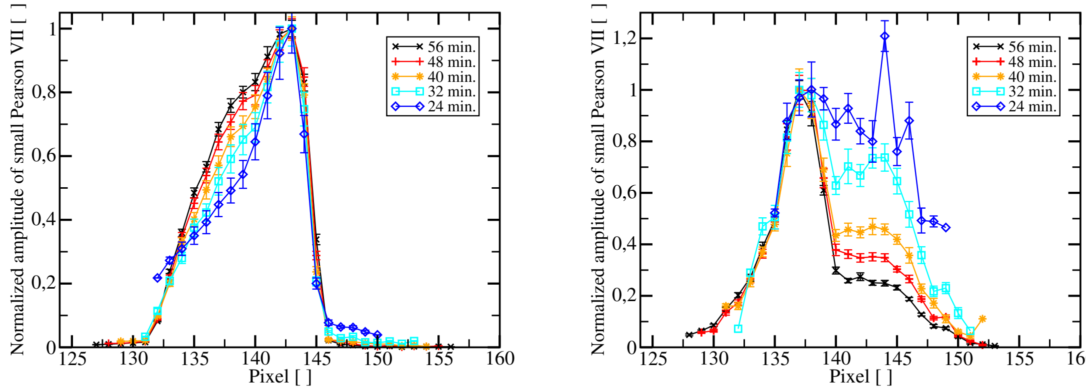

(c) Temporal evolution of intensity from crystallites for sample 1 for $m = 10$, $c = 25$

(d) Temporal evolution of intensity from crystallites for sample 2 for $m = 10$, $c = 25$

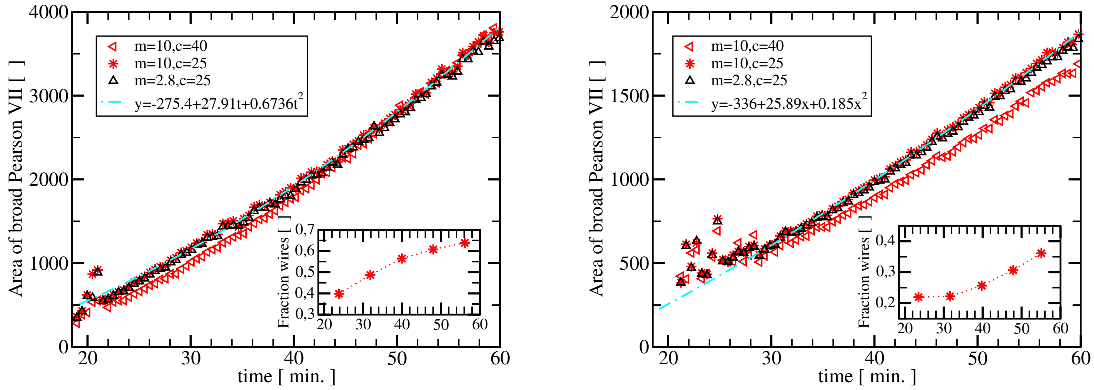

(e) Resulting temporal evolution of intensity of the shape of the nanowire signal for sample 1

(f) Resulting temporal evolution of intensity of the shape of the nanowire signal for sample 2

Figure 4.10.: Results of 1.5 dimensional splitting of parasitic growth and nanowire contribution based on two Pearson VII functions.

then, in a second step a moving average of the fitted amplitudes of the two Pearson VII fits for every q_z was calculated. For this moving average, a successive sequence of $\mathrm{N_F} = 16$ metaframes with temporal resolution of 30s has been included. This way, a temporal resolution of the intensity profiles of 8min is obtained.

First, we need to find estimates for the yet undefined parameters m_1 and s_1. For simplicity, we refer to these two parameters as m and c respectively. From the discussion above, we restrict c to the range 25 to 50 pixel. For m, we consider $m = 2.8$ which is identically to the value used for the broad background, $m = 10$ which corresponds to almost Gaussian tails and, finally, $m = 1.5$ which corresponds to very pronounced, almost Lorentzian tails. Figs. 4.10(a) and 4.10(b) depict the amplitudes of the broad background for all those cases and both samples under consideration as a function of q_z. From the post-growth *ex-situ* measurements presented in Sec. 3.2 we expect this shape to be smooth peak without any fine structure. Clearly, this requirement is not met for $m = 1.5$ for both samples. For $c = 50$ and $m = 1.5$, the background is highly underestimated in the range where the nanowire signal is expected to be most pronounced. For $m = 2.8$, this behavior is also observed for $c = 50$. However, for $m = 1.5$ and $m = 2.8$, the artifact is weaker for decreasing c. In case of sample 1, the background is already a smooth peak as expected for $m = 2.8$ and $c = 25$. For $m = 10$ and sample 1, we obtain almost the identical shape as for $m = 2.8$ and $c = 25$. Only towards the upper bound $c = 50$, a sharp, almost "triangular" peak is observed. Therefore, we conclude that the best background fit is obtained for large $m \approx 10$ and small $c \approx 25$ in case of sample 1. For these values, the resulting profile is rather robust with respect to changes in both parameters (e.g., the depicted cases $m = 2.8$, $c = 25$ and $m = 10$, $c = 40$).

In case of sample 2, input data quality is worse for three reasons: First, the lower density of nanowires on the sample. Second, the smaller mean diameter of the grown nanowires. And third, the incident X-ray flux was lower for sample 2 than for sample 1.[2] Consequently, splitting of the signal is expected to be worse than for sample 1. Most importantly, however, an artifact close to pixel 138 is observed for all depicted values of m and c. We have not been successful in identifying the origin of this artifact. Nevertheless, large $m \approx 10$ and small $c \approx 25$ seem to be a reasonable choice. In fact, robustness with respect to deviations from these parameters is even higher than for sample 1: For $c = 25$, the resulting profiles are almost equal for all three values of m.

The nanowire profiles for $m \approx 10$ and $c \approx 25$ are depicted in Figs. 4.10(c) and 4.10(d). Since we optimized for smoothness of the background in q_z direction, the features of the nanowire profiles remain. On a quantitative level, however, the ratio of the height of the plateau near pixel 145 to the maximum of the peak decreases to approximately 0.27 after 58min of growth in case of sample 2 — as compared to 0.6 for the unprocessed data depicted in Fig. 4.6 and 0.45 for the two-dimensional Gaussian background (see Fig. 4.9(b)). Nevertheless, for early times $t = 24$min and $t = 32$min this ratio is rather similar to the two-dimensional Gaussian background. We point out that the 1.5 dimensional approach for separation of the contributions from the nanowires and crystallites is not capable of extraction of the tails in q_z direction from the experimental data for early growth times.

In Figs. 4.10(e) and 4.10(f), we depict the evolution of the area of the broad Pearson VII for sample 1 and sample 2. Here, the total area of the broad Pearson VII fits $\mathcal{P}(A(q_z, t_\mathrm{G}))$ has been estimated as the area below a Gaussian fit to the amplitudes $A(q_z)$ of the crystallites at given growth time t_G. We observe that this area is again very insensitive to the choice of the parameters m and c. We point out that this estimate for the total area of the crystallites does not incorporate the width c and m-coefficient, which also influence the total number of photon counts originating from the crystallites.[3] Nevertheless, this approximation is only relevant if data with different m and c is compared.

We see that the signal from the crystallites grows faster than linear (positive coefficient

---

[2] Sample 2 was measured just before the electron beam of the synchrotron source ANKA has been dumped and, primary intensity has decayed with respect to the flux directly after injection of the beam several hours ago. On the contrary, sample 1 was measured directly after the subsequent injection and, thus, with higher primary flux.

[3] To be specific, the q_y integration of the Pearson VII has been discarded due to the large uncertainty in

in front of t^2 in the fit[4]). In addition, the fraction of the signal originating from the wire has been roughly estimated and included as inset in these figures.[5] As expected from the discussions in this section of the three subpeaks and the results for the two-dimensional Gaussian background based on the tails of the intensity distribution, we again observe that the signal of the nanowires grows faster than the signal from the crystallites. In fact, this trend is more pronounced than in the latter case. However, the absolute fractions of the scattered intensity originating from the nanowires is much lower than in case of the two-dimensional Gaussian background.

4.2. Comparison with the post-growth *ex-situ* measurements from Sec. 3.2

We now compare the post-growth *ex-situ* results presented in Sec. 3.2 with the *in-situ* data obtained at the NANO beamline at ANKA (see Sec. 4.1).

For comparison, we estimate the zinc blende peak of the NANO data to be at approximately pixel 138. Therefore, we map the data measured at NANO@ANKA by $p \to -1.78 \cdot (p-66)$, where p is the respective pixel and 66 is the center of the diffuse silicon signal.[6] [7] Of course, this is only a rough estimate for this coordinate transformation. Nevertheless, it is sufficient for the quality of the experimental data at hand.

In addition, we point out that the signal obtained at ESRF is obtained with a beamline with very different parameters, in particular the beam profile and the ratio of beam spot size vs. coherence length vs. nano-wire size.

We plotted the profiles obtained at NANO and at ESRF after separation of the nanowire and crystallite signal in Fig. 4.11. All curves have been rescaled such that their global maximum is approximately equal for easy comparison. First, we compare the crystallite signal. For sample S1, we used the signal after $t_\mathrm{G} = 39$min due to the deviations in the later time steps (see Sec. 4.1). None of these signals shows a pronounced fine structure on the scale of the splitting (20 pixel). However, the signal of the crystallites at the NANO

---

the parameters c and m, since

$$B(A,m,b,s) = \int_{-\infty}^{\infty} \mathcal{P}(q_y; A,m,b,s)\ \mathrm{d}q_y = A \cdot s \cdot f(m) \tag{4.3}$$

where the function $f(m)$ is given by

$$f(m) = \int_{-\infty}^{\infty} \frac{2\sqrt{2^{1/m}-1}}{\beta(m-0.5, 0.5)\cdot(1+4\cdot x^2\cdot(2^{1/m}-1))^m}\ \mathrm{d}x\ . \tag{4.4}$$

Since neither s nor $f(m)$ can be estimated reliably from the current data, only the amplitudes $A(q_z, t_\mathrm{G})$ is considered.

[4] For sample 1, the data range from $t_\mathrm{G} = 22$min to $t_\mathrm{G} = 60$min has been used, for sample 2, the data range was limited to 30min to 60min due to the strong noise for $t_\mathrm{G} < 30$min. For both samples, the data for $m = 10$ and $c = 25$ has been employed.

[5] This fraction has been estimated as $\frac{\sum_{q_z} A_\mathrm{NW}(q_z)}{\sum_{q_z} A_\mathrm{NW}(q_z)+A_\mathrm{C}(q_z)}$. Again, the parameters c and m have been discarded as for the total area of the broad Pearson VII function. As a consequence the fraction of photon counts from the nanowires is lower than the calculated and depicted value for the wire fraction. In addition, the errors on the estimates for the wire fraction have large errors, since the tails of $A(q_z, t_\mathrm{G})$ in q_z direction are not known, especially for early growth times t_G.

[6] The prefactor -1.78 is obtained by comparison of the distances from the zinc blende GaAs signal to the center of silicon: $138 - 66 = 72$ pixel at NANO@ANKA compared with -128.25 pixel at ID13@ESRF

[7] Based on this coordinate transformation and our results in Sec. 3.2, we estimate the expected splitting of zinc blende and wurtzite GaAs in the detector frames obtained at the NANO beamline at ANKA to be $16.2\% \cdot (138-66) \approx 12$ pixel. However, we already point out, that the observed splitting in the q_z intensity profiles may be smaller than this maximum value – depending on the properties of the nanowires as will be discussed in Sec. 4.3 (see e.g. Fig. 4.22).

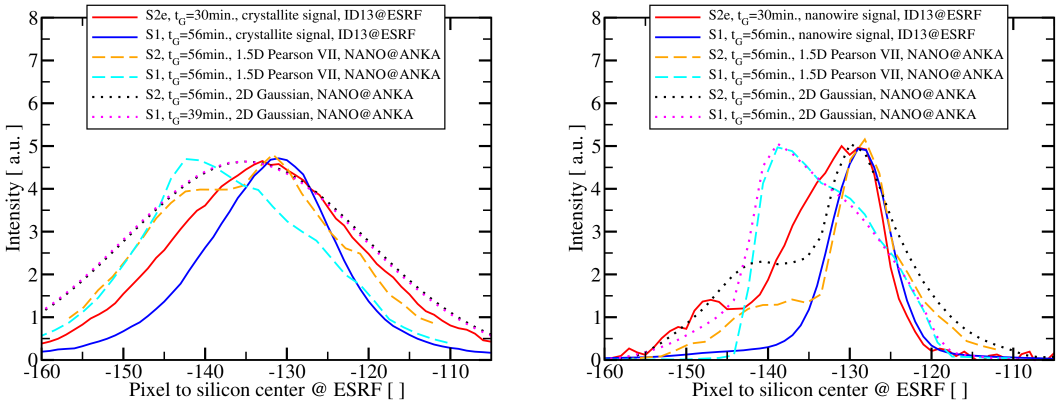

(a) crystallite signal

(b) nanowire signal

Figure 4.11.: Comparison of the preprocessed *in-situ* data obtained at NANO@ANKA with the post-growth *ex-situ* measurements at ID13@ESRF

beamline is broader than the signal measured at ESRF: the differences in width which has been observed at ESRF are not observed at NANO. Moreover, the maximum and the center of mass is far off for sample S1 in case of the 1.5D Pearson VII background.

If we compare the signal originating from the nanowires, we have to keep in mind that sample S2e is not identical to sample 2, but sample S2e has been grown for $t_{\mathrm{G}} = 30\mathrm{min}$ only and the growth conditions (growth temperature, Ga- and As fluxes, properties of the substrate, ...) are only identical up to experimental precision. Nevertheless, the characteristic features and the width of the signal are similar, if we compare sample S2 after 56 minutes of growth with and sample S2e: In addition to a pronounced peak close to position -128, a plateau is observed. The zinc blende peak in the cumulative signal obtained from the ESRF data is broader than the peak obtained at NANO. Both, the ESRF profile and the NANO profile in case of Gaussian background correction decay very similar for pixels smaller than -147. However, in case of the ESRF data, the decay starts also approximately at pixel -147. On the contrary, the profiles obtained at the NANO beamline decay already starting from pixel -144 – both in case of a Pearson VII background subtraction as well as in case of a two-dimensional Gaussian. This behavior is most likely originating in the different coherence properties of the beamlines as well as slight intrinsic deviations between sample S2 and sample S2e.

In contrast, the post-growth *ex-situ* data of sample S1 is *incompatible* with the *in-situ* data measured at NANO@ANKA. We could not identify the origin of these deviation for sample S1. Possible reasons include for example inhomogeneous properties of the grown nanowires and different regions of the sample have been scanned *in-situ* and *ex-situ*. In addition, a drift in the orbit of the electron beam in the synchrotron or a drift in the optics or monochromator of the beamline must also be considered as possible reason, since sample S1 has been measured after a new beam injection at ANKA whereas sample S2 has been measured just before this injection. As a consequence, we discard the shape of the *in-situ* measurements of sample 1 in our further considerations. Nonetheless, sample S1 has been valuable for understanding the composition of the total signal from the contributions of the nanowires and the crystallites.

For proper understanding and interpretation of the obtained nanowire profiles of sample S2 and further future samples, we now model the X-ray signal for nanowires with different distribution of both polytypes. Then, we return to the experimental data of sample S2.

4.3. Numerical simulations of X-ray scattering of polytypic GaAs nanowires

In this section, we discuss numerical simulations for the scattered X-ray intensity of GaAs nanowires constituted by two polytypes. Focus of the discussion will be the $(111)_{\mathrm{z}\curvearrowright\mathrm{c}}$ Bragg reflection which has been measured experimentally as discussed in the previous section. Such simulations require two components: First, appropriate approximations for the scattering under the given experimental conditions of Sec. 4.1 need to be chosen. Second, all relevant aspects of the nanowires for the scattering signal need to be modeled.

4.3.1. Derivation of the X-ray scattering of nanowires

We assume the following approximations for the scattering of the incident X-ray-radiation:

1. First order Born approximation: The nanowires themselves are small enough that kinematic approximation is appropriate [142]. Moreover, the reflected beam from the substrate is weak because the incident angle α_{i} was chosen slightly off the Bragg peak of silicon. Hence, higher order contributions to the scattering signal can be neglected within the precision of the measurements presented in Sec. 4.1.
2. Far field limit: The Fresnel number $\mathcal{F} = \frac{b^2}{\lambda d}$ is much smaller than one for $d \approx 1\mathrm{m}$, $\lambda \approx 1\mathrm{\AA}$ and $b \leq 50\mathrm{nm}$. For that approximate values, the value for the Fresnel number is $\mathcal{F} \leq 2.5 \cdot 10^{-5} \ll 1$. Hence, far field limit is justified.
3. The coherence length is (at least) in the order of the height of a single nanowire, i.e., approximately $2\mu\mathrm{m}$.
4. The size of the impinging beam is so huge that a very large number of coherence volumes is illuminated.

As a consequence of these assumptions the scattered signal is the incoherent sum of the coherent scattering of an individual wire. This coherent scattering contribution is given by the Fourier transformation of the electron density of an individual wire [142].

We characterize a wire by its geometry and its sequence of stacking of GaAs layers. The model for the wire is illustrated in Fig. 4.12.

The geometry contains the wire's height and its diameter. Both quantities vary from wire to wire. Hence, they are assumed to be random quantities for an individual wire with a given average value and a symmetric uniform distribution around this average. For our subsequent discussion of the q_z profile of $(111)_{\mathrm{z}\curvearrowright\mathrm{c}}$ GaAs Bragg reflection, the orientation of the surfaces is irrelevant. Nonetheless, we will include shape effects for both approximations in our discussion of scattering for completeness. Finally, a wire could also be tilted, but we neglect the influence of the tilt of a wire in our simulations.

For the generation of the stacking of a wire, we focus on (i) Markov processes (see Sec. 4.3.2) for growing a wire layer by layer and (ii) alternating phase segments with random length (see Sec. 4.3.3). This random length is determined based on a probability density function such as a Gamma, Weibull, or Poisson distribution. We will also discuss the relation of both approaches to each other and the limiting cases of pure zinc blende wires, pure wurtzite wires or fully random stacking sequences (without direct repetition of the same type of layer like $ABA\underline{BB}ABA$).

From the sequence of stacking, we can approximate the local lattice constant by the neighboring layers. If both neighboring layers are identical, the central layer is part of a wurtzite phase segment and is assigned the lattice constants of wurtzite phase. If both neighboring layers differ, we attribute the zinc blende lattice constant to the current layer. The lattice

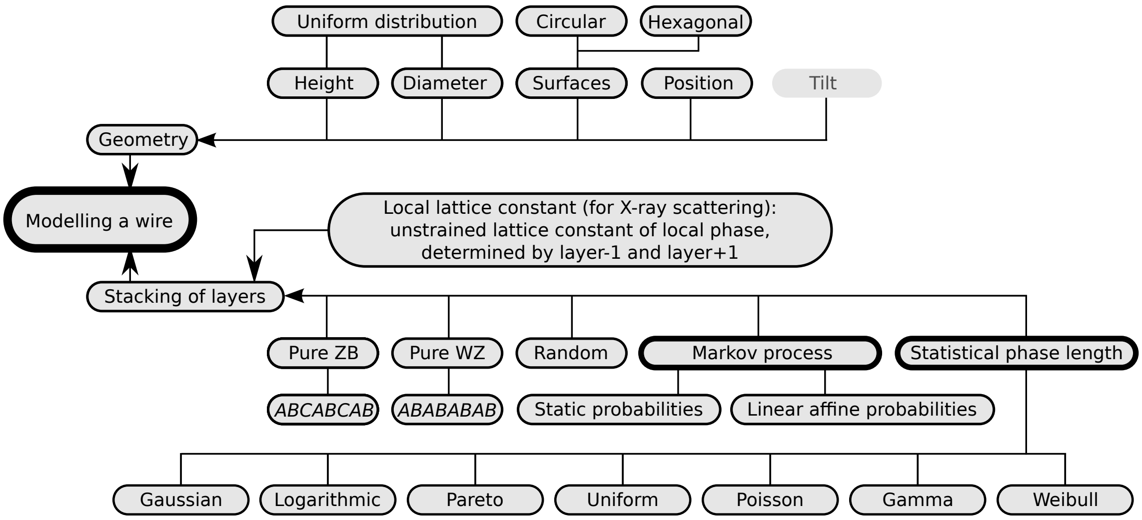

Figure 4.12.: Illustration of the model of a wire for simulations of the diffracted X-ray signal. Markov processes are discussed in Sec. 4.3.2 in detail. Phase segments with statistically generated number of layers are the topic of Sec. 4.3.3.

constant of twin zinc blende phase segments is assumed to be identical to zinc blende itself. Thus, we neglect effects of strain and dislocations. Finally, the first and the last layer of each wire's stacking sequence is attributed to the same phase and lattice constant as its neighboring layer.

We exemplify the translation from stacking sequence to local phase (and thereby also the local lattice constant) by an example (Z=zinc blende, W=wurtzite, T=twin-zinc blende):

```
Stacking sequence = ABCABCABCBCBCABACBACABCABC
Local phase       = ZZZZZZZZWWWWZZWTTTTWZZZZZZ
```

Our approach for modeling the essential properties of thin, self-catalyzed GaAs nanowires on Si(111) substrates are summarized in Fig. 4.12. For simulation a particular set of wires, the developed c++ based simulation tool – parallized by openMP [143] – reads an XML file by TinyXML [144] with a structure as described in appendix F.

Next, we derive the scattered intensity distribution for a given stacking sequence as input.

For this, we model the electron density which we split into a sum of $\mathrm{N_L}$ layers, i.e.,

$$\varrho_{\mathrm{el}}(\boldsymbol{x}) = \sum_{l=1}^{\mathrm{N_L}} \varrho_{\mathrm{el}}^{(l)}(\boldsymbol{x}) \ . \tag{4.5}$$

The electron density $\varrho_{\mathrm{el}}^{(l)}$ of each layer is modeled as an infinitely extended perfectly periodic two dimensional layer of Ga and As atoms at different height $z_{l\alpha}$, $\alpha \in \{\mathrm{Ga}, \mathrm{As}\}$, multiplied by a (possibly layer dependent) shape $\Omega^{(l)}(\boldsymbol{x}_\perp)$. Therefore,

$$\varrho_{\mathrm{el}}^{(l)}(\boldsymbol{x}) = \Omega^{(l)}(\boldsymbol{x}_\perp) \sum_{\alpha\in\{\mathrm{Ga},\mathrm{As}\}} \varrho_{\mathrm{el}}^{(l\alpha)}(\boldsymbol{x}_\perp, z) \ , \tag{4.6}$$

where the single species electron density $\varrho_{\mathrm{el}}^{(l\alpha)}(\boldsymbol{x}_\perp, z)$ of a single layer is approximated by

$$\begin{aligned}\varrho_{\mathrm{el}}^{(l\alpha)}(\boldsymbol{x}_\perp, z) = \varrho_{\mathrm{el}}^{(\alpha)}(\cdot) \otimes_{3\mathrm{D}} \\ \Big[\delta(\cdot\cdot\hat{\mathbf{e}}_z - z_{l\alpha}) \sum_{\boldsymbol{R}_{2\mathrm{D}}\in\mathbb{B}_{2\mathrm{D}}^{(l)}} \delta\big(\cdot\cdot\hat{\mathbf{e}}_x - (\boldsymbol{R}_{2\mathrm{D}}\cdot\hat{\mathbf{e}}_x + x_{l\alpha})\big)\delta\big(\cdot\cdot\hat{\mathbf{e}}_y - (\boldsymbol{R}_{2\mathrm{D}}\cdot\hat{\mathbf{e}}_y + y_{l\alpha})\big)\Big]\end{aligned} \tag{4.7}$$

where $\mathbb{B}_{\mathrm{2D}}^{(l)}$ is the two-dimensional in-plane Bravais lattice and $x_{l\alpha}$ and $y_{l\alpha}$ are (possibly layer dependent) shifts of each layer's origin. $\otimes_{\mathrm{3D}}$ is the three-dimensional convolution operator. $\varrho_{\mathrm{el}}^{(\alpha)}$ is the three dimensional electron density of an atom of type α centered at the origin of three dimensional space. For X-ray scattering, the approximation that the electron density $\varrho_{\mathrm{el}}^{(\alpha)}$ is independent of the chemical binding and the local lattice structure is typically appropriate because most electrons are located in inner shells and almost not influenced by the chemical bonding and the local lattice structure.

The height $z_{l\alpha}$ of a layer can be split as

$$z_{l\alpha} = z_l + \tilde{z}_{l\alpha} \ , \qquad \tilde{z}_{l\alpha} = \begin{cases} 0 & \text{for } \alpha\text{=As} \ , \\ \frac{3}{4} d_l & \text{for } \alpha\text{=Ga} \ , \end{cases} \tag{4.8}$$

where z_l is the beginning of this layer and d_l is the (phase dependent) thickness of this layer. This height d_l is given by

$$\frac{3}{4} d_l = \begin{cases} \frac{1}{4} c_{\mathrm{ZB}}^{(h)} & \text{for the zinc blende polytype ,} \\ \frac{3}{8} c_{\mathrm{WZ}}^{(h)} & \text{for the wurtzite polytype .} \end{cases} \tag{4.9}$$

Consequently, the form factor of a single wire $\mathcal{F}^{(\mathrm{SW})}(\boldsymbol{q})$ can be expressed as

$$\mathcal{F}^{(\mathrm{SW})}(\boldsymbol{q}) \propto \sum_{l=1}^{\mathrm{N_L}} \Big(\tilde{\Omega}^{(l)}(\cdot) \otimes_{\mathrm{2D}} \mathcal{F}_l^{(\mathrm{SL}_{\infty\perp})}(\cdot, q_z) \Big) (\boldsymbol{q}_\perp) \tag{4.10}$$

where

$$\tilde{\Omega}^{(l)}(\boldsymbol{q}_\perp) = \mathbf{FT}_{\boldsymbol{q}_\perp \leftrightarrow \boldsymbol{x}_\perp} \left\{ \Omega^{(l)}(\boldsymbol{x}_\perp) \right\} \tag{4.11a}$$

$$\mathcal{F}_l^{(\mathrm{SL}_{\infty\perp})}(\boldsymbol{q}_\perp, q_z) = \sum_{\alpha \in \{\mathrm{Ga,As}\}} \mathbf{FT}_{q_z \leftrightarrow z} \left\{ \mathbf{FT}_{\boldsymbol{q}_\perp \leftrightarrow \boldsymbol{x}_\perp} \left\{ \varrho_{\mathrm{el}}^{(l\alpha)}(\boldsymbol{x}_\perp, z) \right\} \right\} \tag{4.11b}$$

$$= \mathrm{e}^{-\mathrm{i} q_z z_l} \Big(\sum_{\boldsymbol{R}_{\mathrm{2D}}} \mathrm{e}^{-\mathrm{i} \boldsymbol{q}_\perp \cdot \boldsymbol{R}_{\mathrm{2D}}} \Big) \cdot \Big(\sum_{\alpha \in \{\mathrm{Ga,As}\}} f_\alpha(\boldsymbol{q}) \, \mathrm{e}^{-\mathrm{i} q_z \tilde{z}_{l\alpha}} \, \mathrm{e}^{-\mathrm{i} \boldsymbol{q}_\perp \cdot \boldsymbol{x}_\perp^{(l\alpha)}} \Big) \tag{4.11c}$$

with the atomic form factors $f_\alpha(\boldsymbol{q}) = \mathbf{FT}_{\boldsymbol{q} \leftrightarrow \boldsymbol{x}} \left\{ \varrho_{\mathrm{el}}^{(\alpha)}(\boldsymbol{x}) \right\}$. Note, that we approximate the two dimensional Bravais lattice of the Ga and As plane in a single layer l as identical, but its center might be shifted as incorporated by $\boldsymbol{x}_\perp^{(l\alpha)}$. Up to normalization, the two dimensional infinite sum over the Bravais lattice is

$$\sum_{\boldsymbol{R}_{\mathrm{2D}} \in \mathbb{B}_{\mathrm{2D}}^{(l)}} \mathrm{e}^{-\mathrm{i} \boldsymbol{q}_\perp \cdot \boldsymbol{R}_{\mathrm{2D}}} \propto \sum_{\boldsymbol{G}_\perp^{(l)}} \delta^{(2)}(\boldsymbol{q}_\perp - \boldsymbol{G}_\perp^{(l)}) \ , \tag{4.12}$$

where $\boldsymbol{G}_\perp^{(l)}$ is the reciprocal lattice of $\mathbb{B}_{\mathrm{2D}}^{(l)}$. Thus, the two-dimensional convolution in Eq. (4.10) yields

$$\begin{aligned} \mathcal{F}^{(\mathrm{SW})}(\boldsymbol{q}_\perp, q_z) \propto & \sum_{l=1}^{\mathrm{N_L}} \mathrm{e}^{-\mathrm{i} q_z z_l} \sum_{\alpha \in \{\mathrm{Ga,As}\}} \mathrm{e}^{-\mathrm{i} q_z \tilde{z}_{l\alpha}} \cdot \\ & \cdot \sum_{\boldsymbol{G}_\perp^{(l)}} \int_{\mathbb{R}^2} \tilde{\Omega}^{(l)}(\boldsymbol{q}_\perp - \boldsymbol{\tau}) \, \delta^{(2)}(\boldsymbol{\tau} - \boldsymbol{G}_\perp^{(l)}) \, f_\alpha(\boldsymbol{\tau}, q_z) \, \mathrm{e}^{-\mathrm{i} \boldsymbol{\tau} \cdot \boldsymbol{x}_\perp^{(l\alpha)}} \ \mathrm{d}^2\tau \end{aligned} \tag{4.13a}$$

$$\begin{aligned} = & \sum_{l=1}^{\mathrm{N_L}} \mathrm{e}^{-\mathrm{i} q_z z_l} \sum_{\alpha \in \{\mathrm{Ga,As}\}} \mathrm{e}^{-\mathrm{i} q_z \tilde{z}_{l\alpha}} \cdot \\ & \cdot \sum_{\boldsymbol{G}_\perp^{(l)}} \tilde{\Omega}^{(l)}(\boldsymbol{q}_\perp - \boldsymbol{G}_\perp^{(l)}) \, f_\alpha(\boldsymbol{G}_\perp^{(l)}, q_z) \, \mathrm{e}^{-\mathrm{i} \boldsymbol{G}_\perp^{(l)} \cdot \boldsymbol{x}_\perp^{(l\alpha)}} \end{aligned} \tag{4.13b}$$

The Fourier transform of the shape $\tilde{\Omega}^{(l)}(\boldsymbol{q}_\perp - \boldsymbol{G}_\perp^{(l)})$ decays for increasing magnitude of the argument. Hence, the dominant contribution originates from the element $\boldsymbol{G}_\perp^{(l)}$ nearest to the vector $\boldsymbol{q}_\perp$. Therefore, in lowest order, the sum over $\boldsymbol{G}_\perp^{(l)}$ reduces to the particular $\boldsymbol{G}_\perp^{(l)}(\boldsymbol{q}_\perp)$ closest to the current value of $\boldsymbol{q}_\perp$. Moreover, we approximate the atomic form factor $f_\alpha(\boldsymbol{G}_\perp^{(l)}(\boldsymbol{q}_\perp), q_z)$ by its value at the Bragg peak of the respective close GaAs Bragg peak $f_\alpha(\boldsymbol{Q}_\mathrm{B})$. Thus, we obtain

$$\begin{aligned}\mathcal{F}^{(\mathrm{SW})}(\boldsymbol{q}_\perp, q_z, \boldsymbol{Q}_\mathrm{B}) \propto \sum_{l=1}^{\mathrm{N_L}} \tilde{\Omega}^{(l)}(\boldsymbol{q}_\perp - \boldsymbol{G}_\perp^{(l)}(\boldsymbol{q}_\perp))\, \mathrm{e}^{-\mathrm{i}q_z z_l} \cdot \\ \cdot \sum_{\alpha\in\{\mathrm{Ga,As}\}} f_\alpha(\boldsymbol{Q}_\mathrm{B})\, \mathrm{e}^{-\mathrm{i}q_z \tilde{z}_{l\alpha}}\, \mathrm{e}^{-\mathrm{i}\boldsymbol{G}_\perp^{(l)}(\boldsymbol{q}_\perp)\cdot \boldsymbol{x}_\perp^{(l\alpha)}}\end{aligned} \tag{4.14}$$

in the vicinity of $\boldsymbol{Q}_\mathrm{B}$.

For the rest of this manuscript, we restrict to the q_z profiles of symmetric Bragg reflections. For the q_z profile of these reflections, we have $\boldsymbol{q}_\perp \equiv 0$. The closed reciprocal lattice point for that value of $\boldsymbol{q}_\perp$ is $\boldsymbol{G}_\perp^{(l)}(\boldsymbol{q}_\perp) \equiv 0$. Hence,

$$\mathcal{F}^{(\mathrm{SW})}(q_z, \boldsymbol{Q}_\mathrm{B}) \propto \sum_{l=1}^{\mathrm{N_L}} \tilde{\Omega}^{(l)}(0)\, \mathrm{e}^{-\mathrm{i}q_z z_l} \sum_{\alpha\in\{\mathrm{Ga,As}\}} f_\alpha(\boldsymbol{Q}_\mathrm{B})\, \mathrm{e}^{-\mathrm{i}q_z \tilde{z}_{l\alpha}} \tag{4.15}$$

The term $\tilde{\Omega}^{(l)}(0)$ is equal to the area of the geometrical cross section of the wire at layer l.

We assume constant diameter along the height of the nanowire which renders the in-plane shape of the nanowire a constant prefactor. If pronounced tapering of grown nanowires is revealed, e.g. by post-growth SEM, this geometrical information can be incorporated in a straight-forward manner in the prefactor $\tilde{\Omega}^{(l)}(0)$.

The beginning z_l of a layer l is the sum of all previously grown layers, i.e.,

$$z_0 = 0\ ,\ z_l \overset{l\geq 1}{\equiv} \sum_{k=0}^{l-1} c_k\ , \tag{4.16}$$

where c_k is the thickness of layer k (either the value for zincblende or wurtzite). Hence,

$$\mathcal{F}^{(\mathrm{SW})}(q_z, \boldsymbol{Q}_\mathrm{B}) \propto \sum_{l=1}^{\mathrm{N_L}} \mathrm{e}^{-\mathrm{i}q_z(\sum_{k=0}^{l-1} c_k)} \sum_{\alpha\in\{\mathrm{Ga,As}\}} f_\alpha(\boldsymbol{Q}_\mathrm{B})\, \mathrm{e}^{-\mathrm{i}q_z \tilde{z}_{l\alpha}}\ , \tag{4.17}$$

where the definition of $\tilde{z}_{l\alpha}$ can be found in Eqs. (4.8) and (4.9).

For the rest of this chapter, we restrict to a single wire per coherence volume. Thus, the positions of the center of the wires are irrelevant for the scattering signal and we do not (need to) develop suitable models and approximations for such inter-wire correlations.

In conclusion, the measured intensity distribution $\mathcal{I}(q_z)$ in the vicinity of the Bragg peak $\boldsymbol{Q}_\mathrm{B}$ for $\boldsymbol{q}_\perp = 0$ is given by the sum of the absolute squares of the single wires' form factors $\mathcal{F}_w^{(\mathrm{SW})}$ in Eq. (4.17), i.e.,

$$\mathcal{I}(q_z) \propto \sum_{w=1}^{\mathrm{N_W}} \left|\mathcal{F}_w^{(\mathrm{SW})}(q_z, \boldsymbol{Q}_\mathrm{B})\right|^2\ . \tag{4.18}$$

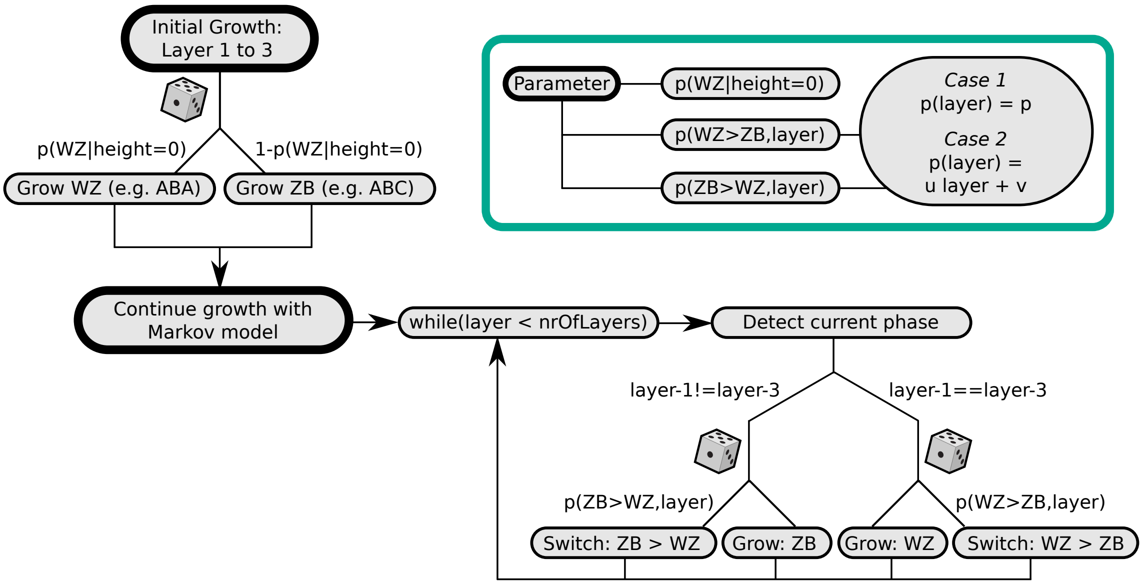

Figure 4.13.: Illustration of the generation of a statistical stacking sequence by a Markov process. The initial condition is determined by the probability $p_{\mathrm{WZ}}^{(0)} = p(\mathrm{WZ}|\mathrm{height} = 0)$ that the first layers of a wire nucleate in wurtzite stacking.

4.3.2. Stacking sequences generated by a Markov model

In this section, we discuss the generation of stacking sequences based on statistical Markov processes and the X-ray scattering signal thereof calculated by Eq. (4.18) in detail. This way of modelling the stacking of the atomic layers in the nanowires is motivated by the results published by Johansson et al. in [24, 110]. In addition, we discuss the effect of (possibly strong) deviations of the initial nucleation probabilities from the behavior of the Markov process after the initial growth stage.

4.3.2.1. Introduction to the Markov model

When forming the first three stacking layers $n = 1, 2, 3$ of a wire (i.e., beginning of first polytype segment), we assume a probability $p_{\mathrm{WZ}}^{(0)}$ for nucleation of a wurtzite stacking. At that stage, no previous history of the wire (i.e., $n \leq 0$) is available: instead, statistical fluctuations of the amorphous substrate surface, pre-patterned masks, gold droplet catalysts, etc. determine that initial behavior. After these initial three layers we assume the previous layers $n-1$, $n-2$ and $n-3$ to determine the behavior for layer n. From layer $n-1$ and layer $n-3$, we identify the current phase of the wire. If both layers are identical, the current phase is wurtzite. If both layers differ, the current layer n grows on top of a zinc blende segment. Depending on the current phase, we switch to the stacking sequence of the other phase with probabilities $p_{\mathrm{ZB}\to\mathrm{WZ}}$ (zinc blende to wurtzite) and $p_{\mathrm{WZ}\to\mathrm{ZB}}$ (wurtzite to zinc blende). Consequently, the current phase segments grows further by one layer with probabilities $1-p_{\mathrm{ZB}\to\mathrm{WZ}}$ (zinc blende segment) and $1-p_{\mathrm{WZ}\to\mathrm{ZB}}$ (wurtzite segment), where we refer to

$$p_{\mathrm{Asym}} = |p_{\mathrm{WZ}\to\mathrm{ZB}} - p_{\mathrm{ZB}\to\mathrm{WZ}}| \tag{4.19}$$

as the asymmetry of the transition probabilities.

Depending on the growth conditions, the probabilities $p_{\mathrm{ZB}\to\mathrm{WZ}}$ and $p_{\mathrm{WZ}\to\mathrm{ZB}}$ can be either almost static or may change during growth even for static “external” growth conditions originating in the complicated dynamics of the nucleation. Hence, the probabilities

$p_{\mathrm{ZB}\to\mathrm{WZ}}$ and $p_{\mathrm{WZ}\to\mathrm{ZB}}$ may become layer-dependent. The lowest and next to lowest order approximations for $p_{\mathrm{ZB}\to\mathrm{WZ}}$ and $p_{\mathrm{WZ}\to\mathrm{ZB}}$ are constant and linear affine functions.[8]

The Markov model for generation of statistic stacking sequences is illustrated in Fig. 4.13.

In the VLS growth model (see Sec. 1.1), the probabilties $p_{\mathrm{ZB}\to\mathrm{WZ}}$ and $p_{\mathrm{WZ}\to\mathrm{ZB}}$ are determined by the content, composition and shape of the droplet and, therefore, are the essential link between models for the properties of the droplet to the stacking sequence of the wire seen in X-ray diffraction. For example, the model presented by Krogstrup et al. in [69] explicitly predicts the behavior of these probabilities in dependence of the properties of the droplet. Moreover, ongoing research by eTEM (see e.g. Refs. [70, 74, 77, 95]) revealed very complicated dynamics at the position of the triple phase point in the framework of the VLS model. However, irrespective of such complicated behavior at the top-edge of the wire below the droplet, any successful physical model for this behavior must be able to quantitatively predict the probabilities $p_{\mathrm{ZB}\to\mathrm{WZ}}$ and $p_{\mathrm{WZ}\to\mathrm{ZB}}$.[9]

In Fig. 4.14, we illustrate the phase distribution in nanowires that results from the Markov model for the stacking sequence: For different (layer-independent) sets of parameters $p_{\mathrm{ZB}\to\mathrm{WZ}}$ and $p_{\mathrm{WZ}\to\mathrm{ZB}}$, three exemplary realizations have been generated and depicted in the range from layer 0 to layer 5000. For simplicity, $p_{\mathrm{WZ}}^{(0)}$ was set to 0.5. Most notably, we observe large fluctuations from segment to segment and from wire to wire.

4.3.2.2. Relation to the exponential distribution

For understanding the influence of the initial growth $p_{\mathrm{WZ}}^{(0)}$ on the "average wire" – and to estimate the requirements on X-ray measurements for its observation – we first derive the probability distribution for a defect-free phase segment to consist of n layers in the framework of a Markov process. By this, we understand the large fluctuations of the lengths of each segment. Then, we extend our treatment to include the initial growth.

The probability that a polytype segment – without loss of generality of the wurtzite polytype – which started growing at layer n_0 will finally consist of exactly $n \geq 1$ layers is

$$p_{\mathrm{WZ}}^{(\mathrm{Markov})}(n_0, n) = \mathcal{N}_{\mathrm{Markov}}(n_0) \left[\prod_{k=2}^{n} \left(1 - p_{\mathrm{WZ}\to\mathrm{ZB}}(n_0 + k - 1)\right) \right] p_{\mathrm{ZB}\to\mathrm{WZ}}(n_0 + n) \quad (4.20\mathrm{a})$$

where $\mathcal{N}_{\mathrm{Markov}}(n_0)$ is a normalization constant to enforce $\sum_{n=1}^{\infty} p_{\mathrm{WZ}}^{(\mathrm{Markov})}(n_0, n) = 1$ for all possible starting layers n_0.

For *layer independent* probabilities $p_{\mathrm{WZ}\to\mathrm{ZB}}$, this expression simplifies to

$$\begin{aligned} p_{\mathrm{WZ}}^{(\mathrm{Markov})}(n) &= \mathcal{N}_{\mathrm{Markov}} \left[\prod_{k=2}^{n} \left(1 - p_{\mathrm{WZ}\to\mathrm{ZB}}\right) \right] p_{\mathrm{ZB}\to\mathrm{WZ}} && (4.21\mathrm{a}) \\ &\overset{n \geq 0}{=} \mathcal{N}_{\mathrm{Markov}} \, p_{\mathrm{ZB}\to\mathrm{WZ}} \left(1 - p_{\mathrm{WZ}\to\mathrm{ZB}}\right)^{n-1} && (4.21\mathrm{b}) \\ &= \frac{\mathcal{N}_{\mathrm{Markov}} \, p_{\mathrm{ZB}\to\mathrm{WZ}}}{1 - p_{\mathrm{WZ}\to\mathrm{ZB}}} \, \mathrm{e}^{\log(1 - p_{\mathrm{WZ}\to\mathrm{ZB}}) \cdot n} && (4.21\mathrm{c}) \\ &= \tilde{\mathcal{N}}_{\mathrm{Markov}}^{(\mathrm{WZ})} \, \mathrm{e}^{-\frac{n}{b_{\mathrm{WZ}}}} \, , && (4.21\mathrm{d}) \end{aligned}$$

---

[8] This way, no discontinuous changes of the transition probabilities can be modelled. As soon as experimental data of better quality is available, a stepwise, iterative estimation of transition probabilities in the time interval t_{i-1} to t_i should be performed – taking into account the transition probabilities up to time t_{i-1} and the resulting phase distributions. This way, a discontinuous change in the transition probabilities can be revealed.

[9] We do not consider defect mediated growth, e.g., by twin-planes.

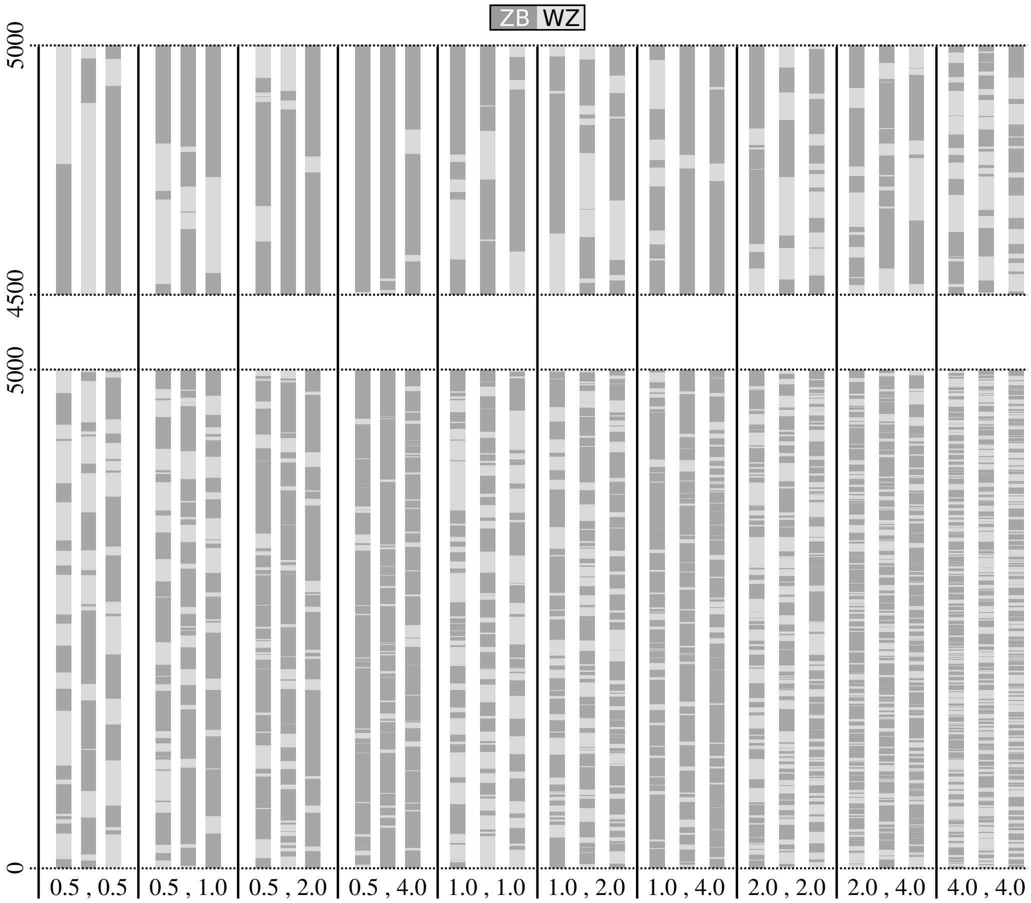

Figure 4.14.: Phase distribution inside nanowires in the framework of the Markov model. For each set of parameters on the abscissa – first the transition probability $p_{\mathrm{ZB}\to\mathrm{WZ}}$ in per cent, then $p_{\mathrm{WZ}\to\mathrm{ZB}}$ in per cent – three exemplary phase distributions have been generated and depicted from layer 0 to layer 5000. The range 4500 to 5000 has been magnified for better visibility of small segments and their frequency of occurrence.

where the new normalization $\tilde{\mathcal{N}}^{(\mathrm{WZ})}_{\mathrm{Markov}} = \frac{\mathcal{N}_{\mathrm{Markov}}\, p_{\mathrm{ZB}\to\mathrm{WZ}}}{1-p_{\mathrm{WZ}\to\mathrm{ZB}}}$ and the *decay constant* $b_{\mathrm{WZ}} = \frac{-1}{\log(1-p_{\mathrm{WZ}\to\mathrm{ZB}})} > 0$ for $0 < p_{\mathrm{WZ}\to\mathrm{ZB}} < 1$ has been defined. The n-dependence of Eq. (4.21d) corresponds to an exponential distribution [129, 145] with mean $\mu_{\mathrm{WZ}} = b_{\mathrm{WZ}}$ if n is considered as a real number and not an integer. This approximation is good if $b_{\mathrm{WZ}} \gg 1$, i.e., $p_{\mathrm{WZ}\to\mathrm{ZB}} \ll 1$.[10] The corresponding normalization for $n \in \mathbb{R}$ is $\tilde{\mathcal{N}}^{(\mathrm{WZ})}_{\mathrm{Markov}} = \frac{1}{b_{\mathrm{WZ}}}$. Eq. (4.21d) will be important for the generalizations discussed in Sec. 4.3.3.

4.3.2.3. Initial growth vs. the stationary limit of growth

We now turn to the second task and investigate the interplay of the parameters $p^{(0)}_{\mathrm{WZ}}$, $p_{\mathrm{WZ}\to\mathrm{ZB}}$ and $p_{\mathrm{ZB}\to\mathrm{WZ}}$: First, the implications from the Markov model for the probabilities $p^{(\mathrm{L})}_{\mathrm{WZ}}(n)$ to find either zinc blende phase or wurtzite phase at a particular layer n of a wire

---

[10] Strictly, the mean phase segment size for phase P is

$$b_{\mathrm{P}} = \sum_{k=0}^{\infty}(k+1)\cdot p^{k}_{\mathrm{P}\to\mathrm{P}}\cdot p_{\mathrm{P}\to\bar{\mathrm{P}}} = \frac{1}{1-p_{\mathrm{P}\to\mathrm{P}}} = \frac{1}{p_{\mathrm{P}\to\bar{\mathrm{P}}}}\ . \tag{4.22}$$

In the limit $p_{\mathrm{P}\to\bar{\mathrm{P}}} \to 0$, which corresponds to the case of long decay length $b_{\mathrm{P}} \gg 1$ and to the approximation of the discrete case by the exponential distribution and continuous n, b_{P} is approximately equal to $b_{\mathrm{P}} \approx -1/\log\left(1-p_{\mathrm{P}\to\bar{\mathrm{P}}}\right)$.

with $\mathrm{N_L}$ layers are discussed. In addition, we consider the average fraction $\bar{p}_{\mathrm{WZ}}(n)$ of wurtzite phase from layer $k = 1$ to $k = n$. Moreover, we discuss the *stationary limit* for height independent switching probabilities $p_{\mathrm{WZ\to ZB}}$ and $p_{\mathrm{ZB\to WZ}}$.

We calculate $p^{(\mathrm{L})}_{\mathrm{WZ}}(n)$ recursively by

$$p^{(\mathrm{L})}_{\mathrm{WZ}}(n) = \begin{cases} p^{(0)}_{\mathrm{WZ}} & n \leq 3 \\ \left(1 - p_{\mathrm{WZ\to ZB}}\right) \cdot p^{(\mathrm{L})}_{\mathrm{WZ}}(n-1) + p_{\mathrm{ZB\to WZ}} \cdot \left(1 - p^{(\mathrm{L})}_{\mathrm{WZ}}(n-1)\right) & n > 3 \end{cases} \tag{4.23}$$

The respective probability for zinc blende is $1 - p^{(\mathrm{L})}_{\mathrm{WZ}}(n)$.

If any switching from one phase to another takes place, i.e., $p_{\mathrm{WZ\to ZB}} + p_{\mathrm{ZB\to WZ}} > 0$, the growth statistics of a wire will approach a *stationary limit* for $\mathrm{N_L} \to \infty$. This stationary limit is independent of the initial growth and is characterized by height independent behavior, i.e., $\breve{p}_{\mathrm{WZ}} = p^{(\mathrm{L})}_{\mathrm{WZ}}(n-1) = p^{(\mathrm{L})}_{\mathrm{WZ}}(n)$ is no longer a function of n. If we solve the case $n > 3$ in Eq. (4.23) for $\breve{p}_{\mathrm{WZ}}$, we obtain

$$\breve{p}_{\mathrm{WZ}} = \frac{p_{\mathrm{ZB\to WZ}}}{p_{\mathrm{WZ\to ZB}} + p_{\mathrm{ZB\to WZ}}} = \frac{1}{1 + \frac{p_{\mathrm{WZ\to ZB}}}{p_{\mathrm{ZB\to WZ}}}} \ . \tag{4.24a}$$

Therefore, the stationary limit is invariant upon the simultaneous scaling $p_{\mathrm{WZ\to ZB}} \to \alpha \cdot p_{\mathrm{WZ\to ZB}}$ and $p_{\mathrm{ZB\to WZ}} \to \alpha \cdot p_{\mathrm{ZB\to WZ}}$, $\alpha \in \mathbb{R}$. Moreover, it is clearly bound by one from above and zero from below. If $p_{\mathrm{WZ\to ZB}} + p_{\mathrm{ZB\to WZ}} = 0$, the stationary limit is simply given by the initial growth behavior, i.e.,

$$\breve{p}_{\mathrm{WZ}} = p^{(0)}_{\mathrm{WZ}} \ . \tag{4.24b}$$

Typical X-ray diffraction measurements however do not reveal the probabilities $p^{(\mathrm{L})}_{\mathrm{WZ}}(n)$, but its average over all layers $k = 1$ to the number of grown layers $k = \mathrm{N_L}$. This average probability (or fraction) of the wurtzite polytype is given by

$$\bar{p}_{\mathrm{WZ}}(\mathrm{N_L}) = \sum_{k=1}^{\mathrm{N_L}} \frac{p^{(\mathrm{L})}_{\mathrm{WZ}}(k)}{\mathrm{N_L}} \tag{4.25}$$

Although our discussion was based on static probabilities $p_{\mathrm{WZ\to ZB}}$ and $p_{\mathrm{ZB\to WZ}}$ independent of n, formulas (4.23) and (4.25) are also valid for height dependent probabilities $p_{\mathrm{WZ\to ZB}}(n)$ and $p_{\mathrm{ZB\to WZ}}(n)$.

The recursive definition (4.23) will now be rewritten in an explicit expression for the case of static probabilities $p_{\mathrm{WZ\to ZB}}$ and $p_{\mathrm{ZB\to WZ}}$. For this purpose, we define the probability $\tilde{p}_{12} \equiv 1 - (p_{\mathrm{WZ\to ZB}} + p_{\mathrm{ZB\to WZ}})$ and rewrite Eq. (4.23) for $n > 3$ as

$$p^{(\mathrm{L})}_{\mathrm{WZ}}(n) \overset{n \geq 3}{=} \tilde{p}_{12} \cdot p^{(\mathrm{L})}_{\mathrm{WZ}}(n-1) + p_{\mathrm{ZB\to WZ}} \ . \tag{4.26}$$

In order to deduce an explicit expression for $p^{(\mathrm{L})}_{\mathrm{WZ}}(n)$ from this recursive relation, it is useful to write down the explicit result for small n:

$$p^{(\mathrm{L})}_{\mathrm{WZ}}(3) = p^{(0)}_{\mathrm{WZ}} \tag{4.27a}$$

$$p^{(\mathrm{L})}_{\mathrm{WZ}}(4) = \tilde{p}_{12} \cdot p^{(0)}_{\mathrm{WZ}} + p_{\mathrm{ZB\to WZ}} \tag{4.27b}$$

$$p^{(\mathrm{L})}_{\mathrm{WZ}}(5) = \tilde{p}_{12}^2 \cdot p^{(0)}_{\mathrm{WZ}} + \tilde{p}_{12} \cdot p_{\mathrm{ZB\to WZ}} + p_{\mathrm{ZB\to WZ}} \tag{4.27c}$$

$$p^{(\mathrm{L})}_{\mathrm{WZ}}(6) = \tilde{p}_{12}^3 \cdot p^{(0)}_{\mathrm{WZ}} + \tilde{p}_{12}^2 \cdot p_{\mathrm{ZB\to WZ}} + \tilde{p}_{12} \cdot p_{\mathrm{ZB\to WZ}} + p_{\mathrm{ZB\to WZ}} \tag{4.27d}$$

From this, we can deduce the explicit expression

$$p^{(\mathrm{L})}_{\mathrm{WZ}}(n) \overset{n\geq 3}{=} \tilde{p}_{12}^{\,n-3}\cdot p^{(0)}_{\mathrm{WZ}} + p_{\mathrm{ZB}\to\mathrm{WZ}}\sum_{k=0}^{n-4}\tilde{p}_{12}^{\,k} \tag{4.28a}$$

$$= \tilde{p}_{12}^{\,n-3}\cdot p^{(0)}_{\mathrm{WZ}} + p_{\mathrm{ZB}\to\mathrm{WZ}}\frac{1-\tilde{p}_{12}^{\,n-3}}{1-\tilde{p}_{12}} = \tilde{p}_{12}^{\,n-3}\cdot p^{(0)}_{\mathrm{WZ}} + \left(1-\tilde{p}_{12}^{\,n-3}\right)\cdot \breve{p}_{\mathrm{WZ}}\ , \tag{4.28b}$$

for arbitrary n. Here, the geometric series $\sum_{k=0}^{n} q^n = \frac{1-q^{n+1}}{1-q}$ for $|q| < 1$ and Eq. (4.24a) have been used. Both limits $\tilde{p}_{12} \to 1$ (which results in $p^{(\mathrm{L})}_{\mathrm{WZ}}(n) \to p^{(0)}_{\mathrm{WZ}}$) and $n \to \infty$ (which results in $p^{(\mathrm{L})}_{\mathrm{WZ}}(n) \to \breve{p}_{\mathrm{WZ}}$) are consistent with the previous discussion.

Eq. (4.28b) is a weighted average[11] for the probabilities $p^{(\mathrm{L})}_{\mathrm{WZ}}(n)$ of the initial statistics $p^{(0)}_{\mathrm{WZ}}$ and the stationary limit $\breve{p}_{\mathrm{WZ}}$. Hence, the weight of the initial growth parameter $p^{(0)}_{\mathrm{WZ}}$ decays as $\tilde{p}_{12}^{\,n-3}$. This weight drops below a given bound ϵ (e.g., $\epsilon = 5\%$) for

$$n > \frac{\log(\epsilon)}{\log(\tilde{p}_{12})} + 3 \overset{\tilde{p}_{12}\approx 1}{\approx} \frac{-\log(\epsilon)}{p_{\mathrm{ZB}\to\mathrm{WZ}} + p_{\mathrm{WZ}\to\mathrm{ZB}}}\ , \tag{4.29}$$

which is *independent* of $p^{(0)}_{\mathrm{WZ}}$. Alternatively, we can define a layer n for which the relative error of $p^{(\mathrm{L})}_{\mathrm{WZ}}(n)$ to the stationary limit $\breve{p}_{\mathrm{WZ}}$ drops below ϵ:

$$\epsilon \overset{!}{\geq} \left|\frac{p^{(\mathrm{L})}_{\mathrm{WZ}}(n) - \breve{p}_{\mathrm{WZ}}}{\breve{p}_{\mathrm{WZ}}}\right| = \tilde{p}_{12}^{\,n-3}\cdot\left(\frac{\left|p^{(0)}_{\mathrm{WZ}} - \breve{p}_{\mathrm{WZ}}\right|}{\breve{p}_{\mathrm{WZ}}}\right) \Rightarrow n \overset{p^{(0)}_{\mathrm{WZ}}\neq\breve{p}_{\mathrm{WZ}}}{\geq} \frac{\log\left(\frac{\epsilon\cdot\breve{p}_{\mathrm{WZ}}}{\left|p^{(0)}_{\mathrm{WZ}}-\breve{p}_{\mathrm{WZ}}\right|}\right)}{\log(\tilde{p}_{12})} + 3 \tag{4.30}$$

This bound depends explicitly on the log of the inverse of the relative difference of the initial behavior and the stationary limit (i.e., $\frac{p^{(0)}_{\mathrm{WZ}}-\breve{p}_{\mathrm{WZ}}}{\breve{p}_{\mathrm{WZ}}}$) and the probability $\tilde{p}_{12}$.

From Eq. (4.28b), we can now calculate analytically and non-recursively the effect of possibly different initial growth behavior $p^{(0)}_{\mathrm{WZ}}$ on layers $n > 3$. For X-ray-measurements we are typically more interested in the result of the average phase content up to some layer $\mathrm{N_L}$ as defined in Eq. (4.25). Evaluation of this average yields

$$\bar{p}_{\mathrm{WZ}}(\mathrm{N_L}) \overset{\mathrm{N_L}>3}{=} \sum_{k=1}^{3}\frac{p^{(0)}_{\mathrm{WZ}}}{\mathrm{N_L}} + \sum_{k=4}^{\mathrm{N_L}}\frac{\tilde{p}_{12}^{\,k-3}\cdot p^{(0)}_{\mathrm{WZ}} + \left(1-\tilde{p}_{12}^{\,k-3}\right)\cdot\breve{p}_{\mathrm{WZ}}}{\mathrm{N_L}} \tag{4.31a}$$

$$= \frac{3}{\mathrm{N_L}}p^{(0)}_{\mathrm{WZ}} + \left(\frac{\mathrm{N_L}-3}{\mathrm{N_L}}\right)\breve{p}_{\mathrm{WZ}} + \left(\frac{p^{(0)}_{\mathrm{WZ}} - \breve{p}_{\mathrm{WZ}}}{\mathrm{N_L}}\right)\tilde{p}_{12}\left(\sum_{k=4}^{\mathrm{N_L}}\tilde{p}_{12}^{\,k-4}\right) \tag{4.31b}$$

$$= \frac{3}{\mathrm{N_L}}p^{(0)}_{\mathrm{WZ}} + \left(\frac{\mathrm{N_L}-3}{\mathrm{N_L}}\right)\breve{p}_{\mathrm{WZ}} + \tilde{p}_{12}\left(\frac{p^{(0)}_{\mathrm{WZ}} - \breve{p}_{\mathrm{WZ}}}{\mathrm{N_L}}\right)\left(\frac{1-\tilde{p}_{12}^{\,\mathrm{N_L}-3}}{1-\tilde{p}_{12}}\right) \tag{4.31c}$$

In the limit $\tilde{p}_{12} \to 1$, we exploit $\lim_{\tilde{p}_{12}\to 1}\frac{1-\tilde{p}_{12}^{\,\mathrm{N_L}-3}}{1-\tilde{p}_{12}} = \mathrm{N_L} - 3$ and obtain

$$\lim_{\tilde{p}_{12}\to 1}\bar{p}_{\mathrm{WZ}}(\mathrm{N_L}) = \frac{3}{\mathrm{N_L}}p^{(0)}_{\mathrm{WZ}} + \left(\frac{\mathrm{N_L}-3}{\mathrm{N_L}}\right)\breve{p}_{\mathrm{WZ}} + \left(\frac{p^{(0)}_{\mathrm{WZ}} - \breve{p}_{\mathrm{WZ}}}{\mathrm{N_L}}\right)\left(\mathrm{N_L}-3\right) = p^{(0)}_{\mathrm{WZ}}\ . \tag{4.32}$$

In the limit $\mathrm{N_L} \to \infty$ (for $\tilde{p}_{12} \neq 1$) or in the limit $p^{(0)}_{\mathrm{WZ}} \to \breve{p}_{\mathrm{WZ}}$ this expression reduces to

$$\lim_{\mathrm{N_L}\to\infty}\bar{p}_{\mathrm{WZ}}(\mathrm{N_L}) = \lim_{p^{(0)}_{\mathrm{WZ}}\to\breve{p}_{\mathrm{WZ}}}\bar{p}_{\mathrm{WZ}}(\mathrm{N_L}) = \breve{p}_{\mathrm{WZ}}\ . \tag{4.33}$$

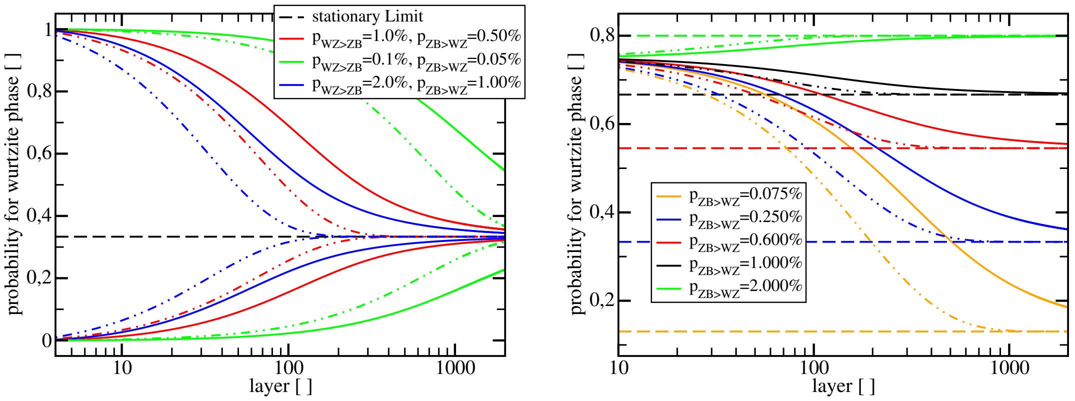

(a) Fixed stationary limit (b) Fixed $p^{(0)}_{\mathrm{WZ}} = 75\%$ and fixed $p_{\mathrm{WZ}\to\mathrm{ZB}} = 0.5\%$

Figure 4.15.: Illustration of the influence of the initial growth behavior $p^{(0)}_{\mathrm{WZ}}$ in the framework of a Markov process. Dashed lines represent stationary limits, dashed-dotted lines represent the probabilities for wurtzite phase in layer n (i.e., $p^{(\mathrm{L})}_{\mathrm{WZ}}(n)$) and continuous lines represent the average fraction of wurtzite phase from layer $k = 1$ to a particular layer n (i.e., $\bar{p}_{\mathrm{WZ}}(n)$). Fig. (a) compares the behavior for fixed stationary limit and different switching probabilities for the extreme cases $p^{(0)}_{\mathrm{WZ}} \in \{0, 1\}$. In Fig. (b), $p^{(0)}_{\mathrm{WZ}}$ and $p_{\mathrm{WZ}\to\mathrm{ZB}}$ are kept fixed and the probability $p_{\mathrm{ZB}\to\mathrm{WZ}}$ is varied.

From Eq. (4.31c), we can understand the interplay of time resolved X-ray data and the initial growth stage under the assumption of static switching probabilities after the initial growth stage. Some results are depicted in Fig. 4.15 for illustration.

Note, that Eq. (4.31c) can be rewritten as

$$\bar{p}_{\mathrm{WZ}}(\mathrm{N_L}) = \left[\frac{3}{\mathrm{N_L}} + \frac{\tilde{p}_{12}}{\mathrm{N_L}}\left(\frac{1-\tilde{p}_{12}^{\mathrm{N_L}-3}}{1-\tilde{p}_{12}}\right)\right] p^{(0)}_{\mathrm{WZ}} + \left[\left(\frac{\mathrm{N_L}-3}{\mathrm{N_L}}\right) - \frac{\tilde{p}_{12}}{\mathrm{N_L}}\left(\frac{1-\tilde{p}_{12}^{\mathrm{N_L}-3}}{1-\tilde{p}_{12}}\right)\right] \breve{p}_{\mathrm{WZ}}\ , \tag{4.34}$$

which expresses the layer average $\bar{p}_{\mathrm{WZ}}(\mathrm{N_L})$ as a weighted average of the initial wurtzite probability $p^{(0)}_{\mathrm{WZ}}$ and the stationary limit $\breve{p}_{\mathrm{WZ}}$ in analogy to Eq. (4.28b). Again, we calculate the layer $\mathrm{N_L}$ for which the weight of the initial growth conditions drops below ϵ, i.e.,

$$\frac{3}{\mathrm{N_L}} + \frac{\tilde{p}_{12}}{\mathrm{N_L}}\left(\frac{1-\tilde{p}_{12}^{\mathrm{N_L}-3}}{1-\tilde{p}_{12}}\right) \leq \epsilon. \tag{4.35}$$

The solution of this equation is

$$\mathrm{N_L} \geq \frac{-\mathrm{LambertW}\left(\frac{\log(\tilde{p}_{12})\ \tilde{p}_{12}^{-2+\frac{3}{\epsilon}+\frac{\tilde{p}_{12}}{\epsilon\,(1-\tilde{p}_{12})}}}{\epsilon\,(1-\tilde{p}_{12})}\right)}{\log(\tilde{p}_{12})} + \frac{3}{\epsilon} + \frac{\tilde{p}_{12}}{\epsilon\,(1-\tilde{p}_{12})} \tag{4.36}$$

and is depicted in Fig. 4.16(a) for various values for ϵ. Again, by construction, this expression does not depend on the initial probability for wurtzite $p^{(0)}_{\mathrm{WZ}}$.

In complete analogy to the case of the local wurtzite probability we can consider the

---

[11] The weights fulfill normalization of the sum to one for all layers n and are positive definite.

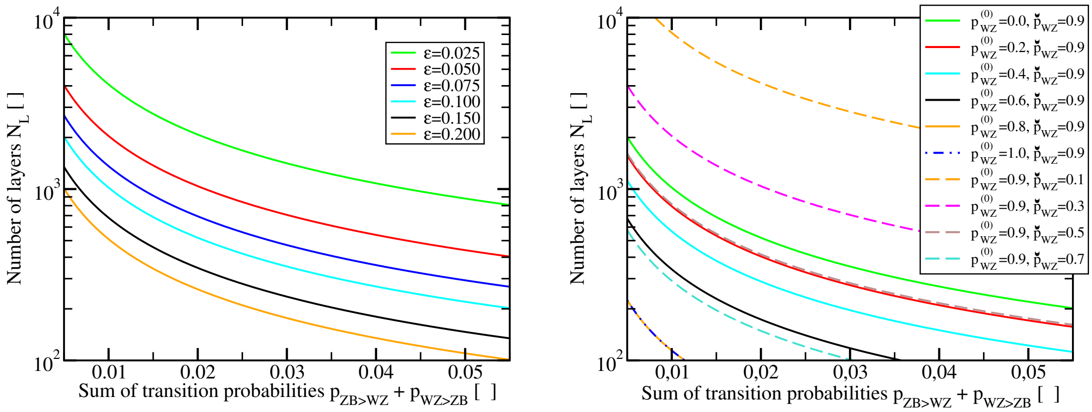

(a) Limited weight according to Eq. (4.36)

(b) Limited relative error according to Eq. (4.37) for $\epsilon = 0.1$.

Figure 4.16.: Illustration of the influence of the initial growth behavior $p^{(0)}_{\mathrm{WZ}}$ in the framework of a Markov process (continuation of Fig. 4.15).

relative deviation of $\bar{p}_{\mathrm{WZ}}(\mathrm{N_L})$ from the stationary limit $\breve{p}_{\mathrm{WZ}}$. In this case, the solution is

$$\mathrm{N_L} \geq \frac{-\mathrm{LambertW}\left(\frac{\log(\tilde{p}_{12})\left|\breve{p}_{\mathrm{WZ}}-p^{(0)}_{\mathrm{WZ}}\right| \tilde{p}_{12}^{\,-2+\frac{\left|\breve{p}_{\mathrm{WZ}}-p^{(0)}_{\mathrm{WZ}}\right|\cdot(3-2\tilde{p}_{12})}{\epsilon\,\breve{p}_{\mathrm{WZ}}\,(1-\tilde{p}_{12})}}}{\epsilon\,\breve{p}_{\mathrm{WZ}}\,(1-\tilde{p}_{12})}\right)}{\log(\tilde{p}_{12})} + \frac{\left|\breve{p}_{\mathrm{WZ}}-p^{(0)}_{\mathrm{WZ}}\right|\cdot(3-2\tilde{p}_{12})}{\epsilon\,\breve{p}_{\mathrm{WZ}}\,(1-\tilde{p}_{12})} \tag{4.37}$$

and is illustrated in Figs. 4.16(b) for various combinations of stationary limit $\breve{p}_{\mathrm{WZ}}$ and initial growth parameter $p^{(0)}_{\mathrm{WZ}}$.

The results depicted in Figs. 4.15 and 4.16 are important for determination if information about the initial growth behavior can be extracted from given experimental data of nanowires with height $\mathrm{N_L}$ or if the influence of the initial growth is negligible for the observed data. Specifically, for the results given in Sec. 4.4.1, the influence of the initial growth is negligible and we can restrict to the parameter space $(p_{\mathrm{ZB\to WZ}}, p_{\mathrm{ZB\to WZ}})$ there.

4.3.2.4. The $(111)_{\mathrm{z\frown c}}$ reflection for static transition probabilities

Next, we consider the X-ray scattering signal $\mathcal{I}(q_z)$ near the $(111)_{\mathrm{z\frown c}}$ GaAs Bragg peak for stacking sequences based on statistical Markov processes. Unless stated otherwise, a set of $\mathrm{N_W} = 2500$ wires has been simulated according to Eq. (4.18). The initial growth parameter $p^{(0)}_{\mathrm{WZ}}$ was set to 0.5 and the number of layers $\mathrm{N_L}$ of each wire was drawn randomly from a uniform distribution in the interval 6500 to 8500. The results have been normalized such that the maximum of the scattering signal is equal to one. Due to space constraints in the captions of the figures, the parameters $p_{\mathrm{ZB\to WZ}}$ and $p_{\mathrm{ZB\to WZ}}$ are sometimes abbreviated as $p_{\mathrm{Z>W}}$ and $p_{\mathrm{W>Z}}$. The transition probability of the symmetric case $p_{\mathrm{ZB\to WZ}} = p_{\mathrm{ZB\to WZ}}$ is sometimes referred to as p_{Switch}.

The results are depicted in Fig. 4.17: Fig. (a) covers symmetric transition probability p_{Switch} from $p_{\mathrm{Switch}} = 0$ to $p_{\mathrm{Switch}} = 1$. Both limits refer to pure wires: Whereas for $p_{\mathrm{Switch}} = 0$ pure wurtzite and zinc blende wires are obtained with fractions determined by $p^{(0)}_{\mathrm{WZ}}$, the limit $p_{\mathrm{Switch}} = 1$ corresponds to pure wires of the 4H polytype (see Sec. 1.4) and we see the $(222)_{\mathrm{z\frown c}}$ reflection of the stacking BABC-BABC-... (i.e., the unit cell BABC). For those extreme cases $p_{\mathrm{Switch}} = 0$ and $p_{\mathrm{Switch}} = 1$, the signal is extremely sharp and shape oscillations are observed. If we increase p_{Switch} from $p_{\mathrm{Switch}} = 0$ to $p_{\mathrm{Switch}} = 0.1\%$,

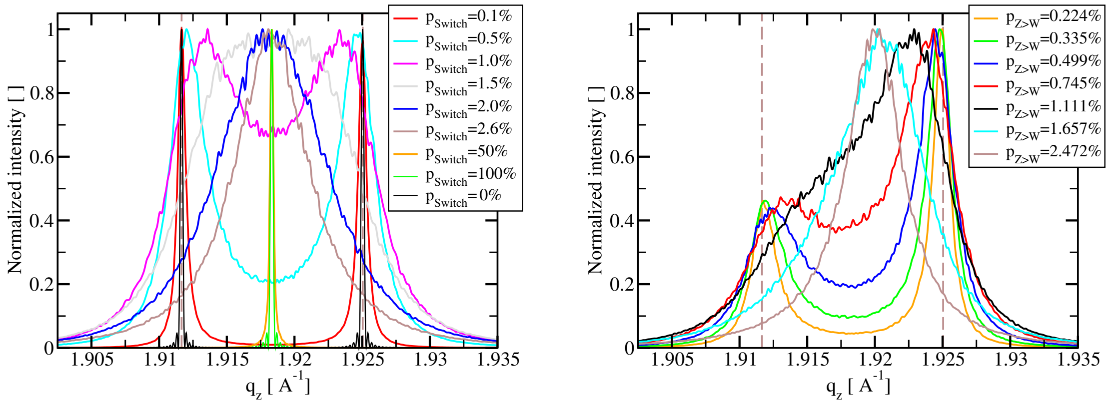

(a) Symmetric cases $p_{\mathrm{ZB}\to\mathrm{WZ}} = p_{\mathrm{WZ}\to\mathrm{ZB}}$ resulting in $\breve{p}_{\mathrm{WZ}} = 0.5$ (see Eq. (4.24a))

(b) Asymmetric cases $p_{\mathrm{ZB}\to\mathrm{WZ}} = 0.667 \cdot p_{\mathrm{WZ}\to\mathrm{ZB}}$ resulting in $\breve{p}_{\mathrm{WZ}} = 0.4$ (see Eq. (4.24a))

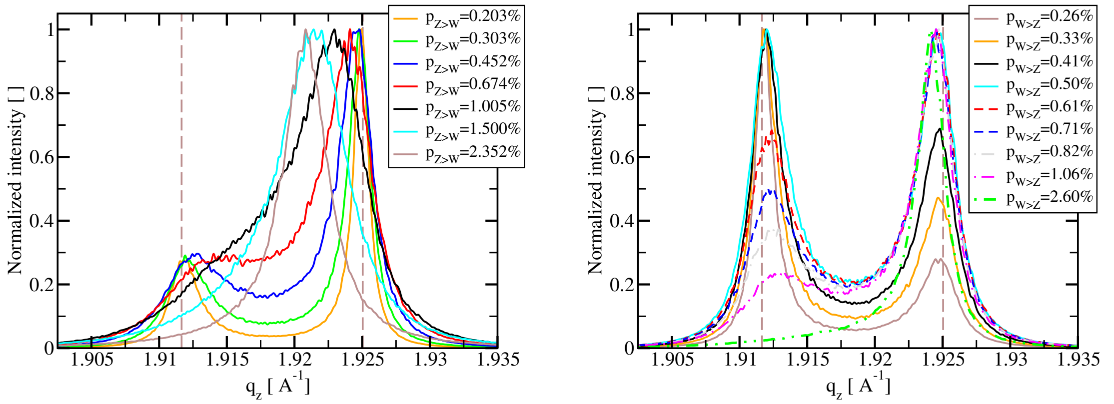

(c) Asymmetric cases $p_{\mathrm{ZB}\to\mathrm{WZ}} = 0.522 \cdot p_{\mathrm{WZ}\to\mathrm{ZB}}$ resulting in $\breve{p}_{\mathrm{WZ}} = 0.34$ (see Eq. (4.24a))

(d) Asymmetric cases with $p_{\mathrm{ZB}\to\mathrm{WZ}} = 0.50\%$

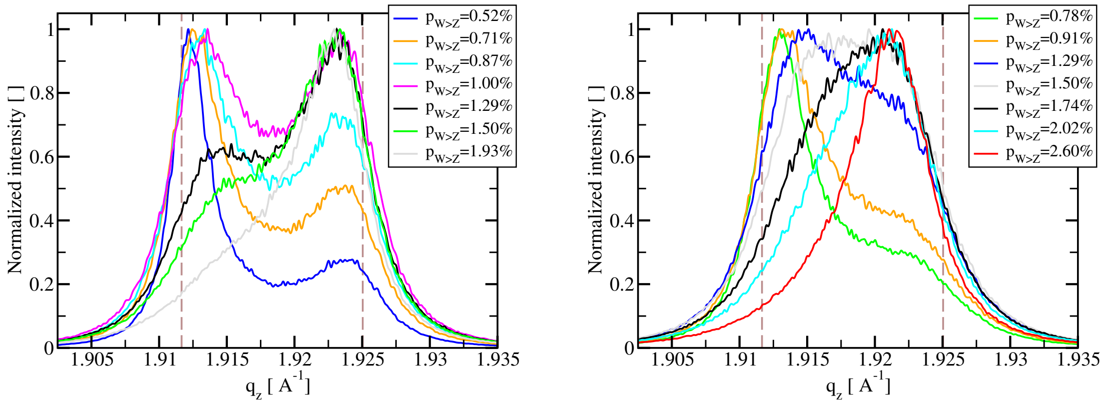

(e) Asymmetric cases with $p_{\mathrm{ZB}\to\mathrm{WZ}} = 1.00\%$

(f) Asymmetric cases with $p_{\mathrm{ZB}\to\mathrm{WZ}} = 1.50\%$

Figure 4.17.: Intensity profile $\mathcal{I}(q_z)$ near the $(111)_{\mathrm{z}\curvearrowright\mathrm{c}}$ GaAs Bragg peak for a Markov process as described in Fig. 4.13.

the peaks from both phases are still distinct, but the size oscillations already vanished due to the statistical fluctuations in the domain sizes. If we increase the switching probability further to $0.5\% \leq p_{\mathrm{Switch}} \leq 1.5\%$, we observe that

- the distinct peaks of extended pure and defect-free zinc blende and wurtzite structures become increasingly broadened and start to overlap significantly,
- the maximum of the two recognizable subpeaks shifts from the native zinc blende

and wurtzite positions towards the center q_C of these two native positions, and,

- that the broadening is stronger than the shift towards the center resulting in a significant weight of the intensity located at q_z values smaller than the pure wurtzite wires' q_z range and larger than the pure zinc blende wires' q_z range.

The drift of the maximum of the two distinct subpeaks towards the center q_C is monotonous in case of our Markov process model (see Fig. 4.13).

For $p_{\text{Switch}} \geq 1.5\%$, both subpeaks merge to a single peak centered at q_C. Its width decreases more and more for increasing switching probabilities p_{Switch}. For $p_{\text{Switch}} = 50\%$, we obtain the limiting case to which we refer as "fully random wires": For every newly grown layer, the probability for switching to the stacking order of the other phase is as big as keeping the stacking sequence of the current phase. From this case of fully random wires, we see that even a very shape single peak (as compared to $p_{\text{Switch}} \approx 2.6\%$) does not imply a structure with high ordering. Note, that by Eq. (4.24a), if the transition probabilities $p_{\text{ZB}\to\text{WZ}} = p_{\text{WZ}\to\text{ZB}}$ are equal, the phase fraction of wurtzite is equal to $\breve{p}_{\text{WZ}} = 50\%$. Moreover, for symmetric switching probabilities, the scattering signal is symmetric with respect to the axis $q_z = q_C$.

If we want to model structures with $\breve{p}_{\text{WZ}} \neq 50\%$ (in the stationary limit), we must consider asymmetric conditions, i.e., $p_{\text{ZB}\to\text{WZ}} \neq p_{\text{WZ}\to\text{ZB}}$. The corresponding X-ray signal (normalized to a maximum of 1) is depicted in Figs. 4.17(b) to 4.17(f):

On the one hand, the phase fractions of both polytypes are equal for all curves in Figs. (b) ($\breve{p}_{\text{WZ}} = 40\%$) and (c) ($\breve{p}_{\text{WZ}} = 34\%$). Again, we observe a transition from two distinct subpeaks to a single merged peak. However, in the intermediate range, a pronounced plateau next to a pronounced peak is observed (e.g., $p_{\text{ZB}\to\text{WZ}} = 0.674\%$ in Fig. (c)). The characteristics of this signal closely resembles the features which we discussed in Sec. 4.1. We point out a drift of the maximum towards zinc blende for decreasing phase fraction $\breve{p}_{\text{WZ}}$ for highly faulty wires.

On the other hand, the phase fractions vary in the Figs. 4.17(d) to 4.17(f). Those figures are dedicated to fixed $p_{\text{ZB}\to\text{WZ}}$ which is set to 0.50%, 1.00% and 1.50% respectively. For $p_{\text{ZB}\to\text{WZ}} = 0.50\%$ (Fig. 4.17(d)), we observe two distinct subpeaks for $p_{\text{WZ}\to\text{ZB}} \leq 1.06\%$. For close values of $p_{\text{WZ}\to\text{ZB}}$, we find a plateau-like behavior of the scattered intensity near the wurtzite reflection. For even higher values for $p_{\text{WZ}\to\text{ZB}}$, the wurtzite subpeak can no longer be observed: only an asymmetric single peak close to zinc blende can be observed. During this increase of $p_{\text{WZ}\to\text{ZB}} = 0.27\%$ to $p_{\text{WZ}\to\text{ZB}} = 2.60\%$, the shape of the wurtzite subpeak becomes more and more broadened and shifts towards zinc blende. At the same time, the shape of the zinc blende subpeak is almost not influenced from the change in $p_{\text{ZB}\to\text{WZ}}$, only its relative height with respect to zinc blende changes.

Qualitatively similar behavior is also observed for $p_{\text{ZB}\to\text{WZ}} = 1.00\%$ (see Fig. 4.17(e)). However, as the average pure phase domains get smaller due to the mostly higher transition probabilities, the peaks are broader and overlap more. Therefore, the drift of the center of the wurtzite peak towards the center is stronger for increasing $p_{\text{WZ}\to\text{ZB}}$ compared to the previous case $p_{\text{ZB}\to\text{WZ}} = 0.50\%$. For $p_{\text{ZB}\to\text{WZ}} = 1.00\%$, the respective subpeak establishes a pronounced plateau already for $p_{\text{WZ}\to\text{ZB}} = 1.29\%$, i.e., for an asymmetry $p_{\text{Asym}} = 0.29\%$ as defined in Eq. (4.19) which is smaller than for the case depicted in Fig. 4.17(d) of $p_{\text{Asym}} \approx 0.6\%$. For $p_{\text{WZ}\to\text{ZB}} \approx 0.52\%$, we observe plateau-like behavior which is comparable to Fig. 4.17(d) if wurtzite and zinc blende parameters are interchanged.

For $p_{\text{WZ}\to\text{ZB}} = p_{\text{ZB}\to\text{WZ}} = 1.50\%$, the broadening is already so strong that the plateau is achieved for vanishing asymmetry ($p_{\text{Asym}} = 0$). Whereas for higher transition probabilities $p_{\text{WZ}\to\text{ZB}} > 1.50\%$, the plateau like behavior vanishes quickly for increasing probability $p_{\text{WZ}\to\text{ZB}}$, the characteristics of the plateau survives even below $p_{\text{WZ}\to\text{ZB}} = 0.78\%$.

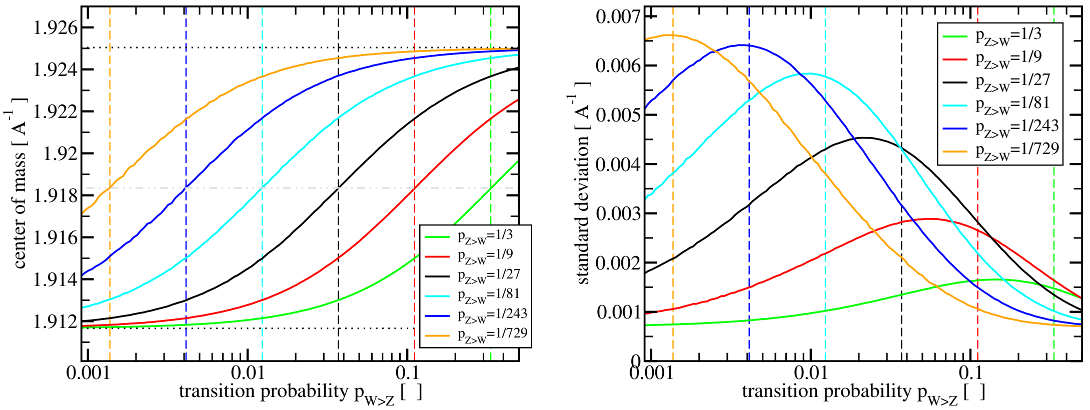

(a) Expectation value μ. The native positions of zinc blende and wurtzite are marked as dotted black line. The mean thereof is the dashed-dotted line.

(b) Width σ

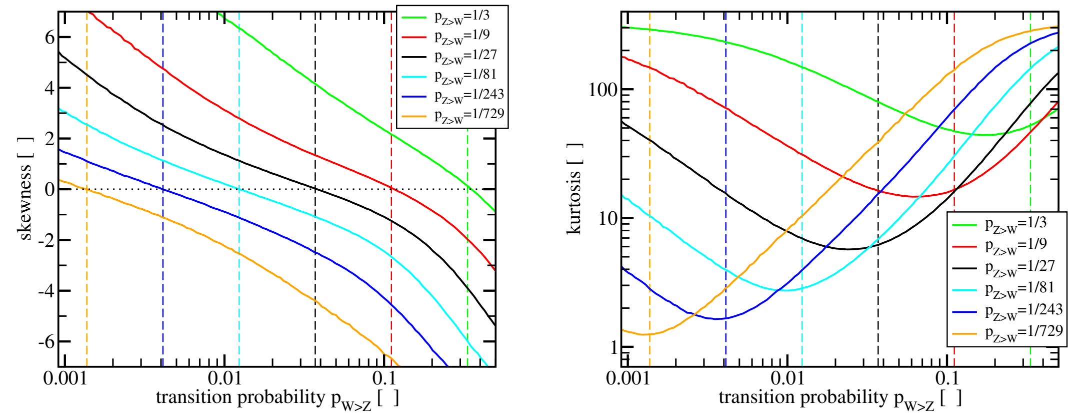

(c) Skewness s. The dotted line highlights the zero of the ordinate.

(d) Kurtosis k

Figure 4.18.: Normalized central moments (as defined in Eq. (4.38)) of the intensity profile $\mathcal{I}(q_z)$ near the $(111)_{z\frown c}$ GaAs Bragg peak for a Markov process as described in Fig. 4.13. All plots depict the respective moment as a function of $p_{\mathrm{WZ}\to\mathrm{ZB}}$ for various fixed values of $p_{\mathrm{ZB}\to\mathrm{WZ}}$. The vertical dashed lines indicate the positions where $p_{\mathrm{WZ}\to\mathrm{ZB}}$ is equal to $p_{\mathrm{ZB}\to\mathrm{WZ}}$ depicted in the respective color.

For further investigation of the X-ray scattering signal, we calculate the center of mass

$$\mu(p_{\mathrm{ZB}\to\mathrm{WZ}}, p_{\mathrm{WZ}\to\mathrm{ZB}}) = \int_{1.90\text{Å}^{-1}}^{1.9367\text{Å}^{-1}} q_z \cdot \tilde{\mathcal{I}}(q_z)\ \mathrm{d}^1 q_z \ , \tag{4.38a}$$

the standard deviation

$$\sigma(p_{\mathrm{ZB}\to\mathrm{WZ}}, p_{\mathrm{WZ}\to\mathrm{ZB}}) = \left(\int_{1.90\text{Å}^{-1}}^{1.9367\text{Å}^{-1}} (q_z - \mu)^2 \cdot \tilde{\mathcal{I}}(q_z)\ \mathrm{d}^1 q_z \right)^{1/2} \ , \tag{4.38b}$$

the skewness

$$s(p_{\mathrm{ZB}\to\mathrm{WZ}}, p_{\mathrm{WZ}\to\mathrm{ZB}}) = \int_{1.90\text{Å}^{-1}}^{1.9367\text{Å}^{-1}} \left(\frac{q_z - \mu}{\sigma} \right)^3 \cdot \tilde{\mathcal{I}}(q_z)\ \mathrm{d}^1 q_z \ , \tag{4.38c}$$

and the kurtosis

$$k(p_{\mathrm{ZB}\to\mathrm{WZ}}, p_{\mathrm{WZ}\to\mathrm{ZB}}) = \int_{1.90\text{Å}^{-1}}^{1.9367\text{Å}^{-1}} \left(\frac{q_z - \mu}{\sigma} \right)^4 \cdot \tilde{\mathcal{I}}(q_z)\ \mathrm{d}^1 q_z \ . \tag{4.38d}$$

of our X-ray profiles. Here, $\tilde{\mathcal{I}}$ is the normalized intensity

$$\tilde{\mathcal{I}}(q_z) = \mathcal{I}(q_z) \Big/ \left(\int_{1.90\text{Å}^{-1}}^{1.9367\text{Å}^{-1}} \mathcal{I}(q_z)\ \mathrm{d}^1 q_z \right) . \tag{4.39}$$

The results are depicted in Fig. 4.18 as a function of $p_{\mathrm{WZ}\to\mathrm{ZB}}$ for various values of $p_{\mathrm{ZB}\to\mathrm{WZ}}$.

In Fig. 4.18(a), the position of the center of mass of the scattered intensity is depicted: As expected, the center of mass is at the average value of the positions of pure zinc blende and wurtzite (grey dashed-dotted line). For very pronounced asymmetry, the center of mass is located essentially at the positions of native zinc blende and wurtzite. However, the center of mass is difficult to estimate for experimental data, since very precise calibrations with a known reference are required. For example, for the post-growth *ex-situ* measurements which we discussed in Sec. 3.2 the estimation of the center of mass is not possible with the required precision. Moreover, in case of highly asymmetric transition probabilities, the magnitude of the slope of the functions in Fig. 4.18(a) is very small, and, thus, would result in huge uncertainties and errors of the retrieved values in such cases.

In contrast, it is typically much simpler to estimate the width σ of an experimentally measured intensity profile. The bahavior of the width σ in the framework of the Markov model is shown in Fig. 4.18(b). Most importantly, we see that the case with the biggest width is *not* the symmetric case $p_{\mathrm{WZ}\to\mathrm{ZB}} = p_{\mathrm{ZB}\to\mathrm{WZ}}$. As a function of one of the two transition probabilities – keeping the other transition probability fixed – the case with the highest asymmetry is close the symmetric case, but slightly shifted towards increased phase purity. In addition, we observe that this maximum width first increases very fast towards wires with higher phase purity. However, once the X-ray signal contains two distinct peaks, this increase slows down and the maximum width converges to its limit.

The skewness – shown in Fig. 4.18(c) – vanishes for the symmetric case $p_{\mathrm{WZ}\to\mathrm{ZB}} = p_{\mathrm{ZB}\to\mathrm{WZ}}$. In contrast to the width σ, the skewness is a strict monotonous function of $p_{\mathrm{WZ}\to\mathrm{ZB}}$ for fixed $p_{\mathrm{ZB}\to\mathrm{WZ}}$.

Finally, in Fig. 4.18(d), the kurtosis is depicted. Interestingly, the kurtosis varies over more than two orders of magnitude. However, the extraction of the value of the kurtosis requires experimental data of very high quality, since it is highly sensitive to the tails of the signal and (statistical as well as systematic) errors in the data. Thus, it should not be used for comparison with experimental data.

Facing the difficulties in determination of the expectation value μ and the kurtosis k, we now turn to the question if knowledge of the width σ and the skewness s is sufficient for interpretation of experimental data. We point out that the transition probabilities of the model underlying Fig. 4.18(d) are assumed to be static. Therefore, the gradient of the nanowire properties with increasing growth time must be small.

Since the skewness is a strict monotonous function of $p_{\mathrm{WZ}\to\mathrm{ZB}}$ for fixed $p_{\mathrm{ZB}\to\mathrm{WZ}}$ with reasonable slope, the equation $s_{\mathrm{Exp}} \overset{!}{=} s(p_{\mathrm{ZB}\to\mathrm{WZ}}, p_{\mathrm{WZ}\to\mathrm{ZB}})$ has a unique solution $p_{\mathrm{WZ}\to\mathrm{ZB}}$ for fixed $p_{\mathrm{ZB}\to\mathrm{WZ}}$. Thus, this solution $p_{\mathrm{WZ}\to\mathrm{ZB}}$ can be understood as a function of $p_{\mathrm{ZB}\to\mathrm{WZ}}$ and the experimental value s_{Exp} (i.e., $p_{\mathrm{WZ}\to\mathrm{ZB}}(p_{\mathrm{ZB}\to\mathrm{WZ}}, s_{\mathrm{Exp}})$). Therefore, the width $\sigma(p_{\mathrm{ZB}\to\mathrm{WZ}}, p_{\mathrm{WZ}\to\mathrm{ZB}})$ can be interpreted as a function $\sigma(p_{\mathrm{ZB}\to\mathrm{WZ}}, p_{\mathrm{WZ}\to\mathrm{ZB}}(p_{\mathrm{ZB}\to\mathrm{WZ}}, s_{\mathrm{Exp}}))$. For given experimental skewness s_{Exp}, the width is now only a function of one *independent* argument $p_{\mathrm{ZB}\to\mathrm{WZ}}$. In addition, the function $p_{\mathrm{WZ}\to\mathrm{ZB}}(p_{\mathrm{ZB}\to\mathrm{WZ}}, s_{\mathrm{Exp}})$ needs to be known for all relevant values for s_{Exp}.

The results for various values for s_{Exp} are depicted in Fig. 4.19. If the skewness s and the width σ of an experimentally measured intensity profile $\mathcal{I}(q_z)$ are known with sufficient accuracy, these plots reveal the transition probabilities $p_{\mathrm{WZ}\to\mathrm{ZB}}$ and $p_{\mathrm{ZB}\to\mathrm{WZ}}$ of the Markov

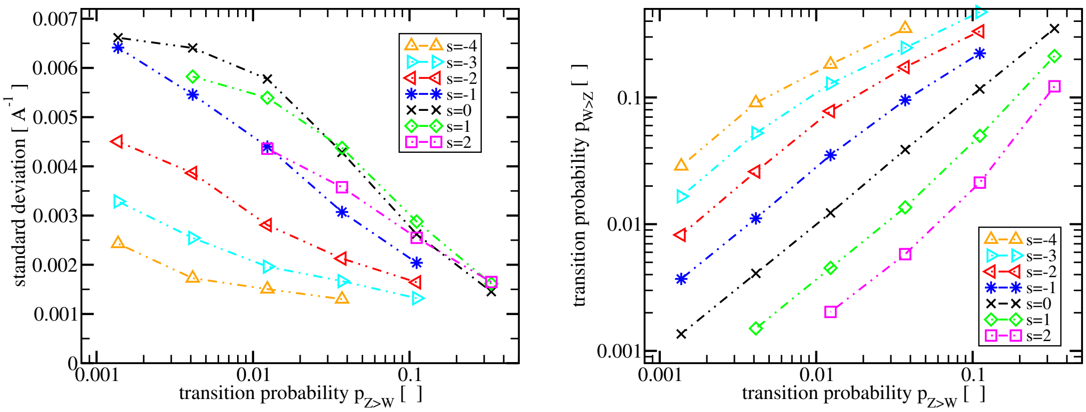

(a) width σ vs. $p_{\mathrm{ZB}\to\mathrm{WZ}}$ (b) $p_{\mathrm{WZ}\to\mathrm{ZB}}$ vs. $p_{\mathrm{ZB}\to\mathrm{WZ}}$

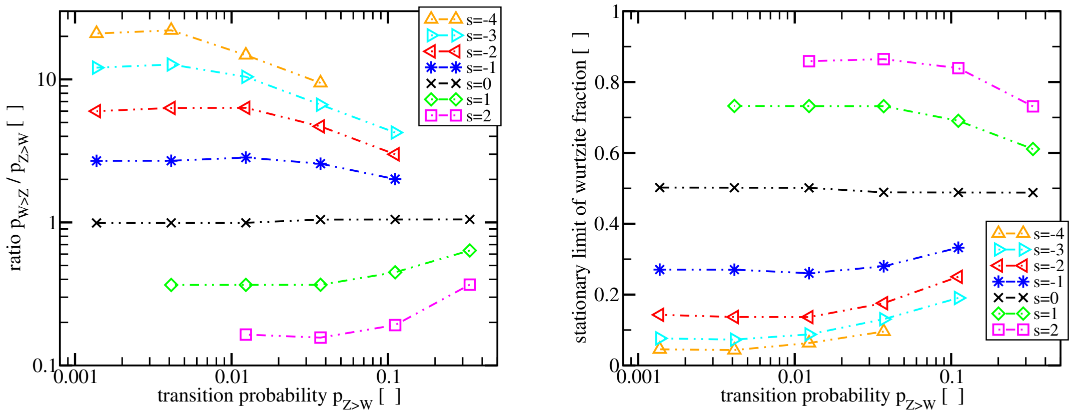

(c) ratio $\frac{p_{\mathrm{WZ}\to\mathrm{ZB}}}{p_{\mathrm{ZB}\to\mathrm{WZ}}}$ vs. $p_{\mathrm{ZB}\to\mathrm{WZ}}$ (d) stationary limit $\breve{p}_{\mathrm{WZ}}$ vs. $p_{\mathrm{ZB}\to\mathrm{WZ}}$

Figure 4.19.: Width σ, transition probability $p_{\mathrm{WZ}\to\mathrm{ZB}}$, the ratio $\frac{p_{\mathrm{WZ}\to\mathrm{ZB}}}{p_{\mathrm{ZB}\to\mathrm{WZ}}}$ and the stationary limit of the wurtzite fraction $\breve{p}_{\mathrm{WZ}}$ as a function of $p_{\mathrm{ZB}\to\mathrm{WZ}}$ for fixed skewness s. If the skewness s and the width σ of an experimentally measured intensity profile $\mathcal{I}(q_z)$ are known with sufficient accuracy, these plots reveal the transition probabilities of the Markov model for polytypism.

model for polytypism: From Fig. (a), it is possible to look up $p_{\mathrm{ZB}\to\mathrm{WZ}}$ for given skewness and width, since the behavior of all functions is strictly monotonous. Fig. (b) maps this value of $p_{\mathrm{ZB}\to\mathrm{WZ}}$ to the corresponding value of $p_{\mathrm{WZ}\to\mathrm{ZB}}$ based on the skewness of the measured intensity profile.

We point out that for $p_{\mathrm{ZB}\to\mathrm{WZ}} \lesssim 4\%$, the functional dependence is almost linear for $-2 \leq s \leq 2$. Thus, in this range, knowledge of the skewness s is already sufficient to estimate the ratio of the transition probabilities $p_{\mathrm{ZB}\to\mathrm{WZ}}/p_{\mathrm{WZ}\to\mathrm{ZB}}$ (see Fig. 4.19(c)). By Eq. (4.24a), this ratio is sufficient for calculation of the stationary limit $\breve{p}_{\mathrm{WZ}}$. The result is depicted in Fig. 4.19(d). This is particularly interesting due to the fact that the skewness s is dimensionless (in contrast to the width σ) and calculated in such a way, that it is insensitive to the q_z calibration of the experimental data.

This approach for interpretation of experimental data is well suited for understanding the Markov model and its relation to the scattering signal and for obtaining a quick rough estimate of the properties of the grown nanowires. However, other means for comparison of experimentally measured data and the Markov model, which are based on pre-computing of a large data set of parameters $(p_{\mathrm{WZ}\to\mathrm{ZB}}, p_{\mathrm{ZB}\to\mathrm{WZ}})$ *once*, include:

- The evaluation of the lowest four moments of each simulated profile and the experi-

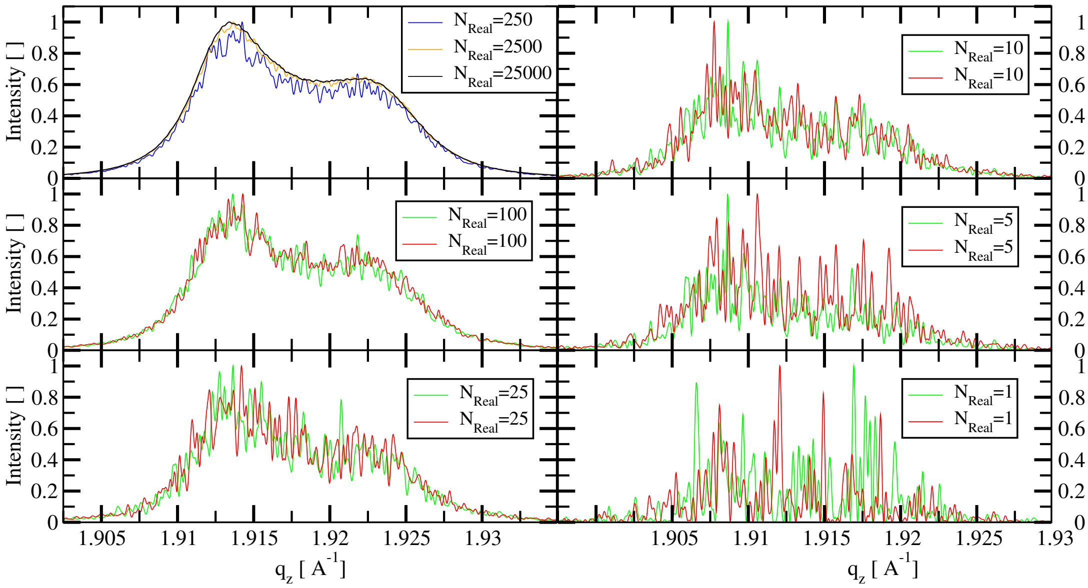

Figure 4.20.: Illustration of the transition of the X-ray intensity q_z profiles of the $(111)_{z\frown c}$ Bragg reflection.

mental data. Then, the weighted error

$$\begin{aligned}\aleph(p_{\mathrm{WZ}\to\mathrm{ZB}}, p_{\mathrm{ZB}\to\mathrm{WZ}}) =& w_\mu \cdot (\mu_{\mathrm{exp}} - \mu(p_{\mathrm{WZ}\to\mathrm{ZB}}, p_{\mathrm{ZB}\to\mathrm{WZ}}))^2 + \\ & w_\sigma \cdot (\sigma_{\mathrm{exp}} - \sigma(p_{\mathrm{WZ}\to\mathrm{ZB}}, p_{\mathrm{ZB}\to\mathrm{WZ}}))^2 + \\ & w_s \cdot (s_{\mathrm{exp}} - s(p_{\mathrm{WZ}\to\mathrm{ZB}}, p_{\mathrm{ZB}\to\mathrm{WZ}}))^2 + \\ & w_k \cdot (k_{\mathrm{exp}} - k(p_{\mathrm{WZ}\to\mathrm{ZB}}, p_{\mathrm{ZB}\to\mathrm{WZ}}))^2 \ . \end{aligned} \tag{4.40}$$

could be considered (or any other suitable error metric). If any of these values cannot be estimated properly, then the respective weight is simply set to zero (typically, $w_{\mu=0}$ and $w_k = 0$). The smallest error metric $\aleph(p_{\mathrm{WZ}\to\mathrm{ZB}}, p_{\mathrm{ZB}\to\mathrm{WZ}})$ reveals the optimal parameters $(p_{\mathrm{WZ}\to\mathrm{ZB}}, p_{\mathrm{ZB}\to\mathrm{WZ}})$ in the set of precomputed profiles.

- Alternatively, a comparison of the full profile for each pixel with the pre-computed profiles can be performed. This approach is advantageous if the tails of the experimentally measured profile are not reliable.

We will compare the experimental and simulated data in Sec. 4.4. We point out, that the effects of the experimental resolution element can be incorporated in all three approaches.

Before we continue with results for the $(333)_{z\frown c}$ reflection, we shortly point out the importance of the statistical nature of our obtained X-ray profiles. If only a single wire (see for example Refs. [101, 123] for such scans of single wires) or few wires are illuminated where each single wire scatters fully coherent and different wires contribute incoherently, we see the large fluctuations in the phase distribution in direct space also in the speckle patterns in reciprocal space. The characteristics of the X-ray profiles of the $(111)_{z\frown c}$ reflection for illumination of $\mathrm{N}_{\mathrm{Real}} = 1$ up to $\mathrm{N}_{\mathrm{Real}} = 25000$ wires are depicted in Fig. 4.20. For the range $\mathrm{N}_{\mathrm{Real}} = 1$ to $\mathrm{N}_{\mathrm{Real}} = 100$, two different volumes with $\mathrm{N}_{\mathrm{Real}}$ wires (generated randomly, but with identical parameters of the random process) are depicted to reveal the large fluctuations from realization to realization. Therefore, scans of few or single wires are much more difficult to interpret (see second part of this manuscript) and contain less statistically relevant information. Such scans are currently only useful if the object under consideration has low fluctuations from object to object.

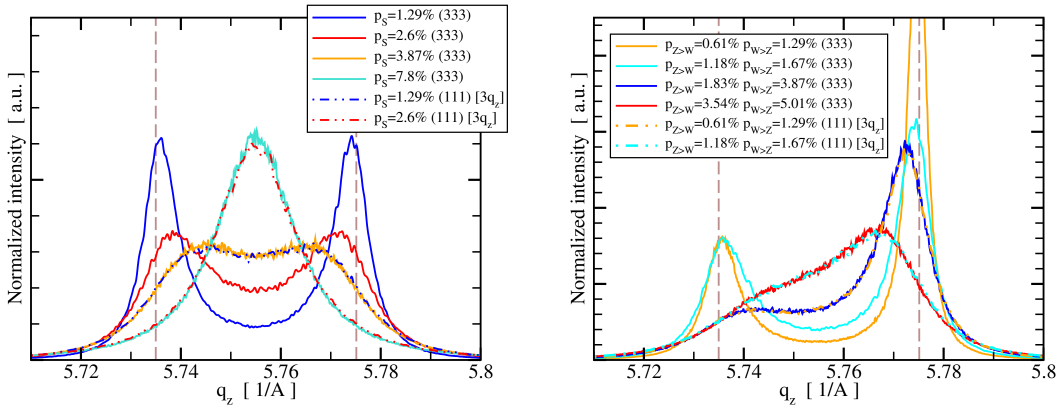

(a) Symmetric conditions $p_{\mathrm{WZ}\to\mathrm{ZB}} = p_{\mathrm{ZB}\to\mathrm{WZ}}$ (b) Asymmetric conditions $p_{\mathrm{WZ}\to\mathrm{ZB}} \neq p_{\mathrm{ZB}\to\mathrm{WZ}}$

Figure 4.21.: Scattered intensity of GaAs nanowires in the framework of the Markov model in the vicinity of the $(333)_{\mathrm{z}\curvearrowright\mathrm{c}}$ Bragg reflection. For comparison, some profiles of the $(111)_{\mathrm{z}\curvearrowright\mathrm{c}}$ reflection are included after transforming $q_z \to 3q_z$.

4.3.2.5. The $(333)_{\mathrm{z}\curvearrowright\mathrm{c}}$ reflection for static transition probabilities

Up to now we studied the $(111)_{\mathrm{z}\curvearrowright\mathrm{c}}$ Bragg reflection, because – as long as only symmetric reflections are considered – the $(222)_{\mathrm{z}\curvearrowright\mathrm{c}}$ reflection is quasi-forbidden and the $(333)_{\mathrm{z}\curvearrowright\mathrm{c}}$ reflection is not available at typical X-ray energies less or similar to 15keV in the current PMBE growth chamber (see Sec. 3.2). Nevertheless, the $(333)_{\mathrm{z}\curvearrowright\mathrm{c}}$ reflection would be available at higher energies or with larger Beryllium windows. Therefore, we shortly discuss the scattering signal in the vicinity of the $(333)_{\mathrm{z}\curvearrowright\mathrm{c}}$ Bragg reflection in the framework of the Markov model. The results are depicted in Fig. 4.21. For comparison, some profiles of the $(111)_{\mathrm{z}\curvearrowright\mathrm{c}}$ reflection are also included – after transforming $q_z \to 3q_z$.

From these results, we observe that the scattering signal of the $(333)_{\mathrm{z}\curvearrowright\mathrm{c}}$ reflection is identical to the $(111)_{\mathrm{z}\curvearrowright\mathrm{c}}$ reflection if the transition probabilities are divided by three (i.e., $p_{\mathrm{WZ}\to\mathrm{ZB}} \to p_{\mathrm{WZ}\to\mathrm{ZB}}/3$ and $p_{\mathrm{ZB}\to\mathrm{WZ}} \to p_{\mathrm{ZB}\to\mathrm{WZ}}/3$) and the q_z values are multiplied by 3 (i.e., $q_z \to 3q_z$). As a consequence access to the $(333)_{\mathrm{z}\curvearrowright\mathrm{c}}$ reflection would enhance the applicability of the presented approach to nanowires with higher transition probabilities (by a factor of 3). Moreover, alternating measurement of the $(111)_{\mathrm{z}\curvearrowright\mathrm{c}}$ and $(333)_{\mathrm{z}\curvearrowright\mathrm{c}}$ reflection during growth would provide highly valuable information for separation of the nanowire signal from the background originating from the parasitic growth since the profile of the nanowire signal would change in a non-trivial way whereas the shape of the smooth Gaussian like background of the crystallites is not expected to change. Finally, the invariance of the profile shapes under the transformation $p_{\mathrm{WZ}\to\mathrm{ZB}} \to p_{\mathrm{WZ}\to\mathrm{ZB}}/3$ and $p_{\mathrm{ZB}\to\mathrm{WZ}} \to p_{\mathrm{ZB}\to\mathrm{WZ}}/3$ might proof useful for the detection of a possibly enhanced amount of the $4H$ polytype in the nanowires (see discussion in Sec. 4.3.3), since the additional contributions from the $4H$ polytype would be already observable for smaller $4H$ segments.

However, since currently no experimental *in-situ* data of the $(333)_{\mathrm{z}\curvearrowright\mathrm{c}}$ reflection during growth has been measured, we do not investigate these benefits further.

4.3.2.6. The $(111)_{\mathrm{z}\curvearrowright\mathrm{c}}$ reflection for non-static transition probabilities

Instead, we discuss the X-ray signal of the $(111)_{\mathrm{z}\curvearrowright\mathrm{c}}$ reflection in presence of a gradient of the transition probabilities along the growth direction. This point is particularly interesting (and has already been mentioned in the motivation for studying polytypism in nanowires with X-ray techniques) because it is currently not feasible with TEM based investigations to reliably detect such gradients – unless the mean thickness of an individual segment is very small. For example, Johansson et al. investigated in Ref. [24] polytypism in highly faulty nanowires with mean segment thicknesses in the order of 3-9 layers. However, the larger the mean segment size is, the more difficult is the detection of this mean value, and in particular a gradient thereof with TEM based investigations. In contrast, highly faulty nanowires are rather difficult to study with X-ray based techniques, but the longer the mean phase segments become, the better is the separation of the contributions from both phases (see Fig. 4.17). Therefore, X-ray diffraction based techniques are very promising for studying polytypism in that range of parameters where TEM based investigations are not well suited.

For illustration, we assume a linear function

$$p_{\mathrm{P}\to\bar{\mathrm{P}}} = u_{\mathrm{P}\to\bar{\mathrm{P}}} \cdot n + v_{\mathrm{P}\to\bar{\mathrm{P}}} \tag{4.41}$$

for both polytypes P (see Fig. 4.13 on page 66).

In Fig. 4.22, illustrations in direct space as well as the results for the scattering signal in reciprocal space are depicted: Clearly, the detection of the gradient in the transition probabilities with increasing height is hardly possible from one or only a few wires – due to the large fluctuations of the length of each individual segment. On the contrary, the X-ray signal changes significantly with increasing number of layers $\mathrm{N_L}$. We observe that

- the overall intensity grows proportionally to the nanowire height $\mathrm{N_L}$ if *no* radial growth is included. This is a consequence of Plancherel's theorem [146], since the scattering factor of both polytypes is almost equal. Radial growth leads to deviations from this linear behavior. However, for the dependence on the diameter of the nanowire, we distinguish two cases: First, the three dimensional information in reciprocal space is available and integrated for the temporal evolution of the nanowires. In this case, Plancherel's theorem holds in three dimensional space and the integrated intensity is simply proportional to the volume of grown crystalline GaAs. To be specific, such newly grown material can originate from radial growth, axial growth, parasitic growth, and, finally, nucleation of additional nanowires with increasing growth time. If we assume linear growth in axial direction as well as absence of all other growth but radial growth, the ratio total integrated intensity of GaAs versus number of grown layers $\mathrm{N_L}$ is proportional to the cross section of the nanowires (or the square of the nanowires' diameter).

  However, if we evaluate the q_z line-profile for $\boldsymbol{q}_\perp = 0$ as in Eq. (4.15) (and, therefore, without integration in q_x and q_y direction), the overall intensity is proportional to the square of the cross section of the nanowires or the fourth power of the nanowires' diameter (see dependence on $\tilde{\Omega}^{(l)}(0)$ in Eq. (4.15) which is squared in order to obtain the scattered intensity). Therefore, in Fig. 4.22(b), which is obtained from the model resulting from Eq. (4.15), a quadratic increase of the scattered intensity (integrated along q_z for $\boldsymbol{q}_\perp = 0$) with $\mathrm{N_L}$ is observed, if the diameter scales as $\mathrm{N_L^{1/4}}$.

  In total, the temporal evolution of the integrated intensities reveals information about the average volumetric growth *independent* of the polytypic behavior of the nanowires. This is particularly interesting in connection with scaling laws which connect radial and axial growth such as described in Sec. 1.3.

  We point out that Plancherel's theorem holds for any Bragg reflection of both polytypes. Thus, temporally resolved reciprocal space mapping of reflections to which both polytypes contribute reveals volumetric growth irrespective of the polytype. If the phase purity of both polytypes is high enough to obtain two well separated sub-peaks, such refections reveal volumetric growth infomation of both polytypes

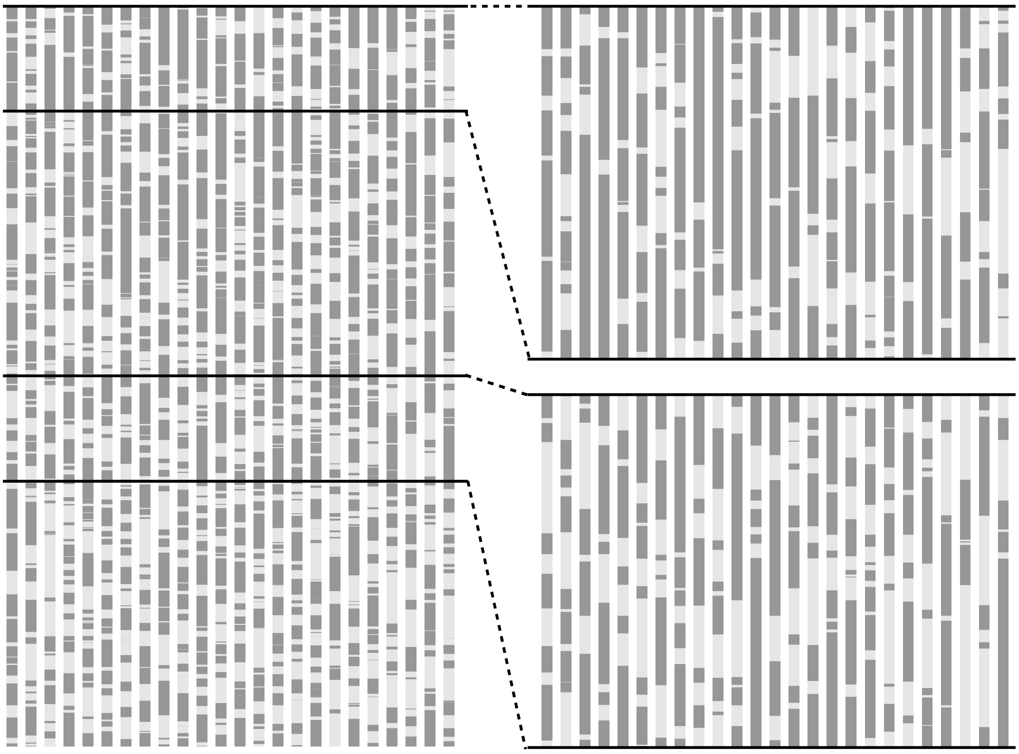

(a) Illustration of the phase distribution (dark gray is zinc blende, light grey is wurtzite) in direct space for 25 GaAs nanowires up to $\mathrm{N_L} = 7000$. The large single segment size fluctuations of the Markov model require consideration of multiple wires to verify the gradient with high statistic significance. The layer ranges 2500–3500 and 6000–7000 are magnified on the right.

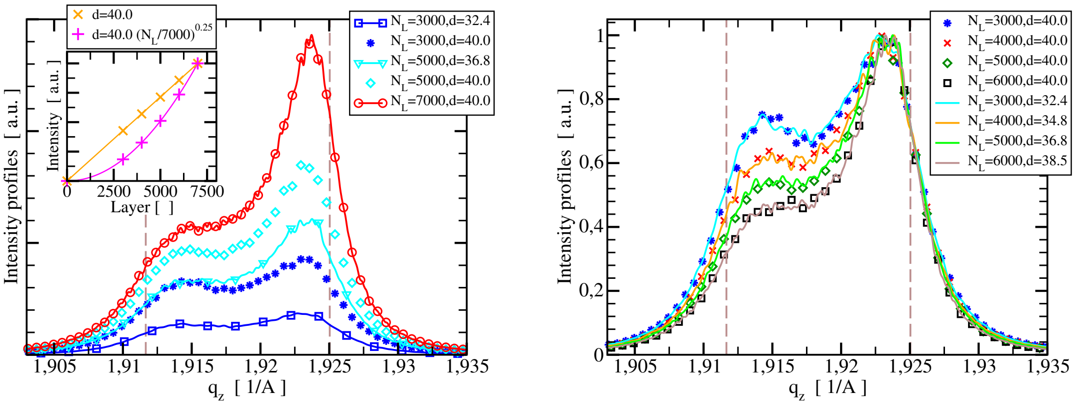

(b) Scattered intensity in the vicinity of the $(111)_{\mathrm{z}\frown\mathrm{c}}$ GaAs reflection for various heights and with or without radial growth of the nanowires.

(c) Comparison of the profiles of the scattered intensity with and without radial growth. The maximum of each profile has been normalized to one.

Figure 4.22.: Results for transition probabilities with a non-zero gradient in growth direction according to Eq. (4.41) with parameters $u_{\mathrm{ZB}\to\mathrm{WZ}} = -8.284 \cdot 10^{-7}$, $u_{\mathrm{ZB}\to\mathrm{WZ}} = 1.176 \cdot 10^{-2}$, $u_{\mathrm{WZ}\to\mathrm{ZB}} = 1.102 \cdot 10^{-6}$, and $v_{\mathrm{WZ}\to\mathrm{ZB}} = 1.089 \cdot 10^{-2}$.

separately. If phase-selective reflections are mapped three dimensionally and in a time-resolved manner, volumetric growth of each polytype can be measured separately in case of highly faulty nanowires.

- the shape close to the $(111)_{\mathrm{z}\frown\mathrm{c}}$ reflection is *independent* of radial growth – as long as the radial growth is epitaxial (see Fig. 4.22(c)). Therefore, by investigation of the shape of the intensity profile, we are able to investigate the evolution of the transition probabilities which determine the fraction of both polytypes, the differential phase

Distribution	Density function	Expectation	Variance
Gamma	$\frac{1}{b\cdot\Gamma(m+1)}\left(\frac{x}{b}\right)^{m}\mathrm{e}^{-\frac{x}{b}}$, $b>0$, $m>-1$	$b\cdot(m+1)$	$b^2\cdot(m+1)$
Weibull	$\frac{\alpha}{b^\alpha}x^{\alpha-1}\,\mathrm{e}^{-\left(\frac{x}{b}\right)^\alpha}$, $\alpha>0$, $b>0$	$b\cdot\Gamma(1+\frac{1}{\alpha})$	$b^2\left(\Gamma(\frac{2+\alpha}{\alpha})-\Gamma^2(\frac{1+\alpha}{\alpha})\right)$
Pareto	$\frac{\gamma}{b}\left(\frac{b}{x}\right)^{\gamma+1}$, $\gamma>0$	$\frac{\gamma b}{\gamma-1}\quad\gamma>1$ $\infty\quad\gamma\leq1$	$\frac{\gamma b^2}{(\gamma-2)(\gamma-1)^2}\quad\gamma>2$ $\infty\quad\gamma\leq2$
Uniform	$\frac{1}{u-l}$, $0.5\leq l<u<\infty$	$\frac{1}{2}(l+u)$	$\frac{1}{12}(u-l)^2$
Poisson	$\frac{\lambda^k}{k!}\,\mathrm{e}^{-\lambda}$, $\lambda>0$	λ	λ
Logarithmic	$\frac{-p^k}{\ln(1-p)\,k}$, $0<p<1$	$\frac{-1}{\ln(1-p)}\frac{p}{1-p}$	$\frac{-p(p+\ln(1-p))}{(1-p)^2\ln^2(1-p)}$
Gaussian	$\frac{1}{\sigma\sqrt{2\pi}}\,\mathrm{e}^{-\frac{1}{2}\left(\frac{x-\mu}{\sigma}\right)^2}$	μ	σ^2

Table 4.1.: Overview over statistical distributions [129, 145, 147] for the generation of phase segments of either zinc blende or wurtzite phase with random length. Gamma and Weibull distribution reduce to a exponential distribution for $m = 0$ and $\alpha = 1$ respectively. $\Gamma(\cdot)$ denotes the Gamma function [129, 145, 147]. Gamma and Weibull distribution are defined for $x \geq 0$, the Pareto distribution for $x \geq b$. The Poisson distribution is only defined for discrete events $k = 0, 1, 2, 3, \ldots$, whereas k is restricted to $k = 1, 2, 3, \ldots$ for the logarithmic distribution. The Gaussian is defined for all $x \in \mathbb{R}$. Gamma, Weibull, Pareto, uniform and Gaussian distribution are two parameter distributions whereas logarithmic and Poisson distribution are one parameter distributions.

fraction (see Sec. E in the appendix) as well as the phase purity (i.e., the mean number of layers without defects in the stacking sequence).

In conclusion, we demonstrated that time-resolved *in-situ* X-ray measurements are well suited for investigation of polytypic nanowire growth. Given proper experimental time-resolved *in-situ* data, the temporal evolution of the integrated intensity reveals the amount of grown crystalline material (possibly phase selective) as well as height-dependent estimates for the phase purity of the nanowires. The first aspect requires no further theoretical investigations. On the contrary, uniqueness of the interpretation as well as characteristic features of the X-ray profiles must be investigated more closely.

For this, we now investigate stackings based on phase segments with random lengths which are determined by drawing random numbers according to a given probability distribution such as a Gamma or Weibull distribution. Thereby, we reveal which aspects of the Markov model are responsible for the characteristics of X-ray profiles. As a result, we understand which deviations from the Markov model could be revealed by studying the $(111)_{\mathrm{z}\frown\mathrm{c}}$ reflection of GaAs nanowires with X-ray radiation. After this, we interpret the experimentally obtained X-ray data of sample S2 in the framework of the Markov model.

4.3.3. Probability distributions for the thickness of defect-free segments

4.3.3.1. Generation of the stacking based on two polytypes

In Sec. 4.3.2, it was proven that the Markov model implies an exponential distribution for the number of layers grown as a defect-free segment of a particular polytype P (see Eq. 4.21d). In this section, we compare the Markov model to a variety of other statistical distributions for the length of a defect-free segment. In particular, we consider Weibull, Gamma, Poisson, uniform, Pareto, logarithmic and Gaussian distributions (see Fig. 4.12 and Tab. 4.1). For those distributions which do not only return integer numbers, the number of layers n for a particular phase segment is obtained by first drawing a *real* number $x \in \mathbb{R}$ and rounding it to the nearest integer value k. The smallest value that is produced by the Gamma, Weibull and Poisson distribution is equal to zero. Hence, the resulting random number is increased by one to achieve a minimum number of layers $\mathrm{N_L} = 1$. For the same reason, we fix $b = 1$ in the Pareto distribution and $l = 1$ for all uniform distributions throughout this chapter. In case of the Gaussian distribution, events resulting in less than one layer are discarded and a new value is drawn until a positive number of layers is generated.

In addition, we will study a simple model for the stacking that results in an enhanced amount of the 4H polytype in the nanowires (see Eq. (4.43b)).

The Gamma distribution and Weibull distribution are particularly interesting because they contain the exponential distribution as a special case. Hence, a smooth transition from the Markov chain to alternative statistical models for the stacking can be investigated.

The Gamma distribution modifies mainly the behavior for short segments ($x \ll b_{\mathrm{P}}$ in Eq. (4.21d)) by introducing a parameter m, $m > -1$. Its decay remains exponential in the form $\mathrm{e}^{-\frac{x}{b_{\mathrm{P}}}}$. Logarithmic distributions correspond to the limiting case $m \to -1$ of the Gamma distribution. Physically, this corresponds to a strongly enhanced probability for short phase segments with exponential (i.e., Markov-like) decay for longer segments at the same time.

The Weibull distribution modifies the decay from $\mathrm{e}^{-\frac{x}{b_{\mathrm{P}}}}$ to $\mathrm{e}^{-\left(\frac{x}{b_{\mathrm{P}}}\right)^{\alpha}}$, $\alpha > 0$, *simultaneously* with modifying the short length behavior. Nevertheless, it reduces to the exponential distribution for $\alpha = 1$. For $\alpha = 2$, the decay of the Weibull distribution corresponds to the decay of a Gaussian distribution. However, the behavior of short segments is different from Gaussian statistics.

Uniform, Pareto and Poisson distributions are representatives of distributions with different characteristics: Uniform distributions show a non-continuous decay to zero, but no decay in length probability up to that bound. Pareto distributions are scale invariant and decay as a power law. Thus, they show a very slow decay in comparison to the exponential decay of the Gamma or Weibull distribution. The Poisson distribution has equal expectation value and variance λ [129, 145]. This is again in strong contrast to the behavior of the Gamma and Weibull distribution with respect to the parameter b: their ratio of variance versus expectation value is proportional to b and not equal to 1 as for the Poisson distribution. This means that for large phase segments (i.e., $b \gg 1$) the fluctuations of the length of the individual segments is strongly suppressed for the Poisson distribution. The Gaussian distribution facilitates independent tuning of the mean value and the variance and, therefore, is employed for studying the transition from high fluctuations of the length of a single segment to low fluctuations.

Before we discuss the respective X-ray profiles, we depict typical realizations of the polytype distribution in nanowires for illustration in Fig. 4.23 – analogous to Fig. 4.14. Having this direction space representations in mind, we now turn to the respective X-ray profiles.

Gamma distribution

Figure 4.24 depicts results for the Gamma distribution. In Fig. 4.24(a) and 4.24(b), we compare the results for fixed decay length b_{P} as a function of m (continuous lines) with the results for a Markov process with the corresponding expectation value (dashed dotted lines in the same color). For $m_Z = m_W = 0$, the results should coincide with $p_{\mathrm{Switch}} = 1.0\%$ – as they do up to statistical fluctuations. We observe that the resulting signal is not identical for identical expectation value of Gamma distribution for $m \neq 0$ and Markov chain. The changes in the scattering signal are significantly smaller than for a Markov process if the expectation value is used for defining the scales to be compared. Even worse, the X-ray scattering signal does not allow a unique identification in the set

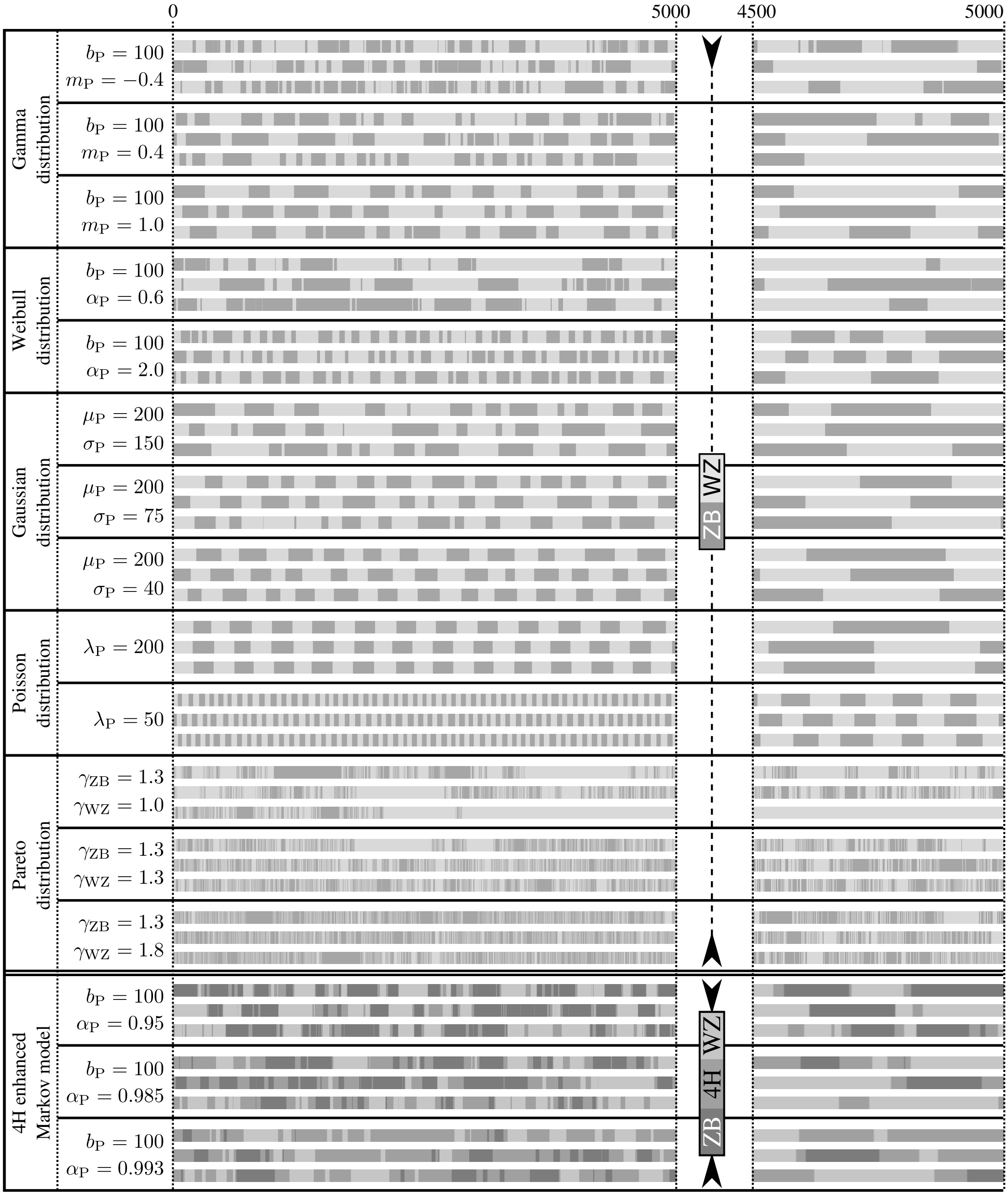

Figure 4.23.: Phase distribution inside nanowires resulting from phase segments with random length. The realizations illustrate some important aspects for the distributions contained in Tab. 4.1. For each set of paramters, three exemplary phase distributions have been generated and depicted from layer 0 to layer 5000. The range 4500 to 5000 has been magnified for better visibility of small segments and the frequency thereof. Examples for the phase distribution in the framework of the Markov model can be found in Fig. 4.14.

of all Gamma distributions: For illustration, in Fig. 4.24(a) the case of $m_Z = m_W = 1.0$ has been depicted which coincides up to very tiny differences with the X-ray signal for $p_{\text{Switch}} = 0.71\%$ – or equivalently $m_Z = m_W = 0.0$ with a decay length of $b = 140$. This ambiguity is also true in the asymmetric case (Fig. 4.24(b)): the scattering signal for $m_Z = m_W = 1.0$ is almost identical to $m_Z = m_W = 0.0$ with expectation value $\mu_Z = 140$ and $\mu_W = 105$. Moreover, this ambiguity demonstrates that X-ray measurements of the $(111)_{z\curvearrowright c}$ Bragg reflection can *not* distinguish if a simple Markov chain – equivalent to

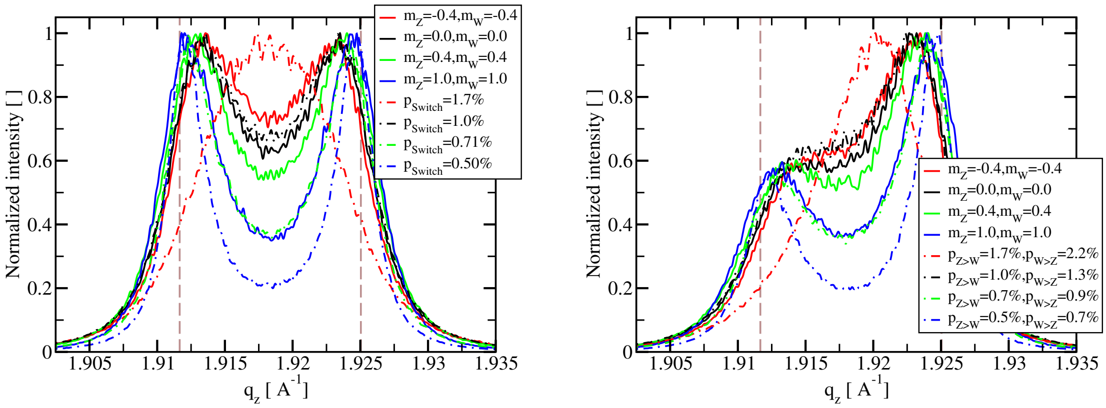

(a) Symmetric case for fixed decay length of 100 layers for zinc blende and wurtzite

(b) Asymmetric case for fixed decay length of 100 layers for zinc blende and 75 layers for wurtzite

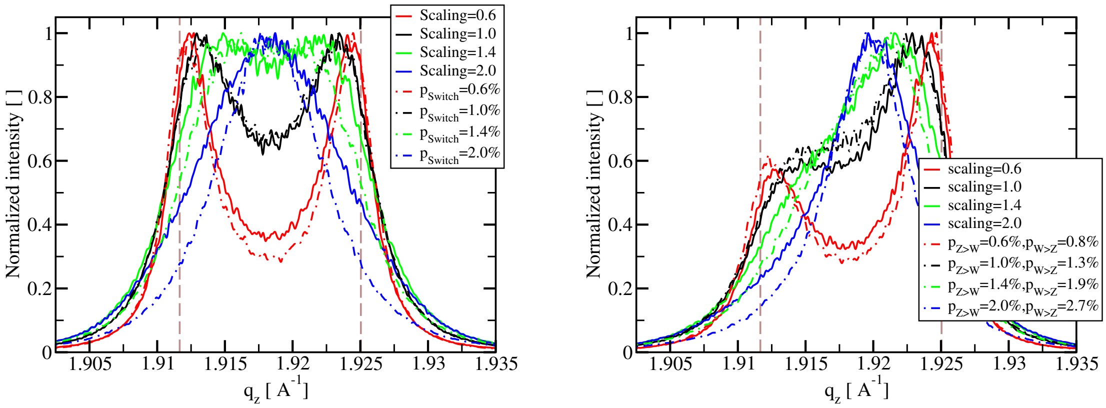

(c) Symmetric case for fixed expectation value of 100 layers for zinc blende and wurtzite

(d) Asymmetric case for fixed expectation value of 100 layers for zinc blende and 75 layers wurtzite

Figure 4.24.: q_z intensity profiles near the $(111)_{\mathrm{z}\frown\mathrm{c}}$ GaAs Bragg peak for a Gamma distribution based phase segment length with parameters as defined in Tab. 4.1. In Figs. (a)-(b), the result for a Markov chain with the transition probability $p_{\mathrm{Switch}} = \left(b_{\mathrm{P}}^{(\mathrm{Markov})}\right)^{-1}$ (see main text) is plotted as a dashed-dotted line in the same color for comparison. In Figs. (c)-(d) the expectation value of all continuous lines is equal. For reference, the q_z profiles for equal decay decay lengths, but $m_{\mathrm{P}} = 0$ (Markovian case) are included as dashed-dotted lines in the respective color in the latter two figures.

an exponential distribution of the phase segment length – is sufficient for describing the stacking sequence of GaAs nanowires or deviations resulting in phase length segments according to a Gamma distribution are present.

The expectation value of the Gamma distribution is invariant upon the simultaneous scaling $m+1 \to s(m+1)$ and $b \to b/s$, since it is given by the product of these two quantities. The influence of this scaling on the X-ray profiles is shown in Figs. 4.24(c) and 4.24(d): Despite equal expectation value the X-ray profiles change significantly (continuous lines). The value for scaling in the legend refers to a multiplication of the decay length with scaling^{-1} and setting $m_{\mathrm{P}} = \text{scaling} - 1$. For reference, the Markovian case with expectation value $b_{\mathrm{P}}^{(\mathrm{Markov})} = b_{\mathrm{P}}^{(\mathrm{Gamma})} \cdot (1 + m_{\mathrm{P}}^{(\mathrm{Gamma})})$ is included (dashed-dotted lines). The major characteristics of the signal are very similar for the cases with equal decay length — irrespective of the variation in m.

Therefore, we can learn from Fig. 4.24: Within the set of Gamma distributions, a unique

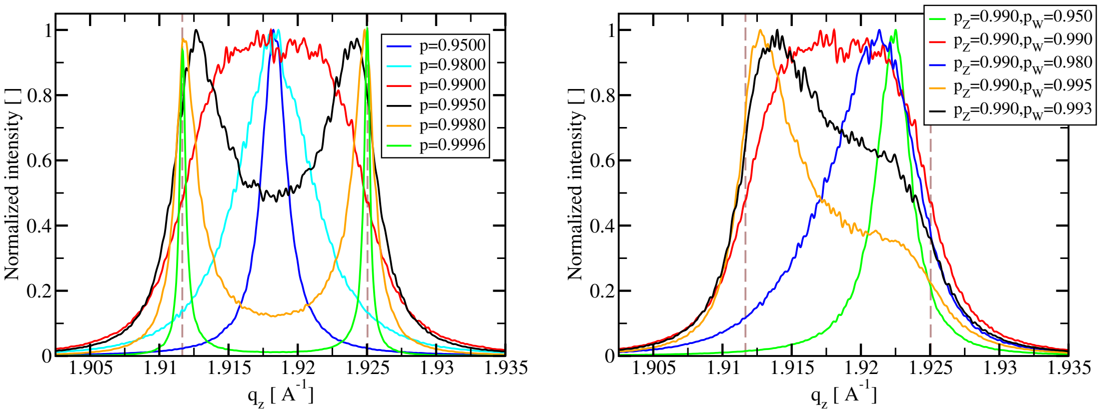

(a) Symmetric case $p = p_Z = p_W$ (b) Asymmetric case $p_Z \neq p_W$

Figure 4.25.: q_z intensity profiles of the $(111)_{\mathrm{z}\frown\mathrm{c}}$ GaAs Bragg peak for a logarithmic phase segment length distribution.

extraction of parameters thereof is not possible. Nevertheless, within the set of Gamma distributions, the decay lengths b_{WZ} and b_{ZB} essentially determine the X-ray signal. The short range behavior m is only of minor importance unless it deviates *strongly* from $m = 0$. Thus, as long as we restrict to the decay lengths b_{WZ} and b_{ZB}, we obtain meaningful estimates even if the full set of Gamma distributions is considered. However, the mean segment length also depends on the parameter m and, therefore, cannot be extracted if the full set of Gamma distributions is admitted as feasible solution: X-rays are not well suited for studying short range deviations from a Markov model described in Sec. 4.3.2.

Logarithmic distribution

In Fig. 4.25, a logarithmic phase segment length distribution is assumed. This distribution corresponds to a strongly enhanced probability for short phase segments and is the limiting case $m \to -1$ of the Gamma distribution. Even such a strong enhancement of short phase length segments in comparison to the Markov model of Sec. 4.3.2 cannot be revealed by X-ray profiles along q_z near the $(111)_{\mathrm{z}\frown\mathrm{c}}$ reflection: the profiles in the symmetric and in the asymmetric cases strongly resemble the features of the pure Markov model (compare Fig. 4.17).

Weibull distribution

We now turn to segment lengths obtained from Weibull distributions (see Tab. 4.1 for definition of parameters and Fig. 4.26 for results). In Fig. 4.26(a) and 4.26(b) we consider fixed decay length b_{WZ} and b_{ZB} and vary the shape α_{WZ} and α_{ZB} (continuous lines).

This scattering signal is compared to a Markov process with expectation value $\mu_{\mathrm{P}}^{(\mathrm{Markov})} = b_{\mathrm{P}}^{(\mathrm{Weibull})}\Gamma(1+\frac{1}{\alpha_{\mathrm{P}}})$ – or equivalently to Weibull distributions with $\tilde{b}_{\mathrm{P}}^{(\mathrm{Weibull})} = b_{\mathrm{P}}^{(\mathrm{Weibull})}\Gamma(1+\frac{1}{\alpha_{\mathrm{P}}})$ and $\tilde{\alpha}_{\mathrm{P}} = 1$ (dashed-dotted lines in the same color). Thus, the mean segment length is equal for the Weibull and Markovian cases and — as for the Gamma distribution — we get by this comparison of profiles with equal mean segment length an impression of the systematic errors if a Weibull distribution with shape parameter α_{P} is erroneously interpreted as Markovian dynamics.

Also as for the Gamma distribution, the two parameters (α_{P},b_{P}) of the distribution (for each polytype) are not mapped on unique scattering profiles which can be seen for example for the shape parameter $\alpha = 0.6$ and the Markov process with $p_{\mathrm{ZB}\to\mathrm{WZ}} = 0.3\%$ and

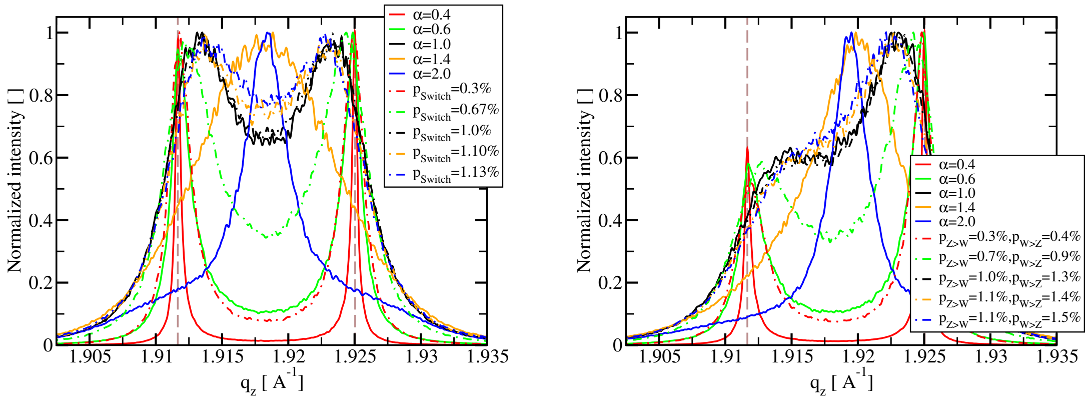

(a) Symmetric case for fixed decay length of 100 layers for zinc blende and wurtzite. For comparison, the signal of the Markov model with equal mean segment lengths is depicted as dashed-dotted line in the same color.

(b) Asymmetric case for fixed decay length of 100 layers for zinc blende and 75 layers for wurtzite. For comparison, the signal of the Markov model with equal mean segment lengths is depicted as dashed-dotted line in the same color.

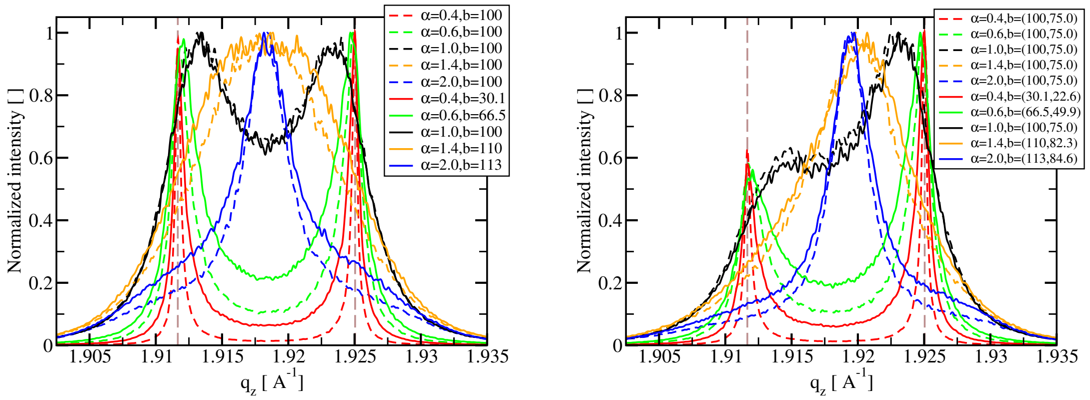

(c) Influence of the shape parameter for fixed expectation value for symmetric conditions of the zinc blende and wurtzite phase (continuous lines). For comparison, the signal with identical shape parameter α_P, but a decay length of $b_\mathrm{P} = 100$ layers is depicted as dashed line in the same color.

(d) Influence of the shape parameter for fixed expectation value for asymmetric conditions of the zinc blende and wurtzite phase (continuous lines). For comparison, the signal with identical shape parameter α_P, but a decay length of $b_\mathrm{ZB} = 100$ layers for zinc blende and $b_\mathrm{WZ} = 75$ layers is depicted as dashed line in the same color.

Figure 4.26.: q_z intensity profiles near the $(111)_{\mathrm{Z}\frown\mathrm{C}}$ GaAs Bragg peak for polytype segment lengths based on Weibull distributions with parameters as defined in Tab. 4.1.

$p_{\mathrm{WZ}\to\mathrm{ZB}} = 0.3\%$ (Fig. 4.26(a)) or $p_{\mathrm{WZ}\to\mathrm{ZB}} = 0.4\%$ (Fig. 4.26(b)) respectively. Note, that for $\alpha > 1.0$, the expectation value changes only very slowly as a function of α. However, the influence of the shape parameter α on the X-ray scattering signal is very strong for *all* α. In particular, the changes induced by values $\alpha \neq 1.0$ for fixed decay length b_P exceed the changes of X-ray profiles if only the expectation value is correspondingly rescaled in the corresponding Markovian case. Therefore, deviations of the decay of the segment length distribution from the Markovian case in the manner of a Weibull distribution ($\alpha \neq 1.0$) would result in strong systematic errors of the extracted values in a Markovian model.

In contrast to Figs. 4.26(a) and 4.26(b), the decay lengths b_P of the Weibull distributions are no longer fixed in Figs. 4.26(c) and 4.26(d). Instead, the decay lengths b_P and and their shape parameters α_P are simultaneously adopted for equal expectation value (continuous lines). For the dashed lines, the decay lengths are fixed and chosen equal to Figs. 4.26(a) and 4.26(b). Clearly, the differences in the corresponding X-ray profiles are much smaller than in Figs. 4.26(a) and 4.26(b).

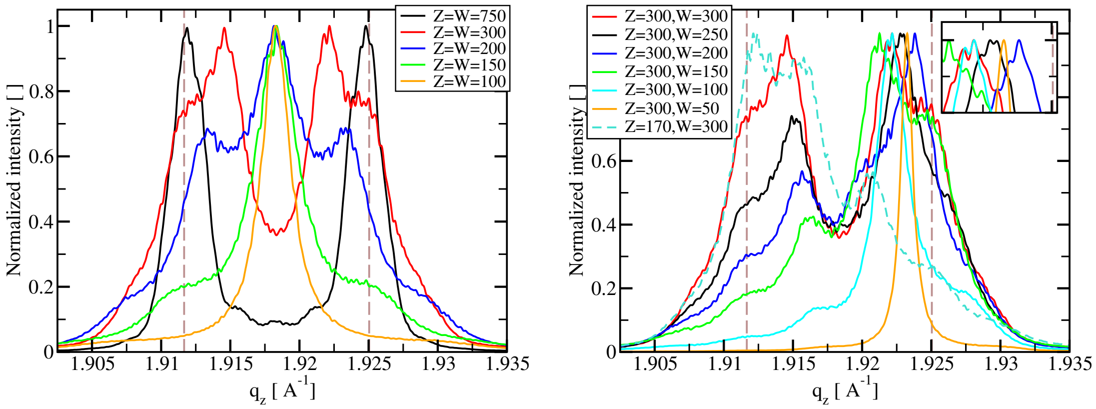

(a) Symmetric case $Z = W$

(b) Asymmetric case $Z = 300$ and $W \neq Z$

Figure 4.27.: q_z intensity profiles near the $(111)_{\mathrm{z}\curvearrowright\mathrm{c}}$ GaAs Bragg peak for a uniform phase segment length distribution with upper bounds Z for zinc blende and W for wurtzite (i.e., uniform distributions bound by $[1, \mathrm{Max}_P]$, $\mathrm{Max}_P \in \{Z, W\}$). The inset in Fig. (b) magnifies the region near the right peak.

This time we identify the higher sensitivity to the shape parameters α_{P} than to the decay lengths b_{P}. If reasonable rough estimates for the decay lengths b_{P} are known, the shape parameters α_{P} can be estimated. However, the strong differences of the changes induces by variations in the shape parameter α_{P} and the decay lengths b_{P} again prevents the extraction of reliable estimates for the mean segment lengths.

If we combine these observations with our observations for the Gamma distribution, we can conclude on the following hierarchical influence on the profile of the X-ray signal:

- Power law exponents in the exponent of the exponential function of the distribution
- Decay length scales b_{P} in the exponent of the exponential function
- Power law exponents in the power law dominating the behavior for small distances

However, it is important to keep in mind, the neither for the Gamma nor for the Weibull distribution a unique identification of both parameters thereof is possible. Given the hierarchical influence, we can only estimate the power law coefficients in the exponent of the exponential function of the distribution in case of a Weibull distribution or the decay length scales b_{P} in the exponent of the exponential function in case of Gamma distributions. It is not possible to distinguish Weibull and Gamma distributions solely by measuring the $(111)_{\mathrm{z}\curvearrowright\mathrm{c}}$ reflection or to identify deviations from the Markov model presented in Sec. 4.3.2. Most importantly, deviations in the stacking sequence for small segment lengths cannot be well investigated by studying $(111)_{\mathrm{z}\curvearrowright\mathrm{c}}$ reflections as a consequence of the small influence of the power law exponents of the power law dominating the behavior for small distances.

Whereas the general features of Gamma, Weibull, exponential and logarithmic distributions are similar for the $(111)_{\mathrm{z}\curvearrowright\mathrm{c}}$ reflection, we will now turn to rectangular, Poisson and Pareto distributions. Each of the latter has characteristic features for a variety of parameters which can be used to distinguish phase segment length distributions grown according to the respective distribution.

Uniform distribution

Fig. 4.27 depicts X-ray profiles along q_z near the $(111)_{\mathrm{z}\curvearrowright\mathrm{c}}$ GaAs reflection for uniform phase segment length distributions bound by $[1, \mathrm{Max}_P]$. $\mathrm{Max}_P \in \{Z, W\}$ is the maximum

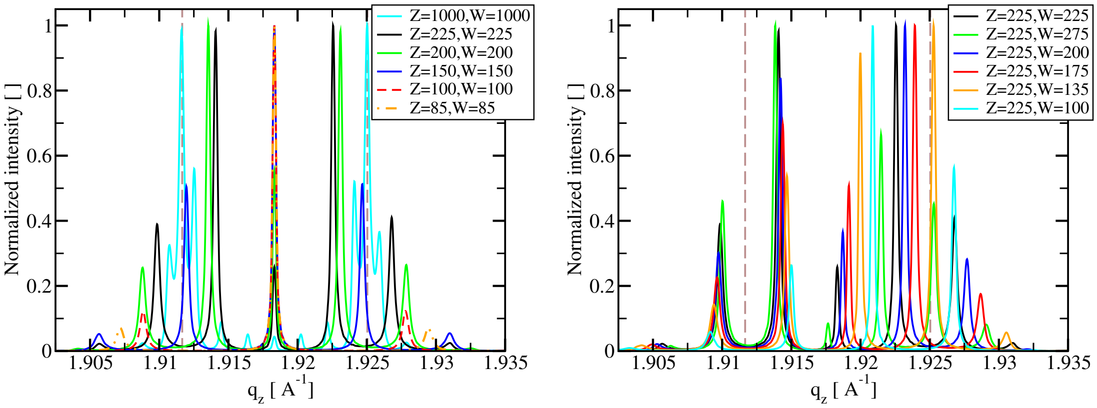

(a) Symmetric case $Z = W$ (b) Asymmetric case $Z = 225$ and $W \neq Z$

Figure 4.28.: q_z intensity profiles near the $(111)_{\text{z}\curvearrowright\text{c}}$ GaAs Bragg peak for a Poisson distributed phase segment length with expectation value Z for zinc blende and W for wurtzite.

number of adjacent layers of phase $P \in \{\text{ZB}, \text{WZ}\}$ before switching the stacking sequence to the alternative phase. Fig. 4.27(a) contains X-ray profiles for equal upper bounds $Z = W$: The q_z profiles for $Z = W \in \{200, 300\}$ differ from the profiles of a Markov chain by the plateau(s) next to peak(s). However, for very high ($Z = W \geq 750$) or very low values ($Z = W \leq 100$) of Z and W, the result is similar to the Markov process. The asymmetric case $Z \neq W$ is considered in Fig. 4.27(b): Whereas for W decreasing from 300 to 200 at $Z = 300$, the right peak shifts towards zinc blende, the peak degenerates to a plateau for $(Z, W) \approx (300, 170)$ (for better visibility, the mirrored case $(Z, W) \approx (170, 300)$ has been depicted instead). For $(Z, W) \approx (300, 150)$, the peak maximum is even left of the symmetric case $W = 300$. For $W = 100$, the peak maximum almost coincides with $W = 300$. Hence, the peak maximum does not drift monotonously towards the native phase positions for a rectangular distribution. Only for even smaller W, the peak shape becomes very narrow and has almost no structure, but shifts continuously towards the limit of pure zinc blende.

The experimentally observed *in-situ* X-ray measurements do not resemble the typical features of the rectangular distribution. Hence, we exclude an (almost) uniform distribution for the length distribution of defect-free segments for the measured GaAs nanowires.

Poisson distribution

Whereas for the Gamma and Weibull distribution (including the Markovian case) we observed a maximum of two peaks, the number of distinct peaks is typically much higher for a Poisson distribution (Fig. 4.28). Note, that the center of some of these subpeaks can be at smaller or higher q_z values than for pure wires. Fig. 4.28(a) depicts results for the symmetric case $Z = W$: In all cases, a peak at the average of the pure wire's q_z value is present. It is the strongest peak for $Z = N \leq 150$. For $Z = N \ll 150$, the side peaks are very weak and basically only the sharp central peak remains – as it is expected in the limit of wires with essentially random stacking. On the contrary, for $Z = N \geq 200$, the maximum intensity of the peaks close to the pure wire's q_z values get stronger and can outruns the central peak ($Z = N = 225$). For $Z = N = 1000$, we see – as expected for very pure wires – that the signal accumulates at the pure wire's positions. Nevertheless, side peaks are still present. We point out that the number of visible side peaks in between the pure wire's position is also not constant: Whereas for $Z = N = 1000$, seven such side peaks are clearly visible, only one peak exists in that q_z range for $Z = N = 100$.

Fig. 4.28(b) depicts a set of q_z profiles for decreasing $100 > W > 275$ at fixed $Z = 225$. Here, we again clearly see the complicated interplay of a statistically distributed number of layers for each polytype segment and partial interference. Although the relative asymmetry for $(Z, N) = (225, 275)$ and $(Z, N) = (225, 175)$ is equal, these two signals are not mirrors of each other. This change in profile can be easily seen from the change in height of the central maximum $q_z \approx 1.9185$ from ≈ 0.08 $[(Z, N) = (225, 275)]$ to ≈ 0.5 $[(Z, N) = (225, 175)]$.

These features of the Poisson distribution are beating phenomena in the X-ray signal despite incoherent averaging of the contribution of different wires: As a consequence of the small standard deviation of the Poisson distribution $\sigma_{\text{Poisson}} = \sqrt{\mu_{\text{Poisson}}} \ll \mu_{\text{Poisson}}$ for expectation values $\mu_{\text{Poisson}} \gg 1$, several rather sharp individual peaks are enclosed by an envelope function. The distance δq_z of two peaks is determined by the height $\mu_Z + \mu_W$ of the "meta-cell" constituted by one average element of zinc blende plus one average element of wurtzite. Due to the small fluctuations of the Poisson distribution, several such meta-cells are stacked with sufficiently small variation to produce distinct and clearly separated peaks similar to diffraction of periodic multilayer structures or multi-slit optical gratings. For example, the distance of two subpeaks of the black curve in Fig. 4.28(a) is $\delta q_z \approx 0.00424\text{Å}^{-1}$ which corresponds to $\delta z = \frac{2\pi}{\delta q_z} \approx 148\text{nm} \,\hat{\approx}\, 450$ layers which is the sum of the expectation value of the zinc blende and wurtzite segments. If we consider the red curve in Fig. 4.28(b), we have $\delta q_z \approx 0.00478\text{Å}^{-1}$ which corresponds to $\delta z = \frac{2\pi}{\delta q_z} \approx 131\text{nm} \,\hat{\approx}\, 400$ layers. Again, this value is the sum of the expectation value of the zinc blende and wurtzite segments.

In addition the distance of the subpeaks, we need to define the center of one subpeak: One subpeak resides at the q_z value of the average lattice constant of the meta-cell. For example, if we again consider the red curve in Fig. 4.28(b), one subpeak is located at the reflection for average layer height of

$$\mathrm{a}_{\text{meta-cell}} \approx \frac{Z}{Z+W}\,\mathrm{a}_Z + \frac{W}{Z+W}\,\mathrm{a}_W \approx 3.2739\text{Å} \quad \Rightarrow \quad q_z \approx 1.919\text{Å}^{-1} \tag{4.42}$$

as observed in the simulated data. As this particular subpeak which has been discussed moves further away from the wurtzite position for decreasing expectation value for wurtzite, while at the same time the distance between to subpeaks increases, the position of the subpeaks close to wurtzite almost coincide for all depicted cases.

Most importantly, the observed experimental peak shapes in Sec. 4.1 do not resemble the characteristics of the profiles depicted in Fig. 4.28. Therefore, we exclude a Poisson distributed length of the phase segments of wurtzite and zinc blende for our experimentally measured X-ray data.

Gaussian distribution

In order to further study the influence of the fluctuations of the length of a single element, we now consider Gaussian distributions for the phase segment length distributions: By varying their standard deviations without modifying their expectation values, we change the relative error of each individual phase segment and tune the degree of long-range correlations in the nanowires' phase segments. If the random event generated by the Gaussian distribution was less than one layer, the event was dropped and new random event has been generated until a positive number of layers has been generated. Therefore, once the standard deviation σ exceeds approximately 25% of the mean value μ, the distribution for generation of the phase segment length is no longer a Gaussian, but a truncated Gaussian. The mean μ and standard deviation σ given in this manuscript are the values of the distribution *before* truncation. For increasing standard deviation σ of the Gaussian distribution, the limit of highly correlated meta cells ($\sigma = 0$) develops towards the case of

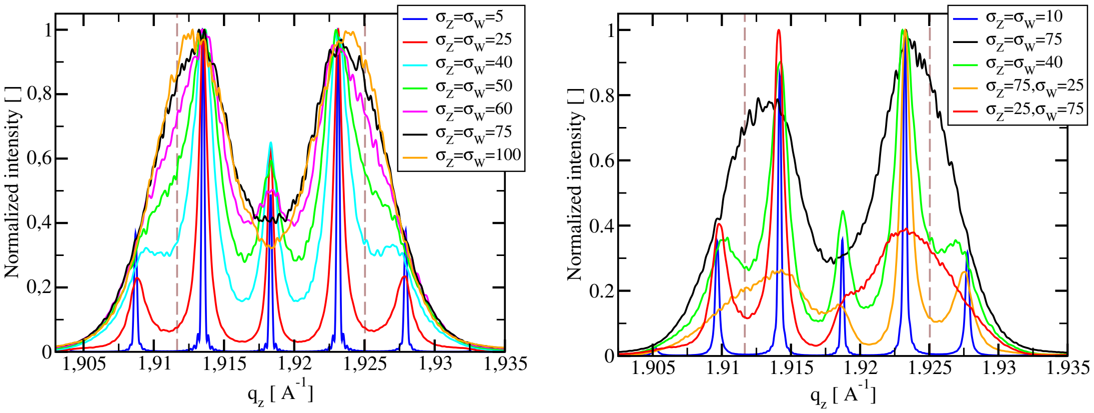

(a) Symmetric case $Z = W = 200$

(b) Asymmetric case $Z = 175$ and $W = 200$

Figure 4.29.: q_z intensity profiles near the $(111)_{z\curvearrowright c}$ GaAs Bragg peak for a Gaussian phase segment length with expectation value Z for zinc blende and W for wurtzite.

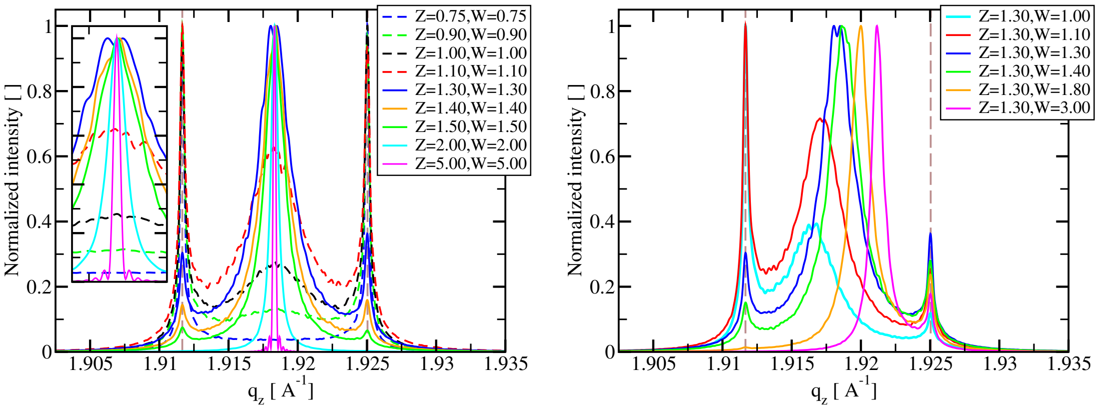

(a) Symmetric case with equal tail index $Z = W$

(b) Asymmetric case $Z = 1.30$ and $W \neq Z$

Figure 4.30.: q_z profile of the intensity near the $(111)_{z\curvearrowright c}$ GaAs Bragg peak for a Pareto distributed phase segment length with a tail index Z for zinc blende and W for wurtzite (i.e., a power law decay with power $Z+1$ and $W+1$ respectively).

high fluctuations ($\sigma \lesssim \mu$). In Fig. 4.29, we observe the transition of the scattering signal from Poisson-like behavior to the characteristics for Gamma, Weibull, etc., distributions for which the standard deviation for the length of a single segment is in the same order as the mean (see Tab. 4.1). Therefore, X-ray investigations of the $(111)_{z\curvearrowright c}$ GaAs Bragg peak are well suited for investigation of the correlations in (and quality of) highly periodic wurtzite-zinc blende super-cell structures ($\sigma_{\mathrm{P}} \ll \mu_{\mathrm{P}}$).

Pareto distribution

In Fig. 4.30, we depict typical scattering signals for a Pareto distribution based phase segment length distribution where the parameter b was set to one. We point out that a power law is scale-free. Therefore, the full depicted range of the polytype distribution in the nanowires from layer 0 to layer 5000 in Fig. 4.23 looks very similar to the magnified region from layer 4500 to 5000. For tail exponents $Z = W \leq 0.9$, two sharp peaks at the pure wires' q_z position are present. Some diffuse intensity is present between these subpeaks. For higher tail index, a third peak emerges in the center of the pure phase subpeaks. At first, this peak is very broad, but it decreases fast in width with increasing

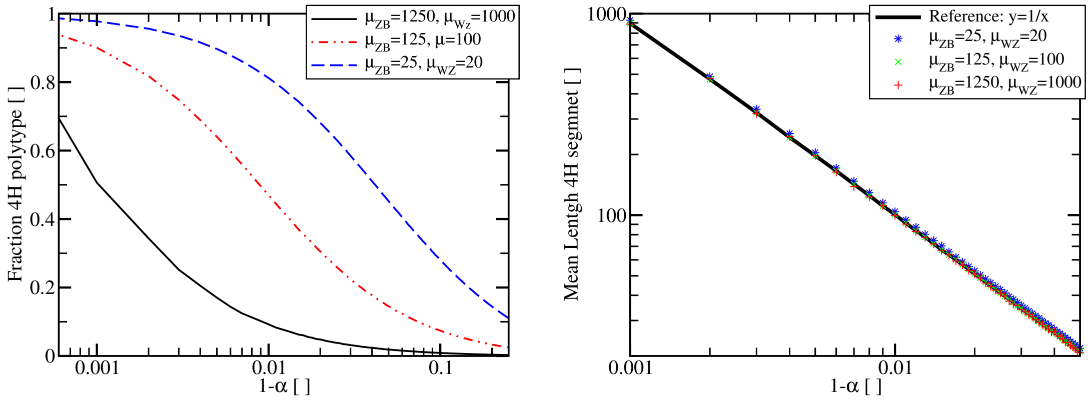

(a) Fraction of 4H polytype vs. α

(b) Mean length of 4H segment vs. α

Figure 4.31.: Fraction and mean length of the 4H polytype in the model (4.43b). The reference solution is taken from Eq. (4.54). The values μ_{ZB} and μ_{WZ} are the decay constants of the exponential distributions underlying the zinc blende and wurtzite segments.

tail index $Z = W$. The maximum intensities of all three subpeaks are almost equal for $Z = W \approx 1.20$ (not depicted). For higher tail indices, the central peak dominates the signal: For $Z = W = 1.5$, the peaks at the pure wires' positions are barely observable any more and have vanished for $Z = W = 2.0$. For very high tail indices, e.g., $Z = W = 5.0$, size oscillations of a meta-cell of alternating phase become visible (as in the Markov model in the limit $p_{\mathrm{ZB}\to\mathrm{WZ}} = p_{\mathrm{WZ}\to\mathrm{ZB}} \to 1.0$), since essentially only phase length segments with a length given by a single layer occur.

In strong contrast to all other probability distributions in Tab. 4.1, the outer peaks do not leave the native wires' position, even for asymmetric tail indices (see Fig. 4.30(b)). This fact originates from the strong influence of the long tails of the Pareto distribution which produces some pure or almost pure wires.[12] Nevertheless, the middle peak changes width and center of mass in case of asymmetric tail indices $Z \neq W$. For the Pareto distribution, this drift is monotonous towards the more likely phase. Plateaus (as e.g., for the Markov model) have not been observed in our simulations. Thus, we also exclude power law phase segment length distributions for our samples discussed in Sec. 4.1.

4.3.3.2. Enhanced occurrence of the 4H polytype

We now investigate the consequences for the X-ray signal near the $(111)_{\mathrm{z}\frown\mathrm{c}}$ Bragg reflection if the content of 4H polytype in the nanowires is increased beyond its purely statistical presence. The 4H structures are constituted by the stacking ABCB (and permutations thereof) as described in Sec. 1.4. Therefore, nearest neighbors define the local polytype to change every layer, i.e., WZWT (see beginning of Sec. 4.3). Hence, 50% of the structure are wurtzite, and 25% of the structure are zinc blende and twinned zinc blende respectively. In order to enhance the 4H wurtzite structures in the stacking sequences of the nanowires, we enhance the probability for a phase segment with length 1. Note, that this is different from enhancing short segment lengths in case of Gamma (for $-1 < m < 0$) or Weibull distribution (for $0 < \alpha < 1$): In those cases, the probability for 4H structure is also enhanced compared to the Markov model (since phase segments with length 1 are enhanced), but the modification is not equally selective as the one which is now investigated.

---

[12] Thus, the influence of the initial growth is much stronger than for the Markov model (see Sec. 4.3.2).

A first simple model is given by the phase length distribution

$$p_{\mathrm{4H+}}^{(\alpha)}(n) = (1-\alpha)\cdot p_{\mathrm{Markov}}(n) + \alpha \cdot p_{1+}(n) \tag{4.43a}$$

$$= (1-\alpha)\frac{1}{b}\,\mathrm{e}^{-n/b}\Theta(n) + \alpha\cdot\delta_{n1} \tag{4.43b}$$

for generation of a polytype segment with n layers. The parameters $\alpha \in [0,1]$ and b are polytype dependent and δ_{ij} is the Kronecker delta. Note, that $b \gg 1$ is assumed which makes the exponential distribution a good approximation to the Markov model. In this model, the limit $\alpha = 0$ corresponds to the original Markov model. The limit $\alpha = 1$ results in pure, perfect 4H nanowires. A phase length of 1 is returned with probability

$$p_{\mathrm{4H+}}^{(\alpha)}(n=1) \overset{b\gg1}{=} \frac{1}{b} + \alpha\frac{b-1}{b} + \mathcal{O}\left(\frac{1}{b^2}\right) = \alpha + \mathcal{O}\left(\frac{1}{b}\right) \tag{4.44}$$

and, therefore, is enhanced by

$$p_{\mathrm{4H+}}^{(\alpha)}(n=1) - p_{\mathrm{4H+}}^{(0)}(n=1) \overset{b\gg1}{=}= \alpha\frac{b-1}{b} + \mathcal{O}\left(\frac{1}{b^2}\right) = \alpha + \mathcal{O}\left(\frac{1}{b}\right) \tag{4.45}$$

All other lengths are correspondingly suppressed by

$$p_{\mathrm{4H+}}^{(\alpha)}(n>1) - p_{\mathrm{4H+}}^{(0)}(n>1) \overset{b\gg1}{=} \frac{-\alpha}{b} + \mathcal{O}\left(\frac{1}{b^2}\right) = 0 + \mathcal{O}\left(\frac{1}{b}\right) \tag{4.46}$$

The mean of $p_{\mathrm{4H+}}^{(\alpha)}(n)$ is

$$\mu\left(p_{\mathrm{4H+}}^{(\alpha)}\right) = (1-\alpha)b + \alpha \overset{b\gg\alpha}{\approx} (1-\alpha)b\ , \tag{4.47}$$

whereas the standard deviation is

$$\sigma\left(p_{\mathrm{4H+}}^{(\alpha)}\right) = \sqrt{(1-\alpha)^2\cdot b^2 + \alpha^2\cdot 0^2} = (1-\alpha)b\ . \tag{4.48}$$

Therefore, the ratio σ/μ equals one, irrespective for the value of α (as long as $\alpha \neq 1$).

The probability for a 4H structures to exceed the lengths $2n$, $n \in \mathbb{N}$, is given by[13]

$$p_{\mathrm{4H}}(\geq 2n) = \left(p_{\mathrm{4H+}}^{(\alpha_{\mathrm{ZB}})}(n=1)\ p_{\mathrm{4H+}}^{(\alpha_{\mathrm{WZ}})}(n=1)\right)^n \tag{4.49a}$$

$$= \left[\left(\frac{1}{b_{\mathrm{ZB}}} + \alpha_{\mathrm{ZB}}\frac{b_{\mathrm{ZB}}-1}{b_{\mathrm{ZB}}}\right)\left(\frac{1}{b_{\mathrm{WZ}}} + \alpha_{\mathrm{WZ}}\frac{b_{\mathrm{WZ}}-1}{b_{\mathrm{WZ}}}\right)\right]^n \tag{4.49b}$$

$$= \mathrm{e}^{\log\left[\left(\frac{1}{b_{\mathrm{ZB}}}+\alpha_{\mathrm{ZB}}\frac{b_{\mathrm{ZB}}-1}{b_{\mathrm{ZB}}}\right)\left(\frac{1}{b_{\mathrm{WZ}}}+\alpha_{\mathrm{WZ}}\frac{b_{\mathrm{WZ}}-1}{b_{\mathrm{WZ}}}\right)\right]\cdot n} = \mathrm{e}^{-2n/b_{\mathrm{4H}}} \tag{4.49c}$$

with

$$b_{\mathrm{4H}} = \frac{-2}{\log\left[\left(\frac{1}{b_{\mathrm{ZB}}} + \alpha_{\mathrm{ZB}}\frac{b_{\mathrm{ZB}}-1}{b_{\mathrm{ZB}}}\right)\left(\frac{1}{b_{\mathrm{WZ}}} + \alpha_{\mathrm{WZ}}\frac{b_{\mathrm{WZ}}-1}{b_{\mathrm{WZ}}}\right)\right]}\ . \tag{4.49d}$$

Hence, the probability of a segment to be smaller than $2n$ is

$$p_{\mathrm{4H}}(< 2n) = 1 - p_{\mathrm{4H}}(\geq 2n) = 1 - \mathrm{e}^{-2n/b_{\mathrm{4H}}}\ . \tag{4.50}$$

If we approximate n as continuous variable x, we have

$$p_{\mathrm{4H}}(< x) = 1 - \mathrm{e}^{-x/b_{\mathrm{4H}}}\ . \tag{4.51}$$

---

[13] For odd length $2n+1$, the result has to multiplied with $p_{\mathrm{4H+}}^{(\alpha_{\mathrm{P}})}(n=1)$ of the terminating phase P.

By differentiating, we obtain

$$p_{\mathrm{4H}}(x) = \frac{1}{b_{\mathrm{4H}}}\,\mathrm{e}^{-x/b_{\mathrm{4H}}} \tag{4.52}$$

for $x > 0$. Therefore, the phase segment length distribution for the 4H structure is well approximated by an exponential distribution with the decay length b_{4H}. However, for the decay length b_{4H} to be significantly larger than 1, either b_{ZB} and b_{WZ} must be in the order of 1, or α_{ZB} and α_{WZ} must be very close to one. It is important to understand that for values of α very close to one, almost all “segments” which are generated are only one layer. On the contrary, every rare event $(1-\alpha)$ typically adds a large number of layers to the stacking. Therefore, a good scale for α can be calculated from the condition $b = b_{\mathrm{ZB}} = b_{\mathrm{WZ}} = b_{\mathrm{4H}}$. Assuming $\alpha = \alpha_{\mathrm{ZB}} = \alpha_{\mathrm{WZ}}$, we isolate

$$b = \frac{-1}{\log\left[\frac{1}{b} + \alpha\frac{b-1}{b}\right]} \quad \Rightarrow \quad \alpha = \frac{1}{b-1}\left(b\,\mathrm{e}^{\frac{-1}{b}} - 1\right) \tag{4.53}$$

from Eq. (4.49d). In the limit $b \gg 1$, we have

$$\alpha \approx \frac{b}{b-1}\left(1 - \frac{1}{b}\right) - \frac{1}{b-1} = 1 - \frac{1}{b-1} \approx 1 - \frac{1}{b}\;. \tag{4.54}$$

For values of α close to 1, the phase fraction of the 4H polytype and the mean segment thickness of the 4H segments are depicted in Fig. 4.31.

Considering the investigations already presented, we expect additional weight at the center of the wurtzite and zinc blende position in the X-ray signal (assuming the average lattice constant of 4H structures equals the average lattice constant of pure zinc blende and pure wurtzite phase). As before, the large fluctuations of the exponential distributions quickly destroy size oscillations and beating phenomena. Moreover, the typically very small mean segment size of the 4H segments (see Fig. 4.31(b)) results in a very broad contribution in reciprocal space. Thus, the amplitude at every point is rather small. Therefore, a deviation from the Markov model according to Eq. (4.43b) cannot by detected experimentally by measuring the vicinity of the $(111)_{\mathrm{z}\curvearrowright\mathrm{c}}$ Bragg reflection if $(1-\alpha)b \gg 1$ (see Fig. 4.32).

For very pure wires (see Fig. 4.32(a)), a third subpeak in between the wurtzite and zinc blende subpeak shows up: Each subpeak is very narrow and they almost do not overlap. Thus, for all practical purposes, the three subpeaks can be treated as independent of each other. Nonetheless, we point out that the characteristics of the signal in this range of parameters closely resembles the features of the Pareto distributed segment lengths with tail indices in the range from 0.9 to 1.5 (see Fig. 4.30).

In contrast, for a decay length in the order of 100 defect-free successive layers of the wurtzite and zinc blende polytype, the incorporation of the 4H polytype results in three strongly overlapping peaks. Most importantly, the enhancement of the polytype 4H can practically not be distinguished from its purely statistical presence because all signals look very similar to the signal of the two phase Markov model without 4H enhancement. Instead, systematically wrong transition probabilities – towards larger values, i.e., less pure wires – would be extracted if the parameter α is not known *a priori*.

Whereas the layer distribution of the wurtzite and zinc blende segments can be easily modified by substituting the contribution p_{Markov} in Eq. (4.43b) by another probability distribution (see Fig. 4.32(c) for a Poisson distribution), the model given in Eq. (4.43b) is no longer applicable, if the layer distribution *of the 4H segments* is not exponential. In this case, the model needs to be extended by specifying

- three distributions for the segment lengths of pure zinc blende, pure wurtzite and 4H and the respective parameters of the distributions, and

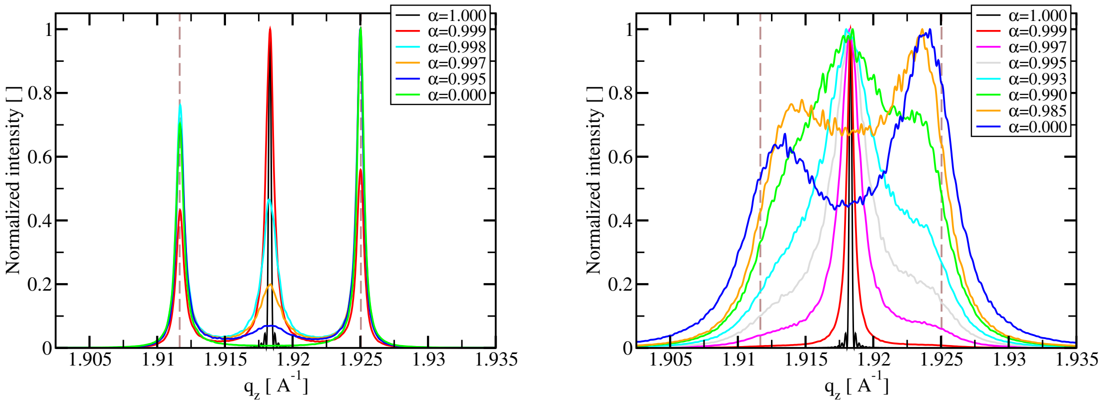

(a) Exponential distribution:μ_{ZB}=1250,μ_{WZ}=1000 (b) Exponential distribution: μ_{ZB}=125, μ_{WZ}=100

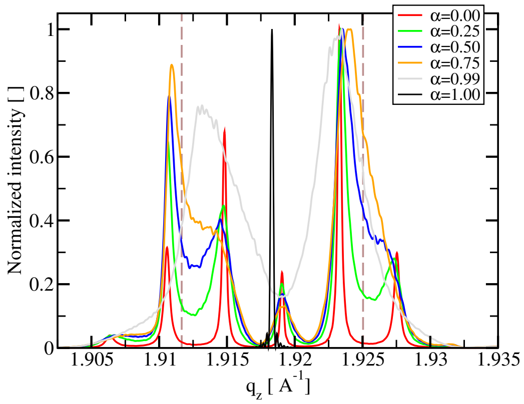

(c) Poisson distribution: μ_{ZB}=250, μ_{WZ}=200

Figure 4.32.: q_z intensity profiles near the $(111)_{\mathrm{z\frown c}}$ GaAs Bragg peak produced by the model defined in Eq. (4.43b). In Fig. (c) the contribution p_{Markov} in Eq. (4.43b) has been substituted by Poisson distributions. The values μ_{ZB} and μ_{WZ} are the mean values of the length distributions of the zinc blende and wurtzite segments.

- three branching ratios to determine the consecutive phase after a segment ended.[14]

However, this extension requires three parameters for the branching ratio, plus the choice of the distribution for the 4H structured segments and its parameters. The model (4.43b) requires only two additional parameters α_{P}, $\mathrm{P} \in \{\mathrm{ZB}, \mathrm{WZ}\}$. Since the experimentally data of Sec. 4.1 can be explained without these extensions and additional parameters, we will not consider the enhancement of the 4H polytype further in this manuscript. However, we have to keep in mind, that an enhancement of the 4H polytype beyond its statistical occurrence cannot be detected from our data, but our wires would seem less pure.

In conclusion, we performed a detailed study of a Markov chain for the stacking sequence of nanowires. First, the influence of initial growth on the probability for a particular phase to occur with increasing height of the wire has been studied for static transition probabilities. Then, the X-ray scattering signal for this class of models was studied and compared to various other probability distributions for the segment lengths of the wurtzite and zinc blende polytype. Within the full set of Weibull and Gamma distributions, which

---

[14] For example: After a pure wurtzite segment, the probability for continuation with a pure zinc blende segment is 30%; after a pure zinc blende segment, the probability for continuation with pure wurtzite segment is 40% and, finally, after a 4H structured segment, the probability for continuation with a pure wurtzite segment is 20%. The alternative continuation is given by the complementary fraction to 100%.

reduce to the Markov model as a special case, the X-ray profile of the $(111)_{\mathrm{z}\curvearrowright\mathrm{c}}$ profile is no longer unique. However, a hierarchy of strong and weak influence on the signal has been identified. For all cases of exponential decay (Markov, Gamma, Weibull and logarithmic), the peak profiles showed the same characteristics. Distributions with non-exponential decay (uniform, Pareto, Poisson) produced different characteristic features for the X-ray q_z profile near the $(111)_{\mathrm{z}\curvearrowright\mathrm{c}}$ Bragg peak and, thus, are excluded for the experimental data presented in Sec. 4.1.

Our simulations demonstrate that the $(111)_{\mathrm{z}\curvearrowright\mathrm{c}}$ reflection only reveals an enhancement of the 4H polytype in case of very pure wires. For the samples which we discuss in this manuscript, an enhancement of the 4H polytype would result in a seemingly reduced phase purity in the framework of our two polytype models.

Moreover, the influence of the variance of the statistical distribution has been discussed in connection to Poisson and Gaussian distributions: For distributions with low length fluctuations, beating phenomena remain despite incoherent averaging of the contributions of different wires as a consequence of the small variance.

Finally, the relation of the $(111)_{\mathrm{z}\curvearrowright\mathrm{c}}$ and $(333)_{\mathrm{z}\curvearrowright\mathrm{c}}$ reflection has been discussed for the Markov model as well as non-static transition probabilities which are necessary for accounting for the changes in the experimental X-ray profiles with advancing growth time presented in Sec. 4.1.

4.4. Implications from the experimental *in-situ* data on the growth dynamics

We now derive the implications from the experimental *in-situ* data of sample S2 on the growth dynamics of nanowires where we employ the insights which have been obtained by the simulations that have been presented in Sec. 4.3. For that purpose, we first extract the time-dependent transition probabilities of a Markov model which correspond to these experimental profiles (see Sec. 4.4.1). Then, we connect these transition probabilities in Sec. 4.4.2 with differences of the nucleation barriers.

4.4.1. Probabilities for transitions of the growing phase in nanowires

The changes in the shape of the experimental intensity profiles (beyond changes originating from changes in the geometry of the nanowires) imply non-static statistical properties of the Markov model. Consequently, we are forced to deal with time-dependent Markov models as discussed in connection with Eq. (4.41) (see Fig. 4.22).

We attribute the gradient in the transition probabilities to a change in the dynamics of growing nanowires with increasing height. We assume a linear relation for the nanowire height (i.e., its number of layers n) and the growth time t_G. Consequently, layer-dependent and height-dependent transition probabilities are synonyms in the subsequent discussion.

For the mapping of the height of the nanowire (number of layers) after a specific growth time t_G, we employ:[15]

layer n [ ]	2802	3585	4368	5151	5934
growth time t_G [min]	26	34	41	49	56

---

[15] This mapping deviates slightly from the mapping in Ref. [131], since a more detailed evaluation of the SEM pictures from this samples revealed a smaller mean height of the wires than used in Ref. [131].

Even for the linearly changing transition probabilities as defined in Eq. (4.41), the extraction of the parameters $u_{\mathrm{P}\rightarrow\bar{\mathrm{P}}}$ and $v_{\mathrm{P}\rightarrow\bar{\mathrm{P}}}$ is highly non-trivial, since neither the beamline parameters (like the resolution element) nor a sufficiently accurate q_z calibration (see discussion close to Fig. 4.18) are available. Consequently, this information needs to be obtained simultaneously with the transition probabilities $p_{\mathrm{P}\rightarrow\bar{\mathrm{P}}}(n)$.

In addition, due to the required correction of the nanowire signal for the contribution from the crystallites, the accuracy of tails of the nanowire signal – which would be very useful for a rough estimation of the nanowires properties as discussed in the framework of Fig. 4.18 – is limited for the available experimental data.

Therefore, we fitted our data in the following way:

1. First, we calculated the “ideal” scattering signal (no resolution element) for a huge set of parameters in Eq. (4.41) at the experimentally observed growth times t_{G}. The bounds for the parameters $u_{\mathrm{P}\rightarrow\bar{\mathrm{P}}}$ and $v_{\mathrm{P}\rightarrow\bar{\mathrm{P}}}$ have been chosen according to the typical features of the X-ray signal for static transition probabilities $p_{\mathrm{P}\rightarrow\bar{\mathrm{P}}}$ with a large safety margin.
2. Then, we performed a Monte-Carlo sampling of the relevant beamline parameters and compared each simulated set of transition probabilities with the experimentally observed profiles.
3. From the large data set of all simulated profiles (each transition probability combined with all beamline parameters), we chose the best fits. In addition to the best overall fit, we exploited these best fits to extract the median of the transition probabilities as well as 25% and 75% quantiles. These quantiles are given as error estimates.

The results are summarized in Fig. 4.33. Before we discuss these results, we first provide more details on the data evaluation itself.

For comparison of the simulated and experimental profiles, we restricted to pixel 136 to 149 (central gray region of the X-ray signal in Fig. 4.33), since the tails of the X-ray signal might be inaccurate due to the imperfect separation of the background from the parasitic growth. Indeed, we see some intensity weight in the region $q_z \gtrapprox 1.9275\text{Å}^{-1}$ which is not fitted by the Markov model. However, we attribute this deviation to the experimental *in-situ* data and the preprocessing thereof, since this additional weight is absent in case of the post-growth *ex-situ* data obtained at ID13@ESRF (see Fig. 4.11). Except for this deviation, all three fits depicted in Fig. 4.33 nicely fit the experimental data. As error metric for the fit, we employed

$$\aleph(p_{\mathrm{P}\rightarrow\bar{\mathrm{P}}}(n), \text{beamline parameters}) = \sqrt{\sum_{t_{\mathrm{Exp}}} \left(1 - \cos\left(\measuredangle(\exp, \mathrm{sim})\right)\right)^2}\ , \qquad (4.55)$$

where

$$\cos\left(\measuredangle(\exp, \mathrm{sim})\right) = \frac{\mathcal{I}^{\exp}(q_z) \cdot \mathcal{I}^{\mathrm{sim}}(q_z)}{\|\mathcal{I}^{\exp}(q_z)\|_2 \cdot \|\mathcal{I}^{\mathrm{sim}}(q_z)\|_2} \qquad (4.56)$$

is evaluated after linear interpolation of the experimental data to the (denser) q_z grid of the simulated profiles.

Here, the resolution element of the beamline is modelled as a (circular) convolution of a Gaussian (width σ) and the intensity profile $\mathcal{I}^{\mathrm{sim}}(q_z)$. The q_z calibration requires two parameters: the distance in reciprocal space which corresponds to the inter-pixel spacing on the detector and the global offset. The three beamline parameters have been Monte-Carlo sampled in these ranges:

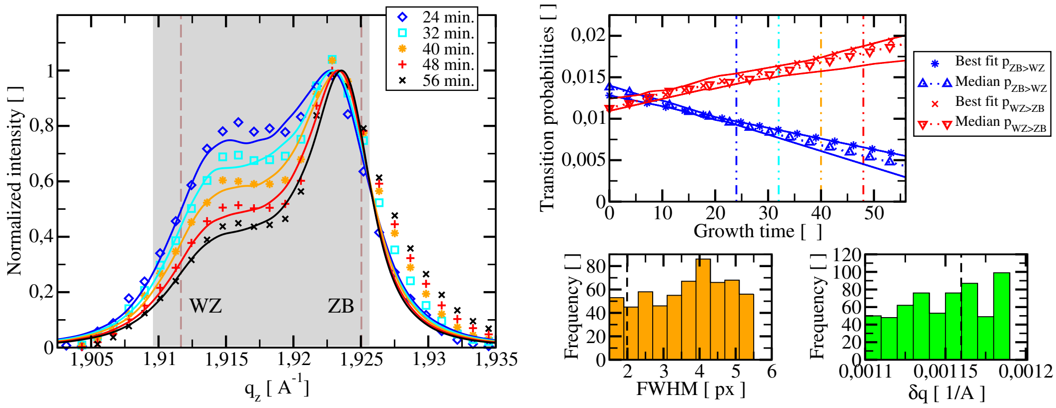

(a) Assumptions: Background modelled as 2 dimensional Gaussian, $d_{\mathrm{WZ}}/d_{\mathrm{ZB}} = 1 + 0.7\%$

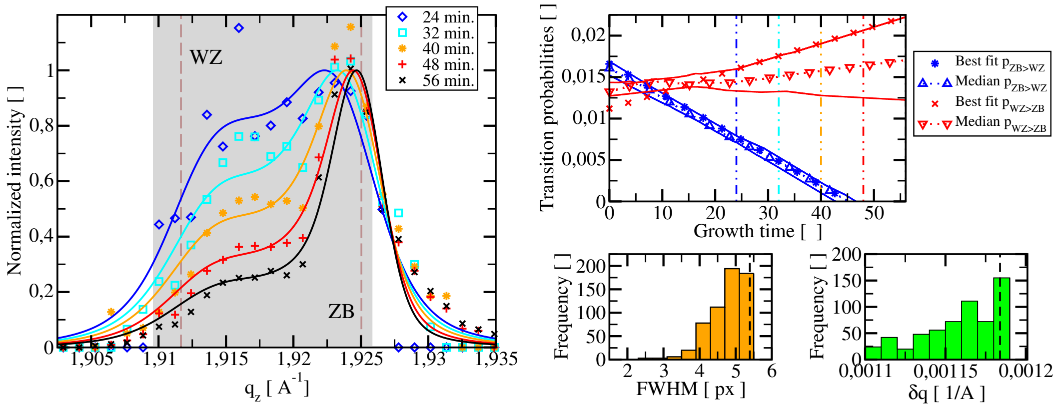

(b) Assumptions: Background modelled as 1.5 dimensional Pearson VII, $d_{\mathrm{WZ}}/d_{\mathrm{ZB}} = 1 + 0.7\%$

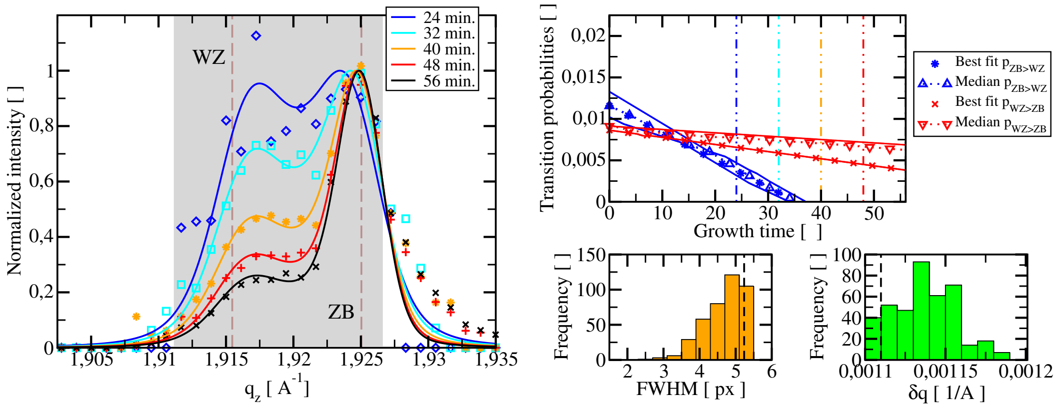

(c) Assumptions: Background modelled as 1.5 dimensional Pearson VII, $d_{\mathrm{WZ}}/d_{\mathrm{ZB}} = 1 + 0.5\%$

Figure 4.33.: Extracted time-dependent transition probabilities of the nanowires grown in the PMBE growth chamber and monitored by *in-situ* X-ray diffraction during their growth at the NANO beamline at the synchrotron ANKA.

parameter	minimal value	maximal value
$q_z(\text{pixel} = 195)$ [Å^{-1}]	1.9445	1.952
δq_z [Å^{-1}]	0.00110	0.00119
σ [pixel]	1.5	5.5

For each fit in Fig. 4.33 we sampled $\mathrm{N_{BL}} = 1000$ combinations of beamline parameters. For a ratio of the interplanar lattice spacing of wurtzite and zincblende of $d_{\mathrm{WZ}}/d_{\mathrm{ZB}} = 1 + 0.7\%$, we simulated $\mathrm{N_{Real}} = 6000$ realizations for $p_{\mathrm{P}\to\bar{\mathrm{P}}}(n)$ according to Eq. (4.41).

For $d_{\mathrm{WZ}}/d_{\mathrm{ZB}} = 1 + 0.5\%$, we simulated $\mathrm{N}_{\mathrm{Real}} = 4000$ realizations for $p_{\mathrm{P}\to\bar{\mathrm{P}}}(n)$.

Consequently, the error metric $\aleph(p_{\mathrm{P}\to\bar{\mathrm{P}}}(n), \text{beamline parameter})$ was evaluated for $\mathrm{N}_{\mathrm{BL}} \cdot \mathrm{N}_{\mathrm{Real}}$ data sets, and the best $(0.01\mathrm{N}_{\mathrm{BL}}) \cdot (0.01\mathrm{N}_{\mathrm{Real}})$ is used for evaluation of the 25% and 75% quantiles of the transition probabilities.

We now discuss the results presented in Fig. 4.33:

In all three cases (different ratio $d_{\mathrm{WZ}}/d_{\mathrm{ZB}}$, different modelling of the contribution from parasitic growth), the transition probability $p_{\mathrm{ZB}\to\mathrm{WZ}}$ decreases at later growth times which results in higher phase purity of zinc blende segments. Within our model, a transition probability less or equal to zero is to be interpreted as growing pure zinc blende wires from that height on. In practice and for the given experimental and model precision, this should be interpreted only in such a way, that wurtzite phase is rare and segments are short. Moreover, we see that, for early growth times, the transition probabilities $p_{\mathrm{ZB}\to\mathrm{WZ}}$ and $p_{\mathrm{WZ}\to\mathrm{ZB}}$ are approach each other for growth times around 20min. Since we could not evaluate the very weak X-ray signal for earlier growth times, one should be careful with interpretation of the extrapolated transition probabilities $p_{\mathrm{ZB}\to\mathrm{WZ}}$ and $p_{\mathrm{WZ}\to\mathrm{ZB}}$ for growth times $t_{\mathrm{G}} \lesssim$ 20min.

For a ratio of the interplanar spacing of the Ga layer in $[111]_{\mathrm{z}\curvearrowright\mathrm{c}}$ direction close to $d_{\mathrm{WZ}}/d_{\mathrm{ZB}} = 1 + 0.7\%$ – as supported by the post-growth *ex-situ* measurements presented in Sec. 3.2 and the results in Refs. [101, 119] – we observe an increase in the transition probability $p_{\mathrm{WZ}\to\mathrm{ZB}}$ with increasing growth time irrespective of employing a two-dimensional Gaussian as background or the 1.5 dimensional Pearson VII model. Even the quantitative values are very similar. However, the errors are different: For the 1.5 dimensional Pearson VII model with $d_{\mathrm{WZ}}/d_{\mathrm{ZB}} = 1 + 0.7\%$, the results is compatible with a slope of zero within the error margins which is not true for the two-dimensional Gaussian background.

Fig. 4.33(c) assumes a smaller ratio of the interplanar spacing $d_{\mathrm{WZ}}/d_{\mathrm{ZB}} = 1 + 0.5\%$. This value has been obtained in Ref. [137]. Under this assumption, both transition probabilities are shifted towards lower absolute values and the trend for wurtzite changes. However, given the results presented in Sec. 3.2, we are confident, that Figs. 4.33(a) and 4.33(b) more accurately represent the transition probabilities in our nanowires.

We point out, that for our wires the transition probabilities fulfil $p_{\mathrm{P}\to\bar{\mathrm{P}}} \lesssim 2\%$ which corresponds to mean phase segment lengths greater than $p^{-1}_{\mathrm{P}\to\bar{\mathrm{P}}} \approx 50$ layer. Consequently, the phase purity of our wires is at least one order of magnitude higher than of the wires investigated by Johansson et al. in Refs. [24, 59] by means of high resolution transmission electron microscopy (HRTEM) where an exponential distribution for the phase segment thickness with mean segment lengths of zinc blende and twinned zinc blende segments in the order of approximately $3 - 9$ layers has been observed. We also point out, that we observe a trend towards higher phase purity of zinc blende despite constant growth parameters – in contrast to the *in-situ* X-ray experiments of Krogstrup et al. [54] where the growth growth conditions have not been kept constant during growth.

In addition, histograms of two beamline parameters (FWHM of resolution element and interpixel spacing δq) of the best $(0.01\mathrm{N}_{\mathrm{BL}}) \cdot (0.01\mathrm{N}_{\mathrm{Real}})$ fits are depicted in Fig. 4.33. Interestingly, the histograms behave differently for a two-dimensional Gaussian background and the 1.5 dimensional Pearson VII background. Whereas for the Pearson VII model a tendency of the resolution element towards $4 - 6$ pixel is observed, the distribution is much broader for the two-dimensional Gaussian background is observed. Only a very small enhancement in the range $3.5 - 5$ pixel is observed. Similar statements hold for the interpixel spacing δq: For the Pearson VII model, a tendency towards higher values (smaller values in case of $d_{\mathrm{WZ}}/d_{\mathrm{ZB}} = 1 + 0.5\%$) is observed, but no enhancement beyond a uniform distribution is observed for the two-dimensional Gaussian background.

Clearly, this behavior is not yet satisfactory: For a robust fitting procedure, the beamline parameters should also "converge" to their true physical solution and not be distributed almost uniformly in a broad range of values as in case of the two-dimensional Gaussian background. From a different perspective, however, one might also say, that this insensitive of the transition probabilities $p_{\mathrm{P}\rightarrow\bar{\mathrm{P}}}$ to the precise parameters of the beamline might also be an advantage. For the Pearson VII model, such "convergence" of the beamline parameters has been observed: However, for $d_{\mathrm{WZ}}/d_{\mathrm{ZB}} = 1 + 0.7\%$, the zinc blende peak should be almost on the native zinc blende position at later growth times, and, thus, we expect a interplanar pixel spacing of only $\delta q \approx \frac{0.078831\text{Å}^{-1}}{(137.5\pm1.0-66.\pm0.5)} = \frac{0.078831\text{Å}^{-1}}{71.5\pm1.5} = 0.001103\text{Å}^{-1} \pm 0.000023\text{Å}^{-1}$. Consequently, the center of mass of the extracted interplanar spacings of the best $(0.01\mathrm{N}_{\mathrm{BL}}) \cdot (0.01\mathrm{N}_{\mathrm{Real}})$ should be located at lower values δq. This accumulation at lower values of δq is observed for $d_{\mathrm{WZ}}/d_{\mathrm{ZB}} = 1 + 0.5\%$. However, for this data set, the splitting of zinc blende and wurtzite is assumed smaller than indicated by the results presented in Sec. 3.2. In order to resolve these inconsistencies completely, a deeper investigation based on additional experimental time-resolved *in-situ* data sets of better data quality taken with the PMBE growth chamber as well as better knowledge of the beamline parameter during these measurements must be performed in future.

4.4.2. Temporal evolution of the differences of nucleation barriers

We now relate the time-resolved transition probabilities $p_{\mathrm{P}\rightarrow\bar{\mathrm{P}}}(n)$ with particular aspects of the energetics of nanowire growth. More specifically, we estimate the nucleation barrier differences

$$\delta E_{\bar{\mathrm{P}}|\mathrm{P}}(n) = E_{\bar{\mathrm{P}}|\mathrm{P}}(n) - E_{\mathrm{P}|\mathrm{P}}(n) \ . \tag{4.57}$$

Here, $E_{\mathrm{P}|\mathrm{P}}$ is the nucleation barrier for growing phase P on phase P. $E_{\bar{\mathrm{P}}|\mathrm{P}}$ is the nucleation barrier for growing the complementary phase $\bar{\mathrm{P}}$ on phase P [59, 88, 105].

For the following discussion it is useful to think of the transition probabilities $p_{\mathrm{P}\rightarrow\bar{\mathrm{P}}}$ as conditional probabilities $p_{\mathrm{P}|\bar{\mathrm{P}}}$ for growing phase P on phase $\bar{\mathrm{P}}$, i.e.

$$p_{\mathrm{WZ}|\mathrm{ZB}} = p_{\mathrm{ZB}\rightarrow\mathrm{WZ}} \ , \qquad p_{\mathrm{ZB}|\mathrm{ZB}} = 1 - p_{\mathrm{ZB}\rightarrow\mathrm{WZ}} \ , \tag{4.58a}$$

$$p_{\mathrm{ZB}|\mathrm{WZ}} = p_{\mathrm{WZ}\rightarrow\mathrm{ZB}} \ , \qquad p_{\mathrm{WZ}|\mathrm{WZ}} = 1 - p_{\mathrm{WZ}\rightarrow\mathrm{ZB}} \ . \tag{4.58b}$$

The link between these conditional probabilities and the nucleation barrier differences is established by

$$p_{\mathrm{P}|\mathrm{P}}(n) = \frac{\nu_{\mathrm{P}|\mathrm{P}}(n) \cdot \mathrm{e}^{-\beta E_{\mathrm{P}|\mathrm{P}}(n)}}{\nu_{\mathrm{P}|\mathrm{P}}(n) \cdot \mathrm{e}^{-\beta E_{\mathrm{P}|\mathrm{P}}(n)} + \nu_{\bar{\mathrm{P}}|\mathrm{P}}(n) \cdot \mathrm{e}^{-\beta E_{\bar{\mathrm{P}}|\mathrm{P}}(n)}} \tag{4.59}$$

where $\beta = 1/(k_{\mathrm{B}}T_{\mathrm{Sub}})$ and k_{B} is the Boltzmann constant [59, 88, 105]. T_{Sub} is the absolute temperature of the growth substrate[16]. The prefactors $\nu_{\mathrm{P}|\mathrm{P}}$ and $\nu_{\bar{\mathrm{P}}|\mathrm{P}}$ incorporate the degeneracies of the number of nuclei which are described by the energies $E_{\mathrm{P}|\mathrm{P}}$ and $E_{\bar{\mathrm{P}}|\mathrm{P}}$ respectively. We point out, that relation (4.59) requires close to equilibrium statistical behavior.

If we combine this equation with the definition (4.57) of the nucleation barrier difference $\delta E_{\bar{\mathrm{P}}|\mathrm{P}}$, we can solve the equation for this nucleation barrier difference $\delta E_{\bar{\mathrm{P}}|\mathrm{P}}$ and obtain

$$\delta E_{\bar{\mathrm{P}}|\mathrm{P}}(n) = k_{\mathrm{B}}T_{\mathrm{Sub}} \cdot \left[\ln\left(\frac{p_{\mathrm{P}|\mathrm{P}}}{p_{\bar{\mathrm{P}}|\mathrm{P}}}\right) + \ln\left(\frac{\nu_{\bar{\mathrm{P}}|\mathrm{P}}}{\nu_{\mathrm{P}|\mathrm{P}}}\right)\right] \tag{4.60a}$$

$$= k_{\mathrm{B}}T_{\mathrm{Sub}} \cdot \left[\ln\left(\frac{1 - p_{\mathrm{P}\rightarrow\bar{\mathrm{P}}}(n)}{p_{\mathrm{P}\rightarrow\bar{\mathrm{P}}}(n)}\right) + \ln\left(\frac{\nu_{\bar{\mathrm{P}}|\mathrm{P}}(n)}{\nu_{\mathrm{P}|\mathrm{P}}(n)}\right)\right] \ , \tag{4.60b}$$

---

[16] Here, it is assumed that the temperature of the substrate is identical to the currently nucleating layer.

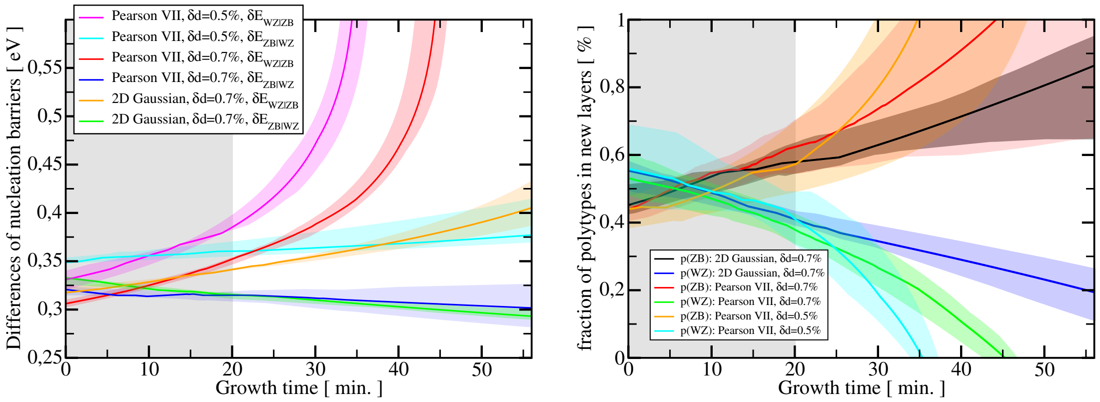

(a) Differences $\delta E_{\bar{\mathrm{P}}|\mathrm{P}}$ of the nucleation barriers

(b) Phase fractions $p_{\mathrm{P}}^{(\mathrm{L})}$

Figure 4.34.: Differences of the nucleation barriers as defined in Eq. (4.60b) and (differential) phase fractions in a quasi-static approximation with increasing growth time for the transition probabilities depicted in Fig. 4.33.

where we returned to the transition probabilities $p_{\mathrm{P}\to\bar{\mathrm{P}}}(n)$ in the last step. This result does not rely on a particular geometrical model for the nucleus, the exact mechanisms of nucleation and the catalyst dynamics [25, 45, 49, 60, 69, 70, 74, 77, 105, 106], but on the validity of a Markov model for the stacking of the grown nanowires.

However, estimation of the degeneracies $\nu_{\mathrm{P}|\mathrm{P}}(n)$ and $\nu_{\bar{\mathrm{P}}|\mathrm{P}}(n)$ requires sophisticated modelling of the mechanism of nucleation. Nevertheless, as long as the degeneracies are almost equal, we have $\frac{\nu_{\bar{\mathrm{P}}|\mathrm{P}}(n)}{\nu_{\mathrm{P}|\mathrm{P}}(n)} \approx 1 \Rightarrow \ln\left(\frac{\nu_{\bar{\mathrm{P}}|\mathrm{P}}(n)}{\nu_{\mathrm{P}|\mathrm{P}}(n)}\right) \approx 0$. The subsequent evaluations are based on this assumption.

We point out, that the extraction of transition probabilities $p_{\mathrm{P}\to\bar{\mathrm{P}}}(n)$ from our measured X-ray data is independent to modelling these parameters $\nu_{\mathrm{P}|\mathrm{P}}(n)$ and $\nu_{\bar{\mathrm{P}}|\mathrm{P}}(n)$, but these parameters – once detailed modelling is available – will change the quantitative numbers for the differences of the nucleation barrier $\delta E_{\bar{\mathrm{P}}|\mathrm{P}}(n)$.

For a substrate temperature of $T_{\mathrm{S}} = 590°\mathrm{C}$, we have $k_{\mathrm{B}}T_{\mathrm{Sub}} = 74.4\mathrm{meV}$. For the transition probabilities depicted in Fig. 4.33 and this value of $k_{\mathrm{B}}T_{\mathrm{Sub}}$, the resulting differences of the nucleation barriers are given in Fig. 4.34(a).

For $p_{\mathrm{P}\to\bar{\mathrm{P}}} = 2\%$, we have $\delta E_{\bar{\mathrm{P}}|\mathrm{P}} \approx 3.9\ k_{\mathrm{B}}T_{\mathrm{Sub}} \approx 290\mathrm{meV}$, and for $p_{\mathrm{P}\to\bar{\mathrm{P}}} = 0.5\%$, we have $\delta E_{\bar{\mathrm{P}}|\mathrm{P}} \approx 5.3\ k_{\mathrm{B}}T_{\mathrm{Sub}} \approx 400\mathrm{meV}$. Consequently, the nucleation barrier differences evolve within these bounds for the two-dimensional Gaussian background correction.

For the Pearson VII background correction, $p_{\mathrm{WZ}\to\mathrm{ZB}}$ drops below 0.5% and, consequently, the respective nucleation barrier difference $E_{\mathrm{WZ}|\mathrm{ZB}}$ exceeds the bound of 400meV. For $p_{\mathrm{WZ}\to\mathrm{ZB}} \to 0$, this quantity diverges. However, within the precision of our model and our data, we should only conclude that $\ln\left(\frac{1-p_{\mathrm{P}\to\bar{\mathrm{P}}}(n)}{p_{\mathrm{P}\to\bar{\mathrm{P}}}(n)}\right) \gg 1$, and, therefore, $E_{\mathrm{WZ}|\mathrm{ZB}} \gg k_{\mathrm{B}}T_{\mathrm{Sub}}$.

We attribute the trend of the transition probabilities and the nucleation barrier differences mainly to the dynamics of the droplet at the nanowire tip, in particular its shape and its composition.

One possible origin is in increase of the supersaturation of As in the liquid droplet during growth. This could lead to a higher probability for the nucleation of zinc blende [56].

Additionally, the volume of the liquid droplet might decrease [69]. Since the droplet mainly consists of Ga, the volume of the liquid droplet is essentially equal to its amount of Ga.

This amount of Gallium might decrease due to a reduction of the Ga-flux towards the droplet via the nanowire side walls as the wire grows longer [87, 148, 149]. This reduction in the volume might have two (non excluding) consequences: First, the diameter of the droplet on the tip might decrease. Secondly, the wetting angle of the droplet with the top-facet of the nanowire might change.

If the diameter of the droplet would decrease, such behavior would most likely produce highly tapered nanowires [46] which has not been observed in the post-growth SEM investigations of the samples [67]. Therefore, the diameter of the droplet likely remains constant with increasing growth time.

Consequently, the reduction of the volume of the Ga droplet probably induces mainly a decrease of the wetting angle of the droplet [69].

Our results imply an increasing phase fraction of zinc blende with increasing growth time (see Fig. 4.34(b)). For the evaluation of the phase fraction, we assume quasi-static probabilities during the mean length of a segment and employ Eq. (4.24a). This is valid as long as the gradient of the transition probabilities is sufficiently small. The result corresponds to the "differential" probabilities $p_{\mathrm{WZ}}^{(\mathrm{L})}(n)$ and not to the global mean fraction $\bar{p}_{\mathrm{WZ}}(n)$ (see Sec. 4.3.2 close to Eq. (4.25)). A discussion of the "differential phase fraction" (i.e., the phase fraction of the newly grown segments) and the global mean phase fraction which is independent of the Markov model is given in Sec. E in the appendix.

The same trend towards a higher phase fraction of zinc blende has also been found by post-growth *ex-situ* investigations by Biermanns et al. [101, 119].[17] However, the authors of these references could not draw any conclusions on the phase *purity* (in the meaning of the mean length of a faultless phase segment) in the nanowires from their data.

In summary, we carefully explored in Sec. 4 the perspectives and limitations of time-resolved *in-situ* X-ray diffraction measurements of the $(111)_{\mathrm{z}\curvearrowright\mathrm{c}}$ Bragg reflection: We demonstrated that — under certain assumptions — estimates for the phase purities — a key quantity for many applications of nanowires — and their evolution during growth can be obtained. From this, the phase fractions and the nucleation barrier differences as well as their evolution during growth could also be estimated. Nonetheless, several aspects must be investigated in future more closely once additional experimental data time-resolved *in-situ* X-ray data is available. For example, the non-uniqueness of the $(111)_{\mathrm{z}\curvearrowright\mathrm{c}}$ X-ray profiles of the nanowire signal and the separation of the contributions from nanowires and parasitic growths should be revisited once the $(111)_{\mathrm{z}\curvearrowright\mathrm{c}}$ and $(333)_{\mathrm{z}\curvearrowright\mathrm{c}}$ reflection can be measured during growth after an upgrade of the PMBE growth chamber. After consideration of the limitations of the $(hhh)_{\mathrm{z}\curvearrowright\mathrm{c}}$ reflections which exploit the tiny differences of the lattice constants of the polytypes but diffract at the same planes, we also propose to supplement measurements of the $(hhh)_{\mathrm{z}\curvearrowright\mathrm{c}}$ reflections by scans of a set of reflections of the asymmetric truncation rod, which are sensitive to polytype specific planes, as discussed in Sec. 2.2. Finally, the simultaneous acquiring of high resolution X-ray diffraction data of specific reflections and RHEED data (which essentially measures many reflections in reciprocal space simultaneously but with low resolution) would also provide significant benefits for data evaluation and should also be considered in future.

---

[17] We would like to mention, that in Ref. [101], a more precise evaluation of the SEM images of the same samples in comparison with Ref. [119] has been performed. Therefore, we advice the reader to consult Ref. [101] instead or in addition to Ref. [119].

5. Conclusion and outlook (Part I.)

In the first part of the manuscript, time-resolved *in-situ* measurements of a two-dimensional cut in reciprocal space close to the $(111)_{\mathrm{z\curvearrowright c}}$ Bragg reflection during the growth of polytypic nanowires have been analyzed. Since this cubic reflection almost coincides with the $(00.2)_{\mathrm{w\curvearrowright h2}}$ wurtzite reflections, where the small shift stems from a small difference in the interplanar spacing of the polytypes in $[111]_{\mathrm{z\curvearrowright c}}$ direction, scattering from the zinc blende and the wurtzite polytype is recorded in that region of reciprocal space. Extensive numerical simulations as well as additional measurements after growth have been performed for optimal interpretation of these time-resolved *in-situ* measurements.

Most notably, post-growth *ex-situ* measurements at the European Synchrotron Radiation Facility (ESRF) with a highly focussed beam (in order to achieve spatial resolution and to simultaneously illuminate a few nanostructures at maximum) revealed important information for the separation of the signal from the growing wires and parasitic growth in the time-resolved *in-situ* measurements. Moreover, indications of high fluctuations in distribution of the polytypes inside the nanowires have been found. Therefore, the averaging over many nanowires in the time-resolved *in-situ* measurements is desired for achieving high statistical significance of results on polytypism. Finally, we could extract the ratio of the interplanar spacing of the two polytypes in $[111]_{\mathrm{z\curvearrowright c}}$ direction from this data.

Nonetheless, some information is lost due to the averaging over a large number of nanowires, in particular if fluctuations are large. The measured time-resolved *in-situ* X-ray measurements can be explained well by a Markov model for the stacking sequence in the nanowires, which is consistent with (and based on) the few statistical segment length studies obtained by TEM of nanowires with very short polytype segments. However, deviations of this Markov model retaining its high fluctuations would not be visible in the q_z profile in the vicinity of the $(111)_{\mathrm{z\curvearrowright c}}$ reflection, but lead to systematic errors with respect to the Markov model at least in some range of parameters. This has been illustrated by investigations of the Gamma- and Weibull distribution (which contain the Markovian behavior as the special case) for the length distribution of the polytypic segments. Moreover, an enhancement of the 4H polytype with respect to the Markovian behavior would not be detected for some range of phase purities. In consequence, additional theoretical modelling to constrain the length distribution as well as additional experimental investigations thereof must be performed in future.

For example, the scaling bahavior of the nanowire signal by comparison of the $(111)_{\mathrm{z\curvearrowright c}}$, $(333)_{\mathrm{z\curvearrowright c}}$, and $(444)_{\mathrm{z\curvearrowright c}}$ reflections might be of importance for such investigations, where we shortly discussed the Markovian case for reference. This scaling might additionally prove highly valuable for separation of the contributions from parasitic growth and nanowire

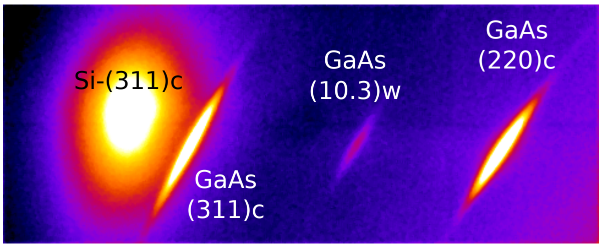

Figure 5.1.: Illustration of the output of a scan of the reflections $(220)_{\mathrm{z}\curvearrowright\mathrm{c}}$, $(10.3)_{\mathrm{w}\curvearrowright\mathrm{h2}}$, $(311)_{\mathrm{z}\curvearrowright\mathrm{c}}$ which is compatible with the current PMBE chamber (X-ray energy 15keV). The demonstration shown here for illustration of the resulting X-ray signal has been emulated *ex-situ* without the PMBE chamber. Incidence angle and detector position is fixed (Pilatus 100K at a distance of 50cm to the sample), no inclination of the chamber is needed. The scan is performed by rotations of the sample around its surface normal by approximately $\delta\varphi \approx 5^\circ$, which has been integrated for the illustration depicted in log-scale.

signal, and for extension of the range of applicability of monitoring symmetric reflections during growth of polytypic nanowires to wires with lower phase purities. However, the $(333)_{\mathrm{z}\curvearrowright\mathrm{c}}$ and $(444)_{\mathrm{z}\curvearrowright\mathrm{c}}$ reflections are not accessible with the current growth chamber at X-ray energies up to 15keV. The alternative is to combine measurements of the symmetric $(111)_{\mathrm{z}\curvearrowright\mathrm{c}}$ reflection with measurements of a series of asymmetric reflections, for example the sequence $(220)_{\mathrm{z}\curvearrowright\mathrm{c}}$, $(10.3)_{\mathrm{w}\curvearrowright\mathrm{h2}}$, $(311)_{\mathrm{z}\curvearrowright\mathrm{c}}$ which has been done based on the results presented in Sec. 2.2 (see Fig. 5.1). A clear advantage of such measurements (compared to the $(111)_{\mathrm{z}\curvearrowright\mathrm{c}}$ reflection) is the better separability of the zinc blende and wurtzite polytype, the separability of the zinc blende twins. However, a rotation of the sample around its normal is required for calibration and scanning of the sample and the scattered intensity is weaker, which both are disadvantageous for time-resolved measurements. Considering these disadvantages, it is very important to achieve a detailed understanding of the prospects and limitations of measurements of the $(111)_{\mathrm{z}\curvearrowright\mathrm{c}}$ reflection.

Therefore, the experimentally available time-resolved *in-situ* measurement of the vicinity of the $(111)_{\mathrm{z}\curvearrowright\mathrm{c}}$ reflection has been interpreted in the framework of the Markov model for the stacking sequence with transition probabilities with non-zero temporal derivative. Specifically, we derived the temporal evolution of the phase purities of both polytypes (and phase fractions) within this model.

The largest systematic uncertainties in the theoretical modelling underlying our results are possible deviations from the Markov model for the stacking in the wires and the absence of higher order contributions in the temporal evolution of the transition probabilities. Whereas the latter can (only) be improved by experimental data of higher quality, the first aspect requires additional research in future. The most important uncertainty in the processing of experimental data is the separation of the signal from parasitic growth and from the wires. Here, further research and improvements are needed for increased precision of results concerning nanowires.

Within the Markov model, approximations for the nucleation barrier differences for continuing growth with the current phase or with the complementary phase can be extracted, if the ratio of the degeneracies of states for nuclei for an additional layer of both cases are known. As a first (rough) estimate, these degeneracies have been assumed equal, but future modelling of the nanowire growth should not only aim for the length distribution of the polytypic segments, but also for the degeneracies of states for nuclei of the currently growing layer in order to reduce the systematic errors in the values for the nucleation barrier differences.

Part II.

Phase retrieval in coherent X-ray diffractive imaging

6. Introduction to coherent X-ray diffractive imaging (CXDI)

In the first part of the manuscript, the evaluation of scattering data from a large number of objects has been investigated. Each object was assumed to interfere coherently with itself, but the scattering from different objects adds up incoherently. Statistical fluctuations were relevant on the level of a single object as well as from one object to another. The combination of large statistical fluctuations in the objects with the partially coherent scattering led to non-unique profiles of the scattered intensity, as was demonstrated in Sec. 4.3.

Additionally, the influence of non-zero strain, which could be located at the interface of the two polytypes or close to the interface to the substrate, and the proper ratio of the interplanar spacings of Ga (or As) planes in growth direction are hard to study from such scattering – at least in some range of parameters. For example, the time-resolved experimental *in-situ* profiles could be fitted well for $d_{\mathrm{WZ}}/d_{\mathrm{ZB}} = 1 + 0.7\%$ as well as for $d_{\mathrm{WZ}}/d_{\mathrm{ZB}} = 1 + 0.5\%$ (see Fig. 4.33). Consequently, this information had to be taken from other measurements and was required as *a priori* knowledge for the interpretation of these profiles. Whereas the latter ratio $d_{\mathrm{WZ}}/d_{\mathrm{ZB}}$ could be estimated from our post-growth *ex-situ* measurements (see Sec. 3.2), an investigation of the strain distribution close to the interfaces is more challanging. The first question has been addressed by TEM and FEM in Ref. [150] for free-standing InAs/InP nanowires and their results give some indication that the assumption to neglect strain in the $[111]_{\mathrm{z}\frown\mathrm{c}}$ direction close to the interfaces of the polytypes is reasonable for the extracted mean segment lengths.

Although some information on the strain distribution inside the nanostructures can be obtained from such TEM investigations, it is important to understand under which conditions the displacement field and the strain distribution inside a nanostructure can be retrieved from the intensity distribution in the vicinity of a Bragg peak ("X-ray diffractive imaging"), because X-ray measurements are non-destructive and can typically be applied more easily *in-situ* and *in-operando* than TEM. Therefore, we now turn to the extraction of the strain distribution and the displacement field inside nanostructures from their scattered intensity in the second part of this manuscript. Since the strain distribution follows from the displacement field by derivation, we mainly speak of the extraction of the displacement field only.

In contrast to the first part of this manuscript, we assume that the scattering volume and the coherence volume coincide ("perfect coherence") and the impinging beam is well

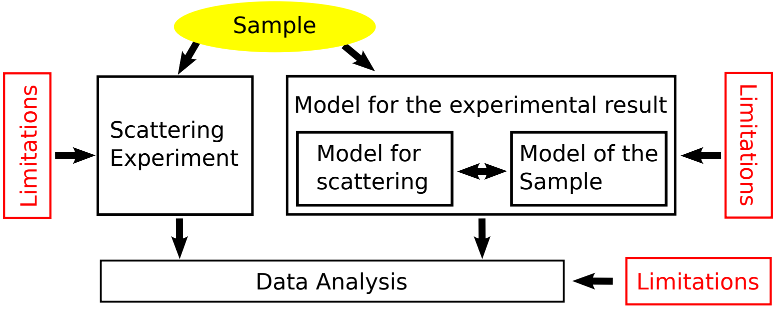

Figure 6.1.: Illustration of the interplay of data analysis, the experimental result of the scattering experiment and the modeling thereof.

approximated by a plane wave inside the scattering volume ("*coherent* X-ray diffractive imaging", abbreviated as "CXDI"). The formalism is not restricted to a particular Bragg reflection $\boldsymbol{Q}_{\mathrm{B}}$. For numerical investigations, we have chosen the Bragg reflection $(004)_{\mathrm{z}\curvearrowright\mathrm{c}}$ which is linked to the third component of the displacement field.

Sections 6.2 and 7.1 to 7.3 are mainly based on the author's work already published in Refs. [1, 2]. Moreover, Secs. 7.4 and 8.1 contain material which has been published in Ref. [2]. Nonetheless, in particular Sec. 7.4 contains a more detailed and more sophisticated discussion of the derivation of the final algorithm in comparison to the presentation in Ref. [2].

For the successful extraction of the displacement field in a sample three aspects must be considered, as illustrated in Fig. 6.1. On the one hand, an appropriate scattering experiment must be performed. On the other hand, an adequate model for the thus obtained experimental data is required. Here, we need to model the relevant properties of the sample as well as the interaction with the impinging X-rays ("scattering"). Finally, this model is employed for analyzing the experimental data ("data analysis").

The focus of this (part of the) manuscript is to improve data analysis in the framework of the current model for CXDI, as introduced and derived in Sec. 6.1.

It is very important to realize that each of the three "aspects" (actual experiment, model of the experiment and data analysis) typically have their own limitations — some independent of the other topic, some dependent. For example, the equations for modelling an experiment may be so complicated (e.g., coupled non-linear partial differential equations) that finding their solutions is barely or not possible. In such a case, either the model has to be simplified which typically implies stronger limitations on the physical system that can be studied. Or, alternatively, data analysis must be improved until the solution can be found in the model in a reliable and robust manner. In the framework of CXDI, the model derived in Sec. 6.1 seems the least complicated physical model worth studying (plane wave illumination, first order Born approximation, far field, . . .) without employing linear elasticity theory as part of the model. Yet data analysis within this model is already rather challenging and fails in many cases even for "ideal data". We are convinced that before proceeding to data analysis within more sophisticated models, it is important to understand and improve data analysis in the simple model given in Sec. 6.1 — as done in this manuscript.

Is is also important to keep in mind that the capabilities of finding the solution within this model strongly depend on the *a priori* knowledge on the sample *and* the particular numerical algorithm that is employed for finding the solution based on the available *a priori* knowledge. As a consequence, data evaluation can (and will) be improved by modification of the numerical algorithm only (without changing the underlying *a priori* knowledge) as well as by modification of the exploited *a priori* knowledge (which also entails modifications of the numerical algorithm).

Throughout this manuscript we assume that the geometry of the nanoobjects under consideration is known and focus on the reconstruction of the displacement field in the interior of this geometry. Nevertheless, we point out that other algorithms aim at simultaneous reconstruction of this geometrical information (see e.g. Refs. [151, 152]). However, such approaches are typically limited to weakly strained objects.

In Sec. 7.3, we demonstrate that the introduction of randomization in data analysis — incorporated in the widely used HIO+ER-algorithm (see Sec. 6.2.3) — improves the reconstruction capabilities without changing the underlying *a priori* knowledge. Numerically, suitable randomization can be incorporated efficiently by overrelaxation of the non-convex and non-linear projection operator in reciprocal space in the HIO+ER-algorithm.

In Sec. 7.4, we then investigate the influence of additional *a priori* knowledge on the sample beyond its shape in direct space and the intensity distribution near a Bragg peak in reciprocal space. Focus of our investigation are direct space constraints on the local scattering magnitude.

The extraction of the displacement field is typically a two-step process: In the first step, a (complex valued) effective electron density is reconstructed. Its phase field is linked to the displacement field, but its determination requires unwrapping of the phase field of the effective electron density. Vortex artifacts in the phase field would imply non-unique phase unwrapping which must be considered non-physical. Therefore, such vortex defects in the phase field must be detected and eliminated. We will discuss their elimination from the reconstructed phase field in Sec. 7.5.

Up to that point, our discussion is based on “ideal” input data within the CXDI model. Neither limitations of the experimental measurements nor the limitations of the model for the scattering experiment (see Fig. 6.1) have been included up to this point. However, these limitations typically lead to inconsistencies during data evaluation. Their influence must be studied and in many cases adequate counter-measures must be incorporated during data evaluation in order to “heal” these inconsistencies. This is the topic of chapter 8.

Specifically, we demonstrate that that a small damping combined with an upper bound (“cut-off”) is beneficial for treating data points of very low intensity (below the given cut-off) in reciprocal space during the iterative reconstruction (see Sec. 8.1). The presence of Poisson photon noise in the experimentally measured intensity distribution – investigated in Sec. 8.2 – induces instabilities of the reconstruction procedure without modifications. If we include small gaps around the constraints in reciprocal space (which are the constraints that are distorted by the Poisson noise) above the before mentioned cut-off, these instabilities are significantly reduced. If the same gaps are applied below the cut-off, the quality of the output of the reconstruction process suffers. Instead, the small damping in addition to the upper bound is preferential below the cut-off.

Whereas these two limitations are more of an experimental nature (limited signal-to-noise ratio and limited incoming X-ray flux), the third limitation which we investigate is related to the model of the nanostructure during reconstruction: Typically, its geometry is truncated artificially in the computational model – in strong contrast to most experimental samples. This artificial truncation causes strong inconsistencies along the crystal truncation rod of the substrate (including its Bragg peak) . Extensions which provide good reconstruction capabilities despite these inconsistencies are finally discussed in Sec. 8.3.

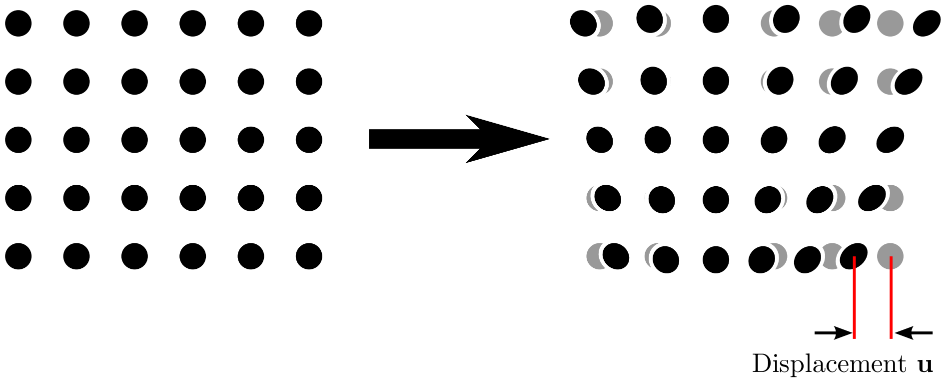

Figure 6.2.: Illustration of the displacement field $\boldsymbol{u}(\boldsymbol{R})$ in a two-dimensional crystal. Each atom located at a Bravais position $\boldsymbol{R}$ is shifted by a displacement $\boldsymbol{u}(\boldsymbol{R})$ from its ideal position.

6.1. Derivation of the model for X-ray scattering in CXDI

In this section, we derive the physical model which constitutes the set of equations which needs to be solved in CXDI. The derivation is based on kinematic approximation and the far-field limit [142]. Absorption is neglected. We do not consider the effect of multiple scattering, since its contribution is negligible as long as the extension of the sample domain under investigation is much smaller as the mean free path of the propagating radiation. Contrarily to "typical" *photonic* crystals for which this length length can decrease even to a single (photonic) unit cell at optical frequencies [153–165], nanocrystalline samples which contain a huge number of (atomic) unit cells can be studied with hard X-ray radiation within this approximation.

Consider an ideal crystal with Bravais lattice $\mathbb{B}$. Its lattice points are referred to as $\boldsymbol{R}$. The basis of each lattice point $\boldsymbol{R}$ is defined as $\varrho_{\mathrm{C}}^{(I)}(\boldsymbol{r})$.

Each lattice point $\boldsymbol{R}$ is now displaced by a displacement $\boldsymbol{u}(\boldsymbol{R})$ (see Fig. 6.2) in a continuous and invertible manner ("elastic deformation"). Such a deformation is accompanied by a modification of the basis at each point and in general breaks the discrete translational symmetry: The basis $\varrho_{\mathrm{C}}^{(I)}(\boldsymbol{r})$ has to be modified to the $\boldsymbol{R}$-dependent quantity $\varrho_{\mathrm{C}}^{(D)}(\boldsymbol{r},\boldsymbol{R})$ which describes the elastically strained unit cell. The full electron density after the elastic deformation can be written as

$$\varrho_{\mathrm{el}}(\boldsymbol{r}) = \sum_{\boldsymbol{R}} \varrho_{\mathrm{C}}^{(D)}(\boldsymbol{r} - (\boldsymbol{R} + \boldsymbol{u}(\boldsymbol{R})), \boldsymbol{R}) \ . \tag{6.1}$$

The term $\boldsymbol{R} + \boldsymbol{u}(\boldsymbol{R})$ shifts each elastically strained cell to its proper position.

If the crystal structure is not infinite, it is useful to introduce the shape function Ω which is equal to one for all points $\boldsymbol{R}$ inside the crystal and zero elsewhere. Then, the electron density reads

$$\varrho_{\mathrm{el}}(\boldsymbol{r}) = \sum_{\boldsymbol{R}} \Omega(\boldsymbol{R})\, \varrho_{\mathrm{C}}^{(D)}(\boldsymbol{r} - (\boldsymbol{R} + \boldsymbol{u}(\boldsymbol{R})), \boldsymbol{R}) \ . \tag{6.2}$$

Fourier transformation of this expression results in

$$\boldsymbol{E}(\boldsymbol{q} = \boldsymbol{Q}_{\mathrm{B}} + \boldsymbol{Q}) = \sum_{\boldsymbol{R}} \Omega(\boldsymbol{R})\, \mathit{\Phi}_{\mathrm{C}}^{(D)}(\boldsymbol{q},\boldsymbol{R})\ \mathrm{e}^{\mathrm{i}(\boldsymbol{Q}_{\mathrm{B}}+\boldsymbol{Q})\cdot\boldsymbol{u}(\boldsymbol{R})}\ \mathrm{e}^{\mathrm{i}\boldsymbol{Q}\cdot\boldsymbol{R}} \ , \tag{6.3}$$

where $\mathit{\Phi}_{\mathrm{C}}^{(D)}(\boldsymbol{q},\boldsymbol{R}) = \mathbf{FT}_{\boldsymbol{q}\leftrightarrow\boldsymbol{r}}\left\{\varrho_{\mathrm{C}}^{(D)}(\,\cdot\,,\boldsymbol{R})\right\}$ and the vector $\boldsymbol{q}$ in reciprocal space has been split as $\boldsymbol{q} = \boldsymbol{Q}_{\mathrm{B}} + \boldsymbol{Q}$ where $\boldsymbol{Q}_{\mathrm{B}}$ is a Bragg point of the Bravais lattice $\mathbb{B}$.

Moreover, the Fourier shift theorem was applied for the shift $\boldsymbol{r} \longrightarrow \boldsymbol{r} + \boldsymbol{R} + \boldsymbol{u}(\boldsymbol{R})$. This shift is the origin of the phase term $\mathrm{e}^{\mathrm{i}(\boldsymbol{Q}_\mathrm{B}+\boldsymbol{Q})\cdot\boldsymbol{u}(\boldsymbol{R})}$. By definition, $\boldsymbol{Q}_\mathrm{B} \cdot \boldsymbol{R}$ is an integer multiple of 2π. Hence, it has been dropped in the last exponential.

Next, we investigate the expression $\varPhi_\mathrm{C}^{(D)}(\boldsymbol{q}, \boldsymbol{R})$ more closely: The electron density of a single, elastically strained cell with N_ApC atoms can be written as

$$\varrho_\mathrm{C}^{(D)}(\boldsymbol{r}, \boldsymbol{R}) = \sum_{i=1}^{N_\mathrm{ApC}} \varrho_i^{(\mathrm{A})} \left(\boldsymbol{r} - (\boldsymbol{R}_i + \boldsymbol{u}(\boldsymbol{R} + \boldsymbol{R}_i) - \boldsymbol{u}(\boldsymbol{R})), \boldsymbol{R}\right) \ . \tag{6.4}$$

In this equation, $\boldsymbol{R}_i$ is the equilibrium position of an atom in the original Bravais lattice $\mathbb{B}$.[1] $\boldsymbol{u}(\boldsymbol{R}+\boldsymbol{R}_i) - \boldsymbol{u}(\boldsymbol{R})$ is the displacement of an atom inside the strained cell with respect to its displaced Bravais point $\boldsymbol{R} + \boldsymbol{u}(\boldsymbol{R})$. Here, we allow atoms from the original (translationally invariant and non-strained) crystal to be locally substituted by atoms of different kind. Therefore, $\varrho^{(\mathrm{A})}$ must be considered as $\boldsymbol{R}$-dependent. Its Fourier transform is

$$\varPhi_\mathrm{C}^{(D)}(\boldsymbol{q}, \boldsymbol{R}) = \sum_{i=1}^{N_\mathrm{ApC}} f_i(\boldsymbol{q}, \boldsymbol{R})\, \mathrm{e}^{\mathrm{i}\boldsymbol{q}\cdot(\boldsymbol{R}_i + \boldsymbol{u}(\boldsymbol{R}+\boldsymbol{R}_i) - \boldsymbol{u}(\boldsymbol{R}))} \ , \tag{6.5}$$

where the Fourier shift theorem has been applied again (shift: $\boldsymbol{r} \longrightarrow \boldsymbol{r} + \boldsymbol{R}_i + \boldsymbol{u}(\boldsymbol{R}+\boldsymbol{R}_i) - \boldsymbol{u}(\boldsymbol{R})$) and $f_i(\boldsymbol{q}, \boldsymbol{R}) = \mathbf{FT}_{\boldsymbol{q}\leftrightarrow\boldsymbol{r}} \left\{ \varrho_i^{(\mathrm{A})}(\,\cdot\,, \boldsymbol{R}) \right\}$ is the atomic form factor of atom i in cell $\boldsymbol{R}$.

Next, we approximate the displacement field $\boldsymbol{u}$ in each cell $\boldsymbol{R}$ by a linear map, i.e.,

$$\boldsymbol{u}(\boldsymbol{R} + \boldsymbol{R}_i) \approx \boldsymbol{u}(\boldsymbol{R}) + \underline{\tau}(\boldsymbol{R})\boldsymbol{R}_i \ \Rightarrow \ \boldsymbol{u}(\boldsymbol{R} + \boldsymbol{R}_i) - \boldsymbol{u}(\boldsymbol{R}) = \underline{\tau}(\boldsymbol{R})\boldsymbol{R}_i \ . \tag{6.6}$$

The quantity $\underline{\tau}$ is referred to as displacement gradient tensor. For continuous displacement fields, this tensor is defined as

$$\underline{\tau} = \begin{pmatrix} \left(\frac{\partial \mathrm{u}_1}{\partial x}\right) & \left(\frac{\partial \mathrm{u}_1}{\partial y}\right) & \left(\frac{\partial \mathrm{u}_1}{\partial z}\right) \\ \left(\frac{\partial \mathrm{u}_2}{\partial x}\right) & \left(\frac{\partial \mathrm{u}_2}{\partial y}\right) & \left(\frac{\partial \mathrm{u}_2}{\partial z}\right) \\ \left(\frac{\partial \mathrm{u}_3}{\partial x}\right) & \left(\frac{\partial \mathrm{u}_3}{\partial y}\right) & \left(\frac{\partial \mathrm{u}_3}{\partial z}\right) \end{pmatrix} \ . \tag{6.7}$$

In our case, the displacement field is defined on a discrete grid only. Hence, the components of the linear approximation (6.6) needs to be calculated by means of a non-linear least square procedure, finite difference schemes or a singular value decomposition [166]. Note that components of the displacement gradient tensor are dimensionless.

With the linearization (6.6), we have

$$\begin{aligned} \varPhi_\mathrm{C}^{(D)}(\boldsymbol{q} = \boldsymbol{Q}_\mathrm{B} + \boldsymbol{Q}, \boldsymbol{R}) &= \sum_{i=1}^{N_\mathrm{ApC}} f_i(\boldsymbol{q}, \boldsymbol{R})\, \mathrm{e}^{\mathrm{i}(\boldsymbol{Q}_\mathrm{B}+\boldsymbol{Q})\cdot(1+\underline{\tau}(\boldsymbol{R}))\boldsymbol{R}_i} && \text{(6.8a)} \\ &= \sum_{i=1}^{N_\mathrm{ApC}} \mathrm{e}^{\mathrm{i}\boldsymbol{Q}_\mathrm{B}\cdot\boldsymbol{R}_i} f_i(\boldsymbol{q}, \boldsymbol{R})\, \mathrm{e}^{\mathrm{i}\boldsymbol{Q}_\mathrm{B}\cdot\underline{\tau}(\boldsymbol{R})\boldsymbol{R}_i}\, \mathrm{e}^{\mathrm{i}\boldsymbol{Q}\cdot\boldsymbol{R}_i}\, \mathrm{e}^{\mathrm{i}\boldsymbol{Q}\cdot\underline{\tau}(\boldsymbol{R})\boldsymbol{R}_i} \ . && \text{(6.8b)} \end{aligned}$$

The first phase term $\mathrm{e}^{\mathrm{i}\boldsymbol{Q}_\mathrm{B}\cdot\boldsymbol{R}_i}$ corresponds to the ideal, non-strained crystal. The other terms vanish at Bragg peaks $\boldsymbol{Q} = \boldsymbol{0}$ or without displacement gradient (i.e., $\underline{\tau} = 0$).

The Takagi-approximation [142, 167] refers to the approximation that the unit cell of the crystal is shifted, but its local deformation is not taken into account for the calculation

---

[1] To be specific, we refer to the position of an atom as its center of mass of the electronic charge distribution.

of the scattering signal. Based on Eq. (6.8b), we can estimate the limitations of this and other approximation.

For these estimations, it is useful to rewrite

$$\boldsymbol{Q}_{\mathrm{B}} = \sum_{i=1}^{d} \eta_i \frac{2\pi}{\mathrm{a}_i} \hat{\boldsymbol{b}}_i \ , \ \eta_i \in \mathbb{Z} \ , \tag{6.9a}$$

$$\boldsymbol{Q} = \sum_{i=1}^{d} \zeta_i \frac{2\pi}{\mathrm{a}_i} \hat{\boldsymbol{b}}_i \ , \ \zeta_i \in \mathbb{R} \ , \tag{6.9b}$$

$$\boldsymbol{R} = \sum_{i=1}^{d} \alpha_i \mathrm{a}_i \hat{\boldsymbol{a}}_i \ , \ \alpha_i \in \mathbb{Z} \ , \tag{6.9c}$$

$$\boldsymbol{R}_i = \sum_{i=1}^{d} \beta_i \mathrm{a}_i \hat{\boldsymbol{a}}_i \ , \ -0.5 \le \beta_i < 0.5 \ , \tag{6.9d}$$

$$\boldsymbol{u}(\boldsymbol{R}) = \sum_{i=1}^{d} \gamma_i(\boldsymbol{R}) \mathrm{a}_i \hat{\boldsymbol{a}}_i \ , \ \gamma_i \in \mathbb{R} \ , \tag{6.9e}$$

where $\hat{\boldsymbol{a}}_i$ are *normalized* crystallographic basis vectors in direct space with lattice constants $\{\mathrm{a}_i\}$ and $\hat{\boldsymbol{b}}_i$ the corresponding *normalized* basis vectors of the reciprocal lattice. Therefore, $\hat{\boldsymbol{a}}_i \cdot \hat{\boldsymbol{b}}_j = \delta_{ij}$ holds by definition.

First, we focus on the contribution of $\mathrm{e}^{\mathrm{i}\boldsymbol{Q}\cdot\boldsymbol{R}_i}$ which can be neglected if $|\boldsymbol{Q}\cdot\boldsymbol{R}_i| \ll 1$. This is guaranteed if the 1-norm of the coefficient vector $\boldsymbol{\zeta}$ in Eq. (6.9b) fulfills

$$\|\boldsymbol{\zeta}\|_1 \ll \frac{1}{\pi} \tag{6.10}$$

because

$$|\boldsymbol{Q}\cdot\boldsymbol{R}_i| = \left| \sum_{m=1}^{d}\sum_{n=1}^{d} \zeta_m \frac{2\pi}{\mathrm{a}_m} \beta_n \mathrm{a}_n \, \hat{\boldsymbol{b}}_m \hat{\boldsymbol{a}}_n \right| = 2\pi \left| \sum_{m=1}^{d} \zeta_m \beta_m \right| \tag{6.11a}$$

$$\le 2\pi \sum_{m=1}^{d} |\zeta_m \beta_m| \overset{|\beta_m|\le 0.5}{\le} \pi \sum_{m=1}^{d} |\zeta_m| = \pi \, \|\boldsymbol{\zeta}\|_1 \tag{6.11b}$$

This implies that only a small region – determined by the condition (6.10) – can be exploited for CXDI if the contribution $\mathrm{e}^{\mathrm{i}\boldsymbol{Q}\cdot\boldsymbol{R}_i}$ is neglected.

This bound has strong implications for the lattice contrast

$$\mathrm{c}_i^{(+)} = \frac{\mathrm{a}_{i,\mathrm{Max}} - \mathrm{a}_{i,\mathrm{Ref}}}{\mathrm{a}_{i,\mathrm{Ref}}} \ , \qquad \mathrm{c}_i^{(-)} = \frac{\mathrm{a}_{i,\mathrm{Min}} - \mathrm{a}_{i,\mathrm{Ref}}}{\mathrm{a}_{i,\mathrm{Ref}}} \tag{6.12}$$

in the sample which can be investigated in the framework of the derived model. For simplicity, we choose the reference lattice constants $\mathrm{a}_{i,\mathrm{Ref}} = (\mathrm{a}_{i,\mathrm{Max}} + \mathrm{a}_{i,\mathrm{Min}})/2$ which simplifies the lattice contrast to

$$\mathrm{c}_i \equiv \mathrm{c}_i^{(+)} = \frac{\mathrm{a}_{i,\mathrm{Max}} - \mathrm{a}_{i,\mathrm{Min}}}{\mathrm{a}_{i,\mathrm{Max}} + \mathrm{a}_{i,\mathrm{Min}}} = -\,\mathrm{c}_i^{(-)} > 0 \ . \tag{6.13}$$

The difference in reciprocal space (in direction i) of the Bragg peaks with lattice constant $\mathrm{a}_{i,\mathrm{Ref}}$ and $\mathrm{a}_{i,\mathrm{c}} = (1+\mathrm{c}_i)\mathrm{a}_{i,\mathrm{Ref}}$ is

$$Q_i = 2\pi h_i \left(\frac{1}{\mathrm{a}_{i,\mathrm{Ref}}} - \frac{1}{(1+\mathrm{c}_i)\mathrm{a}_{i,\mathrm{Ref}}} \right) = h_i \left(\frac{2\pi}{\mathrm{a}_{i,\mathrm{Ref}}} \right) \left(\frac{\mathrm{c}_i}{1+\mathrm{c}_i} \right) \ , \tag{6.14}$$

where h_i is the Miller Bravais index [103, 104] of the respective Bragg reflection in direction i. Comparison with Eq. (6.9b) reveals that the components ζ_i are equal to

$$\zeta_i = h_i \left(\frac{\mathrm{c}_i}{1+\mathrm{c}_i} \right) . \tag{6.15}$$

Thus, the constraint (6.10) constraints the lattice contrast by

$$\sum_{i=1}^{d} |h_i| \left(\frac{\mathrm{c}_i}{1+\mathrm{c}_i} \right) \ll \frac{1}{2\pi} , \tag{6.16}$$

which reduces to

$$\mathrm{c}_3 \ll \tilde{c} \equiv \frac{1}{4\pi - 1} \approx 8.6\% , \tag{6.17}$$

for the $(004)_{\mathrm{z}\curvearrowright\mathrm{c}}$ Bragg reflection. Note, that the lattice contrast should be *much* smaller than the bounds derived from (6.16) because interference effects and shape effects spread the signal to a larger domain in reciprocal space than estimated by Eq. (6.14). A better approximation is to add a fraction $\zeta_i^{(0)}$ to the coefficients (6.15): this fraction $\zeta_i^{(0)}$ estimates the broadening of the signal in per cent of the distance to the neighboring Bragg peaks.

However, as long as no estimate for $\zeta_i^{(0)}$ is available, this constraint can only be evaluated as a function of $\zeta_i^{(0)}$. Hence, we are constrained by

$$\sum_{i=1}^{d} \left[|h_i| \left(\frac{\mathrm{c}_i}{1+\mathrm{c}_i} \right) + \zeta_i^{(0)} \right] \ll \frac{1}{\pi} , \tag{6.18}$$

or

$$\mathrm{c}_3 \ll \frac{1-\pi\zeta_3^{(0)}}{\pi\left(4+\zeta_3^{(0)}\right)-1} \overset{0\leq\zeta_3^{(0)}\ll 1}{\approx} \frac{1-\pi\zeta_3^{(0)}}{4\pi-1} \tag{6.19a}$$

$$= \tilde{c} - \left(\frac{\pi}{4\pi-1} \right) \zeta_3^{(0)} \approx 8.6\% - 0.27 \cdot \zeta_3^{(0)} \tag{6.19b}$$

in the special case of the $(004)_{\mathrm{z}\curvearrowright\mathrm{c}}$ Bragg reflection. For the example of $\zeta_3^{(0)} \approx 5\%$, the lattice contrast is thus limited to $\mathrm{c}_3 \ll 7.2\%$.

Next, we consider $\mathrm{e}^{\mathrm{i}\boldsymbol{Q}\cdot\underline{\tau}(\boldsymbol{R})\boldsymbol{R}_i}$ in Eq. (6.8b): As long as the magnitude of the largest eigenvalue is smaller than one,

$$\boldsymbol{Q} \cdot \underline{\tau}(\boldsymbol{R})\boldsymbol{R}_i \overset{\max_{m=1,\dots,d}(\tau_m)\leq 1}{\leq} |\boldsymbol{Q} \cdot \boldsymbol{R}_i| \tag{6.20}$$

and the respective contribution $\mathrm{e}^{\mathrm{i}\boldsymbol{Q}\cdot\underline{\tau}(\boldsymbol{R})\boldsymbol{R}_i}$ can be neglected. For small strain up to a few per cent, the eigenvalues of the displacement gradient tensor are also in the order of a few per cent. Hence, the restriction on the eigenvalues of $\underline{\tau}(\boldsymbol{R})$ has no implications for the application to real word samples.

Finally, we have to consider the dependence of the atomic form factors $f_i(\boldsymbol{q}, \boldsymbol{R})$ on the scattering vector $\boldsymbol{Q}$: The definition

$$f_i(\boldsymbol{q}, \boldsymbol{R}) = \int_{\mathbb{R}^d} \mathrm{e}^{\mathrm{i}\boldsymbol{q}\cdot\boldsymbol{x}} \varrho_i^{(\mathrm{A})}(\boldsymbol{x}, \boldsymbol{R}) \, \mathrm{d}^d x , \tag{6.21}$$

can be rewritten as

$$f_i(\boldsymbol{q}, \boldsymbol{R}) = \int_{\mathbb{R}^d} \mathrm{e}^{\mathrm{i}\boldsymbol{Q}\cdot\boldsymbol{x}} \, \mathrm{e}^{\mathrm{i}\boldsymbol{Q}_\mathrm{B}\cdot\boldsymbol{x}} \varrho_i^{(\mathrm{A})}(\boldsymbol{x}, \boldsymbol{R}) \, \mathrm{d}^d x , \tag{6.22}$$

where $\boldsymbol{q}$ has been replaced by $\boldsymbol{Q}_\mathrm{B}+\boldsymbol{Q}$. To a good approximation, the electron density of the atom vanishes at distances larger than the lattice constants a_m. Hence, the domain of integration can be reduced from $\mathbb{R}^d$ to $\otimes_{i=1}^{d}[-\mathrm{a}_i,\mathrm{a}_i]$. Thus, each component x_i in $\boldsymbol{Q}\cdot\boldsymbol{x}$ is bound by $[-\mathrm{a}_i,\mathrm{a}_i]$. Therefore, the contribution $\mathrm{e}^{\mathrm{i}\boldsymbol{Q}\cdot\boldsymbol{x}}$ in the atomic form factors can be neglected under the conditions as the expression $\mathrm{e}^{\mathrm{i}\boldsymbol{Q}\cdot\boldsymbol{R}_i}$ in Eq. (6.8b), i.e., the restriction in Eq. (6.10). As a result, it is valid to approximate

$$f_i(\boldsymbol{q},\boldsymbol{R}) \overset{(6.10)}{\approx} f_i(\boldsymbol{Q}_\mathrm{B},\boldsymbol{R}) \ . \tag{6.23}$$

If we combine our recent approximations, we simplified Eq. (6.8b) to

$$\varPhi_\mathrm{C}^{(D)}(\boldsymbol{q}=\boldsymbol{Q}_\mathrm{B}+\boldsymbol{Q},\boldsymbol{R}) \equiv \varPhi_\mathrm{C}^{(D)}(\boldsymbol{Q}_\mathrm{B},\boldsymbol{R}) \overset{(6.10)}{=} \sum_{i=1}^{N_\mathrm{ApC}} \mathrm{e}^{\mathrm{i}\boldsymbol{Q}_\mathrm{B}\cdot\boldsymbol{R}_i} f_i(\boldsymbol{Q}_\mathrm{B},\boldsymbol{R})\,\mathrm{e}^{\mathrm{i}\boldsymbol{Q}_\mathrm{B}\cdot\underline{\tau}(\boldsymbol{R})\boldsymbol{R}_i} \ , \tag{6.24}$$

i.e., a function dependent only on $\boldsymbol{Q}_\mathrm{B}$ and $\boldsymbol{R}$, but no longer dependent on $\boldsymbol{Q}$. Therefore, Eq. 6.3 reads

$$\begin{aligned}\boldsymbol{E}(\boldsymbol{q}=\boldsymbol{Q}_\mathrm{B}+\boldsymbol{Q}) \overset{(6.10)}{=} &\sum_{\boldsymbol{R}}\Omega(\boldsymbol{R})\\ &\varPhi_\mathrm{C}^{(D)}\big(\boldsymbol{Q}_\mathrm{B},\boldsymbol{R},\{f_i(\boldsymbol{Q}_\mathrm{B},\boldsymbol{R})\},\{\underline{\tau}(\boldsymbol{R})\}\big)\,\mathrm{e}^{\mathrm{i}\boldsymbol{Q}_\mathrm{B}\cdot\boldsymbol{u}(\boldsymbol{R})}\,\mathrm{e}^{\mathrm{i}\boldsymbol{Q}\cdot\boldsymbol{u}(\boldsymbol{R})}\,\mathrm{e}^{\mathrm{i}\boldsymbol{Q}\cdot\boldsymbol{R}} \ ,\end{aligned} \tag{6.25}$$

where the dependencies of $\varPhi_\mathrm{C}^{(D)}(\boldsymbol{Q}_\mathrm{B},\boldsymbol{R})$ on the atomic form factors $\{f_i(\boldsymbol{Q}_\mathrm{B},\boldsymbol{R})\}$ and $\{\underline{\tau}(\boldsymbol{R})\}$ have been stated explicitly.

Still, the displacement $\boldsymbol{u}(\boldsymbol{R})$ is coupled to the Fourier variable $\boldsymbol{Q}$ in the term $\mathrm{e}^{\mathrm{i}\boldsymbol{Q}\cdot\boldsymbol{u}(\boldsymbol{R})}$. For

$$|\boldsymbol{Q}\cdot\boldsymbol{u}(\boldsymbol{R})| \ll 1 \ , \tag{6.26}$$

it can be neglected, too. If we exploit the dimensionless coefficients defined in Eq. (6.9), this is equivalent to the constraint

$$|\boldsymbol{Q}\cdot\boldsymbol{u}(\boldsymbol{R})| = \left|\sum_{m=1}^{d}\sum_{n=1}^{d}\zeta_m\frac{2\pi}{\mathrm{a}_m}\gamma_n(\boldsymbol{R})\mathrm{a}_n\hat{\boldsymbol{a}}_n\hat{\boldsymbol{b}}_m\right| = 2\pi\left|\sum_{m=1}^{d}\zeta_m\gamma_m(\boldsymbol{R})\right| \tag{6.27a}$$

$$= 2\pi\,|\boldsymbol{\zeta}\cdot\boldsymbol{\gamma}| \leq 2\pi\,\|\boldsymbol{\zeta}\|_\mathrm{p}\,\|\boldsymbol{\gamma}\|_{\frac{\mathrm{p}}{\mathrm{p}-1}} \ , \tag{6.27b}$$

where in the last step the Hölder inequality [168] – valid for $1\leq p\leq\infty$, $p\in\mathrm{R}$ – has been used. Whereas for $p=2$ the Hölder inequality simplifies to the Cauchy Schwarz inequality [169], for our discussion the case $p=1$ is more suited because the constraint (6.10) refers to $\|\boldsymbol{\zeta}\|_1$. Hence, the previous equation reads

$$|\boldsymbol{Q}\cdot\boldsymbol{u}(\boldsymbol{R})| \leq 2\pi\,\|\boldsymbol{\zeta}\|_1\,\|\boldsymbol{\gamma}\|_\infty \ . \tag{6.28}$$

Therefore the constraint (6.26) is satisfied if

$$\|\boldsymbol{\gamma}\|_\infty \ll \frac{1}{2\pi\,\|\boldsymbol{\zeta}\|_1} \ . \tag{6.29}$$

Since $\boldsymbol{\zeta}$ is constrained by Eq. (6.10), Eq. (6.26) is fulfilled as long as

$$\|\boldsymbol{\gamma}\|_\infty \lesssim 1 \ . \tag{6.30}$$

Therefore, the maximum displacement (in any direction) in the nanostructure under investigation is restricted by the unit cell's lattice constants a_i in the respective direction $\hat{\boldsymbol{a}}_i$.

However, we note that the maximum displacement which may be present in the nanostructure increases with decreasing domain in reciprocal space which is exploited for the reconstruction of the displacement field. For example, if $\|\zeta\|_1$ could be restricted to values as small as one per mill, Eq. (6.29) is well-satisfied even for $\|\gamma\|_\infty \approx 10$. However, for current applications of the resulting model the constraint (6.30) should be considered.

If we define the effective electron density

$$\begin{aligned}\varrho_{\mathrm{eff}}\big(\boldsymbol{Q}_{\mathrm{B}}, \boldsymbol{R}, \{f_i(\boldsymbol{Q}_{\mathrm{B}}, \boldsymbol{R})\}, \{\boldsymbol{u}(\boldsymbol{R})\}, \{\underline{\tau}(\boldsymbol{R})\}\big) &= \\ \varPhi_{\mathrm{C}}^{(D)}\big(\boldsymbol{Q}_{\mathrm{B}}, \boldsymbol{R}, \{f_i(\boldsymbol{Q}_{\mathrm{B}}, \boldsymbol{R})\}, \{\underline{\tau}(\boldsymbol{R})\}\big)\, \mathrm{e}^{\mathrm{i}\boldsymbol{Q}_{\mathrm{B}}\cdot\boldsymbol{u}(\boldsymbol{R})} &\in \mathbb{C} \qquad (6.31)\end{aligned}$$

which is *in*dependent on the distance $\boldsymbol{Q}$ from the Bragg peak $\boldsymbol{Q}_{\mathrm{B}}$, and impose the conditions given in Eq. (6.29), Eq. (6.25) simplifies to

$$\boldsymbol{E}(\boldsymbol{Q}_{\mathrm{B}}, \boldsymbol{Q}) = \sum_{\boldsymbol{R}} \Omega(\boldsymbol{R})\, \varrho_{\mathrm{eff}}\big(\boldsymbol{Q}_{\mathrm{B}}, \boldsymbol{R}, \{f_i(\boldsymbol{Q}_{\mathrm{B}}, \boldsymbol{R})\}, \{\boldsymbol{u}(\boldsymbol{R})\}, \{\underline{\tau}(\boldsymbol{R})\}\big)\, \mathrm{e}^{\mathrm{i}\boldsymbol{Q}\cdot\boldsymbol{R}} \ . \qquad (6.32)$$

Although in this formula only the last term $\mathrm{e}^{\mathrm{i}\boldsymbol{Q}\cdot\boldsymbol{R}}$ depends on $\boldsymbol{Q}$, it is important to understand and investigate under which condition(s) the effective electron density does not depend on the displacement gradient $\underline{\tau}(\boldsymbol{R})$ to a very good approximation. The displacement gradient tensor only contributes by $\mathrm{e}^{\mathrm{i}\boldsymbol{Q}_{\mathrm{B}}\cdot\underline{\tau}(\boldsymbol{R})\boldsymbol{R}_i}$ in Eq. (6.24). Hence, the requirement is

$$\tau_M \ll \frac{1}{2\pi\,\|\eta\|_1} \ . \qquad (6.33)$$

This way, it is guaranteed that

$$|\boldsymbol{Q}_{\mathrm{B}} \cdot \underline{\tau}(\boldsymbol{R})\boldsymbol{R}_i| \ll 1 \qquad (6.34)$$

because

$$\begin{aligned}
|\boldsymbol{Q}_{\mathrm{B}} \cdot \underline{\tau}(\boldsymbol{R})\boldsymbol{R}_i| &\overset{(6.9)}{=} 2\pi \left| \sum_{m=1}^{d} \sum_{n=1}^{d} \eta_m \beta_n \frac{\mathrm{a}_n}{\mathrm{a}_m}\, \hat{\boldsymbol{b}}_m \underline{\tau}(\boldsymbol{R}) \hat{\boldsymbol{a}}_n \right| && (6.35\mathrm{a})\\
&\le 2\pi \sum_{m=1}^{d} \sum_{n=1}^{d} \left| \eta_m \beta_n \frac{\mathrm{a}_n}{\mathrm{a}_m} \right| \left| \hat{\boldsymbol{b}}_m \underline{\tau}(\boldsymbol{R}) \hat{\boldsymbol{a}}_n \right| && (6.35\mathrm{b})\\
&\le 2\pi\ \tau_M \sum_{m=1}^{d} \sum_{n=1}^{d} \left| \eta_m \beta_n \frac{\mathrm{a}_n}{\mathrm{a}_m} \right| && (6.35\mathrm{c})\\
&\approx 2\pi\ \tau_M \sum_{m=1}^{d} \sum_{n=1}^{d} |\eta_m \beta_n| && (6.35\mathrm{d})\\
&= 2\pi\ \tau_M \left(\sum_{m=1}^{d} |\eta_m| \right) \left(\sum_{n=1}^{d} |\beta_n| \right) && (6.35\mathrm{e})\\
&= 2\pi\ \tau_M\, \|\eta\|_1\, \|\beta\|_1 \le 2\pi\ \tau_M\, \|\eta\|_1 \ . && (6.35\mathrm{f})
\end{aligned}$$

Here, τ_M is the largest magnitude of the eigenvalues of the displacement gradient tensor $\underline{\tau}(\boldsymbol{R})$ of all unit cells $\boldsymbol{R}$ and an approximate cubic lattice has been assumed which implies $\mathrm{a}_n/\mathrm{a}_m \approx 1$.

For the $(004)_{\mathrm{z}\frown\mathrm{c}}$ Bragg reflection, the constraint (6.33) implies $\tau_M \ll 4\%$. Given the constraint (6.17) and under the assumption that displacement gradient tensor is bound from above by the lattice contrast, the influence of the displacement gradient tensor on the effective electron density can be neglected and the latter can be approximated as a function $\varrho_{\text{eff}} = \varrho_{\text{eff}}\big(\boldsymbol{Q}_{\text{B}}, \boldsymbol{R}, \{f_i(\boldsymbol{Q}_{\text{B}}, \boldsymbol{R})\}, \{\boldsymbol{u}(\boldsymbol{R})\}\big)$. Thus, we have

$$\boldsymbol{E}(\boldsymbol{Q}_{\text{B}}, \boldsymbol{Q}) = \sum_{\boldsymbol{R}} \Omega(\boldsymbol{R})\, \varrho_{\text{eff}}\big(\boldsymbol{Q}_{\text{B}}, \boldsymbol{R}, \{f_i(\boldsymbol{Q}_{\text{B}}, \boldsymbol{R})\}, \{\boldsymbol{u}(\boldsymbol{R})\}\big)\, \mathrm{e}^{\mathrm{i}\boldsymbol{Q}\cdot\boldsymbol{R}} \,. \tag{6.36}$$

To summarize, the model

$$\mathcal{I}(\boldsymbol{Q}_{\text{B}}, \boldsymbol{Q}) \propto |\boldsymbol{E}(\boldsymbol{Q}_{\text{B}}, \boldsymbol{Q})|^2 \tag{6.37a}$$

$$\boldsymbol{E}(\boldsymbol{Q}_{\text{B}}, \boldsymbol{Q}) \overset{(6.36)}{=} \sum_{\boldsymbol{R}} \Omega(\boldsymbol{R}) \varrho_{\text{eff}}\big(\boldsymbol{Q}_{\text{B}}, \boldsymbol{R}, \{f_i(\boldsymbol{Q}_{\text{B}}, \boldsymbol{R})\}, \{\boldsymbol{u}(\boldsymbol{R})\}\big)\, \mathrm{e}^{\mathrm{i}\boldsymbol{Q}\cdot\boldsymbol{R}} \tag{6.37b}$$

$$\varrho_{\text{eff}}\big(\boldsymbol{Q}_{\text{B}}, \boldsymbol{R}, \{f_i(\boldsymbol{Q}_{\text{B}}, \boldsymbol{R})\}, \{\boldsymbol{u}(\boldsymbol{R})\}\big) \overset{(6.31)}{=} \varPhi_{\text{C}}^{(D)}\big(\boldsymbol{Q}_{\text{B}}, \boldsymbol{R}, \{f_i(\boldsymbol{Q}_{\text{B}}, \boldsymbol{R})\}\big)\, \mathrm{e}^{\mathrm{i}\boldsymbol{Q}_{\text{B}}\cdot\boldsymbol{u}(\boldsymbol{R})} \tag{6.37c}$$

$$\varPhi_{\text{C}}^{(D)}(\boldsymbol{Q}_{\text{B}}, \boldsymbol{R}, \{f_i(\boldsymbol{Q}_{\text{B}}, \boldsymbol{R})\}) \overset{(6.24)}{=} \sum_{i=1}^{N_{\text{ApC}}} \mathrm{e}^{\mathrm{i}\boldsymbol{Q}_{\text{B}}\cdot\boldsymbol{R}_i} f_i(\boldsymbol{Q}_{\text{B}}, \boldsymbol{R}) \tag{6.37d}$$

describes the intensity distribution close to a Bragg peak $\boldsymbol{Q}_{\text{B}}$ under the assumptions:

- Eq. (6.10):
  The experimentally measured intensity $\mathcal{I}$ is only considered in a limited domain in reciprocal space close to the Bragg peak $\boldsymbol{Q}_{\text{B}}$
- Eq. (6.18):
  The maximum lattice contrast is within the limits resulting from the limited domain in reciprocal space
- Eq. (6.30):
  The maximum displacement in any direction i does not exceed approximately one lattice constant
- Moreover, we assume kinematic approximation and illumination with a monochromatic plane wave. This implicitly implies perfect coherence properties and no angular divergence of the impinging beam.

Note, that the sum in Eq. (6.37b) contains all lattice points $\boldsymbol{R}$. Therefore, we now investigate under which conditions this sum can be approximated by an integration over a continuous variable. For this, the functions $\Omega(\boldsymbol{R})$ and $\varrho_{\text{eff}}\big(\boldsymbol{Q}_{\text{B}}, \boldsymbol{R}, \{f_i(\boldsymbol{Q}_{\text{B}}, \boldsymbol{R})\}, \{\boldsymbol{u}(\boldsymbol{R})\}\big)$ need to be defined as a function of $\boldsymbol{r} \in \mathbb{R}^d$ and not only on the Bravais lattice points $\boldsymbol{R}$. For the shape, we define $\Omega(\boldsymbol{r})$ to be one if $\boldsymbol{r}$ is inside the volume of any unit cell $\boldsymbol{R}$ inside the nanostructure and zero otherwise.

For the effective electron density, we define $f_i(\boldsymbol{Q}_{\text{B}}, \boldsymbol{r})$ in analogy to the shape function $\Omega(\boldsymbol{r})$: We map $\boldsymbol{r}$ to the unit cell $\boldsymbol{R}$ in which $\boldsymbol{r}$ is located in. Then we attribute $f_i(\boldsymbol{Q}_{\text{B}}, \boldsymbol{r})$ to $f_i(\boldsymbol{Q}_{\text{B}}, \boldsymbol{R})$ with that $\boldsymbol{R}$. Then, we eliminate the discontinuities of $\varPhi_{\text{C}}^{(D)}\big(\boldsymbol{Q}_{\text{B}}, \boldsymbol{R}, \{f_i(\boldsymbol{Q}_{\text{B}}, \boldsymbol{R})\}\big)$ at the edge of each unit cell by smoothing with a multidimensional Gaussian with FWHM equal to the unit cell dimensions a_i. A full discussion on the limitations resulting from this smoothing goes beyond the scope of this manuscript. However, it is guaranteed that the resulting function is smooth on the scale of the lattice constants a_i.

As long as condition (6.33) is fulfilled, the displacement field $\boldsymbol{u}(\boldsymbol{R})$ can be interpolated smoothly to $\boldsymbol{u}(\boldsymbol{r})$ in such way that the resulting scale of variation is not smaller than the scale of the lattice constants a_i, too.

Therefore, the effective electron density is defined for all points $\boldsymbol{r} \in \mathbb{R}^d$ and is a smooth function on the scale of the lattice constants a_i. We are now able to rewrite

$$\begin{aligned} \boldsymbol{E}(\boldsymbol{Q}_\mathrm{B}, \boldsymbol{Q}) &\overset{(6.36)}{=} \sum_{\boldsymbol{R}} \Omega(\boldsymbol{R}) \varrho_\mathrm{eff}\big(\boldsymbol{Q}_\mathrm{B}, \boldsymbol{R}, \{f_i(\boldsymbol{Q}_\mathrm{B}, \boldsymbol{R})\}, \{\boldsymbol{u}(\boldsymbol{R})\}\big)\, \mathrm{e}^{\mathrm{i}\boldsymbol{Q}\cdot\boldsymbol{R}} && (6.38\mathrm{a}) \\ &= \sum_{\boldsymbol{R}} \int_{\mathbb{R}^d} \delta(\boldsymbol{r} - \boldsymbol{R})\, \Omega(\boldsymbol{r}) \varrho_\mathrm{eff}\big(\boldsymbol{Q}_\mathrm{B}, \boldsymbol{r}, \{f_i(\boldsymbol{Q}_\mathrm{B}, \boldsymbol{r})\}, \{\boldsymbol{u}(\boldsymbol{r})\}\big)\, \mathrm{e}^{\mathrm{i}\boldsymbol{Q}\cdot\boldsymbol{r}}\ \mathrm{d}^d\boldsymbol{r} && (6.38\mathrm{b}) \\ &= \int_{\mathbb{R}^d} \left[\sum_{\boldsymbol{R}} \delta(\boldsymbol{r} - \boldsymbol{R})\right] \Omega(\boldsymbol{r}) \varrho_\mathrm{eff}\big(\boldsymbol{Q}_\mathrm{B}, \boldsymbol{r}, \{f_i(\boldsymbol{Q}_\mathrm{B}, \boldsymbol{r})\}, \{\boldsymbol{u}(\boldsymbol{r})\}\big)\, \mathrm{e}^{\mathrm{i}\boldsymbol{Q}\cdot\boldsymbol{r}}\ \mathrm{d}^d\boldsymbol{r} && (6.38\mathrm{c}) \end{aligned}$$

where we exploited the definition of the Dirac delta distribution [170]

$$\int_{\mathbb{R}^d} f(\boldsymbol{r}) \delta(\boldsymbol{r} - \boldsymbol{r}_0)\ \mathrm{d}^d\boldsymbol{r} = f(\boldsymbol{r}_0) \tag{6.39}$$

for $f(\boldsymbol{r}) = \Omega(\boldsymbol{r}) \varrho_\mathrm{eff}\big(\boldsymbol{Q}_\mathrm{B}, \boldsymbol{r}, \{f_i(\boldsymbol{Q}_\mathrm{B}, \boldsymbol{r})\}, \{\boldsymbol{u}(\boldsymbol{r})\}\big)\, \mathrm{e}^{\mathrm{i}\boldsymbol{Q}\cdot\boldsymbol{r}}$ and $\boldsymbol{r}_0 = \boldsymbol{R}$. Since

$$\sum_{\boldsymbol{R}} \delta(\boldsymbol{r} - \boldsymbol{R}) \propto \sum_{\boldsymbol{G}} \mathrm{e}^{-\mathrm{i}\boldsymbol{G}\cdot\boldsymbol{r}} \tag{6.40}$$

where $\boldsymbol{G}$ is the reciprocal lattice of the Bravais lattice $\mathbb{B}$ with elements $\boldsymbol{R}$, Eq. (6.38c) can be further simplified to

$$\boldsymbol{E}(\boldsymbol{Q}_\mathrm{B}, \boldsymbol{Q}) \propto \sum_{\boldsymbol{G}} \int_{\mathbb{R}^d} \Omega(\boldsymbol{r}) \varrho_\mathrm{eff}\big(\boldsymbol{Q}_\mathrm{B}, \boldsymbol{r}, \{f_i(\boldsymbol{Q}_\mathrm{B}, \boldsymbol{r})\}, \{\boldsymbol{u}(\boldsymbol{r})\}\big)\, \mathrm{e}^{\mathrm{i}(\boldsymbol{Q}-\boldsymbol{G})\cdot\boldsymbol{r}}\ \mathrm{d}^d\boldsymbol{r}\ . \tag{6.41}$$

Since we restrict to the vicinity of a specific Bragg peak $\boldsymbol{Q}_\mathrm{B}$, i.e., the magnitude of $\boldsymbol{Q}$ is much smaller than the spacing to the neighbouring Bragg reflections, the contribution of the points $\boldsymbol{G} \neq 0$ is negligible. Consequently, we drop the outer sum and obtain

$$\boldsymbol{E}(\boldsymbol{Q}_\mathrm{B}, \boldsymbol{Q}) \propto \int_{\mathbb{R}^d} \Omega(\boldsymbol{r}) \varrho_\mathrm{eff}\big(\boldsymbol{Q}_\mathrm{B}, \boldsymbol{r}, \{f_i(\boldsymbol{Q}_\mathrm{B}, \boldsymbol{r})\}, \{\boldsymbol{u}(\boldsymbol{r})\}\big)\, \mathrm{e}^{\mathrm{i}\boldsymbol{Q}\cdot\boldsymbol{r}}\ \mathrm{d}^d\boldsymbol{r} \tag{6.42}$$

as approximation for Eq. (6.36).

Within the validity of this equation, the electric field $\boldsymbol{E}(\boldsymbol{Q}_\mathrm{B}, \boldsymbol{Q})$ in the vicinity of the Bragg reflection $\boldsymbol{Q}_\mathrm{B}$ is given by the Fourier transform of the product of the shape $\Omega(\boldsymbol{r})$ and the effective electron density $\varrho_\mathrm{eff}\big(\boldsymbol{Q}_\mathrm{B}, \boldsymbol{r}, \{f_i(\boldsymbol{Q}_\mathrm{B}, \boldsymbol{r})\}, \{\boldsymbol{u}(\boldsymbol{r})\}\big)$.

For numerical calculations, direct space and reciprocal space are discretized. The discretization grid is chosen as a regular equidistant rectangular grid. This way, the Fourier transform can be evaluated efficiently by the fast Fourier transform (FFT) algorithm [171].

The spacing δx_m (direct space) and δq_m (reciprocal space) of the grid in direction m is connected to the boundaries of the numerical domain ranging from $(-X_m, X_m)$ in direct space and $(-\Omega_m, \Omega_m)$ in reciprocal space via

$$\delta x_m = \frac{2X_m}{N_m}\ , \quad \delta q_m = \frac{2\Omega_m}{N_m}\ , \quad N_m = \frac{2\pi}{\delta q_m\ \delta x_m}\ , \tag{6.43}$$

where N_m is the number of points in direction m. Consequently, by fixing Ω_m and δq_m, we implicitly choose values for N_m, δx_m and X_m.

At this point, we point out a severe deficiency in the conception and the discretization of the model: Typically, we aim to investigate small nanostructures grown epitaxially on a large single-crystalline substrate which, however, is very thick compared to the height of the nanostructures. Thus, the shape $\Omega(\boldsymbol{r})$ of the full object is typically beyond current experimental (perfect plane wave as incident radiation) and computational limitations. However, due to the non-local coupling of all direct space points to each Fourier point, the truncation of the substrate – in order to reduce the computational domain – requires special measures. Nevertheless, it is useful to first study objects numerically which are truncated in the substrate as soon as the displacement field becomes negligible. After this, we return in Sec. 8.3 to the experimental conditions (e.g., a thick substrate which is truncated for the reconstruction).

At this point we can now define the aim of algorithmic reconstruction supported CXDI:

Given the intensity distribution $\mathcal{I}(\boldsymbol{Q}_\mathrm{B}, \boldsymbol{Q})$ in the vicinity of a Bragg peak, the goal is to reconstruct the effective electron density ϱ_eff – optimally including the shape of the object $\Omega(\boldsymbol{r})$. This very general task, however, requires some *a priori* knowledge about the nanoobject under consideration, since the effective electron density is a complex valued object, and, thus, has two degrees of freedom at each spatial point, whereas the intensity distribution is only real-valued. Consequently, without additional *a priori* knowledge, the number of unknowns is twice as large as the measured values.

In the framework of this manuscript, we restrict to the following simplified, yet challenging condition for reconstructions: We always assume that the shape $\Omega(\boldsymbol{r})$ of the nanostructure in direct space is already known. Experimentally, this can be realized by complementary techniques such as atomic force microscopy (AFM) [172–175], scanning electron microscopy (SEM) [176], transmission electron microscopy (TEM) [177] or grazing incidence small angle X-ray scattering (GISAXS) [178]. For weakly strained crystals, the shape can be estimated during the reconstruction by application of the ShrinkWarp algorithm [151]. However, this approach does no longer work for highly strained crystals. Another approach for estimation of the shape is presented in Ref. [152].

This assumption that the shape $\Omega(\boldsymbol{r})$ of the nanostructure is available, is very important for the elimination of two (out of three) intrinsic ambiguities in the extraction of the effective electron density ϱ_eff. This non-uniqueness of the solution of the model results directly from the mathematical properties of the Fourier transform. We specifically have these ambiguities:

- Shifting the object in position space only results in a plane wave modulation in reciprocal space, hence, producing the same intensity distribution $\mathcal{I}(\boldsymbol{Q}_\mathrm{B}, \boldsymbol{Q})$. These ambiguities are removed by fixing the position of the shape Ω in position space.
- If the shape Ω of the nanocrystal is inversion symmetric, an additional twofold ambiguity shows up: Both, $\varrho_\mathrm{eff}(\boldsymbol{r})$ and $\varrho^*_\mathrm{eff}(-\boldsymbol{r})$ fulfill all constraints enforced by the input data and, therefore, constitute two distinct solutions unless $\varrho_\mathrm{eff}(\boldsymbol{r}) \propto \varrho^*_\mathrm{eff}(-\boldsymbol{r})$. We avoid this ambiguity by only investigating nanostructures with non inversion symmetric shape.
- The remaining ambiguity indicated by the mathematical properties of the Fourier transform is a physically irrelevant global phase shift which is not constrained in the reconstruction. Instead, the mathematical measure which we employ for judging upon the success of a reconstruction is insensitive to this ambiguity (see Sec. 6.2.2).

To decrease the number of unknowns below the number of measured points in reciprocal space, the sampling must be chosen accordingly. In particular, the domain limits in direct space must be such that at least half of the domain is outside the scattering volume. This way, the number of complex unknowns in direct space is at least decreased by a factor of 2. The ratio of the number of measured intensity values divided by the number of points in direct space inside the shape $\Omega(\boldsymbol{r})$ is referred to as oversampling ratio σ.

If

- the dimensionality of the structure is at least equal to two,
- the shape $\Omega(\boldsymbol{r})$ is known and finite, and
- the distance $\delta\boldsymbol{q}$ of the measured intensity points $\mathcal{I}(\boldsymbol{Q}_\mathrm{B}, \boldsymbol{Q})$ in reciprocal space is small enough to guarantee a sufficient oversampling ratio σ on the grid ($\sigma \geq 2$ is a lower bound),

it has been proven that the effective electron density ϱ_eff can be retrieved (up to the inherent symmetries mentioned above) [1, 179–182].

In a second step, the extraction of the displacement field $\boldsymbol{u}(\boldsymbol{R})$ from the effective electron density ϱ_eff may require phase unwrapping. For this, many algorithms have already been developed (see for example Ref. [183] and references therein) and, consequently, will not be developed further in this manuscript.

These conditions (known shape $\Omega(\boldsymbol{r})$ and intensity distribution $\mathcal{I}(\boldsymbol{Q}_\mathrm{B}, \boldsymbol{Q})$ on a grid with an oversampling ratio $\sigma \geq 2$) will be investigated in Sec. 7.3. Nevertheless, depending on the nanostructure under consideration, additional *a priori* may be available. Such additional *a priori* knowledge in particular includes the following aspects which are not covered by knowledge of the shape $\Omega(\boldsymbol{r})$ and the intensity distribution $\mathcal{I}(\boldsymbol{Q}_\mathrm{B}, \boldsymbol{Q})$:

1. Far away from the nanostructure, the displacement field $\boldsymbol{u}$ in the substrate typically decays and, finally, results in a negligible phase shift $\boldsymbol{Q}_\mathrm{B} \cdot \boldsymbol{u}(\boldsymbol{R})$ in the effective electron density as defined in Eq. (6.37). Application of this "boundary condition" would fix the yet undetermined global phase in the reconstruction procedure.
2. Additional *a priori* knowledge might also be available for the quantity $\Phi_\mathrm{C}^{(D)}$ as defined in Eq. (6.37). For a crystal of uniform composition of the unit cells, this quantity reduces to a constant. Typically, this scattering magnitude is either a slowly varying function – up to possible material interfaces – or deviates only slightly from its average value – at least in some sub-domains of the nanostructure (e.g. the substrate region). The first case might induce restrictions on the spatial derivatives of the local scattering magnitude $\Phi_\mathrm{C}^{(D)}$. The latter case will be discussed more closely in Sec. 7.4.
3. The phase in the effective electron density is connected to the displacement field $\boldsymbol{u}$. Consequently, restrictions related to the displacement field $\boldsymbol{u}$ translate to restrictions of the phase field of the effective electron density ϱ_eff during the reconstruction. Here, we need to distinguish two important aspects:
    - On the one hand, the phase variation, more specifically, the derivatives of the phase field might be limited. For example, a given maximum amount of strain implies restrictions on the first derivative of the displacement field. A limited strain gradient corresponds to restrictions on the second derivative of the effective electron density. Such restrictions are discussed in detail in Ref. [184].
    - On the other hand, each component of the displacement field is single-valued at any spatial position $\boldsymbol{r}$. Consequently, the phase field must be free of phase vortices. Otherwise, the displacement field components would be multi-valued map. This requirement will be discussed further in Sec. 7.5.

A short summary of the *a priori* knowledge, which considered further in this manuscript, and its importance for eliminition of the intrinsic ambiguities in the CXDI model is given in Fig. 6.3. We point out that the same physical *a priori* knowledge may typically be incorporated in reconstruction algorithms in multiple ways. Consequently, one carefully needs to distinguish between a given set of *a priori* knowledge and the implementation of this set of *a priori* knowledge in the reconstruction process. Consequently, we now introduce the reconstruction *algorithms* which are of importance in this manuscript.

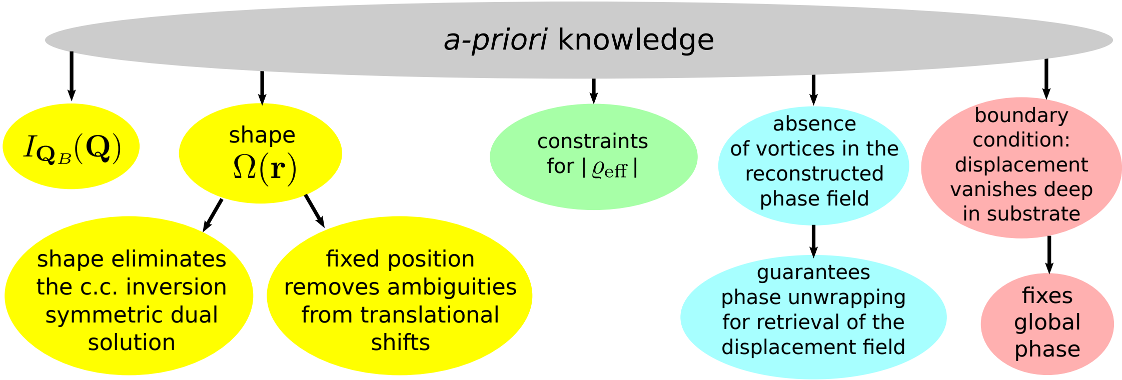

Figure 6.3.: Illustration of the importance of certain *a priori* knowledge for the elimination of the intrinsic ambiguities of the model underlying CXDI reconstructions.

6.2. Theoretical background of the reconstruction procedure

Given a specific set *a priori* knowledge which is theoretically sufficient to determine the solution ϱ_{eff} uniquely (or at least up to ambiguities which are physically not relevant), we still need to find an algorithmic procedure which is capable of retrieving this solution. Whereas very sophisticated and powerful algorithms are available for linear systems of equations, the set of equations (6.37) is non-linear and non-convex. Thus, dedicated algorithms should be developed which are specifically adapted to this set of equations.

In this manuscript we restrict to iterative procedures for extraction of the solution. Such an iterative procedure aims to reduce the distance to the solution by repeatedly performing a set of well-defined operations on a given initial guess.

Therefore, a measure for calculation of the distance of the solution of the set of equations ("ground truth") to any function (defined in the same mathematical space as the solution) is needed. By this measure, the quality of the iterative approximations to the solution is quantified. Consequently, it also reveals the improvements from one iteration to the next iteration. This *error measure* for CXDI phase retrieval is discussed in Sec. 6.2.2.

Consequently, any iterative procedure requires the following ingredients:

1. the error measure which reveals the distance from the current approximation to the desired solution,
2. an initial guess to the final solution, and
3. the operator which is repeatedly applied to this initial guess.

For some iterative procedures, the distance of the current approximation to the desired solution decreases monotonously with every iterative step. Such behavior is desired for optimization problems for which only a single extremum (minimum or maximum) exists. For optimization problems with multiple local minima, such behavior is only adequate if a very good initial guess close to the solution is available. For example, optimization algorithms with monotonously decreasing error can also be used for fine tuning of a low-quality approximation to the solution that has been obtained by other approaches.

If no adequate initial guess is available and many local extrema exist – which is often the case for non-linear and non-convex optimization problems – optimization algorithms must be able to either avoid or escape from unwanted local minima. Consequently, the error measure does typically not decrease with every iteration. Here, one of the most prominent examples is the simulated annealing approach [166].

A good iterative reconstruction algorithm should be successful in all cases and for all conditions. Most importantly, it

1. should not depend on the starting point (as long as no good starting point is available),
2. should perform the reconstructions with little computational effort,
3. should possess these properties for a wide range of its free/internal parameters,
4. should be robust to artifacts (such as noise, . . .) in the input data, and
5. should not require human interaction during execution (like tuning of parameters).

Reaching a success rate of or close to 100% is a challenging task for CXDI reconstructions.

Nevertheless, several inhomogeneously strained nano-sized objects like quantum dots and quantum wires have already been inspected at synchrotron facilities by CXDI [123, 179, 185–200]. In most cases, a combination of the hybrid input output algorithm (HIO-algorithm) and error reduction (ER-algorithm) has been employed [201–203] to solve the highly non-linear, non-local system of equations underlying the reconstruction of the displacement field. This algorithm will be be reviewed and summarized in Sec. 6.2.3.

Despite the success of this algorithm for a number of applications, its capabilities are not fully satisfactory [1, 185, 203], in particular for very inhomogeneously highly strained systems. Consequently, strong efforts are put in the development of novel algorithms in order to overcome the current limitations in CXDI reconstructions (see e.g. Refs. [1, 185, 195, 200, 204–206]).

On the one hand, the incorporation of additional *a priori* knowledge – such as the *a priori* knowledge discussed in Sec. 6.1 – is pursued for retrieving the displacement field $\boldsymbol{u}$ (see for example Refs. [185, 195, 205]).

On the other hand, advances which are not based on additional *a priori* knowledge compared to the existing algorithms have been achieved (see e.g. Refs. [1, 203, 204, 207]).

In this manuscript, we present results for both approaches:

Firstly, we investigate an extension of the above mentioned combination of the HIO- and ER-algorithm based on randomization and overrelaxation of a projection operator [208, 209]. This extension does not require *a priori* knowledge in addition to the shape of the object in direct space and the intensity distribution $\mathcal{I}(\boldsymbol{Q}_\mathrm{B}, \boldsymbol{Q})$ in reciprocal space. This way some residual shortcomings of the traditional HIO+ER-algorithm have been resolved [1, 203]. We will refer to this extension as the $\mathrm{HIO}_{\mathrm{O_R}}$+ER-algorithm [1].

Moreover, we define and discuss suitable operators for incorporating bounds on the magnitude of local scattering amplitude in the traditional HIO+ER-algorithm. We refer to this extension as the $\mathrm{HIO}^{\mathrm{A}}$+$\mathrm{ER}^{\mathrm{A}}$-algorithm, and evaluate the benefits of such direct space constraints [2].

Finally, we combine both approaches – randomization of the overrelaxation of a projection operator and bounds on the magnitude of local scattering amplitude. The respective reconstruction algorithm is referred to as $\mathrm{HIO}^{\mathrm{A}}_{\mathrm{O_R}}$+$\mathrm{ER}^{\mathrm{A}}$-algorithm [2]. Our results demonstrate that the $\mathrm{HIO}^{\mathrm{A}}_{\mathrm{O_R}}$+$\mathrm{ER}^{\mathrm{A}}$-algorithm performs significantly better in extracting the displacement field (and, thus, the strain distribution) in inhomogeneously strained nanocrystals in comparison to the traditional HIO+ER-algorithm.

Throughout this manuscript, we only consider fully automatic reconstructions with no human interaction during the reconstruction.

6.2.1. Multidimensional polynomials with projection maps as argument

The reconstruction algorithms presented in the upcoming sections involve various projection operators. A projection operator is defined by the property that repeated application is identical to a single application of this operator.[2] For the discussion of these algorithms, it is useful to first discuss the simplifications in multidimensional operator polynomials

$$\begin{aligned}\hat{H}_{\mathrm{Op}}(\{\mathbf{M}_i\}) &= c\,1 + \sum_{i_1=1}^{k} c_{i_1}\mathbf{M}_{i_1} + \sum_{i_1=1}^{k}\sum_{i_2=1}^{k} c_{i_1 i_2}\mathbf{M}_{i_1}\mathbf{M}_{i_2} \\ &\quad + \ldots + \left(\sum_{i_1=1}^{k}\sum_{i_2=1}^{k}\cdots\sum_{i_q=1}^{k}\right) c_{i_1 i_2 \ldots i_q}\mathbf{M}_{i_1}\mathbf{M}_{i_2}\ldots\mathbf{M}_{i_q} && (6.44a) \\ &= \sum_{m=0}^{q}\left(\sum_{i_1=1}^{k}\sum_{i_2=1}^{k}\cdots\sum_{i_m=1}^{k}\right) c_{i_1 i_2 \ldots i_m}\mathbf{M}_{i_1}\mathbf{M}_{i_2}\ldots\mathbf{M}_{i_m} && (6.44b)\end{aligned}$$

if the mappings $\mathbf{M}_i$, $1 \leq i \leq k$, of the k-dimensional polynomial of degree q are k (possibly non-commutative and non-linear) projection operators $\mathbf{P}_i$. For our purposes, it is sufficient to restrict to the case $k = 2$.

From the defining property of projection operators, it follows that any combination of *projection* operators $\mathbf{P}_{\xi_1}^{n_1}\mathbf{P}_{\xi_2}^{n_2}\ldots\mathbf{P}_{\xi_m}^{n_m}$ of two different kinds $\xi_j \in \{\Omega, \Gamma\}$, $j \in \{1, \ldots, m\}$, reduces to one of the four building blocks $\mathbf{P}_\Omega\,(\mathbf{P}_\Gamma\mathbf{P}_\Omega)^n$, $\mathbf{P}_\Gamma\,(\mathbf{P}_\Omega\mathbf{P}_\Gamma)^n$, $(\mathbf{P}_\Omega\mathbf{P}_\Gamma)^n$ and $(\mathbf{P}_\Gamma\mathbf{P}_\Omega)^n$ for some integer $n \geq 0$ [1].

The identity operator 1 and the single projection operators are included for $n = 0$ in those building blocks. However, the identity operator is included twice, namely for $n = 0$ for $(\mathbf{P}_\Omega\mathbf{P}_\Gamma)^n$ and $(\mathbf{P}_\Gamma\mathbf{P}_\Omega)^n$. Therefore, the identity operator must be treated separately if those four building blocks are used to simplify Eq. (6.44b).

Taking those considerations into account, we simplify the operator polynomial (6.44b) to

$$\begin{aligned}\hat{H}_{\mathrm{Proj}}(\mathbf{P}_\Gamma, \mathbf{P}_\Omega) = b\,1 &+ \sum_{n=1}^{n_{\mathrm{Max}}^{\mathrm{even}}}\left[c_{\Omega,2n}\,(\mathbf{P}_\Omega\mathbf{P}_\Gamma)^n + c_{\Gamma,2n}\,(\mathbf{P}_\Gamma\mathbf{P}_\Omega)^n\right] + \\ &\sum_{n=0}^{n_{\mathrm{Max}}^{\mathrm{odd}}}\left[c_{\Omega,2n+1}\mathbf{P}_\Omega\,(\mathbf{P}_\Gamma\mathbf{P}_\Omega)^n + c_{\Gamma,2n+1}\mathbf{P}_\Gamma\,(\mathbf{P}_\Omega\mathbf{P}_\Gamma)^n\right]\ , \qquad (6.45a)\end{aligned}$$

if the operators $\mathbf{M}_i$ are projection operators and $n = 2$. The parameter $n_{\mathrm{Max}}^{\mathrm{even}}$ is given by the largest integer smaller or equal to $\frac{p}{2}$. $n_{\mathrm{Max}}^{\mathrm{odd}}$ is determined by the largest integer smaller or equal to $\frac{p-1}{2}$. p is the maximum number of successive projection operators which is included in $\hat{H}_{\mathrm{Proj}}$. If we incorporate the idempotence of projection operators, $\hat{H}_{\mathrm{Proj}}(\mathbf{P}_\Gamma, \mathbf{P}_\Omega)$ constitutes the fundamental structure for two non-commutative projection operators with a maximum of q successive projections.

$\hat{H}_{\mathrm{Proj}}(\mathbf{P}_\Gamma, \mathbf{P}_\Omega)$ as given in Eq. (6.45a) will prove useful for discussing various approaches for the calculation of the next iterative solution in the reconstruction algorithms (e.g., in the manner of Eq. (6.52c) or Eq. (7.7a)).

If the polynomials $\hat{H}_{\mathrm{Proj}}$ are exploited for that purpose, we must imply an additional restriction on the coefficients $(b, \boldsymbol{c}_\Omega, \boldsymbol{c}_\Gamma)$, if the projection operators $\mathbf{P}_\Omega$ and $\mathbf{P}_\Gamma$ reduce to the identity operator 1 if applied to the desired solution $\varrho_{\mathrm{eff}}(\boldsymbol{r})$ (i.e., if the solution $\varrho_{\mathrm{eff}}(\boldsymbol{r})$

---

[2] In the definition, it is sufficient to require $\mathbf{P}_\xi^2 = \mathbf{P}_\xi$. The extension to $\mathbf{P}_\xi^n = \mathbf{P}_\xi$, $n \geq 1$, (idempotence) follows directly by induction.

of the iterative process is a fixed point of both operators $\mathbf{P}_\Gamma$ and $\mathbf{P}_\Omega$). Given the true solution $\varrho_{\text{eff}}(\boldsymbol{r})$ as input, the operator $\hat{H}_{\text{Proj}}$ for determination of the next iterative solution must simplify to the identity operator 1 for any choice of its parameters $(b, \boldsymbol{c}_\Omega, \boldsymbol{c}_\Gamma)$.[3] This requirement is fulfilled *if and only if*

$$b = 1 - \sum_{n=1}^{p} \left[c_{n,\Omega} + c_{n,\Gamma} \right] \ . \tag{6.45b}$$

Consequently, for a maximum of p successive projections in the projection polynomial $\hat{H}_{\text{Proj}}$, $2p$ free parameters appear in $\hat{H}_{\text{Proj}}$.

It is important to keep in mind that in general the product of two non-commutative idempotent operators (like $\mathbf{P}_\Gamma$ and $\mathbf{P}_\Omega$) is no longer idempotent and, hence, the operator $\hat{H}_{\text{Proj}}$ is not idempotent, too.

6.2.2. Error measures and their limitations

In order to investigate the performance and convergence properties of a reconstruction algorithm, three aspects are particularly important:

1. the deviation of the current iterative approximation to the constraints which determine the solution: In our particular case, we consider the dimensionless, normalized error measure

   $$\epsilon^{(i)} = \frac{\langle\, |\widetilde{g}^{(i)}| - \Gamma \,;\, |\widetilde{g}^{(i)}| - \Gamma \,\rangle}{\langle\, \Gamma \,;\, \Gamma \,\rangle} = \frac{1}{\|\Gamma\|_2^2} \sum_{\boldsymbol{Q}} \left(|\widetilde{g}^{(i)}(\boldsymbol{Q})| - \Gamma(\boldsymbol{Q}) \right)^2 \tag{6.46}$$

   for calculation of the distance from the solution $\varrho_{\text{eff}}(\boldsymbol{r})$ from the constraints $\Gamma(\boldsymbol{Q}) = \sqrt{\mathcal{I}(\boldsymbol{Q}_{\text{B}}, \boldsymbol{Q})}$ in reciprocal space. Here, $\|\cdot\|_p$ is the p-norm, $\langle \,\cdot\,;\,\cdot\, \rangle$ the standard scalar product in $\mathbb{R}^n$ (n is the number of points of the intensity distribution which been measured), and $\Gamma(\boldsymbol{Q}) = \sqrt{\mathcal{I}(\boldsymbol{Q}_{\text{B}}, \boldsymbol{Q})}$ are the amplitudes in reciprocal space that are derived from the measured intensity distribution $\mathcal{I}(\boldsymbol{Q}_{\text{B}}, \boldsymbol{Q})$. $\widetilde{g}^{(i)}(\boldsymbol{Q})$ is the (complex valued) Fourier transform of the i-th iterative approximation $\varrho_{\text{eff}}^{(i)}(\boldsymbol{r})$ to the solution.

   We point out that this error measure does not take into account violations of the direct space constraints (shape Ω, ...). More importantly, two quite different direct space objects ϱ_{eff} (hence quite different complex Fourier transforms) may posses an extremely similar distribution of the magnitude Γ in reciprocal space [181, 205]. Consequently, this error measure is – in general – insufficient for judging on the quality of a reconstruction algorithm or a specific reconstruction with a particular reconstruction algorithm. Nevertheless, it may be useful to inspect its capabilities and limitations in details, since it is widely used and can be easily applied to all reconstruction algorithms based on the model (6.37).

   One advantage of this error measure is that it is – by design – insensitive to all inherent ambiguities that are induced by the mathematical properties of the Fourier transform (see Sec. 6.1).

2. the change from iteration $(i-1)$ to iteration (i) of the approximations $\varrho_{\text{eff}}^{(i)}$ to the solution ϱ_{eff}: A naive choice for measuring this change would be the p-norm $\delta^{(i)} = \left\| \varrho_{\text{eff}}^{(i-1)} - \varrho_{\text{eff}}^{(i)} \right\|_p$. However, this difference does not eliminate (physically irrelevant)

---

[3] Strictly speaking, if the solution $\varrho_{\text{eff}}(\boldsymbol{r})$ is not unique, it is sufficient to require that $\hat{H}_{\text{Proj}}$ maps a given solution $\varrho_{\text{eff}}(\boldsymbol{r})$ to another solution $\widetilde{\varrho_{\text{eff}}}(\boldsymbol{r})$. For example, if the global phase of $\varrho_{\text{eff}}(\boldsymbol{r})$ is undefined, it is sufficient to require $\hat{H}_{\text{Proj}}\varrho_{\text{eff}} = \mathrm{e}^{\mathrm{i}\delta}\varrho_{\text{eff}} \equiv \widetilde{\varrho_{\text{eff}}}$, $\delta \in [0, 2\pi[$. However, in this manuscript we restrict to stronger constraint $\hat{H}_{\text{Proj}}\varrho_{\text{eff}} = \varrho_{\text{eff}}$, i.e., we require that the solution ϱ_{eff} is not changed by $\hat{H}_{\text{Proj}}$.

global phase shifts from iteration $(i-1)$ to iteration (i). Consequently, we instead define the angle

$$\chi^{(i)} = \arccos\left[\left|\left\langle \varrho_{\text{eff}}^{(i-1)} \,;\, \varrho_{\text{eff}}^{(i)} \right\rangle\right| \Big/ \sqrt{\left\langle \varrho_{\text{eff}}^{(i-1)} \,;\, \varrho_{\text{eff}}^{(i-1)} \right\rangle \left\langle \varrho_{\text{eff}}^{(i)} \,;\, \varrho_{\text{eff}}^{(i)} \right\rangle}\right] . \tag{6.47}$$

for measuring the change from iteration $(i-1)$ to iteration (i). The absolute value in the nominator of the argument of the arccos function eliminates the dependence on the undetermined, yet irrelevant global phase in $\varrho_{\text{eff}}^{(i)}$. This angle $\chi^{(i)}$ is employed as a measure for the convergence of the algorithm.

Throughout our investigations, we terminated the iterative reconstructions either if a pre-defined maximum number of iterations has been performed or if the change $\chi^{(i)}$ of ϱ_{eff} from iteration to iteration dropped below a certain value.

It is important to keep in mind that the convergence only implies the change from iteration to iteration to vanish. This does – in general – not imply that the converged approximation $\varrho_{\text{eff}}^{(i)}$ is close to the solution ϱ_{eff} [205, 208]. In order to detect whether the result of the iterative procedure resembles to solution ϱ_{eff}, we need to define a third criterion which directly measures this distance and is now defined.

3. the mathematical distance to the (sampled) true solution $\varrho_{\text{eff}}(\boldsymbol{r})$: In complete analogy to the previous discussion for monitoring the change from iteration to iteration, we define the angle

$$\varphi^{(i)} = \arccos\left[\left|\left\langle \varrho_{\text{eff}}^{(i)} \,;\, \varrho_{\text{eff}} \right\rangle\right| \Big/ \sqrt{\left\langle \varrho_{\text{eff}}^{(i)} \,;\, \varrho_{\text{eff}}^{(i)} \right\rangle \left\langle \varrho_{\text{eff}} \,;\, \varrho_{\text{eff}} \right\rangle}\right] . \tag{6.48}$$

However, the reference in this case is not the approximation $\varrho_{\text{eff}}^{(i-1)}$ after iteration $(i-1)$, but the ground truth ϱ_{eff}. For this comparison, it is even more important to eliminate a global phase difference between the ground truth ϱ_{eff} and the result of the reconstruction $\varrho_{\text{eff}}^{(i)}$.

In contrast to the previous two quantities $\epsilon^{(i)}$ and $\chi^{(i)}$, the difference to the ground truth $\varrho_{\text{eff}}(\boldsymbol{r})$ can typically not be determined for experimentally obtained input data of the reconstruction procedure. However, only by this comparison with the ground truth, we are able to judge on the quality of a converged result of the iterative reconstruction procedure. Consequently, it is highly important to carefully investigate the capabilities and limitations of reconstruction algorithms with *simulated* data before they are applied to experimental data.

We point out that the result of a reconstruction should ideally be benchmarked versus the exact quantity that is extracted such as the displacement field, the strain field or the strain gradients – instead of employing Eq. (6.48). However, this is far from trivial since any such derived quantities require additional steps of evaluation with different numerical challenges (e.g. the way derivatives are calculated from the displacement field) or are even not possible in all cases (for example, if the reconstructed phase field contains a phase vortex, unique extraction of the displacement field is not possible, see Sec. 7.5). Consequently, the result of such a benchmark can strongly depend on these additional steps. By the choice (6.48), we benchmark the direct output of the reconstruction procedure and, typically, all further steps will perform well if the input for these further steps is of high quality.

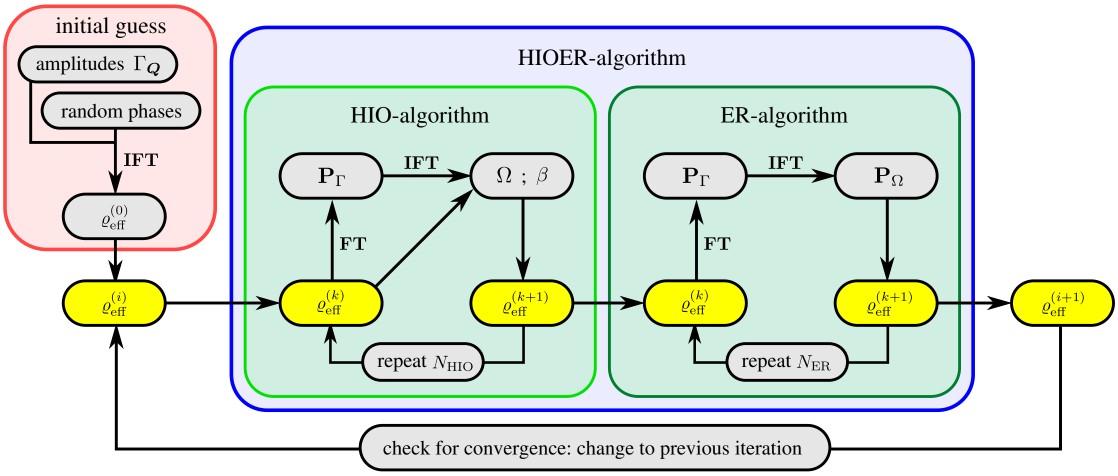

Figure 6.4.: Graphical illustration of the HIO+ER-algorithm including its building blocks.

6.2.3. Overview over current iterative algorithms

A good review of the most important iterative reconstruction algorithms for phase retrieval, which have been proposed, is given in Ref. [203]. The most successful and most widely used algorithm is the HIO+ER-“meta”-algorithm which combines N_{HIO} repetitions of the hybrid input output (HIO-) algorithm with N_{ER} repetitions of the error reduction (ER-) algorithm as follow-up [201, 202]. We now shortly review it before we will extend it in the subsequent sections.

Description of the HIO+ER-algorithm

The first building block – the ER-algorithm [201, 202] – is defined by

$$\varrho_{\text{eff}}^{(i+1)} = \hat{H}_{\text{ER}}\ \varrho_{\text{eff}}^{(i)}\ , \tag{6.49a}$$

where $\hat{H}_{\text{ER}}$ is the projection polynomial

$$\hat{H}_{\text{ER}} = \mathbf{P}_\Omega\,\mathbf{P}_\Gamma\ . \tag{6.49b}$$

Here, $\mathbf{P}_\Omega$ and $\mathbf{P}_\Gamma$ are projection operators in direct and reciprocal space respectively, i.e.,

$$\mathbf{P}_\Omega\,\varrho_{\text{eff}}^{(i)}(\boldsymbol{r}) = \begin{cases} \varrho_{\text{eff}}^{(i)}(\boldsymbol{r}) & \text{if } \boldsymbol{r}\in\Omega\ , \\ 0 & \text{if } \boldsymbol{r}\notin\Omega \end{cases} \tag{6.50a}$$

and

$$\mathbf{P}_\Gamma\,\mathcal{F}^{(i)}(\boldsymbol{Q}) = \Gamma_{\boldsymbol{Q}}\,\mathrm{e}^{\mathrm{i}\arg\left(\mathcal{F}^{(i)}(\boldsymbol{Q})\right)}\ . \tag{6.50b}$$

Here, $\Gamma_{\boldsymbol{Q}} = \sqrt{\mathcal{I}(\boldsymbol{Q}_{\text{B}},\boldsymbol{Q})}$ are the amplitudes in reciprocal space that correspond to the measured intensity distribution $\mathcal{I}(\boldsymbol{Q}_{\text{B}},\boldsymbol{Q})$. $\mathcal{F}^{(i)}(\boldsymbol{Q})$ is defined as $\mathbf{FT}_{\boldsymbol{Q}\leftarrow\boldsymbol{r}}\left\{\varrho_{\text{eff}}^{(i)}\right\}$. The latter operator $\mathbf{P}_\Gamma$ enforces the amplitudes $\Gamma_{\boldsymbol{Q}}$ on the form factor $\mathcal{F}^{(i)}(\boldsymbol{Q})$ of the effective electron density $\varrho_{\text{eff}}^{(i)}$ without modifying its phases $\arg\left(\mathcal{F}^{(i)}(\boldsymbol{Q})\right)$.

The direct space representation of the operator $\mathbf{P}_\Omega$ is

$$\mathbf{P}_\Omega = \begin{cases} 1 & \text{if } \boldsymbol{x}\in\Omega\ , \\ 0 & \text{if } \boldsymbol{x}\notin\Omega\ . \end{cases} \tag{6.51}$$

For notational simplicity, we assume that any operand of the operators $\mathbf{P}_\Gamma$ and $\mathbf{P}_\Omega$ is transformed by Fourier or inverse Fourier transform to the proper space before these operators $\mathbf{P}_\Gamma$ and $\mathbf{P}_\Omega$ are applied.

By alternating projections of a trial solution onto the constraints in direct space and in reciprocal space, the ER-algorithm is a computationally efficient iterative *local* minimizer of a suitable chosen error metrics [201, 202]. However, in practice, CXDI reconstructions typically involve a large number of local minima because the projection operator $\mathbf{P}_\Gamma$ is *non-linear*, *non-convex* and *non-unique* [210]. In consequence, the ER-algorithm typically does converge to a local minimum of the error metrics, but not necessary to the global minimum $\varrho_{\text{eff}}(\boldsymbol{r})$ – as required for a successful CXDI reconstruction. Additionally, the error metric may stagnate for many iterations before decreasing further towards a local minimum.

A very important algorithm which aims to avoid such stagnation and getting caught in local minima other than the global minimum is the hybrid input output (HIO) algorithm proposed by Fienup [201, 202, 211]. This is the second block of the HIO+ER-algorithm in addition to the ER-algorithm.

The HIO-algorithm is also an iterative procedure and is defined by

$$\varrho_{\text{eff}}^{(i+1)}(\boldsymbol{r}) = \begin{cases} \mathbf{P}_\Gamma \varrho_{\text{eff}}^{(i)}(\boldsymbol{r}) & \text{if } \boldsymbol{r} \in \Omega \ , \\ \varrho_{\text{eff}}^{(i)}(\boldsymbol{r}) - \beta \mathbf{P}_\Gamma \varrho_{\text{eff}}^{(i)}(\boldsymbol{r}) & \text{if } \boldsymbol{r} \notin \Omega \ . \end{cases} \tag{6.52a}$$

The parameter β is referred to as feedback parameter and typically chosen from the range $[0.5; 1.0]$ [211]. The success of the HIO+ER-algorithm does not sensitively depend on the value of parameter β in this range [1]. However, it sensitively depends on the choice of the internal parameters N_{HIO} and N_{ER} [1] (see Sec. 7).

This definition is equivalent to

$$\varrho_{\text{eff}}^{(i+1)}(\boldsymbol{r}) = \hat{H}_{\text{HIO}}(\beta) \varrho_{\text{eff}}^{(i)}(\boldsymbol{r}) \tag{6.52b}$$

with the projection polynomial

$$\hat{H}_{\text{HIO}}(\beta) = 1 - \mathbf{P}_\Omega - \beta \mathbf{P}_\Gamma + (1+\beta)\, \mathbf{P}_\Omega \mathbf{P}_\Gamma \ . \tag{6.52c}$$

However, both definitions (6.52a) and (6.52c) motivate different generalizations if additional constraints on the local scattering amplitude are incorporated in the HIO+ER-algorithm in Sec. 7.4.

The convergence properties of the HIO-algorithm have been investigated in Refs. [212–214].

Finally, we must specify the initial guess of the iterative procedure. In most cases no *a priori* knowledge on the phase field in reciprocal space is available. As a result, randomly generated phases $\Phi(\boldsymbol{Q})$ at each point $\boldsymbol{Q}$ in reciprocal space are typically combined with the measured amplitudes $\Gamma_{\boldsymbol{q}}$, i.e.,

$$\mathcal{F}^{(0)}(\boldsymbol{Q}) = \Gamma_{\boldsymbol{Q}} \ \mathrm{e}^{\mathrm{i}\Phi(\boldsymbol{Q})} \ . \tag{6.53}$$

The full HIO+ER-“meta”-algorithm is visualized in Fig. 6.4.

The combination of the HIO- and ER-algorithm is in practice more successful in avoiding stagnation and unwanted local minima than both algorithms on their own [202, 211]. Although the HIO+ER-algorithm is already quite powerful, it is not yet satisfactory as we will illustrate further in Sec. 7.2.

7. Reconstructions in CXDI: Results for simulated ideal data

In this section, we investigate the performance of several reconstruction algorithms for simulated input data. The input data is in this chapter is fully consistent within the theoretical model described in Sec. 6.1. The influence of artifacts (such as noise) on the reconstruction will be investigated in Sec. 8.

As a first step, we introduce in Sec. 7.1 the model systems, which are employed for our investigations. Next, we shortly illustrate in Sec. 7.2 the stagnation of the traditional HIO+ER-algorithm. Then, we demonstrate that proper randomization of the traditional HIO+ER-algorithm is capable of elimination of such stagnation in many cases. If we perform this randomization by overrelaxation of the non-convex non-linear projection operator $\mathbf{P}_\Gamma$ in reciprocal space in the HIO-algorithm, we obtain the $\mathrm{HIO}_{\mathrm{O_R}}$+ER-algorithm which is based on the same *a priori* knowledge as the HIO+ER-algorithm and is equally computationally efficient.

In Sec. 7.4, we will discuss the incorporation of constraints on the local scattering magnitude as additional *a priori* in the HIO+ER-algorithm. We will investigate the benefits of this additional *a priori* knowledge without ($\mathrm{HIO}^{\mathrm{A}}$+$\mathrm{ER}^{\mathrm{A}}$-algorithm) as well as with randomization ($\mathrm{HIO}^{\mathrm{A}}_{\mathrm{O_R}}$+$\mathrm{ER}^{\mathrm{A}}$-algorithm). As for the randomization, we will again discuss two non-equivalent approaches which incorporate the same set of given *a priori* knowledge.

The approximations $\varrho^{(i)}_{\mathrm{eff}}$ to the solution obtained by the before-mentioned algorithms are not guaranteed to be free of phase vortices. However, the fact that the displacement field is a single-valued physical quantity at each point in space, the phase field of the effective electron density must be free of phase vortices. The existence of such phase vortices in the reconstructed effective electron density would prevent unique unwrapping of its phase field. We will provide more details on phase vortices in the framework of CXDI reconstruction in Sec. 7.5.

7.1. Introduction of the test objects

For the investigation of our reconstruction algorithms, we will employ four test objects. First, we consider two smooth, analytically defined phase fields, one photograph of a fireworks during night (truncated in order to obtain a non-inversion symmetric support), and, finally, the displacement field in a periodic arrangement of silicon trenches which is

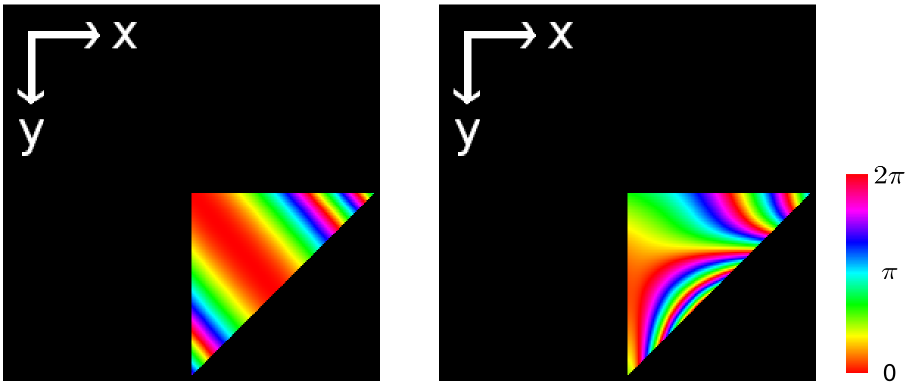

(a) This object belongs to Eq. (7.2a). (b) This object belongs to Eq. (7.2b).

Figure 7.1.: Pure phase objects which we use for the investigation of the convergence of the HIO+ER- and $\mathrm{HIO}_{\mathrm{O_R}}$+ER-algorithm. The magnitude inside both objects is constant. The phase field is plotted in HSV color-bar. The region outside the shape Ω is set to black. (©2012 The Optical Society (OSA), from [1])

calculated by finite element modeling (FEM) of linear elasticity theory (LET). For computationally efficiency and better visualization, we restrict to two-dimensional test objects. An investigation of the HIO+ER and $\mathrm{HIO}_{\mathrm{O_R}}$+ER-algorithm for a three dimensional test object can be found in Ref. [215].

Analytically defined test objects

For the two analytically defined test objects, we define the shape Ω to be a triangular domain defined by the limits $(0,0)$, $(0,a)$ and $(a,0)$ with $a = 0.97$. The object has been sampled on an equidistant grid with $N_1 \times N_2 = 256 \times 256$ data points in the interval $(x,y) = (-1,-1)$ to $(x,y) = (1,1)$. The oversampling ratio for this grid and support Ω is $\sigma = 8.456$.

The magnitude $|\varrho_{\mathrm{eff}}(\boldsymbol{r})|$ inside this shape is set equal to one. Consequently, the two pure phase objects can be written

$$\varrho_{\mathrm{eff}}(\boldsymbol{r}) = \exp\left(\mathrm{i}\,\xi(\boldsymbol{r})\right) \ , \tag{7.1}$$

inside its support Ω, where $\xi(\boldsymbol{r})$ is a real function.

We employ the functions

$$\xi_1(x,y) = (2\pi)^2 \left[(x/b_1)^2 + (y/c_1)^2 \right] \ , \tag{7.2a}$$

$$\xi_2(x,y) = (2\pi) \left[(x-b_2)^3 + (y-c_2)^2 + \frac{x^2 y^3}{c_2^2 b_2^3} \right] \ , \tag{7.2b}$$

where the parameters were chosen as ($b_1 = 1.5515$, $c_1 = -1.835$) and ($b_2 = -0.3515$, $c_2 = 0.535$). The resulting objects are depicted in Fig. 7.1.

Real-word real valued test object

In addition to these two analytically defined test objects with constant magnitude of the effective electron density combined with a smooth phase field (phase variations of 2π extend over several sampling points), we employ the photograph of a fireworks depicted in Fig. 7.2 for investigation of the HIO+ER- and $\mathrm{HIO}_{\mathrm{O_R}}$+ER-algorithm. We define the effective electron density equal to the brightness of the image. Consequently, this object is only real valued in direct space. The support of the image has been modified such

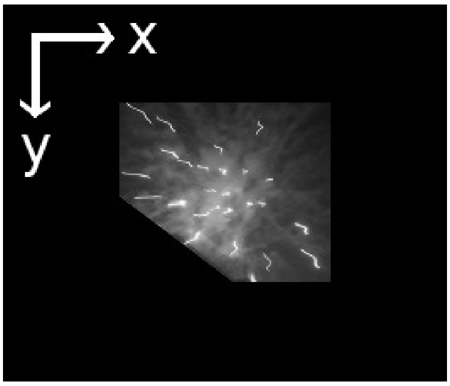

Figure 7.2.: A real valued test object for investigation of the capabilities of CXDI reconstruction algorithms, in particular the HIO+ER- and the $\mathrm{HIO}_{\mathrm{O_R}}$+ER-algorithm. The brightness of the image is set equal to ϱ_{eff}. (©2012 The Optical Society (OSA), from [1])

that it is no longer inversion symmetric. This is required to avoid a two-fold ambiguity of the solution ($\varrho_{\mathrm{eff}}(\boldsymbol{r})$ and $\varrho^*_{\mathrm{eff}}(-\boldsymbol{r})$, see Sec. 6.1). The oversampling ratio of this object is $\sigma = 5.06$.

This object has rather different characteristic features as compared to the previous objects. On the one hand, it contains rather strong variations of its magnitude over short length scales. On the other hand, it also has very weak contrast at the edges of the support Ω. Consequently, it is interesting to also study the performance of the reconstruction algorithms for such kind of objects.

Throughout this manuscript, a reconstruction of these first three test objects is considered successful once the angle $\varphi^{(i)}$ to the test object (see Eq. (6.48)) falls below 0.05°.

Inhomogeneously strained silicon trenches as test object based on FEM

The most important test object which we use for investigating and benchmarking the CDXI reconstruction algorithms under consideration is a periodic array of Si-(001)-nanowires (see Fig. 7.3(a)). The domains between the nanowires ("trenches") are filled with amorphous silicon-oxide $\mathrm{SiO_2}$ (gray domain in Fig. 7.3(a)) during fabrication. Since the thermal expansion coefficients of the crystalline and amorphous region differ, a non-vanishing strain field is observed in the nanostructure after cooling down to room temperature.

We would like to mention that such systems have already been investigated experimentally [216, 217]. In the experimental realization, the periodic nanowires have been fabricated by etching the trenches in a silicon substrate (black domain in Fig. 7.3(a)).

For benchmarking the CXDI reconstructions with such a system, the displacement field $\boldsymbol{u}$ inside this nanostructure has been obtained by Philipp Schroth by finite element modeling (FEM) of linear elasticity theory (LET) with the commercial FEM software "COMSOL Multiphysics" [125, 218–222]. From this displacement field – together with the shape of the nanostructure – we calculated the amplitudes $\Gamma_{\boldsymbol{q}}$ in reciprocal space which are required as input for a CXDI reconstruction.

Both materials (crystalline and amorphous domain) are considered homogeneous in composition. A planar cut perpendicular to the direction of the wires contains all information, since we assume translational symmetry along the wires. Thus, our model system reduces to two dimensions. Moreover, the periodic arrangement of the wires is exploited and the simulation is restricted to a single building block of the periodically repeated wires.

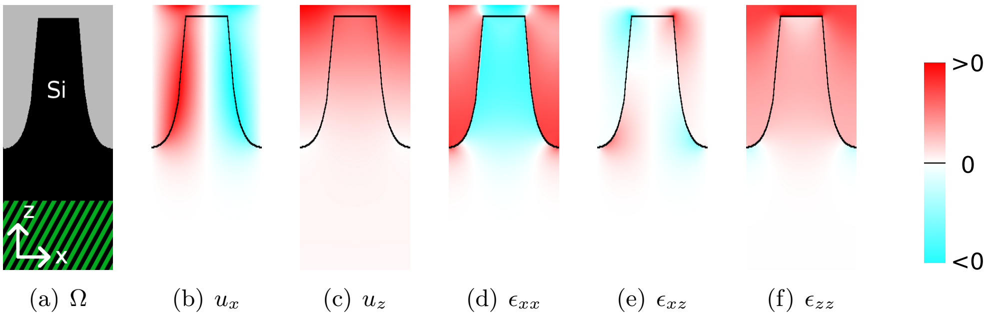

(a) Ω (b) u_x (c) u_z (d) ϵ_{xx} (e) ϵ_{xz} (f) ϵ_{zz}

Figure 7.3.: Fig. (a) shows the geometry and composition of a unit cell of the periodic Si-nanowires. The black domain (including the hatched subdomain) corresponds to the crystalline shape Ω which is relevant for CXDI. The hatched domain will become important in Sec. 7.4. Figs. (b) and (c) show the components of the displacement field obtained by FEM in x- (crystallographic $[100]_{z\frown c}$-direction) and z-direction (crystallographic $[001]_{z\frown c}$-direction). Figs. (d)-(f) show the xx-component, xz-component, and zz-component of the strain tensor ϵ respectively. The interface of the crystalline and amorphous region is marked by a black line. [Fig. (a): (©2013 The Optical Society (OSA), from [2])]

The elastic properties of both materials were characterized by their Poisson ratio ($\nu_{\mathrm{Si}} = 0.28$ and $\nu_{\mathrm{SiO_2}} = 0.17$) and their Young modulus ($Y_{\mathrm{Si}} = 1.3 \cdot 10^{11}$Pa and $Y_{\mathrm{SiO_2}} = 70 \cdot 10^{9}$Pa). We enforced the displacement to vanish in lateral direction at the left and right edges of the domain. Both components of the displacement field have also been set to zero at the bottom of the 1000nm thick substrate. On the upper edge of the domain, no constraints were applied to the displacement field. A free tetrahedral mesh with 25263 elements was generated in order to make this geometry accessible for numerical FEM. The strain in the Si-nanowire was then induced by thermal expansion [125, 223].

The geometry and dimensions of the system are:

- lateral periodicity: 200nm
- vertical etching of the substrate to a depth of 237nm
- filling with amorphous silicon oxide to a height of approximately 258nm (this results in a cap layer of 21nm thickness)
- 1000nm thick substrate domain below the bottom of the nanowire (this way, the displacement field is negligibly small at the bottom edge of the simulation domain)

The resulting displacement field and the strain distribution are depicted in Fig. 7.3. Since the crystalline domain is chemically homogeneous, we set the amplitude of the crystalline silicon domain constant.

We characterize the strain distribution by the maximum strain $\epsilon_{\mathrm{M}} = \max\left(\frac{\partial \mathrm{u_z}}{\partial z}\right)$ on the central axis in the crystalline silicon domain of the simulated wire. Within linear elasticity theory, we are able to increase the strain in the sample by simple linear rescaling of the displacement field $\boldsymbol{u}$.

The phase fields of the effective electron density $\varrho_{\mathrm{eff}}(\boldsymbol{r})$ for different values of the maximum strain ϵ_{M} are collected in Fig. 7.4. We point out the increasing number of phase wraps with increasing maximum strain. In addition, the logarithm of the intensity distribution close to the $(004)_{z\frown c}$ Bragg reflection is also depicted in Fig. 7.4 for the respective effective electron density distribution.

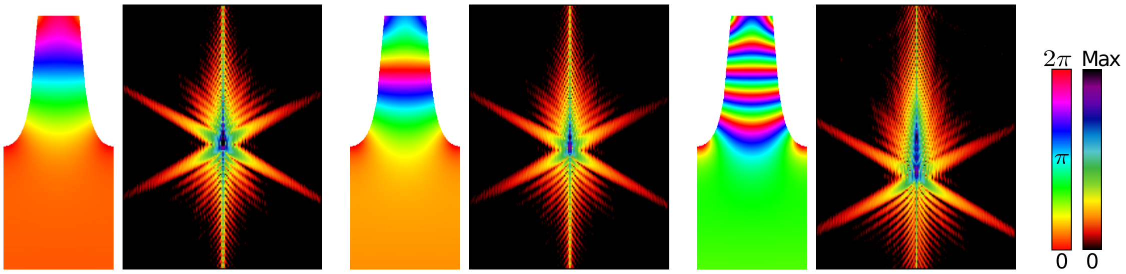

(a) $\epsilon_{\mathrm{M}} = 0.06\%$ (b) $\epsilon_{\mathrm{M}} = 0.10\%$ (c) $\epsilon_{\mathrm{M}} = 0.30\%$

Figure 7.4.: Phase field $\boldsymbol{Q}_{\mathrm{B}} \cdot \boldsymbol{u}(\boldsymbol{r})$ of the effective electron density $\varrho_{\mathrm{eff}}(\boldsymbol{r})$ (left image) and respective intensity distribution (log-scale) close to the Bragg reflection $(004)_{\mathrm{z} \frown \mathrm{c}}$ (right image) for our periodic array of Si-nanowires (see Fig. 7.3). The figures are labelled by the maximum strain ϵ_{M} on the symmetry axis of the wires inside the crystalline silicon domain. [phase field in Figs. (b) and (c): (©2013 The Optical Society (OSA), from [2])]

Direct space has been discretized by a regular rectangular grid with 232x798 pixels ($\mathrm{N}_{\mathrm{Tot}} = 185136$). The distance between two pixels is 0.862nm in x-direction and 1.575nm in z-direction. For the chosen truncation of the substrate the oversampling ratio σ is equal to 3.6326.

For this test object, the reconstruction procedure was terminated, if either $N_{\mathrm{Iter}} = 500$ iterations have been performed or the change of the iterative approximation from the current to the previous iteration as defined in Eq. (6.47) has dropped below 10^{-6} rad.

7.2. Shortcomings of the HIO+ER-algorithm

Before we extend the HIO+ER-algorithm in order to remedy its residual shortcomings, we first need to investigate these shortcomings.

The most important drawbacks of the HIO+ER-algorithm are:

- its breakdown already for rather weak strain,
- its strong sensitivity to the choice of the initial guess, and
- its sensitivity to the choice of its internal parameters N_{HIO} and N_{ER} which balance the tendency for escaping local minima (N_{HIO}) and for converging to the closest local minima (N_{ER}).

For a fixed initial guess, the traditional HIO+ER-algorithm does not involve random behavior. Consequently, for a fixed initial guess, the HIO+ER-algorithm either succeeds or fails. However, (uniformly distributed) *random* phases are typically incorporated for each measured amplitude $\Gamma_{\boldsymbol{Q}}$ in the initial guess of the reconstruction. Therefore, the HIO+ER-algorithm may succeed for some initial guesses, but fail for others. As a result, an investigation of the overall reconstruction procedure requires to consider the success rate $s \in [0\%, 100\%]$ as a statistical quantity which must be estimated from a large number of realizations for the initial guess ($\mathrm{N}_{\mathrm{Real}} \gg 1$). Unless stated otherwise, the success rate s is estimated from $\mathrm{N}_{\mathrm{Real}} = 100$ trials for the initial guess in this manuscript. If the reconstruction algorithm does not depend on the initial guess, the success rate s reduces to a binary function $s \in \{0; 1\}$. Any good reconstruction algorithm should reach a success rate close to 100% within a practical number of iterations N_{Iter}.

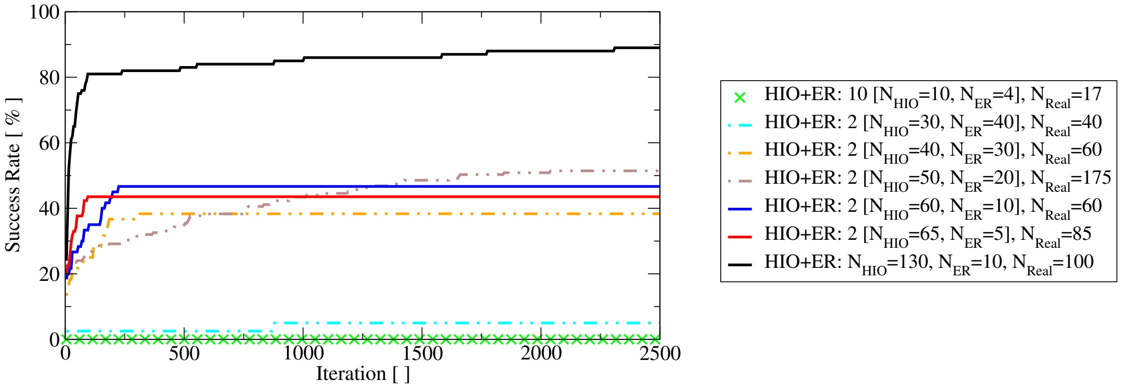

Figure 7.5.: Sensitivity of the HIO+ER-algorithm to the initial guess and its internal parameters N_{HIO} and N_{ER}.

In Fig. 7.5, we depict the success rate s as a function of the number of iterations of the HIO+ER-algorithm for various combinations of the internal parameters N_{HIO} and N_{ER}. β has been set to 0.85.

In order to compare the various combinations of the internal parameters N_{HIO} and N_{ER}, the computational effort (approximated by the number of Fourier transforms) has been normalized to the case $N_{\text{HIO}} = 130$ and $N_{\text{ER}} = 10$. Consequently, ten iterations with $N_{\text{HIO}} = 10$ and $N_{\text{ER}} = 4$ have the same computational effort as a single iteration with $N_{\text{HIO}} = 130$ and $N_{\text{ER}} = 10$. The respective prefactor p of this normalization is given before the square brackets in the legend.

From this figure, we can draw several very important conclusions: First, the success rate is far from being a binary function $s \in \{0; 1\}$ even after the large number of $p \cdot 2500$ iterations. Consequently, the HIO+ER-algorithm strongly depends on the random initial guess. Second, the choice of the internal parameters N_{HIO} and N_{ER} strongly influences the success rate. Third, the dependence on N_{HIO} and N_{ER} is non-trivial: For example, we can compare the two cases $N_{\text{HIO}} = 130$ and $N_{\text{ER}} = 10$ and $N_{\text{HIO}} = 65$ and $N_{\text{ER}} = 5$. Both parameters have been rescaled by the same factor 2. Consequently, the fraction of the building blocks HIO and ER during execution is equal. Nonetheless, the success rate differs strongly. Moreover, we can focus on the five depicted cases with $N_{\text{HIO}} + N_{\text{ER}} = 70$. None of these cases exceeds a success rate of $s = 55\%$. The influence of the choice of N_{HIO} and N_{ER} seems comparably weak in this case: In the range $N_{\text{HIO}} = 40 \ldots 65$, the success rate s after $2 \cdot 2500$ iterations is very similar. For $N_{\text{HIO}} = 30$, we however see a breakdown of the HIO+ER-algorithm.

We point out that this information does not reveal any information on the failed initial trials. Most importantly, we have to consider two possibilities for these trails: First, such a trial could have converged, but not to the solution ϱ_{eff}. Second, it could have stagnated. This stagnation on the level of a single reconstruction refers to a very small decrease of the error metric from one iteration to the next iteration for a large number of successive iteration. Nevertheless, this should not be confused with convergence to a local minima mathematically, although practically both situations may be hardly distinguishable in some cases.

If the success rate remains on a certain plateau for a large number of iterations, we also refer to this situation as stagnation, since some initial trails might still converge after a large number of iterations (see for example $N_{\text{HIO}} = 130$ and $N_{\text{ER}} = 10$ in Fig. 7.5). It will always be clear from the context or explicitly stated, if we refer to stagnation of a single initial guess or to stagnation of the success rate s.

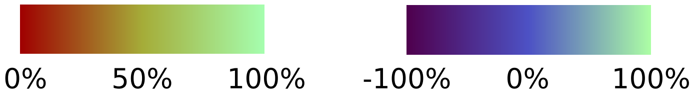

(a) Single success rate s (b) Comparison $s_2 - s_1$

Figure 7.6.: Colorbars for encoding the success rate s (Fig. (a)) or comparisons thereof (Fig. (b)). (©2013 The Optical Society (OSA), from [2])

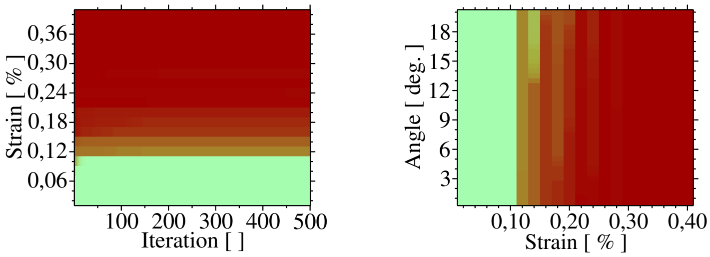

(a) Criterion for success $\varphi^{(i)} \leq \varphi_{\mathrm{Max}} = 1.0°$ (b) Result after $i = 500$ iterations

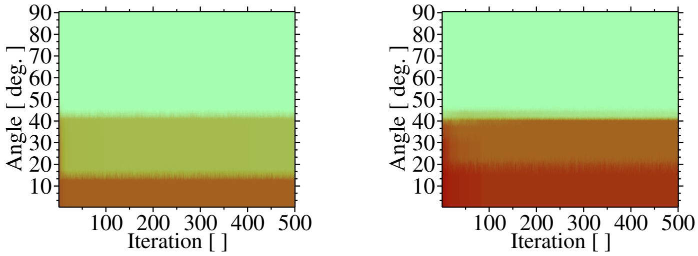

(c) Strain $\epsilon_{\mathrm{M}} = 0.14\%$ (d) Strain $\epsilon_{\mathrm{M}} = 0.16\%$

Figure 7.7.: Reconstruction capabilities of the traditional HIO+ER-algorithm. The discretization step in direction of strain ϵ_{M} is $\delta\epsilon_{\mathrm{M}} = 0.02\%$. The colorbar for all plots is given in Fig. 7.6(a). (©2013 The Optical Society (OSA), from [2])

For comparison, we now apply the HIO+ER-algorithm to our Si nanowire (see Sec. 7.1). Instead of the sensitivity on the internal parameters N_{HIO} and N_{ER}, we now focus on the dependence on the strain ϵ_{M}, the number of iterations i which has been performed and the choice for the success criterion φ_{Max} which is used to distinguish successful reconstructions from failed reconstructions based on Eq. (6.48). For this, we depict two-dimensional cuts from this three dimensional parameter space. The success rate s is encoded by color. The color scheme is identical in all those two-dimensional cuts and given in Fig. 7.6. Fig. 7.6(a) is employed for the range 0% to 100% of the success rate s, whereas Fig. 7.6(b) encodes values of -100% to 100%. The latter is used for comparisons of the success rates of two different cases. The parameters N_{HIO}, N_{ER}, and β of the reconstructions were chosen as $N_{\mathrm{HIO}} = 130$, $N_{\mathrm{ER}} = 10$, and $\beta = 0.8$.

Some results of our simulations are depicted in Fig. 7.7 where ϵ_{M} was sampled in the range 0.02% to 0.40% in steps $\delta\epsilon_{\mathrm{M}} = 0.02\%$.

If we consider all random initial trails as success for which the angle $\varphi^{(i)}$ to the reference solution ϱ_{eff} is below $\varphi_{\mathrm{Max}} = 1.0°$ in iteration (i), all trials converged to the solution within very few iterations up to a maximum strain $\epsilon_{\mathrm{M}} = 0.10\%$ (see Fig. 7.7(a)). However, for larger strain ϵ_{M}, the success rate drops rapidly. For $\epsilon_{\mathrm{M}} = 0.12\%$, the success rate already dropped to $s = 38\%$. For $\epsilon_{\mathrm{M}} > 0.20\%$, success rate is essentially equal to zero.

These observations are rather insensitive to the particular choice of the value $\varphi_{\mathrm{Max}} = 1.0°$

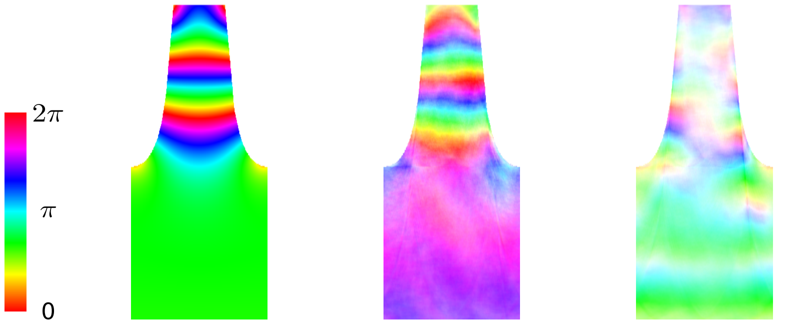

(a) Successful reconstruction (very rare)

(b) Reconstruction with $\varphi \approx 20°$ after 500 iterations ("close to solution")

(c) Reconstruction with $\varphi \approx 40°$ after 500 iterations ("failed reconstruction")

Figure 7.8.: Reconstruction capabilities of the traditional HIO+ER-algorithm for $\epsilon_{\mathrm{M}} = 0.16\%$. The phase field and magnitude are encoded by HSV colorbar (phase encoding identical to Figs. 7.1 and 7.4).

for separating successful and not successful reconstructions in Fig. 7.7(a). This can be seen in Fig. 7.7(b) which illustrates the success rate as function of this angle and strain. Almost no initial guess came even close ($\varphi_{\mathrm{Max}} \leq 20°$) to the solution ϱ_{eff} for $\epsilon_{\mathrm{M}} > 0.2\%$.

In the intermediate range $0.10\% < \epsilon_{\mathrm{M}} \leq 0.20\%$, we can identify at least two pronounced levels of stagnation, most noticeably at approximately $\varphi = 13°$ for $\epsilon_{\mathrm{M}} = 0.14\%$ (see Figs. 7.7(b) and 7.7(c)). For $\epsilon_{\mathrm{M}} = 0.18\%$ and in iteration $i = 500$, $s = 12\%$ of the initial trials dropped below the level of $\varphi_{\mathrm{Max}} = 1.0°$. If we require only the weaker constraint $\varphi_{\mathrm{Max}} = 5.0°$ for a successful reconstruction, $s = 22\%$ of the initial trials have been successful. In other words: 10% of the random initial guesses stagnated at the distance of 4.0° to the solution ϱ_{eff}.

This stagnation becomes more evident in Figs. 7.7(c) and 7.7(d): here, the success rate s is depicted as a function of iteration and the full range of possible angles $\varphi_{\mathrm{Max}} \in [0°, 90°]$ for fixed strain ($\epsilon_{\mathrm{M}} = 0.14\%$ and $\epsilon_{\mathrm{M}} = 0.16\%$). For both values of strain, we observe two pronounced levels of stagnation. Once a reconstruction performed with the traditional HIO+ER-algorithm stagnates, the mean number of iterations that the iterative procedure stagnates is very high, *even if this level is far from the solution* ϱ_{eff}. For illustration, we depict a typical result of a successful reconstruction as well as the output of reconstructions with an error of $\varphi \approx 20°$ and $\varphi \approx 40°$ after $i = 500$ iterations in Fig. 7.8.

Based on the results and discussion in this section on the shortcomings of the traditional HIO+ER-algorithm, we modify the HIO+ER-algorithm in the next section. These modifications will significantly reduce the sensitivity to the random initial guess and the internal parameters N_{HIO} and N_{ER}. Moreover, these modifications increase the maximum strain ϵ_{M} which can be reconstructed successfully.

7.3. Elimination of stagnation by randomization

The origin of the shortcomings in projection based phase retrieval algorithms such as the HIO+ER-algorithm are the mathematical properties of the projection operator $\mathbf{P}_{\Gamma}$: Its non-convexity allows for the existence of traps and tunnels [208] during iterative optimization or minimization schemes.

In this section, we aim to avoid stagnation or local minima other than the global minimum by randomization *during* the iterative reconstruction. This randomization is performed such that the solution ϱ_{eff} – the fix point of the iterative procedure – remains a fix point irrespective of this randomization. However, by randomization of the iterative procedure, we hope to change the traps and tunnels from iteration to iteration. Consequently, "convergence" and stagnation in such "non-static" traps and tunnels is no longer possible – in contrast to the solution ϱ_{eff} which remains a "static" fix point of the iterative procedure.

Marchesini demonstrated in Ref. [207] that for his particular numerical example an additional low-dimensional subspace saddle-point optimization was also able to overcome stagnation of the traditional HIO+ER-algorithm. In our approach, such additional optimization procedures are not required.

As a consequence of our approach, random numbers influence the reconstruction at two stages: first, the initial guess itself is based on random phases for the given amplitudes Γ, and, second, for algorithms that exploit randomization during reconstruction, the iterative approximation to the solution varies for each repeated instance of the reconstruction *even for the same initial trial.*

In this section we pursue two approaches for such a randomization:

1. We exploit the concept of overrelaxation [208, 209, 224] and substitute the projection operator $\mathbf{P}_\Gamma$ in the HIO-operator by its overrelaxed analogue

   $$\mathbf{Q}_{\Gamma;\lambda_\Gamma} = 1 + \lambda_\Gamma \left(\mathbf{P}_\Gamma - 1\right) \ . \tag{7.3}$$

   The direct space assembly in Eq. (6.52a) of the HIO-algorithm remains unchanged. Since we have $\mathbf{Q}_{\Gamma;\lambda_\Gamma} = \mathbf{P}_\Gamma = 1$ for the solution $\varrho_{\text{eff}}(\boldsymbol{r})$ (irrespective of the value for the *relaxation parameter* λ_Γ) randomization of λ_Γ seems promising for achieving "non-static" traps and tunnels. Consequently, the relaxation parameter λ_Γ is drawn *each iteration* of the HIO-algorithm from a uniform random distribution in the interval $[1-\nu, 1+\nu]$, $\nu \geq 0$. Unless stated otherwise, we choose $\nu = 0.5$.

   The limiting case $\mathbf{Q}_{\Gamma;\lambda_\Gamma} \to \mathbf{P}_\Gamma$ is obtained for $\lambda_\Gamma \to 1$ (equivalent to $\nu \to 0$) which corresponds to the traditional HIO+ER-algorithm.

2. We randomize some coefficients in projection polynomial $\hat{H}_{\text{HIO}}$ of the HIO-algorithm. For this purpose, we split the coefficients $c_{\xi,n}$, $\xi \in \{\Omega, \Gamma\}$, $n \geq 1$, in Eq. (6.45a) in a deterministic part $c_{\xi,n}^{(D)}$ and a random part $r_{\xi,n}\, c_{\xi,n}^{(R)}$, i.e.,

   $$c_{\xi,n} = c_{\xi,n}^{(D)} + r_{\xi,n}\, c_{\xi,n}^{(R)} \ . \tag{7.4}$$

   Here, we set the deterministic contribution $c_{\xi,n}^{(D)}$ equal to the traditional HIO-algorithm (see Eq. (6.52c)). $r_{\xi,n}$ is uniformly distributed in the range $[-1, 1]$. The reconstructions contains randomization if at least one coefficient $c_{\xi,n}^{(R)}$ is non-zero. In this approach, Eq. (6.45b) guarantees that the solution ϱ_{eff} remains a fixed point of the iterative procedure irrespective of the randomization.

We point out that overrelaxation without randomization has been investigated for convex problems [209] and in connection with the ER-algorithm for phase retrieval [208]. Moreover, overrelaxation is also included in the difference map algorithm proposed by Elser in Ref. [224]. In the difference map algorithm with overrelaxation, the iterative step for our set of constraints is given by [203]

$$\varrho_{\text{eff}}^{(i+1)}(\boldsymbol{r}) = \left[1 + \beta \left(\mathbf{P}_\Omega \mathbf{Q}_{\Gamma;\lambda_\Gamma} - \mathbf{P}_\Gamma \mathbf{Q}_{\Omega;\lambda_\Omega}\right)\right] \varrho_{\text{eff}}^{(i)}(\boldsymbol{r}) \equiv \hat{H}_{\text{Diff}}(\beta, \lambda_\Gamma, \lambda_\Omega) \varrho_{\text{eff}}^{(i)}(\boldsymbol{r}) \ , \tag{7.5}$$

where Elser proposes to choose the relaxation parameters as $\lambda_\Gamma = \lambda_\Omega = \beta^{-1}$ [224]. However, as will be shown, *randomization* turned out to be indispensable for overcoming stagnation in the traditional HIO+ER-algorithm.

A comparison of both approaches can also be nicely performed in the framework of projection polynomials.

The replacement Eq. (7.3) of the (non-linear and non-convex) projection operator $\mathbf{P}_\Gamma$ in reciprocal space in the HIO-algorithm corresponds to changing Eq. (6.52c) to

$$\varrho_{\text{eff}}^{(i+1)}(\boldsymbol{r}) = \left[1 - \mathbf{P}_\Omega - \beta\mathbf{Q}_{\Gamma;\lambda_\Gamma} + (1+\beta)\,\mathbf{P}_\Omega\mathbf{Q}_{\Gamma;\lambda_\Gamma}\right]\varrho_{\text{eff}}^{(i)}(\boldsymbol{r}) \equiv \hat{H}_{\text{HIO+O}_\text{R}}(\beta,\lambda_\Gamma)\varrho_{\text{eff}}^{(i)}(\boldsymbol{r}) \; . \tag{7.6}$$

Here, we defined the operator $\hat{H}_{\text{HIO+O}_\text{R}}(\beta,\lambda_\Gamma)$ of the $\text{HIO}_{\text{O}_\text{R}}$-algorithm.

If we exploit the *linearity* of $\mathbf{P}_\Omega$, we can re-express the operator polynomial (7.6) as a projection polynomial in the original projection operators $\mathbf{P}_\Omega$ and $\mathbf{P}_\Gamma$ as

$$\hat{H}_{\text{HIO+O}_\text{R}}(\beta,\lambda_\Gamma) \equiv [1 + \beta\,(\lambda_\Gamma - 1)] + [\beta - \lambda_\Gamma - \beta\lambda_\Gamma]\,\mathbf{P}_\Omega - \beta\lambda_\Gamma\mathbf{P}_\Gamma + [(1+\beta)\lambda_\Gamma]\,\mathbf{P}_\Omega\mathbf{P}_\Gamma \; . \tag{7.7a}$$

For the subsequent discussions, it is useful to split the contribution of the traditional HIO+ER-algorithm ($\lambda_\Gamma = 1$) from the modifications induces by overrelaxation. For that purpose, we substitute $\lambda_\Gamma = 1 + \gamma_\Gamma$ and obtain

$$\begin{aligned} \hat{H}_{\text{HIO+O}_\text{R}}(\beta,\lambda_\Gamma = 1+\gamma_\Gamma) = [1 + \beta\gamma_\Gamma] + [-1 - \gamma_\Gamma(1+\beta)]\,\mathbf{P}_\Omega + \\ [-\beta(1+\gamma_\Gamma)]\,\mathbf{P}_\Gamma + [(1+\beta)(1+\gamma_\Gamma)]\,\mathbf{P}_\Omega\mathbf{P}_\Gamma \; . \end{aligned} \tag{7.7b}$$

Hence, γ_Γ is distributed uniformly in $[-\nu,\nu]$.

The deviation $\beta\gamma_\Gamma = \beta\,(\lambda_\Gamma - 1)$ from the identity operator in the first term can neither be represented by the traditional HIO-algorithm for any value of β (see Eq. (6.52c)) nor by the difference map algorithm for any combination of values for β, λ_Γ, and λ_Ω (see Eq. (7.5)). In both cases, the previous iterative result $\varrho_{\text{eff}}^{(i)}(\boldsymbol{r})$ is weighted with 1 or projected at least once either in direct space (by $\mathbf{P}_\Omega$) or in reciprocal space (by $\mathbf{P}_\Gamma$) before being included in the calculation of the next approximative solution $\varrho_{\text{eff}}^{(i+1)}(\boldsymbol{r})$.

From these projection polynomials, we can read of the coefficients

$$b = 1 + \beta\,(\lambda_\Gamma - 1) = 1 + \beta\gamma_\Gamma \; , \tag{7.8a}$$

$$c_{\Omega,1} = \beta - \lambda_\Gamma - \beta\lambda_\Gamma = -1 - \gamma_\Gamma(1+\beta) \; , \tag{7.8b}$$

$$c_{\Omega,2} = (1+\beta)\lambda_\Gamma = (1+\beta)(1+\gamma_\Gamma) \; , \tag{7.8c}$$

$$c_{\Gamma,1} = -\beta\lambda_\Gamma = -\beta(1+\gamma_\Gamma) \; , \tag{7.8d}$$

$$c_{\Gamma,2} = 0 \tag{7.8e}$$

in the projection polynomial

$$\hat{H}_{\text{Proj}}(b, c_{\Omega,1}, c_{\Omega,1}, c_{\Gamma,1}, c_{\Gamma,2}) \equiv b\,1 + c_{\Omega,1}\mathbf{P}_\Omega + c_{\Gamma,1}\mathbf{P}_\Gamma + c_{\Omega,2}\mathbf{P}_\Omega\mathbf{P}_\Gamma + c_{\Gamma,2}\mathbf{P}_\Gamma\mathbf{P}_\Omega \; , \tag{7.8f}$$

of the $\text{HIO}_{\text{O}_\text{R}}$-algorithm. We point out, that these coefficients fulfill the constraint $b = 1 - \sum_{n=1}^{2}\left[c_{n,\Omega} + c_{n,\Gamma}\right]$ by construction (see Eq. (6.45b)).

Also by construction, the deterministic contribution $c_{\xi,n}^{(D)}$ (for $\gamma_\Gamma = 0$) reproduces the traditional HIO-algorithm (see Eq. (6.52c))

$$c_{\Omega,1}^{(D)} = -1 \; , \quad c_{\Gamma,1}^{(D)} = -\beta \; , \quad c_{\Omega,2}^{(D)} = 1 + \beta \; , \quad c_{\Gamma,2}^{(D)} = 0 \; . \tag{7.9}$$

The coefficients $c_{\xi,n}^{(R)}$ in Eq. (7.4) however are not constant, but parametrized by ν and β. Specifically, we find

$$c_{\Omega,1}^{(R)} = -\nu(1+\beta) \; , \quad c_{\Gamma,1}^{(R)} = -\nu\beta \; , \quad c_{\Omega,2}^{(R)} = \nu(1+\beta) \; , \quad c_{\Gamma,2}^{(R)} = 0 \; . \tag{7.10}$$

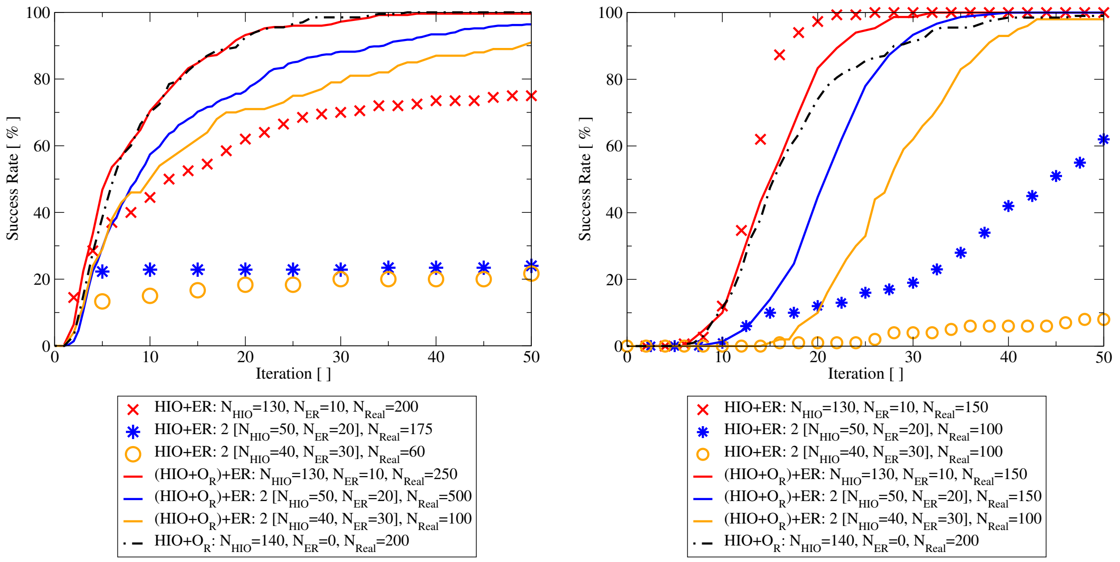

(a) First phase object defined in Eq. (7.2a).

(b) Second phase object defined in Eq. (7.2b).

Figure 7.9.: Comparison of the success rate s of reconstructions of the pure phase objects defined by Eqs. (7.1), (7.2a) and (7.2b) (see Fig. 7.1) with the HIO+ER- and the $\text{HIO}_{\text{O}_\text{R}}$+ER-algorithm. The parameter β was fixed to 0.85. Continuous lines represent results of the $\text{HIO}_{\text{O}_\text{R}}$+ER-algorithm, isolated dots of the HIO+ER-algorithm. A pure $\text{HIO}_{\text{O}_\text{R}}$-calculation without ER is included as black, dash-dotted curve. (©2012 The Optical Society (OSA), from [1])

For $\nu \to 0$, the amplitudes $c^{(R)}_{\xi,n}$ of the randomization vanish and we obtain again the traditional HIO+ER-algorithm. In addition to these correlations in $c^{(R)}_{\xi,n}$, we only have a *single* common random number $r = r_{\xi,n}$ for all coefficients. Consequently, the random contributions are not statistically independent, but highly correlated.

This is in strong contrast to a statistically independent randomization of each coefficient $c_{\xi,n}$ separately: These correlations in $c^{(R)}_{\xi,n}$ and $r_{\xi,n}$ induced by overrelaxation are absent, if we set some coefficients $c^{(R)}_{\xi,n} \neq 0$ and draw statistically independent random values $r_{\xi,n}$.

This way, we can distinguish whether the benefits from randomization require the precise correlations induced by overrelaxation or if other approaches for randomization are similarly successful. For the same purpose, we will also consider the overrelaxation (7.3) with a pre-defined fixed relaxation parameter λ_Γ throughout the entire iterative reconstruction.

If we apply the concept (7.3) to our model systems (see Sec. 7.1), we obtain the results depicted in Fig. 7.9 for the two analytically defined pure phase objects (see Fig. 7.1) and in Fig. 7.2 for the real valued test object with strong amplitude variation on short length scales and weak contrast at the edge of the support (see Fig. 7.2). Every trial has its own random initial guess and its own set of random overrelaxation parameters λ_Γ.

Again, for the traditional HIO+ER-algorithm, we observe stagnation and a strong influence of the choice of the internal parameters N_{HIO} and N_{ER} (see also Fig. 7.5). In contrast, the incorporation of randomization ($\text{HIO}_{\text{O}_\text{R}}$+ER-algorithm) succeeds in overcoming stagnation for these three test objects as well as strongly reducing the sensitivity to the choice of the internal parameters N_{HIO} and N_{ER}. For all choices of these parameters, the success rate s is close to 100% after few iterations. Here, the number of iterations for the different parameters N_{HIO} and N_{ER} is again normalized with respect to the case $N_{\text{HIO}} = 130$ and $N_{\text{ER}} = 10$ as described for Fig. 7.5. The recon-

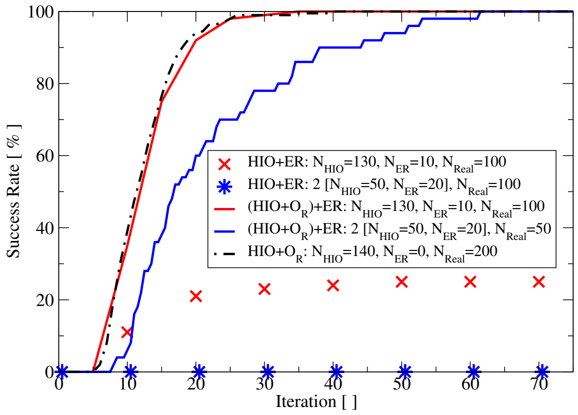

Figure 7.10.: Comparison of the success rate s of reconstructions of the purely real test object with strong variation of its magnitude over short length scales and weak contrast at the edge of the support (see Fig. 7.2) with the HIO+ER- and the HIO$_{\mathrm{O_R}}$+ER-algorithm. The parameter β was fixed to 0.8. Continuous lines represent the HIO$_{\mathrm{O_R}}$+ER-algorithm, isolated dots the HIO+ER-algorithm. A pure HIO$_{\mathrm{O_R}}$-calculation without ER is included as black, dash-dotted curve. (©2012 The Optical Society (OSA), from [1])

struction with the HIO$_{\mathrm{O_R}}$+ER-algorithm was even successful if the success rate of the HIO+ER-algorithm was close to zero (for example: $(N_{\mathrm{HIO}}, N_{\mathrm{ER}}) = (50, 20)$ in Fig. 7.10 or $(N_{\mathrm{HIO}}, N_{\mathrm{ER}}) = (40, 30)$ in Fig. 7.9(b)). Moreover, very good performance has also been observed if no ER has been included (HIO$_{\mathrm{O_R}}$-algorithm). Only for the second phase object (Fig. 7.9(b)) and the choice $(N_{\mathrm{HIO}}, N_{\mathrm{ER}}) = (130, 10)$, the traditional HIO+ER-algorithm performed slightly better than the HIO$_{\mathrm{O_R}}$+ER- or HIO$_{\mathrm{O_R}}$-algorithm. In all other cases, we observe significant improvements as a consequence of the incorporation of randomized overrelaxation.

We point out that the behavior of those initial guesses which did not reach the criterion for success ($\varphi^{(i)} \leq 0.05°$; see Eq. (6.48)) is different for these three test objects: Whereas the failed reconstruction of the second phase object (Fig. 7.9(b)) and the real valued test object (Fig. 7.10) are typically at least close to the solution ϱ_{eff} (angles $\varphi^{(i)} \leq 5°$) and plagued by very persistent stripe artifacts, the failed reconstructions of the first phase object (Fig. 7.9(a)) are far from the solution ϱ_{eff} (angles $\varphi^{(i)} \geq 55°$).

Before we study these results in more detail, we also apply the HIO$_{\mathrm{O_R}}$+ER-algorithm to the simulated Si-nanowires (see Sec. 7.1) and compare the results to the HIO+ER-algorithm (see Fig. 7.7).

Fig. 7.11(a) is the direct analogue to Fig. 7.7(a) after incorporation of randomized overrelaxation. For better comparison, the difference of the success rate of those two cases is directly given in Fig. 7.11(b). Strong advantage of the HIO$_{\mathrm{O_R}}$+ER-algorithm in comparison to the HIO+ER-algorithm is observed in the range $\epsilon_{\mathrm{M}} = 0.12\%$ to $\epsilon_{\mathrm{M}} = 0.28\%$. Here, the HIO$_{\mathrm{O_R}}$+ER-algorithm is clearly superior to the traditional HIO+ER-algorithm. Successful reconstructions are achieved independent of the random initial guess with a success probability close to 100% within $i = 500$ iterations. In the range $\epsilon_{\mathrm{M}} \leq 0.10\%$, no negative penalty of randomized overrelaxation has been discovered. Consequently, the incorporation of randomized overrelaxation shifted the maximum strain ϵ_{M} which could be reconstructed successfully towards higher values. At the same time, the influence of the initial guess is reduced tremendously.

Figs. 7.11(c) to 7.11(f) are the analogue of Figs. 7.7(c) and 7.7(d) which were devoted to the traditional HIO+ER-algorithm. These figures nicely illustrate the ability of the

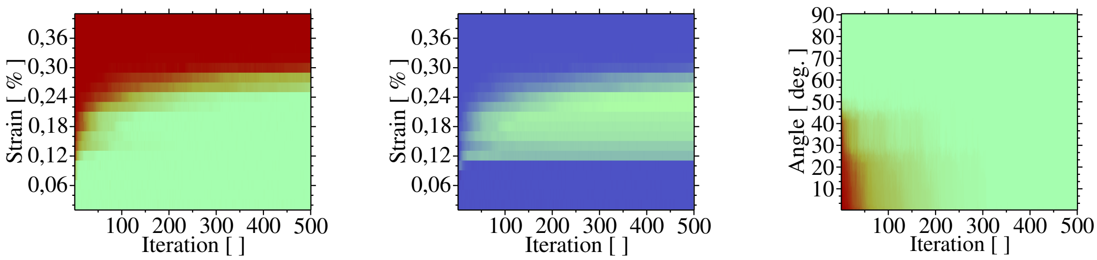

(a) Criterion for success $\varphi^{(i)} \leq \varphi_{\mathrm{Max}} = 1.0°$ (©2013 The Optical Society (OSA), from [2])

(b) Comparison to the classical HIO+ER-algorithm (Fig. 7.7(a))

(c) Strain $\epsilon_{\mathrm{M}} = 0.22\%$ (©2013 The Optical Society (OSA), from [2])

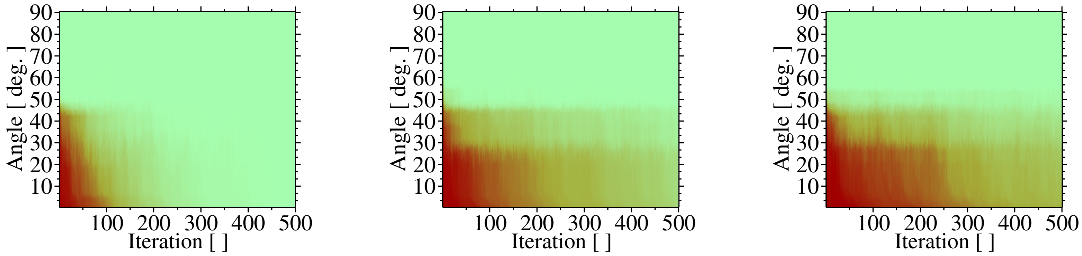

(d) Strain $\epsilon_{\mathrm{M}} = 0.24\%$ (©2013 The Optical Society (OSA), from [2])

(e) Strain $\epsilon_{\mathrm{M}} = 0.26\%$ (©2013 The Optical Society (OSA), from [2])

(f) Strain $\epsilon_{\mathrm{M}} = 0.28\%$

Figure 7.11.: Reconstruction capabilities of the $\mathrm{HIO}_{\mathrm{O_R}}$+ER-algorithm for the Si-nanowires depicted in Figs. 7.3 and 7.4. The discretization step in direction of strain ϵ_{M} is $\delta\epsilon_{\mathrm{M}} = 0.02\%$. The colorbar for all plots except (b) is given in Fig. 7.6(a). The colorbar for Fig. (b) is given by Fig. 7.6(b).

$\mathrm{HIO}_{\mathrm{O_R}}$+ER-algorithm to escape from stagnation more successfully than the traditional HIO+ER-algorithm. Moreover, they illustrate the breakdown of the reconstruction process with increasing strain: We observe that with increasing strain the number of iterations which is required to escape from stagnation by randomized overrelaxation is increasing more and more. Nevertheless, the characteristics near the breakdown of the $\mathrm{HIO}_{\mathrm{O_R}}$+ER-algorithm is clearly different from the breakdown behavior of the traditional HIO+ER-algorithm.

However, for strain $\epsilon_{\mathrm{M}} > 0.30\%$, almost no random initial trial succeeded in coming close to the solution $\varrho_{\mathrm{eff}}(\boldsymbol{r})$ after $i = 500$ iterations, even if randomized overrelaxation is incorporated. In order to extent the applicability to higher values of ϵ_{M}, we will investigate possible benefits from additional physical knowledge which allows to constrain the local magnitude of the effective electron density $|\varrho_{\mathrm{eff}}(\boldsymbol{r})|$ in Sec. 7.4. Before, we investigate the modification (7.3) in the HIO+ER-algorithm more detailed.

First, we investigate the sensitivity of the $\mathrm{HIO}_{\mathrm{O_R}}$+ER-algorithm on the choice of its internal parameters other than N_{HIO} and N_{ER}. Therefore, we depict in Fig. 7.12 the sensitivity of the $\mathrm{HIO}_{\mathrm{O_R}}$+ER-algorithm on the choice of the parameter β (feedback parameter) (see Fig. 7.12(a)) and on the bounds of the uniform distribution for the relaxation parameter λ_Γ for the first phase object which has been defined in Eq. (7.2a) (see Fig. 7.12(b)).

The star symbols in Fig. 7.12(a) correspond to the traditional HIO+ER-algorithm ($\nu = 0$) and the continuous blue line to the value $\nu = 0.5$ which is employed if not specified otherwise. After same transient behavior ($\nu \lesssim 0.3$) the success rate s is almost independent of the value for ν in the range $\nu = 0.4$ to $\nu = 0.6$. As for the traditional HIO+ER-algorithm, the influence of the parameter β is minor in the range $\beta \in (0.65, 0.85)$. Consequently, the $\mathrm{HIO}_{\mathrm{O_R}}$+ER is also robust to changes of the parameters β and ν.

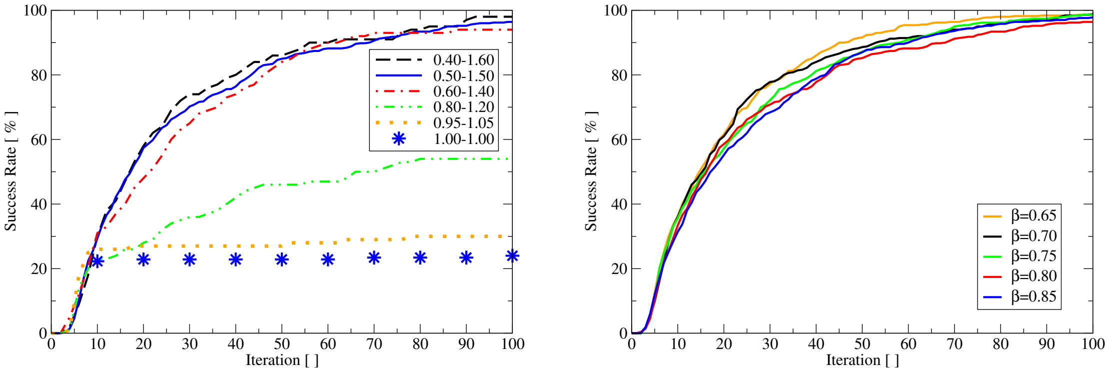

(a) Dependence of the success rate on the bounds of a uniformly distributed relaxation parameter λ_Γ.

(b) Dependence of the success rate on the parameter β of the $\mathrm{HIO}_{\mathrm{O_R}}$+ER-algorithm.

Figure 7.12.: Investigation of the sensitivity of the $\mathrm{HIO}_{\mathrm{O_R}}$+ER-algorithm on the choice of the parameter β (feedback parameter) and on the bounds of the uniform distribution for the relaxation parameter λ_Γ for the first phase object (defined in Eq. 7.2a). The parameters N_{HIO} and N_{ER} have been set to $N_{\mathrm{HIO}} = 50$ and $N_{\mathrm{ER}} = 20$. (©2012 The Optical Society (OSA), from [1])

Fig. 7.13 demonstrates that randomization of the relaxation parameter is essential for overcoming the shortcomings of the traditional HIO+ER-algorithm: overrelaxation with a *fixed* relaxation parameter λ_Γ typically even decreases the performance of the HIO+ER-algorithm. For a deviation of λ_Γ greater than ten percent from $\lambda_\Gamma = 1.00$, almost no successful reconstructions have been observed for any of the three test objects. However, the strong dependence of the results on the precise choice of the value of λ_Γ is an indication that the traps and tunnels induced by the non-convex projection operator $\mathbf{P}_\Gamma$ in reciprocal space can indeed be influenced by overrelaxation – as has been argued at the beginning of this section. Consequently, it is interesting to investigate whether other modifications of the iterative operator $\hat{H}_{\mathrm{HIO}}$ (see Eq. (6.52c)) such as Eq. (7.4) provide similar benefits in combination with randomization or if these benefits rely on the specific mathematical features of overrelaxation (see Eq. (7.10)).

For that, we investigate the approach defined by Eq. (7.4) for three sets of coefficients:

$$\begin{array}{llll} c^{(D)}_{\Omega,1} = -1.0 & c^{(D)}_{\Omega,2} = 1.85 & c^{(D)}_{\Gamma,1} = -0.85 & c^{(D)}_{\Gamma,2} = 0.0 \\ c^{(R)}_{\Omega,1} = 0.2 & c^{(R)}_{\Omega,2} = 0.2 & c^{(R)}_{\Gamma,1} = 0.2 & c^{(R)}_{\Gamma,2} = 0.2 \end{array} \tag{7.11a}$$

$$\begin{array}{llll} c^{(D)}_{\Omega,1} = -1.3 & c^{(D)}_{\Omega,2} = 1.5 & c^{(D)}_{\Gamma,1} = -0.5 & c^{(D)}_{\Gamma,2} = 0.3 \\ c^{(R)}_{\Omega,1} = 0.2 & c^{(R)}_{\Omega,2} = 0.2 & c^{(R)}_{\Gamma,1} = 0.1 & c^{(R)}_{\Gamma,2} = 0.1 \end{array} \tag{7.11b}$$

$$\begin{array}{llll} c^{(D)}_{\Omega,1} = -1.0 & c^{(D)}_{\Omega,2} = 1.3 & c^{(D)}_{\Gamma,1} = -0.3 & c^{(D)}_{\Gamma,2} = 0.0 \\ c^{(R)}_{\Omega,3} = 0.1 & c^{(R)}_{\Omega,4} = 0.1 & c^{(R)}_{\Gamma,3} = 0.1 & c^{(R)}_{\Gamma,4} = 0.1 \end{array} \tag{7.11c}$$

All parameters which are not listed – except b which is defined by Eq. (6.45) – are zero. The respective results are depicted in Fig. 7.14.

The deterministic contribution in Eq. (7.11a) is given by the traditional HIO-algorithm (see Eq. (7.9)) for $\beta = 0.85$, whereas the amplitudes $c^{(R)}_{\Omega,1}$, $c^{(R)}_{\Gamma,1}$, $c^{(R)}_{\Omega,2}$, and $c^{(R)}_{\Gamma,2}$ for the randomized contribution are all set equal to $c^{(R)} = 0.2$. Consequently, it is useful for judging on the importance of the correlations in Eq. (7.10).

For the parameters (7.11b), the deterministic contribution has been slightly modified and can no longer be mapped to the traditional HIO-algorithm. Moreover, the noise amplitudes $c^{(R)}_{\Gamma,1}$ and $c^{(R)}_{\Gamma,2}$ have been decreased.

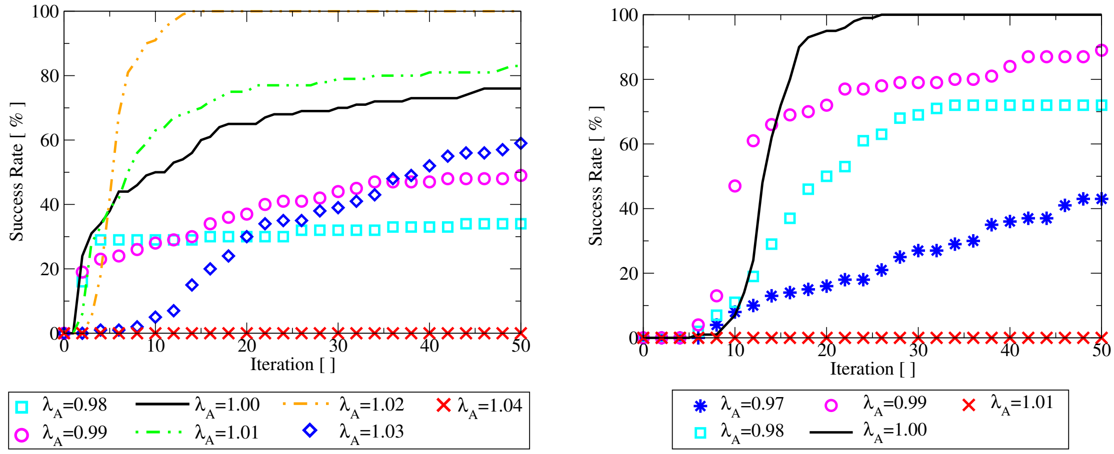

(a) First phase object defined in Eq. (7.2a).

(b) Second phase object defined in Eq. (7.2b).

Figure 7.13.: Success rate of the HIO+ER-algorithm modified by overrelaxation with *fixed* relaxation parameter λ_Γ (no randomization). The parameters are set to $N_{\mathrm{HIO}} = 130$, $N_{\mathrm{ER}} = 10$ and $\beta = 0.85$. (©2012 The Optical Society (OSA), from [1])

Finally, the deterministic contribution in Eq. (7.11c) corresponds to the traditional HIO-algorithm for $\beta = 0.3$. However, randomization is here included only in coefficients $c_{\xi,n}$ with $n > 2$ – in strong contrast to the randomization based on overrelaxation. Consequently, the random contribution differs strongly from the case of randomized overrelaxation and Eqs. (7.11a) and (7.11b).

For none of the sets of parameters defined in Eq. (7.11), we observe stagnation for any of our test objects in Fig. 7.14. However, performance of the different parameter sets differs: Whereas the parameters (7.11a) are equally efficient as randomized overrelaxation, the other two set of parameters are less efficient than $\mathrm{HIO}_{\mathrm{O_R}}$-based reconstructions, in particular for the second phase object and the purely real test object. The worst performance on average is observed if the deterministic coefficients no longer coincide with the traditional HIO+ER-algorithm. Consequently, such deviations should be avoided without good reason. Although randomization of the coefficients $c_{\xi,n}$ with $n > 2$ is also capable of overcoming stagnation, randomization of the coefficients $c_{\xi,n}$ with $n \leq 2$ seems more efficient. Finally, we observe that the correlations contained in Eq. (7.10) seem of minor importance for the benefits which are achieved by randomization of the HIO-algorithm.

The latter point however is important if we consider computational efficiency and simplicity of implementation of the reconstruction algorithms and their number of free internal parameters: In comparison to a randomization of the coefficients $c_{\xi,n}$, $\xi \in \{\Omega, \Gamma\}$, $n \geq 1$, (see Eqs. (6.45a) and (7.4)), the $\mathrm{HIO}_{\mathrm{O_R}}$-algorithm is computationally more efficient (only two Fourier transformations for each iteration), is more straight forward to implement and, finally, has less internal degrees of freedom (only one uniform random distributions defined by ν instead of four). Consequently, we prefer the $\mathrm{HIO}_{\mathrm{O_R}}$-algorithm over independent randomization of the coefficients $c_{\xi,n}$, $\xi \in \{\Omega, \Gamma\}$.

In summary, we demonstrated that the concept of randomization remedies the shortcomings of the traditional HIO+ER-algorithm as described in Sec. 7.2 to a large degree. Nonetheless, the computational effort of the $\mathrm{HIO}_{\mathrm{O_R}}$+ER-algorithm scales identical to the traditional HIO+ER-algorithm and its implementation is simple and straight-forward (including parallelization). Finally, we could not find any indication of a negative penalty of our proposed extension.

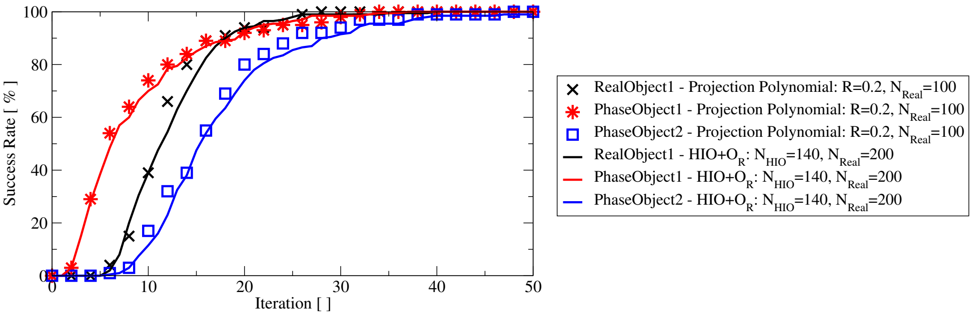

(a) Parameters according to Eq. (7.11a). (©2012 The Optical Society (OSA), from [1])

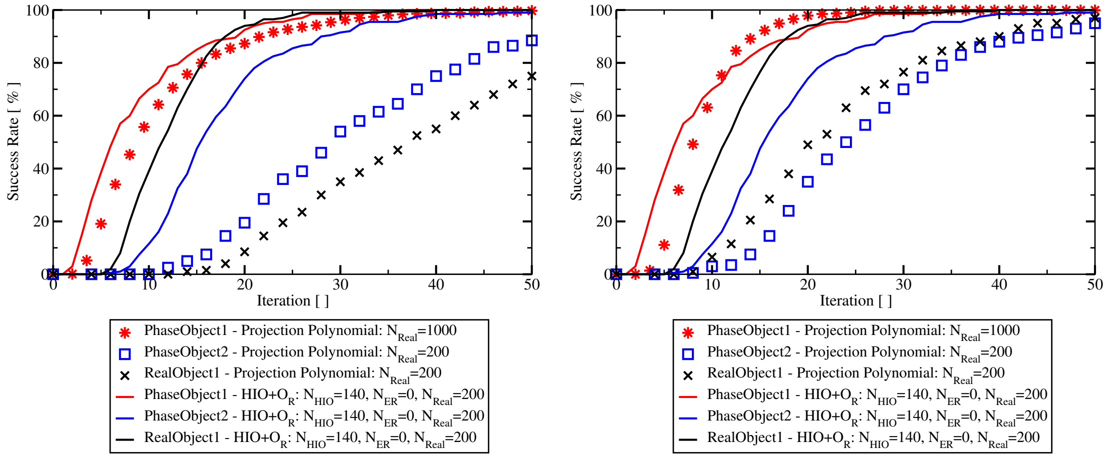

(b) Parameters according to Eq. (7.11b).

(c) Parameters according to Eq. (7.11c).

Figure 7.14.: Comparison of the success rate of both frameworks (7.3) [$\mathrm{HIO}_{\mathrm{O_R}}$-algorithm] and (7.4) which provide a generalization of the traditional HIO-algorithm based on randomization. No ER has been performed. The parameters of the projection polynomials are found in Eq. (7.11). The parameters of the traditional HIO-algorithm are $N_{\mathrm{HIO}} = 140$ and $\beta = 0.85$. Continuous lines illustrate the behavior for randomized overrelaxation of $\mathbf{P}_\Gamma$, whereas dots represent the behavior of the success rate resulting from uncorrelated randomization of the coefficients $c_{\xi,n}$ in a projection polynomial.

7.4. Regularization by constraining the scattering magnitude

For a reconstruction of experimental data, additional *a priori* knowledge was valuable in some cases [184, 185, 195, 205]. However, a thorough investigation of the benefits – and possible drawbacks – of such additional *a priori* knowledge has not yet been performed. In this section, we will provide such a detailed investigation for additional constraints on the magnitude of the effective electron ϱ_{eff} density in direct space (see also the discussion in Sec. 6.1). Typically, such constraints are relevant for materials with low contrast in the local scattering magnitude $\Phi_{\mathrm{C}}^{(D)}$ in Eq. (6.37), in particular for chemically homogeneous materials such as our Si-nanowire model system.

Whereas the improvements of the traditional HIO-algorithm based on randomized overrelaxation in Sec. 7.3 did not modify the *a priori* knowledge of the reconstruction procedure, but yet succeeded in significant improvements of the reconstruction capabilities, we now incorporate the above described additional *a priori* constraints in the traditional HIO+ER-algorithm ($\mathrm{HIO^A}$+$\mathrm{ER^A}$-algorithm). We again point out that the same set of physical *a priori* knowledge can typically be incorporated in various ways in a reconstruction algorithm.

We will also unify these direct space constraints on the scattering magnitude with the concepts of randomized overrelaxation ($\mathrm{HIO}^{\mathrm{A}}_{\mathrm{O_R}}$+$\mathrm{ER}^{\mathrm{A}}$-algorithm). For this unification, the suggested implementation of the direct space constraints on the local scattering magnitude differs from the implementation previously published in Refs. [195, 205]. Again, we will observe advantages from randomization during the iterative reconstruction (i.e., $\mathrm{HIO}^{\mathrm{A}}_{\mathrm{O_R}}$+$\mathrm{ER}^{\mathrm{A}}$-algorithm compared to the $\mathrm{HIO}^{\mathrm{A}}$+$\mathrm{ER}^{\mathrm{A}}$-algorithm).

Throughout this section, we restrict to the Si-nanowires as test system (see Sec. 7.1).

In the first part of this section, we define and discuss operators that are suited for constraining the local scattering magnitude ("gapped homogeneity constraints") in the HIO+ER-algorithm before we discuss the results of our numerical simulations in the second part of this section. It will turn out that the incorporation of such additional *a priori* knowledge in the HIO+ER-algorithm will shift the range of applicability of phase retrieval to significantly higher values of strain and, moreover, improve the robustness of the method for equal strain distribution.

The $\mathbf{HIO}^{\mathrm{A}}$+$\mathbf{ER}^{\mathrm{A}}$-algorithm

Since the magnitude of the effective electron density $|\varrho_{\mathrm{eff}}|$ (or the local scattering magnitude $|\Phi_{\mathrm{C}}^{(D)}|$ is typically both, a slowly varying function (up to material interfaces where chemical contrast might give rise to a strong variation on short length scales) and a function which deviates only slightly from its average value (at least in some sub-domains $\Omega_j \subseteq \Omega$ of the sample with geometry Ω), we first motivate why we give preference of the second property for our investigation over the first.

First, the local scattering magnitude $|\Phi_{\mathrm{C}}^{(D)}|$ may be inconsistent with the first property at material boundaries. At boundaries changes of the chemical composition and, therefore, of the local scattering magnitude can occur on very short length scales which violates the first property (unless the chemical gradient at the interface is smooth e.g. as a result of high temperature annealing induced diffusion). Consequently, in addition to limits on the gradient inside the material domains, good estimates of the internal material distribution and the resulting boundaries would be required. However, such kind of *a priori* knowledge is difficult to obtain. In contrast, the deviation from the mean value is small at least at interfaces with small chemical contrast and we do not require estimates of such inner boundaries.

Both approaches could be applied in specific sub-domains $\Omega_j \subseteq \Omega$ only. The unification of the domains Ω_j does not need to coincide with the full sample Ω. Moreover, the domains may even overlap. An important example for such a sub-domain is the substrate region which can typically be considered chemically homogeneous and almost unstrained irrespective of the nanostructure which is grown on top. Hence, the local scattering magnitude in this sub-domain of the full structure is a slowly varying function as well as a function that deviates only slightly from its average. This is independent of additional constraints for the nanostructure on top of the substrate or a global constraint for the full domain Ω.

The most stringent case for both assumptions is a chemically homogeneous material. In that case, the scattering magnitude $\Phi_{\mathrm{C}}^{(D)}(\boldsymbol{r})$ is constant – as long as we neglect the changes originating in strain. As a result, the derivatives of $\Phi_{\mathrm{C}}^{(D)}(\boldsymbol{r})$ are equal to zero as well as the deviation from its average.

Consequently, physically both approaches are interesting with a preference for constraints on the local scattering magnitude since such *a priori* knowledge can typically be obtained more easily for a specific sample.

If we instead look at these two types of constraints from a mathematical and numerical point, we have to account for the following aspects:

1. The first approach — slow variation of $|\Phi_{\mathrm{C}}^{(D)}|$ — focuses *only* on near-distance constraints in direct space. Since however the intensity distributions $\mathcal{I}(\boldsymbol{Q}_{\mathrm{B}}, \boldsymbol{Q})$ typically decay very fast, the total intensity weight at large $|\boldsymbol{Q}|$-values – which corresponds to near-distance fluctuations – is typically very weak and erroneous short range fluctuations already suppressed by the decay of $\Gamma(\boldsymbol{Q})$.

   Contrarily, the second approach — constraining the local scattering magnitude $|\Phi_{\mathrm{C}}^{(D)}|$ to the interval [average-gap, average+gap] — eliminates physically non-feasible contributions on *all* length scales up to the dimensions of the respective domain Ω_j. Consequently, such constraints are likely to have a larger impact on the intensity distribution in reciprocal space at smaller $|\boldsymbol{Q}|$-values where more intensity weight is located. Consequently, we may expect that reconstructions should benefit more from the second approach than from the first.

2. Finally, we point out that the second approach is also more advantageous from the perspective of implementation and computational efficiency, since it can be incorporated as a point operation (i.e., local, single pixel operation) with projection property (as long as the average value is assumed to be known, see detailed discussion later). In contrast, derivatives of a function cannot be implemented as point operations, but require higher computational effort.

As a conclusion of the entire discussion, we now focus on restrictions for the magnitude of the magnitude of the effective electron density $|\varrho_{\mathrm{eff}}|$.

More specifically and expressed mathematically, we consider the constraints

$$\mathrm{A_{L,j}}\bar{\zeta}_j \leq |\varrho_{\mathrm{eff}}(\boldsymbol{r})| \leq \mathrm{A_{H,j}}\bar{\zeta}_j \;\forall\; \boldsymbol{r} \in \Omega_j \subseteq \Omega \;, \tag{7.12}$$

where Ω_j are the domains to be constrained. $\mathrm{A_{L,j}} \leq 1$ and $\mathrm{A_{H,j}} \geq 1$ are additional parameters which need to be known *a priori* for every domain j. The averages $\bar{\zeta}_j$ are defined as[1]

$$\bar{\zeta}_j = \sqrt{\left\langle\, \mathbf{P}_{\Omega_j}\, |\varrho_{\mathrm{eff}}| \,;\, \mathbf{P}_{\Omega_j}\, |\varrho_{\mathrm{eff}}| \,\right\rangle / \left\langle\, \mathbf{P}_{\Omega_j} \,;\, \mathbf{P}_{\Omega_j} \,\right\rangle} \;. \tag{7.14}$$

The parametrization of the two independent parameters $\mathrm{A_{L,j}}\bar{\zeta}_j$ and $\mathrm{A_{H,j}}\bar{\zeta}_j$ of each domain Ω_j by three variables (the relative values $\mathrm{A_{L,j}} \leq 1$ and $\mathrm{A_{H,j}} \geq 1$ and the average value $\bar{\zeta}_j$) will be useful for incorporation of the fact that for typical experimental conditions the averages $\bar{\zeta}_j$ are not *a priori* known. Instead, they also need to be extracted during the reconstruction process. We will return to this additional difficulty later. For now, we assume that the averages $\bar{\zeta}_j$ are *a priori* knowledge at hand.

For implementation of these constraits, we define the set of projection operators

$$\mathbf{P}_{\mathrm{A}}^{(j)}\, \varrho_{\mathrm{eff}}^{(i)}(\boldsymbol{r}) = \begin{cases} \mathrm{A}_j^{(i)}(\boldsymbol{r})\;\; \mathrm{e}^{\mathrm{i}\,\arg\left(\varrho_{\mathrm{eff}}^{(i)}(\boldsymbol{r})\right)} & \text{if } \boldsymbol{r} \in \Omega_j \;, \\ \varrho_{\mathrm{eff}}^{(i)}(\boldsymbol{r}) & \text{if } \boldsymbol{r} \notin \Omega_j \;, \end{cases} \tag{7.15a}$$

with

$$\mathrm{A}_j^{(i)}(\boldsymbol{r}) = \min\left(\mathrm{A_{H,j}}\bar{\zeta}_j ; \max\left(\mathrm{A_{L,j}}\bar{\zeta}_j ; \left|\varrho_{\mathrm{eff}}^{(i)}(\boldsymbol{r})\right|\right)\right) \;, \tag{7.15b}$$

where (i) labels iterations and (j) labels the domains Ω_j.

We particularly point out four properties of the operators $\mathbf{P}_{\mathrm{A}}^{(j)}$:

---

[1] If the constraints (7.12) are applied to the full domain Ω, we could alternatively define the average $\bar{\zeta}$ by

$$\bar{\zeta} = \sqrt{\langle\, |\varrho_{\mathrm{eff}}| \,;\, |\varrho_{\mathrm{eff}}| \,\rangle / \langle\, \mathbf{P}_{\Omega} \,;\, \mathbf{P}_{\Omega} \,\rangle} \;, \tag{7.13}$$

which would additionally take the behavior of $|\varrho_{\mathrm{eff}}(\boldsymbol{r})|$ outside the support Ω into account. However, Eq. (7.14) allows for a unified discussion and algorithm irrespective of the geometry of the domains Ω_j, even it coincides with the full support Ω. Therefore, we give preference to Eq. (7.14).

1. They are *nonlinear* (i.e., it is not guaranteed that $\mathbf{P}_{\mathrm{A}}^{(j)}\left(\alpha_1\varrho_{\mathrm{eff}\,1}^{(i)}+\alpha_2\varrho_{\mathrm{eff}\,2}^{(i)}\right)$ is equal to $\alpha_1\mathbf{P}_{\mathrm{A}}^{(j)}\varrho_{\mathrm{eff}\,1}^{(i)}+\alpha_2\mathbf{P}_{\mathrm{A}}^{(j)}\varrho_{\mathrm{eff}\,2}^{(i)}$ for all α_1, $\alpha_2 \in \mathbb{R}$).
2. They *commute* with $\mathbf{P}_\Omega$ (i.e., $[\mathbf{P}_\Omega, \mathbf{P}_{\mathrm{A}}^{(j)}] = \mathbf{P}_\Omega\mathbf{P}_{\mathrm{A}}^{(j)} - \mathbf{P}_{\mathrm{A}}^{(j)}\mathbf{P}_\Omega = 0$ for all j).
3. $\mathbf{P}_{\mathrm{A}}^{(m)}$ and $\mathbf{P}_{\mathrm{A}}^{(n)}$ also commute pairwise (i.e., $[\mathbf{P}_{\mathrm{A}}^{(m)}, \mathbf{P}_{\mathrm{A}}^{(n)}] = 0$ for all n and m) .
4. None of the operators $\mathbf{P}_{\mathrm{A}}^{(j)}$ and $\mathbf{P}_\Omega$ commutes with the projection operator $\mathbf{P}_\Gamma$.

The second feature is a consequence of the fact, that $\mathbf{P}_\Omega$ reduces to the identity operator in $\Omega_j \subset \Omega$ (see Eq. (6.51)).

For the third property, we have to distinguish two cases: First, if the domains Ω_m and Ω_n do not intersect, one of the operators reduces the identity map for every point $\boldsymbol{r}$. Second, if both domains intersect, they commute if $\mathrm{A}_{\mathrm{H,m}}\bar{\zeta}_m \geq \mathrm{A}_{\mathrm{L,n}}\bar{\zeta}_n$ and $\mathrm{A}_{\mathrm{L,m}}\bar{\zeta}_m \leq \mathrm{A}_{\mathrm{H,n}}\bar{\zeta}_n$. The interpretation of this conditions is simple: The lower and upper bounds of the domains Ω_n and Ω_m must not be contradictory for any point $\boldsymbol{r}$. Consequently, for reasonably chosen bounds $\mathrm{A}_{\mathrm{L,j}}$ and $\mathrm{A}_{\mathrm{H,j}}$, the operators $\mathbf{P}_{\mathrm{A}}^{(m)}$ and $\mathbf{P}_{\mathrm{A}}^{(n)}$ commute pairwise.

Keeping these properties in mind, we now turn to the implementation of such *a priori* knowledge as an extension to the traditional HIO-algorithm.

As for the implementation of randomization in Sec. 7.3, we again address two non-equivalent approaches for the mathematical realization of the same *a priori* knowledge:

1. The first way of including our constraints is based on the substitution of the shape operator $\mathbf{P}_\Omega$ in the projection polynomials of the HIO- and ER-algorithm (see Eqs. (6.49b) and (6.52c)) by the operator $\mathbf{P}_{\Omega,\mathrm{A}}$ which is defined as

   $$\mathbf{P}_{\Omega,\mathrm{A}} = \mathbf{P}_\Omega\mathbf{P}_{\mathrm{A}} = \mathbf{P}_\Omega \prod_j \mathbf{P}_{\mathrm{A}}^{(j)} \ . \tag{7.16a}$$

   The composite operator $\mathbf{P}_{\Omega,\mathrm{A}}$ is again a projection operator, since the defining property $\mathbf{P}_{\Omega,\mathrm{A}}^2 = \mathbf{P}_{\Omega,\mathrm{A}}$ of a projection operator (idempotence) is fulfilled due to the the permutation properties described above.

   After this substitution, the projection polynomials of the HIO+ER-algorithm read

   $$\hat{H}_{\mathrm{HIO+A}}^{(\mathrm{PP})} = 1 - \mathbf{P}_{\Omega,\mathrm{A}} - \beta\,\mathbf{P}_\Gamma + (1+\beta)\;\mathbf{P}_{\Omega,\mathrm{A}}\mathbf{P}_\Gamma \ , \tag{7.16b}$$

   $$\hat{H}_{\mathrm{ER,A}}^{(\mathrm{PP})} = \mathbf{P}_{\Omega,\mathrm{A}}\mathbf{P}_\Gamma \ . \tag{7.16c}$$

2. The second approach of incorporating the constraints (7.12) is specifically targeted at the HIO-algorithm. Its direct space assembly (6.52a) can be read as

   $$\varrho_{\mathrm{eff}}^{(i+1)}(\boldsymbol{r}) = \begin{cases} \mathbf{M}_{\mathrm{C}}\varrho_{\mathrm{eff}}^{(i)}(\boldsymbol{r}) & \text{if } \boldsymbol{r} \in \Omega \ , \\ \varrho_{\mathrm{eff}}^{(i)}(\boldsymbol{r}) - \beta\mathbf{M}_{\mathrm{C}}\varrho_{\mathrm{eff}}^{(i)}(\boldsymbol{r}) & \text{if } \boldsymbol{r} \notin \Omega \ , \end{cases} \tag{7.17a}$$

   $$\mathbf{M}_{\mathrm{C}} = \mathbf{P}_\Gamma \tag{7.17b}$$

   where the mapping $\mathbf{M}_{\mathrm{C}}$ incorporates all constraints *except* the geometry Ω. Reading the HIO-algorithm like this, natural generalizations for $\mathbf{M}_{\mathrm{C}}$ are obtained by

   $$\mathbf{M}_{\mathrm{C}} = \mathbf{P}_{\mathrm{A}}\mathbf{P}_\Gamma \ , \tag{7.18a}$$

   $$\mathbf{M}_{\mathrm{C}} = \mathbf{P}_\Gamma\mathbf{P}_{\mathrm{A}} \ , \tag{7.18b}$$

   $$\mathbf{M}_{\mathrm{C}} = 0.5 \cdot \{\,\mathbf{P}_{\mathrm{A}}, \mathbf{P}_\Gamma\} \ , \tag{7.18c}$$

where $\{\cdot,\cdot\}$ denotes the common anticommutator in physics.

Whereas the mapping $\mathbf{M}_\mathrm{C}$ in case of the traditional HIO-algorithm as defined in Eq. (7.17b) is a projection operator (i.e., $\mathbf{M}_\mathrm{C}^2 = \mathbf{M}_\mathrm{C}$), this is no longer true for the extensions (7.18).

Nevertheless, the solution $\varrho_\mathrm{eff}(\boldsymbol{r})$ is a fixed point of $\mathbf{M}_\mathrm{C}$ for the extensions (7.18), since $\mathbf{M}_\mathrm{C}$ reduces simply to the identity operator 1 if applied to $\varrho_\mathrm{eff}(\boldsymbol{r})$.

We restrict to Eq. (7.18a) which results in the projection polynomials

$$\begin{aligned} \hat{H}_\mathrm{HIO,A} &= 1 - \mathbf{P}_\Omega - \beta \mathbf{P}_\mathrm{A}\mathbf{P}_\Gamma + (1+\beta)\,\mathbf{P}_\Omega\mathbf{P}_\mathrm{A}\mathbf{P}_\Gamma && (7.19\mathrm{a}) \\ &= 1 - \mathbf{P}_\Omega - \beta \mathbf{P}_\mathrm{A}\mathbf{P}_\Gamma + (1+\beta)\,\mathbf{P}_{\Omega,\mathrm{A}}\mathbf{P}_\Gamma\ , && (7.19\mathrm{b}) \end{aligned}$$

where the definition (7.16a) has been used in the second expression.

The ER-algorithm is modified in the same way as in our first approach (see Eq. (7.16c)).

The second approach for modifying the HIO-algorithm is clearly different from our first approach resulting in Eq. (7.16b), because it is composed of three "basis projection operators" ($\mathbf{P}_\Omega$, $\mathbf{P}_\Gamma$, and ($\mathbf{P}_{\Omega,\mathrm{A}}$ or $\mathbf{P}_\mathrm{A}$)) instead of two ($\mathbf{P}_\Gamma$ and $\mathbf{P}_{\Omega,\mathrm{A}}$).

For comparison, it is useful to rewrite the action of $\hat{H}^{(\mathrm{PP})}_\mathrm{HIO+A}$ on the effective electron density $\varrho_\mathrm{eff}(\boldsymbol{r})$ – given in Eq. (7.16b) – for points $\boldsymbol{r}$ inside and outside the shape Ω separately as

$$\varrho_\mathrm{eff}^{(i+1)}(\boldsymbol{r}) = \begin{cases} \hat{H}_\mathrm{HIO}\left(\beta; \mathbf{P}_\Omega \to \mathbf{P}_\mathrm{A}\right) \varrho_\mathrm{eff}^{(i)}(\boldsymbol{r}) & \text{if } \boldsymbol{r} \in \Omega\ , \\ \left(1 - \beta \mathbf{P}_\Gamma\right) \varrho_\mathrm{eff}^{(i)}(\boldsymbol{r}) & \text{if } \boldsymbol{r} \notin \Omega\ , \end{cases} \tag{7.20}$$

where $\hat{H}_\mathrm{HIO}\left(\beta; \mathbf{P}_\Omega \to \mathbf{P}_\mathrm{A}\right)$ is the HIO-operator defined in Eq. (6.52c) after the substitution $\mathbf{P}_\Omega \to \mathbf{P}_\mathrm{A}$. This equation needs to be compared to Eq. (7.17a) together with Eq. (7.18a).

We now face the complication that the averages $\bar{\zeta}_j$ are typically not known for "real world" reconstructions of experimental data. Consequently, it is necessary to estimate these averages $\bar{\zeta}_j$ during reconstruction.

For this task, we modify Eq. (7.15b) to

$$\begin{aligned} \bar{\zeta}_j^{(i)} &= \sqrt{\left\langle \mathbf{P}_{\Omega_j} \left|\varrho_\mathrm{eff}^{(i)}\right|\ ;\ \mathbf{P}_{\Omega_j} \left|\varrho_\mathrm{eff}^{(i)}\right| \right\rangle \Big/ \left\langle \mathbf{P}_{\Omega_j}\ ;\ \mathbf{P}_{\Omega_j} \right\rangle}\ , && (7.21\mathrm{a}) \\ \mathrm{A}_j^{(i)}(\boldsymbol{r}) &= \min\left(\mathrm{A}_\mathrm{H,j}\bar{\zeta}_j^{(i)}; \max\left(\mathrm{A}_\mathrm{L,j}\bar{\zeta}_j^{(i)}; \left|\varrho_\mathrm{eff}^{(i)}(\boldsymbol{r})\right|\right)\right)\ . && (7.21\mathrm{b}) \end{aligned}$$

To distinguish the projection operator (7.15) from its modified counterpart based on Eqs. (7.15a) and (7.21), we refer to these new mappings by $\mathbf{M}_\mathrm{A}^{(j)}$.

We again analyse the properties of these operators $\mathbf{M}_\mathrm{A}^{(j)}$ before we consider the implications for the reconstruction procedure:

- The essential property $\mathbf{P}_\mathrm{A}^{(j)}\varrho_\mathrm{eff}(\boldsymbol{r}) = \varrho_\mathrm{eff}(\boldsymbol{r})$ is still valid for the mappings $\mathbf{M}_\mathrm{A}^{(j)}$.
- In general, two operators $\mathbf{M}_\mathrm{A}^{(n)}$ and $\mathbf{M}_\mathrm{A}^{(m)}$ do no longer commute, if the domains Ω_n and Ω_m intersect. Nonetheless, they still commute for disjoint domains Ω_n and Ω_m.
- The operators $\mathbf{P}_\mathrm{A}^{(j)}$ still commute with $\mathbf{P}_\Omega$ as long as $\Omega_j \subset \Omega$.
- The mappings $\mathbf{M}_\mathrm{A}^{(j)}$ are in general no longer projection operators: If applied repeatedly to an object, the average during the next action may be different from the current one. Thus, the operator is no longer idempotent as required for a projection operator. An exception is the case $\mathrm{A}_\mathrm{L,j} = \mathrm{A}_\mathrm{H,j} = 1$. In this case, applying a mapping $\mathbf{M}_\mathrm{A}^{(j)}$ repeatedly yields in the same result as applying it once.

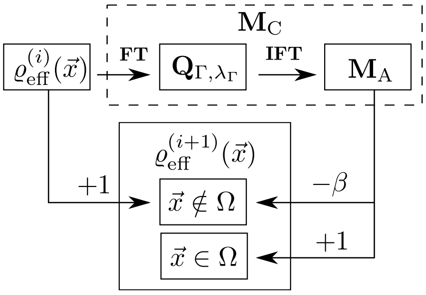

Figure 7.15.: Schematics of the $\mathrm{HIO}^\mathrm{A}_{\mathrm{O_R}}$-algorithm: The difference to the $\mathrm{HIO}_{\mathrm{O_R}}$-algorithm is the application of the operator $\mathbf{M}_\mathrm{A}$ before the feedback based calculation of the next iterative candidate $\varrho_\mathrm{eff}^{(i+1)}(\boldsymbol{r})$.

As a consequence, a generalization of Eq. (7.16b) in the framework of projection polynomials is no longer possible once the estimation (7.21) of the averages $\bar{\zeta}_j^{(i)}$ is included in the iterative solution procedure.

In contrast, the approach (7.17a) together with (7.18) includes the estimation of the averages $\bar{\zeta}_j$ by substituting

$$\mathbf{P}_\mathrm{A}^{(j)} \longrightarrow \mathbf{M}_\mathrm{A}^{(j)} \ , \ \mathbf{M}_\mathrm{A} = \prod_j \mathbf{M}_\mathrm{A}^{(j)} \tag{7.22}$$

in Eq. (7.18) in a straight forward way and without conceptional changes (since the mappings $\mathbf{M}_\mathrm{C}$ as defined in Eq. (7.18a) are no projection operators even if the averages $\bar{\zeta}_j$ are not estimated during the reconstruction).

In consequence, we will restrict ourselves to the framework defined by Eq. (7.17a) together with

$$\mathbf{M}_\mathrm{C} = \mathbf{M}_\mathrm{A}\mathbf{P}_\Gamma \tag{7.23}$$

and refer to it as HIO^A-algorithm. For the ER^A-algorithm, we employ

$$\hat{H}_\mathrm{ER,A}^\mathrm{(OP)} = \mathbf{P}_\Omega\mathbf{M}_\mathrm{A}\mathbf{P}_\Gamma \ . \tag{7.24}$$

We refer to the combination of those building blocks as the HIO^A+ER^A-algorithm.

Considering the benefits from randomization (see Sec. 7.3), the next step is the incorporation of randomized overrelaxation in the HIO^A-algorithm.

The $\mathbf{HIO}^\mathrm{A}_{\mathbf{O_R}}$+$\mathbf{ER}^\mathrm{A}$-algorithm

The combination of randomized overrelaxation with the modifications described by Eqs. (7.17a) and (7.23) can be done in the same manner as without the constraints $\mathbf{M}_\mathrm{A}$ by the substitution $\mathbf{P}_\Gamma \longrightarrow \mathbf{Q}_{\Gamma;\lambda_\Gamma}$ in the HIO^A-algorithm.

Consequently, we have

$$\mathbf{M}_\mathrm{C}(\lambda_\Gamma) = \mathbf{M}_\mathrm{A}\mathbf{Q}_{\Gamma;\lambda_\Gamma} \tag{7.25}$$

instead of Eq. (7.23). The direct space assembly as defined in Eq. (7.17a) is not modified.

Since overrelaxation was only employed in the HIO-algorithm, error reduction is still given by Eq. (7.24).

The final scheme of the $\mathrm{HIO}^\mathrm{A}_{\mathrm{O_R}}$-algorithm is illustrated graphically in Fig. 7.15 and its combination with the ER-algorithm analog to the traditional HIO+ER-algorithm (see Fig. 6.4 on page 125). The $\mathrm{HIO}^\mathrm{A}_{\mathrm{O_R}}$+$\mathrm{ER}^\mathrm{A}$ is computational equally efficient as the standard HIO+ER-algorithm. The computational efficiency is limited by the $N\log(N)$-scaling of the FFT algorithm.

We point out that over-relaxation (irrespective of randomization) also destroys the idempotence of the operator $\mathbf{M}_\mathrm{C}$ for $\lambda_\Gamma \neq 1$ – irrespective of the introduction of the magnitude constraints $\mathbf{M}_\mathrm{A}$.

We stress the different nature of our modifications: Whereas randomized overrelaxation succeeds in utilizing the *same* given *a priori* knowledge more successfully, the constraints $\mathbf{M}_\mathrm{A}$ aim at a regularization of the reconstruction with *additional a priori* knowledge.

In Sec. G in the appendix, we shortly comment on the operator polynomial approach for combining the magnitude constraints $\mathbf{M}_\mathrm{A}$ and randomized overrelaxation $\mathbf{Q}_{\Gamma;\lambda_\Gamma}$.

Numerical results for the HIO$^\mathrm{A}$+ER$^\mathrm{A}$- and HIO$^\mathrm{A}_{\mathrm{O_R}}$+ER$^\mathrm{A}$-algorithm

We now present results for three particular cases for the magnitude constraints given in Eq. (7.12):

- Firstly, we investigate the case $\mathrm{A}_{\mathrm{L},} = \mathrm{A}_{\mathrm{H},} = 1.0$ in the full domain Ω.
- Secondly, we consider the case $\mathrm{A}_{\mathrm{L},} = \mathrm{A}_{\mathrm{H},} = 1.0$, but only applied deep in the substrate and no magnitude constraints elsewhere.
- Finally, we allow for a gap of ±0.3, i.e., $\mathrm{A}_{\mathrm{L},} = 0.7$ and $\mathrm{A}_{\mathrm{H},} = 1.3$ and apply this limitation in the full domain Ω.

The benefits of each of these three exemplary constraints will be investigated separately for the HIO$^\mathrm{A}$+ER$^\mathrm{A}$-algorithm and for the HIO$^\mathrm{A}_{\mathrm{O_R}}$+ER$^\mathrm{A}$-algorithm. For the latter, we will also apply the second and third constraint simultaneously, since it closely resembles typical experimental conditions: strong constraints in the (practically unstrained) substrate domain, and some weaker constraints for the inhomogeneously strained domain on top.

We perform our investigations in the same manner as for the HIO+ER- and HIO$_{\mathrm{O_R}}$+ER-algorithm based on the Si nanowire test system (see Sec. 7.1 and Figs. 7.7 and 7.11). This way, a straight forward comparison of our results is possible.

We stop our simulations at latest at $\epsilon_\mathrm{M} = 1.0\%$ for two reasons: On the one hand, we exceed the validity of the model (6.37). On the other hand, the number of pixels in our discrete numerical grid representing the fastest 2π-oscillation in the effective electron density ϱ_eff dropped to approximately eight pixels. Consequently, for higher values of ϵ_M, a denser numerical grid in direct space would be required. However, we prefer to keep the numerical grid identical throughout our numerical investigations.

Investigation of the HIO$^\mathrm{A}$+ER$^\mathrm{A}$-algorithm

The result for applying $\mathrm{A}_{\mathrm{L},} = \mathrm{A}_{\mathrm{H},} = 1.0$ to the full domain Ω is depicted in Fig. 7.16. First, we observe, that the range of successful convergence to the solution ϱ_eff is shifted to higher strain values $\epsilon_\mathrm{M} = 0.56\%$ as compared to the classical HIO+ER-algorithm (see Fig. 7.16(b)). Moreover, we see, that for strain $\epsilon_\mathrm{M} > 0.56\%$, stagnation typically takes place at angles φ greater than 20.0°, so again on a level far from the solution ϱ_eff (compare Fig. 7.7). Nevertheless, a reasonable fraction of the random initial trials successfully converged to the solution ϱ_eff even for strain values as high as $\epsilon_\mathrm{M} = 0.80\%$. In some rare cases, we even observe a successful reconstruction up to 1.0% of strain (see Fig. 7.17). Hence, homogeneous structures can be reconstructed successfully for much higher values of strain if the constraint $\mathrm{A}_{\mathrm{L},} = \mathrm{A}_{\mathrm{H},} = 1.0$ is exploited during the reconstruction. However, the regularization by this additional *a priori*-knowledge is insufficient for elimination of the influence of the chosen initial guess for large strain ϵ_M. Moreover, the reconstructed effective electron density often suffers from phase vortices which are non-physical and will be discussed in Sec. 7.5.

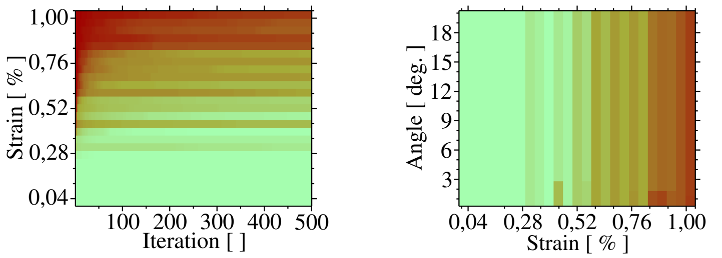

(a) Criterion for success $\varphi^{(i)} \leq \varphi_{\mathrm{Max}} = 1.0°$

(b) Result after $i = 500$ iterations

Figure 7.16.: Reconstruction capabilities of the $\mathrm{HIO}^{\mathrm{A}}$+$\mathrm{ER}^{\mathrm{A}}$-algorithm, where the magnitude constraints $\mathbf{M}_{\mathrm{A}}$ defined in Eqs. (7.15a) and (7.21) with $\mathrm{A}_{\mathrm{L},} = 1.0$ and $\mathrm{A}_{\mathrm{H},} = 1.0$ are applied in the full direct space domain Ω. The discretization step in direction of strain ϵ_{M} is $\delta\epsilon_{\mathrm{M}} = 0.04\%$. Colorbar for both plots is given in Fig. 7.6(a). (©2013 The Optical Society (OSA), from [2])

In Fig. 7.18, we apply the constraint $\mathrm{A}_{\mathrm{L},} = \mathrm{A}_{\mathrm{H},} = 1.0$ only in a substrate region with thickness in z-direction equal to 80 pixel (see hatched domain in Fig. 7.3(a)). The highest strain ϵ_{M} for which the reconstruction is independent of the random initial trail, almost does not change in comparison to the traditional HIO+ER-algorithm. However, we still observe three improvements: First, the upper bound of the "transition range" – the range of strain ϵ_{M} for which at least some initial guesses have been reconstructed successfully – changes from strain values of $\epsilon_{\mathrm{M}} \approx 0.20\%$ (in case of the traditional HIO+ER-algorithm) to approximately $\epsilon_{\mathrm{M}} = 0.30\%$. Second, the success rate s in this transition range improves to higher values as compared to the traditional HIO+ER-algorithm. Yet, it typically does not reach values close to $s = 100\%$ in most cases in that range. Finally, in the transition range, we observe several local minima *close* to the true solution after $i = 500$ iterations (i.e., angles $\varphi \leq 20.0°$). Nevertheless, the success rate s is almost independent of φ_{Max} in the range $\varphi_{\mathrm{Max}} \leq 10.0°$.

The most complicated bahavior is observed for the "relaxed" constraint $\mathrm{A}_{\mathrm{L},} = 0.7$ and $\mathrm{A}_{\mathrm{H},} = 1.3$ applied to full domain Ω. The respective results are depicted in Fig. 7.19.

In this case, the success rate does depend on the choice of the value of φ_{Max} even below $\varphi_{\mathrm{Max}} = 10.0°$ (compare Figs. 7.19(a) and 7.19(b)). If we only look $\varphi_{\mathrm{Max}} = 1.0°$ (Fig. 7.19(a)), it seems that most benefits of the strict magnitude constraint $\mathrm{A}_{\mathrm{L},} = \mathrm{A}_{\mathrm{H},} = 1.0$ (see Fig. 7.16) are lost for a gap of ±0.3 – corresponding to $\mathrm{A}_{\mathrm{L},} = 0.7$ and $\mathrm{A}_{\mathrm{H},} = 1.3$. Almost no reconstructions which drop below the distance $\varphi_{\mathrm{Max}} = 1.0°$ are observed for $\epsilon_{\mathrm{M}} > 0.22\%$.

However, we see that many local minima *near* the true solution emerge, as can be seen in Fig. 7.19(c). This observation explains the differences of the success rate for $\varphi_{\mathrm{Max}} = 1.0°$ and $\varphi_{\mathrm{Max}} = 10.0°$.

It is interesting to compare these results in greater detail with the traditional HIO+ER-algorithm and the $\mathrm{HIO}_{\mathrm{O_R}}$+ER-algorithm:

In Fig. 7.19(d), we compare the gapped magnitude constraints to the classical HIO+ER-algorithm. This plot demonstrates that our modification to incorporate constraints on $\mathit{\Phi}_{\mathrm{C}}^{(D)}$ results in no penalty in comparison to traditional HIO+ER-algorithms for gaps as large as ±0.3. The most pronounced advantages are observed in the range $\epsilon_{\mathrm{M}} = 0.12\%$ to $\epsilon_{\mathrm{M}} = 0.20\%$ where some reconstructions with the traditional HIO+ER-algorithm have been successful, but many stagnated far from the solution. For $\epsilon_{\mathrm{M}} \gtrsim 0.20\%$, where the success rate s of the traditional HIO+ER-algorithm is essentially equal to zero, also the

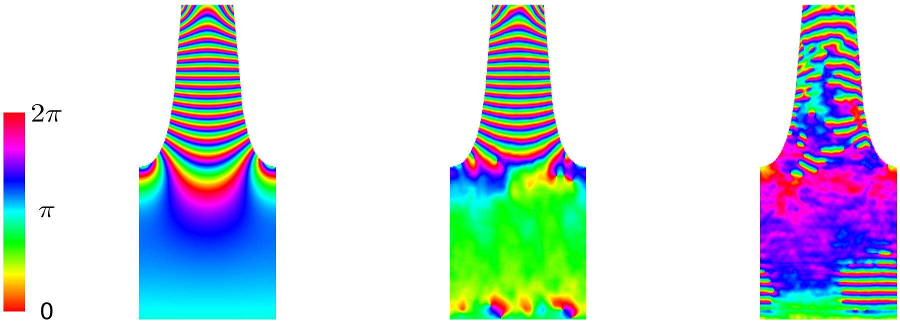

(a) Successful reconstruction (very rare)

(b) Failed reconstruction after 500 iterations: Output contains non-physical phase vortices

(c) Failed reconstruction after 500 iterations: Output contains non-physical phase vortices

Figure 7.17.: Illustration of the output of reconstructions with the HIO$^{\mathrm{A}}$+ER$^{\mathrm{A}}$-algorithm for $\epsilon_{\mathrm{M}} = 1.0\%$, where the magnitude constraints $\mathbf{M}_{\mathrm{A}}$ defined in Eqs. (7.15a) and (7.21) with $\mathrm{A}_{\mathrm{L},} = 1.0$ and $\mathrm{A}_{\mathrm{H},} = 1.0$ are applied in the full direct space domain Ω. The phase field and magnitude are encoded by HSV colorbar (phase encoding identical to Figs. 7.1 and 7.4).

benefits of the additional constraints $\mathrm{A}_{\mathrm{L},} = 0.7$ and $\mathrm{A}_{\mathrm{H},} = 1.3$ applied to full domain Ω are less pronounced.

In addition, Fig. 7.19(e) and 7.19(f) compare the results for the ± 0.3 gapped magnitude constraints $\mathrm{A}_{\mathrm{L},} = 0.7$ and $\mathrm{A}_{\mathrm{H},} = 1.3$ applied to full domain Ω with the HIO$_{\mathrm{O_R}}$+ER-algorithm. Both plots clearly demonstrate the power of randomized overrelaxation. In the range $\epsilon_{\mathrm{M}} = 0.12\%$ to $\epsilon_{\mathrm{M}} = 0.28\%$, the benefits from randomized overrelaxation – a pure modification of data evaluation without modification of the underlying *a priori* knowledge – exceed the benefits provided by adding additional *a priori* knowledge to the HIO+ER-algorithm. In contrast, this additional *a priori* knowledge is essential for strain values higher than $\epsilon_{\mathrm{M}} \gtrsim 0.28\%$ (see Fig. 7.19(f)): For such values of ϵ_{M}, the HIO$^{\mathrm{A}}$+ER$^{\mathrm{A}}$-algorithm was more successful than the HIO$_{\mathrm{O_R}}$+ER-algorithm. Thus, the combination of both modifications – randomized overrelaxation in the projection operator in reciprocal space and the direct space constraints on $|\varrho_{\mathrm{eff}}(\boldsymbol{r})|$ – seems very promising for improving data evaluation in the framework of CXDI and will therefore now investigated.

Investigation of the HIO$^{\mathrm{A}}_{\mathrm{O_R}}$+ER$^{\mathrm{A}}$-algorithm

For the investigation of the HIO$^{\mathrm{A}}_{\mathrm{O_R}}$+ER$^{\mathrm{A}}$-algorithm, we focus on the same three cases for the magnitude constraints on $|\varrho_{\mathrm{eff}}(\boldsymbol{r})|$ in framework of HIO$^{\mathrm{A}}$+ER$^{\mathrm{A}}$-algorithm. Moreover, we investigate the combination of the ± 0.3 gapped magnitude constraints applied to the full structure Ω and strict magnitude constraints ± 0.0 in the essentially unstrained substrate region as an additional fourth case.

Again, we first look at the result for strict magnitude constraints $\mathrm{A}_{\mathrm{L},} = \mathrm{A}_{\mathrm{H},} = 1.0$ in the full domain Ω. The respective results are depicted in Fig. 7.20. Even for strain as high as $\epsilon_{\mathrm{M}} = 1.0\%$, the success rate s reaches almost 100% in few iterations (see Fig. 7.20(a)): $s \geq 90\%$ [$s \geq 95\%$] is realized after $N_{\mathrm{Iter}} = 104$ [$N_{\mathrm{Iter}} = 153$] iterations. A direct comparison to reconstructions based on the same *a priori* knowledge, but performed without randomized overrelaxation (i.e., with the HIO$^{\mathrm{A}}$+ER$^{\mathrm{A}}$-algorithm) is given in Fig. 7.20(b). Clearly, randomized overrelaxation provides strong benefits in escaping stagnation also in presence of magnitude constraints on $|\varrho_{\mathrm{eff}}(\boldsymbol{r})|$. The characteristic features of the improvement are identical to those which are obtained by incorporating randomized overrelaxation in the

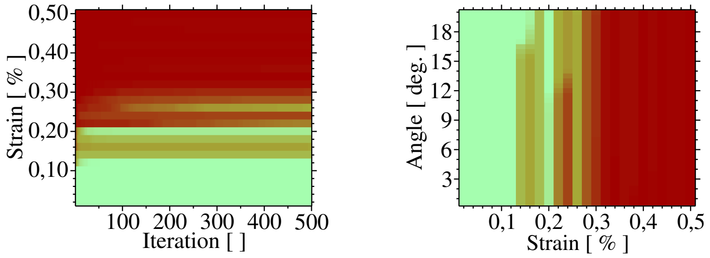

(a) Criterion for success $\varphi^{(i)} \leq \varphi_{\mathrm{Max}} = 1.0^\circ$

(b) Result after $i = 500$ iterations (©2013 The Optical Society (OSA), from [2])

Figure 7.18.: Reconstruction capabilities of the $\mathrm{HIO}^{\mathrm{A}}$+$\mathrm{ER}^{\mathrm{A}}$-algorithm, where the magnitude constraints $\mathbf{M}_{\mathrm{A}}$ defined in Eqs. (7.15a) and (7.21) with $\mathrm{A}_{\mathrm{L},} = 1.0$ and $\mathrm{A}_{\mathrm{H},} = 1.0$ are applied in the substrate domain (hatched domain in Fig. 7.3(a)) inside the direct space object. The discretization step in direction of strain ϵ_{M} is $\delta\epsilon_{\mathrm{M}} = 0.02\%$. Colorbar for both plots is given in Fig. 7.6(a).

classical HIO+ER-algorithm (see Fig. 7.11(b)): Long term stagnation of certain random initial trials during the iterative reconstruction is almost absent.

If we limit the magnitude constraints to the same deep substrate domain as before, we also observe a significantly more robust reconstruction process than without randomized overrelaxation (see Fig. 7.21): Up to $\epsilon_{\mathrm{M}} = 0.42\%$, distances of $\varphi \leq 1.0^\circ$ are reached in less than $i = 500$ iterations independent of the random initial phases (see Fig. 7.21(a) and 7.21(b)). From Fig. 7.21(b), we see a smooth increase in distance to the true solution after $i = 500$ iterations up to $\epsilon_{\mathrm{M}} = 0.50\%$. The behavior for $\epsilon_{\mathrm{M}} = 0.44\%$ – the first value for which the criterion $\varphi \leq 1.0^\circ$ could not be reached in almost all cases – is depicted in Fig. 7.21(c). We recognize a level of stagnation at approximately 20.0° which is left by more and more initial trails with increasing number of iterations. Moreover, a second level of stagnation at approximately 10.0° can be observed. The attraction of this level is so strong, that even with randomized overrelaxation the iterative process barely manages to escape from this level.

In the remaining three figures of Fig. 7.21, we compare this behavior to the $\mathrm{HIO}_{\mathrm{O_R}}$+ER- and $\mathrm{HIO}^{\mathrm{A}}$+$\mathrm{ER}^{\mathrm{A}}$-algorithm:

In Fig. 7.21(d), we compare to reconstructions including randomization and focus on the benefits from the additional physical knowledge of the sample's constant local magnitude constraint $|\varrho_{\mathrm{eff}}(\boldsymbol{r})|$ in the substrate region ($\mathrm{HIO}_{\mathrm{O_R}}$+ER-algorithm). In contrast to this, the advantage of the incorporation of randomized overrelaxation – a purely mathematical modification of the reconstruction process without employing any additional physical knowledge – in the $\mathrm{HIO}^{\mathrm{A}}$+$\mathrm{ER}^{\mathrm{A}}$-algorithm is highlighted in Figs. 7.21(e) (strain vs. iteration) and 7.21(f) (angle vs. strain). As each of these two modifications on their own showed no drawbacks compared to the traditional HIO+ER-algorithm, we also observe no drawbacks of the $\mathrm{HIO}^{\mathrm{A}}_{\mathrm{O_R}}$+$\mathrm{ER}^{\mathrm{A}}$-algorithm compared to the special cases of the $\mathrm{HIO}_{\mathrm{O_R}}$+ER- and $\mathrm{HIO}^{\mathrm{A}}$+$\mathrm{ER}^{\mathrm{A}}$-algorithm for this set of given *a priori* knowledge.

For better illustration of the output of the $\mathrm{HIO}^{\mathrm{A}}$+$\mathrm{ER}^{\mathrm{A}}$-algorithm and the $\mathrm{HIO}^{\mathrm{A}}_{\mathrm{O_R}}$+$\mathrm{ER}^{\mathrm{A}}$-algorithm for the effective electron density ϱ_{eff} based on this set of constraints, we depict a typical result for ϱ_{eff} of these algorithms for $\epsilon_{\mathrm{M}} = 0.18\%$ in Fig. 7.22. We remind the reader that for this value of ϵ_{M} a large fraction of initial trials failed in coming close to the true solution with the $\mathrm{HIO}^{\mathrm{A}}$+$\mathrm{ER}^{\mathrm{A}}$-algorithm.

Next, we investigate the influence of randomized overrelaxation on the reconstruction

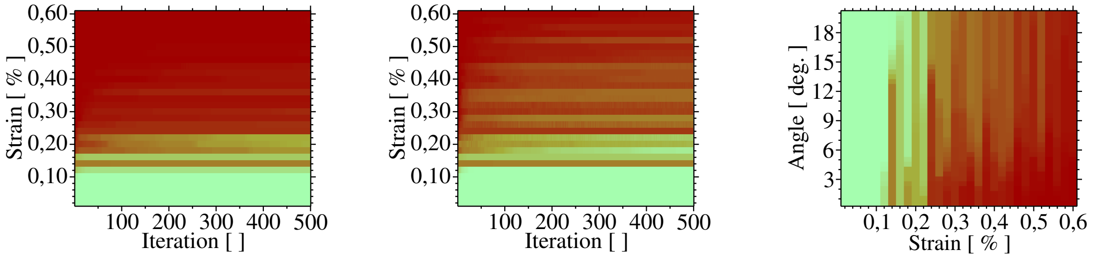

(a) Criterion for success $\varphi^{(i)} \leq \varphi_{\mathrm{Max}} = 1.0°$

(b) Criterion for success $\varphi^{(i)} \leq \varphi_{\mathrm{Max}} = 10.0°$

(c) Result after $i = 500$ iterations (©2013 The Optical Society (OSA), from [2])

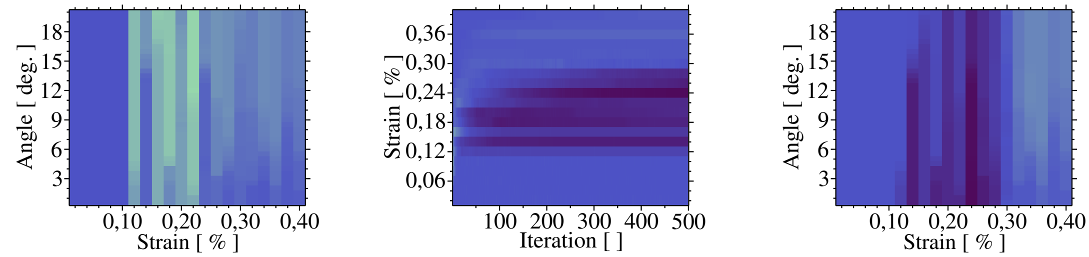

(d) Comparison to HIO+ER-algorithm at iteration $i = 500$ (Fig. 7.7(b))

(e) Comparison to $\mathrm{HIO}_{\mathrm{O_R}}$+ER-algorithm for $\varphi_{\mathrm{Max}} = 1.0°$ (Fig. 7.11(a))

(f) Comparison to $\mathrm{HIO}_{\mathrm{O_R}}$+ER-algorithm at iteration $i = 500$

Figure 7.19.: Reconstruction capabilities of the $\mathrm{HIO}^{\mathrm{A}}$+$\mathrm{ER}^{\mathrm{A}}$-algorithm, where the magnitude constraints $\mathbf{M}_{\mathrm{A}}$ defined in Eqs. (7.15a) and (7.21) with $\mathrm{A}_{\mathrm{L},} = 0.7$ and $\mathrm{A}_{\mathrm{H},} = 1.3$ are applied in the full direct space shape Ω. The discretization step in direction of strain ϵ_{M} is $\delta\epsilon_{\mathrm{M}} = 0.02\%$. Colorbar for plots (a)-(c) is given in Fig. 7.6(a), for plots (d)-(f) in Fig. 7.6(b).

process for the case of a ±30% gapped magnitude constraint in the entire direct space domain Ω of the object, i.e., choosing $\mathrm{A}_{\mathrm{L},} = 0.7$ and $\mathrm{A}_{\mathrm{H},} = 1.3$. The results are summarized in Fig. 7.23. As for the $\mathrm{HIO}^{\mathrm{A}}$+$\mathrm{ER}^{\mathrm{A}}$-algorithm, the success rate s depends on the choice for φ_{Max} in this case: In Figs. 7.23(a) and 7.23(b), we depict the success rates s as a function of strain and iteration for $\varphi_{\mathrm{Max}} = 1.0°$ and $\varphi_{\mathrm{Max}} = 10.0°$. The corresponding figures for the $\mathrm{HIO}^{\mathrm{A}}$+$\mathrm{ER}^{\mathrm{A}}$-algorithm are Figs. 7.19(a) and 7.19(b) respectively.

In contrast to the behavior of the $\mathrm{HIO}^{\mathrm{A}}$+$\mathrm{ER}^{\mathrm{A}}$-algorithm, the dependence of the success rate on the success criterion is, by far, more systematic: The dependence of the success rate s on φ_{Max} can be seen nicely in Fig. 7.23(c) which shows s as a function of strain ϵ_{M} and φ_{Max} after $i = 500$ iterations. In Fig. 7.23(c) all initial trials end up at a similar distance to the solution ϱ_{eff}. Up to $\epsilon_{\mathrm{M}} = 0.28\%$ – approximately the same strain ϵ_{M} which could be solved by the $\mathrm{HIO}_{\mathrm{O_R}}$+ER-algorithm without incorporating constraints on $|\varrho_{\mathrm{eff}}(\boldsymbol{r})|$ – all random initial trials still converge successfully to the solution ϱ_{eff} with an error smaller than $\varphi_{\mathrm{Max}} = 1.0°$. Beyond this value $\epsilon_{\mathrm{M}} = 0.28\%$, a single pronounced level of stagnation shows up. Its typical distance φ to the solution ϱ_{eff} as a function of strain ϵ_{M} increases monotonically, but slowly to values $\varphi_{\mathrm{Max}} > 1.0°$ – up to a strain ϵ_{M} of almost $\epsilon_{\mathrm{M}} \lesssim 1.0\%$. Up to this bound ϵ_{M}, the level of stagnation is *close* to the true solution *and* is reached by the $\mathrm{HIO}^{\mathrm{A}}_{\mathrm{O_R}}$+$\mathrm{ER}^{\mathrm{A}}$-algorithm independent of the random initial trial. Both observations do not hold for the $\mathrm{HIO}^{\mathrm{A}}$+$\mathrm{ER}^{\mathrm{A}}$-algorithm, as can be seen from the direct comparison of Figs. 7.19(c) and 7.23(c) given in Fig. 7.23(d).

Fig. 7.23(e) shows the success rate s as a function of the angle φ_{Max} and iteration i for the value $\epsilon_{\mathrm{M}} = 0.60\%$. This plot demonstrates that the achieved quality of the result of the iterative process is almost independent of the iteration i which is underlying Fig. 7.23(c)

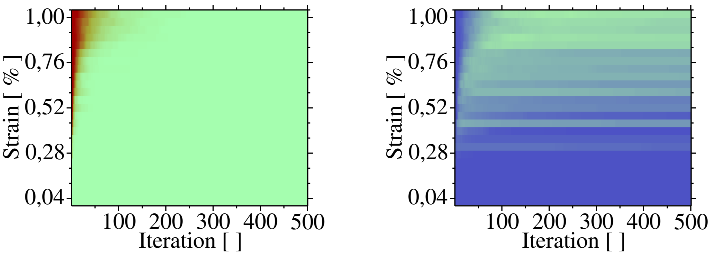

(a) Criterion for success $\varphi^{(i)} \leq \varphi_{\mathrm{Max}} = 1.0°$ (©2013 The Optical Society (OSA), from [2])

(b) Comparison to $\mathrm{HIO}^{\mathrm{A}}$+$\mathrm{ER}^{\mathrm{A}}$-algorithm (Fig. 7.16(a))

Figure 7.20.: Reconstruction capabilities of the $\mathrm{HIO}^{\mathrm{A}}_{\mathrm{O_R}}$+$\mathrm{ER}^{\mathrm{A}}$-algorithm, where the magnitude constraints $\mathbf{M}_{\mathrm{A}}$ defined in Eqs. (7.15a) and (7.21) with $\mathrm{A}_{\mathrm{L},} = 1.0$ and $\mathrm{A}_{\mathrm{H},} = 1.0$ are applied in the full direct space shape Ω. The discretization step in direction of strain ϵ_{M} is $\delta\epsilon_{\mathrm{M}} = 0.04\%$. Colorbar of Fig. (a) is given in Fig. 7.6(a), for Fig. (b) in Fig. 7.6(b).

after the initial phase of the reconstruction. Those levels of long-term stagnation close to the solution ϱ_{eff} are so strong that they are not left successfully despite randomized overrelaxation. For completeness, the direct comparison to the $\mathrm{HIO}^{\mathrm{A}}$+$\mathrm{ER}^{\mathrm{A}}$-algorithm of s as a function of φ_{Max} and i for $\epsilon_{\mathrm{M}} = 0.60\%$ can be found in Fig. 7.23(f).

Finally, we focus on the combination of ±0.3 gapped magnitude constraints in the entire sample ($\mathbf{M}^{(1)}_{\mathrm{A}}$) plus strict magnitude constraints in the substrate region ($\mathbf{M}^{(2)}_{\mathrm{A}}$) in the framework of the $\mathrm{HIO}^{\mathrm{A}}_{\mathrm{O_R}}$+$\mathrm{ER}^{\mathrm{A}}$-algorithm. The results are collected in Fig. 7.24.

Again, the success rate s depends on the choice for φ_{Max}, but the behavior is still different compared to employing each of the magnitudes constraints $\mathbf{M}^{(1)}_{\mathrm{A}}$ and $\mathbf{M}^{(2)}_{\mathrm{A}}$ on their own. For strain values $\epsilon_{\mathrm{M}} \leq 0.48\%$, almost no dependence on φ_{Max} can be observed for values greater or equal to 0.5° (see Fig. 7.24(c)). Then, an almost linear behavior separates the regions of successful and not successful reconstructions in the plot from $\epsilon_{\mathrm{M}} = 0.52\%$ to $\epsilon_{\mathrm{M}} = 0.76\%$. At this bound $\epsilon_{\mathrm{M}} = 0.76\%$, the success rate for angles $\varphi_{\mathrm{Max}} \gtrsim 9.0°$ is almost 100% and quickly drops to almost 0% for angles $\varphi_{\mathrm{Max}} \lesssim 9.0°$. However, by employing the strict substrate constraints on $|\varrho_{\mathrm{eff}}(\boldsymbol{r})|$ (i.e., $\mathbf{M}^{(2)}_{\mathrm{A}}$) in addition to $\mathbf{M}^{(1)}_{\mathrm{A}}$, this quality (defined by the error of approximately 9.0°) remains constant for strain up to $\epsilon_{\mathrm{M}} = 1.0\%$ for almost all initial trails. In order to exclude effects from the specific value $i = 500$ – the basis of Fig. 7.24(c) – we depict the behavior of the success rate s as a function of φ_{Max} and iteration i for $\epsilon_{\mathrm{M}} = 0.60\%$ and $\epsilon_{\mathrm{M}} = 1.00\%$ in Fig. 7.24. From this we see that the value $i = 500$ has been chosen reasonable for the before-mentioned considerations.

Investigation of the $\mathrm{HIO}^{\mathrm{A}}_{\mathrm{O_R}}$-algorithm ($\mathrm{HIO}^{\mathrm{A}}_{\mathrm{O_R}}$+$\mathrm{ER}^{\mathrm{A}}$-algorithm with $N_{\mathrm{ER}} = 0$)

Up to now, the results are based on the internal parameters $N_{\mathrm{HIO}} = 130$ and $N_{\mathrm{ER}} = 10$ of the HIO+ER-based algorithms. In Sec. 7.3, we demonstrated that the concept of randomized overrelaxation is powerful enough to even eliminate the need for error reduction in many cases entirely – as long as no additional *a priori* information was added to the traditional HIO+ER-algorithm. We now discuss this special case $N_{\mathrm{ER}} = 0$ ($\mathrm{HIO}^{\mathrm{A}}_{\mathrm{O_R}}$-algorithm) of the $\mathrm{HIO}^{\mathrm{A}}_{\mathrm{O_R}}$+$\mathrm{ER}^{\mathrm{A}}$-algorithm. For this, we consider the two cases $\mathrm{A}_{\mathrm{L},} = \mathrm{A}_{\mathrm{H},} = 1.0$ and $\mathrm{A}_{\mathrm{L},} = 0.7$ and $\mathrm{A}_{\mathrm{H},} = 1.3$ in the entire domain Ω.

The results for the $\mathrm{HIO}^{\mathrm{A}}_{\mathrm{O_R}}$-algorithm ($N_{\mathrm{ER}} = 0$) and the direct comparisons to the $\mathrm{HIO}^{\mathrm{A}}_{\mathrm{O_R}}$+$\mathrm{ER}^{\mathrm{A}}$-algorithm with $N_{\mathrm{HIO}} = 130$ and $N_{\mathrm{ER}} = 10$ are depicted in Fig. 7.25. The differences to the $\mathrm{HIO}^{\mathrm{A}}_{\mathrm{O_R}}$+$\mathrm{ER}^{\mathrm{A}}$-algorithm with $N_{\mathrm{ER}} = 10$ are minor:

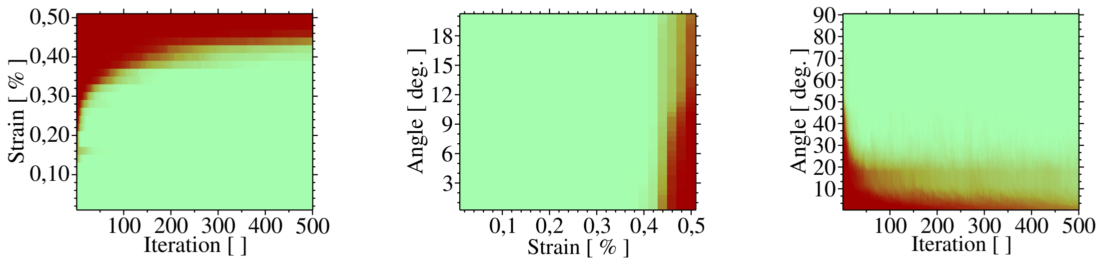

(a) Criterion for success $\varphi^{(i)} \leq \varphi_{\mathrm{Max}} = 1.0°$

(b) Result after $i = 500$ iterations (©2013 The Optical Society (OSA), from [2])

(c) Strain $\epsilon_{\mathrm{M}} = 0.44\%$

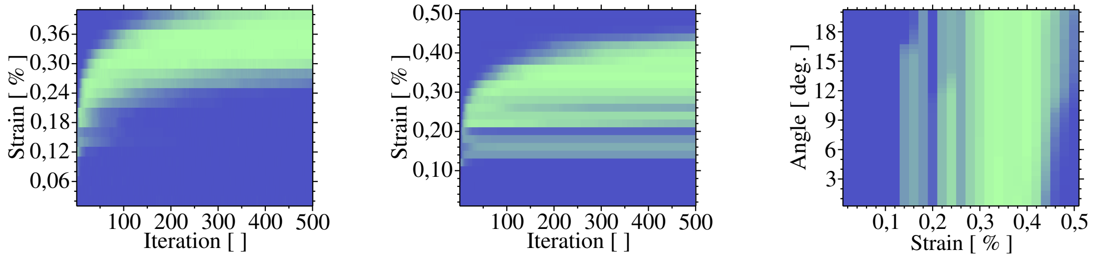

(d) Comparison to $\mathrm{HIO}_{\mathrm{O_R}}$+ER-algorithm (Fig. 7.11(a))

(e) Comparison to $\mathrm{HIO}^{\mathrm{A}}$+$\mathrm{ER}^{\mathrm{A}}$-algorithm (strain vs. iteration)

(f) Comparison to $\mathrm{HIO}^{\mathrm{A}}$+$\mathrm{ER}^{\mathrm{A}}$-algorithm (angle vs. strain)

Figure 7.21.: Reconstruction capabilities of the $\mathrm{HIO}^{\mathrm{A}}_{\mathrm{O_R}}$+$\mathrm{ER}^{\mathrm{A}}$-algorithm, where the magnitude constraints $\mathbf{M}_{\mathrm{A}}$ defined in Eqs. (7.15a) and (7.21) with $\mathrm{A}_{\mathrm{L},} = 1.0$ and $\mathrm{A}_{\mathrm{H},} = 1.0$ are applied in the substrate domain in the direct space object only (see hatched domain in Fig. 7.3(a)). The discretization step in direction of strain ϵ_{M} is $\delta\epsilon_{\mathrm{M}} = 0.02\%$. Colorbar for plots (a)-(c) is given in Fig. 7.6(a), for the remaining plots in 7.6(b).

In case of strict magnitude constraints, error reduction *slightly* speeds up convergence for low strain $\epsilon_{\mathrm{M}} \lesssim 0.30\%$ which, however, is achieved after few iterations for low strain anyway. For larger strain, it *slightly* slows down convergence to the solution (for better visibility the x-axis only covers the range up to iteration 100 – instead of 500 in most related plots). In case of the ±0.3 gapped magnitude constraints, the efforts of the HIO-algorithm to escape from local minima lift the average quality of the solution to a slightly higher value φ since the “polishing” of the ER-algorithm is missing. Apart from this, the behavior is very similar.

Thus, we demonstrated that also in presence of constraints on the magnitude of the effective electron density, the differences in the behavior of the reconstruction with and without error reduction are minor if randomized overrelaxation is included in the reciprocal space projection of the hybrid input output algorithm.

At this point, we shortly summarize our results on the $\mathrm{HIO}^{\mathrm{A}}_{\mathrm{O_R}}$+$\mathrm{ER}^{\mathrm{A}}$-algorithm: On the one hand, we demonstrated the benefits which are obtained by adding additional physical *a priori* knowledge to the reconstruction process where our focus of discussion were constraints on the magnitude of the effective electron density $|\varrho_{\mathrm{eff}}(\boldsymbol{r})|$, since such constraints can typically be employed for experimental samples and, at the same time, tremendously extend the range of applicability of the currently most widely used reconstruction algorithm in CXDI. On the other hand, we demonstrated that the given *a priori* information – with and without such magnitude constraints – is exploited more efficiently, if the concept of randomized overrelaxation is included in data evaluation based on the HIO+ER-algorithm. In particular, the influence of the initial guess of the reconstruction becomes negligible.

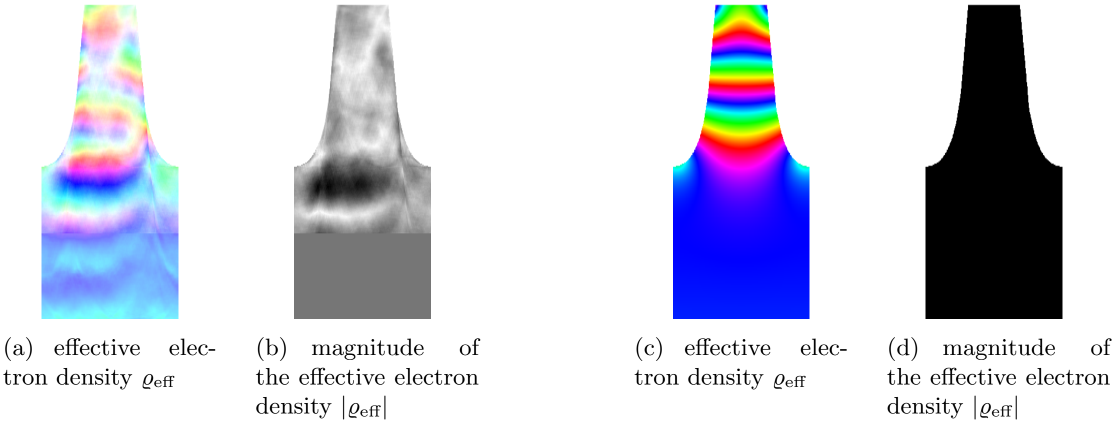
(a) effective electron density ϱ_{eff}
(b) magnitude of the effective electron density $|\varrho_{\text{eff}}|$
(c) effective electron density ϱ_{eff}
(d) magnitude of the effective electron density $|\varrho_{\text{eff}}|$

Figure 7.22.: Illustration of the output of reconstructions with the $\text{HIO}^{\text{A}}+\text{ER}^{\text{A}}$- and the $\text{HIO}^{\text{A}}_{\text{O}_\text{R}}+\text{ER}^{\text{A}}$-algorithm (see Figs. 7.18 and 7.21) for $\epsilon_{\text{M}} = 0.18\%$, where the magnitude constraints $\mathbf{M}_{\text{A}}$ defined in Eqs. (7.15a) and (7.21) with $\text{A}_{\text{L},} = 1.0$ and $\text{A}_{\text{H},} = 1.0$ are applied in the substrate domain in the direct space object only (see hatched domain in Fig. 7.3(a)). Figs. (a)-(b) show a stagnated initial guess of a reconstruction with the $\text{HIO}^{\text{A}}+\text{ER}^{\text{A}}$-algorithm, whereas Figs. (c)-(d) illustrate the output of the $\text{HIO}^{\text{A}}_{\text{O}_\text{R}}+\text{ER}^{\text{A}}$-algorithm: a successful reconstruction independent of the initial guess. The complex valued effective electron densities are encoded by HSV colorbar (phase encoding identical to Figs. 7.1 and 7.4), whereas their magnitudes are encoded by a black (max) and white (zero) colorbar separately for better visibility.

7.5. Elimination of vortices in the reconstructed phase field

Despite the benefits from randomized overrelaxation and the constraints $\mathbf{M}_{\text{A}}$ defined in Eqs. (7.15a) and (7.21), further investigations (and improvements) are still required before CXDI becomes an easily applicable method for the investigation of inhomogeneously strained nanocrystals.

On the one hand, experimentally measured data is not “ideal” – like the input data which is employed in this section. Several typical deviations will be investigated in Sec. 8.

On the other hand, neither the traditional HIO+ER-algorithm nor the $\text{HIO}^{\text{A}}_{\text{O}_\text{R}}+\text{ER}^{\text{A}}$-algorithm guarantee that the phase field of the iterative approximations to the solution ϱ_{eff} can be unwrapped globally without inconsistencies. Since the unwrapping of the phase field is required for obtaining the displacement field in highly strained nanostructures, this drawback is unsatisfactory.

Such inconsistencies have already been observed in failed reconstruction in this manuscript, for example in Fig. 7.17(b), and will now be investigated more closely.

We remind the reader that the possible existence of such inconsistencies already imposed restrictions on the choice of the error metric for judging on the quality of our reconstructed effective electron densities (see discussion in Sec. 6.2.2). Therefore, a deep understanding thereof is even more important.

In Fig. 7.26, we magnified the bottom of Fig. 7.17(b) which is nicely suited for a thorough discussion of vortex artifacts.

The phase field of the effective electron density $\varrho_{\text{eff}}(\boldsymbol{r})$ is given by $\Phi(\boldsymbol{r}) = \boldsymbol{Q}_{\text{B}} \cdot \boldsymbol{u}(\boldsymbol{r})$ (see Sec. 6.1). Since each component of the displacement field $\boldsymbol{u}(\boldsymbol{r})$ is a single-valued function of the position $\boldsymbol{r}$, also the phase field $\Phi(\boldsymbol{r})$ is a single-valued function at each position $\boldsymbol{r}$.

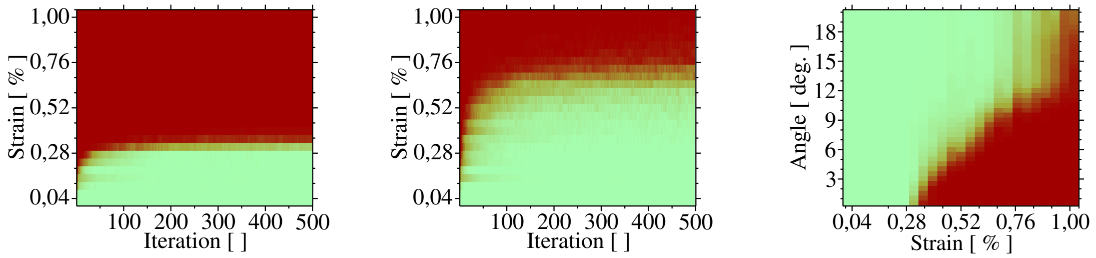

(a) Criterion for success $\varphi^{(i)} \leq \varphi_{\text{Max}} = 1.0°$ (compare to Fig. 7.19(a))

(b) Criterion for success $\varphi^{(i)} \leq \varphi_{\text{Max}} = 10.0°$ (compare to Fig. 7.19(b))

(c) Result after $i = 500$ iterations (©2013 The Optical Society (OSA), from [2])

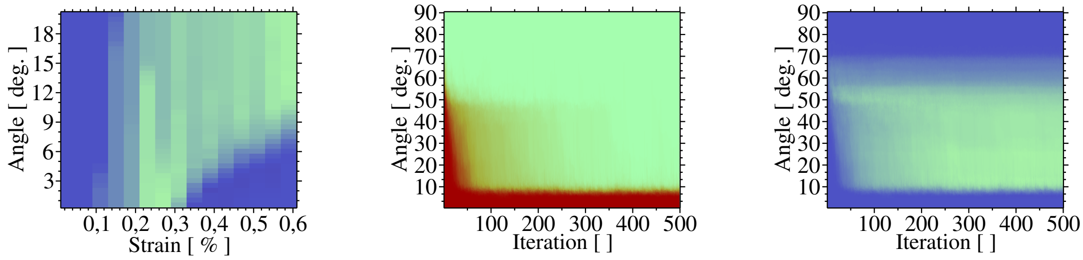

(d) Comparison with ±0.3 gapped HIO$^{\text{A}}$+ER$^{\text{A}}$-algorithm at iteration 500 (Fig. 7.19(c))

(e) Strain $\epsilon_{\text{M}} = 0.60\%$

(f) Comparison for $\epsilon_{\text{M}} = 0.60\%$ to ±0.3 gapped HIO$^{\text{A}}$+ER$^{\text{A}}$-algorithm

Figure 7.23.: Reconstruction capabilities of the $\text{HIO}^{\text{A}}_{\text{O}_\text{R}}$+ER$^{\text{A}}$-algorithm, where the magnitude constraints $\mathbf{M}_{\text{A}}$ defined in Eqs. (7.15a) and (7.21) with $\text{A}_{\text{L},} = 0.7$ and $\text{A}_{\text{H},} = 1.3$ are applied to the entire object domain Ω. The discretization step in direction of strain ϵ_{M} is $\delta\epsilon_{\text{M}} = 0.04\%$. Colorbar for plots (a)-(c) and (e) is given in Fig. 7.6(a), for the remaining plots in Fig. 7.6(b).

This phase field can therefore be understood as the anti-derivative ("potential") of a vector field ("force field") $\boldsymbol{F}(\boldsymbol{r}) = \nabla\Phi(\boldsymbol{r})$. By construction, this vector field is conservative and non-vortical, i.e., $\nabla \otimes \boldsymbol{F} \equiv 0$ *in the entire nanostructure* (which is assumed to constitute a simply connected domain Ω). As a consequence, the integration $\int_\gamma \boldsymbol{F}(\boldsymbol{r})\, \mathrm{d}\boldsymbol{r}$ of the vector field $\boldsymbol{F}$ is equal for all paths γ as long as its starting and end point are identical. Most importantly, this implies that

$$\oint_\gamma \boldsymbol{F}(\boldsymbol{r})\, \mathrm{d}\boldsymbol{r} = 0 \tag{7.26}$$

for any closed path γ (i.e., its starting and end point coincide).

The phase field $\Phi(\boldsymbol{r})$ in Fig. 7.26 is however *not* non-vortical in the entire depicted domain: Consider for example the integration paths γ_i as depicted in Fig. 7.26(b). If we decompose these paths into its straight line contributions, we reduce the integration $\oint_\gamma \boldsymbol{F}(\boldsymbol{r})\, \mathrm{d}\boldsymbol{r}$ to one-dimensional integrations. Since the phase field is a mathematically "well behaved" function along the paths γ_i, the anti-derivative $\Phi(\boldsymbol{r}_{\text{End}}) - \Phi(\boldsymbol{r}_{\text{Begin}})$ directly gives the result. We point out, that – depending on the phase field – *one-dimensional* local unwrapping of the phase field of the effective electron density $\varrho_{\text{eff}}(\boldsymbol{r})$ may be required which, however is a straight forward task as long as the data is not corrupted by noise and not undersampled numerically. By this approach, we have:

path	γ_1	γ_2	γ_3	γ_4	γ_5	γ_6	γ_7	γ_8
integral [$\cdot(2\pi)$]	0	0	1	-1	2	0	1	-1

Consequently, we detected violations of Eq. (7.26) which however are only multiples of 2π. The deviations stem from four point vortices inside the paths γ_i, $i = 3, 4, 7, 8$. The exact

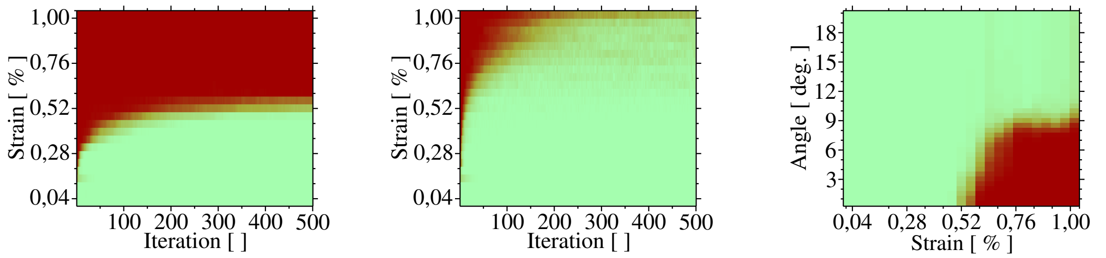

(a) Criterion for success $\varphi^{(i)} \leq \varphi_{\mathrm{Max}} = 1.0°$

(b) Criterion for success $\varphi^{(i)} \leq \varphi_{\mathrm{Max}} = 10.0°$

(c) Result after $i = 500$ iterations (©2013 The Optical Society (OSA), from [2])

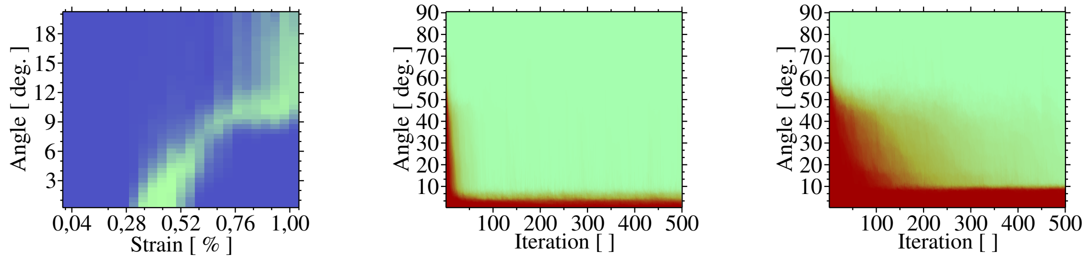

(d) Comparison to absence of strict magnitude constraints in the substrate (Fig. 7.23(c))

(e) Strain $\epsilon_{\mathrm{M}} = 0.60\%$

(f) Strain $\epsilon_{\mathrm{M}} = 1.00\%$

Figure 7.24.: Reconstruction capabilities of the $\mathrm{HIO}^{\mathrm{A}}_{\mathrm{O_R}}$+$\mathrm{ER}^{\mathrm{A}}$-algorithm with magnitude constraints $\mathbf{M}^{(1)}_{\mathrm{A}}$ with zero gap in the substrate domain ($\mathrm{A}_{\mathrm{L},1} = 1.0$, $\mathrm{A}_{\mathrm{H},1} = 1.0$) supplemented by $\mathbf{M}^{(2)}_{\mathrm{A}}$ with ± 0.3 gap in entire support Ω ($\mathrm{A}_{\mathrm{L},2} = 0.7$, $\mathrm{A}_{\mathrm{H},2} = 1.3$). The discretization step in direction of strain ϵ_{M} is $\delta\epsilon_{\mathrm{M}} = 0.04\%$. Colorbar for all plots except (d) is given in Fig. 7.6(a), for the remaining plot in Fig. 7.6(b).

positions of these point vortices can be located by shrinking the paths continuously until only a single pixel is contained in the interior of the paths γ_i.

If each pixel is scanned by a rectangular path through the neighbouring pixels, we attribute the result of this (numerical) integration after division by 2π to each pixel as its *vortex charge*. This charge is quantized and can only take integer values.

After detection of point vortices, we are able to actively manipulate them: Although many different interesting and promising possibilities for manipulation of vortex defects can be considered, we here restrict to the annihilation of point vortices by creating and super-imposing an anti-vortex: Such an anti-vortex is charged oppositely as the original vortex. Our approach closely resembles the mathematical concepts of second quantization in quantum field theory which is employed for the description of matter and anti-matter [225, 226].

We point out that identical or similar mathematical and formal concepts as described here are of high importance in various aspects of physics and mathematics such as electrodynamics (Maxwell's equations), quantum mechanics (discretization), advanced calculus (winding number), . . . , but, to the best of the authors' knowledge, such advanced concepts for detection and, more importantly, for active manipulation and control have not yet been incorporated in CXDI phase retrieval algorithms [227, 228]. As a result, the behavior of such vortices has not yet been thoroughly investigated.

In this manuscript, we pursue the following approach for incorporation of control over the vortices in the iterative approximations $\varrho^{(i)}_{\mathrm{eff}}$:

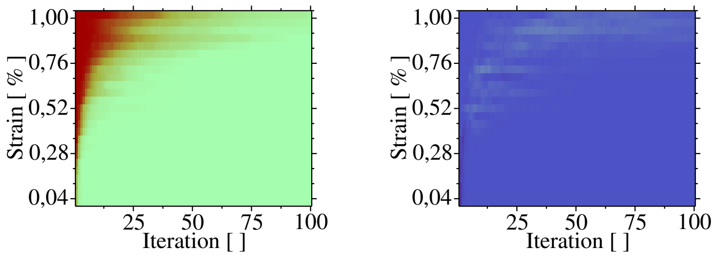

(a) Pure HIO$^{\mathrm{A}}_{\mathrm{O_R}}$-based reconstructions (no ER) with zero gap constraints $\mathrm{A}_{\mathrm{L},} = \mathrm{A}_{\mathrm{H},} = 1.0$, where $\varphi_{\mathrm{Max}} = 1.0°$.

(b) Comparison to HIO$^{\mathrm{A}}_{\mathrm{O_R}}$+ER$^{\mathrm{A}}$-algorithm with $N_{\mathrm{HIO}} = 130$ and $N_{\mathrm{ER}} = 10$, where $\varphi_{\mathrm{Max}} = 1.0°$

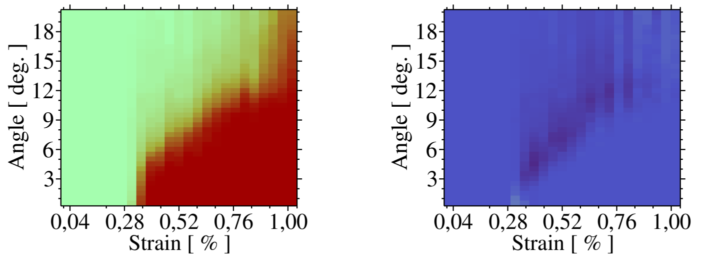

(c) Pure HIO$^{\mathrm{A}}_{\mathrm{O_R}}$-based reconstructions (no ER) with $\mathrm{A}_{\mathrm{L},} = 0.7$ and $\mathrm{A}_{\mathrm{H},} = 1.3$ after $i = 500$ iterations

(d) Comparison to HIO$^{\mathrm{A}}_{\mathrm{O_R}}$+ER$^{\mathrm{A}}$-algorithm with $N_{\mathrm{HIO}} = 130$ and $N_{\mathrm{ER}} = 10$ for $\mathrm{A}_{\mathrm{L},} = 0.7$ and $\mathrm{A}_{\mathrm{H},} = 1.3$

Figure 7.25.: Behavior of the HIO$^{\mathrm{A}}_{\mathrm{O_R}}$-algorithm (HIO$^{\mathrm{A}}_{\mathrm{O_R}}$+ER$^{\mathrm{A}}$-algorithm with $N_{\mathrm{ER}} = 0$).

After each "meta-iteration" of the HIO$^{\mathrm{A}}_{\mathrm{O_R}}$+ER$^{\mathrm{A}}$-algorithm (i.e., N_{HIO} iterations of the HIO$^{\mathrm{A}}_{\mathrm{O_R}}$- and N_{ER} iterations of the ER$^{\mathrm{A}}$-algorithm), we extract the current phase $\Phi^{(i)}(\boldsymbol{r}) = \arg\left(\varrho^{(i)}_{\mathrm{eff}}(\boldsymbol{r})\right)$ and store the current values $\rho^{(i)}(\boldsymbol{r}) = |\varrho^{(i)}_{\mathrm{eff}}(\boldsymbol{r})|$. For this phase field $\Phi^{(i)}(\boldsymbol{r})$, we detect the charge κ of each pixel (x, y) by contour integration of the closed path

$$(x, y) \rightarrow (x, y + 1) \rightarrow (x + 1, y + 1) \rightarrow (x + 1, y) \rightarrow (x, y) \tag{7.27}$$

after local unwrapping of the two neighbouring pixels.[2] If any of these points is outside the geometrical shape Ω, the charge κ is set to zero. At the edges of the computational domain, we employ periodic boundary conditions.

Based on this charge distribution we construct a field $\Psi^{(i)}(\boldsymbol{r})$ for compensation by creation of the respective anti-vortices. For each position (x_k, y_k) (pixel coordinates) with non-zero charge, we add the field

$$\Psi^{(i)}_k(\boldsymbol{r}) = -\kappa \operatorname{atan}_2(y - y_k, x - x_k) \tag{7.29}$$

to the compensation field $\Psi^{(i)}(\boldsymbol{r})$. We point out that the field configuration (7.29) is not unique. Without additional constraints, any spatial field distribution which has a single point vortex at position (x_k, y_k) is applicable. The field (7.29) is circular with respect to the distance in pixels. For a non-equal pixel spacing in the orthogonal directions – for

---

[2] Of course, also other paths such as

$$\begin{aligned}(x-1, y+1) \rightarrow (x, y+1) \rightarrow (x+1, y+1) \rightarrow (x+1, y) \rightarrow (x+1, y-1) \rightarrow \\ \rightarrow (x, y-1) \rightarrow (x-1, y-1) \rightarrow (x-1, y) \rightarrow (x-1, y+1)\end{aligned} \tag{7.28}$$

can be used. For simplicity, we restrict to Eq. (7.27) in this manuscript.

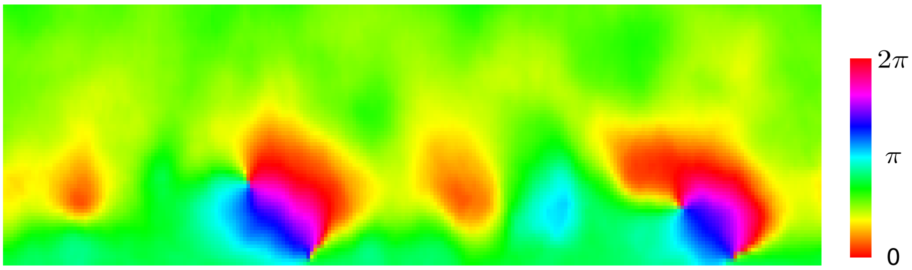

(a) Magnification of the bottom 74 pixels of Fig. 7.17(b)

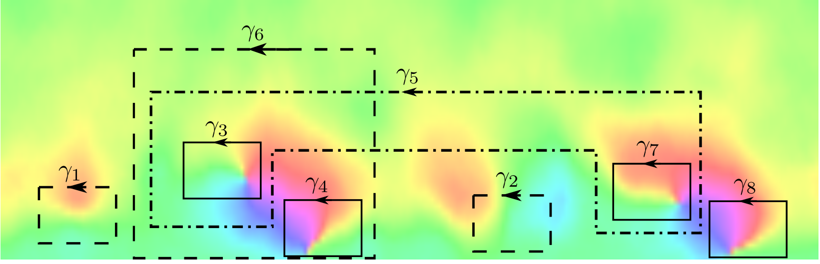

(b) Exemplary integration paths γ_i, $i = 1, \ldots, 8$ for Fig. (a)

Figure 7.26.: Illustration of vortices in the phase field of the reconstructed effective electron density ϱ_{eff} which prevent a globally consistent phase unwrapping.

example in case of our Si nanowire test system – we could also employ the field

$$\tilde{\Psi}_k^{(i)}(\boldsymbol{r}) = -\,\kappa\ \operatorname{atan}_2\left(s_y \cdot (y - y_k)\,, s_x \cdot (x - x_k)\right) \tag{7.30}$$

where the factors $s_{x/y}$ correspond to the distance of two neighbouring pixels in x and y direction. As a result, the point vortex would posses circular symmetry in physical length dimensions instead of pixels.

Both field configurations (7.29) and (7.30) have a non-vanishing gradient throughout the entire domain Ω. As a consequence, these corrections will also change the gradient of the effective electron density ϱ_{eff} throughout the entire geometry Ω. In contrast, the field

$$\dot{\Psi}_k^{(i)}(\boldsymbol{r}) = -\operatorname{sgn}(\kappa) \begin{cases} 0 & \text{if } y > y_k \\ \pi & \text{if } y < y_k \\ \frac{1}{2}\pi & \text{if } y = y_k \text{ and } x \geq x_k \\ \frac{3}{2}\pi & \text{if } y = y_k \text{ and } x < x_k \end{cases} \tag{7.31}$$

also constitutes a point vortex at (x_k, y_k) with charge $|\kappa| = 1$.[3] However, its gradient vanishes everywhere expect on the line y_k. Nonetheless, it induces a phase shift by π of regions below and above this line.

We would like to mention the cancellation effects of close-by point vortices of opposite charge. In such cases, the long-ranged modifications strongly cancel each other – similar to the cancellation effects in the far-field of multipoles in electrodynamics.

For simplicity, we restrict to the field (7.29) for the remainder of this manuscript.

After construction of the compensation field $\Psi^{(i)}(\boldsymbol{r})$, we add it to the current phase field $\Phi^{(i)}(\boldsymbol{r})$, i.e.,

$$\Phi^{(i)}(\boldsymbol{r}) \longrightarrow \Phi^{(i)}(\boldsymbol{r}) + \Psi^{(i)}(\boldsymbol{r})\ . \tag{7.32}$$

---

[3] This field configuration is only applicable for point vortices with charge $|\kappa| = 1$. For higher charges, this field configuration can no longer be locally unwrapped.

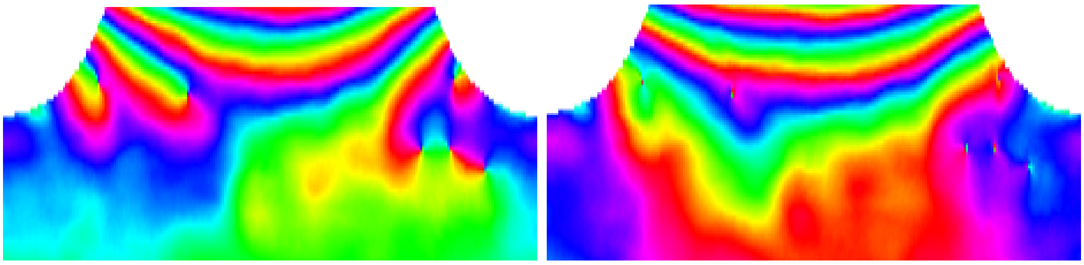

(a) Magnification of the central region of the phase field in Fig. (d)

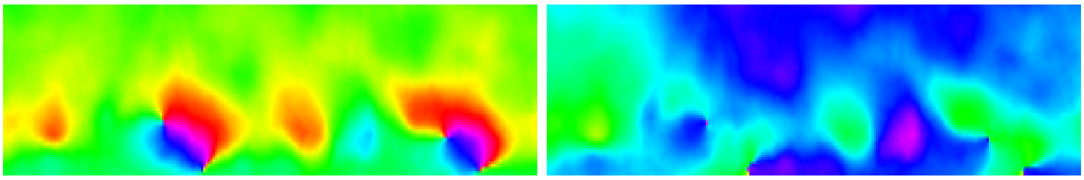

(b) Magnification of the bottom region of the phase field in Fig. (d) (left image identical to Fig. 7.26)

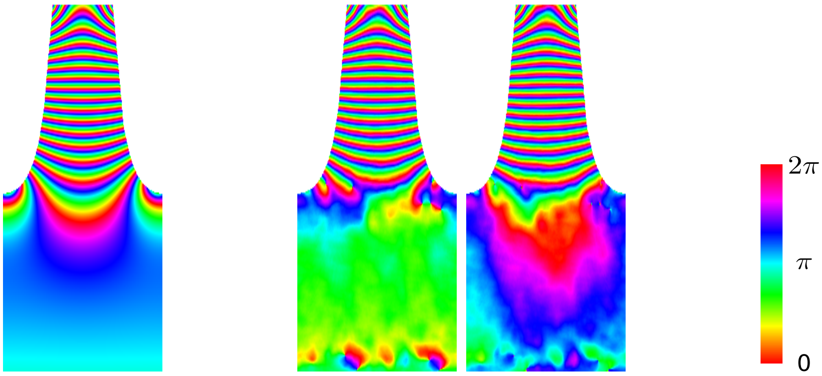

(c) Solution for ϱ_{eff} as reference

(d) $\mathrm{HIO}^{\mathrm{A}}+\mathrm{ER}^{\mathrm{A}}$-algorithm with $\mathrm{A}_{\mathrm{L},} = 1.0$ and $\mathrm{A}_{\mathrm{H},} = 1.0$ (10 vortices corrected)

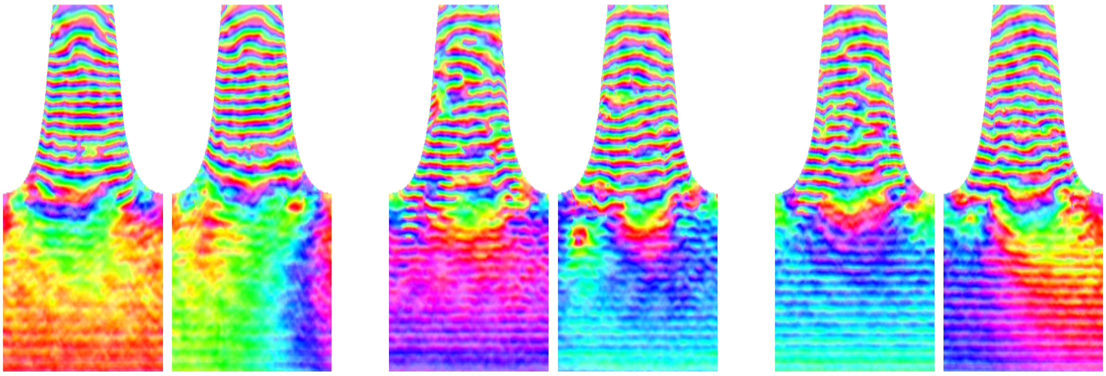

(e) $\mathrm{HIO}^{\mathrm{A}}_{\mathrm{O_R}}+\mathrm{ER}^{\mathrm{A}}$-algorithm with $\mathrm{A}_{\mathrm{L},} = 0.7$ and $\mathrm{A}_{\mathrm{H},} = 1.3$ (25 vortices corrected)

(f) $\mathrm{HIO}^{\mathrm{A}}_{\mathrm{O_R}}+\mathrm{ER}^{\mathrm{A}}$-algorithm with $\mathrm{A}_{\mathrm{L},} = 0.7$ and $\mathrm{A}_{\mathrm{H},} = 1.3$ (57 vortices corrected)

(g) $\mathrm{HIO}^{\mathrm{A}}_{\mathrm{O_R}}+\mathrm{ER}^{\mathrm{A}}$-algorithm with $\mathrm{A}_{\mathrm{L},} = 0.7$ and $\mathrm{A}_{\mathrm{H},} = 1.3$ (43 vortices corrected)

Figure 7.27.: Illustration of the correction for phase vortices by superposition of anti-vortex excitations for failed reconstructions (output for ϱ_{eff} after 500 iterations) at $\epsilon_{\mathrm{M}} = 1.0\%$ despite magnitude constraints $\mathbf{M}_{\mathrm{A}}$ in the domain Ω in direct space and randomized overrelaxation. In each figure, the left image depicts the phase field of the effective electron density before vortex correction, whereas the right image shows the output after vortex correction.

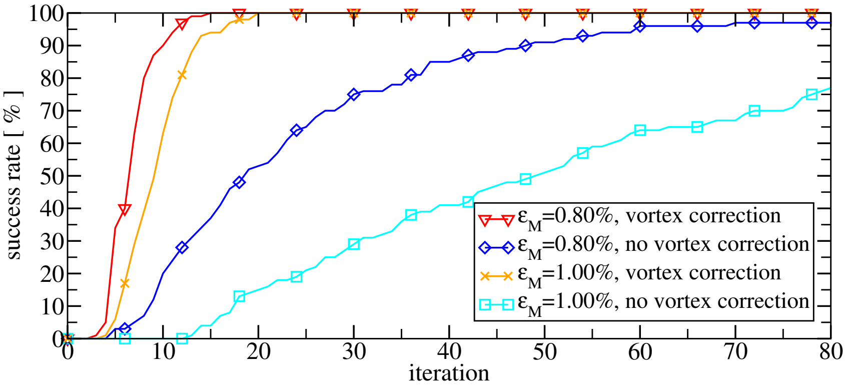

Figure 7.28.: Success rate of the $\mathrm{HIO}^{\mathrm{A}}_{\mathrm{O_R}}$+$\mathrm{ER}^{\mathrm{A}}$-algorithm for strict amplitude constraints $\mathrm{A}_{\mathrm{L},} = 1.0$ and $\mathrm{A}_{\mathrm{H},} = 1.0$ in the full domain Ω with and without vortex correction as a function of iteration for $\epsilon_{\mathrm{M}} \in \{0.80\%, 1.00\%\}$. Criterion for success is $\varphi^{(i)} \leq \varphi_{\mathrm{Max}} = 1.0°$.

We point out, that only the vortex detection is restricted to the geometry Ω, but the fields $\Phi^{(i)}$ and $\Psi^{(i)}$ in general extend beyond this geometry.

The final step is to combine the stored amplitudes $\rho^{(i)}(\boldsymbol{r})$ with these corrected phases $\Phi^{(i)}(\boldsymbol{r})$ in the natural way, i.e, $\varrho^{(i)}_{\mathrm{eff}}(\boldsymbol{r}) = \rho^{(i)}(\boldsymbol{r}) \cdot \mathrm{e}^{\mathrm{i}\,\Phi^{(i)}(\boldsymbol{r})}$. This iterative approximation $\varrho^{(i)}_{\mathrm{eff}}(\boldsymbol{r})$ is now free of vortices and taken as input for the next “meta-iteration” of the $\mathrm{HIO}^{\mathrm{A}}_{\mathrm{O_R}}$+$\mathrm{ER}^{\mathrm{A}}$-algorithm.

Before we discuss the performance of the combination of the $\mathrm{HIO}^{\mathrm{A}}_{\mathrm{O_R}}$+$\mathrm{ER}^{\mathrm{A}}$-algorithm and this way of vortex elimination, we give in Fig. 7.27 some examples for the effective electron density ϱ_{eff} before and after vortex correction – without running additional meta-iterations of the $\mathrm{HIO}^{\mathrm{A}}_{\mathrm{O_R}}$+$\mathrm{ER}^{\mathrm{A}}$-algorithm. Clearly, we see the non-local character — also intrinsic to the Fourier transform itself as to our magnitude constraints discussed in Sec. 7.4 — of the vortex correction. After this correction, all depicted failed reconstructions resemble the solution ϱ_{eff}, which is given in Fig. 7.27(c) for reference, much better than before this correction. We also nicely observe the localization of the effects of the vortex correction in case two oppositely charged point vortices are close to each other, for example the configuration close to the bottom in Fig. 7.27(d). Away from these pairs of vortices, the influence on the gradient of the phase field $\Phi(\boldsymbol{r})$ is only very small.

Moreover, and more importantly, the phase field $\Phi(\boldsymbol{r})$ of any of the corrected approximations can be unwrapped and, as a consequence, error metrics which measure the error of the reconstructed strain field and the reconstructed displacement field can be investigated (see also the discussion in Sec. 6.2.2). For illustration, we compare the number of phase wraps from the center of the substrate domain to the center of the top: For the true solution 7.27(c), we see approximately 14.5 phase wraps. After vortex correction, we find approximately 15, 13.5, 14.5 and 14.25 phase wraps in the examples depicted in Figs. 7.27(d) to 7.27(g) respectively. Consequently, the relative error of the displacement of the nanowire top versus its bottom is smaller than 7% in these examples – despite the fact that no further iterations of $\mathrm{HIO}^{\mathrm{A}}_{\mathrm{O_R}}$+$\mathrm{ER}^{\mathrm{A}}$-algorithm are performed after vortex correction.

These examples clearly demonstrate the power and importance of control over the point vortex structure in the reconstructed phase field.

A disadvantage of the vortex correction is that the required computational effort is not *a priori* known since the number of vortices which are corrected each meta-iteration is not *a priori* known. As a consequence, the number of meta-iterations of the $\mathrm{HIO}^{\mathrm{A}}_{\mathrm{O_R}}+\mathrm{ER}^{\mathrm{A}}$-algorithm is no longer a valid measure for comparison of the computational efficiency. Nonetheless, the behavior of the success rate as a function of the number of meta-iterations is still interesting: A significant reduction of the number of iterations which is required to achieve success rates close to 100% would indicate a high value of the vortex correction as additionally employed *a priori* knowledge – irrespective of the computational efficiency. We compare the success rate of the $\mathrm{HIO}^{\mathrm{A}}_{\mathrm{O_R}}+\mathrm{ER}^{\mathrm{A}}$-algorithm for strict magnitude constraints ($\mathrm{A}_{\mathrm{L},} = 1.0$ and $\mathrm{A}_{\mathrm{H},} = 1.0$ in the full domain Ω) for reconstructions with and without vortex correction as a function of iteration for $\epsilon_{\mathrm{M}} \in \{0.80\%, 1.00\%\}$ in Fig. 7.28. In fact, we see that the number of iterations which is required to achieve success rates close to 100% is significantly reduced in case of vortex correction after each meta-iteration. Since, however, the $\mathrm{HIO}^{\mathrm{A}}_{\mathrm{O_R}}+\mathrm{ER}^{\mathrm{A}}$-algorithm is already able to achieve success rates close to 100% with a well defined computational effort, the incorporation of our approach for vortex corrections is of minor importance for *ideal* data. Nonetheless, it will become important in Sec. 8.3 where we discuss the impact of the inconsistencies in the experimental and theoretical scattering data if the substrate is artificially truncated in direct space.

8. Reconstructions in CXDI: Results for simulated non-ideal data

In Sec. 7, we performed a thorough analysis of the reconstruction capabilities of the HIO+ER-algorithm in the framework of CXDI as described in Sec. 6.1. Based on these results, we developed several extensions and modifications which all provide significant improvements of the HIO+ER-algorithm.

These investigations of the HIO+ER-algorithm and its extensions have – up to now – been performed with *ideal* data in the framework of the CXDI model for the scattering of an inhomogeneously strained nanostructure in the vicinity of a Bragg peak.

In this chapter, we now consider the impact of typical deviations of experimentally measured data from the CXDI model on reconstructions based on the extensions of the HIO+ER-algorithm which we developed in Sec. 7.

Specifically, we focus on three such deviations:

- First, we investigate different approaches for treating (the typically large fraction of) reciprocal space data points which do not exceed the noise level. This investigation and its implications are presented in Sec. 8.1.
- Second, we consider in Sec. 8.2 the consequences of Poisson noise for the number of photons at each measured $\boldsymbol{q}$ point in reciprocal space.
- Third, we deal in Sec. 8.3 with the inconsistencies along the crystal truncation rod (CTR) of the substrate for nanostructures that are grown epitaxial on a crystalline substrate.

We point out the different nature of the three investigations: The first deviation mainly stems from technological and experimental limitations which will change in future. The second deviation is an intrinsic characteristics of the quantization of the light field as photons. The last deviation is a systematic error in the CXDI model for typical experimental structures: On the one hand, consideration of the full substrate is computationally not feasible and cannot be described by kinematic theory. On the other hand, truncation of the substrate near the nanoobject results in inconsistencies on the crystal truncation rod.

We mention that further aspects have to be investigated before CXDI might become applicable to experimental data in a robust way. Since CXDI is based on proper sampling of the reciprocal space intensity distribution, the following aspects should be investigated

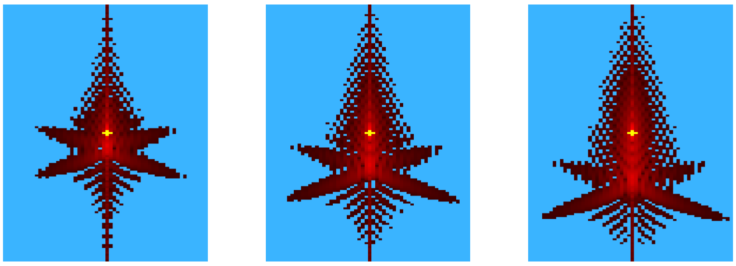

(a) $\epsilon_{\mathrm{M}} = 0.10\%$ (b) $\epsilon_{\mathrm{M}} = 0.20\%$ (c) $\epsilon_{\mathrm{M}} = 0.28\%$

Figure 8.1.: Scattering signal in presence of a low signal cutoff Γ_{N}. Only the central region of the scattering signal around the Bragg peak $\boldsymbol{Q}_{\mathrm{B}}$ is shown (58x133 pixels, corrected for non-square direct space pixel dimensions). The Bragg Peak $\boldsymbol{Q}_{\mathrm{B}}$ is located in the center of the images and highlighted in yellow. The data points in reciprocal space below the noise level Γ_{N} are masked in dark cyan. The scattering signal above noise level is logarithmic from black (low intensity) to red (high intensity). (©2013 The Optical Society (OSA), from [2])

carefully: First, the influence of the experimental resolution function should be considered. Proper sampling is typically only obtained if the spread of the resolution element is much smaller than the distance of neighbouring points of the $\boldsymbol{q}$-grid in reciprocal space. Second, typical experimental measurements of reciprocal space with one-dimensional or two-dimensional pixel detector do not sample a regular rectangular $\boldsymbol{q}$-grid in reciprocal space (due to the non-linear transformations from the geometrical scattering angles to reciprocal space [142]). Third, the robustness with respect to deviations of the geometrical shape Ω (or approaches for its simultaneous reconstruction) also need to be investigated.

8.1. Strategies for treating points of low intensity

The signal to noise ratio of our simulated input data for the reciprocal space amplitudes $\Gamma_{\boldsymbol{q}}$ in the previous chapter was only limited only by finite digit precision. In contrast, the signal to noise ratio of the experimental scattering data $\Gamma_{\boldsymbol{q}}$ given in Refs. [196, 197] is in the order of approximately 100 (excluding the central Bragg peak). As a consequence, the true value $\Gamma_{\boldsymbol{q}}$ of most data points in reciprocal space is not accessible by current experimental measurements. Possible reasons include detector noise or additional diffuse scattering, e.g. by optical elements, Be windows of vacuum flight tubes, etc.. Nonetheless, we know that the “background level” Γ_{N} (as estimated from the signal to noise ratio) constitutes an upper bound of these inaccessible data points, i.e., $\Gamma_{\boldsymbol{q}} \leq \Gamma_{\mathrm{N}}$.

In order to make CXDI of inhomogeneously strained nanostructures a robust technique of experimental value, we face this problem and compare in this section six strategies for treating these data points $\Gamma_{\boldsymbol{q}} \leq \Gamma_{\mathrm{N}}$ in reciprocal space.

To be specific, we define for every value of strain ϵ_{M} the low cutoff Γ_{N} as $\Gamma_{\mathrm{N}} = \mu \ \max_{\boldsymbol{q}} (\Gamma_{\boldsymbol{q}})$ where $\mu = 0.005$. If we exclude the Bragg peak, this value for μ corresponds approximately to the experimental value for the signal to noise ratio of current experimental data mentioned above. Fig. 8.1 shows which part of the scattering signal for the particular values of strain $\epsilon_{\mathrm{M}} = 0.10\%$, $\epsilon_{\mathrm{M}} = 0.20\%$ and $\epsilon_{\mathrm{M}} = 0.28\%$ exceeds this cutoff level Γ_{N}. In Tab. 8.1, we quantify the effects of this cutoff $\mu = 0.005$ in reciprocal space. For this purpose, we define the *effective oversampling ratio* σ_{eff} as the ratio of the number of data points exceeding the cutoff level Γ_{N} divided by the number of data points inside the direct space support. It is listed in Tab. 8.1 together with the number and percentage of data points in the scattering signal which exceed the cutoff Γ_{N}. Moreover, this table contains the

ϵ_{M}	0.10%	0.20%	0.28%
σ_{eff}	0.0304	0.0392	0.0442
# points $> \Gamma_{\mathrm{N}}$	1548	2000	2255
(# points $> \Gamma_{\mathrm{N}}$)/$\mathrm{N}_{\mathrm{Tot}}$	0.84%	1.08%	1.22%
$\Vert\Gamma_{\boldsymbol{q}} < \Gamma_{\mathrm{N}}\Vert_1 \,/\, \Vert\Gamma_{\boldsymbol{q}}\Vert_1$	64.6%	59.7%	56.3%
$\Vert\Gamma_{\boldsymbol{q}} < \Gamma_{\mathrm{N}}\Vert_2 \,/\, \Vert\Gamma_{\boldsymbol{q}}\Vert_2$	0.433%	0.401%	0.396%

Table 8.1.: Characteristics of the input data in case of the finite signal to noise ratio Γ_{N} defined by $\mu = 0.005$. (©2013 The Optical Society (OSA), from [2])

fraction of the $\mathcal{L}_1$- and $\mathcal{L}_2$-norm which is accumulated in the ideal scattering signal below the cutoff Γ_{N}.

The effective oversampling ratio is only in the range of $\sigma_{\mathrm{eff}} = 0.03$ to $\sigma_{\mathrm{eff}} = 0.05$ for the three cases which we employ for illustration. This values are not only much smaller than for the ideal system ($\sigma = 3.6326$), but also below the lower bound $\sigma = 2$ for the traditional HIO+ER-algorithm (see Sec. 6.1).

For the cutoff $\mu = 0.005$ and our discretization in direct and reciprocal space, only for approximately 1% of the points in reciprocal space a better estimate than the upper bound Γ_{N} is known. The "residual" approximately 99% of data points must be treated in such a way that the small fraction of data points exceeding Γ_{N} is sufficient for a successful reconstruction.

It is interesting to observe that these few data points $> \Gamma_{\mathrm{N}}$ contain more than 99.5% of the scattered *intensity* ($1 - \Vert\Gamma_{\boldsymbol{q}} < \Gamma_{\mathrm{N}}\Vert_2 \,/\, \Vert\Gamma_{\boldsymbol{q}}\Vert_2$ from Tab. 8.1). The large number of data points below the cutoff Γ_{N} accounts *in total* only to less than 0.5% of the scattered intensity. In contrast, more of 50% of the weight of the amplitudes $\Gamma_{\boldsymbol{q}}$ – which is the relevant input for a CXDI reconstruction with the HIO+ER-algorithm and its extensions – is below the cutoff Γ_{N}.

Of course, the precise values in Tab. 8.1 depend on the spacings of the discretization grid in direct space: A grid with larger inter-pixel spacing in direct space will suffer from aliasing artifacts, whereas a finer grid will reduce the effective oversampling even further and, therefore, relies even more on an efficient approach for low signal data points. However, the optimal choice of the direct space grid goes beyond the scope of this manuscript.

Based on this discussion, the importance of an adequate treatment of the data points below a cutoff comparable to the scale in current experiments is evident. In consequence, we investigate the behavior of $\mathrm{HIO}_{\mathrm{O_R}}$+ER and $\mathrm{HIO}^{\mathrm{A}}_{\mathrm{O_R}}$+$\mathrm{ER}^{\mathrm{A}}$-algorithm for $\Gamma_{\mathrm{N}} > 0$.

Our approaches modify the definition of $\mathbf{P}_\Gamma$ given in Eq. (6.50b) to

$$\mathbf{P}_\Gamma \; \mathcal{F}^{(i)}(\boldsymbol{q}) = \kappa_{\boldsymbol{q}} \;\; \mathrm{e}^{\mathrm{i}\; \arg\left(\mathcal{F}^{(i)}(\boldsymbol{q})\right)} \; , \tag{8.1}$$

but differ in the definition of $\kappa_{\boldsymbol{q}}$.

The first, naive approach is based on

$$\kappa_{\boldsymbol{q}}^{(A)} = \begin{cases} \Gamma_{\boldsymbol{q}} & \text{if } \Gamma_{\boldsymbol{q}} > \Gamma_{\mathrm{N}} \; , \\ |\mathcal{F}^{(i)}(\boldsymbol{q})| & \text{if } \Gamma_{\boldsymbol{q}} \le \Gamma_{\mathrm{N}} \; . \end{cases} \tag{8.2a}$$

With other words: the reciprocal space amplitudes may evolve unconstrained in the entire noisy domain. Of course, we expect bad performance of this approach because the available information – namely the upper bound of the signal – is completely discarded. Nevertheless, it is useful for comparison and therefore included for completeness.

The second approach incorporates the noisy region as the weak signal limit, i.e., approximating all amplitudes below the lower cutoff Γ_N as zero. Hence, we define

$$\kappa_{\boldsymbol{q}}^{(B)} = \begin{cases} \Gamma_{\boldsymbol{q}} & \text{if } \Gamma_{\boldsymbol{q}} > \Gamma_\mathrm{N} \ , \\ 0 & \text{if } \Gamma_{\boldsymbol{q}} \leq \Gamma_\mathrm{N} \ . \end{cases} \tag{8.2b}$$

The third, fourth and fifth approach are combinations of the first and second approach: they allow the reciprocal space amplitude at every $\boldsymbol{q}$-point to evolve freely until it exceeds the given cutoff Γ_N. The approaches differ in the behavior if the cutoff is exceeded during the iterative procedure: In the third approach, the respective amplitude is reset to zero. In the fourth approach, it is reset to a random value (uniform distribution) in the interval $[0, \Gamma_\mathrm{N}]$. The fifth approach resets the amplitude only to its upper bound Γ_N. In formulas, these approaches correspond to defining $\kappa_{\boldsymbol{q}}$ as

$$\kappa_{\boldsymbol{q}}^{(C)} = \begin{cases} \Gamma_{\boldsymbol{q}} & \text{if } \Gamma_{\boldsymbol{q}} > \Gamma_\mathrm{N} \ , \\ |\mathcal{F}^{(i)}(\boldsymbol{q})| & \text{if } (\Gamma_{\boldsymbol{q}} \leq \Gamma_\mathrm{N}) \wedge (|\mathcal{F}^{(i)}(\boldsymbol{q})| \leq \Gamma_\mathrm{N}) \ , \\ 0 & \text{if } (\Gamma_{\boldsymbol{q}} \leq \Gamma_\mathrm{N}) \wedge (|\mathcal{F}^{(i)}(\boldsymbol{q})| > \Gamma_\mathrm{N}) \ , \end{cases} \tag{8.2c}$$

in case of the third approach,

$$\kappa_{\boldsymbol{q}}^{(D)} = \begin{cases} \Gamma_{\boldsymbol{q}} & \text{if } \Gamma_{\boldsymbol{q}} > \Gamma_\mathrm{N} \ , \\ |\mathcal{F}^{(i)}(\boldsymbol{q})| & \text{if } (\Gamma_{\boldsymbol{q}} \leq \Gamma_\mathrm{N}) \wedge (|\mathcal{F}^{(i)}(\boldsymbol{q})| \leq \Gamma_\mathrm{N}) \ , \\ \mathrm{rand}\,(0; \Gamma_\mathrm{N}) & \text{if } (\Gamma_{\boldsymbol{q}} \leq \Gamma_\mathrm{N}) \wedge (|\mathcal{F}^{(i)}(\boldsymbol{q})| > \Gamma_\mathrm{N}) \ , \end{cases} \tag{8.2d}$$

where $\mathrm{rand}\,(0; \Gamma_\mathrm{N})$ is a uniform random distribution in the interval $[0, \Gamma_\mathrm{N}]$, for the fourth approach and, finally,

$$\kappa_{\boldsymbol{q}}^{(E)} = \begin{cases} \Gamma_{\boldsymbol{q}} & \text{if } \Gamma_{\boldsymbol{q}} > \Gamma_\mathrm{N} \ , \\ |\mathcal{F}^{(i)}(\boldsymbol{q})| & \text{if } (\Gamma_{\boldsymbol{q}} \leq \Gamma_\mathrm{N}) \wedge (|\mathcal{F}^{(i)}(\boldsymbol{q})| \leq \Gamma_\mathrm{N}) \ , \\ \Gamma_\mathrm{N} & \text{if } (\Gamma_{\boldsymbol{q}} \leq \Gamma_\mathrm{N}) \wedge (|\mathcal{F}^{(i)}(\boldsymbol{q})| > \Gamma_\mathrm{N}) \ , \end{cases} \tag{8.2e}$$

for the fifth approach.

Moreover, we include a sixth approach which is based on

$$\kappa_{\boldsymbol{q}}^{(F)} = \begin{cases} \Gamma_{\boldsymbol{q}} & \text{if } \Gamma_{\boldsymbol{q}} > \Gamma_\mathrm{N} \ , \\ c_\mathrm{D}|\mathcal{F}^{(i)}(\boldsymbol{q})| & \text{if } (\Gamma_{\boldsymbol{q}} \leq \Gamma_\mathrm{N}) \wedge (|\mathcal{F}^{(i)}(\boldsymbol{q})| \leq \Gamma_\mathrm{N}) \ , \\ \Gamma_\mathrm{N} & \text{if } (\Gamma_{\boldsymbol{q}} \leq \Gamma_\mathrm{N}) \wedge (|\mathcal{F}^{(i)}(\boldsymbol{q})| > \Gamma_\mathrm{N}) \ , \end{cases} \tag{8.2f}$$

where $c_\mathrm{D} \lesssim 1$ models a small damping of the intensity in regions below Γ_N. This way, we regularize the corrupted data points such that their respective spatial frequencies in the direct space effective electron density $\varrho_\mathrm{eff}(\boldsymbol{x})$ are slightly damped each iteration. The idea behind this approach is that this slight damping will be compensated by the direct space constraints on the (oversampled) grid if “incorrectly” damped, but still accounts for the fact that most data points below the upper bound Γ_N are (much) smaller than this upper bound.

Note, that the last approach (F) reduces to the fifth approach (E) in the limit $c_\mathrm{D} \to 1$. Throughout this manuscript, we consider $c_\mathrm{D} = 0.99$.

For a proper investigation of these models defined in Eq. (8.2), we must eliminate the amplitude information $\Gamma_{\boldsymbol{q}}$ from the initial guess (6.53) for all points $\Gamma_{\boldsymbol{q}} \leq \Gamma_\mathrm{N}$. For that purpose, we set $\Gamma_{\boldsymbol{q}} = 0$ for all point $\Gamma_{\boldsymbol{q}}$ in the initial guess for which $\Gamma_{\boldsymbol{q}} \leq \Gamma_\mathrm{N}$ is fulfilled.

We first investigate the behavior of the angle $\varphi^{(i)}$ (see Eq. (6.48)) as a function of iteration on the level of a single reconstruction and for a fixed strain ϵ_M (see Fig. 8.2). The behavior

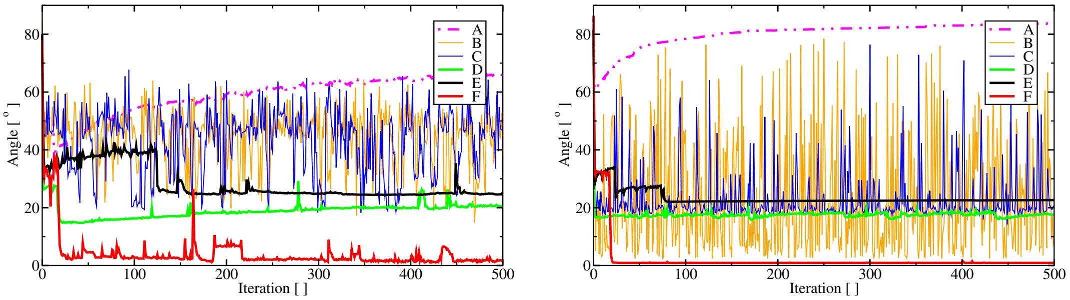

(a) $\mathrm{HIO_{OR}}$+ER-algorithm for $\epsilon_{\mathrm{M}} = 0.20\%$

(b) $\mathrm{HIO^{A}_{OR}}$+$\mathrm{ER^{A}}$-algorithm for $\epsilon_{\mathrm{M}} = 0.28\%$ with $\mathrm{A_{L,}} = \mathrm{A_{H,}} = 1.0$ in entire domain Ω

Figure 8.2.: Illustration of the typical behavior of $\varphi^{(i)}$ for the models (A) to (F) (as defined in Eq. (8.2)) as a function of iteration for a *single* reconstruction.

of the models is very similar for the HIO+ER- for $\epsilon_{\mathrm{M}} = 0.20\%$ (Fig. 8.2(a)) and the $\mathrm{HIO^{A}_{OR}}$+$\mathrm{ER^{A}}$-algorithm for $\epsilon_{\mathrm{M}} = 0.28\%$ (Fig. 8.2(b)):

As expected, model (A) – which completely disregards the upper bound information in the low cutoff domain – fails completely. Model (B), i.e., setting the low signal amplitudes simply to zero, results in very unstable behavior: As soon as the solution is approached to some level, the projection of the low signal amplitudes $\Gamma_{\boldsymbol{q}}$ to zero redistributes scattering amplitude from the interior of the object's domain Ω to its exterior. As a consequence, the iterative reconstruction procedure is unable to consistently fit the reciprocal space signal from sharp surfaces which is very pronounced due to the discontinuity of the effective electron density at surfaces. The inconsistencies in the scattering signal are strong enough to produce the pronounced instabilities visible in Fig. 8.2 for model (B). Model (C), (D) and (E) all allow for free variation of $\Gamma_{\boldsymbol{q}}$ in the low signal region until the upper bound Γ_{N} is exceeded. The instabilities in model (C) are less pronounced than in model (B), but still rather strong. The origin of the instabilities is identical to model (B). Model (D) and model (E) avoid these strict zeros in reciprocal space and thus are more stable than model (C), but achieve almost equal quality of the iterative reconstruction. model (E) shows almost no instabilities. However, model (E) only achieves angles φ which are too big for obtaining high-quality reconstruction: the best results for our parameters underlying Fig. 8.2 are only in the order of 18.0°. The drawback of all models (A) to (E) is that no "regularization" for the data points $\Gamma_{\boldsymbol{q}} \leq \Gamma_{\mathrm{N}}$ is included. For that purpose, the small damping has been added to model (F). With this modification, very small angles in the range of 0.5° to 2.0° are achieved without instabilities of practical importance (see Fig. 8.2).

Next, we again focus on the success rate s as a statistical quantity (see Fig. 8.3). However, we should take into account the observed instabilities during a single reconstruction procedure. For this, we distinguish two cases and extract two numbers for each of the $\mathrm{N_{Real}} = 100$ initial trials (with new random initial phases):

- First, we extract the smallest distance $\varphi^{(i)}$ which was achieved at any iteration $i \leq 500$ (left bars in Fig. 8.3).
- Second, we extract the distance $\varphi^{(500)}$, i.e., the distance to the solution ϱ_{eff} after $i = 500$ iterations (right bars in Fig. 8.3).

If the reconstruction algorithm is stable and the error is an approximately monotonously decreasing function of the number of performed iterations, the error after $i = 500$ iterations should be similar to the error of the best reconstruction. If the reconstruction algorithm is unstable, it is likely that the error after $i = 500$ iterations of a large fraction of the initial

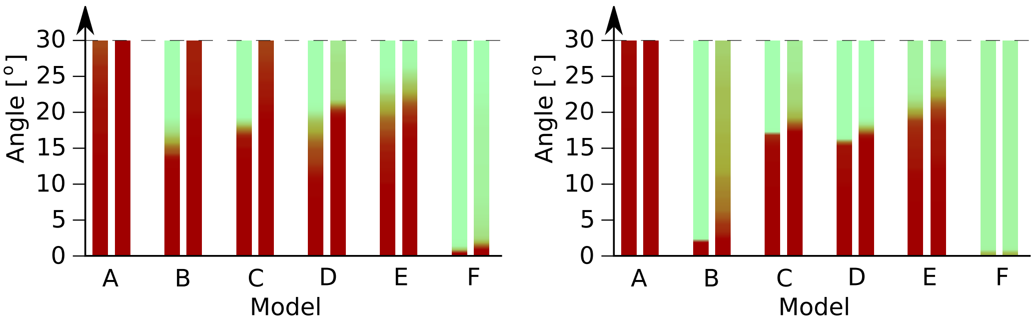

(a) $\mathrm{HIO}_{\mathrm{O_R}}$+ER-algorithm for $\epsilon_{\mathrm{M}} = 0.20\%$

(b) $\mathrm{HIO}^{\mathrm{A}}_{\mathrm{O_R}}$+$\mathrm{ER}^{\mathrm{A}}$-algorithm for $\epsilon_{\mathrm{M}} = 0.28\%$ with $\mathrm{A}_{\mathrm{L},} = \mathrm{A}_{\mathrm{H},} = 1.0$ in entire domain Ω

Figure 8.3.: Comparison of the success rate s for the models defined in Eq. (8.2) for fixed strain ϵ_{M}. For every model the left bar shows the success rate s if the best iterative approximation $\varrho_{\mathrm{eff}}^{(i)}$ at any iteration $i \leq 500$ is compared to the angle $\varphi_{\mathrm{Max}} \in [0°, 30°]$ on the ordinate. The right bar evaluates s for $\varphi_{\mathrm{Max}} \in [0°, 30°]$ if only the result $\varrho_{\mathrm{eff}}^{(i)}$ after iteration $i = 500$ is considered. Colorbar for the success rate s is given by Fig. 7.6(a).

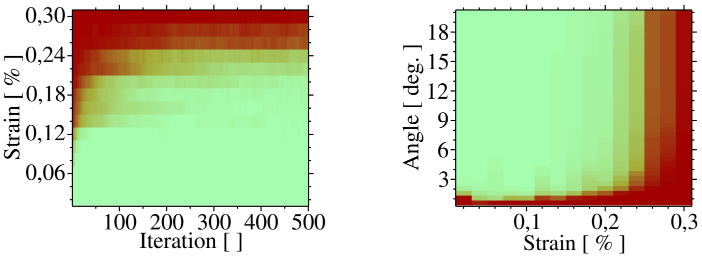

(a) Criterion for success $\varphi^{(i)} \leq \varphi_{\mathrm{Max}} = 10.0°$

(b) Result after $i = 500$ iterations

Figure 8.4.: Reconstruction capabilities of the $\mathrm{HIO}_{\mathrm{O_R}}$+ER-algorithm in case of a non-zero low cutoff (see Tab. 8.1) and treatment according to Eq. (8.2f). The discretization step in direction of strain ϵ_{M} is $\delta\epsilon_{\mathrm{M}} = 0.02\%$. Colorbar for both plots is given in Fig. 7.6(a). (©2013 The Optical Society (OSA), from [2])

trials is much larger than the best solution that has been found throughout the entire reconstruction process. Consequently, the comparison of the two bars in Fig. 8.3 contains valuable information on the instability of the approaches (A) to (F).

Nonetheless, the left bars in Fig. 8.3 become important if we find some robust and practical criterion for selecting the best approximation $\varrho_{\mathrm{eff}}^{(i)}$ from the N_{Iter} iterations ($N_{\mathrm{Iter}} = 500$ in our example). In contrast, the right bars are important as long as such a criterion is not available.

Fig. 8.3 confirms our observations on the level of a single reconstruction: Model (A) is not useful at all. Model (B) can get quite close to the true solution (especially in presence of strict magnitude constraints), but is extremely unstable. Model (C) does not approach the solution as good as model (B) and is still very unstable without magnitude constraints. Instability decreases further for model (D) and (E), but typical distances to the solution ϱ_{eff} are big. Model (F) achieves much better quality *and* stability than the models (A) to (E). Therefore, model (F) is clearly the winner of our comparison in the framework of the HIO+ER- and the $\mathrm{HIO}^{\mathrm{A}}_{\mathrm{O_R}}$+$\mathrm{ER}^{\mathrm{A}}$-algorithm.

For the best model (F) and the cut-off $\mu = 0.005$ (see Tab. 8.1), the success rate s is

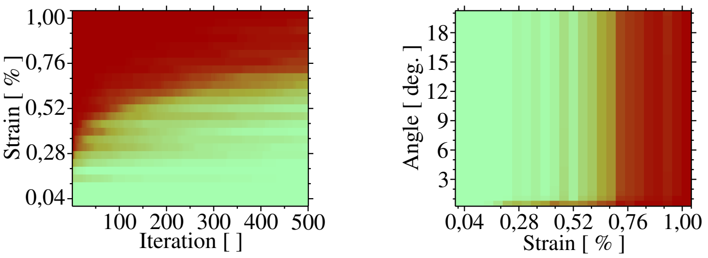

(a) Criterion for success $\varphi^{(i)} \leq \varphi_{\mathrm{Max}} = 10.0°$

(b) Result after $i = 500$ iterations

Figure 8.5.: Reconstruction capabilities of the $\mathrm{HIO}^{\mathrm{A}}_{\mathrm{O_R}}$+$\mathrm{ER}^{\mathrm{A}}$-algorithm in case of a non-zero low cutoff (see Tab. 8.1) and treatment according to Eq. (8.2f). The constraints (7.21) with $\mathrm{A}_{\mathrm{L},} = 1.0$ and $\mathrm{A}_{\mathrm{H},} = 1.0$ were applied in the full direct space shape Ω. The discretization step in direction of strain ϵ_{M} is $\delta\epsilon_{\mathrm{M}} = 0.04\%$. Colorbar of both plots is given in Fig. 7.6(a). (©2013 The Optical Society (OSA), from [2])

depicted as a function of strain ϵ_{M} vs. iteration i and angle φ_{Max} vs. strain ϵ_{M} – analogous to our discussion in case of ideal data in Sec. 7.4. Fig. 8.4 depicts the case without magnitude constraints (i.e., $\mathrm{HIO}_{\mathrm{O_R}}$+ER-algorithm) whereas Fig. 8.5 considers the case of strict magnitude constraints for $|\varrho_{\mathrm{eff}}(\boldsymbol{r})|$ in the entire direct space domain Ω.

In both cases, the success rate is almost independent of the choice φ_{Max} for $\varphi_{\mathrm{Max}} \in [3.0°, 20.0°]$. In comparison to reconstructions without the cutoff $\mu = 0.005$ in reciprocal space, the maximum strain ϵ_{M} which has been reconstructed successfully in the framework of model (F) dropped from $\epsilon_{\mathrm{M}} \approx 0.28\%$ to $\epsilon_{\mathrm{M}} \approx 0.24\%$ without constraints on $|\varrho_{\mathrm{eff}}(\boldsymbol{r})|$ and from $\epsilon_{\mathrm{M}} \geq 1.0\%$ to $\epsilon_{\mathrm{M}} \approx 0.68\%$ with strict constraints on $|\varrho_{\mathrm{eff}}(\boldsymbol{r})|$ in the entire domain Ω.

Fig. 8.6 gives a graphical summary of our numerical investigation for $\mu = 0$ and $\mu = 0.005$:

Starting from the standard HIO+ER-algorithm, the improvements which are achieved by including randomized overrelaxation and additional magnitude constraints $\mathbf{M}_{\mathrm{A}}$ separately or combined can be found. Two values are extracted from every set of parameters which we presented in this manuscript: The upper value in each rectangular box is the maximum strain ϵ_{M} for which an almost perfect solution could be reconstructed within $i = 500$ iterations and for almost all random initial trails. The lower value is the maximum strain ϵ_{M} for which the reconstruction of the effective electron density $\varrho^{(500)}_{\mathrm{eff}}$ was successful if the requirement for success is relaxed: Any strain ϵ_{M} for which at least a non-negligible fraction of initial guesses managed to achieve a result close to the solution ϱ_{eff} ($\varphi_{\mathrm{Max}} \lesssim 10.0°$) is classified as suitable for the respective algorithm.

From this figure, our four major results can be read off easily:

- First, additional magnitude constraints $\mathbf{M}_{\mathrm{A}}$ tremendously enhance the range of applicability, but the result still depends on the random initial guess.
- Second, randomized overrelaxation manages to eliminate the sensitivity to the random initial guess to a large degree (with and without the constraints $\mathbf{M}_{\mathrm{A}}$).
- Third, randomized overrelaxation manages to increase the range of applicability further (without any additional *a priori* knowledge) in all cases we presented.
- Finally, model (F) succeeds in reconstruction of input data with a signal to noise ratio that is comparable to current experimental data – despite corresponding effective oversampling ratios in the order of $\sigma_{\mathrm{eff}} \lesssim 0.05 \ll 2$.

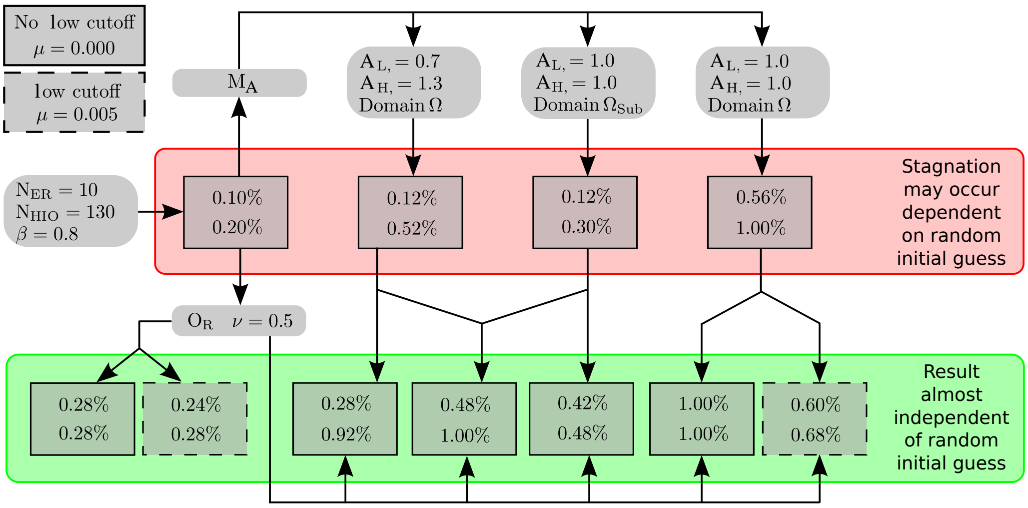

Figure 8.6.: Intermediate summary of our numerical investigations: Starting from standard HIO+ER, the improvements which are achieved by randomized overrelaxation and additional constraints $\mathbf{M}_{\mathrm{A}}$ on the local scattering magnitude $|\varrho_{\mathrm{eff}}(\boldsymbol{r})|$ are simplified to two values. The upper value in each rectangular box is the maximum strain ϵ_{M} for which an almost perfect solution could be reconstructed within $i = 500$ iterations and for almost all random initial trails. The lower value is the maximum strain ϵ_{M} for which the reconstruction of the effective electron density $\varrho_{\mathrm{eff}}^{(500)}$ was at least successful for a non-negligible fraction of initial guesses and/or with a reduced requirement on the quality of the result. [(©2013 The Optical Society (OSA), from [2]), notation adopted]

Therefore, we are confident that the combination of randomized overrelaxation $\mathbf{Q}_{\Gamma;\lambda_\Gamma}$, magnitude constraints $\mathbf{M}_{\mathrm{A}}$ and a small damping of low-intensity domains in reciprocal space provides a major advance in CXDI data analysis.

8.2. Consequences of Poisson photon noise

In the previous section, we investigated the reconstruction capabilities if a low cut off of the reciprocal space data is taken into account. In this section, we extend our considerations and discuss the impact of Poisson noise in the measured *intensity* data, since the measured intensity is directly proportional to the number photons. Some detectors even count the discrete number of detected photons as measure for the intensity. We will not consider other sources of noise (e.g., electronic noise and non-linearity of photon response in CCD detectors) and other detection artifacts (e.g., dead time in counting detectors).

Within these assumptions, the following relation

$$\mathcal{I}(\boldsymbol{q}) = |\Gamma_{\boldsymbol{q}}|^2 = c\, N_{\boldsymbol{q}}^{(\mathrm{Ph})} \tag{8.3}$$

holds.

This implies that a change $\delta\mathcal{I}(\boldsymbol{q})$ of the intensity is related to a change of the amplitude via

$$\delta\mathcal{I}(\boldsymbol{q}) \approx 2\,|\Gamma_{\boldsymbol{q}}|\;\delta\,|\Gamma_{\boldsymbol{q}}| \quad \Rightarrow \quad \delta\,|\Gamma_{\boldsymbol{q}}| = \frac{\delta\mathcal{I}(\boldsymbol{q})}{2\,|\Gamma_{\boldsymbol{q}}|}\,. \tag{8.4}$$

Therefore, the relative change of the amplitude

$$\frac{\delta\,|\Gamma_{\boldsymbol{q}}|}{|\Gamma_{\boldsymbol{q}}|} = \frac{1}{2}\cdot\frac{\delta\mathcal{I}(\boldsymbol{q})}{\mathcal{I}(\boldsymbol{q})} \tag{8.5}$$

is half the relative change of the intensity.

We now assume Poisson statistics for the number of incident photons $N_{\boldsymbol{q}}^{(\mathrm{Ph})}$ for each measured point $\boldsymbol{q}$. In this case, a good estimate for the deviation of the number of photons $\delta N_{\boldsymbol{q}}^{(\mathrm{Ph})}$ is provided by the standard deviation $\sqrt{N_{\boldsymbol{q}}^{(\mathrm{Ph})}}$ of this distribution, i.e., we approximate

$$\delta N_{\boldsymbol{q}}^{(\mathrm{Ph})} \approx \sqrt{N_{\boldsymbol{q}}^{(\mathrm{Ph})}} \ . \tag{8.6}$$

Therefore, we have

$$\delta \mathcal{I}(\boldsymbol{q}) \approx c\sqrt{N_{\boldsymbol{q}}^{(\mathrm{Ph})}} \quad , \quad \delta\left|\Gamma_{\boldsymbol{q}}\right| = \frac{\delta \mathcal{I}(\boldsymbol{q})}{2\left|\Gamma_{\boldsymbol{q}}\right|} = \frac{\sqrt{c}}{2} \tag{8.7a}$$

and

$$\frac{\delta \mathcal{I}(\boldsymbol{q})}{\mathcal{I}(\boldsymbol{q})} = \frac{1}{\sqrt{N_{\boldsymbol{q}}^{(\mathrm{Ph})}}} \quad , \quad \frac{\delta\left|\Gamma_{\boldsymbol{q}}\right|}{\left|\Gamma_{\boldsymbol{q}}\right|} = \frac{1}{2\sqrt{N_{\boldsymbol{q}}^{(\mathrm{Ph})}}} \tag{8.7b}$$

in case of Poisson noise. It is important to recognize that the expected deviation of the amplitude $\delta\left|\Gamma_{\boldsymbol{q}}\right|$ is *in*dependent of the number of photons, but does depend on the constant of proportionality c. In contrast, the relative deviations of intensity and amplitude are *in*dependent of this proportionality constant c, but depend on the number of photons.

We have already seen in the previous section that the reconstruction process is very sensitive to enforced inconsistencies of the constraints in direct space and reciprocal space (model (B)) and typically instabilities are observed. A corruption of the reciprocal space amplitudes by Poisson noise also leads to inconsistencies of the constraints in direct space and reciprocal space.

In order to avoid the expected instabilities, we now study the influence of a gap for the reciprocal space projection amplitudes in the projection operator $\mathbf{P}_{\Gamma}$: within a certain range around the given input amplitude Γ_{N}, the reconstructed amplitudes $\Gamma_{\mathrm{N}}^{(i)}$ are allowed to vary freely. This way, we strongly reduce the inconsistencies of the direct space and reciprocal space constraints and might avoid instabilities. However, such gaps render the constraints in reciprocal space less tighten which might hinder the reconstruction.

Based on our above discussion, the gap should allow for a *constant* (i.e., $\boldsymbol{q}$-independent) deviation $\delta\left|\Gamma_{\boldsymbol{q}}\right| = \frac{\sqrt{c}}{2}$ from the given input value $\left|\Gamma_{\boldsymbol{q}}\right|$ in case of Poisson noise.

In our simulations, we will predefine the total number of collected photons $N_{\mathrm{Tot}}^{(\mathrm{Ph})}$ from all $\boldsymbol{q}$ points. The corresponding value of c which is required for defining the gap interval $\delta\left|\Gamma_{\boldsymbol{q}}\right|$ is obtained by summation of Eq. (8.3) with respect to $\boldsymbol{q}$, i.e.,

$$c = \sum_{\boldsymbol{q}} \left|\Gamma_{\boldsymbol{q}}\right|^2 / N_{\mathrm{Tot}}^{(\mathrm{Ph})} \ . \tag{8.8}$$

Hence, we directly obtain an estimate for the gaps $\delta\left|\Gamma_{\boldsymbol{q}}\right| = \frac{\sqrt{c}}{2}$. This way, we can study the performance of the reconstruction algorithm for gapped projections in reciprocal space even if the input data $\Gamma_{\boldsymbol{q}}$ is not corrupted by noise. Since the gaps $\delta\left|\Gamma_{\boldsymbol{q}}\right|$ only define the order of magnitude, we also investigate the reconstruction capabilities if the gap is chosen as $2\delta\left|\Gamma_{\boldsymbol{q}}\right| = \sqrt{c}$, i.e., twice as large as the above defined gap $\delta\left|\Gamma_{\boldsymbol{q}}\right|$.

Moreover, we also substitute the ideal amplitudes $\Gamma_{\boldsymbol{q}}$ for every $\boldsymbol{q}$ — alternatively or in addition to the gaps $\delta\left|\Gamma_{\boldsymbol{q}}\right|$ — by random Poisson events with mean $N_{\boldsymbol{q}}^{(\mathrm{Ph})}$, which can be obtained directly from Eq. (8.3) once c is calculated according to Eq. (8.8). It is important to keep in mind that a random event drawn from a Poisson distribution is an integer number. As a result, a reasonable fraction of the amplitudes $\Gamma_{\boldsymbol{q}}$ is exactly zero for a low

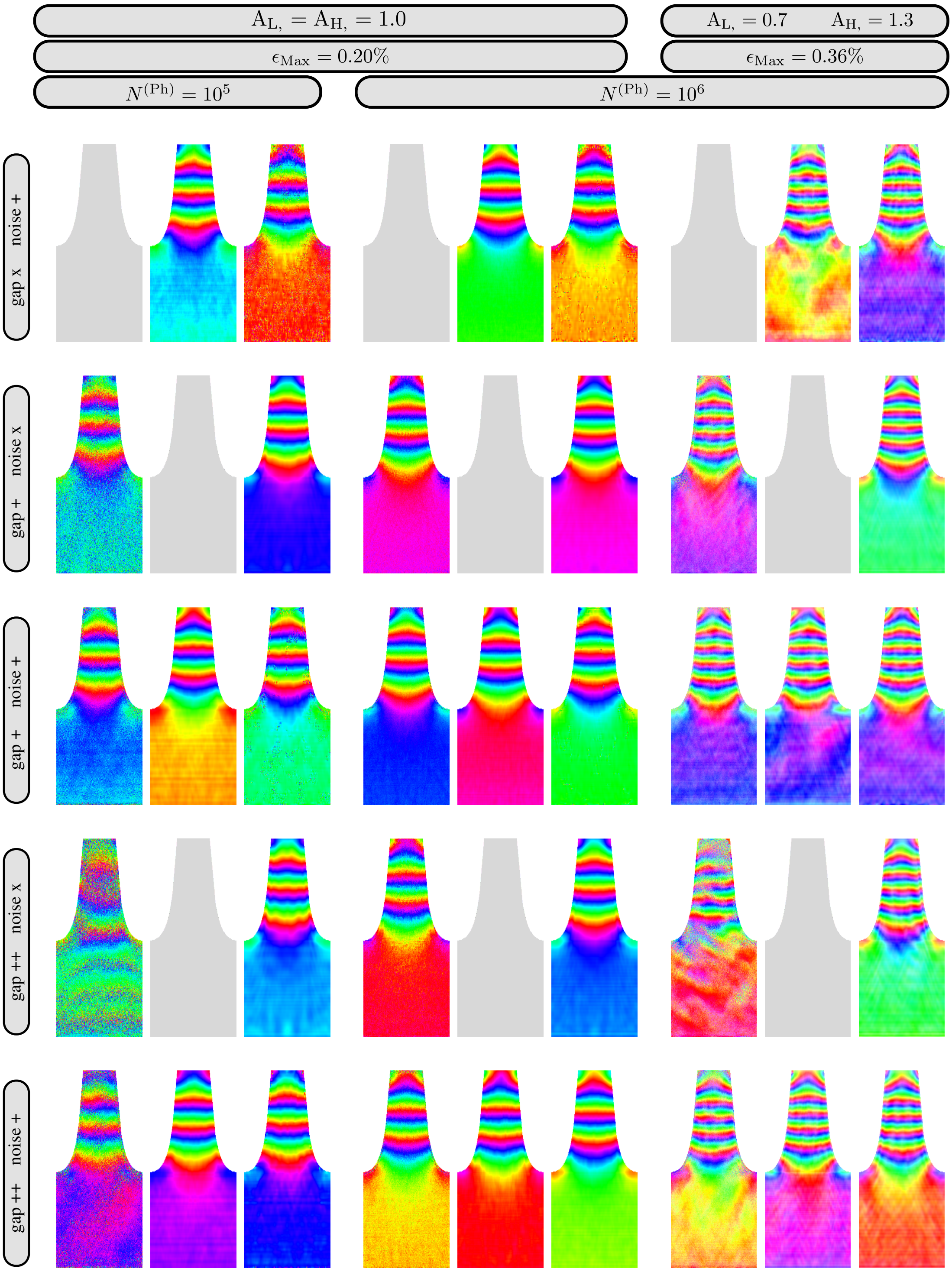

Figure 8.7.: $\mathrm{HIO}^{\mathrm{A}}_{\mathrm{O_R}}$+$\mathrm{ER}^{\mathrm{A}}$-algorithm with strict magnitude constraints $\mathbf{M}_{\mathrm{A}}$ in the full direct space domain Ω (see Eqs. (7.15a) and (7.21)). In each sub-figure, the left image is a typical result if the projections are gapped in the entire domain in reciprocal space. The middle image enforces a zero in reciprocal space for all pixels which measure zero photons in a random Poisson noise realization, and gaps elsewhere. The right figure shows the result of a typical reconstruction if points below the low cutoff $\mu = 0.005$ are treated by model (F) as described in Sec. 8.1 and the remaining points as gapped projections in reciprocal space.

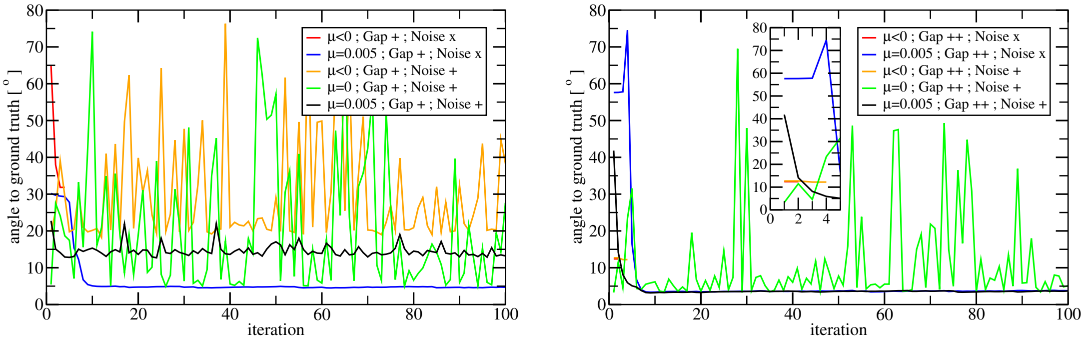

(a) Comparison for "Gap +" with $N_{\mathrm{Tot}}^{(\mathrm{Ph})} = 10^5$ (b) Comparison for "Gap ++" with $N_{\mathrm{Tot}}^{(\mathrm{Ph})} = 10^6$

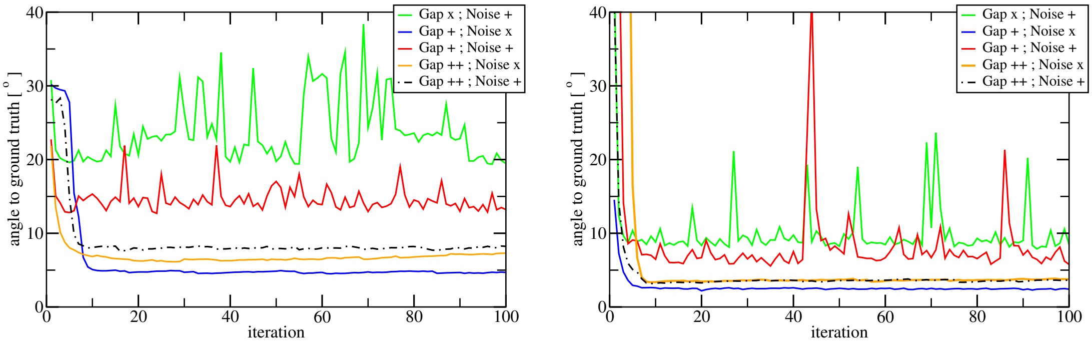

(c) $\epsilon_{\mathrm{M}} = 0.20\%$, $\mu = 0.005$, $N_{\mathrm{Tot}}^{(\mathrm{Ph})} = 10^5$ (d) $\epsilon_{\mathrm{M}} = 0.20\%$, $\mu = 0.005$, $N_{\mathrm{Tot}}^{(\mathrm{Ph})} = 10^6$

Figure 8.8.: Quantitative analysis of the behavior illustrated in Fig. 8.7.

number of collected photons $N_{\mathrm{Tot}}^{(\mathrm{Ph})}$. This fact resembles the highly unstable model (B) in the previous section, but now these instabilities might be reduced by the gaps $\delta\,|\Gamma_{\boldsymbol{q}}|$ for the remaining points above the cutoff.

In Fig. 8.7, the *best* reconstruction results have been collected which have been achieved after $N_{\mathrm{Iter}} = 250$ iterations and given the following input data and data treatment during reconstruction:

- the input amplitudes $\delta\,|\Gamma_{\boldsymbol{q}}|$ are either free of noise ("noise x"), or corrupted by (discrete) Poisson noise ("noise +")
- for amplitudes $\Gamma_{\boldsymbol{q}}$ above the cutoff $\mu \in \{-1, 0, 0.005\}$ (see Sec. 8.1), the projection $\mathbf{P}_\Gamma$ in reciprocal space is not gapped ("gap x"), gapped by $\delta\,|\Gamma_{\boldsymbol{q}}| = \frac{\sqrt{c}}{2}$ ("gap +") or gapped by $2 \cdot \delta\,|\Gamma_{\boldsymbol{q}}|$ ("gap ++")
- for amplitudes $\Gamma_{\boldsymbol{q}}$ below or equal to the cutoff μ, the projection $\mathbf{P}_\Gamma$ is done according to model (F) as described in Sec. 8.1 (see Eq. (8.2f))

We point out, that no amplitude $\Gamma_{\boldsymbol{q}}$ – with or without Poisson noise – is below the cutoff $\mu = -1 < 0$, and in this case, all points $\boldsymbol{q}$ are treated as gapped projections. Moreover, we emphasize, that for $\mu = 0$ and in presence of noise in the input data $\Gamma_{\boldsymbol{q}}$, all $\boldsymbol{q}$ points for which the outcome of the discrete Poisson event was zero, are forced to be strictly zero. Consequently, this case will reveal if model (B) from Sec. 8.1 is significantly less unstable if the $\boldsymbol{q}$-points with high intensity weight are gapped.

These cases have been depicted in Fig. 8.7 for $\epsilon_{\mathrm{M}} = 0.20\%$, $\mathrm{A}_{\mathrm{L},} = 1.0$ and $\mathrm{A}_{\mathrm{H},} = 1.0$ in the full domain Ω and $N_{\mathrm{Tot}}^{(\mathrm{Ph})} \in \{10^5, 10^6\}$ as well as for $\epsilon_{\mathrm{M}} = 0.36\%$, $\mathrm{A}_{\mathrm{L},} = 0.7$ and $\mathrm{A}_{\mathrm{H},} = 1.3$ in the full domain Ω and $N_{\mathrm{Tot}}^{(\mathrm{Ph})} = 10^6$.

From this collection, we first observe that the results for $\mu < 0$ typically are worst in quality, in particular in the case “gap ++ ; noise x”. In contrast, the quality of reconstructions for $\mu = 0$ and $\mu = 0.005$ is very acceptable. In most cases, the reconstruction for $\mu = 0$ seems slightly superior to the case $\mu = 0.005$. Fig. 8.8 gives quantitative information on the comparison depicted in Fig. 8.7: In Fig. 8.8(a), we compare the distance φ of the iterative approximation to the solution ϱ_{eff} for $N_{\text{Tot}}^{(\text{Ph})} = 10^5$ and the case “gap+”. On the one hand, we observe strong instabilities in presence of noise (“noise +”) for $\mu = 0$ and $\mu < 0$. In absence of noise, the gaps in the projection operator result in negligible change of the solution from iteration to iteration ($\chi \leq 10^{-6}$rad) after very few iterations and the iterative reconstruction is terminated. The by far best behavior with respect to stability is found for $\mu = 0.005$, i.e. the projection $\mathbf{P}_\Gamma$ for low-intensity $\boldsymbol{q}$-points is bound from above and slightly damped, while gaps $\delta\,|\Gamma_{\boldsymbol{q}}|$ are applied for those $\boldsymbol{q}$-points with high intensity.

Fig. 8.8(b) considers the case of ten times more photons and twice as large gaps. For this case, our results are similar: For $\mu < 0$, the gaps are large and the change from iteration to iteration vanishes very early (only two and four iterations) which ends the reconstruction procedure. For these larger gaps $2\delta\,|\Gamma_{\boldsymbol{q}}|$, this termination even took place in presence of noise in the input data. As in the previous case (Fig. 8.8(a)), the best quality for $\mu = 0$ is very good, but the overall behavior is very unstable and thus unwanted. For $\mu = 0.005$, the best quality and stability is observed – with and without noise corruption in the input data $\Gamma_{\boldsymbol{q}}$.

Figs. 8.8(c) and 8.8(d) are therefore dedicated to this case $\mu = 0.005$ in greater detail: From these figures, we see that a reconstruction *without gaps* in the projection $\mathbf{P}_\Gamma$ performs significantly less stable and produces worse quality of the reconstructed approximations to ϱ_{eff} than reconstructions with gaps (“gap +” and “gap ++”). Whereas for the smaller gaps “gaps +”, we still observe some instabilities, these instabilities are absent for our larger gaps $2 \cdot \delta\,|\Gamma_{\boldsymbol{q}}|$ (“gaps ++”).

In conclusion, we observe that the domains with low intensity (in total many $\boldsymbol{q}$ points, but few photon counts only (see Tab. 8.1)) and with high intensity should be treated differently. In our investigations, the combination of model (F) (as described in Sec. 8.1) for the low intensity domains with gapped projections in reciprocal space with $\boldsymbol{q}$-independent gaps $2\delta\,|\Gamma_{\boldsymbol{q}}| = \sqrt{c}$ for $\boldsymbol{q}$ points with amplitudes $\Gamma_{\boldsymbol{q}}$ above the cutoff μ produced the best results. This approach provided high stability and good quality at the same time.

8.3. Artificial truncation of the substrate during a reconstruction

In this section, we now turn to a wide-spread inconsistency in experimentally measured scattering data and the intensity distribution $\mathcal{I}(\boldsymbol{Q}_{\text{B}}, \boldsymbol{Q})$ simulated within the framework of the CXDI model as discussed in Sec. 6.1. Specifically, the Bragg peak as well as the crystal truncation rod (CTR) require special attention: The reason is that in many cases of experimental relevance the signal from the substrate below the nanostructure is not equal to the signal thereof modelled in reconstruction algorithms based on kinematic theory (such as the HIO+ER-based reconstruction algorithms).

Typically, the contribution from the substrate cannot be modelled by kinematic theory, and, moreover, is very thick in comparison to the nanostructure. Its proper computational modelling would therefore require non-kinematic modelling as well as huge computational resources (in comparison the the kinematic approximation). Therefore, it would be preferential to truncate the substrate during the reconstruction in the computational model for the nanostructure artificially as soon as the displacement field is expected to be negligible. We now study which modifications of a reconstruction algorithm (such as the

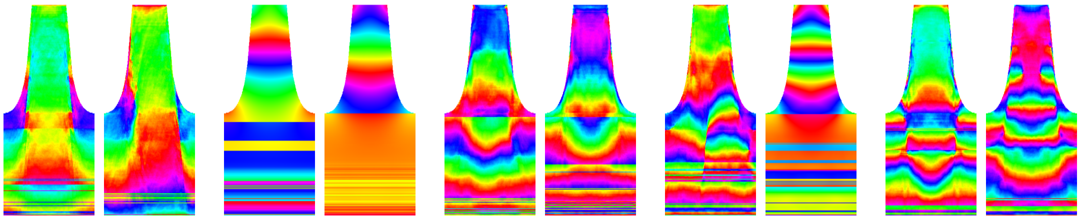

(a) $\epsilon_{\mathrm{M}} = 0.04\%$ (b) $\epsilon_{\mathrm{M}} = 0.08\%$ (c) $\epsilon_{\mathrm{M}} = 0.12\%$ (d) $\epsilon_{\mathrm{M}} = 0.16\%$ (e) $\epsilon_{\mathrm{M}} = 0.20\%$

Figure 8.9.: Examples for the output of reconstructions with the $\mathrm{HIO}^{\mathrm{A}}_{\mathrm{O_R}}$+$\mathrm{ER}^{\mathrm{A}}$-algorithm in case the crystal truncation rod is ignored in the projections $\mathbf{P}_\Gamma$.

HIO+ER-algorithm and its extensions) are required to facilitate such a truncation in the computational model of the nanostructure.

Since the contributions from the diffraction of the primary beam deep in the substrate, where the displacement field is negligible, are restricted to the crystal truncation rod[1], most data points $\mathcal{I}(\boldsymbol{Q}_{\mathrm{B}}, \boldsymbol{Q})$ in reciprocal space are still well described by the CXDI model defined in Sec. 6.1. However, the data on the crystal truncation rod (including the Bragg peak) is inconsistent and must be ignored if the substrate is truncated artificially in the computational model of the nanostructure. This is particularly important, since the crystal truncation rod contains a significant fraction of the scattered intensity weight close to a Bragg peak $\boldsymbol{Q}_{\mathrm{B}}$.

Throughout this section, we restrict our presentation to the $\mathrm{HIO}^{\mathrm{A}}_{\mathrm{O_R}}$+$\mathrm{ER}^{\mathrm{A}}$-algorithm with magnitude constraints $\mathbf{M}_{\mathrm{A}}$ as defined in Eqs. (7.15a) and (7.21) with $\mathrm{A}_{\mathrm{L},} = 1.0$ and $\mathrm{A}_{\mathrm{H},} = 1.0$ which are applied in the full direct space domain Ω. Moreover, we assume ideal data (no low cutoff or photon noise) for the investigations in this section – apart from the crystal truncation rod.

Fig. 8.9 gives an impression of the results of reconstructions for various small amounts of strain ϵ_{M} if the crystal truncation rod is ignored in the projection operator $\mathbf{P}_\Gamma$ in reciprocal space (so that the respective amplitudes $\Gamma_{\boldsymbol{q}}$ evolve freely) and no other modifications of the $\mathrm{HIO}^{\mathrm{A}}_{\mathrm{O_R}}$+$\mathrm{ER}^{\mathrm{A}}$-algorithm or the employed *a priori* knowledge are done.

Without the information on the crystal truncation rod, no information about the substrate domains without lateral gradient is contained in the scattering data, and horizontal stripes are to be expected. This behavior is best seen in Fig. 8.9(b), where the effective electron density inside the nanowire is reconstructed nicely, but the substrate is full of such stripe "artifacts". These "artifacts" however are unavoidable for the given constraints.

More importantly, most reconstructions in Fig. 8.9 reveal complete failure even in the nanowire region. Out of $\mathrm{N}_{\mathrm{Real}} = 5$ initial trials for each value of strain ϵ_{M} in Fig. 8.9, only 6 out of the 25 reconstructions succeeded (5 out of 5 for $\epsilon_{\mathrm{M}} = 0.08\%$ and 1 out of 5 for $\epsilon_{\mathrm{M}} = 0.16\%$) – despite the strongest magnitude constraints we can apply and the improvements from randomized overrelaxation. Clearly, this performance is not satisfactory and adequate modifications must be developed and thoroughly investigated. Without special measures for incorporating the inconsistencies along the crystal truncation rod, CXDI reconstructions with the $\mathrm{HIO}^{\mathrm{A}}_{\mathrm{O_R}}$+$\mathrm{ER}^{\mathrm{A}}$-algorithm are not sufficiently robust for application to experimental data.

---

[1] Unless the Bragg condition for the substrate is fulfilled, the "secondary" beam which stems from the diffraction of the substrate is much weaker than the primary beam. The contributions from small angle scattering of this "secondary" beam at the nanostructure – which are not included in the first order Born approximation – are very small.

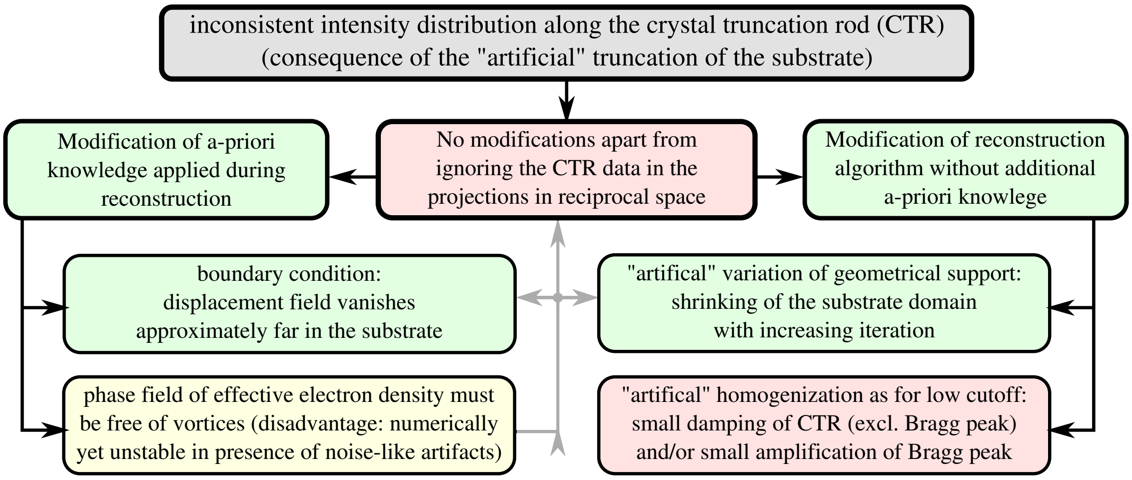

Figure 8.10.: Overview over the discussed approaches for resolving the inconsistent intensity distribution along the crystal truncation rod (CTR). Green boxes correspond to approaches which turn out to be helpful without known drawbacks. Yellow boxes correspond to approaches which also turn out to be helpful, but some aspects need to be resolved before they can be applied to experimental data. Finally, red boxes correspond to approaches which did not provide any benefits or even made the performance worse.

It is likely that the origin of this reduction in reconstruction performance are the intrinsic ambiguities in the CXDI model which stem from the mathematical properties of the Fourier transform. Once the full crystal truncation rod is ignored, the inhomogeneously strained domains in the nanowire can be shifted to laterally homogeneous regions, for which no constraints are contained any more. As a consequence, many additional traps and tunnels complicate the non-linear, non-local and non-convex task to reconstruct the effective electron density.

Fig. 8.10 gives an overview over the approaches which we discuss in this section in order to resolve the inconsistent intensity distribution along the crystal truncation rod (CTR).

As in Secs. 7.3 and 7.4, we can either modify the reconstruction algorithm without modifications of the “physical” *a priori* knowledge or we can incorporate additional *a priori* knowledge in order to improve the reconstruction capabilities.

For the latter approach, we investigated model (F) as described in Sec. 8.1 (see Eq. (8.2f)) for the $\boldsymbol{q}$-points on (i) the crystal truncation rod excluding the Bragg peak and (ii) for the Bragg peak. We investigated values for the “damping constant” c_D slightly below and above 1.0 (the limiting case of a freely evolving amplitude) in both domains separately and the all four combinations of damping and amplification in both domains simultaneously. No benefits in the reconstruction capabilities have been observed if model (F) is applied along the crystal truncation rod instead of the domains of weak intensity. In fact, in most cases the performance of the thus modified $\mathrm{HIO}^{\mathrm{A}}_{\mathrm{O_R}}$+$\mathrm{ER}^{\mathrm{A}}$-algorithm was even worse.

A modification of the employed *a priori* knowledge with respect to the $\mathrm{HIO}^{\mathrm{A}}_{\mathrm{O_R}}$+$\mathrm{ER}^{\mathrm{A}}$-algorithm which already proofed valuable for ideal data, has already been discussed in Sec. 7.5: the elimination of point vortices in the phase field of the approximated effective electron density after each meta-iteration of the $\mathrm{HIO}^{\mathrm{A}}_{\mathrm{O_R}}$+$\mathrm{ER}^{\mathrm{A}}$-algorithm. Since for ideal data, the $\mathrm{HIO}^{\mathrm{A}}_{\mathrm{O_R}}$+$\mathrm{ER}^{\mathrm{A}}$-algorithm was already capable of retrieving the effective electron density rather efficiently and with a well-defined estimation for the computational effort of each iterative step, vortex elimination was non-essential for ideal data. We now return to our approach for elimination of point vortices as described in Sec. 7.5 and apply it after each meta-iteration of the $\mathrm{HIO}^{\mathrm{A}}_{\mathrm{O_R}}+\mathrm{ER}^{\mathrm{A}}$-algorithm.

Since the error metrics defined in Eq. (6.48) is also sensitive to the deviations in the reconstructed effective electron density which are now to be expected (such as horizontal stripe artifacts or a smooth gradient in vertical direction), it is no longer suited for determination of the quality of the reconstructed result. Equally, we cannot employ Eq. (6.46) (deviation of amplitudes Γ) without modification, since the inconsistencies on the crystal truncation rod would also falsify the interpretation. In contrast, Eq. (6.47) (change from iteration to iteration) can still be applied for determination of the convergence of the algorithm. Nonetheless, Eqs. (6.46) and (6.48) can be expressed as a standard scalar product in $\mathbb{R}^{\mathrm{N_{Tot}}}$. Since the Fourier transform is a unitary transformation, both equations can be equally evaluated in direct and reciprocal space. Therefore, both formulas are applicable if we evaluate them in reciprocal space and *ignore the crystal truncation rod in the evaluation.* Since Eq. (6.48) is not applicable in case of experimental data, we give preference to Eqs. (6.46) and (6.47) (values given in radians) in this section on non-ideal data and which are both of high relevance for experimental data.

In Fig. 8.11, we depict details for reconstructions with the $\mathrm{HIO}^{\mathrm{A}}_{\mathrm{O_R}}+\mathrm{ER}^{\mathrm{A}}$-algorithm without as well as with vortex elimination if the scattered intensity $\mathcal{I}(\boldsymbol{Q}_{\mathrm{B}}, \boldsymbol{Q})$ is ignored along the crystal truncation rod. Without vortex correction, the depicted reconstructions for $\epsilon_{\mathrm{M}} = 0.20\%$ and $\epsilon_{\mathrm{M}} = 0.36\%$ fail. Neither the error ϵ in the reciprocal space amplitudes (ignoring the CTR) nor the change from iteration to iteration χ decreases with increasing iteration. Most importantly, the depicted approximations to the effective electron density are far from the solution.

In contrast, after the incorporation of vortex elimination after each meta-iteration of the $\mathrm{HIO}^{\mathrm{A}}_{\mathrm{O_R}}+\mathrm{ER}^{\mathrm{A}}$-algorithm, we observe nice reconstructions away from the homogeneous substrate regions, as depicted in Fig. 8.11(m) for $\epsilon_{\mathrm{M}} = 0.20\%$ and in Fig. 8.11(q) for $\epsilon_{\mathrm{M}} = 0.36\%$. Interestingly, the error metrics behave very differently in both cases: Whereas two pronounced sudden drops in the error metrics are observed for the depicted example $\epsilon_{\mathrm{M}} = 0.36\%$ (in both error metrics) and good reconstruction quality at the bottom part of the inhomogeneously strained nanowire is observed after the error ϵ dropped to approximately 10^{-5} (iteration $i = 22$), we observe only one drop in the error metrics for $\epsilon_{\mathrm{M}} = 0.20\%$ after $i = 11$ iterations. From that point on, the errors χ and ϵ do not decrease further, but remain (up to a short spike at iteration $i \approx 200$) close to the level 10^{-2}. Nonetheless, even the bottom part of the nanowire is reconstructed well – despite the fact that the error ϵ is approximately three orders of magnitude larger than for $\epsilon_{\mathrm{M}} = 0.36\%$. Most importantly, the level $\epsilon \approx 10^{-2}$ is very similar to the completely failed reconstructions without vortex correction. This observation is more important than it seems at first:

Typically, it is more difficult to achieve a given error level ϵ with vortex elimination than without vortex elimination. The reason for this is that the set of mathematical functions which can occur as a phase field $\Phi(\boldsymbol{r})$ of the effective electron density ϱ_{eff} after vortex elimination is tremendously reduced: instead of arbitrary functions $\Phi(\boldsymbol{r})$, the phase field $\Phi(\boldsymbol{r})$ is enforced to be free of vortices. All phase field $\Phi(\boldsymbol{r})$ with a non-vanishing number of vortices which would produce an error level similar to the given error level ϵ are eliminated. From this reduced underlying set of possible phase fields $\Phi(\boldsymbol{r})$, it is typically less likely that functions which significantly differ from the solution ϱ_{eff} result in an error level close to or below the given error level ϵ. In consequence, the error level ϵ is only meaningful in combination with the set of applied constraints during the reconstruction. An error level in the order of $\epsilon \approx 10^{-2}$ without vortex correction does not indicate a good reconstruction. In contrast, an error level in the order of $\epsilon \approx 10^{-2}$ is already an indication for a high-quality reconstruction.

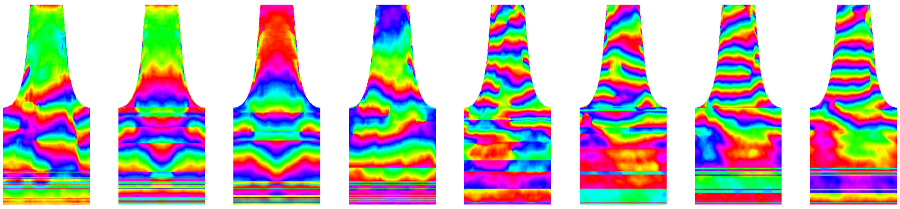

(a) $\epsilon_{\mathrm{M}} = 0.20\%$, $i = 1$ (b) $\epsilon_{\mathrm{M}} = 0.20\%$, $i = 50$ (c) $\epsilon_{\mathrm{M}} = 0.20\%$, $i = 140$ (d) $\epsilon_{\mathrm{M}} = 0.20\%$, $i = 250$ (e) $\epsilon_{\mathrm{M}} = 0.36\%$, $i = 1$ (f) $\epsilon_{\mathrm{M}} = 0.36\%$, $i = 50$ (g) $\epsilon_{\mathrm{M}} = 0.36\%$, $i = 140$ (h) $\epsilon_{\mathrm{M}} = 0.36\%$, $i = 250$

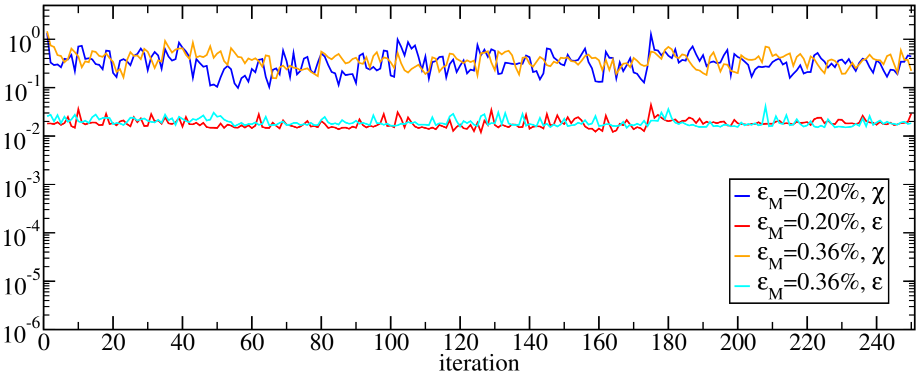

(i) Error metrics

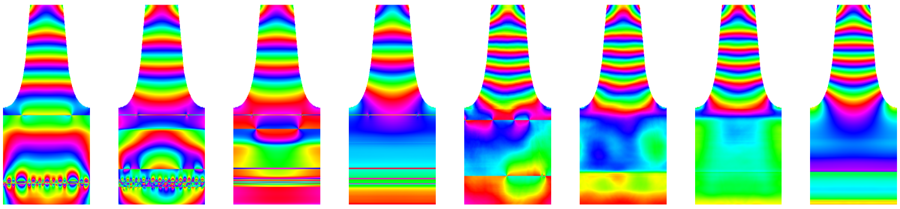

(j) $\epsilon_{\mathrm{M}} = 0.20\%$, $i = 6$ (k) $\epsilon_{\mathrm{M}} = 0.20\%$, $i = 7$ (l) $\epsilon_{\mathrm{M}} = 0.20\%$, $i = 9$ (m) $\epsilon_{\mathrm{M}} = 0.20\%$, $i = 11$ (n) $\epsilon_{\mathrm{M}} = 0.36\%$, $i = 6$ (o) $\epsilon_{\mathrm{M}} = 0.36\%$, $i = 7$ (p) $\epsilon_{\mathrm{M}} = 0.36\%$, $i = 9$ (q) $\epsilon_{\mathrm{M}} = 0.36\%$, $i = 22$

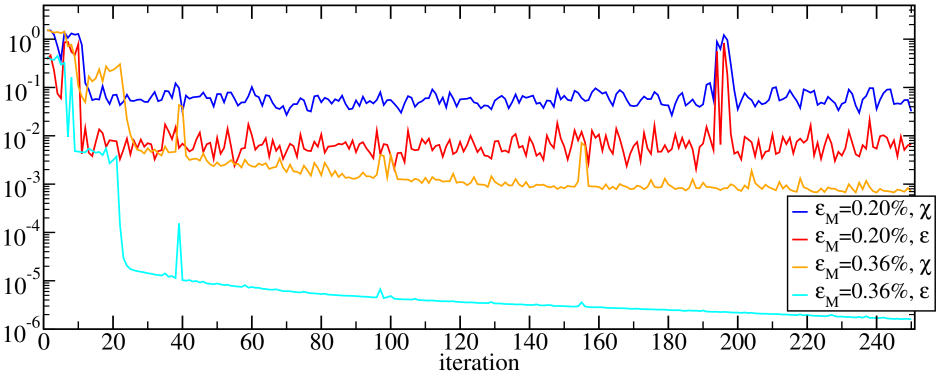

(r) Error metrics

Figure 8.11.: Investigation of the $\mathrm{HIO}^{\mathrm{A}}_{\mathrm{O_R}}$+$\mathrm{ER}^{\mathrm{A}}$-algorithm if the scattered intensity $\mathcal{I}(\boldsymbol{Q}_{\mathrm{B}}, \boldsymbol{Q})$ along the crystal truncation rod is ignored. The Figs. (a)-(i) provide details on reconstructions without any further modifications. In Figs. (j)-(r), vortex elimination is performed after each meta-iteration of the $\mathrm{HIO}^{\mathrm{A}}_{\mathrm{O_R}}$+$\mathrm{ER}^{\mathrm{A}}$-algorithm.

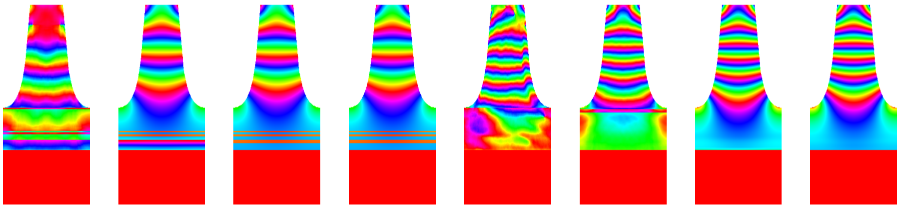

(a) $\epsilon_{\mathrm{M}} = 0.20\%$, $i = 81$ (b) $\epsilon_{\mathrm{M}} = 0.20\%$, $i = 86$ (c) $\epsilon_{\mathrm{M}} = 0.20\%$, $i = 184$ (d) $\epsilon_{\mathrm{M}} = 0.20\%$, $i = 186$ (e) $\epsilon_{\mathrm{M}} = 0.36\%$, $i = 21$ (f) $\epsilon_{\mathrm{M}} = 0.36\%$, $i = 25$ (g) $\epsilon_{\mathrm{M}} = 0.36\%$, $i = 30$ (h) $\epsilon_{\mathrm{M}} = 0.36\%$, $i = 250$

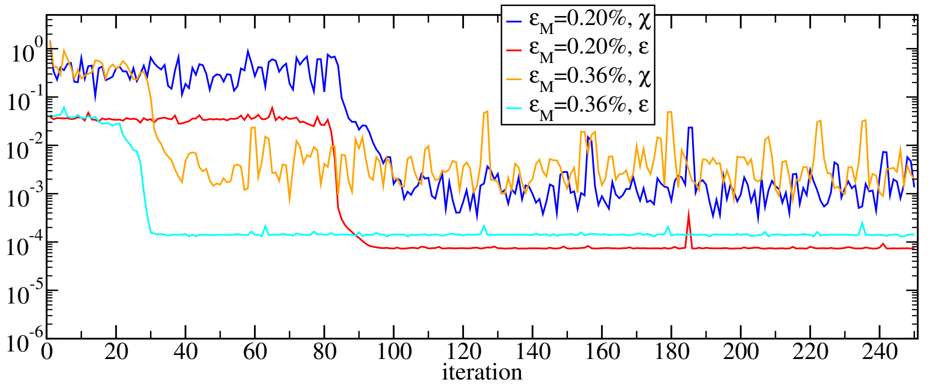

(i) Error metrics

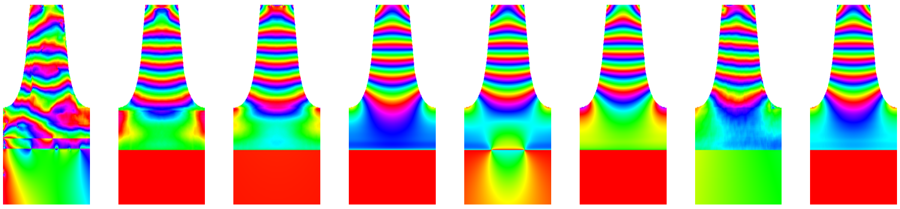

(j) $\epsilon_{\mathrm{M}} = 0.36\%$, $i = 7$ (k) $\epsilon_{\mathrm{M}} = 0.36\%$, $i = 10$ (l) $\epsilon_{\mathrm{M}} = 0.36\%$, $i = 11$ (m) $\epsilon_{\mathrm{M}} = 0.36\%$, $i = 15$ (n) $\epsilon_{\mathrm{M}} = 0.36\%$, $i = 16$ (o) $\epsilon_{\mathrm{M}} = 0.36\%$, $i = 22$ (p) $\epsilon_{\mathrm{M}} = 0.36\%$, $i = 161$ (q) $\epsilon_{\mathrm{M}} = 0.36\%$, $i = 162$

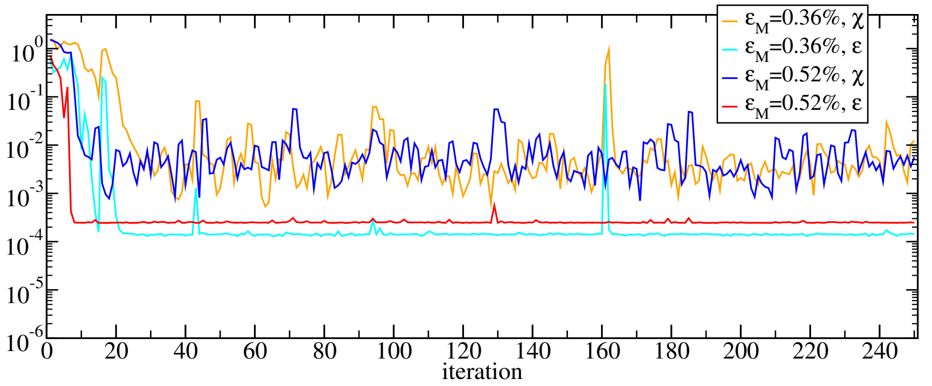

(r) Error metrics

Figure 8.12.: Investigation of the $\mathrm{HIO}^{\mathrm{A}}_{\mathrm{O_R}}+\mathrm{ER}^{\mathrm{A}}$-algorithm if the scattered intensity $\mathcal{I}(\boldsymbol{Q}_{\mathrm{B}}, \boldsymbol{Q})$ along the crystal truncation rod is ignored, but additionally a vanishing displacement deep in the substrate (hatched region in Fig. 7.3(a)) is enforced as a boundary condition after every iteration of the HIO- and the ER-algorithm (Figs. (a)-(i) without vortex elimination, Figs. (j)-(r) with vortex elimination after each meta-iteration of the $\mathrm{HIO}^{\mathrm{A}}_{\mathrm{O_R}}+\mathrm{ER}^{\mathrm{A}}$-algorithm).

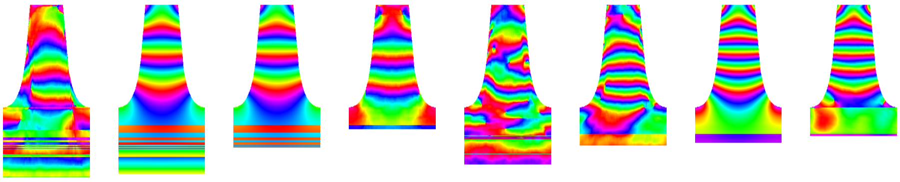

(a) $\epsilon_{\mathrm{M}} = 0.20\%$, $i = 63$ (b) $\epsilon_{\mathrm{M}} = 0.20\%$, $i = 73$ (c) $\epsilon_{\mathrm{M}} = 0.20\%$, $i = 150$ (d) $\epsilon_{\mathrm{M}} = 0.20\%$, $i = 204$ (e) $\epsilon_{\mathrm{M}} = 0.36\%$, $i = 100$ (f) $\epsilon_{\mathrm{M}} = 0.36\%$, $i = 156$ (g) $\epsilon_{\mathrm{M}} = 0.36\%$, $i = 165$ (h) $\epsilon_{\mathrm{M}} = 0.36\%$, $i = 184$

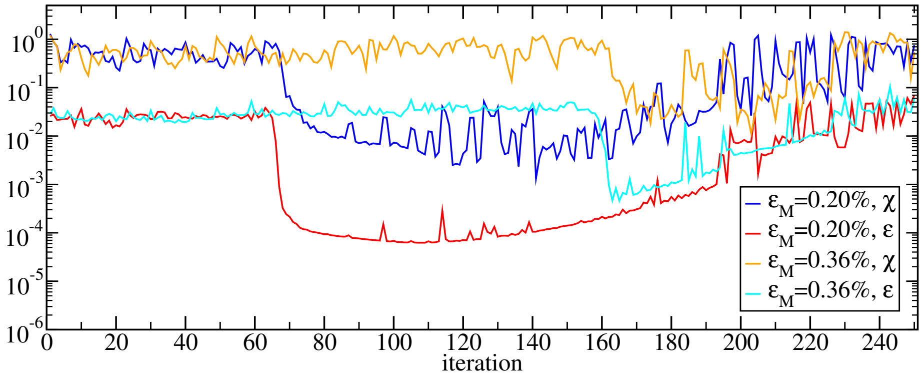

(i) Error metrics

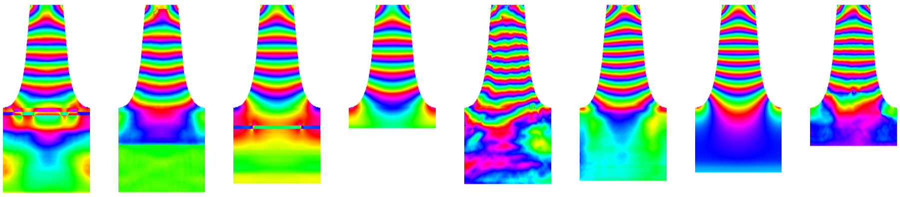

(j) $\epsilon_{\mathrm{M}} = 0.36\%$, $i = 19$ (k) $\epsilon_{\mathrm{M}} = 0.36\%$, $i = 21$ (l) $\epsilon_{\mathrm{M}} = 0.36\%$, $i = 47$ (m) $\epsilon_{\mathrm{M}} = 0.36\%$, $i = 208$ (n) $\epsilon_{\mathrm{M}} = 0.52\%$, $i = 44$ (o) $\epsilon_{\mathrm{M}} = 0.52\%$, $i = 54$ (p) $\epsilon_{\mathrm{M}} = 0.52\%$, $i = 79$ (q) $\epsilon_{\mathrm{M}} = 0.52\%$, $i = 156$

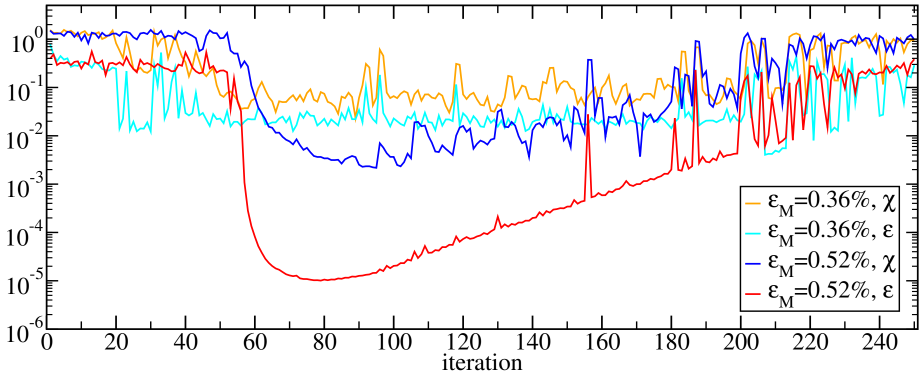

(r) Error metrics

Figure 8.13.: Investigation of the $\mathrm{HIO}^{\mathrm{A}}_{\mathrm{O_R}}$+$\mathrm{ER}^{\mathrm{A}}$-algorithm if the intensity $\mathcal{I}(\boldsymbol{Q}_{\mathrm{B}}, \boldsymbol{Q})$ on the crystal truncation rod is ignored, and the support Ω shrinks by one pixel every two meta-iterations of the $\mathrm{HIO}^{\mathrm{A}}_{\mathrm{O_R}}$+$\mathrm{ER}^{\mathrm{A}}$-algorithm. The support begins at pixel $z = 500$ at iteration 1 and at pixel $z = 625$ after 250 iterations (Figs. (a)-(i) without vortex elimination, Figs. (j)-(r) with vortex elimination after each meta-iteration of the $\mathrm{HIO}^{\mathrm{A}}_{\mathrm{O_R}}$+$\mathrm{ER}^{\mathrm{A}}$-algorithm).

This observation also holds for the results depicted in Figs. 8.12 and 8.13 where we compare two further approaches – each without as well as with vortex elimination – for resolving the inconsistencies of the amplitudes $\Gamma(\boldsymbol{q})$ along the crystal truncation rod.

Once we consider experimental data, the error metrics for the perfect solution ϱ_{eff} is no longer zero, but a lower bound larger than zero is implied by noise and other artifacts in the input data. Once this lower bound exceeds the error level ϵ which would reveals a successful reconstruction, it can no longer be used for detection of a successful reconstruction. Therefore, the larger the value of ϵ is which reveals a successful reconstruction, the better. Vortex elimination therefore is not only important for making the reconstruction itself a success, but also for the detection of this success.

Nonetheless, the results obtained by the combination of the $\mathrm{HIO}^{\mathrm{A}}_{\mathrm{O_R}}$+$\mathrm{ER}^{\mathrm{A}}$-algorithm and vortex correction are not net satisfactory for the following reasons: Firstly, the detection of point vortices (as described in Sec. 7.5) is not sufficiently robust against the stripe artifacts in the homogeneous substrate domain (see for example Figs. 8.11(j) and 8.11(k)). Secondly, the current detection of the point vortices is not sufficiently robust against the noise-like artifacts in the reconstructed approximations to the effective electron density which originate from a low cutoff or Poisson photon noise.

Consequently, the detection of point vortices must be improved further in future, for example by combination with phase smoothing constraints based on conjugate gradient optimization [166, 229, 230] or Fourier filtering.

Instead, we now discuss two further approaches to resolve the inconsistencies of the amplitudes $\Gamma(\boldsymbol{q})$ along the crystal truncation rod. Both approaches aim to reduce the above discussed ambiguities during the reconstruction which arise from the non-constraint domains deep in the substrate if the intensity distribution along the crystal truncation rod is not constrained.

The first approach assumes an *a priori* guess for the depth below the nanostructure for which the lateral gradient of the phase field $\Phi(\boldsymbol{r})$ of the effective electron density ϱ_{eff} becomes negligible. Below this depth, the phase field $\Phi(\boldsymbol{r})$ is set to zero after every iteration of the HIO- and the ER-algorithm. This boundary condition eliminates the global phase ambiguity in the reconstructed effective electron density if the full data within the CXDI model (including the crystal truncation rod) would be available. However, if the data on the crystal truncation rod is ignored during the reconstruction, the global phase which is indicated by this boundary condition, is no longer enforced away from the phase-constrained region. Nonetheless, a large fraction of the many additional traps and tunnels induced by the unconstrained direct space domains should be eliminated by this boundary condition from the iterative approximation procedure and the performance of the $\mathrm{HIO}^{\mathrm{A}}_{\mathrm{O_R}}$+$\mathrm{ER}^{\mathrm{A}}$-algorithm for reconstruction of the effective electron density should (at least partially) recover.

In Fig. 8.12, we depict examples for reconstructions performed with this approach: Specifically, the phase in the hatched region in Fig. 7.3(a) is set to zero after every iteration of the HIO- and the ER-algorithm. Without (Figs. (a)-(i)) as well as with vortex elimination after each meta-iteration of the $\mathrm{HIO}^{\mathrm{A}}_{\mathrm{O_R}}$+$\mathrm{ER}^{\mathrm{A}}$-algorithm (Figs. (j)-(r)) the inhomogeneously strained regions in the nanowire have been reconstructed nicely. As expected from our discussion,

- the number of horizontal stripe artifacts reduces,
- the incorporation of vortex elimination significantly reduces the number of meta-iterations of the $\mathrm{HIO}^{\mathrm{A}}_{\mathrm{O_R}}$+$\mathrm{ER}^{\mathrm{A}}$-algorithm before a very good approximation to the solution ϱ_{eff} is found (see Sec. 7.5),

- vortex detection may become unstable in presence of horizontal stripe artifacts (see Figs. 8.12(n) and 8.12(p)), and
- the phase correlation from the boundary condition (global phase) is lost in the interior of the nanostructure.

Strictly speaking, this first approach adds additional *a priori* information to the reconstruction process and would fix the global phase for ideal data. However, since the "only" benefit of this additional *a priori* information in presence of CTR-inconsistencies is a reduction of the traps and tunnels, we should be able to observe similar benefits if this region where the phase was set to zero is completely discarded from the geometry Ω.

Consequently, our second approach investigates the influence of a reduction in the geometrical shape Ω below the nanostructure. More specifically, we investigate a dynamic shrinking of the support starting from some depth z_{S}. After a given number of iterations z_δ, the beginning of the support is shifted towards larger z_{S} and, thereby, reducing the height of the geometry $\Omega = \Omega(z_{\mathrm{S}})$. At all steps, the lower truncation of the substrate is horizontal so that the contributions from the scattering from this artificial truncation are limited to the ignored domain in reciprocal space. By the dynamic shrinking of the support $\Omega(z_{\mathrm{S}})$, we avoid an *a priori* estimate for the depth where the lateral gradient becomes negligible. We point out that instead of shrinking the geometry Ω in the second approach we could also dynamically grow the boundary condition $\Phi(\boldsymbol{r}) = 0$ of the previous approach. We emphasize that the second approach does not employ any additional *a priori* knowledge during the reconstruction (and, hence, does not fix the global phase of the reconstructed effective electron density even for ideal data).

In our simulations, we start at pixel $z_{\mathrm{S}} = 500$ at iteration $i = 1$ and increase z_{S} by one every two meta-iterations of the $\mathrm{HIO}^{\mathrm{A}}_{\mathrm{O_R}}$+$\mathrm{ER}^{\mathrm{A}}$-algorithm. Exemplary results without as well as with vortex elimination are given in Fig. 8.13. We observe, that successful reconstructions have been achieved by this second approach. The characteristics in all depicted cases is rather similar: After some initial iterations, a fast decrease in the error metrics is observed and a reasonable approximation is found. However, this number of initial iterations varies strongly from $i = 21$ for $\epsilon_{\mathrm{M}} = 0.36\%$ with vortex elimination to $i \approx 165$ without vortex elimination. However, the result after $i = 21$ for $\epsilon_{\mathrm{M}} = 0.36\%$ with vortex elimination is only a "local attractor" close to the solution. Nonetheless, the error metrics is in the order of $\epsilon \approx 10^{-2}$ which is again an indication of a good approximation – in contrast to the case without vortex correction where an error metrics in the order of 10^{-2} does not indicate good approximations. At iteration $i = 208$, the error metrics ϵ decreases by one order of magnitude. We interpret this decrease as the escape of the reconstruction procedure from the local attractor in favor of the attractor of the solution ϱ_{eff}.

After the abrupt decrease of the error metrics ϵ (and "polishing" of the approximation in some cases for some iterations), the further shrinkage of the support implies that domains with small lateral gradient are removed from the shape Ω. As a result, small deviations of the reconstructed amplitudes $\Gamma_{\boldsymbol{q}}$ away from the crystal truncation rod are induced which is the reason for the slowly increasing error metrics ϵ with increasing number of iterations.

With further shrinkage of the support $\Omega(z_{\mathrm{S}})$, more and more regions with non-zero lateral gradient are no longer contained in the geometry $\Omega(z_{\mathrm{S}})$ and the error metrics ϵ increases further. In addition, more and more spikes indicate instabilities in the reconstruction procedure (for example iteration $i \approx 155$ to $i \approx 230$ for $\epsilon_{\mathrm{M}} = 0.52\%$ with vortex elimination). At some point, the geometry Ω is so small that the inconsistencies away from the crystal truncation rod become so strong, that the reconstruction inside this "residual" shape $\Omega(z_{\mathrm{S}})$ breaks down (for example iteration $i \gtrsim 230$ for $\epsilon_{\mathrm{M}} = 0.52\%$ with vortex elimination).

The benefit of vortex elimination is also in this approach that a good approximation to the solution ϱ_{eff} is typically found after fewer iterations. However, in the framework of the second approach, this essentially means that the reconstruction ϱ_{eff} of a larger geometry $\Omega(z_{\mathrm{S}})$ is possible which corresponds to an increased sensitivity to weak gradients in lateral direction deep in the substrate.

Further optimization of the treatment of the inconsistencies is possible. For example, we could also grow the support Ω dynamically starting from an intentionally too small domain – instead of dynamic shrinking. In contrast to shrinking, the initial phases of this new line have to be fixed. If a fixed global phase of the reconstruction is desired, one approach would be to constrain the phase as in the first approach, but start from an artificially big domain (e.g., full shape Ω) and shrink it dynamically towards the lower truncation of the sample.

Moreover, it would also be interesting to investigate and compare the linear increase of the parameter z_{S} with a non-linear (possibly randomized and/or non-monotonous) variation of this parameter z_{S}, i.e. the thickness of the support Ω.

Nonetheless, in summary, both approaches which we presented are capable of improving the performance of the $\mathrm{HIO}^{\mathrm{A}}_{\mathrm{O_R}}+\mathrm{ER}^{\mathrm{A}}$-algorithm for CXDI reconstruction if the data along the crystal truncation rod cannot be taken as input data $\Gamma(\boldsymbol{q})$ for the reconstruction. Dynamically shrinking of the substrate avoids additional *a priori* knowledge.

Before further optimization of the treatment of the inconsistencies along the crystal truncation rod between model and experiment are pursued, it would be more important to improve the robustness of the detection of point vortices in presence of noise-like artifacts and extend the underlying concepts to three dimensional non-physical “defects” in the phase field of the reconstructed effective electron densities. Moreover, other experimental artifacts (see introduction of this chapter) are still to be investigated, most importantly violations of the strict, ideal sampling in reciprocal space.

9. Conclusion and outlook (Part II.)

The second part of this manuscript has been devoted to improving the extraction of the displacement field and strain distribution in inhomogeneoulsy strained nanostructures from the coherently scattered intensity distribution in the vicinity of a Bragg peak. We assume first order Born approximation ("kinematic approximation") and far-field conditions to be fulfilled. Yet, the extraction of the displacement field requires finding the solution of a set of coupled, non-linear, and non-local equations.

One approach to solving these equations, which utilizes only the object's geometry and the intensity distribution in the vicinity of a Bragg peak as *a priori* knowledge, is the HIO+ER-algorithm. Although this algorithm succeeds in reconstruction of a variety of objects, reconstructions of highly strained nanostructures typically fail. Moreover, the algorithm strongly depends on the initial guess and the choice of the parameters N_{HIO} and N_{ER}, as illustrated in Sec. 7.2. We investigated improvements with respect to these shortcoming by two approaches in detail: exploiting given physical *a priori* knowledge more efficiently and incorporating additional *a priori* knowledge.

It was shown in Sec. 7.3, that the incorporation of adequate randomization in the HIO+ER-algorithm significantly reduces the sensitivity to the choice of the parameters N_{HIO} and N_{ER} as well as to the initial guess, and, consequently, is of high relevance for data analysis in coherent X-ray diffractive imaging. Overrelaxation $\mathbf{Q}_{\Gamma;\lambda_\Gamma}$ of the projection operator $\mathbf{P}_\Gamma$ in reciprocal space with randomly drawn relaxation parameter provides a computationally efficient and easy to implement approach for randomization. The developed algorithm has been named $\mathrm{HIO}_{\mathrm{O_R}}$+ER-algorithm.

In contrast to the modifications for randomized overrelaxation in the HIO+ER-algorithm, the $\mathrm{HIO}^{\mathrm{A}}$+$\mathrm{ER}^{\mathrm{A}}$-algorithm takes advantage of additional *a priori* knowledge for the local scattering magnitude $|\varrho_{\mathrm{eff}}(\boldsymbol{r})|$ in domains Ω_j. We limit the deviation of $|\varrho_{\mathrm{eff}}(\boldsymbol{r})|$ in a domain Ω_j with respect to its mean value in this domain Ω_j by the two parameters $\mathrm{A_{L,j}} \leq 1$ and $\mathrm{A_{H,j}} \geq 1$. These constraints are applicable to many samples and the parameters $\mathrm{A_{L,j}}$ and $\mathrm{A_{H,j}}$ are typically easily estimated.

Although the limits of applicability are shifted towards significantly higher values of strain by incorporation of such constraints, the success of the $\mathrm{HIO}^{\mathrm{A}}$+$\mathrm{ER}^{\mathrm{A}}$-algorithm still strongly depends on the initial guess in many cases. Therefore, we introduced the $\mathrm{HIO}^{\mathrm{A}}_{\mathrm{O_R}}$+$\mathrm{ER}^{\mathrm{A}}$-algorithm (see Fig. 9.1) which includes both, randomized overrelaxation and the constraints $\mathbf{M}_{\mathrm{A}}$ on the local scattering magnitude. Our results demonstrate that this algorithm aggregates the benefits from both concepts: reconstructions of highly strained objects, which are very likely to fail without our modifications, became possible with barely no failures. Moreover, the $\mathrm{HIO}^{\mathrm{A}}_{\mathrm{O_R}}$+$\mathrm{ER}^{\mathrm{A}}$-algorithm inherits the good computational scaling of the traditional HIO+ER-algorithm and is easy to implement.

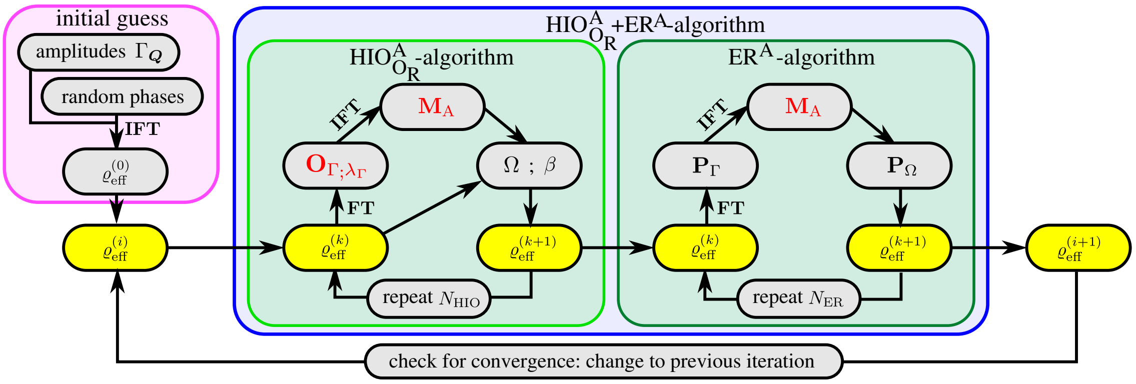

Figure 9.1.: Summary of the $\mathrm{HIO}^{\mathrm{A}}_{\mathrm{O_R}}$+$\mathrm{ER}^{\mathrm{A}}$-algorithm (compare Figs. 6.4 and 7.15).

Given the tremendously improved performance of the $\mathrm{HIO}^{\mathrm{A}}_{\mathrm{O_R}}$+$\mathrm{ER}^{\mathrm{A}}$-algorithm for "ideal data", we started with an investigation of the consequences of experimental artifacts and limitations for a reconstruction.

Specifically, we investigated various strategies for treating data points $\Gamma_{\boldsymbol{q}}$ below a cut-off Γ_{N}. For cut-offs Γ_{N} adequate for current experimental data quality, a large fraction of the number of data points $\Gamma_{\boldsymbol{q}}$ in smaller than this cut-off Γ_{N} (typically leading to effective oversampling ratios $\sigma_{\mathrm{eff}} \ll 1$), but only a low fraction of the scattered photons. For these data points, a small artificial damping in addition to limiting the reciprocal space amplitude by Γ_{N} from above during the reconstruction performed best in our simulations.

Moreover, instabilities during the iterative reconstruction typically occur in presence of Poisson photon noise in the input data $\Gamma_{\boldsymbol{q}}$ without appropriate modifications. We demonstrated that these instabilities can be avoided to a large degree by the introduction of small gaps in the projection operator $\mathbf{P}_{\Gamma}$ in reciprocal space. The gap can be chosen independent of $\boldsymbol{q}$. Its optimal size can estimated from the total number of photons detected in the scattered intensity distribution $\mathcal{I}(\boldsymbol{Q}_{\mathrm{B}}, \boldsymbol{Q})$.

Finally, we propose to dynamically shrink the substrate during the iterative reconstruction in order to circumvent inconsistencies in the input data $\Gamma_{\boldsymbol{q}}$ on the crystal truncation rod. At the same time, the crystal truncation rod is ignored in projections $\mathbf{P}_{\Gamma}$ in reciprocal space. The elimination of phase vortices after each "meta-iteration" of the $\mathrm{HIO}^{\mathrm{A}}_{\mathrm{O_R}}$+$\mathrm{ER}^{\mathrm{A}}$-algorithm proved highly valuable for achieving good reconstruction capabilities despite such discrepancies on the crystal truncation rod.

Despite the various advancements for ideal and non-ideal data, many further improvements are needed before CXDI becomes a robust and easily applicable method of practical value. Most notably, the follwling aspects must be resolved: First, the vortex detection as presented in this manuscript is not yet robust in presence of noise-like artifacts in the input data. Consequently, the reliability of the detection must be improved, for example by combination with suitable phase smoothing before detection. In addition, the elimination of vortex defects must be extended to three dimensional space. Second, the required precision of the shape Ω must be reduced for reliable experimental results. For example, the shape Ω could be replaced by a "minimal shape" Ω_{-}, which establishes a lower bound for the true shape Ω, and a "maximal shape" Ω_{+} as upper bound for Ω. However, the extension of the reconstruction algorithms to such bounds is not straight forward and must be investigated in detail. Finally, the impact of the current experimental limitations with respect to sampling (typically interpolation of data recorded by a two dimensional detector instead of proper sampling), the experimental resolution element and deviations of the incident beam from a plane wave (coherence) must also be investigated.

Appendix

A. Generation of random events for given probability density

For a given probability density distribution $p(x)$, random events according to this distribution can be generated by the following procedure:

1. Make sure $p(x)$ is normalized properly to an area of 1, i.e.,

$$\tilde{p}(x) = \frac{p(x)}{\int_{\mathbb{R}} p(y)\ \mathrm{d}y} \tag{9.1}$$

2. Implement a function to calculate the anti-derivative

$$V(x) = \int_{-\infty}^{x} \tilde{p}(y)\ \mathrm{d}y\ . \tag{9.2}$$

   If possible, evaluate this integral analytically. If not, use numerical integration. The function $V(x)$ is restricted to the interval 0 (for $x \to -\infty$) to 1 (for $x \to \infty$).

3. Draw a random number r from a uniform distribution on $]0, 1[$.

4. Solve the equation

$$V(x_r) = r \tag{9.3}$$

   for $x_r = V^{-1}(r)$ and return x_r as event.[1] This way, events can be generated for distributions $p(x)$ for which no third party library implementation is available.

   If $V(x)$ is not available in analytical form or cannot be inverted analytically, numerical solvers need to be employed. However, if $p(x)$ is not equal to zero on the interval on which it is defined, a unique solution exists and can be easily found by bisection approaches. Depending on the distribution and its properties, methods based on the derivative of $V(x)$ (which is $\tilde{p}(x)$) like the Newton method [166] may accelerate convergence.

This procedure is based on the fact that the change $\mathrm{d}V(x)$ is given by

$$\mathrm{d}V(x) = \frac{\mathrm{dV(x)}}{\mathrm{dx}}\mathrm{d}x = \tilde{p}(x)\mathrm{d}x\ . \tag{9.4}$$

If every value $y = V(x)$ is drawn equally likely, it is equivalent to drawing a particular $x = V^{-1}(y)$ with probability $\tilde{p}(x)$.

The GNU scientific library (GSL) [147] provides the functions gsl_integration_qag (for definite integrations) and gsl_integration_qagiu for indefinite integrations which have been exploited in this work. GSL also provides the solver methods gsl_root_fsolver_bisection and gsl_root_fsolver_falsepos [147] which are suitable for solving $V(x_r) = r$ numerically

---

[1] Trivially, for this procedure to work properly, a unique inverse map V^{-1} must exist.

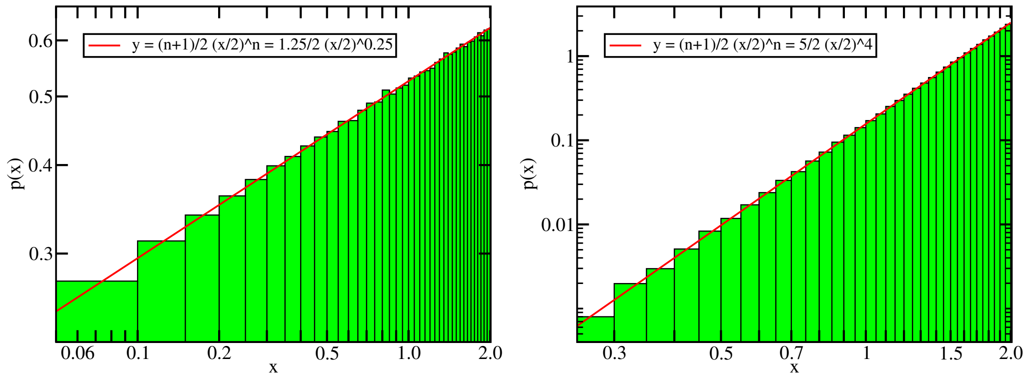

(a) Exponent $n = 0.25$ (b) Exponent $n = 4.00$

Figure A.1.: Comparison of the analytical probability distribution function $p(x) = (n+1)/2 \cdot (x/2)^n$, $x \in [0, 2]$, with a normalized histogram based on $N = 10^6$ randomly generated events as described in the main text.

if required. Both methods do not rely on the derivative of $V(x)$. For verification of the quality of the solution, the residuum ϵ_r of $|V(x_r) - r|$ can be employed. However, if the distance either from 0 or 1 to the drawn random number r is smaller than the predefined upper bound for ϵ_r, special care is required.[2] Moreover, if the distribution $p(x)$ is equal to zero for some values or on some domain, iterative Newton methods will typically become unstable and should not be used.

This procedure will now be illustrated for three probability density distributions $p(x)$. The first two distributions permit analytic integration and inversion. The last example is the most important probability density distribution in Sec. 1.2 for which neither analytic normalization nor integration (and, thus, also inversion) is possible.

First, consider the power law distribution

$$p(x) = (n+1)/2 \cdot (x/2)^n \quad , \quad x \in [0, 2] \ . \tag{9.5}$$

For this distribution, the procedure above yields:

1. Already normalized.
2. $V(x) = (x/2)^{n+1}$.
3. $r \in]0, 1[$ from uniform distribution.
4. $x_r = 2 \sqrt[n+1]{r}$.

This way, one million events have been generated for $n = 0.25$ and $n = 4$, arranged as a histogram and compared to the analytical density $p(x)$ in Fig. A.1. Clearly, the events resemble the given distribution $p(x)$.

As a second example, the exponential distribution $p(x) = 1/b \cdot \mathrm{e}^{-x/b}$, $x \in [0, \infty[$ has been chosen. In this case, the procedure described above yields

1. Already normalized.
2. $V(x) = 1 - \mathrm{e}^{-x/b}$.

---

[2] In this work, a random number r is drawn as long as it is smaller than the upper bound for the residuum or its difference $1 - r$ is smaller than this bound.

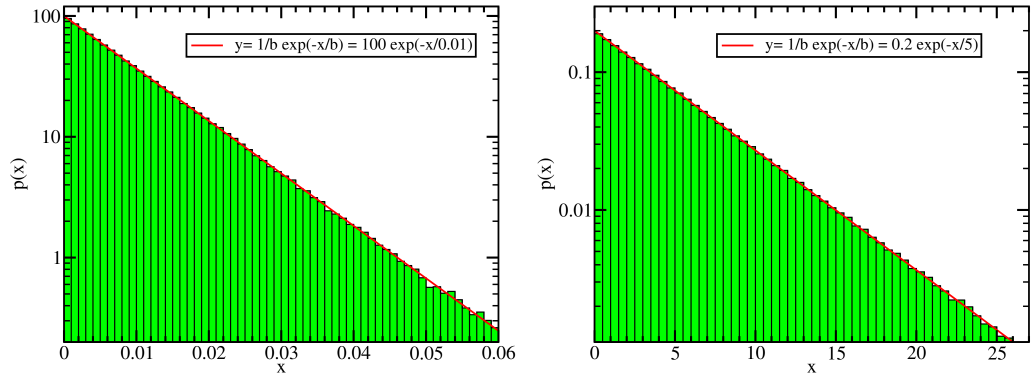

(a) Decay length $b = 0.01$

(b) Decay length $b = 5.00$

Figure A.2.: Comparison of the analytical probability distribution function $p(x) = 1/b \cdot \mathrm{e}^{-x/b}$, $x \in [0, \infty[$, with a normalized histogram based on $N = 10^6$ randomly generated events as described in the main text.

3. $r \in]0, 1[$ from uniform distribution.
4. $x_r = -b \ln(1 - r)$.

Again, one million events have been generated. In this case, the parameter b was chosen as $b = 0.01$ and $b = 5.00$. The events have been arranged as a histogram and compared to the analytical density $p(x)$ in Fig. A.2. Clearly, the events resemble the given distribution $p(x)$ also in case of the exponential distribution.

In the last example, all integrations and solutions are obtained by numerical methods. As example, we choose the structure of an exponential distribution, but with non-constant parameter μ, i.e.,

$$p(x) = \Theta(x) \frac{1}{\mu(x)} \, \mathrm{e}^{-x/\mu(x)} \tag{9.6a}$$

$$\mu(x) = \frac{1 + \mu_{\mathrm{Min}} \cdot f(N(x))}{f(N(x))} \tag{9.6b}$$

$$f(N(x)) = \alpha \cdot \Theta\left(N(x) - N_{\mathrm{Min}}\right) \left(\frac{N(x)}{N_{\mathrm{Min}}} - 1\right)^{\beta} \tag{9.6c}$$

$$N(x) = r \cdot x + \xi \tag{9.6d}$$

For a motivation of the distribution, we refer the reader to Sec. 1.2.

These steps four steps are now employed (function calls as given in Ref. [147]):

1. normalization with
   gsl_integration_qagiu(p , 0 , . . . , resultNormalization , errorEstimate)
2. anti-derivative of $\tilde{p}(x)$ with
   gsl_integration_qag(p , 0 , x , . . . , resultAntiDerivative , errorEstimate)
   and divide by resultNormalization.
3. r = gsl_rng_uniform_pos(. . .)
4. First, get upper bound (smaller than infinity for numerical treatment). By construction, $V(0) - r < 0$ is smaller than zero for the distribution which we consider. From the expectation value of $\tilde{p}(x)$, we obtain a scale x suitable for starting the search of an upper bound for which $V(x) - r > 0$. If $V(x) - r < 0$ for some x, we increase

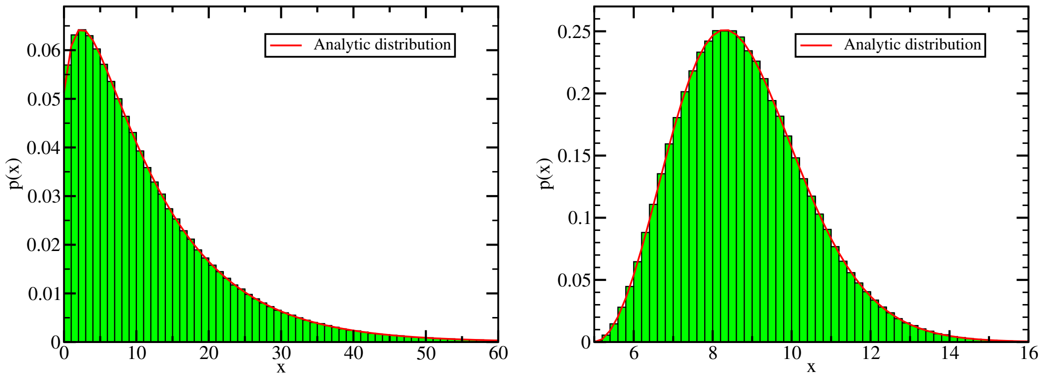

(a) Parameter: $\xi = 0.2$, $r = 0.03$, $\alpha = 0.25$, $\beta = 1$, $N_{\text{Min}} = 0.15$, $\mu_{\text{Min}} = 10$

(b) Parameter: $\xi = 0.0$, $r = 0.03$, $\alpha = 0.25$, $\beta = 2$, $N_{\text{Min}} = 0.15$, $\mu_{\text{Min}} = 1$

Figure A.3.: Comparison of the analytical probability distribution function $p(x)$, $x \in [0, \infty[$, as defined in Eq. (9.6) with a normalized histogram based on $N = 10^6$ randomly generated events as described in the main text. In this case, the integration of the density $p(x)$ is performed numerically. For all figures, numerical integration was bound by 10^{-8} on relative and absolute scale. Root bracketing with gsl_root_fsolver_falsepos was stopped when the residuum dropped below an absolute error of 10^{-6}.

x by a factor (e.g. of 3) and set the lower bound to the previous limit of the upper bound. Thus, a possible algorithm for finding the bounds is structured as:

- Set lowBound = 0 and uppBound = expectation value of $\tilde{p}(x)$.
- While $V(\text{uppBound}) - r < 0$: lowBound = uppBound ; uppBound *= 3.0 ;

Then, we use the solver gsl_root_fsolver_falsepos to obtain the solution x_r numerically. Return x_r.

B. Bragg reflections of a rotated substrate

Here, we add additional tables relevant for the discussions on the X-ray reflections available with the *in-situ* MBE growth chamber (see Sec. 2.2, in particular Fig. 2.3). We focus on rotations of the substrate by 60° and multiples thereof and provide tables and transformation matrices for X-ray Bragg reflections. Only scattering for which the incoming window and outgoing window is not equal is considered. The scan range for each index of the Miller indices was $-8\ldots8$.

First, we discuss cubic GaAs on $[111]_{\mathrm{z}\curvearrowright\mathrm{c}}$-oriented substrates. If the crystalline structure is rotated by 60° around the $[111]_{\mathrm{z}\curvearrowright\mathrm{c}}$ surface normal, the reflection indices are transformation by the matrix

$$\mathbf{M}_{60^\circ}^{(111)c} = \begin{pmatrix} 2/3 & -1/3 & 2/3 \\ 2/3 & 2/3 & -1/3 \\ -1/3 & 2/3 & 2/3 \end{pmatrix} . \tag{9.7}$$

If the rotation is 120° instead, the reflection indices are transformed by the matrix

$$\mathbf{M}_{120^\circ}^{(111)c} = \begin{pmatrix} 0 & 0 & 1 \\ 1 & 0 & 0 \\ 0 & 1 & 0 \end{pmatrix} , \tag{9.8}$$

i.e., a rotation by 120° around the $[111]_{\mathrm{z}\curvearrowright\mathrm{c}}$ axis corresponds to a shift of each index to the next position with periodic back-folding. Note that a rotation by 60° typically does not yield a valid reflection, but there are exceptions, e.g., if all indices are equal as $(111)_{\mathrm{z}\curvearrowright\mathrm{c}}$ or for example $\left(\bar{1}31\right)_{\mathrm{z}\curvearrowright\mathrm{c}}$.

We now consider a hexagonal basis: In direct space, the angle between our first two basis vectors is 120°. In contrast, the angle between the first two basis vectors in reciprocal space is 60°. Consequently, the transformation matrices for direct space indices and reciprocal space indices (such as Bragg reflections) are different. For indices with respect to the hexagonal direct space basis, the transformation matrix for a rotation by 60° around the $[00.1]_{\mathrm{w}\curvearrowright\mathrm{h2}}$ direction[3] is

$$\mathbf{M}_{d,60^\circ}^{(00.1)w} = \begin{pmatrix} 1 & -1 & 0 \\ 1 & 0 & 0 \\ 0 & 0 & 1 \end{pmatrix} \tag{9.9}$$

and the respective rotation by 120° is resembled by the matrix

$$\mathbf{M}_{d,120^\circ}^{(00.1)w} = \begin{pmatrix} 0 & -1 & 0 \\ 1 & -1 & 0 \\ 0 & 0 & 1 \end{pmatrix} . \tag{9.10}$$

The transformation matrix for a rotation by 60° around the $[00.1]_{\mathrm{w}\curvearrowright\mathrm{h2}}$ direction for indices related to the reciprocal hexagonal basis is

$$\mathbf{M}_{r,60^\circ}^{(00.1)w} = \begin{pmatrix} 0 & -1 & 0 \\ 1 & 1 & 0 \\ 0 & 0 & 1 \end{pmatrix} \tag{9.11}$$

and the respective rotation by 120° is resembled by the matrix

$$\mathbf{M}_{r,120^\circ}^{(00.1)w} = \begin{pmatrix} -1 & -1 & 0 \\ 1 & 0 & 0 \\ 0 & 0 & 1 \end{pmatrix} . \tag{9.12}$$

For convenience, we now add two tables which contain details about all reflections that can be measured with the current PMBE growth chamber (see Sec. 2.2 and appendix C).

---

[3] The $[00.1]_{\mathrm{w}\curvearrowright\mathrm{h2}}$ direction in direct space is parallel to the $(00.1)_{\mathrm{w}\curvearrowright\mathrm{h2}}$ direction in reciprocal space, and, thus, does not need to be distinguished.

Table B.1.: List of Bragg reflections of *cubic* GaAs which can be studied with the current PMBE growth chamber at an X-ray energy of 15keV and $[111]_{\mathrm{z}\curvearrowright\mathrm{c}}$ oriented surface. Constraints are $\Theta_{\mathrm{In}}^{(\mathrm{Max})} = 18°$, $\Theta_{\mathrm{Out}}^{(\mathrm{Max})} = 18°$.

0°	60°	120°	180°	240°	300°	$\lvert\mathcal{S}\rvert^2$
[-2 2 2]	[-0.67 -0.67 3.3]	[2 -2 2]	[3.3 -0.67 -0.67]	[2 2 -2]	[-0.67 3.3 -0.67]	4
[-1 -1 3]	[1.7 -2.3 1.7]	[3 -1 -1]	[1.7 1.7 -2.3]	[-1 3 -1]	[-2.3 1.7 1.7]	2050
[-1 1 1]	[-0.33 -0.33 1.7]	[1 -1 1]	[1.7 -0.33 -0.33]	[1 1 -1]	[-0.33 1.7 -0.33]	2050
[-1 1 3]	[1 -1 3]	[3 -1 1]	[3 1 -1]	[1 3 -1]	[-1 3 1]	2050
[-1 3 -1]	[-2.3 1.7 1.7]	[-1 -1 3]	[1.7 -2.3 1.7]	[3 -1 -1]	[1.7 1.7 -2.3]	2050
[-1 3 1]	[-1 1 3]	[1 -1 3]	[3 -1 1]	[3 1 -1]	[1 3 -1]	2050
[0 0 2]	[1.3 -0.67 1.3]	[2 -0 -0]	[1.3 1.3 -0.67]	[-0 2 -0]	[-0.67 1.3 1.3]	4
[0 0 4]	[2.7 -1.3 2.7]	[4 0 0]	[2.7 2.7 -1.3]	[0 4 0]	[-1.3 2.7 2.7]	4096
[0 2 0]	[-0.67 1.3 1.3]	[-0 -0 2]	[1.3 -0.67 1.3]	[2 -0 -0]	[1.3 1.3 -0.67]	4
[0 2 2]	[0.67 0.67 2.7]	[2 0 2]	[2.7 0.67 0.67]	[2 2 0]	[0.67 2.7 0.67]	4096
[0 4 0]	[-1.3 2.7 2.7]	[0 0 4]	[2.7 -1.3 2.7]	[4 0 0]	[2.7 2.7 -1.3]	4096
[1 -1 1]	[1.7 -0.33 -0.33]	[1 1 -1]	[-0.33 1.7 -0.33]	[-1 1 1]	[-0.33 -0.33 1.7]	2050
[1 -1 3]	[3 -1 1]	[3 1 -1]	[1 3 -1]	[-1 3 1]	[-1 1 3]	2050
[1 1 -1]	[-0.33 1.7 -0.33]	[-1 1 1]	[-0.33 -0.33 1.7]	[1 -1 1]	[1.7 -0.33 -0.33]	2050
[1 1 1]	[1 1 1]	[1 1 1]	[1 1 1]	[1 1 1]	[1 1 1]	2050
[1 1 3]	[2.3 0.33 2.3]	[3 1 1]	[2.3 2.3 0.33]	[1 3 1]	[0.33 2.3 2.3]	2050
[1 3 -1]	[-1 3 1]	[-1 1 3]	[1 -1 3]	[3 -1 1]	[3 1 -1]	2050
[1 3 1]	[0.33 2.3 2.3]	[1 1 3]	[2.3 0.33 2.3]	[3 1 1]	[2.3 2.3 0.33]	2050
[2 -2 2]	[3.3 -0.67 -0.67]	[2 2 -2]	[-0.67 3.3 -0.67]	[-2 2 2]	[-0.67 -0.67 3.3]	4
[2 0 0]	[1.3 1.3 -0.67]	[-0 2 -0]	[-0.67 1.3 1.3]	[-0 -0 2]	[1.3 -0.67 1.3]	4
[2 0 2]	[2.7 0.67 0.67]	[2 2 0]	[0.67 2.7 0.67]	[0 2 2]	[0.67 0.67 2.7]	4096
[2 2 -2]	[-0.67 3.3 -0.67]	[-2 2 2]	[-0.67 -0.67 3.3]	[2 -2 2]	[3.3 -0.67 -0.67]	4
[2 2 0]	[0.67 2.7 0.67]	[0 2 2]	[0.67 0.67 2.7]	[2 0 2]	[2.7 0.67 0.67]	4096
[2 2 2]	[2 2 2]	[2 2 2]	[2 2 2]	[2 2 2]	[2 2 2]	4
[3 -1 -1]	[1.7 1.7 -2.3]	[-1 3 -1]	[-2.3 1.7 1.7]	[-1 -1 3]	[1.7 -2.3 1.7]	2050
[3 -1 1]	[3 1 -1]	[1 3 -1]	[-1 3 1]	[-1 1 3]	[1 -1 3]	2050
[3 1 -1]	[1 3 -1]	[-1 3 1]	[-1 1 3]	[1 -1 3]	[3 -1 1]	2050
[3 1 1]	[2.3 2.3 0.33]	[1 3 1]	[0.33 2.3 2.3]	[1 1 3]	[2.3 0.33 2.3]	2050
[4 0 0]	[2.7 2.7 -1.3]	[0 4 0]	[-1.3 2.7 2.7]	[0 0 4]	[2.7 -1.3 2.7]	4096

Table B.2.: List of Bragg reflections of *wurtzite* GaAs which can be studied with the current PMBE growth chamber at an X-ray energy of 15keV and $[00.1]_{\mathrm{w}\curvearrowright\mathrm{h2}}$ oriented surface. Constraints are $\Theta_{\mathrm{In}}^{(\mathrm{Max})} = 18°$, $\Theta_{\mathrm{Out}}^{(\mathrm{Max})} = 18°$.

0°	60°	120°	180°	240°	300°	$\lvert\mathcal{S}\rvert^2$
[-2 0 1]	[0 -2 1]	[2 -2 1]	[2 0 1]	[0 2 1]	[-2 2 1]	452
[-2 0 2]	[0 -2 2]	[2 -2 2]	[2 0 2]	[0 2 2]	[-2 2 2]	512
[-2 0 3]	[0 -2 3]	[2 -2 3]	[2 0 3]	[0 2 3]	[-2 2 3]	2623
[-2 1 2]	[-1 -1 2]	[1 -2 2]	[2 -1 2]	[1 1 2]	[-1 2 2]	2050
[-2 2 1]	[-2 0 1]	[0 -2 1]	[2 -2 1]	[2 0 1]	[0 2 1]	452
[-2 2 2]	[-2 0 2]	[0 -2 2]	[2 -2 2]	[2 0 2]	[0 2 2]	512
[-2 2 3]	[-2 0 3]	[0 -2 3]	[2 -2 3]	[2 0 3]	[0 2 3]	2623
[-1 -1 2]	[1 -2 2]	[2 -1 2]	[1 1 2]	[-1 2 2]	[-2 1 2]	2050
[-1 0 1]	[0 -1 1]	[1 -1 1]	[1 0 1]	[0 1 1]	[-1 1 1]	452
[-1 0 2]	[0 -1 2]	[1 -1 2]	[1 0 2]	[0 1 2]	[-1 1 2]	513
[-1 0 3]	[0 -1 3]	[1 -1 3]	[1 0 3]	[0 1 3]	[-1 1 3]	2623
[-1 0 4]	[0 -1 4]	[1 -1 4]	[1 0 4]	[0 1 4]	[-1 1 4]	1
[-1 1 1]	[-1 0 1]	[0 -1 1]	[1 -1 1]	[1 0 1]	[0 1 1]	452
[-1 1 2]	[-1 0 2]	[0 -1 2]	[1 -1 2]	[1 0 2]	[0 1 2]	513
[-1 1 3]	[-1 0 3]	[0 -1 3]	[1 -1 3]	[1 0 3]	[0 1 3]	2623
[-1 1 4]	[-1 0 4]	[0 -1 4]	[1 -1 4]	[1 0 4]	[0 1 4]	1
[-1 2 2]	[-2 1 2]	[-1 -1 2]	[1 -2 2]	[2 -1 2]	[1 1 2]	2050
[0 -2 1]	[2 -2 1]	[2 0 1]	[0 2 1]	[-2 2 1]	[-2 0 1]	452
[0 -2 2]	[2 -2 2]	[2 0 2]	[0 2 2]	[-2 2 2]	[-2 0 2]	513
[0 -2 3]	[2 -2 3]	[2 0 3]	[0 2 3]	[-2 2 3]	[-2 0 3]	2623
[0 -1 1]	[1 -1 1]	[1 0 1]	[0 1 1]	[-1 1 1]	[-1 0 1]	452
[0 -1 2]	[1 -1 2]	[1 0 2]	[0 1 2]	[-1 1 2]	[-1 0 2]	512
[0 -1 3]	[1 -1 3]	[1 0 3]	[0 1 3]	[-1 1 3]	[-1 0 3]	2623
[0 -1 4]	[1 -1 4]	[1 0 4]	[0 1 4]	[-1 1 4]	[-1 0 4]	1
[0 0 2]	[0 0 2]	[0 0 2]	[0 0 2]	[0 0 2]	[0 0 2]	2050
[0 0 4]	[0 0 4]	[0 0 4]	[0 0 4]	[0 0 4]	[0 0 4]	4
[0 1 1]	[-1 1 1]	[-1 0 1]	[0 -1 1]	[1 -1 1]	[1 0 1]	452
[0 1 2]	[-1 1 2]	[-1 0 2]	[0 -1 2]	[1 -1 2]	[1 0 2]	512
[0 1 3]	[-1 1 3]	[-1 0 3]	[0 -1 3]	[1 -1 3]	[1 0 3]	2623
[0 1 4]	[-1 1 4]	[-1 0 4]	[0 -1 4]	[1 -1 4]	[1 0 4]	1
[0 2 1]	[-2 2 1]	[-2 0 1]	[0 -2 1]	[2 -2 1]	[2 0 1]	452
[0 2 2]	[-2 2 2]	[-2 0 2]	[0 -2 2]	[2 -2 2]	[2 0 2]	513
[0 2 3]	[-2 2 3]	[-2 0 3]	[0 -2 3]	[2 -2 3]	[2 0 3]	2623
[1 -2 2]	[2 -1 2]	[1 1 2]	[-1 2 2]	[-2 1 2]	[-1 -1 2]	2050
[1 -1 1]	[1 0 1]	[0 1 1]	[-1 1 1]	[-1 0 1]	[0 -1 1]	452
[1 -1 2]	[1 0 2]	[0 1 2]	[-1 1 2]	[-1 0 2]	[0 -1 2]	513
[1 -1 3]	[1 0 3]	[0 1 3]	[-1 1 3]	[-1 0 3]	[0 -1 3]	2623
[1 -1 4]	[1 0 4]	[0 1 4]	[-1 1 4]	[-1 0 4]	[0 -1 4]	1
[1 0 1]	[0 1 1]	[-1 1 1]	[-1 0 1]	[0 -1 1]	[1 -1 1]	452
[1 0 2]	[0 1 2]	[-1 1 2]	[-1 0 2]	[0 -1 2]	[1 -1 2]	513
[1 0 3]	[0 1 3]	[-1 1 3]	[-1 0 3]	[0 -1 3]	[1 -1 3]	2623
[1 0 4]	[0 1 4]	[-1 1 4]	[-1 0 4]	[0 -1 4]	[1 -1 4]	1
[1 1 2]	[-1 2 2]	[-2 1 2]	[-1 -1 2]	[1 -2 2]	[2 -1 2]	2050
[2 -2 1]	[2 0 1]	[0 2 1]	[-2 2 1]	[-2 0 1]	[0 -2 1]	452
[2 -2 2]	[2 0 2]	[0 2 2]	[-2 2 2]	[-2 0 2]	[0 -2 2]	512
[2 -2 3]	[2 0 3]	[0 2 3]	[-2 2 3]	[-2 0 3]	[0 -2 3]	2623
[2 -1 2]	[1 1 2]	[-1 2 2]	[-2 1 2]	[-1 -1 2]	[1 -2 2]	2050
[2 0 1]	[0 2 1]	[-2 2 1]	[-2 0 1]	[0 -2 1]	[2 -2 1]	452
[2 0 2]	[0 2 2]	[-2 2 2]	[-2 0 2]	[0 -2 2]	[2 -2 2]	512
[2 0 3]	[0 2 3]	[-2 2 3]	[-2 0 3]	[0 -2 3]	[2 -2 3]	2623

C. Extended tables to Sec. 2.2

Here, we add additional tables relevant for the discussions on the X-ray reflections available with the *in-situ* MBE growth chamber (see Sec. 2.2, in particular Fig. 2.3).[4] All data is based on 15keV energy of the incident X-ray radiation and 0.7% increased vertical lattice constant of wurtzite in comparison to zinc blende [119]. Only scattering for which the incoming window and outgoing window is not equal is considered. The scan range for each index of the Miller indices was $-8\ldots8$.

Table C.3.: List of Bragg reflections of *cubic* GaAs which can be studied with the current PMBE growth chamber at an X-ray energy of 15keV and $[111]_{z\curvearrowright c}$ oriented surface. Constraints are $\Theta_{\text{In}}^{(\text{Max})} = 18°$, $\Theta_{\text{Out}}^{(\text{Max})} = 18°$.

reflection (cubic)	$\lvert\mathcal{S}\rvert^2$ [electrons]	(q_z,q_r) [1/Å]	$\lVert\boldsymbol{G}\rVert_2$ [1/Å]	$\Theta_{\text{Bragg}}^{\text{reflec.}}$ [°]	reflection (wurtzite)
[-2 2 2]	4	(1.2834,3.6299)	3.8501	14.67	[-2 2 1.3]
[-1 -1 3]	2050	(0.6417,3.6299)	3.6862	14.03	[-2 0 0.67]
[-1 1 1]	2050	(0.6417,1.8149)	1.9250	7.27	[-1 1 0.67]
[-1 1 3]	2050	(1.9250,3.1436)	3.6862	14.03	[-2 1 2]
[-1 3 -1]	2050	(0.6417,3.6299)	3.6862	14.03	[0 2 0.67]
[-1 3 1]	2050	(1.9250,3.1436)	3.6862	14.03	[-1 2 2]
[0 0 2]	4	(1.2834,1.8149)	2.2228	8.41	[-1 0 1.3]
[0 0 4]	4096	(2.5667,3.6299)	4.4457	17.00	[-2 0 2.7]
[0 2 0]	4	(1.2834,1.8149)	2.2228	8.41	[0 1 1.3]
[0 2 2]	4096	(2.5667,1.8149)	3.1436	11.93	[-1 1 2.7]
[0 4 0]	4096	(2.5667,3.6299)	4.4457	17.00	[0 2 2.7]
[1 -1 1]	2050	(0.6417,1.8149)	1.9250	7.27	[0 -1 0.67]
[1 -1 3]	2050	(1.9250,3.1436)	3.6862	14.03	[-1 -1 2]
[1 1 -1]	2050	(0.6417,1.8149)	1.9250	7.27	[1 0 0.67]
[1 1 1]	2050	(1.9250,0.0000)	1.9250	7.27	[0 0 2]
[1 1 3]	2050	(3.2084,1.8149)	3.6862	14.03	[-1 0 3.3]
[1 3 -1]	2050	(1.9250,3.1436)	3.6862	14.03	[1 1 2]
[1 3 1]	2050	(3.2084,1.8149)	3.6862	14.03	[0 1 3.3]
[2 -2 2]	4	(1.2834,3.6299)	3.8501	14.67	[0 -2 1.3]
[2 0 0]	4	(1.2834,1.8149)	2.2228	8.41	[1 -1 1.3]
[2 0 2]	4096	(2.5667,1.8149)	3.1436	11.93	[0 -1 2.7]
[2 2 -2]	4	(1.2834,3.6299)	3.8501	14.67	[2 0 1.3]
[2 2 0]	4096	(2.5667,1.8149)	3.1436	11.93	[1 0 2.7]
[2 2 2]	4	(3.8501,0.0000)	3.8501	14.67	[0 0 4]
[3 -1 -1]	2050	(0.6417,3.6299)	3.6862	14.03	[2 -2 0.67]
[3 -1 1]	2050	(1.9250,3.1436)	3.6862	14.03	[1 -2 2]
[3 1 -1]	2050	(1.9250,3.1436)	3.6862	14.03	[2 -1 2]
[3 1 1]	2050	(3.2084,1.8149)	3.6862	14.03	[1 -1 3.3]
[4 0 0]	4096	(2.5667,3.6299)	4.4457	17.00	[2 -2 2.7]

---

[4] For information on rotations of the substrate by 60° and multiples thereof, see appendix B.

Table C.4.: List of Bragg reflections of *wurtzite* GaAs which can be studied with the current PMBE growth chamber at an X-ray energy of 15keV and $[00.1]_{\mathrm{w}\frown\mathrm{h2}}$ oriented surface. Constraints are $\Theta_{\mathrm{In}}^{(\mathrm{Max})} = 18^\circ$, $\Theta_{\mathrm{Out}}^{(\mathrm{Max})} = 18^\circ$.

reflection (wurtzite)	$\lvert\mathcal{S}\rvert^2$ [electrons]	(q_z,q_r) [1/Å]	$\lVert\boldsymbol{G}\rVert_2$ [1/Å]	$\Theta^{\mathrm{reflec.}}_{\mathrm{Bragg}}$ [°]	reflection (cubic)
[-2 0 1]	452	(0.9558,3.6299)	3.7536	14.29	[-0.83 -0.83 3.2]
[-2 0 2]	512	(1.9117,3.6299)	4.1025	15.65	[-0.33 -0.33 3.7]
[-2 0 3]	2623	(2.8675,3.6299)	4.6258	17.71	[0.17 0.17 4.2]
[-2 1 2]	2050	(1.9117,3.1436)	3.6792	14.00	[-1 1 3]
[-2 2 1]	452	(0.9558,3.6299)	3.7536	14.29	[-2.2 1.8 1.8]
[-2 2 2]	512	(1.9117,3.6299)	4.1025	15.65	[-1.7 2.3 2.3]
[-2 2 3]	2623	(2.8675,3.6299)	4.6258	17.71	[-1.2 2.8 2.8]
[-1 -1 2]	2050	(1.9117,3.1436)	3.6792	14.00	[1 -1 3]
[-1 0 1]	452	(0.9558,1.8149)	2.0512	7.75	[-0.17 -0.17 1.8]
[-1 0 2]	513	(1.9117,1.8149)	2.6360	9.98	[0.33 0.33 2.3]
[-1 0 3]	2623	(2.8675,1.8149)	3.3936	12.90	[0.83 0.83 2.8]
[-1 0 4]	1	(3.8233,1.8149)	4.2322	16.16	[1.3 1.3 3.3]
[-1 1 1]	452	(0.9558,1.8149)	2.0512	7.75	[-0.83 1.2 1.2]
[-1 1 2]	513	(1.9117,1.8149)	2.6360	9.98	[-0.33 1.7 1.7]
[-1 1 3]	2623	(2.8675,1.8149)	3.3936	12.90	[0.17 2.2 2.2]
[-1 1 4]	1	(3.8233,1.8149)	4.2322	16.16	[0.67 2.7 2.7]
[-1 2 2]	2050	(1.9117,3.1436)	3.6792	14.00	[-1 3 1]
[0 -2 1]	452	(0.9558,3.6299)	3.7536	14.29	[1.8 -2.2 1.8]
[0 -2 2]	513	(1.9117,3.6299)	4.1025	15.65	[2.3 -1.7 2.3]
[0 -2 3]	2623	(2.8675,3.6299)	4.6258	17.71	[2.8 -1.2 2.8]
[0 -1 1]	452	(0.9558,1.8149)	2.0512	7.75	[1.2 -0.83 1.2]
[0 -1 2]	512	(1.9117,1.8149)	2.6360	9.98	[1.7 -0.33 1.7]
[0 -1 3]	2623	(2.8675,1.8149)	3.3936	12.90	[2.2 0.17 2.2]
[0 -1 4]	1	(3.8233,1.8149)	4.2322	16.16	[2.7 0.67 2.7]
[0 0 2]	2050	(1.9117,0.0000)	1.9117	7.22	[1 1 1]
[0 0 4]	4	(3.8233,0.0000)	3.8233	14.57	[2 2 2]
[0 1 1]	452	(0.9558,1.8149)	2.0512	7.75	[-0.17 1.8 -0.17]
[0 1 2]	512	(1.9117,1.8149)	2.6360	9.98	[0.33 2.3 0.33]
[0 1 3]	2623	(2.8675,1.8149)	3.3936	12.90	[0.83 2.8 0.83]
[0 1 4]	1	(3.8233,1.8149)	4.2322	16.16	[1.3 3.3 1.3]
[0 2 1]	452	(0.9558,3.6299)	3.7536	14.29	[-0.83 3.2 -0.83]
[0 2 2]	513	(1.9117,3.6299)	4.1025	15.65	[-0.33 3.7 -0.33]
[0 2 3]	2623	(2.8675,3.6299)	4.6258	17.71	[0.17 4.2 0.17]
[1 -2 2]	2050	(1.9117,3.1436)	3.6792	14.00	[3 -1 1]
[1 -1 1]	452	(0.9558,1.8149)	2.0512	7.75	[1.8 -0.17 -0.17]
[1 -1 2]	513	(1.9117,1.8149)	2.6360	9.98	[2.3 0.33 0.33]
[1 -1 3]	2623	(2.8675,1.8149)	3.3936	12.90	[2.8 0.83 0.83]
[1 -1 4]	1	(3.8233,1.8149)	4.2322	16.16	[3.3 1.3 1.3]
[1 0 1]	452	(0.9558,1.8149)	2.0512	7.75	[1.2 1.2 -0.83]
[1 0 2]	513	(1.9117,1.8149)	2.6360	9.98	[1.7 1.7 -0.33]
[1 0 3]	2623	(2.8675,1.8149)	3.3936	12.90	[2.2 2.2 0.17]
[1 0 4]	1	(3.8233,1.8149)	4.2322	16.16	[2.7 2.7 0.67]
[1 1 2]	2050	(1.9117,3.1436)	3.6792	14.00	[1 3 -1]
[2 -2 1]	452	(0.9558,3.6299)	3.7536	14.29	[3.2 -0.83 -0.83]
[2 -2 2]	512	(1.9117,3.6299)	4.1025	15.65	[3.7 -0.33 -0.33]
[2 -2 3]	2623	(2.8675,3.6299)	4.6258	17.71	[4.2 0.17 0.17]
[2 -1 2]	2050	(1.9117,3.1436)	3.6792	14.00	[3 1 -1]
[2 0 1]	452	(0.9558,3.6299)	3.7536	14.29	[1.8 1.8 -2.2]
[2 0 2]	512	(1.9117,3.6299)	4.1025	15.65	[2.3 2.3 -1.7]
[2 0 3]	2623	(2.8675,3.6299)	4.6258	17.71	[2.8 2.8 -1.2]

D. Exemplary SEM images from the samples S1, S2 and S2e

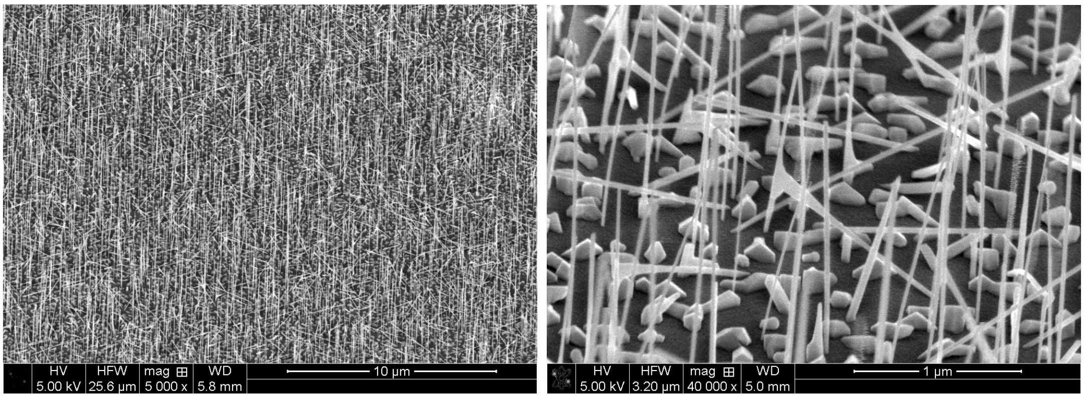

(a) sample 1

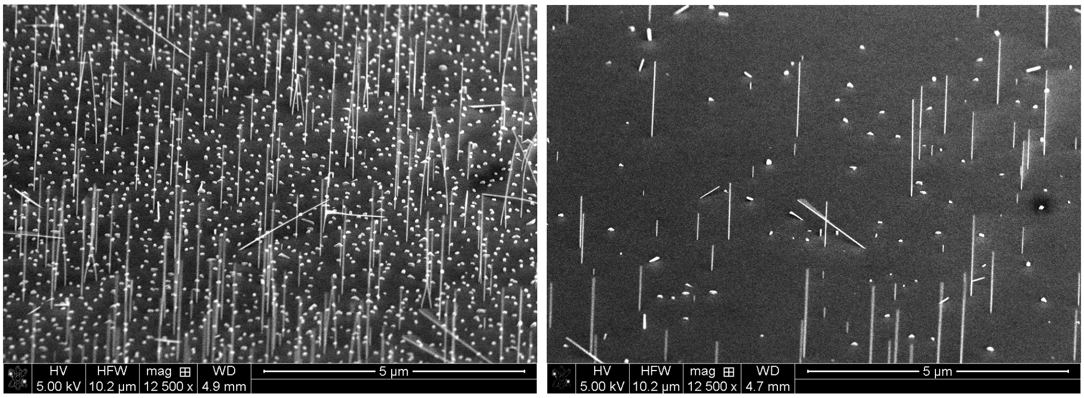

(b) sample 2

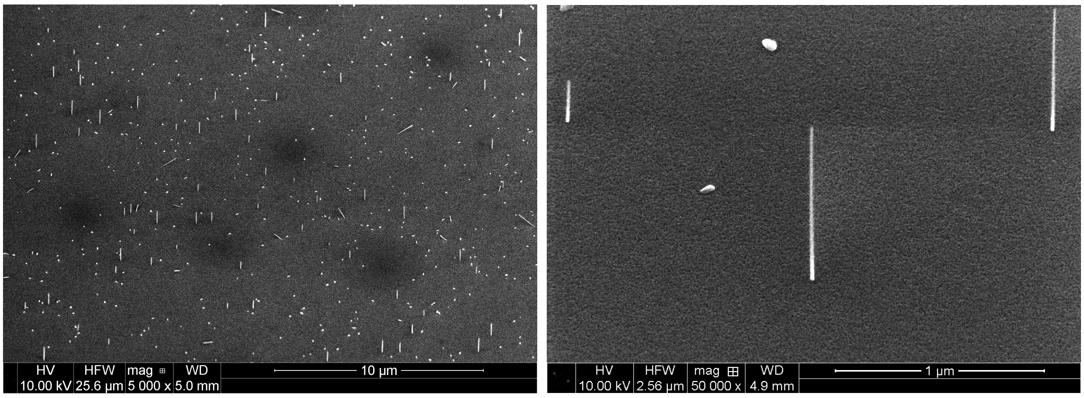

(c) sample 2e

Figure D.4.: Post-growth *ex-situ* SEM images of the samples which are discussed in Secs. 3 and 4. Colors have been adopted for better contrast. Images have been taken by Philipp Schroth, Jean-Wolfgang Hornung and Robby Prang and are reproduced with permission.

E. Relation between mean and currently growing polytype fractions

Here, we derive the relation between the *total* fractions f_P of a particular phase $P \in \{\mathrm{ZB}, \mathrm{WZ}\}$ in the entire set of wires at times t and $t+\delta t$ and their relation to the fraction of that particular phase in the *newly grown fragments* during the time δt at the top of the wire. We refer to this fraction of phase P in the newly grown domains during the time t to $t+\delta t$ as *differential* phase fraction $\tilde{f}_\mathrm{P}(t, t+\delta t)$.

We assume:

1. No phase transformations take place in the part of the wires already grown before time t.
2. The diameter of the wires is constant ("no radial growth").
3. The height of the wires is a linear function of time after an incubation time t_Inc.

Based on the first assumption, we can express total fraction $f_\mathrm{P}(t+\delta t)$ of a single wire as

$$f_\mathrm{P}(t+\delta t) = \left(\frac{V(t)}{V(t)+\delta V(t,t+\delta t)}\right) f_\mathrm{P}(t) + \left(\frac{\delta V(t,t+\delta t)}{V(t)+\delta V(t,t+\delta t)}\right) \tilde{f}_\mathrm{P}(t,t+\delta t) \tag{9.13}$$

where $V(t)$ is volume of the wire at time t and $\delta V(t, t+\delta t)$ is the volume grown in the time interval t to $t+\delta t$. The second assumption implies that $V(t) = A_0\, h(t)$ and $\delta V(t,t+\delta t) = A_0\, \delta h(t,t+\delta t)$ where $h(t)$ is wire's height after time t and $\delta h(t,t+\delta t)$ is the change of height from t to $t+\delta t$. Finally, the third approximation induces the equivalences

$$h(t) = g\cdot(t-t_\mathrm{Inc}) \ , \tag{9.14a}$$

$$\delta h(t,t+\delta t) = h(t+\delta t) - h(t) = g\cdot\delta t \ , \tag{9.14b}$$

where g is the growth rate of the wires in height with dimension $[\,g\,] = 1\frac{\mathrm{m}}{\mathrm{s}}$. Therefore, Eq. (9.13) simplifies to

$$f_\mathrm{P}(t+\delta t) = \left(\frac{t-t_\mathrm{Inc}}{t-t_\mathrm{Inc}+\delta t}\right) f_\mathrm{P}(t) + \left(\frac{\delta t}{t-t_\mathrm{Inc}+\delta t}\right) \tilde{f}_\mathrm{P}(t,t+\delta t) \ . \tag{9.15}$$

Hence, the *finite difference* approximation for the differential phase fraction $\tilde{f}_\mathrm{P}(t,t+\delta t)$ is

$$\tilde{f}_\mathrm{P}(t,t+\delta t) = \left(\frac{t-t_\mathrm{Inc}+\delta t}{\delta t}\right) f_\mathrm{P}(t+\delta t) - \left(\frac{t-t_\mathrm{Inc}}{\delta t}\right) f_\mathrm{P}(t) \ . \tag{9.16}$$

However, this finite difference approximation is very sensitive to noise. Typically, it is better to fit the (less noisy, discrete) total fraction $f_\mathrm{P}(t)$ by a time-continuous model function (e.g., a polynomial of degree n) and calculate the differential phase fraction $\tilde{f}_\mathrm{P}(t,t+\delta t)$ analytically in the limit $\delta t \to 0$. Hence, $\tilde{f}_\mathrm{P}(t,t+\delta t)$ simplifies to $\tilde{f}_\mathrm{P}(t) \equiv \lim_{\delta t\to 0} \tilde{f}_\mathrm{P}(t,t+\delta t)$. In the limit $\delta t \to 0$, it is valid to approximate $f_\mathrm{P}(t+\delta t)$ by

$$f_\mathrm{P}(t+\delta t) \approx f_\mathrm{P}(t) + \delta t \left(\frac{\partial \mathrm{f_P(t)}}{\partial t}\right) \ . \tag{9.17}$$

Therefore, we obtain from Eq. (9.16) the result

$$\begin{aligned}
\tilde{f}_\mathrm{P}(t) &= \lim_{\delta t\to 0} \tilde{f}_\mathrm{P}(t,t+\delta t) && (9.18\mathrm{a})\\
&= \lim_{\delta t\to 0} \left[\left(\frac{t-t_\mathrm{Inc}+\delta t}{\delta t}\right)\left(f_\mathrm{P}(t) + \delta t\left(\frac{\partial \mathrm{f_P(t)}}{\partial t}\right)\right) - \left(\frac{t-t_\mathrm{Inc}}{\delta t}\right) f_\mathrm{P}(t)\right] && (9.18\mathrm{b})\\
&= f_\mathrm{P}(t) + (t-t_\mathrm{Inc})\left(\frac{\partial \mathrm{f_P(t)}}{\partial t}\right) \ . && (9.18\mathrm{c})
\end{aligned}$$

Suppose, the total fraction $f_\mathrm{P}(t)$ can be modeled well by a polynomial of degree n, i.e.,

$$f_\mathrm{P}(t) = \sum_{k=0}^{n} p_k (t - t_\mathrm{Inc})^k \ . \tag{9.19}$$

The differential fraction $\tilde{f}_\mathrm{P}(t)$ is then given by the polynomial

$$\tilde{f}_\mathrm{P}(t) = \sum_{k=0}^{n} (1+k)\, p_k\, (t - t_\mathrm{Inc})^k \tag{9.20}$$

of the same degree n, but coefficients $\tilde{p}_k = (1+k)\, p_k$. For the special case of a polynomial of degree 2, the result for $\tilde{f}_\mathrm{P}(t)$ is

$$\tilde{f}_\mathrm{P}(t) = p_0 + 2p_1(t - t_\mathrm{Inc}) + 3p_2(t - t_\mathrm{Inc})^2 \ . \tag{9.21}$$

However, it is important to keep in mind, that our derivation is based on a single wire. Therefore, errors in $\tilde{f}_\mathrm{P}$ are induced by the fact that different wires are not identical in height and incubation time, but may have a broad distribution for these quantities. In addition, radial growth might need to be included – depending on the ratio of the axial and radial growth rate.

F. Structure of the XML File for simulations of GaAs nanowires on Si(111)

In this section, we exemplary add detailed information on the structure of the XML-based configuration files for the simulations concerning polytypic GaAs nanowires as discussed in Sec. 4.3.

The basic structure of the XML file is as follows:

```
<?xml version="1.0" ?>
<InSituWireScattering debugLevel="0"
 maxNumberOfThreads="24" logFilename="inSitu.log">
  [List of Tasks]
</InSituWireScattering>
```

The list of tasks to be done can be any number of entries from the two possible topics:

- Extraction of some statistical information for a given model for the stacking sequence. No X-ray simulations are performed. In this case, the task to be done has the following structure:

  ```
  <ExtractStatistics fileBasename="./output" numberOfVolumes="1">
    [Properties]
  </ExtractStatistics>
  ```

- Calculation of the q_z intensity profile for some X-ray Bragg reflection. In this case, the task to be done has the following structure:

  ```
  <LineProfileQZ fileBasename="./output" qx="0.0" qy="0.0"
   qzMin="1.907" qzStep="0.000025" qzMax="1.93" qzResolution="0.001"
   hklHex="(0,0,3)" numberOfIncoherentVolumes="2500">
    [Properties]
  </LineProfileQZ>
  ```

  Here, “hklHex” refers to the indices of $(hkl)_{\mathrm{z}\frown\mathrm{h1}}$ as defined in Sec. 1.4.

In both cases, properties must contain a section WireModeling in the follow structure:

```
<WireModeling wiresInSingleCoherenceVolume="1">

  <LatticeParameter
   cGaAsWz="6.573563633494758628"
   cGaAsZnB="9.791802830429134003"
   aGaAsWz="3.9974868"
   aGaAsZnB="3.9974868"
  />

  <StackingModel>
    [SpecificModels]
  </StackingModel>

</WireModeling>
```

Lattice parameters are in Angstroms. Specific models, which have been implemented, are:

```
<pureZnB probability="0.0">
  [Geometry]
</pureZnB>

<pureWz probability="0.0">
  [Geometry]
</<pureWz>

<randomStackingLayersWithoutRepetitions probability="0.0">
  [Geometry]
</randomStackingLayersWithoutRepetitions>

<randomStackingHexOrZnB probability="0.0" pZnB="0.75">
  [Geometry]
</randomStackingHexOrZnB>

<markovChain probability="0.00"
 pStartWz="0.75" pSwitchHexToZnB="0.01" pSwitchZnBToWz="0.0075">
  [Geometry]
</markovChain>

<markovChainLayerDependentProbabilityLinear probability="0.0"
 pStartWz="0.75"
 pSwitchHexToZnBSlopePerLayer="0.0" pSwitchHexToZnBLayerZero="0.01"
 pSwitchZnBToWzSlopePerLayer="0.0" pSwitchZnBToWzLayerZero="0.0075">
  [Geometry]
</markovChainLayerDependentProbabilityLinear>

<phaseLengthDistributionBasedWires probability="1.0" pStartWz="0.5">
  [Geometry]
  <StatisticalDistributionLengthLayersZnB>
    [DistributionDefinition]
  </StatisticalDistributionLengthLayersZnB>
  <StatisticalDistributionLengthLayersWz>
    [DistributionDefinition]
  </StatisticalDistributionLengthLayersWz>
</phaseLengthDistributionBasedWires>
```

In principle, the stacking model and its particular values within a wire can depend on the geometry of a wire. Therefore, we defined that the geometry is a sub-element of the specific models. The geometry contains information about the diameter, the height and position of the center of each wire in the following format:

```
<Diameter
 shapeGeometry="0"
 shapeDistributionMean="400"
 shapeDistributionWidth="50"
/>

<Height model="0" mean="5500" width="500" />

<WirePosition model="0"/>
```

For the definition of the models, we refer the reader directly to the source code. In case of "phaseLengthDistributionBasedWires", an element to which we referred as DistributionDefinition needs to be defined and must be *one* of the following elements:

```
<Exponential mu="100" pDeviateMarkov4HEnhance="0.0"/>
<Gamma powerLawExp="0.0" expInvDecayConst="100.0"
 pDeviateMarkov4HEnhance="0.0"/>
<Weibull shape="2.0" expInvDecayConst="100.0"
 pDeviateMarkov4HEnhance="0.0"/>
<Rectangular minimumLayers="1" maximumLayers="100"
 pDeviateMarkov4HEnhance="0.0"/>
<Pareto tailIndex="0.4" minimumLayers="1.0"
 pDeviateMarkov4HEnhance="0.0"/>
<Poisson mu="100" pDeviateMarkov4HEnhance="0.0"/>
<Logarithmic p="0.5" pDeviateMarkov4HEnhance="0.0"/>

<Gauss mu="100" sigma="5" pDeviateMarkov4HEnhance="0.0"/>
<Laplace mu="100" shift="30" pDeviateMarkov4HEnhance="0.0"/>
<LevySkew scale="1.0" exponent="0.5"
 skewness="0.0" shiftOffset="0.0"
 pDeviateMarkov4HEnhance="0.0"/>
<Logistisch mu="100.0" expInvDecayConst="100.0"
 pDeviateMarkov4HEnhance="0.0"/>
```

Random numbers according to these distributions are generated with the GSL [147]. The first group of distributions (up to logarithmic) yields a non-negative number of layers only. If zero is a possible result of the respective distribution, an offset of one is added to achieve a minimum number of one layer. If the respective distribution can yield negative numbers, parameters are used as they are typically referred to, but for negative results a new random number is drawn, i.e., the distribution is truncated from below at one layer. In the main text, we only discuss results for the first group of distributions and the Gaussian distribution. The parameter pDeviateMarkov4HEnhance refers to α in Eq. (4.43b) where p_{Markov} is substituted by any of the above distributions.

In addition to the WireModeling-element, the calculation of the q_z profile via <LineProfileQZ/> requires additionally the element

```
<AtomicScattering Ga="1.0" As="1.0"/>
```

as sub-element.

Finally, a full XML file for a calculation of the X-ray profile near the $(111)_{\mathrm{z}\curvearrowright\mathrm{c}}$ reflection with enhanced $4H$ polytype might look like this:

```
<?xml version="1.0" ?>

<InSituWireScattering debugLevel="0"
 maxNumberOfThreads="24" logFilename="inSitu.log" >

  <LineProfileQZ fileBasename="./output"
   qx="0.0" qy="0.0" qzMin="1.90" qzMax="1.94" qzStep="0.00002"
   qzResolution="0.0" hklHex="(0,0,3)" numberOfIncoherentVolumes="2500">
```

```
    <AtomicScattering Ga="5.605" As="5.8977"/>

    <WireModeling wiresInSingleCoherenceVolume="1"
     exportWireStackingToFile="0" exportWireStackingFilename="wires.log">

      <LatticeParameter
       cGaAsWz="6.573563633494758628" cGaAsZnB="9.791802830429134003"
       aGaAsWz="3.9974868"            aGaAsZnB="3.9974868"/>

      <StackingModel>

        <phaseLengthDistributionBasedWires probability="1.0"
         nrOfEventsForDistributionVerification="0" pStartWz="0.5">

          <StatisticalDistributionLengthLayersZnB>
            <Exponential mu="125.0" pDeviateMarkov4HEnhance="0.995"/>
          </StatisticalDistributionLengthLayersZnB>

          <StatisticalDistributionLengthLayersWz>
            <Exponential mu="100.0" pDeviateMarkov4HEnhance="0.990"/>
          </StatisticalDistributionLengthLayersWz>

          <Diameter shapeGeometry="0"
           shapeDistributionMean="400" shapeDistributionWidth="50"/>

          <Height model="0" mean="7500" width="1000"/>

          <WirePosition model="0"/>

        </phaseLengthDistributionBasedWires>

      </StackingModel>

    </WireModeling>

  </LineProfileQZ>

</InSituWireScattering>
```

The simulations presented in Sec. 1.2 and in part II of this manuscript are also configured by XML files. However, in those cases we refer the reader to the respective source codes and the example XML file therein.

G. Operator polynomial approach for combining $\mathbf{M}_{\mathrm{A}}$ and $\mathbf{Q}_{\Gamma;\lambda_\Gamma}$

Here, we shortly comment on the combination of randomized overrelaxation $\mathbf{Q}_{\Gamma;\lambda_\Gamma}$ and our magnitude constraints $\mathbf{M}_{\mathrm{A}}$ starting from HIO as a projection polynomial (i.e., Eq. (6.52c)). For the understanding of this discussion, it is required to study Sec. 7.4 in detail first.

In this approach, it is important to distinguish if we introduce overrelaxation $\mathbf{Q}_{\Gamma;\lambda_\Gamma}$ or magnitude constraints $\mathbf{M}_{\mathrm{A}}$ first in Eq. (6.52c):

The transformation from the operator polynomial (7.6) to an projection polynomial (7.7b) relies on the *linearity* of the operator $\mathbf{P}_\Omega$. Therefore, this transformation can no longer be performed if the substitution (7.16a) is performed first – irrespective of taking into account the estimation of the averages $\bar{\zeta}_j$ by Eq. (7.21a) or not. Only if we introduce overrelaxation first and then include the constraints $\mathbf{M}_{\mathrm{A}}$ by substitution of $\mathbf{P}_\Omega$ as a second step, the resulting operator is a projection polynomial as long as we assume the averages $\bar{\zeta}_j$ to be known *a priori*. Therefore, this sequence of incorporation of randomized overrelaxation and the magnitude constraints should be preferred.

However, once we include the estimation of the averages $\bar{\zeta}_j$ as defined in Eq. (7.21a), the operator is no longer contained in the set of projection polynomials irrespective of the order of substitution. Nonetheless, it can still be employed as an iterative prescription during the reconstruction.

In analogy to Eq. (7.16b), but after the substitutions $\mathbf{P}_\Omega \to \mathbf{P}_{\Omega,\mathrm{A}}$ (see Eq. (7.16a)) and (7.22) in the projection polynomial of the $\mathrm{HIO}_{\mathrm{O_R}}$-algorithm (see Eq. (7.7b)), we obtain

$$\begin{aligned}\hat{H}^{(\mathrm{OP})}_{\mathrm{HIO+O_R+A}}(\beta, \lambda_\Gamma = 1 + \gamma_\Gamma) = {} & [1 + \beta\gamma_\Gamma] + [-1 - \gamma_\Gamma(1+\beta)]\, \mathbf{P}_\Omega \mathbf{M}_{\mathrm{A}} - \\ & [-\beta(1+\gamma_\Gamma)]\, \mathbf{P}_\Gamma + [(1+\beta)(1+\gamma_\Gamma)]\, \mathbf{P}_\Omega \mathbf{M}_{\mathrm{A}} \mathbf{P}_\Gamma \ . \qquad (9.22)\end{aligned}$$

γ_Γ is still uniformly distributed in $[-\nu, \nu]$. Still, the property $\hat{H}^{(\mathrm{OP})}_{\mathrm{HIO+O_R+A}}(\beta, \lambda_\Gamma)\, \varrho_{\mathrm{eff}} = \varrho_{\mathrm{eff}}$ is guaranteed for all β and λ_Γ by construction.

This formula establishes the result of the combination randomized overrelaxation and our magnitude constraints starting from the projection polynomial approach.

Acknowledgements

Ich danke meinem Referenten Prof. Dr. Tilo Baumbach dafür, dass ich meine Dissertation am Institut für Photonenforschung und Synchrotronstrahlung am Karlsruher Institut für Technologie (KIT) anfertigen durfte. Im Besonderen danke ich ihm für das Vertrauen, mich in meiner Dissertation mit zwei großen Themenkomplexen beschäftigen und innerhalb dieser Themenkomplexe eigene Schwerpunkte setzen zu dürfen. Darüber hinaus danke ich ihm auch für seine Unterstützung bei der Veröffentlichung der im Rahmen dieser Arbeit erzielten Ergebnisse in wissenschaftlichen Zeitschriften.

Prof. RNDr. Václav Holý, CSc., bin ich sehr dankbar dafür, dass er diese Arbeit als Korreferent begutachtet hat.

Ein besonderer Dank gilt meinem langjährigen Freund und Kollegen Philipp Schroth. Ich hoffe, er hat unsere enge und konstruktive Zusammenarbeit im Rahmen des ersten Teils dieser Arbeit als ebenso gewinnbringend und inspirierend empfunden wie ich.

Weiterhin danke ich Dr. Andrey A. Minkevich, der mein Interesse für kohärente Röntgenbildgebung weckte und mich in die aktuellen Fragestellungen und Probleme einführte.

Ohne die Unterstützung von Dr. Wolfgang Mexner und Robert Sabo und deren Wissen über die IT-Infrastruktur im KIT, das beide jederzeit bereitwillig mit mir geteilt haben, wäre mir die erfolgreiche Einrichtung und Administration eines Clusters von linux-basierten “number crunchern” nicht möglich gewesen. Ohne dieses Cluster wären die numerischen Berechnungen in dieser Arbeit nur schwer oder gar nicht realisierbar gewesen.

Für konstruktives Feedback zur Struktur dieser Arbeit und gründliches Korrekturlesen von Teilen davon danke ich besonders Dr. Timo Aschenbrenner, Dr. Jannik Dreier, Jean-Wolfgang Hornung, Dr. Michael König und Philipp Schroth.

Ich freue mich, dass ich einige meiner Kollegen auch zu meinen Freunden zählen darf und danke ihnen genauso wie weiteren Freunden, die mich teils seit dem Beginn des Physik-Studiums auf meinem Weg in Karlsruhe begleitet haben, für die vielen anregenden fachlichen und nicht-fachlichen Diskussionen sowie die schönen, gemeinsamen Unternehmungen der letzten Jahre.

Ich danke meinen Eltern dafür, dass sie *immer* mit Rat und Tat für mich da waren.

Bibliography

[1] Martin Köhl, A. A. Minkevich, and Tilo Baumbach. „Improved success rate and stability for phase retrieval by including randomized overrelaxation in the hybrid input output algorithm". In: *Opt. Express* 20.15 (2012), pp. 17093–17106.

[2] Martin Köhl, Philipp Schroth, A. A. Minkevich, and Tilo Baumbach. „Retrieving the displacement of strained nanoobjects: the impact of bounds for the scattering magnitude in direct space". In: *Opt. Express* 21.23 (2013), pp. 27734–27749.

[3] Martin Köhl, Philipp Schroth, A. A. Minkevich, Jean-Wolfgang Hornung, Emmanouil Dimakis, Claudio Somaschini, Lutz Geelhaar, Timo Aschenbrenner, Sergey Lazarev, Daniil Grigoriev, Ullrich Pietsch, and Tilo Baumbach. „Polytypism in GaAs nanowires: Determination of the interplanar spacing of wurtzite GaAs by X-ray diffraction". In: *Journal of Synchrotron Radiation* 22 (2015), pp. 67–75.

[4] The Optical Society (OSA). *Optics InfoBase: Optics Express - Copyright & Permissions.* 2013. URL: `http://www.opticsinfobase.org/oe/submit/review/copyright_permissions.cfm` (visited on 11/18/2013).

[5] The Optical Society (OSA). *Copyright Transfer Agreement.* URL: `http://www.opticsinfobase.org/submit/forms/copyxfer.pdf` (visited on 11/18/2013).

[6] International Union of Crystallography (IUCr). *Transfer of Copyright Agreement.* 2014. URL: `http://journals.iucr.org/services/copyrightform.pdf` (visited on 10/26/2014).

[7] Jon Cartwright. „Qubit in a nanowire". In: *Nature News* (Dec. 2010).

[8] Michael E. Reimer, Gabriele Bulgarini, Nika Akopian, Moïra Hocevar, Maaike Bouwes Bavinck, Marcel A. Verheijen, Erik P. A. M. Bakkers, Leo P. Kouwenhoven, and Val Zwiller. „Bright single-photon sources in bottom-up tailored nanowires". In: *Nature Communications* 3 (Mar. 2012), p. 737.

[9] V. Mourik, K. Zuo, S. M. Frolov, S. R. Plissard, E. P. A. M. Bakkers, and L. P. Kouwenhoven. „Signatures of Majorana Fermions in Hybrid Superconductor-Semiconductor Nanowire Devices". In: *Science* 336.6084 (2012), pp. 1003–1007.

[10] Oliver Hayden, Ritesh Agarwal, and Wei Lu. „Semiconductor nanowire devices". In: *Nano Today* 3.5-6 (Oct. 2008), pp. 12–22.

[11] Katsuhiro Tomioka, Tomotaka Tanaka, Shinjiro Hara, Kenji Hiruma, and Takashi Fukui. „III-V Nanowires on Si Substrate: Selective-Area Growth and Device Applications". In: *IEEE Journal of Selected Topics in Quantum Electronics* 17.4 (July 2011), pp. 1112–1129.

[12] Timo Aschenbrenner. „Wachstum und Charakterisierung von nitrid-basierten Halbleiterstrukturen für optoelektronische Anwendungen: Nanosäulen, Bragg-Reflektoren und Laserdioden". Dissertation. Universität Bremen, 2010.

[13] Katsuhiro Tomioka, Masatoshi Yoshimura, and Takashi Fukui. „A III-V nanowire channel on silicon for high-performance vertical transistors". In: *Nature* 488.7410 (Aug. 2012), pp. 189–192.

[14] Jie Xiang, Wei Lu, Yongjie Hu, Yue Wu, Hao Yan, and Charles M. Lieber. „Ge/Si nanowire heterostructures as high-performance field-effect transistors“. In: *Nature* 441.7092 (May 2006), pp. 489–493.

[15] Dhruv Saxena, Sudha Mokkapati, Patrick Parkinson, Nian Jiang, Qiang Gao, Hark Hoe Tan, and Chennupati Jagadish. „Optically pumped room-temperature GaAs nanowire lasers“. In: *Nature Photonics* 7.12 (Dec. 2013), pp. 963–968.

[16] Xiangfeng Duan, Yu Huang, Ritesh Agarwal, and Charles M. Lieber. „Single-nanowire electrically driven lasers“. In: *Nature* 421.6920 (Jan. 2003), pp. 241–245.

[17] Bozhi Tian, Xiaolin Zheng, Thomas J. Kempa, Ying Fang, Nanfang Yu, Guihua Yu, Jinlin Huang, and Charles M. Lieber. „Coaxial silicon nanowires as solar cells and nanoelectronic power sources“. In: *Nature* 449.7164 (Oct. 2007), pp. 885–889.

[18] Allon I. Hochbaum, Renkun Chen, Raul Diaz Delgado, Wenjie Liang, Erik C. Garnett, Mark Najarian, Arun Majumdar, and Peidong Yang. „Enhanced thermoelectric performance of rough silicon nanowires“. In: *Nature* 451.7175 (Jan. 2008), pp. 163–167.

[19] Eric Stern, James F. Klemic, David A. Routenberg, Pauline N. Wyrembak, Daniel B. Turner-Evans, Andrew D. Hamilton, David A. LaVan, Tarek M. Fahmy, and Mark A. Reed. „Label-free immunodetection with CMOS-compatible semiconducting nanowires“. In: *Nature* 445.7127 (Feb. 2007), pp. 519–522.

[20] Yi Cui, Qingqiao Wei, Hongkun Park, and Charles M. Lieber. „Nanowire Nanosensors for Highly Sensitive and Selective Detection of Biological and Chemical Species“. In: *Science* 293.5533 (Aug. 2001). PMID: 11509722, pp. 1289–1292.

[21] Stevan Nadj-Perge. „Single Spins in Semiconductor Nanowires“. PhD thesis. Technische Universiteit Delft, 2010.

[22] P. Caroff, K. A. Dick, J. Johansson, M. E. Messing, K. Deppert, and L. Samuelson. „Controlled polytypic and twin-plane superlattices in III-V nanowires“. In: *Nature Nanotechnology* 4.1 (Jan. 2009), pp. 50–55.

[23] Hannah J. Joyce, Callum J. Docherty, Qiang Gao, H. Hoe Tan, Chennupati Jagadish, James Lloyd-Hughes, Laura M. Herz, and Michael B. Johnston. „Electronic properties of GaAs, InAs and InP nanowires studied by terahertz spectroscopy“. In: *Nanotechnology* 24.21 (May 2013), p. 214006.

[24] Jonas Johansson, Lisa S. Karlsson, C. Patrik T. Svensson, Thomas Mårtensson, Brent A. Wacaser, Knut Deppert, Lars Samuelson, and Werner Seifert. „Structural properties of (111)B-oriented III-V nanowires“. In: *Nature Materials* 5.7 (July 2006), pp. 574–580.

[25] Philippe Caroff, Jessica Bolinsson, and J. Johansson. „Crystal Phases in III-V Nanowires: From Random Toward Engineered Polytypism“. In: *IEEE Journal of Selected Topics in Quantum Electronics* 17.4 (2011), pp. 829–846.

[26] Steffen Breuer, Carsten Pfüller, Timur Flissikowski, Oliver Brandt, Holger T. Grahn, Lutz Geelhaar, and Henning Riechert. „Suitability of Au- and Self-Assisted GaAs Nanowires for Optoelectronic Applications“. In: *Nano Letters* 11.3 (Mar. 2011), pp. 1276–1279.

[27] Karen L. Kavanagh. „Misfit dislocations in nanowire heterostructures“. In: *Semiconductor Science and Technology* 25.2 (Feb. 2010), p. 024006.

[28] Frank Glas. „Critical dimensions for the plastic relaxation of strained axial heterostructures in free-standing nanowires“. In: *Physical Review B* 74.12 (Sept. 2006).

[29] Xu Zhang, Vladimir G. Dubrovskii, Nickolay V. Sibirev, and Xiaomin Ren. „Analytical Study of Elastic Relaxation and Plastic Deformation in Nanostructures on Lattice Mismatched Substrates“. In: *Crystal Growth & Design* 11.12 (Dec. 2011), pp. 5441–5448.

[30] Robin F.C. Farrow. *Molecular Beam Epitaxy: Applications to Key Materials.* New Jersey, United States: Noyes Publications, 1995.

[31] E.H.C. Parker. *The Technology and Physics of Molecular Beam Epitaxy.* New York, United States: Plenum Press, 1985.

[32] Sebastian Lehmann, Daniel Jacobsson, Knut Deppert, and KimberlyA. Dick. „High crystal quality wurtzite-zinc blende heterostructures in metal-organic vapor phase epitaxy-grown GaAs nanowires“. In: *Nano Research* 5.7 (2012), pp. 470–476.

[33] Motoshi Shibata, Stoyan S. Stoyanov, and Masakazu Ichikawa. „Selective growth of nanometer-scale Ga dots on Si(111) surface windows formed in an ultrathin SiO2 film“. In: *Physical Review B* 59.15 (Apr. 1999), pp. 10289–10295.

[34] S. C. Hardy. „The surface tension of liquid gallium“. In: *Journal of Crystal Growth* 71.3 (May 1985), pp. 602–606.

[35] J. M. Dona and J. Gonzalez-Velasco. „Mechanism of surface diffusion of gold adatoms in contact with an electrolytic solution“. In: *The Journal of Physical Chemistry* 97.18 (1993), pp. 4714–4719.

[36] C. Alonso, R. C. Salvarezza, J. M. Vara, A. J. Arvia, L. Vazquez, A. Bartolome, and A. M. Baro. „The Evaluation of Surface Diffusion Coefficients of Gold and Platinum Atoms at Electrochemical Interfaces from Combined STM-SEM Imaging and Electrochemical Techniques“. In: *Journal of the Electrochemical Society* 137.7 (1990), pp. 2161–2166.

[37] Yiyi Wang, Ahmet S. Özcan, Karl F. Ludwig, and Anirban Bhattacharyya. „Real-time studies of gallium adsorption and desorption kinetics on sapphire (0001) by grazing incidence small-angle x-ray scattering and x-ray fluorescence“. In: *Journal of Applied Physics* 103.10, 103538 (2008), pp. –.

[38] Ann I. Persson, Magnus W. Larsson, Stig Stenstrom, B. Jonas Ohlsson, Lars Samuelson, and L. Reine Wallenberg. „Solid-phase diffusion mechanism for GaAs nanowire growth“. In: *Nat Mater* 3.10 (2004), pp. 677–681.

[39] T. I. Kamins, R. Stanley Williams, D. P. Basile, T. Hesjedal, and J. S. Harris. „Ti-catalyzed Si nanowires by chemical vapor deposition: Microscopy and growth mechanisms“. In: *Journal of Applied Physics* 89.2 (2001), pp. 1008–1016.

[40] P. J. Poole, J. Lefebvre, and J. Fraser. „Spatially controlled, nanoparticle-free growth of InP nanowires“. In: *Applied Physics Letters* 83.10 (2003), pp. 2055–2057.

[41] S. Hertenberger, D. Rudolph, S. Bolte, M. Döblinger, M. Bichler, D. Spirkoska, J. J. Finley, G. Abstreiter, and G. Koblmüller. „Absence of vapor-liquid-solid growth during molecular beam epitaxy of self-induced InAs nanowires on Si“. In: *Applied Physics Letters* 98.12 (Mar. 2011), pp. 123114–123114–3.

[42] D. Rudolph, S. Hertenberger, S. Bolte, W. Paosangthong, D. Spirkoska, M. Döblinger, M. Bichler, J.J. Finley, G. Abstreiter, and G. Koblmüller. „Direct observation of a noncatalytic growth regime for GaAs nanowires“. In: *Nano Letters* 11.9 (2011), pp. 3848–3854.

[43] Xuezhe Yu, Hailong Wang, Jun Lu, Jianhua Zhao, Jennifer Misuraca, Peng Xiong, and Stephan von Molnár. „Evidence for Structural Phase Transitions Induced by the Triple Phase Line Shift in Self-Catalyzed GaAs Nanowires“. In: *Nano Letters* 12.10 (Oct. 2012), pp. 5436–5442.

[44] F.M. Davidson, D.C. Lee, D.D. Fanfair, and B.A. Korgel. „Lamellar Twinning in Semiconductor Nanowires“. In: *Journal of Physical Chemistry C* 111.7 (Feb. 2007), pp. 2929–2935.

[45] R. S. Wagner and W. C. Ellis. „Vapor-Liquid-Solid mechanism of single crystal growth“. In: *Applied Physics Letters* 4.5 (1964), pp. 89–90.

[46] J. C. Harmand, G. Patriarche, N. Péré-Laperne, M.-N. Mérat-Combes, L. Travers, and F. Glas. „Analysis of vapor-liquid-solid mechanism in Au-assisted GaAs nanowire growth“. In: *Applied Physics Letters* 87.20 (Nov. 2005), p. 203101.

[47] Brent A. Wacaser, Kimberly A. Dick, Jonas Johansson, Magnus T. Borgström, Knut Deppert, and Lars Samuelson. „Preferential Interface Nucleation: An Expansion of the VLS Growth Mechanism for Nanowires“. In: *Advanced Materials* 21.2 (2009), pp. 153–165.

[48] Björn Eisenhawer, Vladimir Sivakov, Silke Christiansen, and Fritz Falk. „A Time-Resolved Numerical Study of the Vapor-Liquid-Solid Growth Kinetics Describing the Initial Nucleation Phase as well as Pulsed Deposition Processes“. In: *Nano Letters* 13.3 (Mar. 2013), pp. 873–883.

[49] V. G. Dubrovskii, G. E. Cirlin, N. V. Sibirev, F. Jabeen, J. C. Harmand, and P. Werner. „New Mode of Vapor-Liquid-Solid Nanowire Growth“. In: *Nano Letters* 11.3 (Mar. 2011), pp. 1247–1253.

[50] J. Motohisa, J. Noborisaka, J. Takeda, M. Inari, and T. Fukui. „Catalyst-free selective-area {MOVPE} of semiconductor nanowires on (111)B oriented substrates“. In: *Journal of Crystal Growth* 272.1-4 (2004). The Twelfth International Conference on Metalorganic Vapor Phase Epitaxy, pp. 180 –185.

[51] Sébastien Plissard, Kimberly A Dick, Guilhem Larrieu, Sylvie Godey, Ahmed Addad, Xavier Wallart, and Philippe Caroff. „Gold-free growth of GaAs nanowires on silicon: arrays and polytypism“. In: *Nanotechnology* 21.38 (Sept. 2010), p. 385602.

[52] Peter Krogstrup, Ronit Popovitz-Biro, Erik Johnson, Morten Hannibal Madsen, Jesper Nygård, and Hadas Shtrikman. „Structural Phase Control in Self-Catalyzed Growth of GaAs Nanowires on Silicon (111)“. In: *Nano Letters* 10.11 (2010), pp. 4475–4482.

[53] Emmanouil Dimakis, Jonas Lähnemann, Uwe Jahn, Steffen Breuer, Maria Hilse, Lutz Geelhaar, and Henning Riechert. „Self-Assisted Nucleation and Vapor-Solid Growth of InAs Nanowires on Bare Si(111)“. In: *Crystal Growth & Design* 11.9 (Sept. 2011), pp. 4001–4008.

[54] Peter Krogstrup, Morten Hannibal Madsen, Wen Hu, Miwa Kozu, Yuka Nakata, Jesper Nygård, Masamitu Takahasi, and Robert Feidenhans'l. „In-situ x-ray characterization of wurtzite formation in GaAs nanowires“. In: *Applied Physics Letters* 100.9 (Feb. 2012), pp. 093103–093103–4.

[55] Abdul Mazid Munshi, Dasa L. Dheeraj, Jelena Todorovic, Antonius T.J. van Helvoort, Helge Weman, and Bjørn-Ove Fimland. „Crystal phase engineering in self-catalyzed GaAs and GaAs/GaAsSb nanowires grown on Si(111)“. In: *Journal of Crystal Growth* 372 (June 2013), pp. 163–169.

[56] Masahito Yamaguchi, Ji-Hyun Paek, and Hiroshi Amano. „Probability of twin formation on self-catalyzed GaAs nanowires on Si substrate“. In: *Nanoscale Research Letters* 7.1 (Oct. 2012), p. 558.

[57] Torsten Rieger, Mihail Ion Lepsa, Thomas Schäpers, and Detlev Grützmacher. „Controlled wurtzite inclusions in self-catalyzed zinc blende III-V semiconductor nanowires“. In: *Journal of Crystal Growth* 378.0 (2013). The 17th International Conference on Molecular Beam Epitaxy, pp. 506 –510.

[58] AF. Morral. „Gold-Free GaAs Nanowire Synthesis and Optical Properties“. In: *Selected Topics in Quantum Electronics, IEEE Journal of* 17.4 (2011), pp. 819–828.

[59] Jonas Johansson, Lisa S. Karlsson, Kimberly A. Dick, Jessica Bolinsson, Brent A. Wacaser, Knut Deppert, and Lars Samuelson. „Effects of Supersaturation on the Crystal Structure of Gold Seeded III-V Nanowires“. In: *Crystal Growth & Design* 9.2 (Feb. 2009), pp. 766–773.

[60] Hannah J. Joyce, Jennifer Wong-Leung, Qiang Gao, H. Hoe Tan, and Chennupati Jagadish. „Phase Perfection in Zinc Blende and Wurtzite III-V Nanowires Using Basic Growth Parameters“. In: *Nano Letters* 10.3 (Mar. 2010), pp. 908–915.

[61] Kimberly A. Dick, Philippe Caroff, Jessica Bolinsson, Maria E. Messing, Jonas Johansson, Knut Deppert, L. Reine Wallenberg, and Lars Samuelson. „Control of III-V nanowire crystal structure by growth parameter tuning“. In: *Semiconductor Science and Technology* 25.2 (Feb. 2010), p. 024009.

[62] Frank Glas. „Chemical potentials for Au-assisted vapor-liquid-solid growth of III-V nanowires“. In: *Journal of Applied Physics* 108.7 (Oct. 2010), p. 073506.

[63] Maria Tchernycheva, Laurent Travers, Gilles Patriarche, Frank Glas, Jean-Christophe Harmand, George E. Cirlin, and Vladimir G. Dubrovskii. „Au-assisted molecular beam epitaxy of InAs nanowires: Growth and theoretical analysis“. In: *Journal of Applied Physics* 102.9 (Nov. 2007), p. 094313.

[64] Michael J. Tambe, Shenqiang Ren, and Silvija Gradecak. „Effects of Gold Diffusion on n-Type Doping of GaAs Nanowires“. In: *Nano Letters* 10.11 (Nov. 2010), pp. 4584–4589.

[65] D. V. Lang, H. G. Grimmeiss, E. Meijer, and M. Jaros. „Complex nature of gold-related deep levels in silicon“. In: *Physical Review B* 22.8 (Oct. 1980), pp. 3917–3934.

[66] Vladimir G. Dubrovskii. *Nucleation Theory and Growth of Nanostructures.* Heidelberg, New York, Dordrecht, London: Springer, 2014.

[67] Philipp Schroth. „In-situ Studies of MBE grown self-ctalyzed GaAs nanowires (preliminary title)“. Dissertation (in preparation). Karlsruhe Institute of Technology, 2015 (planned).

[68] Torsten Rieger, Sonja Heiderich, Steffi Lenk, Mihail Ion Lepsa, and Detlev Grützmacher. „Ga-assisted MBE growth of GaAs nanowires using thin HSQ layer“. In: *Journal of Crystal Growth* 353.1 (2012), pp. 39 –46.

[69] Peter Krogstrup, Stefano Curiotto, Erik Johnson, Martin Aagesen, Jesper Nygård, and Dominique Chatain. „Impact of the Liquid Phase Shape on the Structure of III-V Nanowires“. In: *Physical Review Letters* 106.12 (Mar. 2011), p. 125505.

[70] Michael Moseler, Felipe Cervantes-Sodi, Stephan Hofmann, Gábor Csányi, and Andrea C. Ferrari. „Dynamic Catalyst Restructuring during Carbon Nanotube Growth“. In: *ACS Nano* 4.12 (2010), pp. 7587–7595.

[71] Steffen Breuer, Lou-Fé Feiner, and Lutz Geelhaar. „Droplet Bulge Effect on the Formation of Nanowire Side Facets“. In: *Crystal Growth & Design* 13.7 (July 2013), pp. 2749–2755.

[72] Givargizov E. I. and Chernov A. A. In: *Kristallografiya* 18 (1973).

[73] V.G. Dubrovskii and N.V. Sibirev. „General form of the dependences of nanowire growth rate on the nanowire radius“. In: *Journal of Crystal Growth* 304.2 (2007), pp. 504 –513.

[74] A. D. Gamalski, J. Tersoff, R. Sharma, C. Ducati, and S. Hofmann. „Metastable Crystalline AuGe Catalysts Formed During Isothermal Germanium Nanowire Growth". In: *Phys. Rev. Lett.* 108 (25 2012), p. 255702.

[75] V.G. Dubrovskiĭ, N.V. Sibirev, R.A. Suris, G.É. Cirlin, V.M. Ustinov, M. Tchernysheva, and J.C. Harmand. „The role of surface diffusion of adatoms in the formation of nanowire crystals". In: *Semiconductors* 40.9 (2006), pp. 1075–1082.

[76] V. Consonni, V. G. Dubrovskii, A. Trampert, L. Geelhaar, and H. Riechert. „Quantitative description for the growth rate of self-induced GaN nanowires". In: *Phys. Rev. B* 85 (15 2012), p. 155313.

[77] A. D. Gamalski, C. Ducati, and S. Hofmann. „Cyclic Supersaturation and Triple Phase Boundary Dynamics in Germanium Nanowire Growth". In: *The Journal of Physical Chemistry C* 115.11 (2011), pp. 4413–4417.

[78] C.-Y. Wen, J. Tersoff, K. Hillerich, M. C. Reuter, J. H. Park, S. Kodambaka, E. A. Stach, and F. M. Ross. „Periodically Changing Morphology of the Growth Interface in Si, Ge, and GaP Nanowires". In: *Phys. Rev. Lett.* 107 (2 2011), p. 025503.

[79] Frank Glas, Jean-Christophe Harmand, and Gilles Patriarche. „Nucleation Antibunching in Catalyst-Assisted Nanowire Growth". In: *Physical Review Letters* 104.13 (Mar. 2010), p. 135501.

[80] Jean-Christophe Harmand, Frank Glas, and Gilles Patriarche. „Growth kinetics of a single InP(1-x)As(x) nanowire". In: *Physical Review B* 81.23 (June 2010), p. 235436.

[81] Peter Hänggi, Peter Talkner, and Michal Borkovec. „Reaction-rate theory: fifty years after Kramers". In: *Rev. Mod. Phys.* 62 (2 1990), pp. 251–341.

[82] Vladimir G. Dubrovskii, Vincent Consonni, Lutz Geelhaar, Achim Trampert, and Henning Riechert. „Scaling growth kinetics of self-induced GaN nanowires". In: *Applied Physics Letters* 100.15, 153101 (2012), pp. –.

[83] J. H. Paek, T. Nishiwaki, M. Yamaguchi, and N. Sawaki. „Catalyst free MBE-VLS growth of GaAs nanowires on (111)Si substrate". In: *physica status solidi (c)* 6.6 (2009), pp. 1436–1440.

[84] S. Ambrosini, M. Fanetti, V. Grillo, A. Franciosi, and S. Rubini. „Vapor-liquid-solid and vapor-solid growth of self-catalyzed GaAs nanowires". In: *AIP Advances* 1.4 (Nov. 2011), p. 042142.

[85] Tim Burgess, Steffen Breuer, Philippe Caroff, Jennifer Wong-Leung, Qiang Gao, Hark Hoe Tan, and Chennupati Jagadish. „Twinning Superlattice Formation in GaAs Nanowires". In: *ACS Nano* 7.9 (Sept. 2013), pp. 8105–8114.

[86] S. Cahangirov and S. Ciraci. „First-principles study of GaAs nanowires". In: *Physical Review B* 79.16 (Apr. 2009), p. 165118.

[87] V. G. Dubrovskii, N. V. Sibirev, G. E. Cirlin, J. C. Harmand, and V. M. Ustinov. „Theoretical analysis of the vapor-liquid-solid mechanism of nanowire growth during molecular beam epitaxy". In: *Physical Review E* 73.2 (Feb. 2006), p. 021603.

[88] Frank Glas, Mohammed Reda Ramdani, Gilles Patriarche, and Jean-Christophe Harmand. „Predictive modeling of self-catalyzed III-V nanowire growth". In: *Phys. Rev. B* 88 (19 2013), p. 195304.

[89] Toru Akiyama, Kosuke Sano, Kohji Nakamura, and Tomonori Ito. „An Empirical Potential Approach to Wurtzite-Zinc-Blende Polytypism in Group III-V Semiconductor Nanowires". In: *Japanese Journal of Applied Physics* 45.9 (2006), pp. L275–L278.

[90] Jonas Johansson, C. Patrik T. Svensson, Thomas Mårtensson, Lars Samuelson, and Werner Seifert. „Mass Transport Model for Semiconductor Nanowire Growth“. In: *The Journal of Physical Chemistry B* 109.28 (2005), pp. 13567–13571.

[91] Jonas Johansson, Brent A Wacaser, Kimberly A Dick, and Werner Seifert. „Growth related aspects of epitaxial nanowires“. In: *Nanotechnology* 17.11 (2006), S355.

[92] Dominik Kriegner, Christian Panse, Bernhard Mandl, Kimberly A. Dick, Mario Keplinger, Johan M. Persson, Philippe Caroff, Daniele Ercolani, Lucia Sorba, Friedhelm Bechstedt, Julian Stangl, and Günther Bauer. „Unit Cell Structure of Crystal Polytypes in InAs and InSb Nanowires“. In: *Nano Letters* 11.4 (Apr. 2011), pp. 1483–1489.

[93] Bernhard Mandl, Julian Stangl, Thomas Mårtensson, Anders Mikkelsen, Jessica Eriksson, Lisa S. Karlsson, Günther Bauer, Lars Samuelson, and Werner Seifert. „Au-Free Epitaxial Growth of InAs Nanowires“. In: *Nano Letters* 6.8 (2006), pp. 1817–1821.

[94] Kiyoshi Takahashi and Toyosaka Morizumi. „Growth of InAs Whiskers in Wurtzite Structure“. In: *Japanese Journal of Applied Physics* 5.8 (1966), p. 657.

[95] He Zheng, Jian Wang, Jian Yu Huang, Jianbo Wang, Ze Zhang, and Scott X. Mao. „Dynamic Process of Phase Transition from Wurtzite to Zinc Blende Structure in InAs Nanowires“. In: *Nano Letters* (Nov. 2013).

[96] Rienk E. Algra, Marcel A. Verheijen, Magnus T. Borgström, Lou-Fé Feiner, George Immink, Willem J. P. van Enckevort, Elias Vlieg, and Erik P. A. M. Bakkers. „Twinning superlattices in indium phosphide nanowires“. In: *Nature* 456.7220 (Nov. 2008), pp. 369–372.

[97] M. Hjort, S. Lehmann, J. Knutsson, R. Timm, D. Jacobsson, E. Lundgren, K.A. Dick, and A. Mikkelsen. „Direct Imaging of Atomic Scale Structure and Electronic Properties of GaAs Wurtzite and Zinc Blende Nanowire Surfaces“. In: *Nano Letters* 13.9 (Sept. 2013), pp. 4492–4498.

[98] Jiming Bao, David C. Bell, Federico Capasso, Jakob B. Wagner, Thomas Mårtensson, Johanna Trägårdh, and Lars Samuelson. „Optical Properties of Rotationally Twinned InP Nanowire Heterostructures“. In: *Nano Letters* 8.3 (Mar. 2008), pp. 836–841.

[99] D. Spirkoska, J. Arbiol, A. Gustafsson, S. Conesa-Boj, F. Glas, I. Zardo, M. Heigoldt, M. H. Gass, A. L. Bleloch, S. Estrade, M. Kaniber, J. Rossler, F. Peiro, J. R. Morante, G. Abstreiter, L. Samuelson, and A. Fontcuberta i Morral. „Structural and optical properties of high quality zinc-blende/wurtzite GaAs nanowire heterostructures“. In: *Physical Review B* 80.24 (Dec. 2009), p. 245325.

[100] Martin Heiss, Sonia Conesa-Boj, Jun Ren, Hsiang-Han Tseng, Adam Gali, Andreas Rudolph, Emanuele Uccelli, Francesca Peiró, Joan Ramon Morante, Dieter Schuh, Elisabeth Reiger, Efthimios Kaxiras, Jordi Arbiol, and Anna Fontcuberta i Morral. „Direct correlation of crystal structure and optical properties in wurtzite/zinc-blende GaAs nanowire heterostructures“. In: *Phys. Rev. B* 83 (4 2011), p. 045303.

[101] Andreas Biermanns. „X-ray diffraction from single GaAs nanowires“. Dissertation. Universität Siegen, 2012.

[102] Ioffe Institute (St. Petersburg, Russian Federation). *GaAs – Gallium Arsenide: Basic parameters at 300 K*. 2001. URL: `http://www.ioffe.ru/SVA/NSM/Semicond/GaAs/basic.html` (visited on 04/11/2014).

[103] N. W. Ashcroft and N. D. Mermin. *Festkörperphysik*. Oldenbourg Wissenschaftsverlag, 1976.

[104] C. Kittel. *Einführung in die Festkörperphysik.* München: Springer, 2002.

[105] Frank Glas, Jean-Christophe Harmand, and Gilles Patriarche. „Why Does Wurtzite Form in Nanowires of III-V Zinc Blende Semiconductors?“ In: *Physical Review Letters* 99.14 (Oct. 2007), p. 146101.

[106] V. G. Dubrovskii, N. V. Sibirev, J. C. Harmand, and F. Glas. „Growth kinetics and crystal structure of semiconductor nanowires“. In: *Physical Review B* 78.23 (Dec. 2008), p. 235301.

[107] Tomoki Yamashita, Toru Akiyama, Kohji Nakamura, and Tomonori Ito. „Theoretical investigation on the structural stability of GaAs nanowires with two different types of facets“. In: *Physica E: Low-dimensional Systems and Nanostructures* 42.10 (Sept. 2010), pp. 2727–2730.

[108] Rita Magri, Marcello Rosini, and Flavio Casetta. „Structural stability of clean GaAs nanowires grown along the [111] direction“. In: *physica status solidi (c)* 7.2 (2010), pp. 374–377.

[109] J. Johansson, K. A. Dick, P. Caroff, M. E. Messing, J. Bolinsson, K. Deppert, and L. Samuelson. „Diameter Dependence of the Wurtzite-Zinc Blende Transition in InAs Nanowires“. In: *The Journal of Physical Chemistry C* 114.9 (Mar. 2010), pp. 3837–3842.

[110] Jonas Johansson, Jessica Bolinsson, Martin Ek, Philippe Caroff, and Kimberly A. Dick. „Combinatorial Approaches to Understanding Polytypism in III-V Nanowires“. In: *ACS Nano* 6.7 (July 2012), pp. 6142–6149.

[111] V. G. Dubrovskii and N. V. Sibirev. „Growth thermodynamics of nanowires and its application to polytypism of zinc blende III-V nanowires“. In: *Phys. Rev. B* 77 (3 2008), p. 035414.

[112] Alexander Fian, Monica Lexholm, Rainer Timm, Bernhard Mandl, Ulf Håkanson, Dan Hessman, Edvin Lundgren, Lars Samuelson, and Anders Mikkelsen. „New Flexible Toolbox for Nanomechanical Measurements with Extreme Precision and at Very High Frequencies“. In: *Nano Letters* 10.10 (2010), pp. 3893–3898.

[113] Emelie Hilner, Ulf Håkanson, Linus E. Fröberg, Martin Karlsson, Peter Kratzer, Edvin Lundgren, Lars Samuelson, and Anders Mikkelsen. „Direct Atomic Scale Imaging of III-V Nanowire Surfaces“. In: *Nano Letters* 8.11 (2008), pp. 3978–3982.

[114] Anders Mikkelsen, Niklas Skold, Lassana Ouattara, Magnus Borgstrom, Magnus Borgstrom, Jesper N. Andersen, Lars Samuelson, Werner Seifert, and Edvin Lundgren. „Direct imaging of the atomic structure inside a nanowire by scanning tunnelling microscopy“. In: *Nature Materials* 3.8 (2004), pp. 519–523.

[115] Tao Yang, Simon Hertenberger, Stefanie Morkötter, Gerhard Abstreiter, and Gregor Koblmüller. „Size, composition, and doping effects on In(Ga)As nanowire/Si tunnel diodes probed by conductive atomic force microscopy“. In: *Applied Physics Letters* 101.23, 233102 (2012), pp. –.

[116] Rainer Timm, Olof Persson, David L. J. Engberg, Alexander Fian, James L. Webb, Jesper Wallentin, Andreas Jönsson, Magnus T. Borgström, Lars Samuelson, and Anders Mikkelsen. „Current-Voltage Characterization of Individual As-Grown Nanowires Using a Scanning Tunneling Microscope“. In: *Nano Letters* 13.11 (2013), pp. 5182–5189.

[117] B. Mattias Borg, Martin Ek, Bahram Ganjipour, Anil W. Dey, Kimberly A. Dick, Lars-Erik Wernersson, and Claes Thelander. „Influence of doping on the electronic transport in GaSb/InAs(Sb) nanowire tunnel devices“. In: *Applied Physics Letters* 101.4, 043508 (2012), pp. –.

[118] Chin-Yu Yeh, Z. W. Lu, S. Froyen, and Alex Zunger. „Zinc-blende-wurtzite polytypism in semiconductors“. In: *Phys. Rev. B* 46 (16 1992), pp. 10086–10097.

[119] Andreas Biermanns, Steffen Breuer, Anton Davydok, Lutz Geelhaar, and Ullrich Pietsch. „Structural evolution of self-assisted GaAs nanowires grown on Si(111)“. In: *physica status solidi (RRL) - Rapid Research Letters* 5.4 (2011), pp. 156–158.

[120] *Technical Specification and Operating Procedure — PILATUS 100K-S Detector System, Version 1.7.* DECTRIS Ltd., Neuenhoferstrasse 107, 5400 Baden, Switzerland: DECTRIS – Next Generation X-Ray Detectors, July 2011.

[121] Simon O Mariager, Søren L Lauridsen, Claus B Sørensen, Asmus Dohn, Phillip R Willmott, Jesper Nyg?rd, and Robert Feidenhans?l. „Stages in molecular beam epitaxy growth of GaAs nanowires studied by x-ray diffraction“. In: *Nanotechnology* 21.11 (2010), p. 115603.

[122] Anton Davydok, Steffen Breuer, Andreas Biermanns, Lutz Geelhaar, and Ullrich Pietsch. „Lattice parameter accommodation between GaAs(111) nanowires and Si(111) substrate after growth via Au-assisted molecular beam epitaxy“. In: *Nanoscale Research Letters* 7.1 (Feb. 2012). PMID: 22315928, p. 109.

[123] Andreas Biermanns, Anton Davydok, Hendrik Paetzelt, Ana Diaz, Volker Gottschalch, Till Hartmut Metzger, and Ullrich Pietsch. „Individual GaAs nanorods imaged by coherent X-ray diffraction“. In: *J. Synchrotron Radiat.* 16.6 (2009), pp. 796–802.

[124] T. Slobodskyy, P. Schroth, D. Grigoriev, A. A. Minkevich, D. Z. Hu, D. M. Schaadt, and T. Baumbach. „A portable molecular beam epitaxy system for in situ x-ray investigations at synchrotron beamlines“. In: *Review of Scientific Instruments* 83.10 (Oct. 2012), pp. 105112–105112–7.

[125] P. Schroth, T. Slobodskyy, D. Grigoriev, A. Minkevich, M. Riotte, S. Lazarev, E. Fohtung, D.Z. Hu, D.M. Schaadt, and T. Baumbach. „Investigation of buried quantum dots using grazing incidence X-ray diffraction“. In: *Mater. Sci. Eng., B* 177.10 (2012), pp. 721 –724.

[126] Jean Wolfgang Hornung. „Growth and Characterization of self-catalyzed GaAs Nanowires“. Diplomarbeit. Karlsruhe Institute of Technology, 2013.

[127] Philipp Schroth. „In-situ Untersuchung von selbstorganisierten InAs/GaAs Quantenpunkten“. Diplomarbeit. Karlsruhe Institute of Technology, 2011.

[128] S. Rembold. *Wachstumskammer kompl. (Zeichnungsnummer: SY083-200-000-001-G).* CreaTec Fischer & Co. GmbH, 74391 Erligheim, Germany, Apr. 2008.

[129] I. N. Bronstein, K. A. Semendjajew, G. Musiol, and H. Mühlig. *Taschenbuch der Mathematik.* Frankfurt am Main, Deutschland: Verlag Harri Deutsch GmbH; Auflage: 7., vollst. überarb. u. erg. Aufl., 2008.

[130] Gerhard Merziger and Thomas Wirth. *Repetitorium der höheren Mathematik.* Springe: Binomi Verlag; 4. Auflage, 2002.

[131] P. Schroth, M. Köhl, J.-W. Hornung, E. Dimakis, C. Somaschini, L. Geelhaar, A. Biermanns, U. Pietsch, S. Bauer, S. Lazarev, and T. Baumbach. *Evolution of polytypism in GaAs nanowires during growth revealed by time-resolved in-situ X-ray diffraction.* to be published.

[132] Andrey Minkevich, Martin Köhl, Philipp Schroth, Jean-Wolfgang Hornung, Sergey Lazarev, Daniil Grigoriev, and Tilo Baumbach. *ESRF proposal MA-1849: GaAs/Si(111) nanorods by improved CXDI reconstruction algorithm using quasi-forbidden reflexes.*

[133] Wayne Rasband, National Institutes of Health, USA. *ImageJ 1.44o – Image Processing and Analysis in Java*. Dec. 2013. URL: `http://imagej.nih.gov/ij` (visited on 04/11/2014).

[134] S. K. Gupta. „Peak Decomposition using Pearson Type VII Function“. In: *Journal of Applied Crystallography* 31.3 (1998), pp. 474–476.

[135] M. I. McMahon and R. J. Nelmes. „Observation of a Wurtzite Form of Gallium Arsenide“. In: *Phys. Rev. Lett.* 95 (21 2005), p. 215505.

[136] Christian Panse, Dominik Kriegner, and Friedhelm Bechstedt. „Polytypism of GaAs, InP, InAs, and InSb: An ab initio study“. In: *Physical Review B* 84.7 (Aug. 2011), p. 075217.

[137] M Tchernycheva, J C Harmand, G Patriarche, L Travers, and G E Cirlin. „Temperature conditions for GaAs nanowire formation by Au-assisted molecular beam epitaxy“. In: *Nanotechnology* 17.16 (2006), p. 4025.

[138] Steffen Breuer. „Molecular Beam Epitaxy of GaAs Nanowires and their Suitability for Optoelectronic Applications“. PhD thesis. Humboldt-Universität Berlin, 2011.

[139] KIT - University of the State of Baden-Wuerttemberg and National Laboratory of the Helmholtz Association. *Nano beamline*. Feb. 2014. URL: `http://www.anka.kit.edu/784.php` (visited on 04/11/2014).

[140] *ANKA Instrumentation Book 2012*. Karlsruhe Institute of Technology, Hermann-von-Helmholtz-Platz 1, 76344 Eggenstein-Leopoldshafen, Germany: ANKA Synchrotron Radiation Facility and Institute of Photon Science and Synchrotron Radiation, Sept. 2013.

[141] Sergey Stepanov. *X0h Request Form*. Dec. 2013. URL: `http://x-server.gmca.aps.anl.gov/cgi/WWW_form.exe?template=x0h_form.htm` (visited on 04/11/2014).

[142] U. Pietsch, V. Holy, and T. Baumbach. *High-Resolution X-ray Scattering From Thin Films to Lateral Nanostructures*. New York: Springer, 2004.

[143] OpenMP Architecture Review Board. *OpenMP Application Program Interface, Version 3.1*. July 2011. URL: `http://www.openmp.org/mp-documents/OpenMP3.1.pdf` (visited on 03/26/2013).

[144] Lee Thomason, Yves Berquin, and Andrew Ellerton. *TinyXml Documentation, Version 2.6.0*. Mar. 2010. URL: `http://www.grinninglizard.com/tinyxmldocs/index.html` (visited on 03/26/2013).

[145] Horst Rinne. *Taschenbuch der Statistik*. Frankfurt am Main, Deutschland: Verlag Harri Deutsch GmbH; Auflage: 4., überarb. u. erw. Aufl., 2008.

[146] Michel Plancherel and Mittag Leffler. „Contribution À LÉtude de la reprÉsentation D’une fonction arbitraire par des intÉgrales dÉfinies“. In: *Rendiconti del Circolo Matematico di Palermo* 30.1 (1910), pp. 289–335.

[147] Mark Galassi, Jim Davies, James Theiler, Brian Gough, Gerard Jungman, Patrick Alken, Michael Booth, Fabrice Rossi, and Rhys Ulerich. *GNU Scientific Library: Reference Manual, Edition 1.16*. 2013. URL: `http://www.gnu.org/software/gsl/manual/gsl-ref.pdf` (visited on 12/12/2013).

[148] C. Colombo, D. Spirkoska, M. Frimmer, G. Abstreiter, and A. Fontcuberta i Morral. „Ga-assisted catalyst-free growth mechanism of GaAs nanowires by molecular beam epitaxy“. In: *Physical Review B* 77.15 (Apr. 2008).

[149] Volker Pankoke, Sung Sakong, and Peter Kratzer. „Role of sidewall diffusion in GaAs nanowire growth: A first-principles study“. In: *Physical Review B* 86.8 (Aug. 2012), p. 085425.

[150] Magnus W Larsson, Jakob B Wagner, Mathias Wallin, Paul Håkansson, Linus E Fröberg, Lars Samuelson, and L Reine Wallenberg. „Strain mapping in free-standing heterostructured wurtzite InAs/InP nanowires“. In: *Nanotechnology* 18.1 (2007), p. 015504.

[151] S. Marchesini, H. He, H. N. Chapman, S. P. Hau-Riege, A. Noy, M. R. Howells, U. Weierstall, and J. C. H. Spence. „X-ray image reconstruction from a diffraction pattern alone“. In: *Phys. Rev. B* 68 (14 2003), p. 140101.

[152] Shunsuke Hattanda, Hiroyuki Shioya, Yosuke Maehara, and Kazutoshi Gohara. „K-means clustering for support construction in diffractive imaging“. In: *J. Opt. Soc. Am. A* 31.3 (2014), pp. 470–474.

[153] John D. Joannopoulos, Steven G. Johnson, Joshua N. Winn, and Robert D. Meade. *Photonic Crystals - Molding the Flow of Light - 2nd Edition.* 2nd. New Jersey: Princeton University Press, 2008.

[154] Kazuaki Sakoda. *Optical Properties of Photonic Crystals.* 1st. Berlin, Heidelberg, New York: Springer, 2001.

[155] K. Busch, G. von Freymann, S. Linden, S. F. Mingaleev, L. Tkeshelashvili, and M. Wegener. „Periodic nanostructures for photonics“. In: *Phys. Rep.* 444 (2007), p. 101.

[156] Kurt Busch, Christian Blum, Alexandra M. Graham, Daniel Hermann, Martin Köhl, Patrick Mack, and Christian Wolff. „The photonic Wannier function approach to photonic crystal simulations: status and perspectives“. In: *J. Mod. Opt.* 58.5-6 (2011), pp. 365–383.

[157] Martin Köhl, Christian Wolff, and Kurt Busch. „Cluster coherent potential approximation for disordered photonic crystals using photonic Wannier functions“. In: *Opt. Lett.* 37.4 (2012), pp. 560–562.

[158] Kurt Busch, Sergei F Mingaleev, Antonio Garcia-Martin, Matthias Schillinger, and Daniel Hermann. „The Wannier function approach to photonic crystal circuits“. In: *J. Phys. Condens. Matter* 15.30 (2003), R1233.

[159] Sajeev John. „Strong localization of photons in certain disordered dielectric superlattices“. In: *Phys. Rev. Lett.* 58 (23 1987), pp. 2486–2489.

[160] Eli Yablonovitch. „Inhibited Spontaneous Emission in Solid-State Physics and Electronics“. In: *Phys. Rev. Lett.* 58.20 (1987), pp. 2059–2062.

[161] A. Birner, K. Busch, and F. Müller. „Photonische Kristalle“. In: *Physikalische Blätter* 55 (1999), p. 27.

[162] A. Birner, R. B. Wehrspohn, U. Gösele, and K. Busch. „Silicon-based Photonic Crystals“. In: *Advanced Materials* 13.6 (2001), p. 377.

[163] S. John, O. Toader, and K. Busch. „Photonic Band Gap Materials: A Semiconductor for Light“. 2001.

[164] Susumu Noda. „Recent Progresses and Future Prospects of Two- and Three-Dimensional Photonic Crystals“. In: *J. Lightwave Technol.* 24.12 (2006), pp. 4554–4567.

[165] R. B. Wehrspohn, H. Kitzerow, and K. Busch. *Nanophotonic Materials - Photonic Crystals, Plasmonics, and Metamaterials.* Wiley-VCH, 2008.

[166] William H. Press, Saul A. Teukolsky, William T. Vetterling, and Brian P. Flannery. *Numerical Recipes – The Art of Scientific Computing (3rd Edition).* New York, USA: Cambridge University Press, 2007.

[167] Satio Takagi. „A Dynamical Theory of Diffraction for a Distorted Crystal“. In: *J. Phys. Soc. Jpn.* 26.5 (1969), pp. 1239–1253.

[168] O. Hölder. „Ueber einen Mittelwertsatz." In: *Gött. Nachr.* 1889 (1889), pp. 38–47.

[169] G. Strang. *Linear Algebra and Its Applications.* Thomson, Brooks/Cole, 2006.

[170] Antonis Gonis. *Green functions for ordered and disordered systems.* 1st. New York: Elsevier Science Publishers B.V., 1992.

[171] M. Frigo and S.G. Johnson. „The Design and Implementation of FFTW3". In: *Proc. IEEE* 93.2 (2005), pp. 216–231.

[172] G. Binnig, C. F. Quate, and Ch. Gerber. „Atomic Force Microscope". In: *Phys. Rev. Lett.* 56 (9 1986), pp. 930–933.

[173] Franz J. Giessibl. „Advances in atomic force microscopy". In: *Rev. Mod. Phys.* 75 (3 2003), pp. 949–983.

[174] Stéphane Cuenot, Christian Frétigny, Sophie Demoustier-Champagne, and Bernard Nysten. „Surface tension effect on the mechanical properties of nanomaterials measured by atomic force microscopy". In: *Phys. Rev. B* 69 (16 2004), p. 165410.

[175] Nader Jalili and Karthik Laxminarayana. „A review of atomic force microscopy imaging systems: application to molecular metrology and biological sciences". In: *Mechatronics* 14.8 (2004), pp. 907 –945.

[176] Ludwig Reimer. *Scanning electron microscopy: physics of image formation and microanalysis.* Ed. by P. W. Hawkes. 2nd. Vol. 45. Springer Series in Optical Sciences, 1998.

[177] Ludwig Reimer and Helmut Kohl. *Transmission Electron Microscopy.* 5th. Vol. 36. Springer Series in Optical Sciences, 2008.

[178] Gilles Renaud, Rémi Lazzari, and Frédéric Leroy. „Probing surface and interface morphology with Grazing Incidence Small Angle X-Ray Scattering". In: *Surf. Sci. Rep.* 64.8 (2009), pp. 255 –380.

[179] R.P. Millane. „Phase retrieval in crystallography and optics". In: *J. Opt. Soc. Am. A* 7.3 (1990), pp. 394–411.

[180] R. P. Millane. „Multidimensional phase problems". In: *J. Opt. Soc. Am. A* 13.4 (1996), pp. 725–734.

[181] J. H. Seldin and J. R. Fienup. „Numerical investigation of the uniqueness of phase retrieval". In: *J. Opt. Soc. Am. A* 7.3 (1990), pp. 412–427.

[182] R. H. T. Bates. „Fourier phase problems are uniquely solvable in more than one dimension". In: *Optik (Stuttgart)* 61 (1982), pp. 247–262.

[183] Jing-Feng Weng and Yu-Lung Lo. „Novel rotation algorithm for phase unwrapping applications". In: *Opt. Express* 20.15 (2012), pp. 16838–16860.

[184] A. A. Minkevich, M. Köhl, S. Escoubas, O. Thomas, and T. Baumbach. „Retrieval of the atomic displacements in the crystal from the coherent X-ray diffraction pattern". In: *Journal of Synchrotron Radiation* 21.4 (2014), pp. 774–783.

[185] Jose A. Rodriguez, Rui Xu, Chien-Chun Chen, Yunfei Zou, and Jianwei Miao. „Oversampling smoothness: an effective algorithm for phase retrieval of noisy diffraction intensities". In: *J. Appl. Crystallogr.* 46.2 (2013), pp. 312–318.

[186] Ana Diaz, Virginie Chamard, Cristian Mocuta, Rogerio Magalhães-Paniago, Julian Stangl, Dina Carbone, Till H Metzger, and Günther Bauer. „Imaging the displacement field within epitaxial nanostructures by coherent diffraction: a feasibility study". In: *New J. Phys.* 12.3 (2010), p. 035006.

[187] S. T. Haag, M.-I. Richard, S. Labat, M. Gailhanou, U. Welzel, E. J. Mittemeijer, and O. Thomas. „Anomalous coherent diffraction of core-shell nano-objects: a methodology for determination of composition and strain fields“. In: *Phys. Rev. B* 87 (3 2013), p. 035408.

[188] P. Godard, G. Carbone, M. Allain, F. Mastropietro, G. Chen, L. Capello, A. Diaz, T.H. Metzger, J. Stangl, and V. Chamard. „Three-dimensional high-resolution quantitative microscopy of extended crystals“. In: *Nat. Commun.* 2 (2011), p. 568.

[189] M. Dierolf, A. Menzel, P. Thibault, P. Schneider, C.M. Kewish, R. Wepf, O. Bunk, and F. Pfeiffer. „Ptychographic X-ray computed tomography at the nanoscale“. In: *Nature* 467 (2010), p. 436.

[190] Ian Robinson and Ross Harder. „Coherent X-ray diffraction imaging of strain at the nanoscale“. In: *Nat. Mater.* 8.4 (2009), pp. 291–298.

[191] Y. Nishino, Y. Takahashi, N. Imamoto, T. Ishikawa, and K. Maeshima. „Three-dimensional visualization of a human chromosome using coherent x-ray diffraction“. In: *Phys. Rev. Lett.* 102 (2009), p. 018101.

[192] C. G. Schroer, P. Boye, J. M. Feldkamp, J. Patommel, A. Schropp, A. Schwab, S. Stephan, M. Burghammer, S. Schöder, and C. Riekel. „Coherent x-ray Diffraction Imaging with Nanofocused Illumination“. In: *Phys. Rev. Lett.* 101.9, 090801 (2008), p. 090801.

[193] Jianwei Miao, Pambos Charalambous, Janos Kirz, and David Sayre. „Extending the methodology of X-ray crystallography to allow imaging of micrometre-sized non-crystalline specimens“. In: *Nature* 400.6742 (1999), pp. 342–344.

[194] Mark A. Pfeifer, Garth J. Williams, Ivan A. Vartanyants, Ross Harder, and Ian K. Robinson. „Three-dimensional mapping of a deformation field inside a nanocrystal“. In: *Nature* 442.7098 (2006), pp. 63–66.

[195] A. A. Minkevich, M. Gailhanou, J.-S. Micha, B. Charlet, V. Chamard, and O. Thomas. „Inversion of the diffraction pattern from an inhomogeneously strained crystal using an iterative algorithm“. In: *Phys. Rev. B* 76 (2007), p. 104106.

[196] A. A. Minkevich, E. Fohtung, T. Slobodskyy, M. Riotte, D. Grigoriev, T. Metzger, A. C. Irvine, V. Novák, V. Holý, and T. Baumbach. „Strain field in (Ga,Mn)As/GaAs periodic wires revealed by coherent X-ray diffraction“. In: *Europhys. Lett.* 94.6 (2011), p. 66001.

[197] A. A. Minkevich, E. Fohtung, T. Slobodskyy, M. Riotte, D. Grigoriev, M. Schmidbauer, A. C. Irvine, V. Novák, V. Holý, and T. Baumbach. „Selective coherent x-ray diffractive imaging of displacement fields in (Ga,Mn)As/GaAs periodic wires“. In: *Phys. Rev. B* 84 (2011), p. 054113.

[198] S. G. Podorov, K. M. Pavlov, and D. M. Paganin. „A non-iterative reconstruction method for direct and unambiguous coherent diffractive imaging“. In: *Opt. Express* 15.16 (2007), pp. 9954–9962.

[199] I. A. Vartanyants and I. K. Robinson. „Partial coherence effects on the imaging of small crystals using coherent x-ray diffraction“. In: *J. Phys.: Condens. Matter* 13 (2001), pp. 10593–10611.

[200] Y. Chushkin and F. Zontone. „Upsampling speckle patterns for coherent X-ray diffraction imaging“. In: *J. Appl. Crystallogr.* 46.2 (2013), pp. 319–323.

[201] J.R. Fienup. „Phase retrieval algorithms: a comparison“. In: *Appl. Opt.* 21.15 (1982), pp. 2758–2769.

[202] J.R. Fienup. „Reconstruction of a complex-valued object from the modulus of its Fourier transform using a support constraint“. In: *J. Opt. Soc. Am. A* 4.1 (1986), pp. 118–123.

[203] S. Marchesini. „A unified evaluation of iterative projection algorithms for phase retrieval“. In: *Rev. Sci. Instrum.* 78.1, 011301 (2007), p. 011301.

[204] Daniel E. Adams, Leigh S. Martin, Matthew D. Seaberg, Dennis F. Gardner, Henry C. Kapteyn, and Margaret M. Murnane. „A generalization for optimized phase retrieval algorithms“. In: *Opt. Express* 20.22 (2012), pp. 24778–24790.

[205] A. A. Minkevich, T. Baumbach, M. Gailhanou, and O. Thomas. „Applicability of an iterative inversion algorithm to the diffraction patterns from inhomogeneously strained crystals“. In: *Phys. Rev. B* 78 (2008), p. 174110.

[206] Russell Trahan and David Hyland. „Mitigating the effect of noise in the hybrid input-output method of phase retrieval“. In: *Appl. Opt.* 52.13 (2013), pp. 3031–3037.

[207] Stefano Marchesini. „Phase retrieval and saddle-point optimization“. In: *J. Opt. Soc. Am. A* 24.10 (2007), pp. 3289–3296.

[208] Aharon Levi and Henry Stark. „Image restoration by the method of generalized projections with application to restoration from magnitude“. In: *J. Opt. Soc. Am. A* 1.9 (1984), pp. 932–943.

[209] D. C. Youla and H. Webb. „Image restoration by the method of convex projections: part 1 - theory“. In: *IEEE Trans. Med. Imaging* 1.2 (1982), pp. 81–94.

[210] Heinz H. Bauschke, Patrick L. Combettes, and D. Russell Luke. „Phase retrieval, error reduction algorithm, and Fienup variants: a view from convex optimization“. In: *J. Opt. Soc. Am. A* 19.7 (2002), pp. 1334–1345.

[211] J. R. Fienup and C. C. Wackerman. „Phase-retrieval stagnation problems and solutions“. In: *J. Opt. Soc. Am. A* 3.11 (1986), pp. 1897–1907.

[212] Hiroaki Takajo, Tohru Takahashi, Ryuzo Ueda, and Makoto Taninaka. „Study on the convergence property of the hybrid input–output algorithm used for phase retrieval“. In: *J. Opt. Soc. Am. A* 15.11 (1998), pp. 2849–2861.

[213] Hiroaki Takajo, Tohru Takahashi, and Takao Shizuma. „Further study on the convergence property of the hybrid input–output algorithm used for phase retrieval“. In: *J. Opt. Soc. Am. A* 16.9 (1999), pp. 2163–2168.

[214] J. Miao, D. Sayre, and H. N. Chapman. „Phase retrieval from the magnitude of the Fourier transforms of nonperiodic objects“. In: *J. Opt. Soc. Am. A* 15.6 (1998), pp. 1662–1669.

[215] Florian Sutterlüti. „Reconstruction of the displacement field from inhomogeneously strained nanostructures from far-field scattering data: Properties of the (HIO-OR)+ER algorithm in 3 dimensions“. Bachelor thesis. Karlsruhe Institute of Technology, 2013.

[216] M. Eberlein, S. Escoubas, M. Gailhanou, O. Thomas, J.-S. Micha, P. Rohr, and R. Coppard. „Investigation by High Resolution X-ray Diffraction of the local strains induced in Si by periodic arrays of oxide filled trenches“. In: *Phys. Status Solidi A* 204.8 (2007), pp. 2542–2547.

[217] M. Eberlein, S. Escoubas, M. Gailhanou, O. Thomas, P. Rohr, and R. Coppard. „Influence of crystallographic orientation on local strains in silicon: a combined high-resolution X-ray diffraction and finite element modelling investigation“. In: *Thin Solid Films* 516.22 (2008), pp. 8042 –8048.

[218] T. Benabbas, Y. Androussi, and A. Lefebvre. „A finite-element study of strain fields in vertically aligned InAs islands in GaAs“. In: *J. Appl. Phys.* 86.4 (1999), pp. 1945–1950.

[219] M Hanke, D Grigoriev, M Schmidbauer, P Schäfer, R Köhler, U.W Pohl, R.L Sellin, D Bimberg, N.D Zakharov, and P Werner. „Diffuse X-ray scattering of InGaAs/GaAs quantum dots“. In: *Physica E* 21.2-4 (2004). Proceedings of the Eleventh International Conference on Modulated Semiconductor Structures, pp. 684 –688.

[220] M. Hanke, D. Grigoriev, M. Schmidbauer, P. Schäfer, R. Köhler, R. L. Sellin, U. W. Pohl, and D. Bimberg. „Vertical composition gradient in InGaAs/GaAs alloy quantum dots as revealed by high-resolution x-ray diffraction“. In: *Appl. Phys. Lett.* 85.15 (2004), p. 3062.

[221] G R Liu and S S Quek Jerry. „A finite element study of the stress and strain fields of InAs quantum dots embedded in GaAs“. In: *Semicond. Sci. Technol.* 17.6 (June 2002), pp. 630–643.

[222] M. Hanke, Yu. I. Mazur, Jr. E. Marega, Z. Y. AbuWaar, G. J. Salamo, P. Schäfer, and M. Schmidbauer. „Shape transformation during overgrowth of InGaAs/GaAs(001) quantum rings“. In: *Appl. Phys. Lett.* 91.4, 043103 (2007), p. 043103.

[223] H. She and B. Wang. „Finite element analysis of conical, dome and truncated InAs quantum dots with consideration of surface effects“. In: *Semicond. Sci. Technol.* 24 (2009), p. 025002.

[224] Veit Elser. „Phase retrieval by iterated projections“. In: *J. Opt. Soc. Am. A* 20.1 (2003), pp. 40–55.

[225] M. E. Peskin and D. V. Schroeder. *An Introduction to Quantum Field Theory.* Addison-Wesley Publishing Company, 1995.

[226] G. Czycholl. *Theoretische Festkörperphysik.* Berlin: Springer, 2007.

[227] G. J. Williams, M. A. Pfeifer, I. A. Vartanyants, and I. K. Robinson. „Internal structure in small Au crystals resolved by three-dimensional inversion of coherent x-ray diffraction“. In: *Phys. Rev. B* 73 (9 2006), p. 094112.

[228] Ross Harder, Meng Liang, and I. K. Robinson. *Investigation of complex objects through coherent x-ray diffraction in the Bragg geometry.* Presentation on the conference “Coherence”. 2007.

[229] Neculai Andrei. „Another nonlinear conjugate gradient algorithm for unconstrained optimization“. In: *Optimization Methods and Software* 24.1 (2009), pp. 89–104.

[230] Gonglin Yuan. „Modified nonlinear conjugate gradient methods with sufficient descent property for large-scale optimization problems“. In: *Optimization Letters* 3.1 (2009), pp. 11–21.